NASA TR R-131

NATIONAL AERONAUTICS AND SPACE ADMINISTRATION

TECHNICAL REPORT
R-131

FINAL REPORT
ON THE
TIROS I METEOROLOGICAL SATELLITE SYSTEM

By the Staffs
of
GODDARD SPACE FLIGHT CENTER
and
U.S. WEATHER BUREAU

1962

For sale by the Superintendent of Documents, U.S. Government Printing Office, Washington, D.C., 20402. Yearly subscription, $15: foreign, $19; single copy price varies according to size - - - - - - - - - Price $2.25

FINAL REPORT ON THE TIROS I METEOROLOGICAL SATELLITE SYSTEM

SUMMARY

The TIROS I Meteorological Satellite was designed to observe cloud cover over most of the earth by means of television techniques. The satellite instrumentation was remotely programmed from strategically located ground stations; the returned data were received and processed by these same stations.

TIROS I was launched on April 1, 1960, by a Thor-Able rocket from Cape Canaveral, Florida, into a near-circular orbit with an apogee of 465.9 statute miles and an inclination of 48.36 degrees to the equator. The satellite's spin axis was normal to the earth at 23.5 degrees north latitude. The Minitrack network tracked the satellite. The NASA Space Computing Center provided ephemeris information, and illumination and earth aspect data, which were converted to data-collection programs by the NASA TIROS Technical Control Center, Goddard Space Flight Center, and sent to the primary command stations for transmission to the satellite. Observed cloud information was received from the satellite, recorded, and transmitted to the agencies responsible for processing and evaluation.

The satellite traversed 1,302 orbits before the end of its three-month functional life, and returned slightly fewer than 23,000 pictures—over 60 percent of them having high meteorological information content. Technical difficulties reduced the number of pictures taken during its final month of operation, and were responsible for the decision not to continue operations beyond the initially scheduled life span. However, TIROS I has demonstrated the feasibility of observing the weather by satellite.

CONTENTS

PREFACE

The days following April 1, 1960, were historic for meteorology: the first full-scale meteorological satellite, TIROS I, was in orbit, being tried out, and sending to the ground stations television pictures of the cloud-cover of large areas of the earth. This report documents many aspects of the complex technological developments culminating in those historic days, many of the problems encountered in the operation of the complex satellite, and the results of the analyses of those first pictures of the earth obtained from a satellite.

The non-uniform distribution of incoming solar radiation and its re-radiation as reflected and thermal energy produces variations in the temperature of the atmosphere over the earth's surface. Weather is a result of the efforts of the atmosphere to adjust itself to these variations within the constraints of the laws of physics. The success of the present meteorological observation network of ground and radiosonde stations in the areas of both research and forecasting depends heavily on the density of stations. Many areas of the earth have no stations or so few that serious weather disturbances arise and move, undetected, toward inhabited regions until adequate forecasting occurs too late to be effective. In many instances even the relatively dense continental U.S. network of stations is not adequate, particularly when disturbances move in from oceanic or arctic areas where weather observations are not made. Because it can provide a truly global means of observing a global phenomenon, the satellite is an ideal tool for the meteorological exploration of the earth.

TIROS I was a first step; it brought under scrutiny the clouds, the visible manifestations of the thermodynamic processes of the atmosphere. It has provided a means of detecting and tracking air masses across the surface of the earth. But its measurements have been qualitative, not quantitative, and fundamental understanding of the global weather processes will have to await successful quantitative radiation studies.

To recognize and honor all those scientists and engineers who labored for and contributed to the success of TIROS I would require many columns of names. But these names are known to our colleagues in this adventure. Our appreciation and thanks go to all.

W. G. Stroud
Project Manager, TIROS I
Goddard Space Flight Center
National Aeronautics and Space Administration
Greenbelt, Maryland

April 1, 1961.

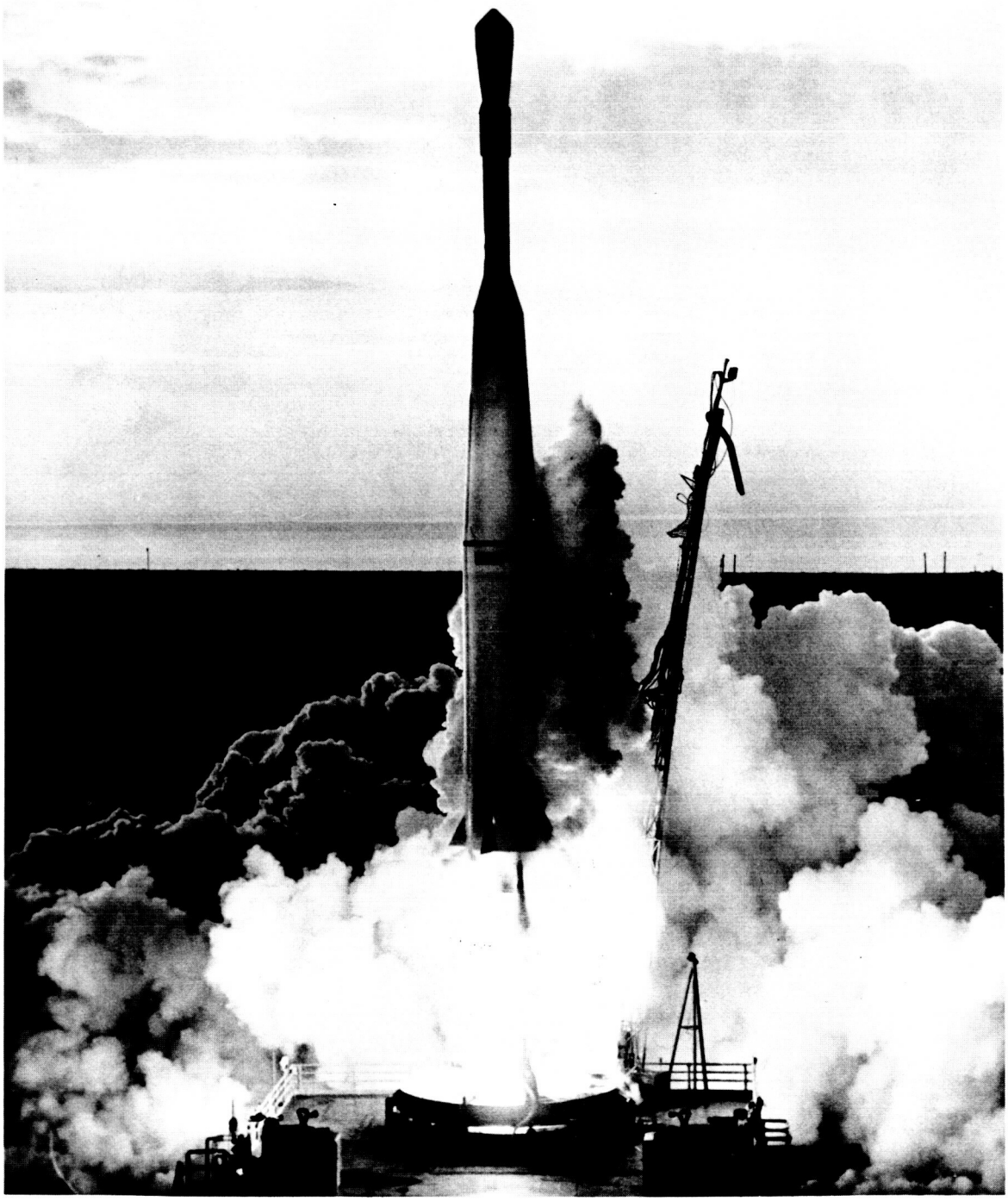

The launching of the TIROS I satellite by a Thor-Able rocket, April 1, 1960.

FINAL REPORT
ON THE
TIROS I METEOROLOGICAL SATELLITE SYSTEM

PART I

Edited by
Lewis J. Allison and Ernest A. Neil
Goddard Space Flight Center

CHAPTER 1

BACKGROUND OF THE TIROS PROGRAM

EARLY INVESTIGATIONS OF THE ATMOSPHERE

Man lives at the bottom of a vast "ocean" of air that covers the entire globe and extends upward with diminishing density.[1] It is an ocean in constant motion, its properties constantly changing. Early scientists soon recognized that particular atmospheric motions produced particular weather patterns, and so it became necessary to observe and describe the basic atmospheric motions. Early weather scientists used kites, manned balloons, and later the heavier-than-air flying machine to enlarge their knowledge of the atmopshere.[2]

Pascal of France was one of the first, if not the first, to attempt measurements of the atmosphere as a function of altitude. In 1643, Torricelli, a student of Galileo, invented the mercury-filled glass-tube barometer. Soon thereafter, Pascal carried one of these tubes up a mountainside and observed that the atmospheric pressure decreased as he climbed.

While mountaintop observatories began to explore the atmosphere at higher altitudes, the major step forward came when the instruments themselves could actually be carried aloft and beyond the influences of the ground surface.

The use of kites to lift thermometers was recorded as early as 1749 in Glasgow, 3 years earlier than Franklin's noted experiment with the kite, key, and thunderstorm. Kites had little practical importance, however, until Hargrove invented the powerful box kite in 1893. The large box kites were able to lift temperature and pressure recorders, called meteorographs, as high as 10,000 feet. At one time, the U.S. Weather Bureau maintained a series of kite stations for routine soundings.

Even prior to the box kite and free balloons of the 1890's the adventurous meteorologist could take to the free-balloon in the quest of scientific knowledge. After the first ascent of the Montgolfier balloon in 1783, the balloon was quickly put to use in lifting curious investigators into the previously unattainable atmosphere. In December 1783, J. A. C. Charles, the French physicist and discoverer of the gas law which bears his name, rode a hydrogen filled balloon to a height of 9,000 feet. He carried both a barometer and thermometer. Thus, he must be ranked as one of the first meteorological adventurers. The famous French chemist, Gay-Lussac, ventured to 23,000 feet in 1804 and made measurements of temperature, pressure, and electric field. He also took samples of the air in evacuated glass bulbs and so proved that the composition of the air did not change with altitude.

The suggestion to expand the scope of meteorological observations to include instrumental explorations of the atmosphere aloft by small unmanned balloon-borne instruments was first made in 1809. However, such a flight into the upper air did not take place until 1893 when a height of 16 kilometers or almost 53,000 feet, was reached. This was a start. A long series of frequent soundings into the upper air was begun in 1898, by Teisserenc de Bort at Trappes, France, which resulted in discovery of the stratosphere. The French observations showed that the atmosphere has at least two layers, distinguishable by the way the temperature changes with altitude. In the lower levels the temperature generally decreases with height. Above 30,000 or 40,000 feet, the temperature was found to no longer decrease with increasing altitude but to remain nearly constant.

Thus the concept of the atmosphere as not a single gaseous envelope surrounding the earth but a series of layers, each with its own characteristics, was established. The lower layer, the region of decreasing temperature, is called the troposphere; the layer above that, the stratosphere.

NOTE: Superior figures throughout the text of Part I identify references listed in Chapter 7.

These observations began a trend that still continues and probably will continue as long as man is curious about his atmosphere: new observations continue to reveal an atmosphere more complex than was previously suspected.

In the early 1900's kites and balloons were gradually supplanted by the airplane, which could carry the weather-sensing meteorograph to ten or fifteen thousand feet and then return quickly to its field. This eliminated the problem of recovering balloon-borne instruments that might be carried miles away. However, regular ascents into the stratosphere could not be made by the aircraft of 1920. Not until the advent of balloon-borne radio-transmitting meteorological instruments in 1927 was the stratosphere opened to regular observation. By the mid-1930's the radiosonde, as this instrument is now called, was supplying regular observations of upper-air conditions from stations around the world.

Radiosonde techniques have been continually improved until, in the recent IGY program, the average altitude of upper-air sounding balloons has been raised to 90,000 feet. This average has been exceeded often enough to permit meteorologists routinely to draw upper-air weather maps to altitudes of around 100,000 feet.

STATE OF THE ART OF METEOROLOGICAL DATA ACQUISITION

The first weather charts covered an area of only a few thousand square miles and were restricted to surface observations taken more or less simultaneously at prescribed times.[1] The more these charts were studied and used for forecasting weather, the larger was the area covered by observations and the stronger became the realization that knowledge of the interaction of atmospheric processes vertically and horizontally over hemispheric dimensions was required if meteorological motions and their time variations were to be fully understood. Out of this realization there developed the existing world radiosonde network covering many land areas, islands, and oceanic shipping routes. Each station in this network is an upper air-sounding station where the atmospheric pressure, temperature, and moisture are sampled vertically to about 100,000 feet twice, and at some places, four times daily. Recently, with the development and use of the sounding rocket, measurements are also being made from time to time of the upper 1 percent of the atmospheric mass beyond the reach of the radiosonde balloon.

The distribution of observing stations in the radiosonde network is such that only a very small portion of the atmosphere can be sounded by this conventional technique. The observing stations, by and large, are manned and consequently are located primarily in areas where year-round residence is feasible. Thus, large storms can reside undetected for days in many desert, polar and oceanic areas where there are very few stations, if any at all. The oceanic areas of the Southern Hemisphere are particularly devoid of upper air sounding stations. Yet, information from this region is highly desirable since by virtue of the global nature of the atmospheric flow, such information would be most helpful in explaining events in the Northern Hemisphere.

Even in the areas where there appears to be a more dense distribution of observing stations, the available information is often inadequate, particularly with regard to the existence and movement of smaller-scale storms. In these areas, storms of limited areal extent may develop and produce significant weather without being properly recognized by conventional techniques. The transient and often extremely violent storms may strike an unsuspecting locality with little possibility of timely warning.

RECENT EARTH-VIEWING EXPERIMENTS

EARTH OBSERVATION FROM ROCKETS

For many years prior to World War II, a small amount of work was carried on with high altitude rockets for upper atmosphere research; but with the advent of the war, most of it had to be discontinued. Shortly after VE-day, a number of German V–2 rockets were captured virtually intact. The U.S. Army proposed using these rockets for high altitude research programs and invited the U.S. Navy and various universities to participate. It appeared logical to install cameras for high altitude cloud photography, and the first V–2 rocket picture was taken and recovered on October 24, 1946.[3] Figure 1 shows an early composite rocket photograph taken by a V–2 at an altitude of 100 miles on March 7, 1947.[4, 5, 6] Little improvement in definition or altitude was obtained until the flight of the Viking 11 rocket on May 24,

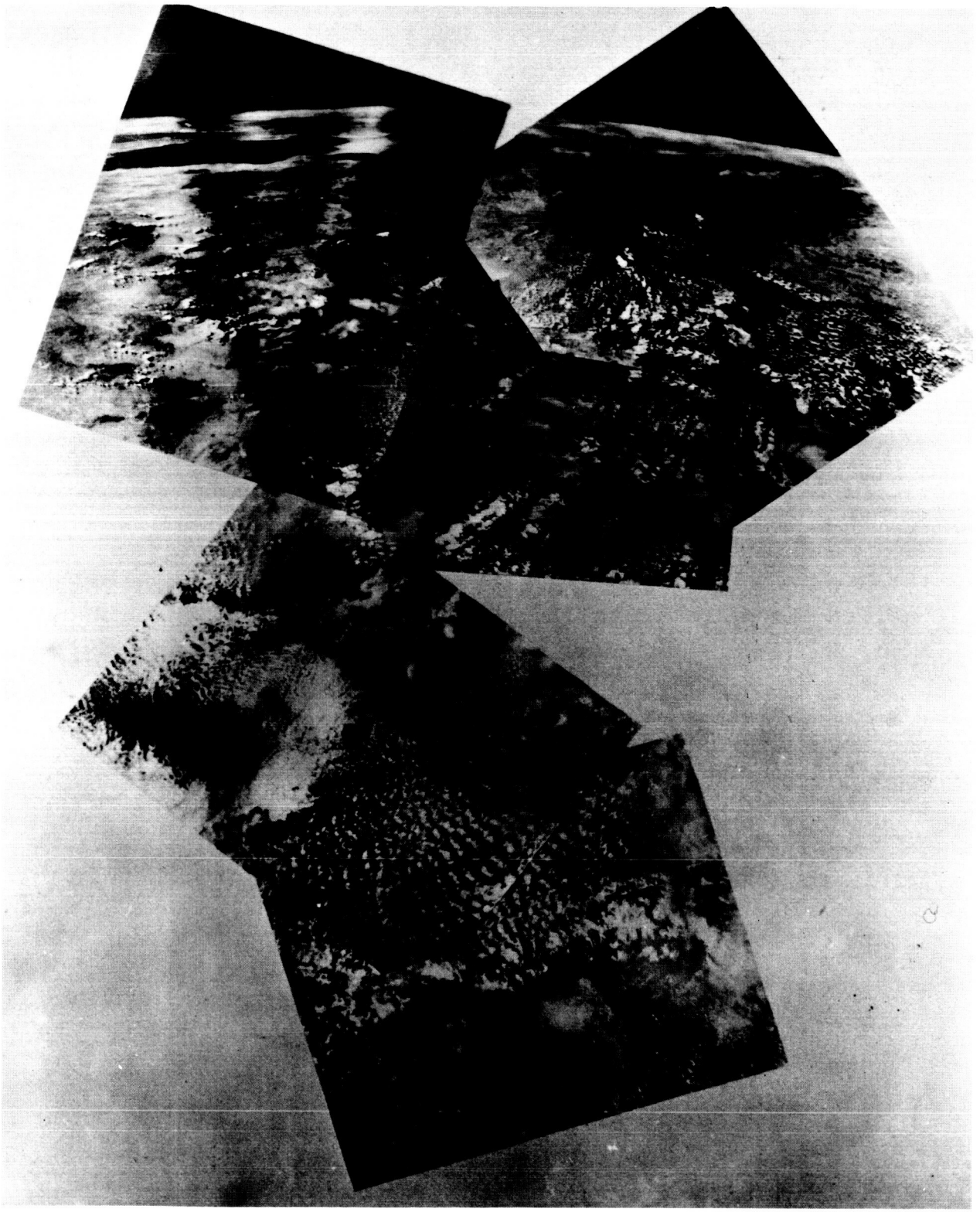

FIGURE 1.—Composite of photographs taken from a V–2 rocket, March 7, 1947.

1954.[7] Pictures from this and later Viking rockets* covered the altitudes from 64 miles on ascent through a peak of 158 miles to 33 miles on the descent. Good photographs of cloud cover, terrain formation, the atmospheric layer on the horizon, and the earth's curvature were obtained.[8] An area to the left of White Sands Proving Ground, New Mexico, is shown in Figure 2, a photograph from the Viking 12 rocket.

The first really fortunate attempt at high altitude cloud photography was made on October 5, 1954 at White Sands, New Mexico, by an Aerobee rocket equipped with two 16 mm motion picture cameras designed by the Naval Research Laboratory.[9] Figure 3 shows a mosiac picture of towering clouds spiraling out of a tropical storm near Del Rio, Texas, taken from this rocket.

During the next few years, cloud photographs were taken by motion picture cameras in the recoverable nose cones of a variety of research rockets. Excellent cloud pictures were made from a Nike-Cajun rocket at a peak altitude of 86 miles on December 5, 1958, during Project Hugo.[10, 11] On August 24, 1959, classic motion pictures were taken from the recoverable nose cone of an Atlas missile flying over the Atlantic Missile Range.[12, 13] A mosaic of several photographs taken at an altitude of 300 nautical miles (Figure 4) reveals the global sweep of the weather. For comparison, the U.S. Weather Bureau synoptic weather chart for

*Viking was a U.S. Navy rocket developed to replace the dwindling supply of V–2's.

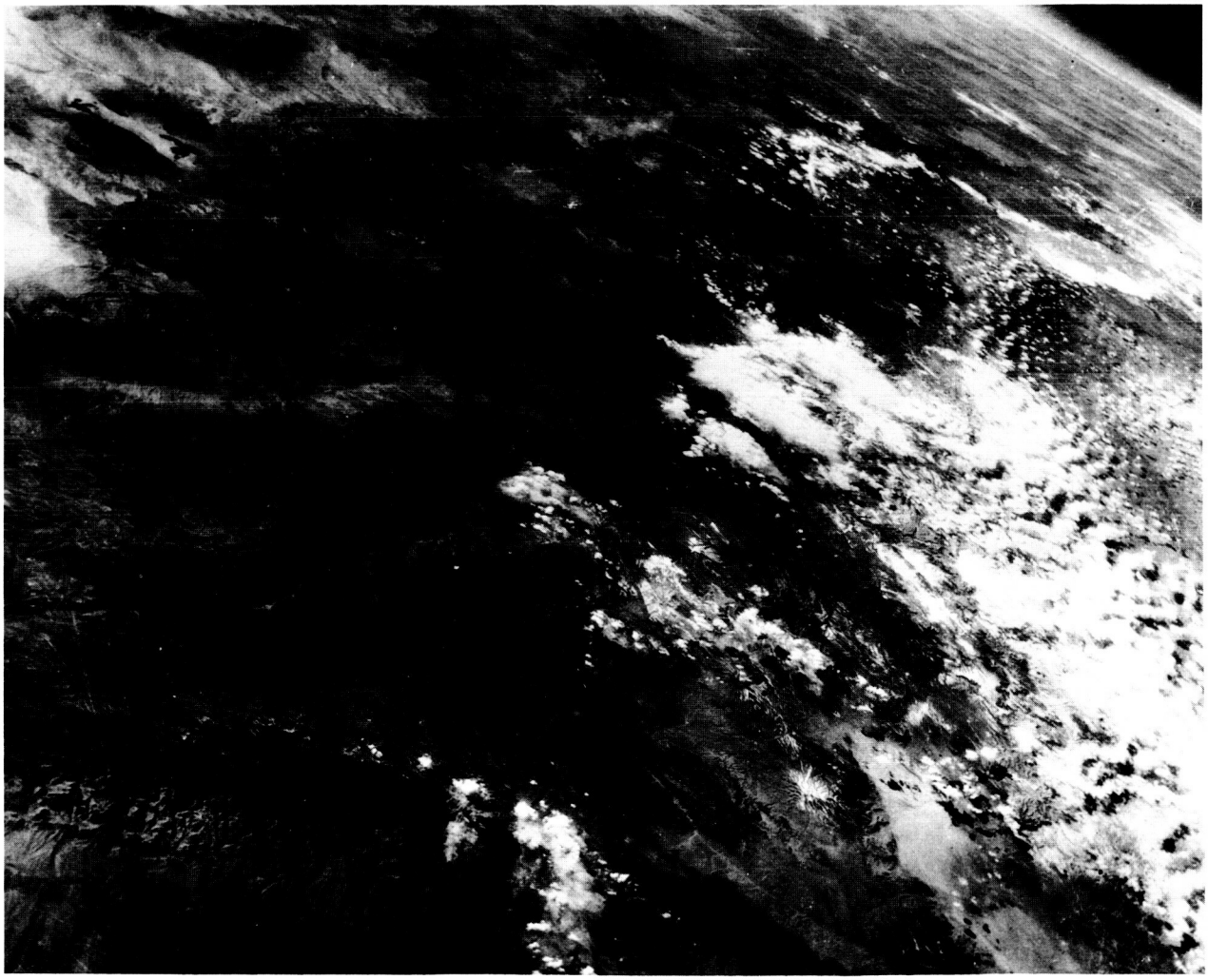

FIGURE 2.—Photograph taken from the Viking 12 rocket, February 4, 1955.

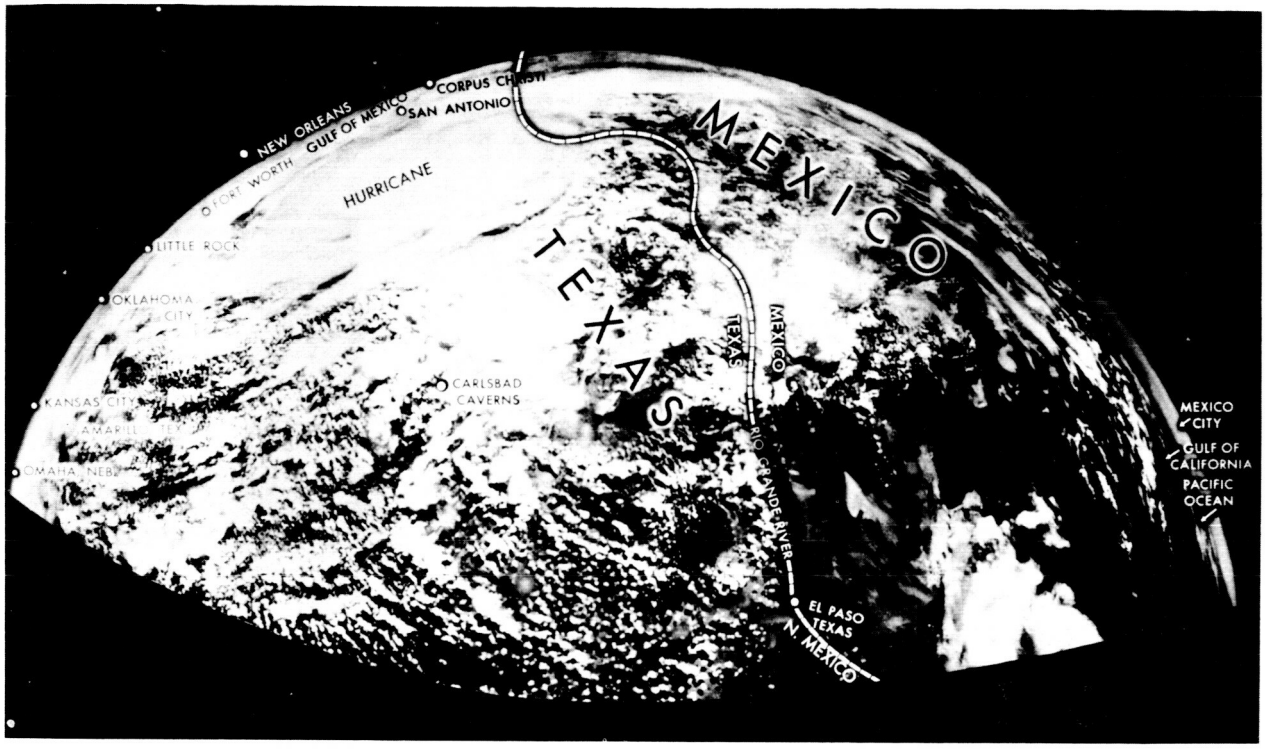

FIGURE 3.—Composite of photographs of a tropical storm taken from an Aerobee rocket, October 5, 1954.

this day is also shown in Figure 4.[14] More recently, NASA scientists fired camera-equipped Aerobee rockets from Fort Churchill, Canada.[15] Figure 5 was taken at an altitude of 140 miles, by two 70 mm Maurer Model 220 cameras, mounted 180 degrees apart. Details of cloud structure and the counterclockwise flow pattern around a low pressure system in the left center of the photograph are readily discernible with a stereo viewer.

EARTH OBSERVATIONS FROM SATELLITES

Although rocket photography provides a sampling of the potentialities of weather observations from space, greater continuity of observation is essential for operational weather analysis. The feasibility of weather observation from a satellite was discussed by S. M. Greenfield and W. W. Kellogg in 1951.[16] As early as 1954, Harry Wexler presented the idea of a satellite weather observatory equipped with infrared detectors, radars and television cameras,[17, 18] and S. F. Singer specified the requirements for meteorological measurements from a minimum satellite vehicle.[19, 20] An early attempt at image-sensing from an earth satellite was made in the Vanguard II cloud-cover experiment, devised by W. G. Stroud and his associates while at the U.S. Army Signal Research and Development Laboratories.[21-24] The Vanguard II satellite (1959 Alpha) was launched February 17, 1959. A simple form of image scanning, induced by the motion of the spinning satellite, was used. The satellite spin provided "line" scanning and the travel along the trajectory gave "frame" scanning, as shown in Figure 6. The optical sensor system utilized had an included angle of view of 1 degree, and was sensitive to radiation between the wavelengths of about 0.6 and 0.8 micron. The arrangement of the satellite instrumentation can be seen in Figures 7 and 8. Two sensors were utilized, pointing in opposite directions, with their optical axes 45 degrees from the satellite spin axis. As the spinning satellite moved in its orbit, one of the two sensors would always scan the earth's surface. With the proper spin rate and altitude, the individual scan strips would be contiguous. The output of the sensors was amplified and the information stored on a magnetic tape recorded for relay to the earth when the satellite was interrogated by a ground station.

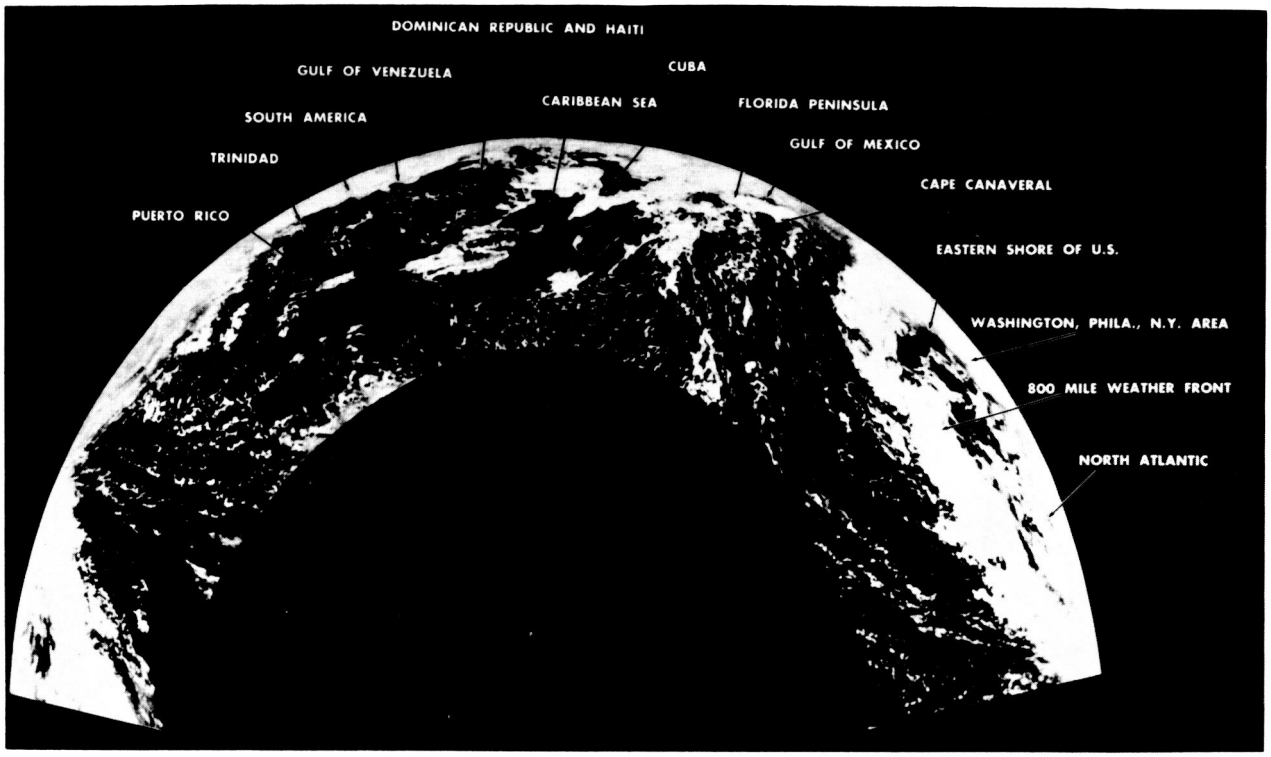

(a) Photo-mosaic of motion-picture frames taken from an Atlas rocket, August 24, 1959.

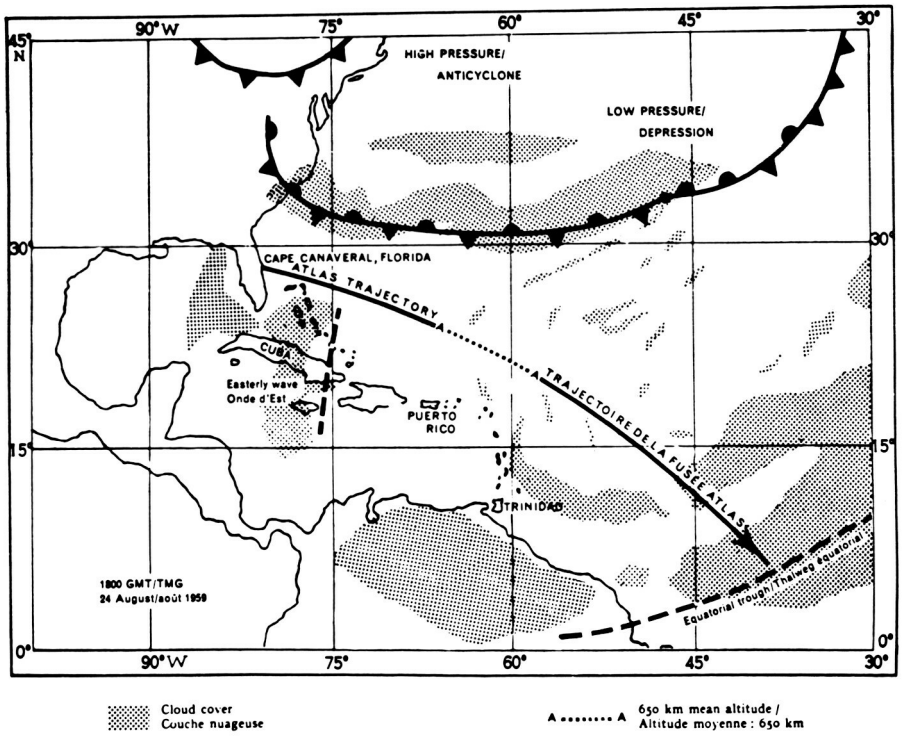

(b) Composite U.S. Weather Bureau frontal analysis for 1800 GMT, August 24, 1959, with cloud cover obtained from photographs taken from an Atlas rocket at 650 km.

FIGURE 4.

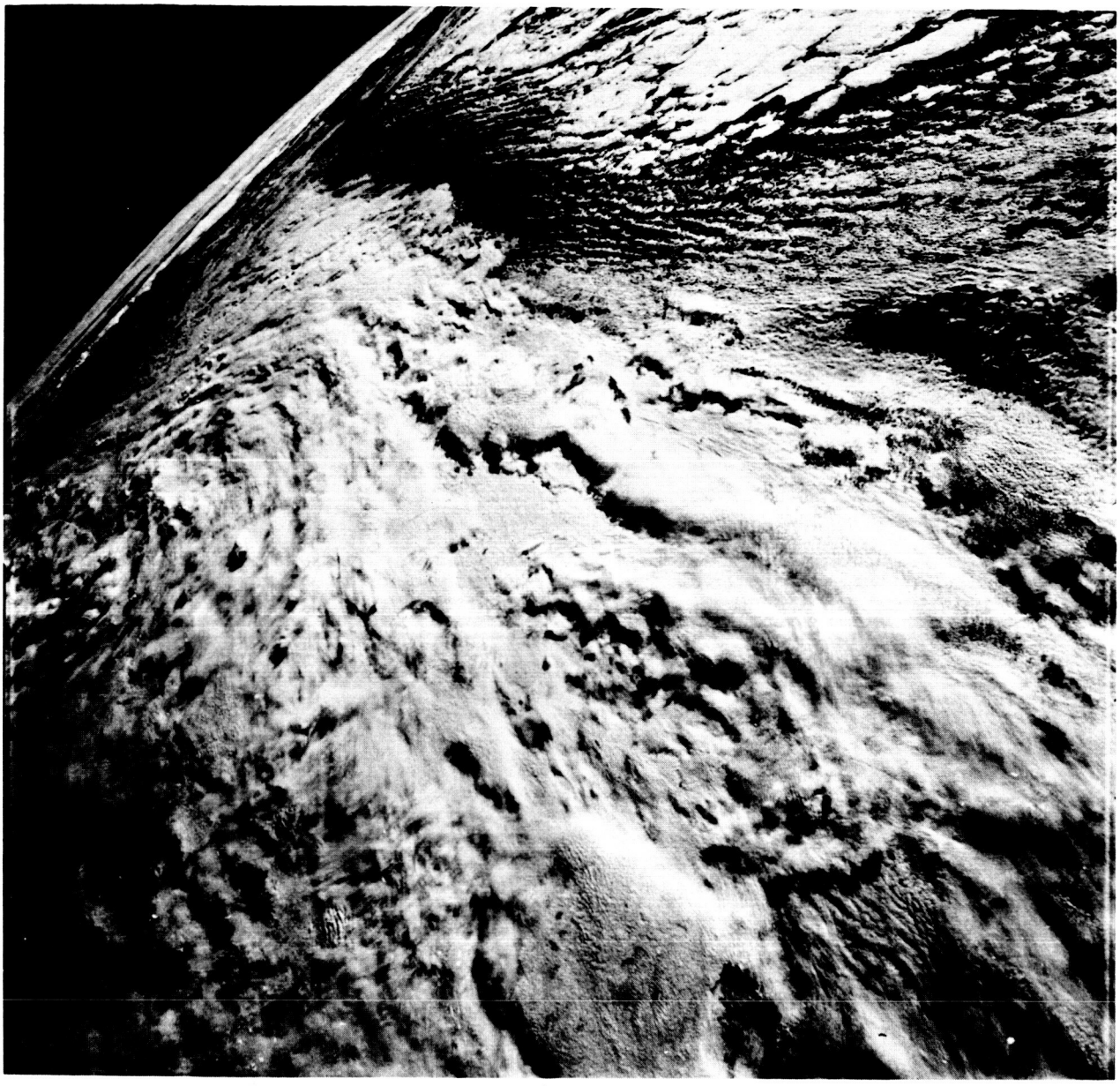

FIGURE 5.—Photograph taken from an Aerobee rocket at Fort Churchill, Canada, 1960.

For optimum results, this system required a nearly circular orbit and a stable spin axis. In the case of the Vanguard II experiment the orbit was quite elliptical, the spin axis had large perturbations, and the spin rate was considerably less than the design value. Therefore, even though the instruments worked perfectly, it has so far not been possible to reconstruct the data in the form of cloud photographs.

Pioneers I and II, which were launched in October and November 1958, were also equipped with low-speed "spot" scanning systems similar to that of the Vanguard II satellite.[25, 26] However, Pioneer I viewed the major portion of the earth while it was in darkness, and Pioneer II did not attain an orbit.

The basic television system designed for the Pioneer II satellite was modified and repackaged for the Explorer VI satellite (1959 Delta) launched on August 7, 1959.[27] This satellite returned TV data to earth, and some pictures were synthesized. A tip-down of the velocity vector,

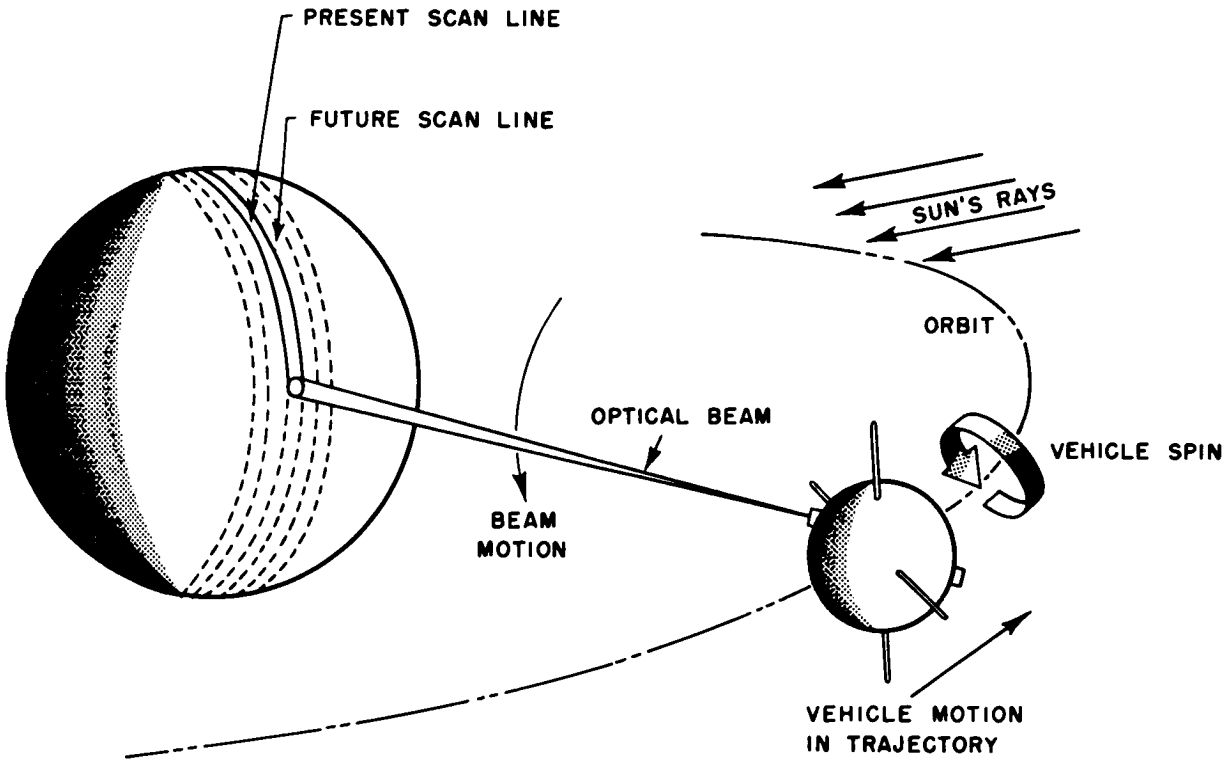

FIGURE 6.—Operation of the imaging system aboard the Vanguard II satellite.

combined with a malfunction in the TV circuit logic, resulted in considerable degradation of the intended picture resolution. A TV picture, and an analogous representation of the prevailing weather, are shown in Figure 9.

The Explorer VII satellite (1959 Iota 1) launched October 13, 1959, carried, among other instrumentation, equipment for measurements of the earth's radiation balance. This is part of an experiment, under the cognizance of Verner E. Suomi, to determine the influence of the thermal radiation budget on the earth's weather.[28–33]

Although it was not considered a weather satellite, Lunik III (1959 Theta), launched October 4, 1959, is worthy of mention here because of its picture-taking function. It succeeded in taking the first satellite pictures of the moon, with two camera systems employing, respectively, an f/5.6, 200 mm focal length lens and an f/9.5, 500 mm focal length lens. Electronic telemetry techniques were used to transmit the photographic data to the earth.[34]

During 1959, the imminence of television satellites to observe large-area cloud cover reawakened interest in nephanalysis as a diagnostic tool and as basic research data. In preparation for the handling of data from TIROS I (1960 Beta 2) and subsequent cloud-cover satellites, a Cloud Conference was held on December 14–15, 1959, at Washington, D.C., sponsored by the U.S. Weather Bureau, to discuss the current state of cloud research and the expected impact of satellite-observed data. A conference report was published in July 1960 by the Meteorological Satellite Laboratory of the U.S. Weather Bureau.[35]

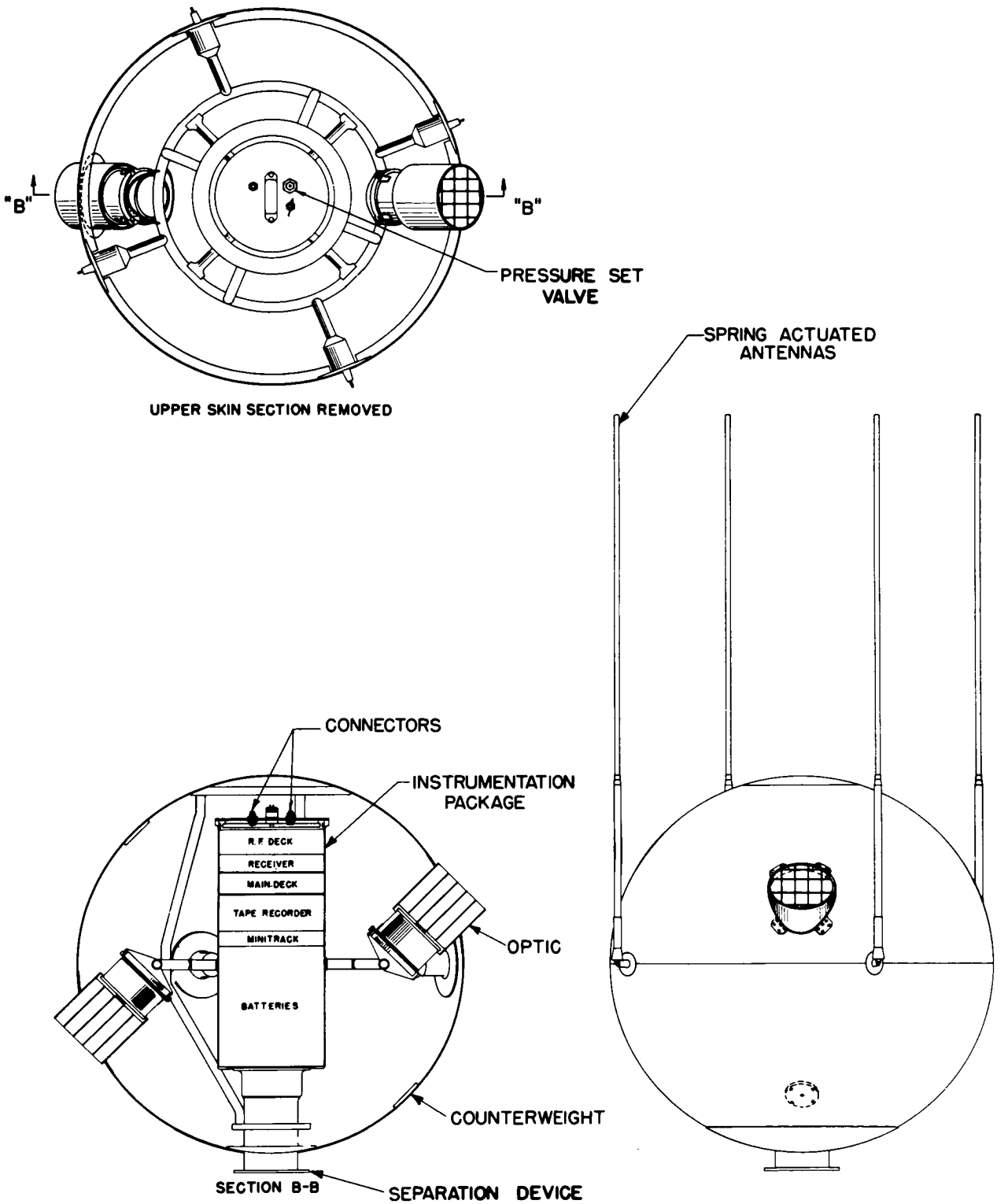

FIGURE 7.—Arrangement of components in the Vanguard II satellite, showing relation of sensors and their optics.

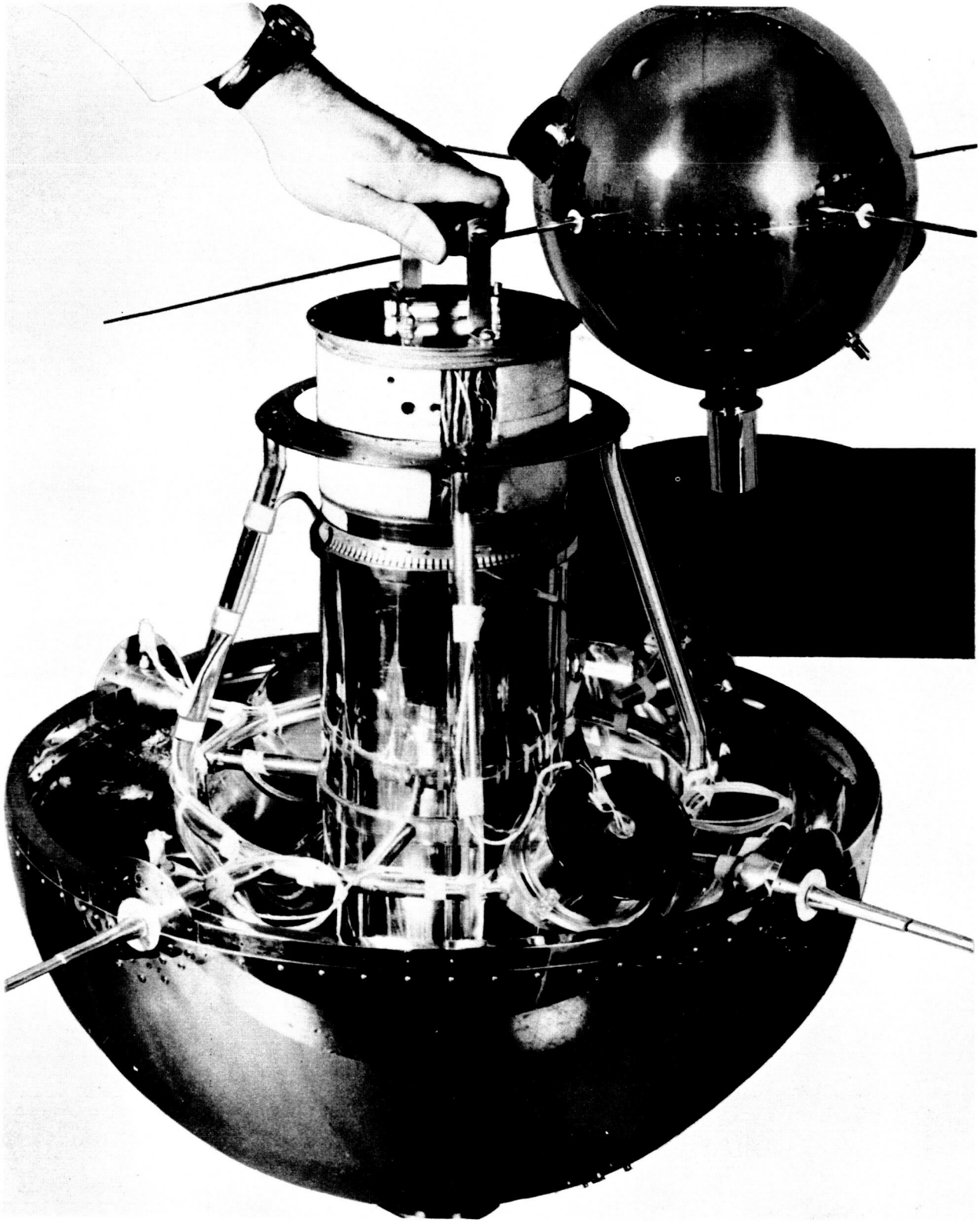

FIGURE 8.—Vanguard II satellite, showing internal components.

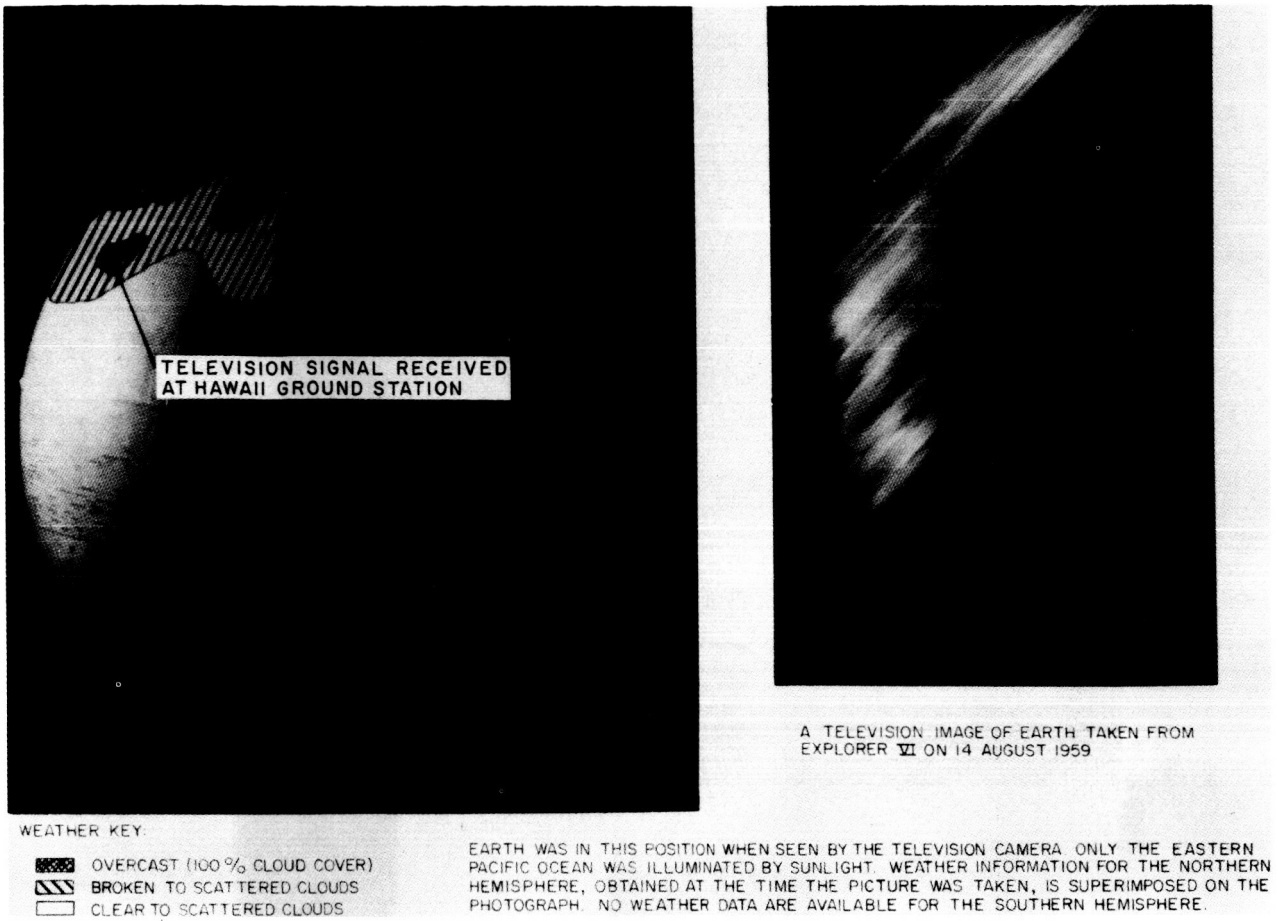

FIGURE 9.—**Photograph of the earth made by TV scanning techniques from the Explorer VI satellite.**

CHAPTER 2

DESIGN AND DEVELOPMENT OF THE TIROS SYSTEM

EVOLUTION OF THE TIROS I PROJECT

HISTORY OF PROJECT MANAGEMENT

A brief history of the TIROS I project will help to place in proper prospective the design considerations and the changes which took place.[36] This history was drastically shaped by a series of governmental management decisions. The significant element in the development was the growing awareness in the scientific and engineering communities of the possibility of having satellites and, in particular, of having satellites for meteorological uses. The early Rand Report by Greenfield & Kellogg, the early papers by Wexler, Stroud and Nordberg, and Glaser, all brought to the fore the possibilities of applying the satellite to the meteorologist's needs.

In the military services, of course, consideration of reconnaissance systems was quite active; and the U.S. Air Force, the Army Ballistic Missile Agency, and the Signal Corps all had under consideration satellites for reconnaissance and surveillance. In mid-1958, there was a major reorientation of mission responsibilities in the Defense Department, and Army interest was directed specifically to meteorological satellites. The Advanced Research Projects Agency (ARPA) established an Ad Hoc Committee on Meteorology chaired by W. W. Kellogg of the Rand Corporation and Mr. Roger Warner of ARPA. This committee—with participation from the Office of Naval Research, the Air Force Cambridge Research Center, the Air Research and Development Command, the U.S. Weather Bureau, the U.S. Army Signal Research & Development Laboratories, NASA, and the Astro-Electronics Division of the Radio Corporation of America, with appropriate scientific advisers—was responsible for the conceptual design of the TIROS meteorological satellite. The implementation of the design fell to the Astro-Electronics Division of RCA.

The launch vehicle, and therefore the satellite itself, went through several configuration changes but finally settled on the THOR-ABLE II configuration, thereby fixing the payload weight at around 280 pounds.

In April 1959, overall systems management of TIROS was transferred from the Department of Defense to NASA. NASA was responsible for directing the efforts of the Ballistic Missile Division of the Air Force, the U.S. Army Signal Research and Development Laboratories, its own Minitrack network and Space Computing Center, the Naval Photographic Interpretation Center, and the Meteorological Satellite Laboratory of U.S. Weather Bureau.

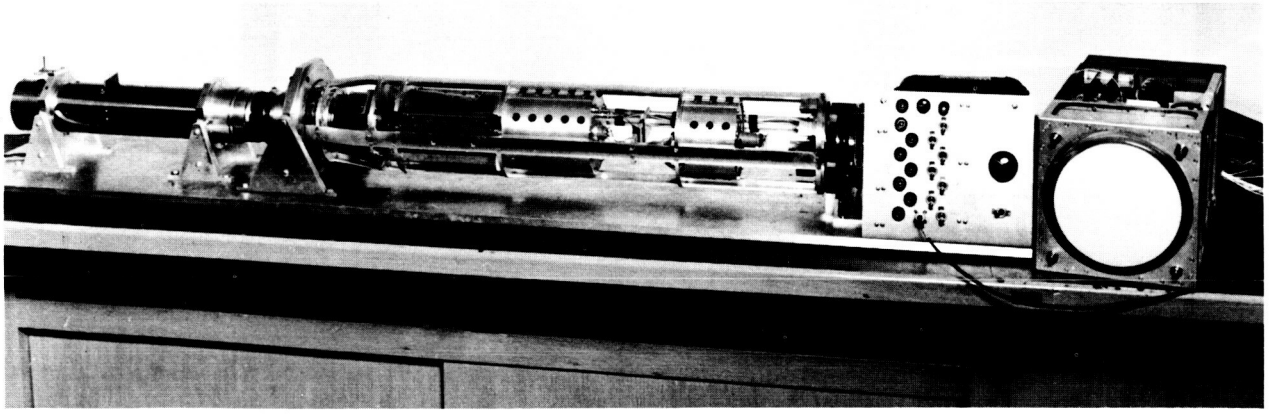

FIGURE 10.—Model of an early-feasibility satellite (Project Janus).

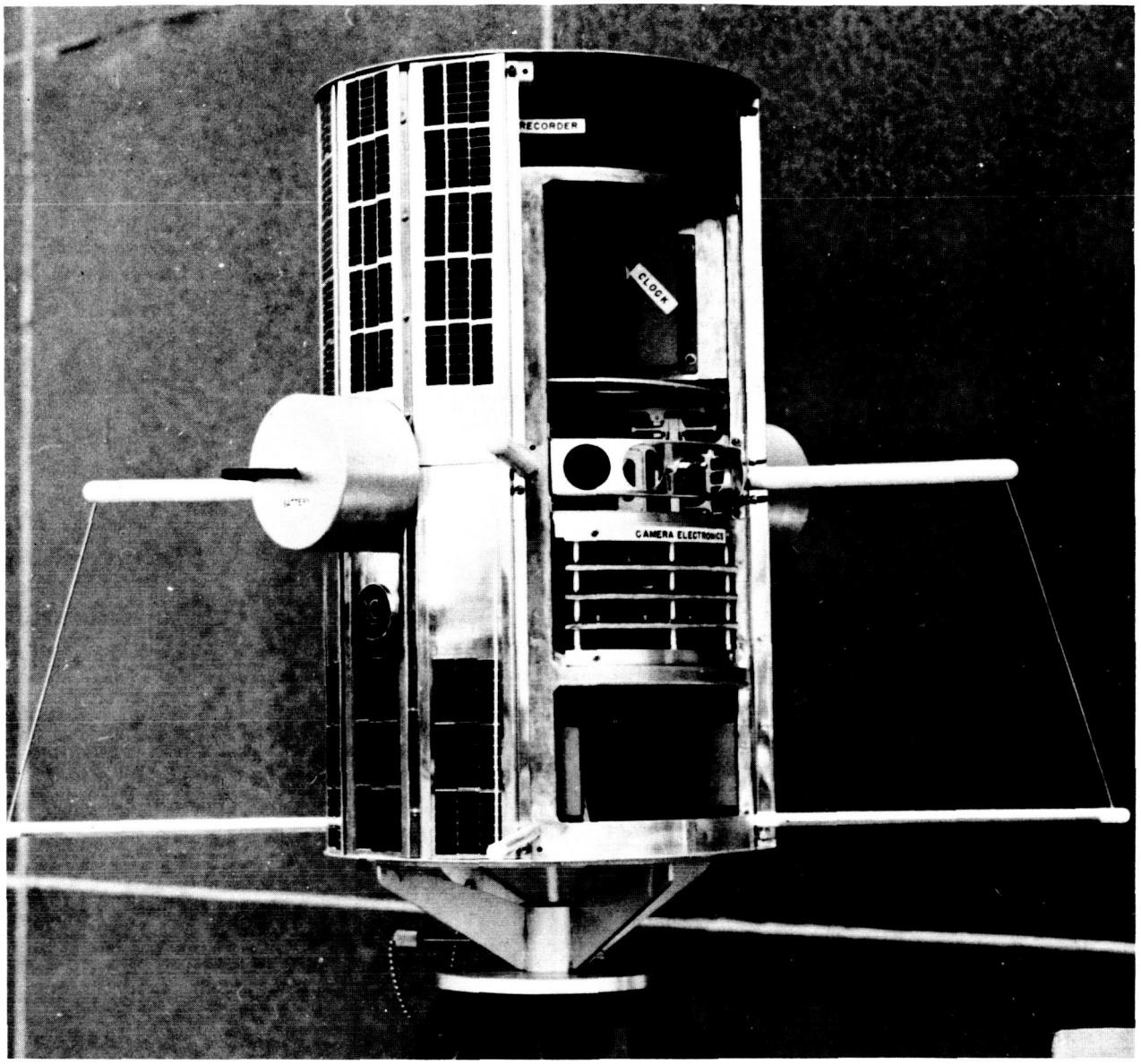

FIGURE 11.—Model of the Janus II satellite.

HISTORY OF TECHNICAL DEVELOPMENT

The changing management approach in the TIROS program caused a sequence of technical decisions both in the launch vehicle and the satellite itself. The satellite ranged from the 20-pound JUPITER C payload through the JUNO II configuration to the final payload capability of the THOR-ABLE II (Figures 10–12).

By the time of the shift of project responsibility to NASA, the payload had settled down to the two-television-camera system and a family of infrared radiation experiments designed and developed by a group of scientists and engineers of U.S. Army Signal Research and Development Laboratories (who later transferred to GSFC). This experiment was not included in the first TIROS launch because of schedule considerations.

THE TIROS I SATELLITE SYSTEM

SYSTEM CONCEPTS AND IMPLEMENTATION

The objectives for the TIROS I Satellite system were extended to the practical limitations imposed by technical, temporal, safety, and budgetary problems. The system was to include a

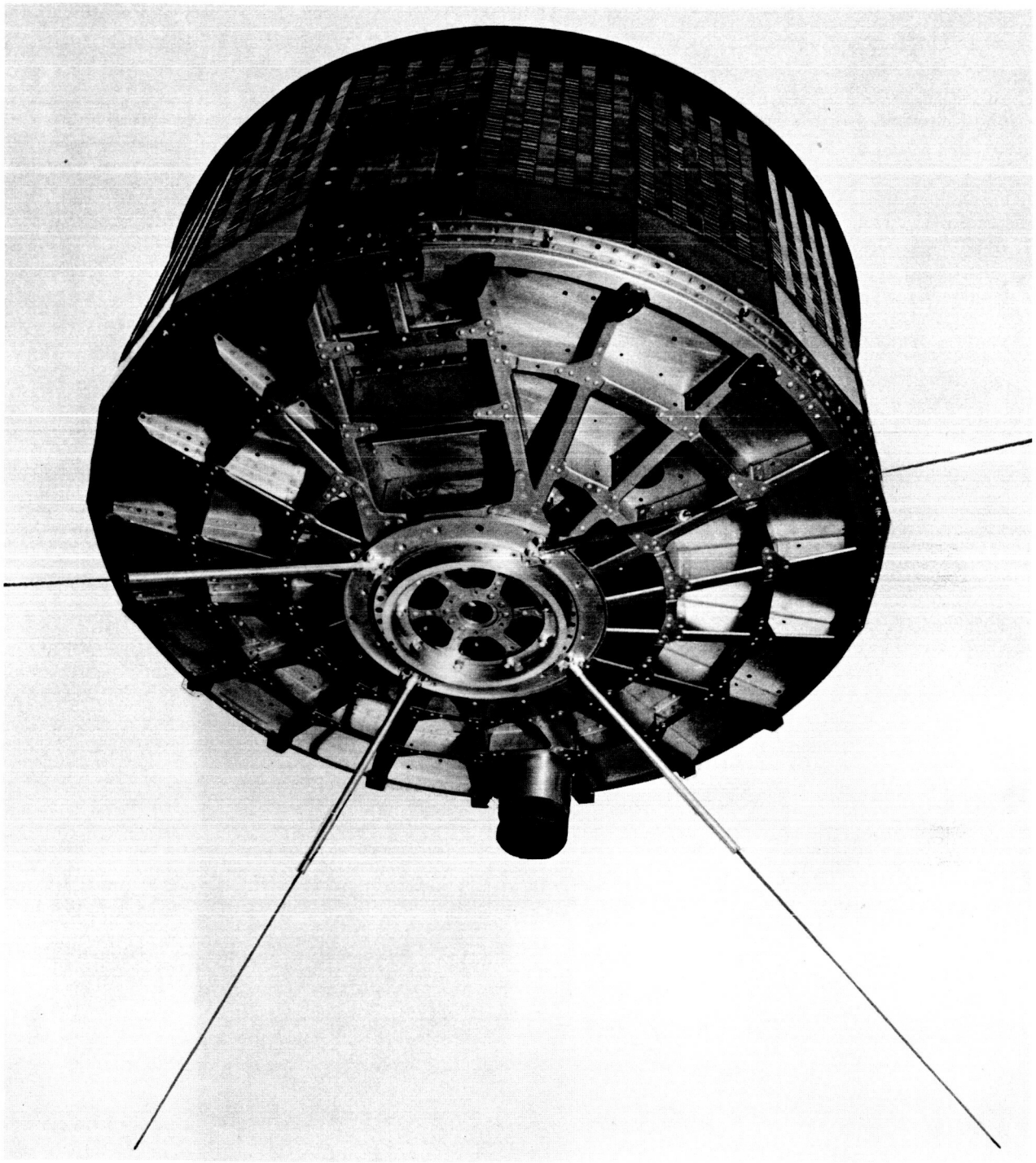

FIGURE 12.—The TIROS I satellite.

single, three-camera (later changed to two) satellite, and two ground stations capable of programming the satellite instrumentation and of receiving and processing the satellite-transmitted data. Although complete orbital coverage of the earth is possible only with polar orbits, missile-range firing restrictions were such that the best orbital inclination obtainable was in the neighborhood of 50 degrees. Also, although three ground stations would have permitted communications contact with the satellite during every orbit, two ground stations provided contact for all but three or four orbits a day, and were considered sufficient. State-of-the-art techniques were used to the greatest extent possible. However, space and weight limitations for the various payload components, imposed by the rocket capacity and the unique requirements encountered in adopting lower-atmosphere components for space use, engendered highly advanced state-of-the-art designs. An important consideration in component design was the specified life-span of the satellite. A 90-day operational life was specified for TIROS I.

Orbital characteristics.—Earth-seeking satellites were beyond the state of the art when the TIROS design was considered. Also, the vidicon-equipped television cameras required the illumination provided by sunlight to take satisfactory pictures. Consequently, TIROS was planned as a spin-stabilized satellite with its spin axis fixed in space. As it orbited around the earth, the cameras faced towards or away from the earth, depending upon the orbital position. The time of launch was selected such that the sun was "behind" the satellite (within 60 degrees of the optical axis), illuminating the earth while the cameras faced it. The

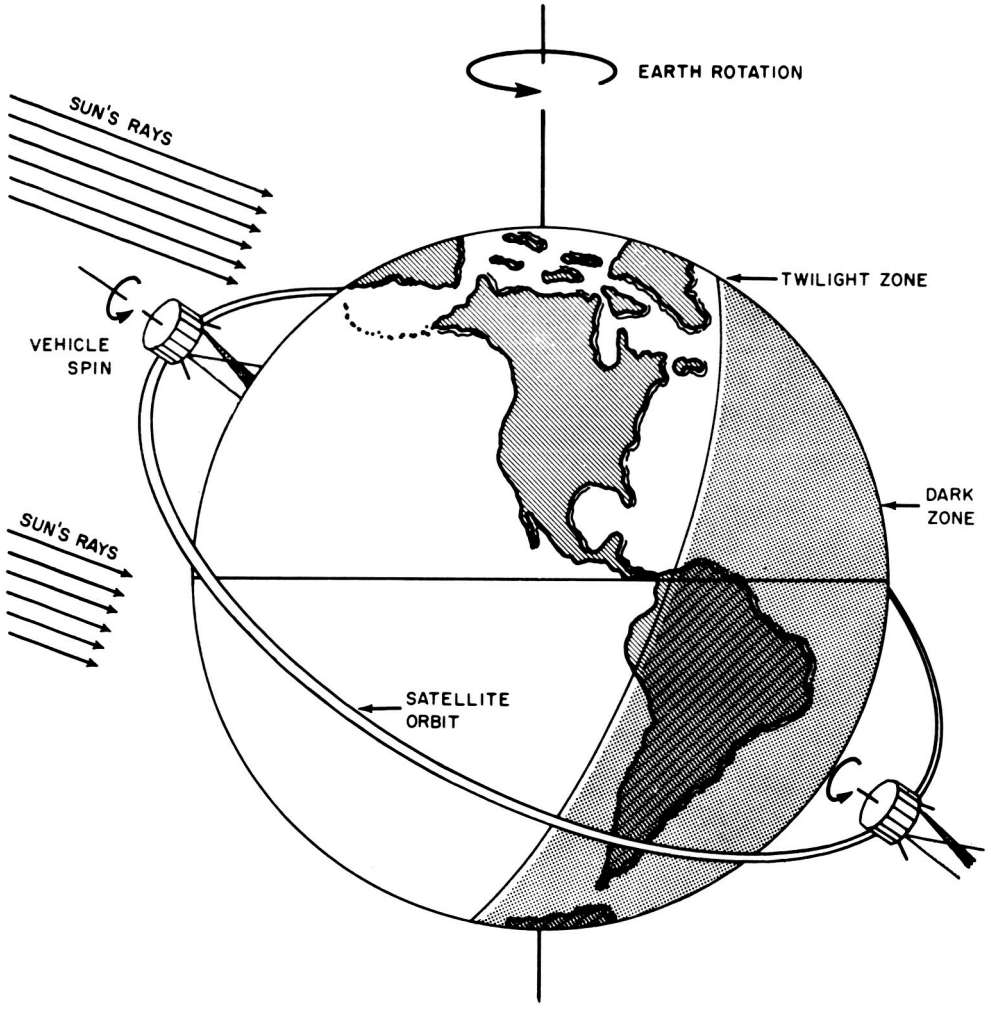

FIGURE 13.—Extreme positions of TIROS I with respect to the earth during the orbit.

extreme positions of TIROS I in an orbit are shown in Figure 13. TIROS I orbited from 50 degrees North latitude to 50 degrees South. As the earth precessed, all portions of this global belt were covered many times during the satellite's operational life. The change of photographic coverage from orbit to orbit is illustrated in Figure 14.

Although the operational life of TIROS I was limited to 90 days, the actual time the satellite would remain in orbit was estimated to be from 75 to 125 years. Atmospheric drag will eventually cause a satellite to spiral into the lower atmosphere and be destroyed. An early development of equations permitting a relatively accurate estimation of the lifetimes of satellites in a circular orbit was published by Henry [37] in 1957; and confirmed by Newton [38] in 1958.

Picture-taking criteria.—The television (picture-taking and transmission) design concepts were based largely on a study by Arnold Glaser,[39] who initiated guidelines for acceptable optical parameters for cloud pictures. Other studies, based on the planned orbital characteristics for TIROS I, determined the maximum number of pictures that could be taken oven the sunlit portion of the orbit. Practical considerations (e.g., the desirability of constructing mosaics) dictated a 50 percent overlap for the wide-angle pictures (see Figure 15).

The usefulness of the television camera can be best measured in terms of the dimensions in the

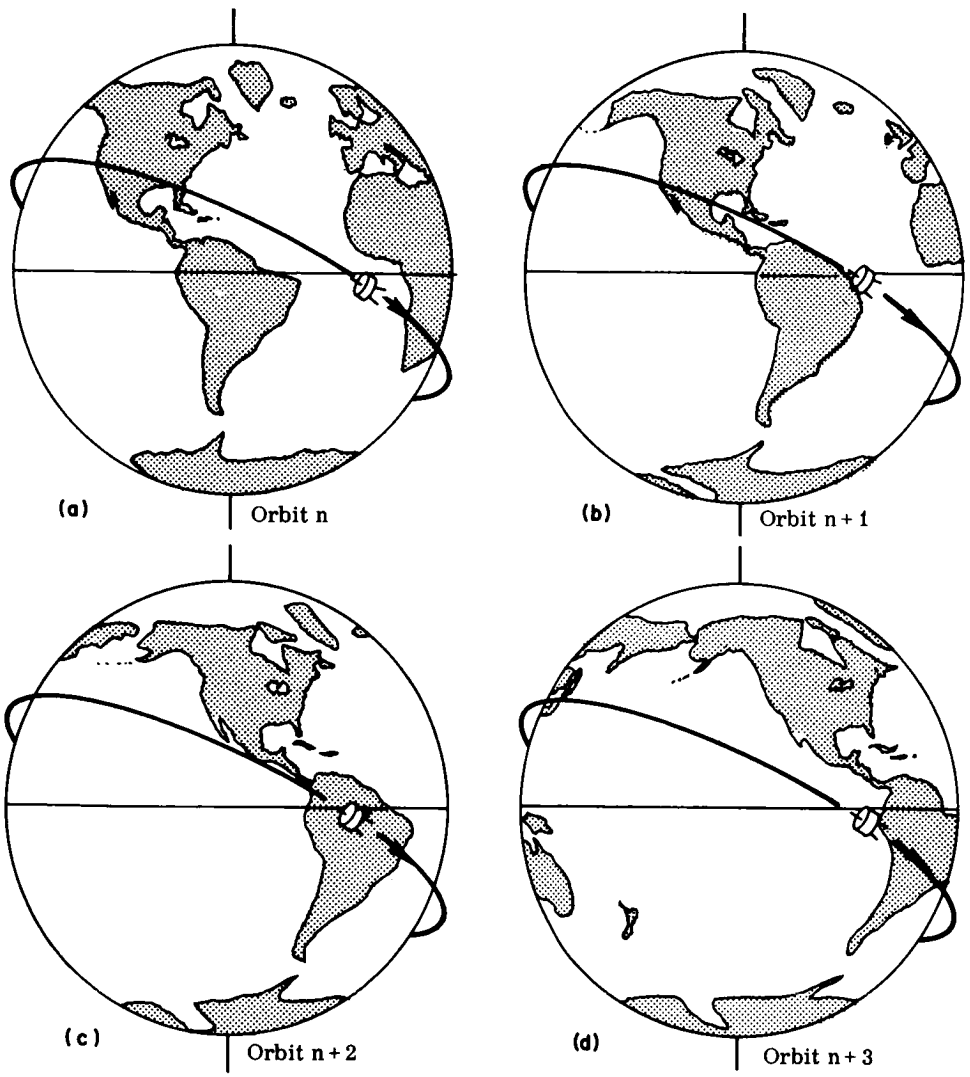

FIGURE 14.—Progression of photographic coverage due to the earth's precession.

scene it is capable of resolving, and in the minimum illumination required for an exposure.[40] The scene detail is established as a factor indicating the best resolution of the photosensor and the selected focal length of the optical system. The half-inch vidicon has a resolution of 35 optical lines per millimeter on axis. The relationship which will yield scene resolution is expressed by the equation

$$G_r = \frac{S}{300} R,$$

where G_r is the desired ground (or scene) resolution, S is the scale factor (equal to the ratio of altitude to focal length) and R is the sensor resolution in optical lines per meter.*

*One optical line is equivalent to two TV lines.

With reference to the minimum required scene brightness, typical vidicon operation will permit the following operating conditions: with 0.03 ft-candle-sec impinging on the photoconductor through the lens, an image bright enough to produce a good picture on the television screen will result with an effective lens aperture ratio of f/2 and a 1-millisecond exposure. A scene illuminance of 480 foot-lamberts will be required. (Special vidicons capable of responding to 0.01 ft-candle-sec have been built.) Photography is then limited to the time when the position of the satellite with respect to the sun and the scene is favorable, so that this minimum value is exceeded. Future payload capacity will permit the use of the image orthicon and other television sensors

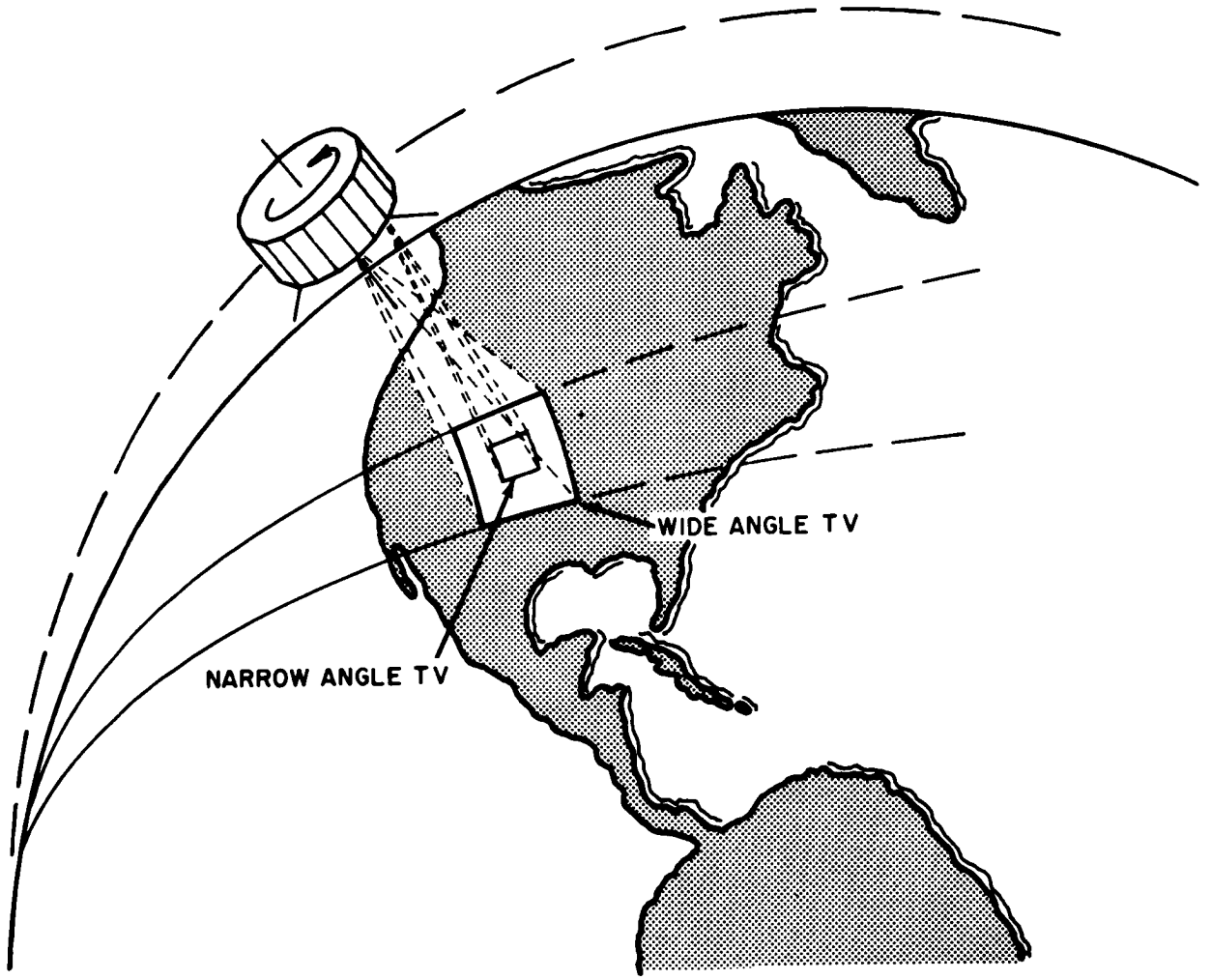

FIGURE 15.—Relative coverage of the two TIROS I cameras.

which possess several thousand times the sensitivity of the vidicon.

Also to be considered is how much of the earth is seen at various viewing angles off-vertical (i.e., when the satellite's optical axis is not pointed directly at the subpoint on the earth). Approximation formulas have been developed which yield direct solutions for the slant range S, and the distance along the ground, W, from the subpoint.[41] Referring to Figure 16, the exact solutions for S and W are:

$$S=[h+R(1-\cos\theta)]\sec\phi,$$

$$W=R\theta\ (\theta \text{ in radians}),$$

$$\theta=\sin^{-1}\left[\frac{R+h}{R}\sin\phi\right]-\phi$$

$$\theta<90°.$$

However, a good approximation is

$$S=\left[h+\frac{1}{2}\frac{h^2}{R}\tan^2\phi\right]\sec\phi,$$

$$W=[(S\sin\phi)^2+(S\cos\phi-h)^2]^{1/2};$$

and the flat-earth approximation is

$$S=h\sec\phi,$$

$$W=h\tan\phi.$$

Table 1 gives the values of S and W for satellite altitudes ranging from 100 to 10,000 miles for three values of ϕ: 30 degrees, 45 degrees, and 60 degrees. Values were computed for each method given above.

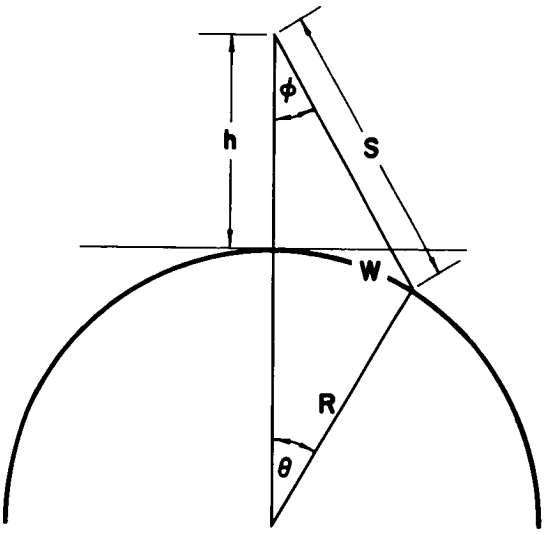

FIGURE 16.—Geometry of earth coverage from an observation satellite.

THE SATELLITE

Design of the satellite.—The TIROS satellite shown in Figure 17, is an 18-sided right polyhedron about 42 inches in diameter and 22.5 inches

TABLE 1.—VALUES OF SLANT RANGE S AND GROUND DISTANCE W (FROM THE SUBPOINT) FOR VARIOUS SATELLITE ALTITUDES AND VIEWING ANGLES

h (statute miles)	ϕ (deg)	Distances (statute miles)					
		Based on Exact Formula		Based on Approximate Formula		Based on Flat Earth Approximation	
		S	W	S	W	S	W
100	30	116.0	58.0	116.0	58.0	115.5	57.7
	45	143.2	101.2	143.2	101.2	141.4	100.0
	60	208.2	180.4	207.5	179.7	200.0	173.2
200	30	232.9	116.4	232.9	116.4	230.9	115.5
	45	290.3	205.2	289.9	205.1	282.8	200.0
	60	435.8	378.2	430.0	372.7	400.0	346.4
300	30	350.8	175.7	350.7	175.4	346.4	173.2
	45	441.6	312.4	440.2	311.5	424.3	300.0
	60	689.6	599.2	667.5	579.1	600.0	519.6
500	30	590.0	295.5	589.4	294.9	577.4	288.7
45	45	758.1	537.6	751.3	532.2	707.1	500.0
	60	1,348.9	1,185.7	1,187.5	1,032.7	1,000.0	866.1
1,000	30	1,208.2	606.5	1,203.3	603.1	1,154.7	577.4
	45	1,668.7	1,198.1	1,592.8	1,133.4	1,414.2	1,000.0
2,000	The maximum value of ϕ possible is 53 deg, at which $W=2558$ miles.						
5,000	The maximum value of ϕ possible is 41.6 deg, at which $W=3342$ miles.						
10,000	The maximum value of ϕ possible is 26.2 deg, at which $W=4410$ miles.						
	The maximum value of ϕ possible is 16.5 deg, at which $W=5075$ miles.						

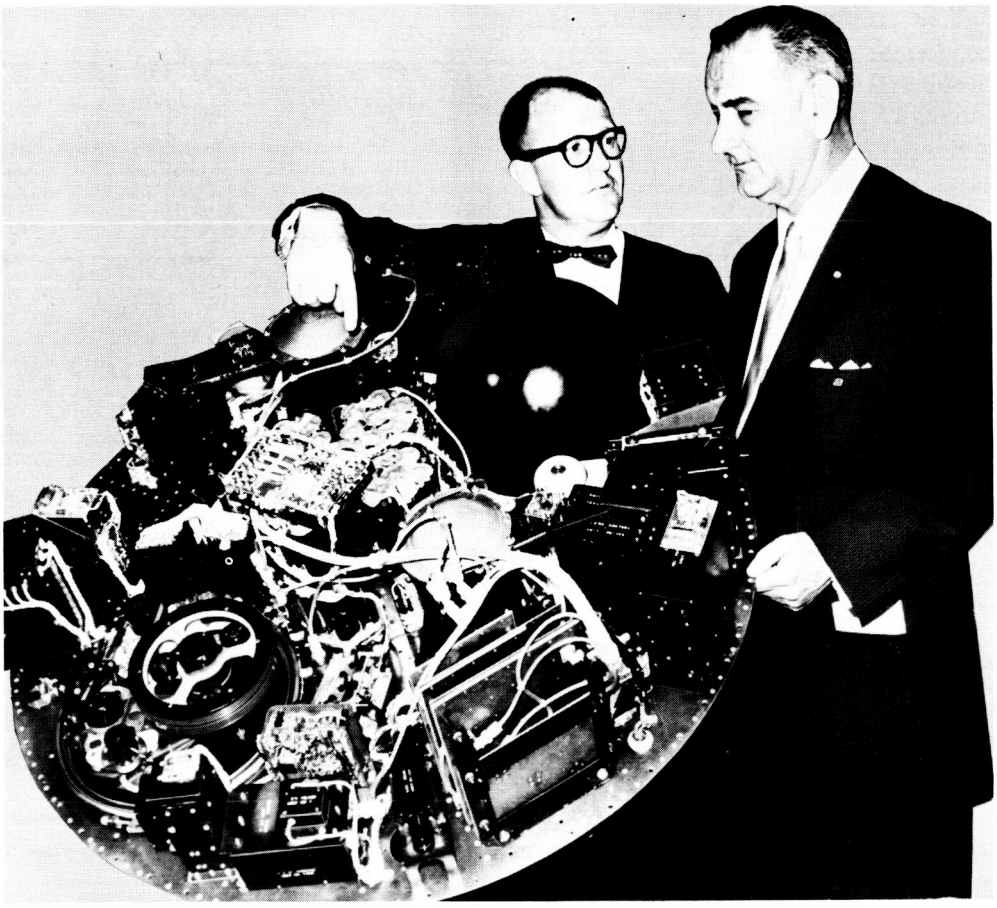

(a) Internal top view.

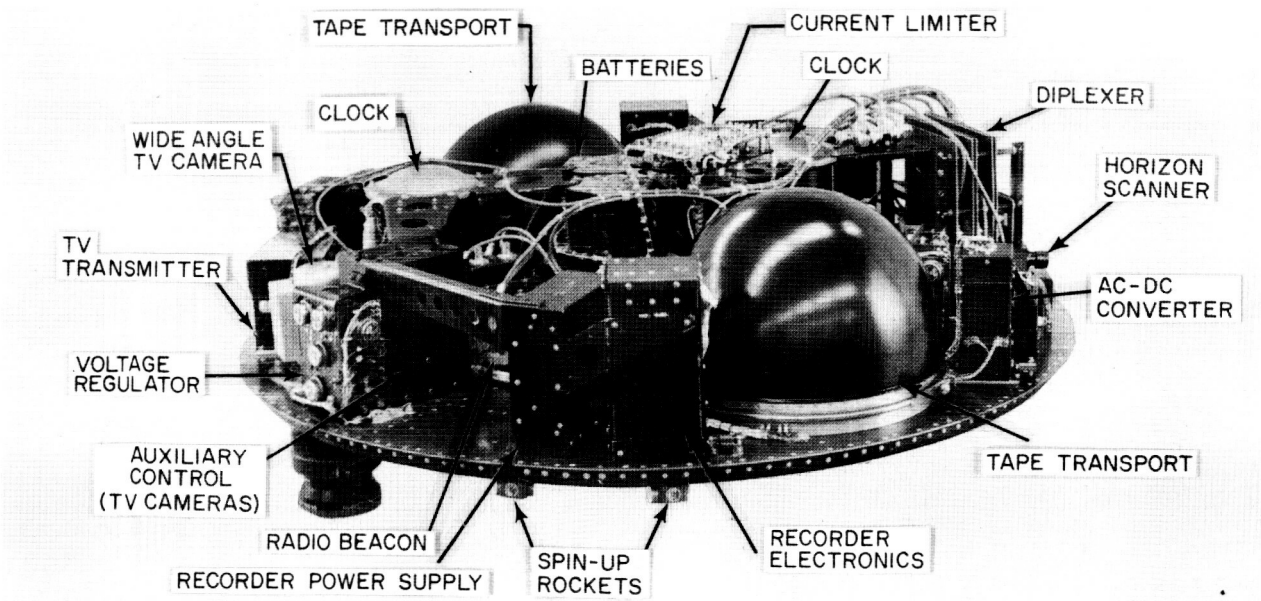

(b) Detailed internal view.

FIGURE 17.—The TIROS I satellite.

high with a design weight limit of 270 lbs.[42] Four elements of the transmitting antenna project from the bottom, and the single receiving antenna element projects from the top. The top and sides are covered with 9,260 solar cells which form the primary electrical power source. The TV cameras look down from the baseplate. The equipment contained in the satellite may be broadly considered (separately, or in conjunction with complementary ground station components) as a series of independent but coordinated subsystems, which will be discussed separately below.

TV picture subsystem.—The TV picture subsystem consists of the wide-angle and narrow-angle camera chains which are identical, except for the camera optics, and completely independent of each other. Two distinct modes of operation are available for each chain: *direct* mode to operate within line-of-sight range of the ground station, and *remote* mode to store pictures on the magnetic tapes for playback during interrogation by the ground station. An FM–FM system is used to transmit the picture information to the ground station. Each chain consists of a camera, magnetic tape recorder, record and playback amplifiers, transmitter, and the associated control circuitry for each. Diagrams of the TV picture subsystem are shown in Figure 18.

The RCA-developed TV cameras use a specially-constructed, ruggedized ½-inch vidicon. A diagrammatic representation of the vidicon is shown in Figure 19. Inscribed on the vidicon are "center" cross hairs and picture-corner reference marks. A solenoid-operated, focal plane shutter is used to expose the vidicon. The video information passes through a transistorized amplifier to bring it up to a useful level. The wide-angle camera with its associated electronic package[40] is shown

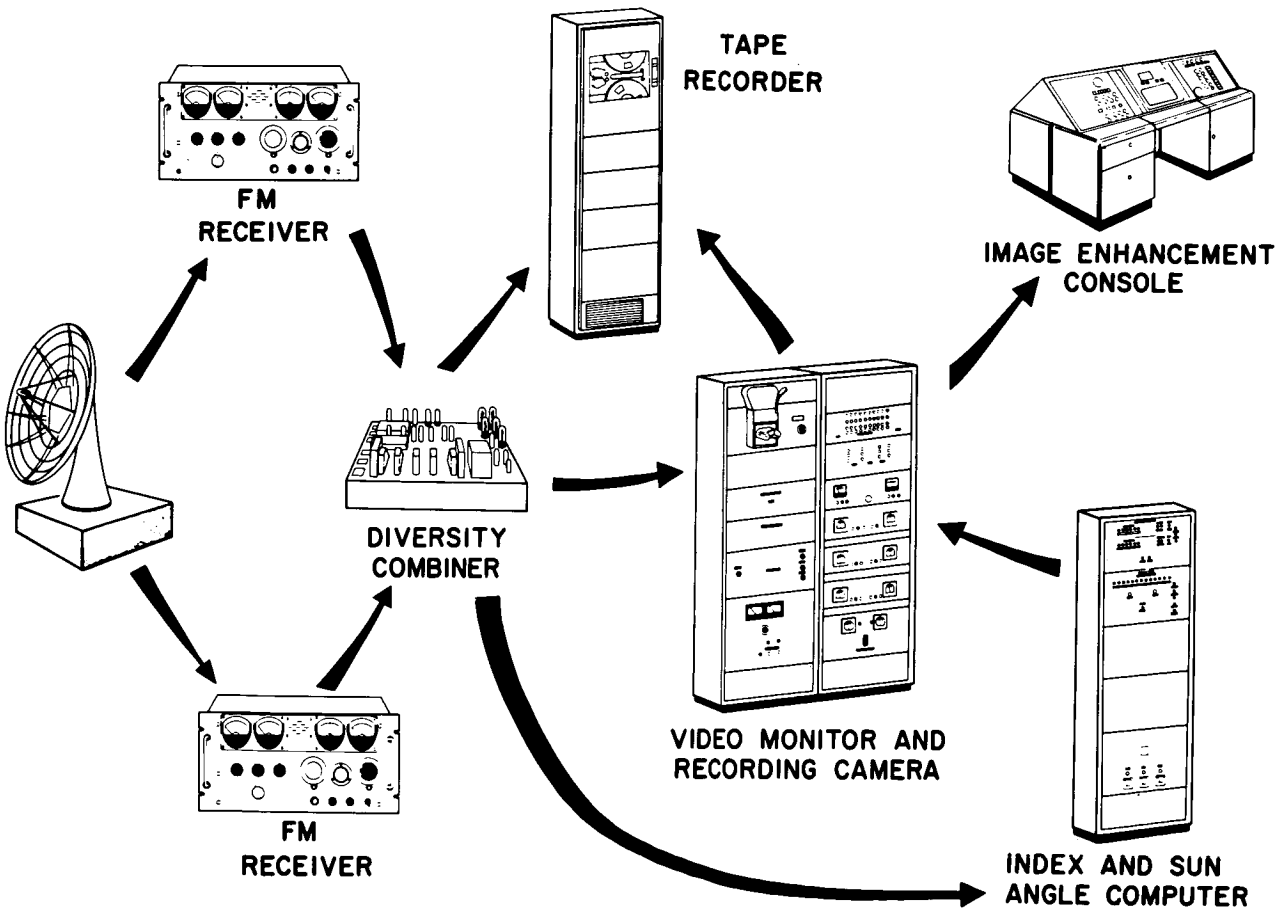

(a) Pictorial representation of components.

FIGURE 18.—TV picture subsystem.

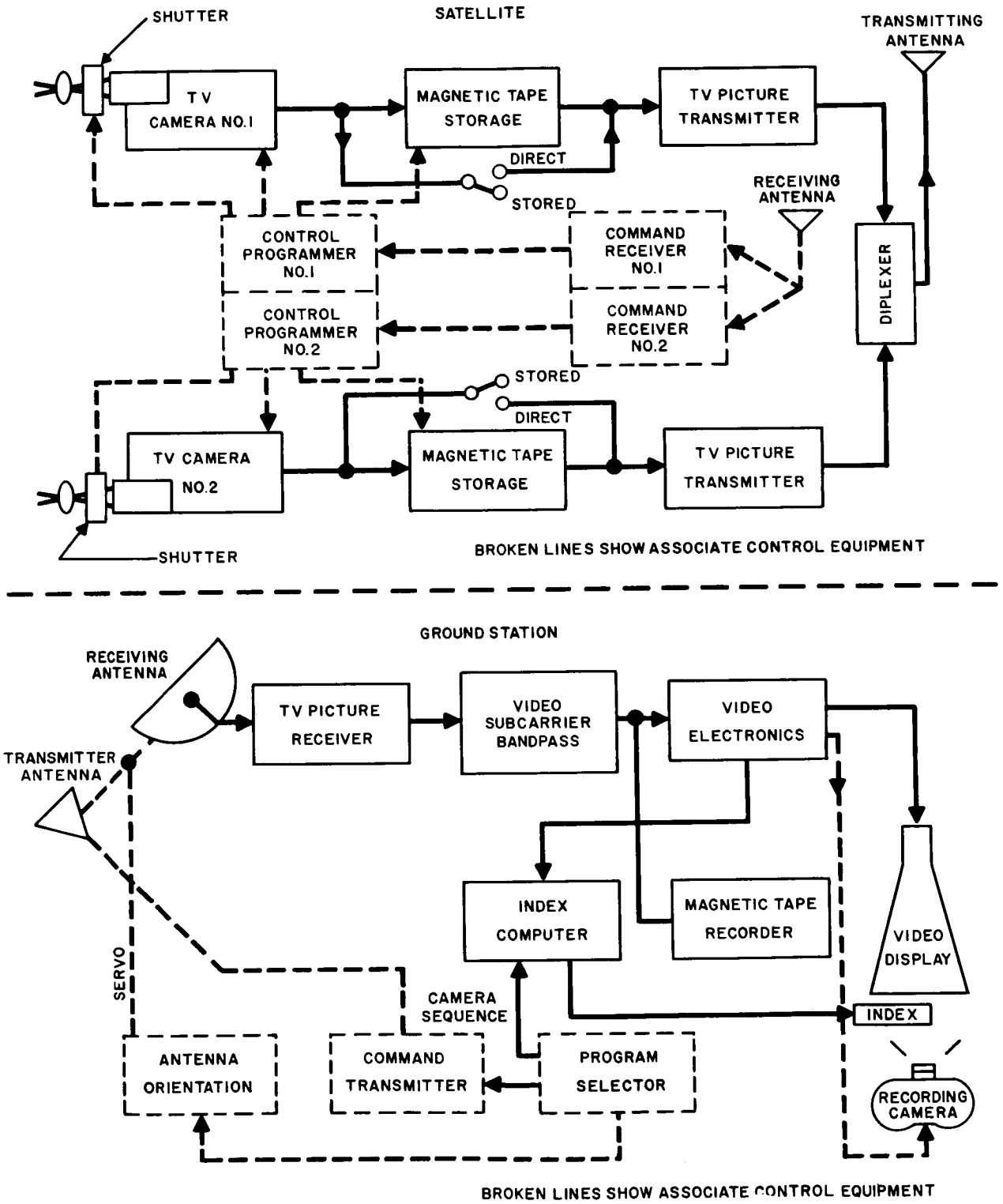

(b) Block diagram.

FIGURE 18.—TV picture subsystem.

in Figure 20. Some of the more significant parameters of the TV cameras are given in Table 2.

Table 2.—Significant Parameters of the TIROS I TV Cameras

TV Camera Parameters	Camera Chain	
	Wide Angle	Narrow Angle
Field of view	104 deg.	12.67 deg.
Lens aperture	f/1.5	f/1.8
Shutter speed	1.5 msec	1.5 msec
Lines per frame	500	500
Vertical sweep duration	2 sec	2 sec
Frames per second	1/2	1/2
Video bandwidth	62.5 kc	62.5 kc
Power consumption (average).	9 w	9 w
Resolution	1½ mi	1000 ft
Peak spectral sensitivity (visible spectrum).	0.7 to 0.9μ	0.7 to 0.9μ

Both wide and narrow angle cameras are aligned parallel to the spin axis. When viewing vertically, the wide-angle camera covers an area approximately 750 miles on a side, the narrow-angle camera, approximately 65 miles on a side with its field of view centered in the larger area of the wide-angle camera. Pictures can be taken at 10-second or 30-second intervals. The 30-second picture interval is intended to provide a 50-percent overlap of the wide-angle pictures.

Each magnetic tape recorder has two separate channels—one for video and one for an index to indicate satellite rotational position. The latter channel is part of the Position Indicator Subsystem and will be discussed later. The tape recorder electronics provide the transport power.

Video from the camera is fed to the all-transistorized tape recorder electronics, where it is changed to a frequency-modulated signal on an 85-kc subcarrier. Full deviation of the signal is from 70 to 100 kc. This information flows either directly to the transmitter, after position-reference mixing, or to the tape transport, depending on whether the satellite is operating in the direct or remote mode. In the remote mode of operation, the FM signal is recorded on tape and, during playback, the two channels of information on the tape are mixed before fed to the transmitter.

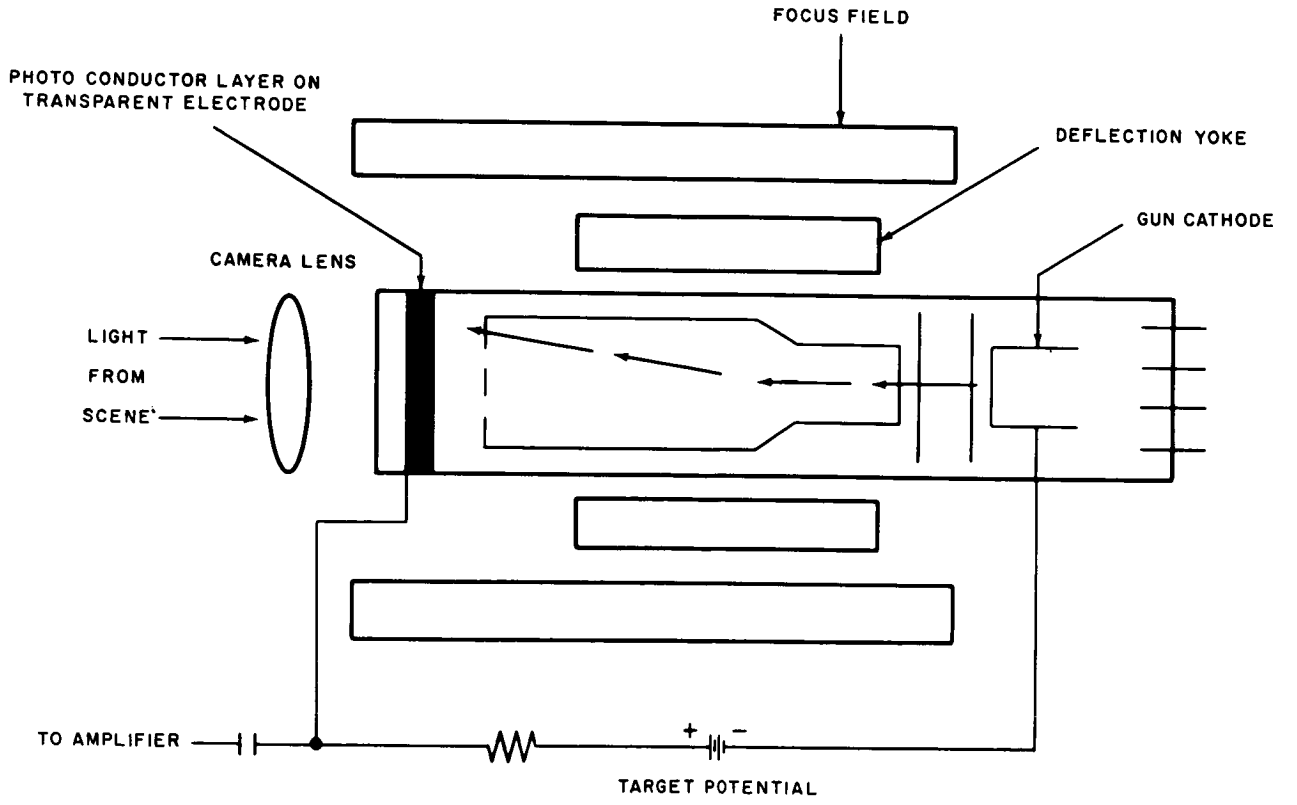

FIGURE 19.—Diagrammatic representation of the vidicon used in TIROS I TV cameras.

The pressurized tape transport mechanism, shown in Figure 21, was developed especially for satellite operation from the standpoint of weight, power consumption, and electronic performance. Four hundred feet of 3/8-inch Mylar-base tape is used with both record and playback speeds of 50 inches per second. During the record cycle, the transports operate only during the picture readout time and a total of 32 pictures taken at 30-second intervals can be stored on each tape. During the playback cycle, the transports run continuously until all information is played back and the end-of-tape switch is actuated in preparation for another record cycle. Each transport is housed in a hemispherical aluminum dome to protect against contamination during ground handling.

The FM information, mixed with the rotational index from the tape recorder electronics, is fed to a 2-watt FM transmitter operating at 235 Mc. The power required for the transmitters in each of the two systems is supplied by dc-to-dc converters. These transmitters operate for 4 to 10 minutes out of each 100-minute orbit, during interrogation of the satellite by the ground station.

Telemetry and tracking subsystems.—Telemetered satellite parameters, satellite attitude data (to be discussed under *Position indicator subsystem*), and a radio beacon signal for tracking purposes were broadcast to the ground by the beacon transmitters. Included in this subsystem are the telemetry switches and the required subcarrier oscillators. A block diagram of this subsystem is shown in Figure 22.

Two completely transistorized 30-milliwatt beacon transmitters operated simultaneously at 108.00 and 108.03 Mc from the time of launch. During the launch phase, a 1,300-cps tone was transmitted for tracking purposes and for a positive indication of third-stage separation. Upon

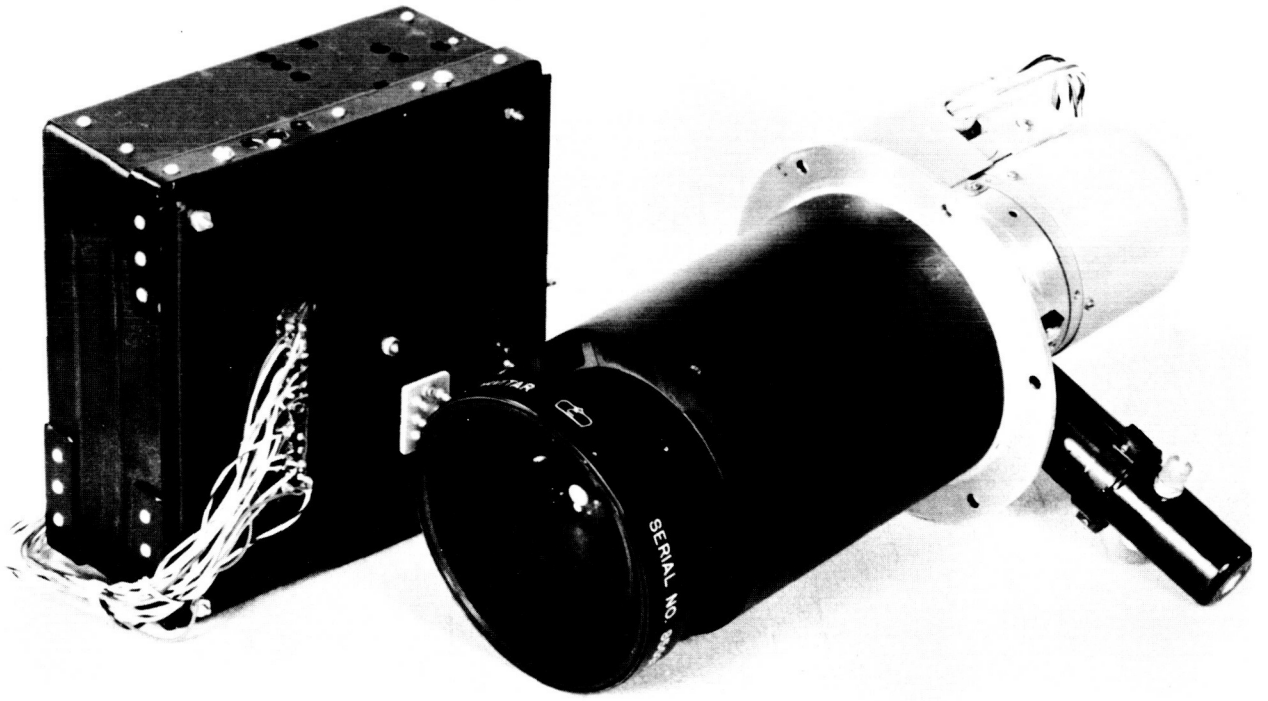

FIGURE 20.—The TIROS I wide-angle TV camera and its associated electronic package.

separation, the 1,300-cps tone was turned off and was used only for telemetering purposes thereafter. After the satellite began orbiting the carrier was amplitude-modulated continuously by horizon-scanner data and, during interrogation by the ground station, telemetered information was transmitted over the beacons. For the sake of reliability, all information was transmitted over both beacons. The maximum power consumption for each beacon is 0.45 watt.

The two telemetry switches were solenoid-operated 40-position units. The telemetered parameters, as is shown in Table 3, were connected through the contacts on each switch for duplicate transmission through both beacon transmitters. The switches ran through a complete cycle in about 30 seconds whenever the satellite was interrogated by the ground station.

Satellite function-control subsystem.—The satellite function-control subsystem includes the command receiver; the function controls; timing and remote-sequencing equipment; and the auxiliary equipment controls which are duplicated for each camera channel. Because of its complexity, only a general description of the system will be given here, with references to the various possible modes of operation. A more detailed description can be found in the TIROS I Final Comprehensive Technical Report, May 1961, prepared by the Astro-Electronics Division of RCA.

The command receiver provided the link between the ground station and the satellite control subsystem. A common antenna was used for the two receivers (one in each camera channel), but the receiver output was distributed to each control circuit. The receiver was transistorized through-

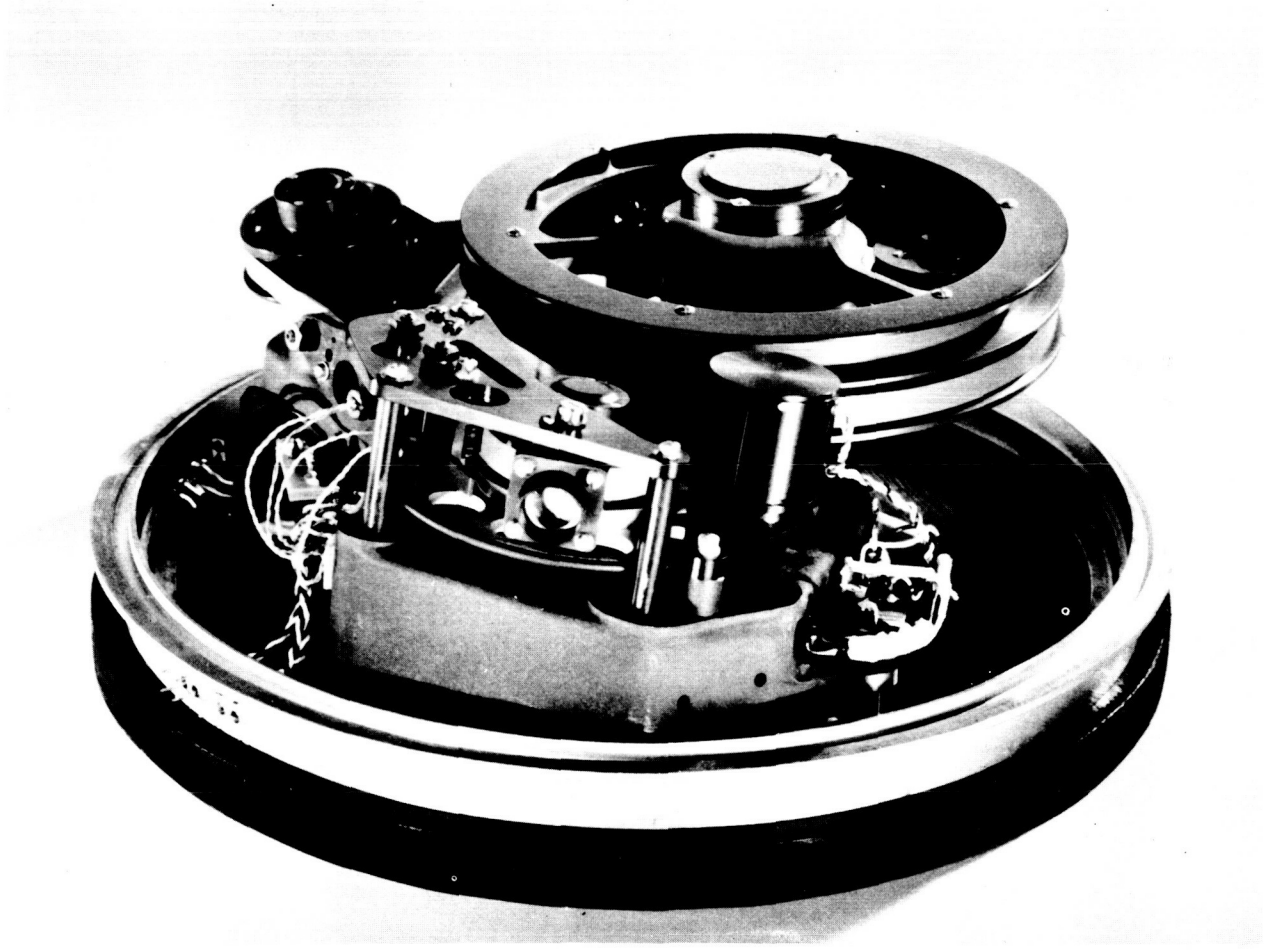

FIGURE 21.—The TIROS I tape transport mechanism.

646-770 O—64——3

out and, with negligible power consumption, was kept energized at all times.

All control systems in the satellite used bandpass filters to distinguish between the control tones transmitted from the ground station. Eight tones were used for all satellite instrumentation control, and combinations of these tones were used for different sequencing of events. The logic in the controls is such as to prevent damage to the satellite by improper sequencing or combinations. Typical control configurations for "Tape Playback," and "Direct Picture" functions are shown

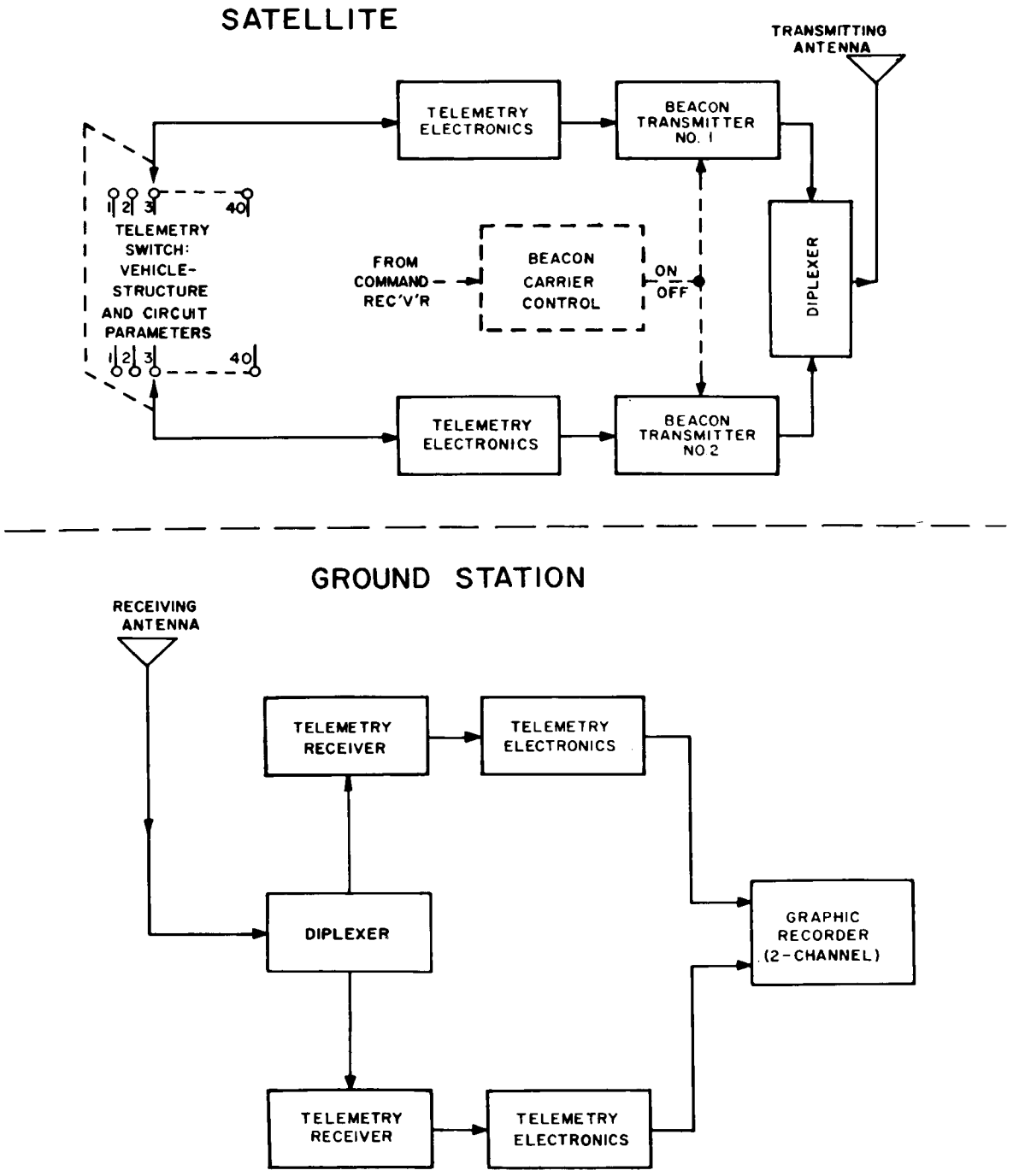

FIGURE 22.—The TIROS I telemetry and tracking beacon subsystem.

TABLE 3.—TELEMETERED PARAMETERS OF THE TIROS I SATELLITE

TEL. SW. POS. NO.	Parameter Transmitted Through Beacon No. 1	Parameter Transmitted Through Beacon No. 2
1	Ground Calibrate	Ground Calibrate
2	−2.5 Volts Reference	−2.5 Volts Reference
3	Top Skin Temperature (1)	Base Plate Temperature (40°)
4	Top Skin Temperature (2)	Base Plate Temperature (90°) 19″ r.
5	Side Skin Temp. (Top Panel 2)	Base Plate Temperature (190°)
6	Side Skin Temp. (Bot. Panel 2)	Base Plate Temperature (90°) 6″ r.
7*	−28 Volts, Battery String "X"	−28 Volts, Battery String "X"
8*	−28 Volts, Battery String "Y"	−28 Volts, Battery String "Y"
9*	−28 Volts, Battery String "Z"	−28 Volts, Battery String "Z"
10	−28 Volts, Main Load Buss	−28 Volts, Main Load Buss
11	Voltage Regulator No. 1, −24.5V	Voltage Regulator No. 1, −24.5V
12	Voltage Regulator No. 2, −24.5V	Voltage Regulator No. 2, −24.5V
13	Voltage Regulator No. 1, −13.0V	Voltage Regulator No. 1, −13.0V
14	Voltage Regulator No. 2, −13.0V	Voltage Regulator No. 2, −13.0V
15	Clock No. 2 Vertical Sync	Transmitter Converter No. 1
16	Clock No. 2 Horizontal Sync	Transmitter Converter No. 2
17	Clock No. 1 Vertical Sync	Transmitter No. 1
18	Clock No. 1 Horizontal Sync	Transmitter No. 2
19	Vidicon No. 1 High Voltage	Vidicon No. 1 High Voltage
20	Vidicon No. 2 High Voltage	Vidicon No. 2 High Voltage
21	Vidicon No. 1 Fil. and Focus Cur	Vidicon No. 1 Fil. and Focus Cur.
22	Vidicon No. 2 Fil and Focus Cur	Vidicon No. 2 Fil and Focus Cur.
23	Spin-Up Rocket Firing Index	Spin-Up Rocket Firing Index
24	TV Camera No. 1 Video Output	Solar Cells, Top
25	TV Camera No. 2 Video Output	Solar Cells, Side
26	Solar Cells, Top	Recorder Head No. 1
27	Solar Cells, Side	Recorder Head No. 2
28	Motor Power Convertor No. 1	Motor Power Convertor No. 1
29	Motor Power Convertor No. 2	Motor Power Convertor No. 2
30	Playback Amplifier No. 2	Playback Amplifier No. 1
31	Playback Amplifier No. 2	Playback Amplifier No. 2
32	Transmitter Converter No. 1	Clock No. 2 Vertical Sync
33	Transmitter Converter No. 2	Clock No. 2 Horizontal Sync
34	Transmitter No. 1	Clock No. 1 Vertical Sync
35	Transmitter No. 2	Clock No. 1 Horizontal Sync
36	Base Plate Temperature (40°)	Top Skin Temperature (1)
37	Base Plate Temperature (90°) 19″r	Top Skin Temperature (2)
38	Base Plate Temperature (190°)	Side Skin Temperature (Top Pan. 2)
39	Base Plate Temperature (90°) 6″r	Side Skin Temperature (Bot. Pan. 2)
40	Home Contact	Home Contact

*The storage battery strings X, Y, and Z are monitored separately by the telemetry subsystem.

in Figure 23. Only the tones for "Direct Camera I," "Direct Camera II," "Playback I," and "Playback II" could activate the circuits of the satellite. All other control tones were rejected until after the resulting 30-second warm-up period. This allowed tube filaments time to warm-up and minimized the possibility of jamming and unauthorized readouts. To allow for maximum usage of ground station contact time, one system would be warming while the second was transmitting data.

Control configurations for "Set Clock I," "Set Clock II," and "Start Clock," are shown in Figure 24. Set Clock, Start Clock and Spin-Up tones were transmitted during interruptions of any one of the four basic control tones listed in the preceding paragraph.

The timing and remote-sequencing equipment consisted of the clocks and their associated "Set" and "Start" circuits. A TIROS I clock [43] with its control crystal is shown in Figure 25. With this equipment, cameras and tape recorders were se-

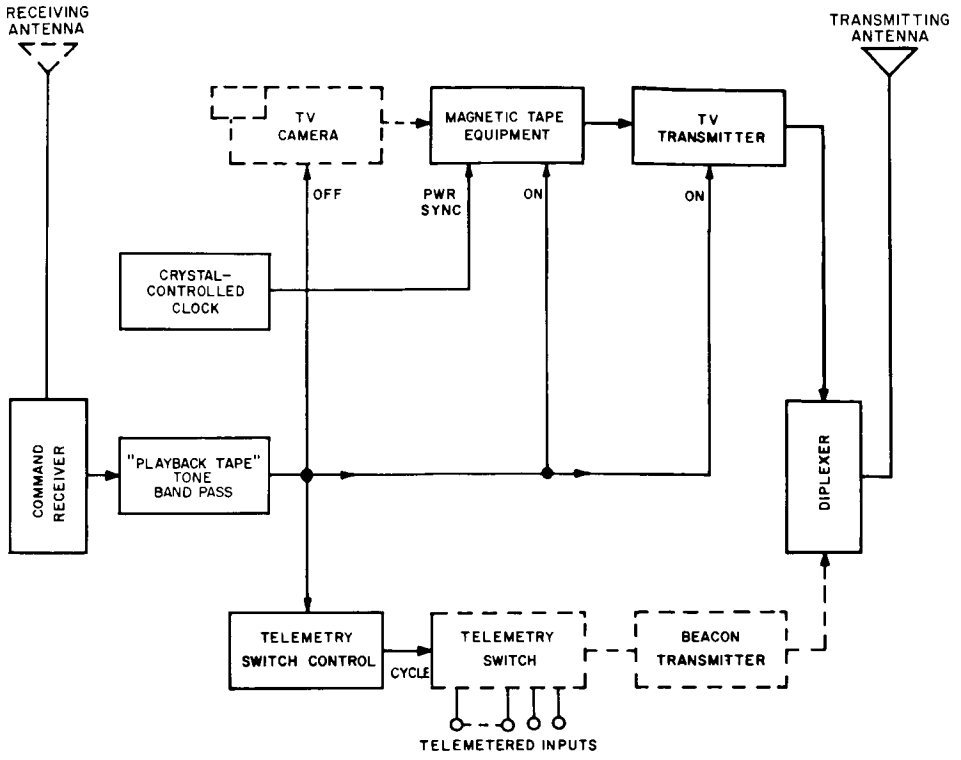

(a) Transmission of remote (tape-stored) pictures to ground.

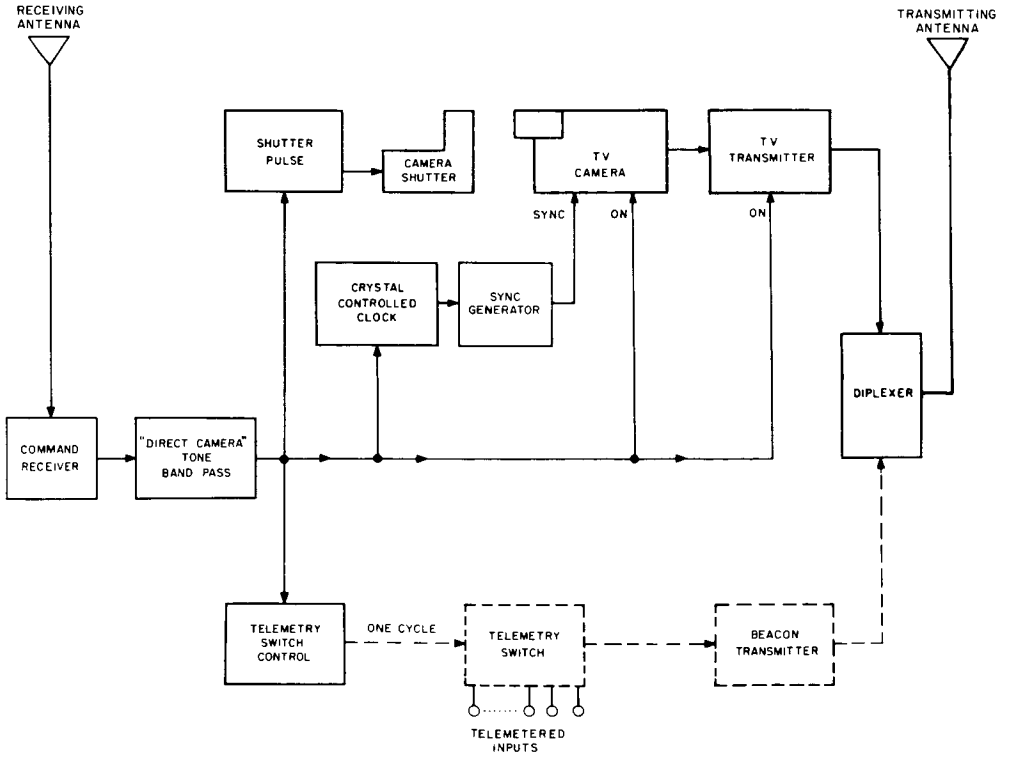

(b) Transmission of direct (non-stored) pictures to ground.

FIGURE 23.—Component grouping for functional modes of TIROS I satellite.

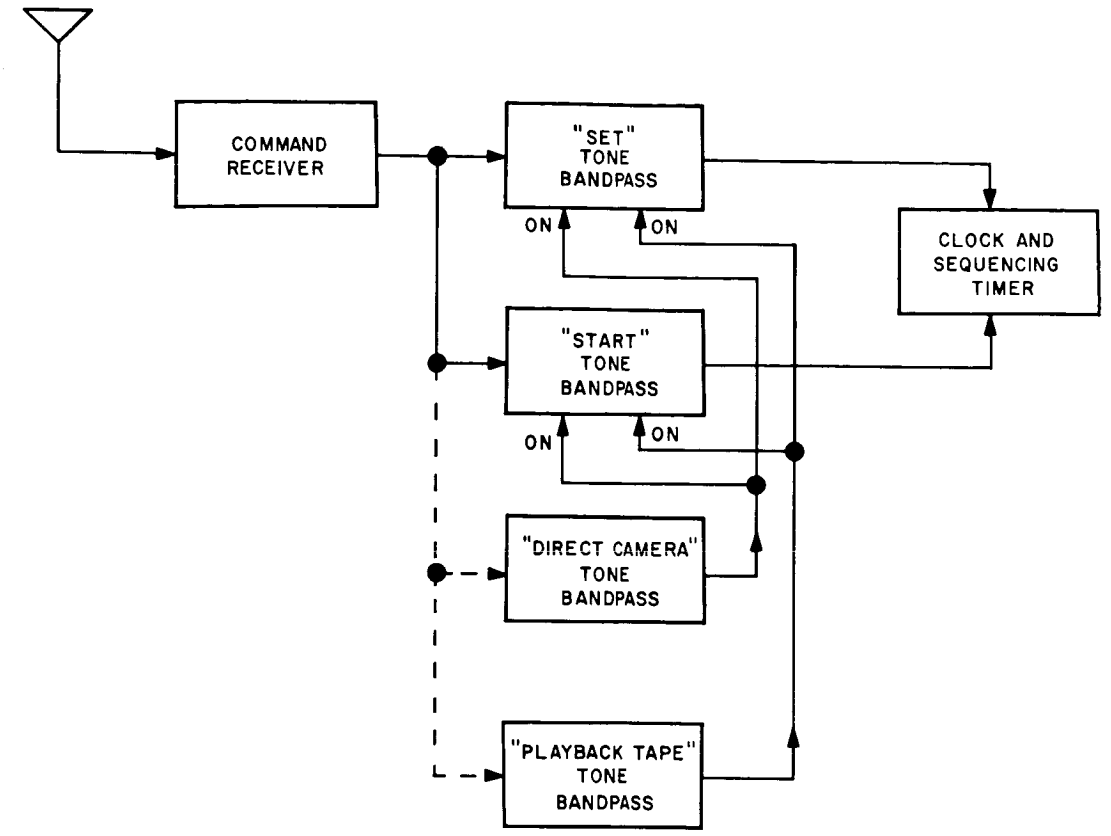

(a) Component block diagram.

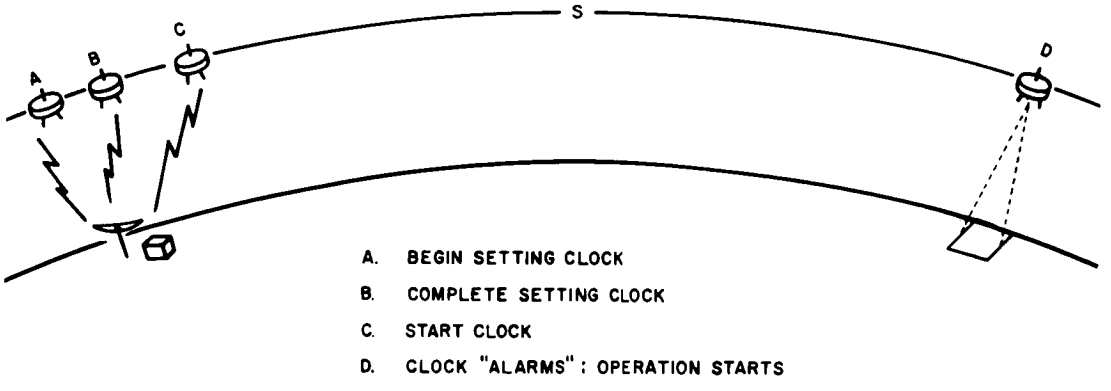

(b) Physical relations in delayed operation.

FIGURE 24.—Arrangement for delayed photography from TIROS I satellite.

quenced automatically at a preselected time in the orbit when the satellite is beyond radio range of the station.

A 9,000-count register was the basic element read in the clock. This register could be filled with pulses from either the ground station at a 130-pps rate or from within the clock at a 0.5-pps rate after the "clock start" tone had been transmitted. When the 9,000-count register was filled, the clock "alarmed" and provided horizontal and vertical sync to the cameras, 500-cps sync to the recorder power supply, and the necessary switching for sequencing. At the alarm time a solenoid-operated stepper, driving actuating cams, began a 16-minute sequence of picture-taking every 30 seconds. At the end of the 16-minute sequence the

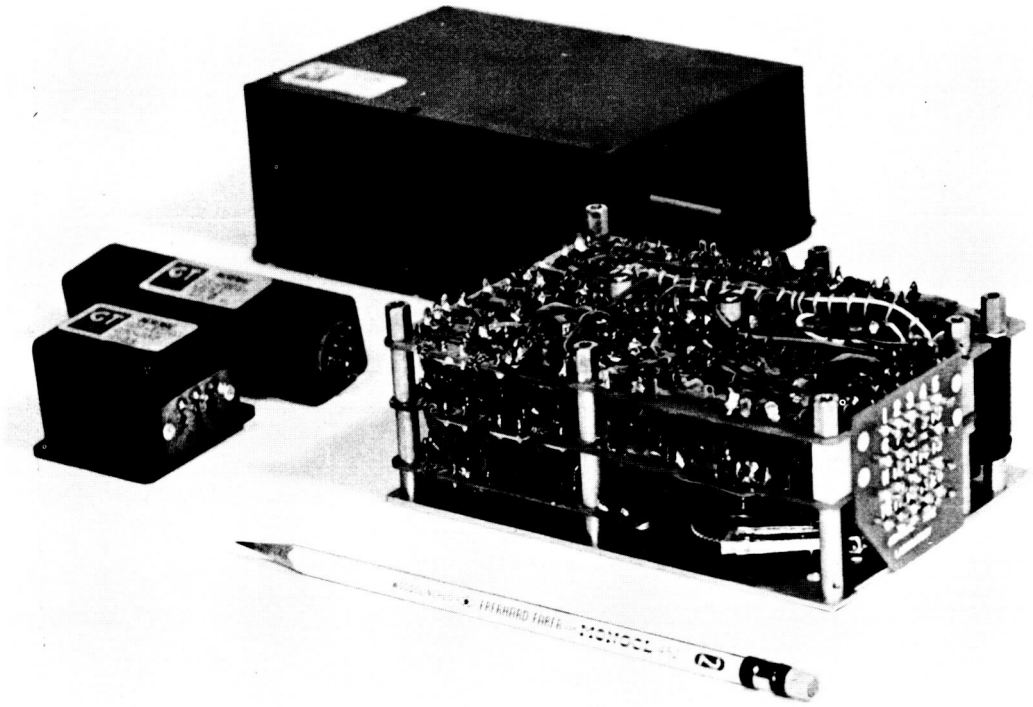

(a)

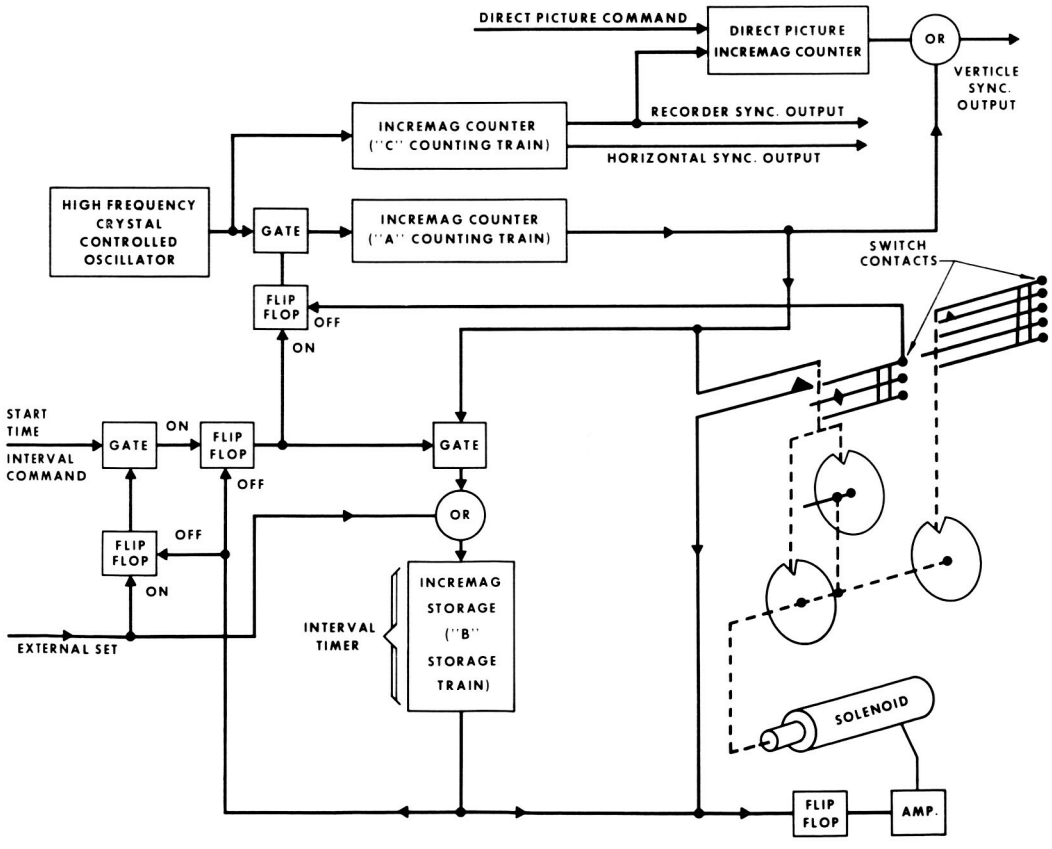

(b)

FIGURE 25.—The TIROS I clock.

clock shut off automatically. The basic timing for the clocks was derived from either of two 18-kc oscillators, gated for reliability. The clocks could be run either synchronously or separately, and could be set and started in any of the four basic operating modes described earlier.

Auxiliary equipment and controls provided for back-up control of the precession dampers and despin weights (both to be described in the section on the *Dynamics control subsystem*), control of the spin-up rockets, and on-off control of the power output of the beacon transmitters. A control circuit configuration for these is shown in the block diagram of Figure 26. At separation of the third rocket stage and the payload, the precession dampers and despin weights were released by action of lift-off switches. Had they not been, manually initiated signal transmission from the ground of the spin-up tone could have activated a solenoid-operated rotary switch to "step" for back-up firing. The first step of this switch would release the precession dampers and the second (which requires a separate manual command) would release the despin weights. This manual back-up was provided to assure operation of the attitude control mechanisms.

For proper operation of the satellite, it was required that the rotational speed remain between 9 and 12 rpm. When the vehicle slowed to approximately 9 rpm, transmission of the spin-up

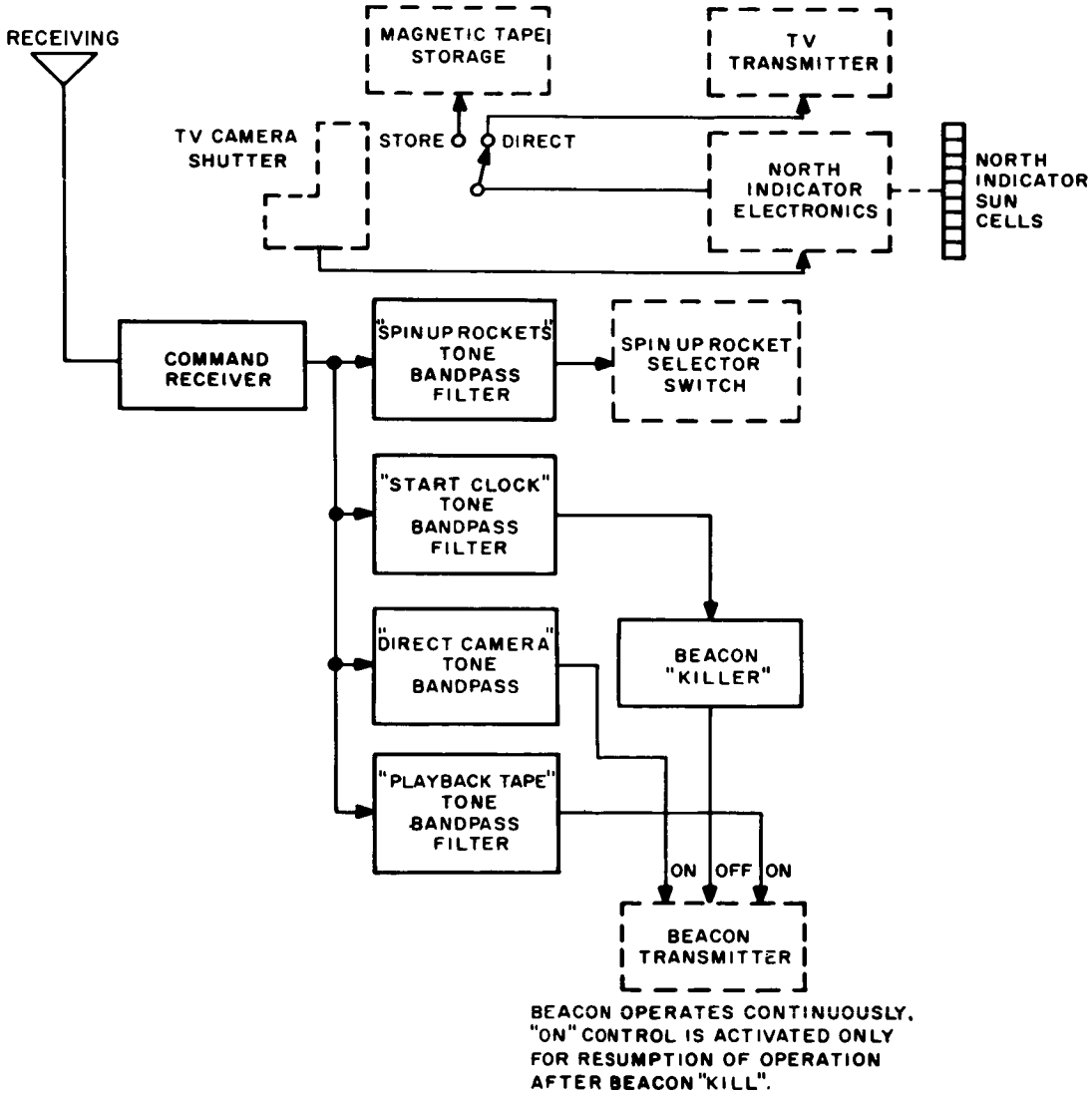

FIGURE 26.—TIROS I control circuitry for spin-up motors, sun-angle indicator, and beacon transmitter "kill".

tone for the third time would cause the stepping switch to select a pair of diametrically-opposite rockets to fire immediately. This would then cause the spin rate to increase by 3 rpm.

At the end of the useful life of a satellite, it is desirable to shut down the beacon transmitters. Provisions were incorporated at the ground station to send a tone which would activate a beacon-shutdown circuit. If it became desirable to reactivate the satellite, transmission of either a direct or playback control tone for the required warm-up time would have caused the beacons to come back into operation.

Satellite position indicator subsystem.—The satellite position indicator subsystem includes the horizon scanner and the sun-angle sensors. These units provided spin-axis attitude data and sun-angle reference (for locating "north" on the pictures taken).

Attitude information for the spin-axis orientation was derived from an infrared sensor, developed by the Barnes Engineering Corporation, which was mounted at right angles to the spin axis. As the satellite rotated, the IR cell sensed outer space temperatures. When it intercepted the earth, the discrete changes of temperature were used to trigger a multivibrator. Information obtained in this way was telemetered to earth continuously on the beacon transmitters. The beamwidth of the IR sensor lens system was 1 degree. A block diagram of this subsystem is shown in Figure 27.

Knowledge of the satellite's rotational position with respect to the sun provides a means of locating "north" in the picture transmitted to the earth. The angle from a baseplate reference to the sun is measured by means of 9 solar cells located every 40 degrees on the satellite's periphery, with each cell installed in a well and covered by an aperture slit. This arrangement allows the solar cell to see the sun for about 7 degrees of satellite rotation.

The electrical output of each cell triggers one of three multivibrators (each with a different pulse length), and the cells are connected in such an order that the output of any two adjacent cell-multivibrator combinations is unique. From the time at which the pulses are sent with respect to vertical sync to the cameras, the sun angle may be computed. These pulses are returned to the ground station simultaneously with the picture information, for both direct and remote pictures. A block diagram of this subsystem is shown in Figure 28.

Satellite dynamics control subsystem.—Control of the satellite dynamics was exercised by means of the spin-reduction device, the precession dampers, and the spin-up rockets. The effect of all of

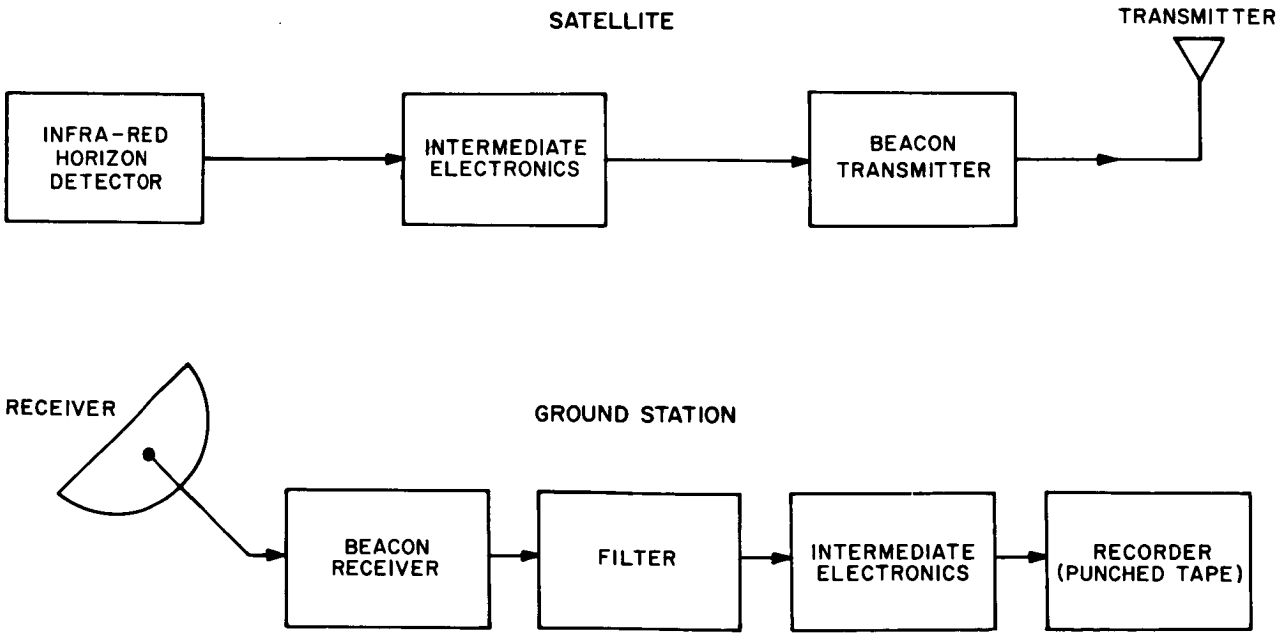

FIGURE 27.—The TIROS I position-indicator circuits.

these devices was to effect and maintain a stable spin axis with a rotational velocity of 9 to 12 rpm about the axis.

At the time of separation from the third stage, the satellite was rotating about its spin axis at approximately 85 rpm. The equipment aboard was designed for an optimum spin rate of 12 rpm. To effect a permanent reduction in the spin rate, it was necessary to reduce the satellite's kinetic energy of rotation. This was accomplished by extending masses on cables until the desired rate was attained, and then releasing the masses. Two cables were attached at points 180 degrees apart, and each cable was wrapped 360 degrees around the satellite and the weight locked in place. Upon the firing of a pair of squibs, the weights were released and unwrapped by "centrifugal force" until the cables were radial to the spin axis. At that time, the cables slipped from open hooks and departed. A close-up picture of the device showing a weight, cable, and hook, are shown in Figure 29.

The initial wobble of the satellite (due to precession or nutation) after release from the third-stage rocket was damped out by a unique device utilizing a tuned energy-absorbing mass (TEAM) which opposes forces that tend to oscillate the satellite body. This is illustrated in Figure 30. Two similar mechanisms were installed vertically along the satellite side wall, 180 degrees apart. Each mechanism weighs just under 1 pound. During the launching the movement of the weights was restrained. At the time of satellite separation, squibs were fired which released the weights and they rolled freely along the rods. The device was tuned to the precession frequency of the satellite and it rapidly absorbed the energy causing the wobble. When the satellite stabilized, the weights came to rest at the center of the rods.

The earth's magnetic field, by acting upon magnetic materials in the satellite, was expected to reduce the spin rate of the vehicle to below 9 rpm after a time in orbit. To compensate for this, two pairs of spin-up rockets were provided, mounted

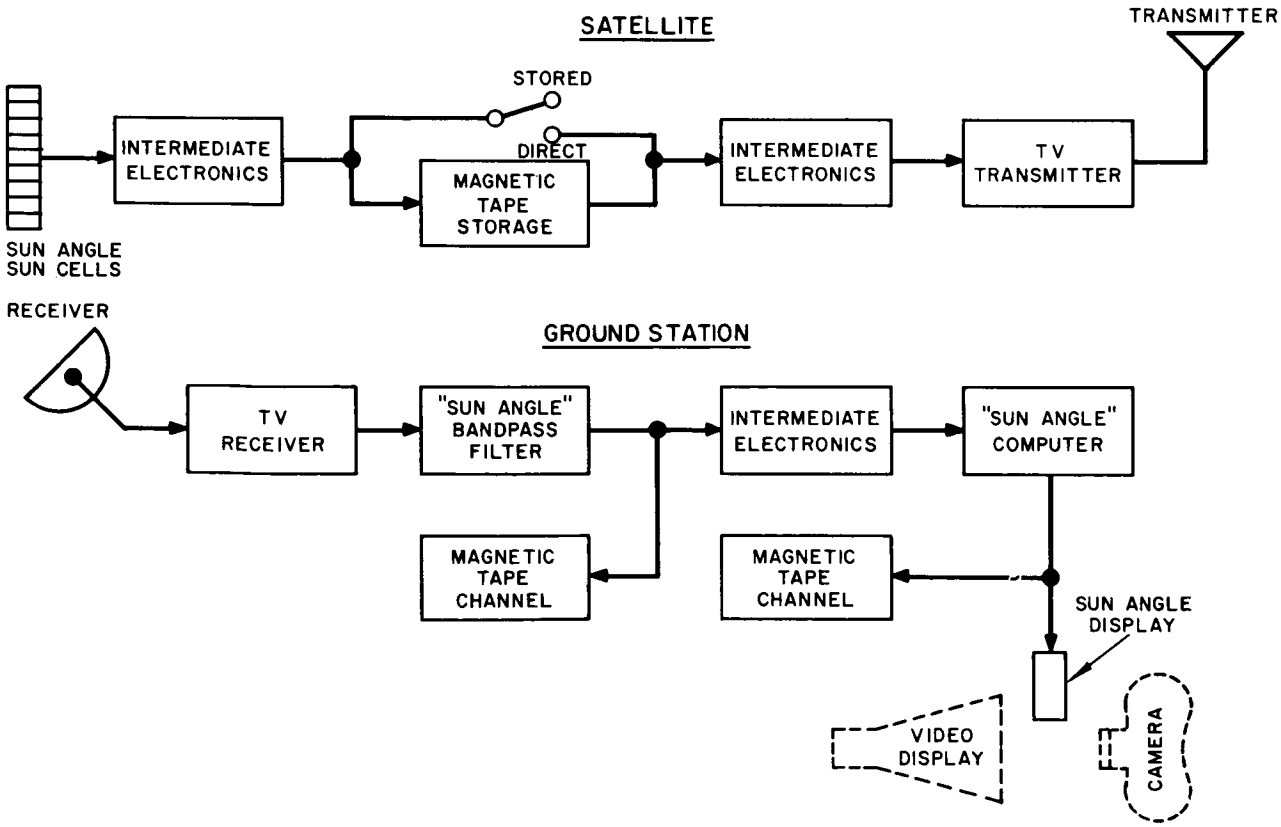

FIGURE 28.—The sun-angle sensor subsystem.

at diametrically opposite points around the periphery of the satellite. On command from the ground, one pair of these solid-propellant rocket motors would fire. Each rocket has an impulse of 1.4 pound-seconds. It was confirmed that this force increased the spin rate by about 3 rpm. Two of these rockets are shown in Figure 31.

Electrical power subsystem.—The electrical power subsystem consists of the solar cells, batteries, voltage and current regulators, and power converters. Figure 32 is a functional block diagram, showing voltages and branch circuits.

Primary electrical power for the satellite is derived from 9120 solar cells (developed by International Rectifier Corp.) mounted on the walls and top of the satellite. (140 more are used only for "control" measurements by the telemetry system.) These cells, 1 by 2 centimeters in size, have an average minimum conversion efficiency of 7.5 percent including the effects of an optical coating added to improve their thermal efficiency. Eighty solar cells comprising sixteen "shingles" are connected in series-parallel through protective diodes, as a module. A total of 115 such modules are used, with many connections taken off to the batteries as a fail-safe measure. Although the total output of the cells is primarily a function of incident sun and temperature, an average power output of 25,000 watt-minutes per day was realized.

The solar cells charged 63 nickel-cadmium hermetically sealed storage batteries (developed by the Sonotone Corporation) which are used to provide power for the equipment, even during periods of little or no illumination of the solar cells. The bank of batteries is mounted at the center of the baseplate, as shown in Figure 33. The batteries are connected in three paralleled strings of 21 batteries each to provide an unregulated dc

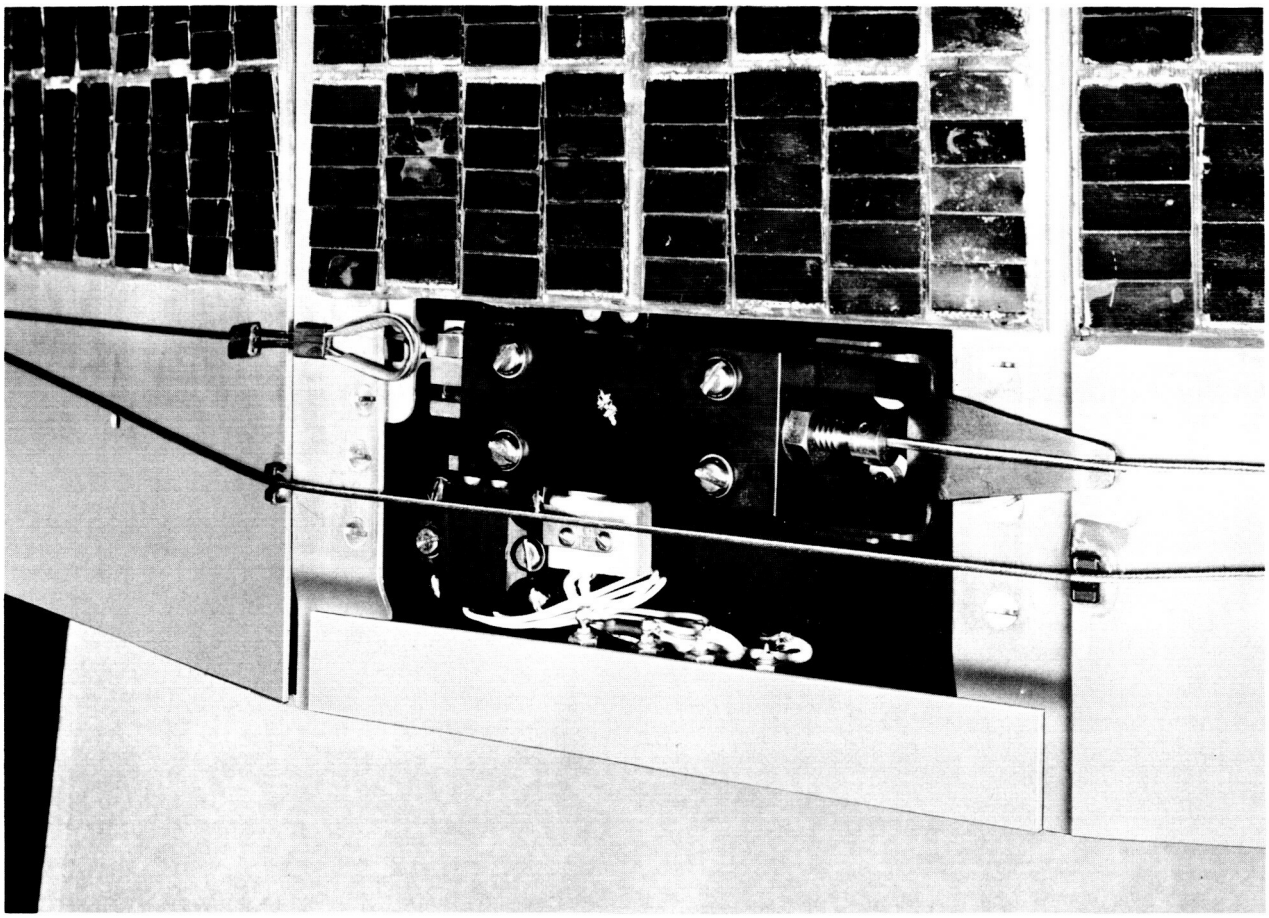

FIGURE 29.—The TIROS I Yo-Yo despin mechanism, showing a weight, cable and hook.

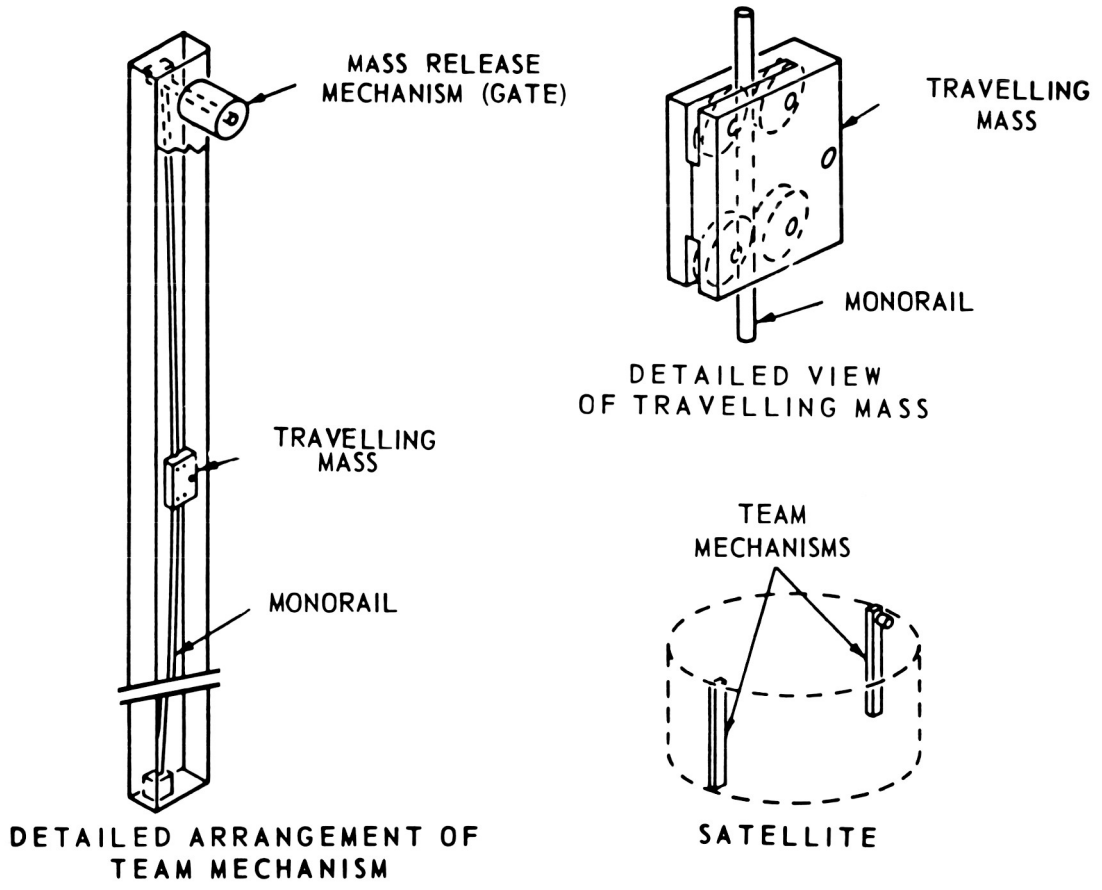

(a)

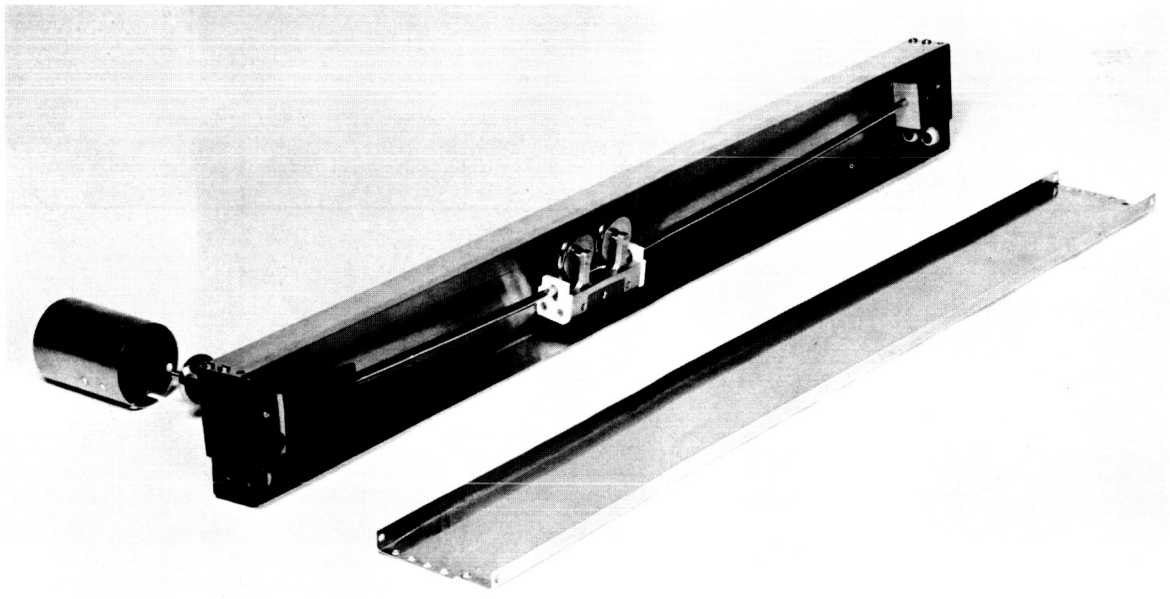

(b)

FIGURE 30.—The TIROS I TEAM (precession damping) mechanism.

voltage of 26 to 33 volts to the system. The three battery strings are isolated from each other by fusing and diode decoupling to prevent circulating currents and catastrophic failure due to a malfunction in one string. The total capacity of the batteries is about 300 watt-hours under normal operating conditions.

The three strings of batteries are isolated from the solar cells by three current regulators. This prevents damage to the batteries due to excessive charge rates. Power in excess of that required to maintain the batteries is diverted through bypass voltage regulators to the main battery output bus. Voltage regulators reduce the bus voltage to 24.5 volts ±1 percent, and 13 volts ±1 percent for the various electronic circuits.

Unregulated battery voltage is supplied to the non-critical circuits such as the tape-transport drive converter, transmitter power supply, camera power supply, and solenoid-actuated switches. The tape-transport drive converter supplies 500-cps 115-volt two-phase power to drive the tape transport. The transmitter power supply provides +250 volts dc and 6.3 volts ac for the filaments. The camera power converter supplies +300 volts and −50 volts dc for camera operation.

Antenna subsystem.—The antenna subsystem consists of the transmitting antenna, the receiving antenna, and the balun diplexer network shown in Figure 34.

The transmitting antenna consists of a pair of crossed dipoles fed in quadrature to achieve circular polarization. Each radiating element consists of a rod equivalent to 0.19 wavelength at 108 Mc. This rod is the center conductor of a coaxial sleeve which is equivalent to 0.25 wavelength at 235 Mc. The rod and sleeve are joined at the drive and form a short-circuited transmission line within the sleeve. This antenna system provided a nearly isotropic pattern with little distortion caused by the satellite.

The receiving antenna is a quarter-wave monopole situated in the neutral plane of the transmitting antenna. By virtue of its position alone, there was approximately 45 db attenuation between the receiving and transmitting antenna.

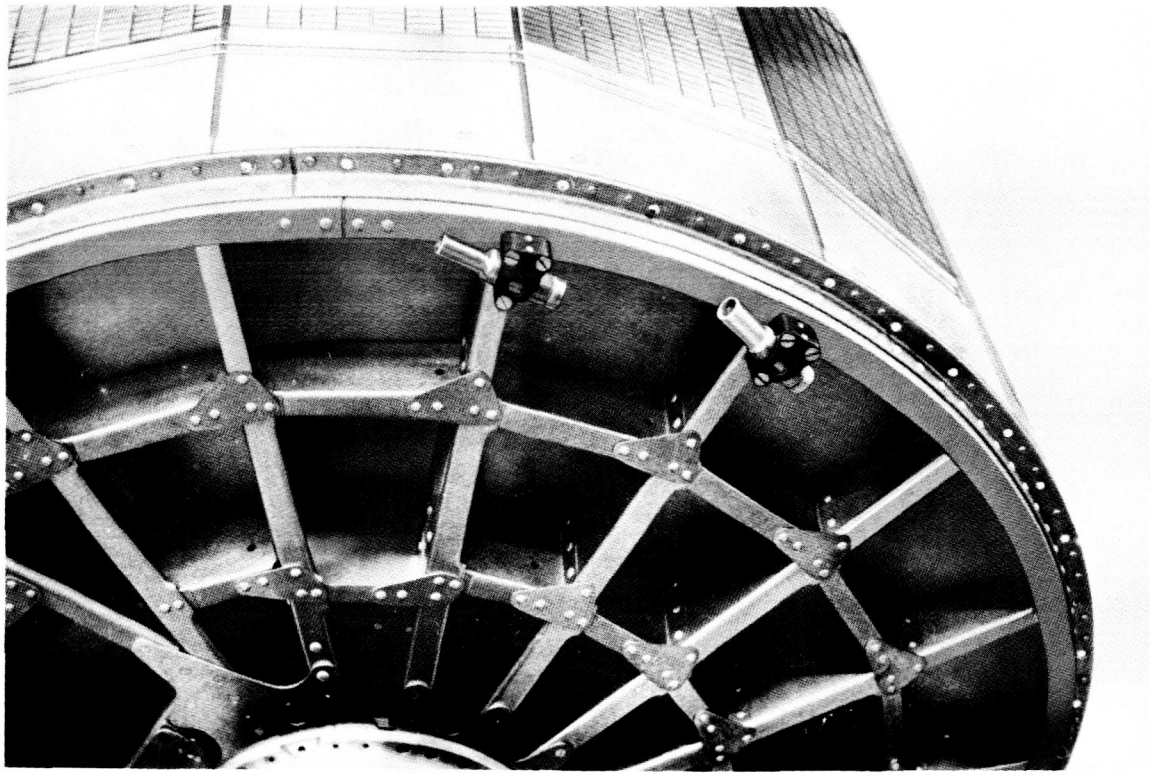

FIGURE 31.—View of a pair of TIROS I spin-up rocket motors.

This is enough isolation to prevent blocking of the satellite receivers by the transmitted signal.

The matching and coupling network was developed specifically to couple the various TIROS transmitters to the antenna, and to provide isolation between transmitters of different frequencies. It also divides the currents properly to each of the transmitting antennas and provides the proper impedance match. Separate though similar network sections are used for the 108-Mc and 235-Mc frequencies; each section contains a diplexer and two balun transformers. The diplexer is a transmission-line bridge network which permits the "generators" to be connected symmetrically across the bridge input while the antennas are driven from the output. The balun transformer is essentially a delay line to selectively phase the RF currents in the respective dipoles. To achieve

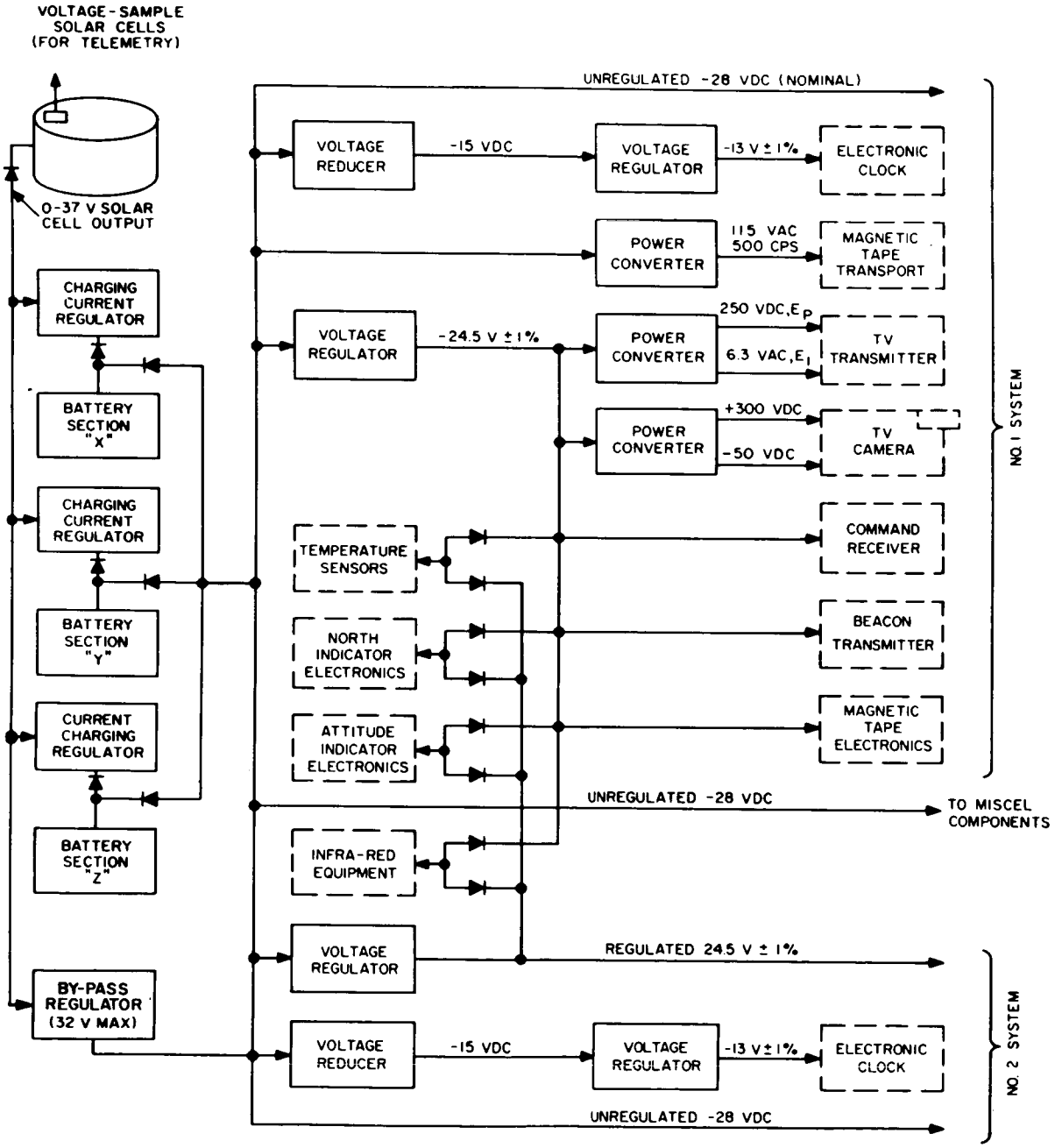

FIGURE 32.—The TIROS I electrical power subsystem.

FIGURE 33.—The TIROS I storage batteries in position on the satellite baseplate.

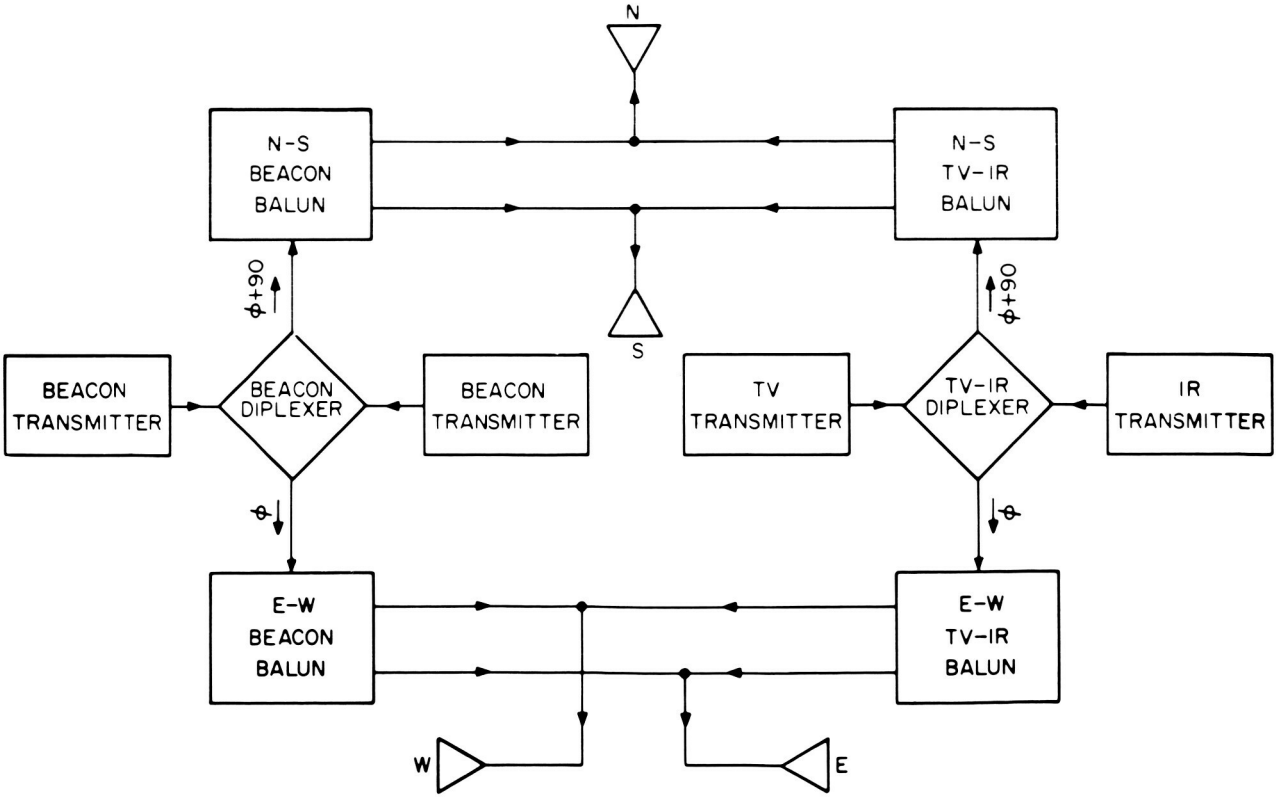

FIGURE 34.—The matching and coupling network for the TIROS I transmitting antenna.

circular polarization, the two cables coupling the diplexer outputs to their respective baluns are cut to differ in electrical length by 90 degrees.

Mechanical structure.—The satellite structure is essentially a right cylinder 42 inches in diameter and 22.5 inches high. The vertical skin consists of 18 side panels attached to a skeleton framework connecting the top and baseplate. Figure 35 shows some of the construction details.

Substantially all of the payload components were mounted to the radial ribs under the baseplate. These are contoured in accordance with the average load and moment forces generated along the ribs. The reinforced baseplate gives peripheral support to the integrated top and side panel assembly. The total loads are passed to the center of the baseplate, to the hub, and then to the carrier rocket through the mating ring.

The structure was designed for high strength, to withstand the rigorous ascent loads and environmental factors, with sufficient rigidity to provide a suitable mounting surface for the brittle solar cells and with sufficient strength to maintain the required tolerances for optical mountings.

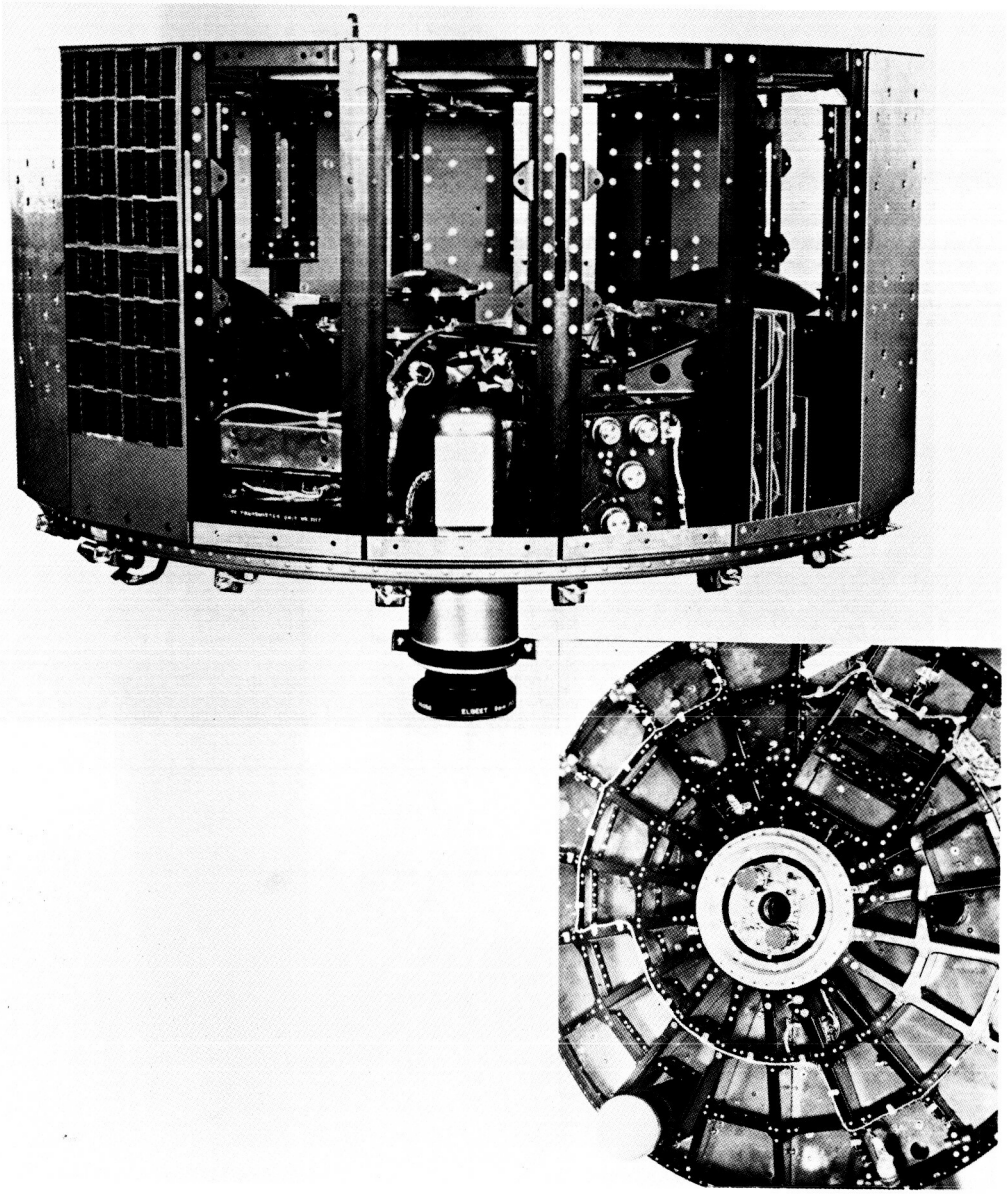

FIGURE 35.—Structural details of the TIROS I satellite housing.

Load levels of 50 g in the axial direction and 30 g in the radial direction could be applied to the satellite without damage. The top and side structure, where the solar cells are mounted, have metal stress limit levels of the order of 3,000 psi.

The structure, with its payload, was statically and dynamically balanced to eliminate disturbances during launch and to insure rotation about an axis parallel to the optical axis while it is in orbit.

The location of the various subsystem components on the baseplate is shown in the illustration (Figure 36, a and b).

Subsystem integration tests.—Integration of the TIROS I subsystems was started on the original electrical prototype satellite, No. T–1, in conjunction with the prototype (Princeton) ground station. As soon as the more advanced prototype, No. T–2, was available, it was substituted for the T–1, and was utilized for the remaining part of the integration, test, and evaluation program. Satellite No. T–1 was the original electrical prototype. It was used only during the study of the original mechanical layout and electrical integration problems. A typical series of problems encountered included system logic errors, grounding problems, inadequate filtering and decoupling, and incompatibility of units. Several units required changes as a result of the investigation. Handling techniques and test procedures were developed as a result of the test made on this model. (This model was later rebuilt as a complete prototype and designated model T–1A.) The advanced prototype, No. T–2, showed several of the

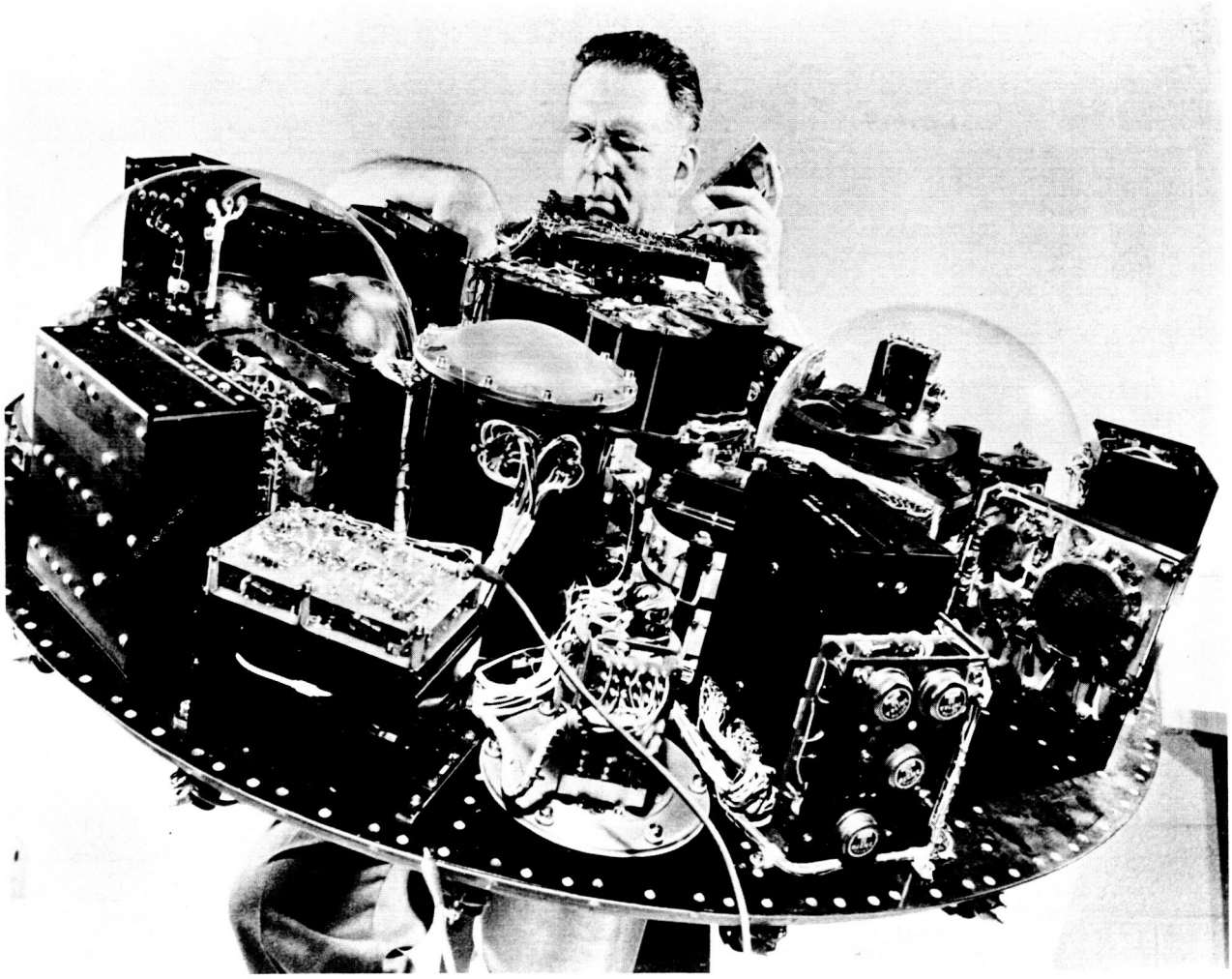

FIGURE 36(a).—Physical layout of components of the TIROS I satellite.

same type of problems encountered in T–1 because of minor harness and grounding changes. Subtle logic errors continued to be located, but before the flight models were completed, a foolproof logic system had been developed. The T–2 satellite was primarily used as a test prototype for the environmental tests required for the program. The results of this were excellent, since there was not a serious failure on any flight model during their tests that could be attributed to design problems.

Specific-performance tests.—To evaluate the satellites completely as required by the specifications, a series of special specific-performance tests were set up. These tests were separate from the usual calibration and environmental tests, and were not necessarily repeated on complete satellites because of the nature of the tests. This special series includes despin, antenna pattern, camera light-threshold, solar cells and batteries, precession dampers, magnetic field drag, structural, and thermal tests.

Despin tests.—The despin mechanism (Yo-Yo) was designed to reduce the satellite's rotational speed from the design speed of 120 rpm, to be acquired during launch, to the operating speed of approximately 9–12 rpm. The elements of the system were designed and tested with a dummy vehicle. After the elements were installed in the actual satellites, special tests were required to test the proper functioning of the system. The final spin down, as recorded on the ground, would not be the same as in space because of the effect of the air drag on the weights.

The satellite was mounted outdoors on a special fixture designed to spin it at launch speeds. By a command signal to the satellite, the squibs were fired, and the despin weights were released. A photograph of the test fixture is shown in Figure

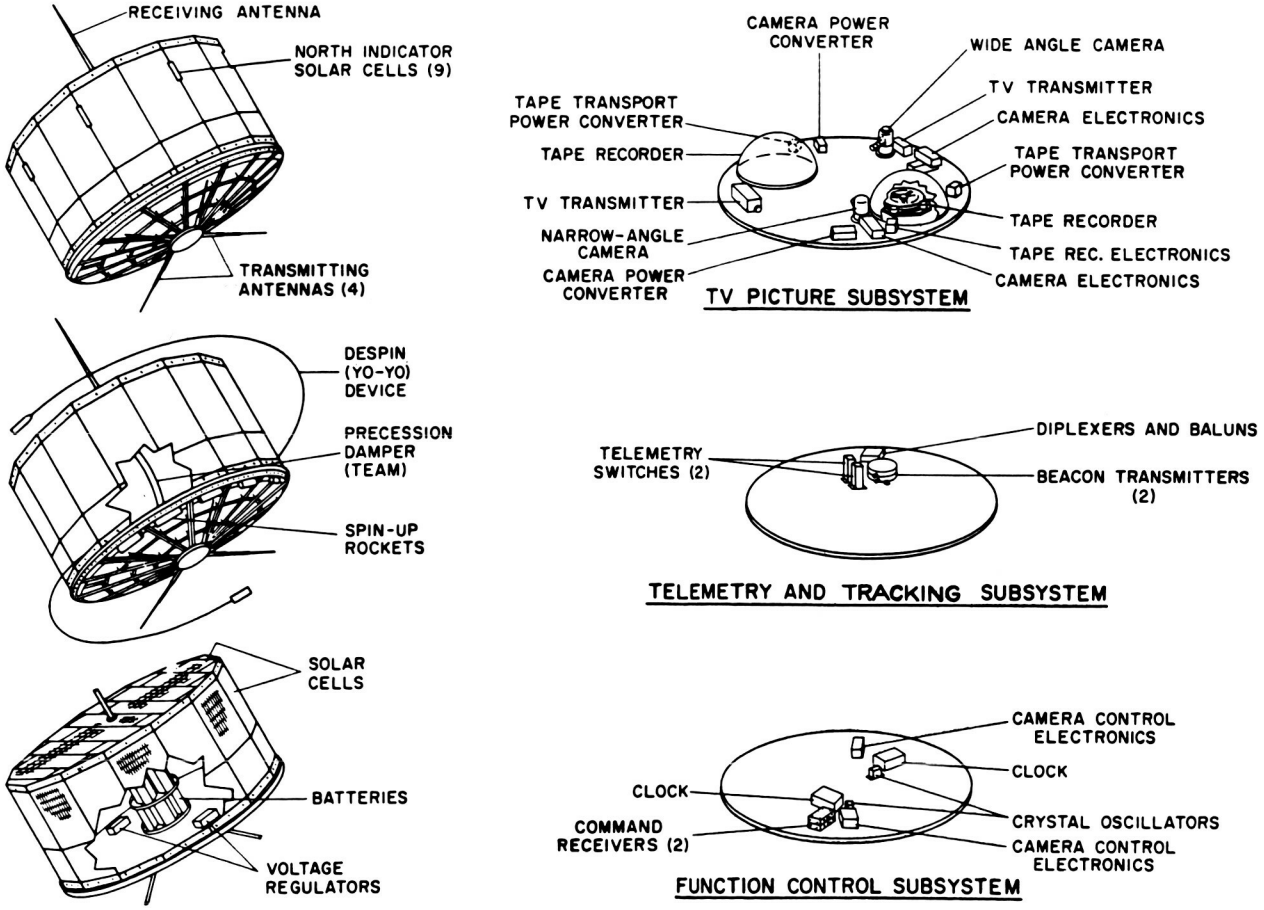

FIGURE 36(b).—Physical layout of components of the TIROS I satellite.

646–770 O—64——4

37. Four tests were conducted using the test-model satellites, succeeding thirty on a simulation model. All tests were successful within the limitations of the atmospheric environment. Actual space conditions could not be duplicated for these tests.

Antenna pattern measurements.—Special facilities were constructed to permit maximum accuracy of field strength measurements to determine the antenna patterns. Measurements were made on both reduced-scale and full-scale models of the satellite. The measurements with the actual satellite configuration were made with the vehicle mounted on a tall wooden structure in an attempt to simulate free space conditions. It was determined in this manner that the critical transmitting antenna pattern was isotropic within ±3 db for 236 Mc and within +4 and −8 db for 108 Mc.

Camera light-threshold measurements.—Discussions held among all interested parties on the reflected light expected from the clouds led to the conclusion that 10,000 foot-lamberts was a realistic value. Further discussion as to expected wavelengths, vidicon response, and many other related subjects helped define the test lamp used for setting up vidicon sensitivity. Two 500-watt lamps of known characteristics were used, and the dynamic range of the vidicons were set with limits of 200 and 13,000 foot-lamberts. Sensitivity curves were run on each camera and included with the alignment data.

Solar cells and battery tests.—Several special test devices were developed for use in evaluating and selecting the solar cells to be used on the flight model satellites. An indoor unit was designed for solar cell evaluation under controlled conditions; an outdoor fixture was used for direct sunlight observations of small numbers of cells; a second outdoor unit was built to evaluate and test the completed satellite units; and a production-type unit was built for rapid selection of cells. Original evaluation of various types of solar cells was carried out with the use of two basic tests units. These are the indoor and outdoor units shown in Figure 38. Each of these units provides a separate and precisely controllable test to evaluate the basic solar cell unit. The use of large quantities of these cells necessitated quick and accurate quality control and final assembly check-out. A "mass" solar cell tester developed at RCA provided the quality control necessary by allowing checks of up to 5,000 cells per day with variable conditions to simulate a standard June 21st solar illumination, from sea level to orbital conditions. The final assembly checkout was done by shading various sections of the completed

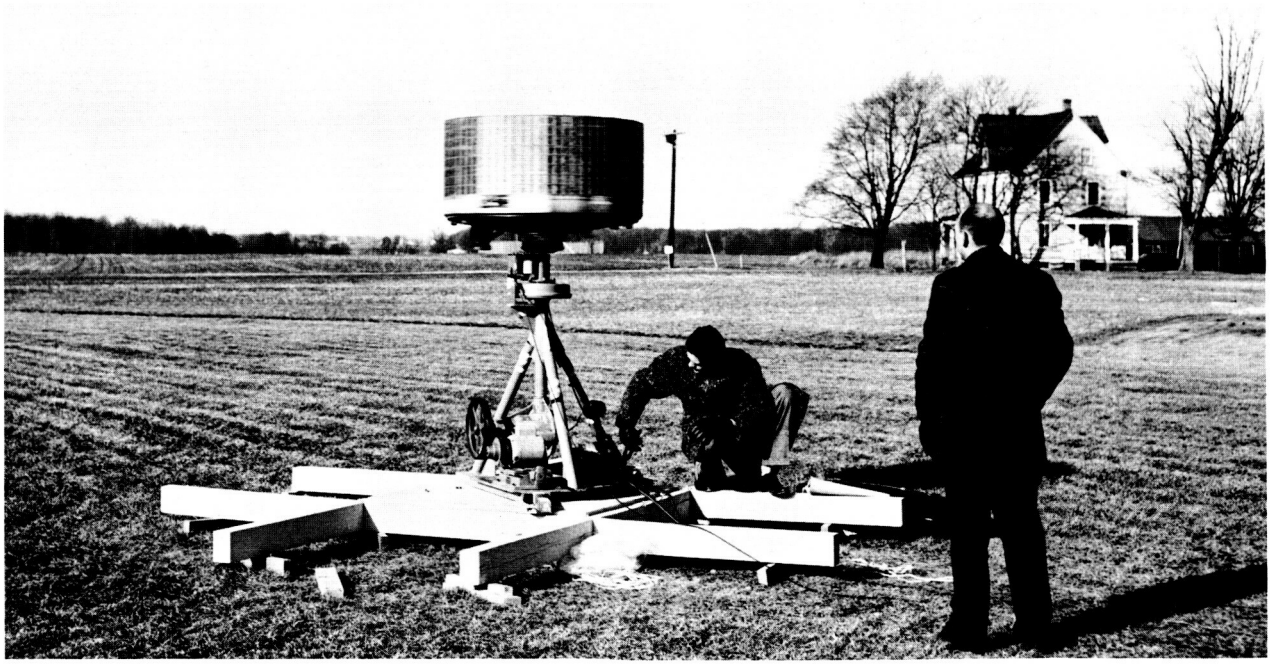

FIGURE 37.—The TIROS I despin field test fixture.

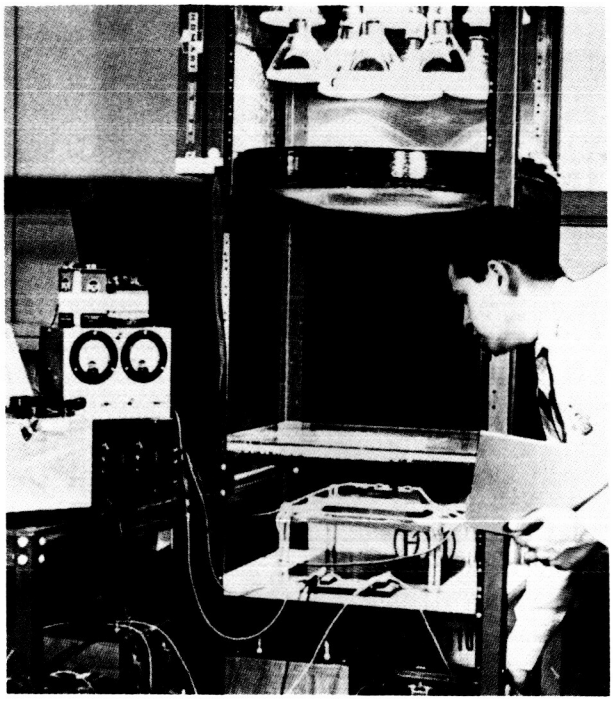

(a) Simulated solar-source "indoor" fixture.

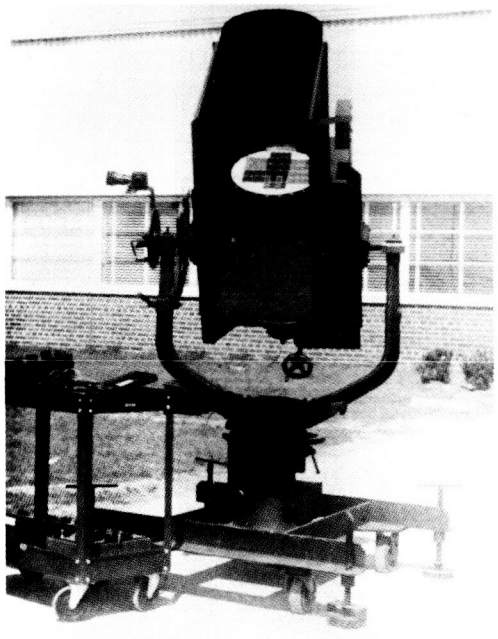

(b) Natural solar-source "outdoor" fixture.

FIGURE 38.—Solar cell text fixtures.

units in the sunlight and using pyroheliometer measurements with voltage and current readings as a final check of power output capabilities.

Magnetic field tests.—To properly evaluate the effect of the earth's magnetic field on the satellite, a special test fixture was constructed with field coils capable of producing up to 200 gauss and with hydrostatic bearings for minimum friction at the speeds of interest. Reproducible data were taken from tests made on a complete satellite; and extrapolations made from this data, together with calculations, provided necessary information on the effects of the earth's field on the spin rate. A photograph of this fixture in use during test is shown in Figure 39.

Structural loading tests.—The structural loading tests were made with a unique test fixture designed by RCA. A view of a satellite structure under test is shown in Figure 40. This facility allowed individual tests to be carried out on either the baseplate alone or the complete satellite structure. Loading to 80 percent of the design limit was used, and significant stress and deflection measurements were made to prove the design. Mass-distribution plates were used to load the baseplate, and a Mylar pressure bag provided even distribution of the load applied to the top of the

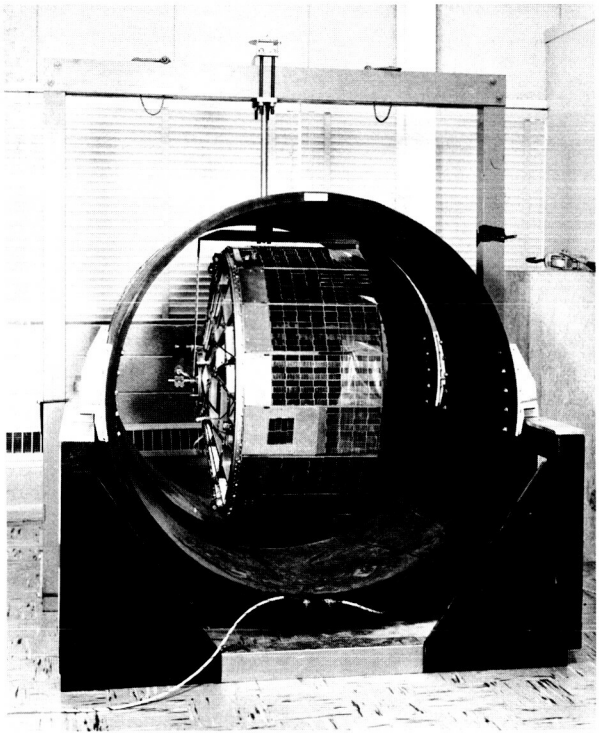

FIGURE 39.—The TIROS I satellite in the magnetic-field "drag" test fixture.

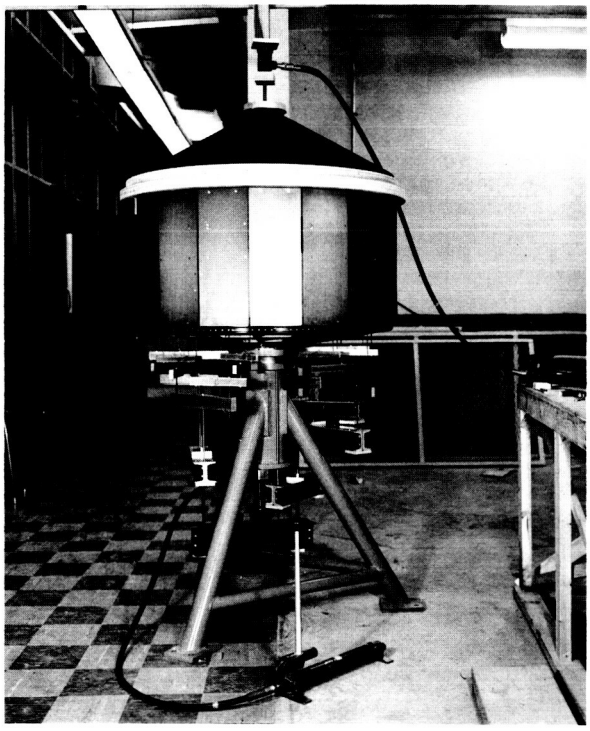

FIGURE 40.—Structural-loading test fixture designed for the TIROS satellites.

structure by a hydraulic jack. Forces up to 40 g were applied.

Thermal tests.—The accuracy of the thermal balance condition calculated for the satellite was proven by placing the entire payload in a 48-inch vacuum-thermal chamber, shown in Figure 41, under controlled conditions. A specially designed heat source was placed near the top of the satellite and heated to 278° F to simulate heat from the sun. The walls of the environmental facility were cooled to −78° F, the lowest possible with the large heat load, to simulate the temperature of outer space. Under vacuum conditions with the satellite operating, stabilized temperatures were measured at 22 locations.

Environmental (qualification) tests.—The TIROS I environmental test program was based on the requirement that one prototype satellite and at least two flight models be qualified by the launch date. The determination of the environmental test program was made by the Environmental Committee which reported to the NASA Project Manager. The program was itemized in detail and could be modified or changed only by the Committee. Whether or not a prototype or flight model was qualified by environmental testing was determined by the Environmental Committee with the concurrence of the Project Manager.

The goal of the environmental tests was to insure that the odds would be at least 20 to 1 against disabling of a satellite by the launching environment. Ideally this requires the demonstration by tests-to-failure of 5 to 10 vehicles that the scatter of strength of "identical" vehicles will not permit failure in flight in more than 1 out of 20 cases. The only practical way to avoid this large program is to demonstrate by test that one or two vehicles possess such a large margin of strength over the expected environment that further testing is not required. The initial goal in testing a vehicle should be to find, first, whether this large margin of strength already exists in the design or whether it can be obtained with reasonable effort. If this large margin is not obtained, the design may still be acceptable; but this should be demonstrated by tests of additional *identical* units. The number of units required depends upon how low the strengths of the units are found to be.

A series of tests were arranged to insure the adequacy of the payload for the orbital conditions that were expected. Environmental tests were monitored closely and very complete electrical calibration checks were made at the conclusion of each test to note any change in operation due to the tests. Prior to shipment, each payload was given a final calibration check with careful alignment checks of all sensors and a static and dynamic balance. The payload was then considered to be ready for launch. The types of tests conducted included vibration, shock, acceleration, temperature extremes, low pressure, and thermal low pressure combination. A view of the satellite undergoing vibration test is shown in Figure 42. In view of the fact that only one prototype vehicle was subjected to the vibration test, this test was conducted at three times the g level.

The philosophy was to test flight units at least at the level of the expected flight environment and either two prototypes at twice that level or one prototype at three times the flight level. Wherever uncertainties in the expected numbers existed, a conservative approach was chosen. To test, for example, for a possible resonance burning in the third stage rocket, the prototype was subjected

to a sinusoidal vibration from 550 cps to 650 cps at about 50 g peak-to-peak. Surprisingly, the payload survived this test well on the first attempt.

Prototype and flight models* were tested in a vacuum chamber at 0° C and 50° C. The test was considered successfully completed after the unit passed 10 days of continuous operation without malfunction. Many shortcomings, serious ones and minor ones, were discovered.

Table 4 shows a breakdown of problems revealed by the environmental test program. The terms used are defined as follows: "Design failure" covers major redesigns, such as mechanical tape drive mechanism and new power supply circuits, as well as minor changes such as underrated fuses and components. A "design weakness" is a malfunction which would not jeopardize the mission of the satellite: an example is a constant error in a frequency divider circuit. If necessary, ground stations could have compensated for the error in the data reduction process. "Component failures" are malfunctions caused by components properly rated and not overloaded. In two out

TABLE 4.—PROBLEMS REVEALED BY THE ENVIRONMENTAL TEST PROGRAM

Problem	Prototype	D_1	D_2	D_3	Total
Design failure	7	2	1	1	11
Design weakness	2	1	1	1	5
Component failure	4	0	0	1	5
Insufficient testing and inspection of subassemblies in testing	3	1	2	1	7
Human errors and accidents	3	2	2	0	7
Total	19	6	6	4	--

*Satellites Nos. T1A and T2 were designated as prototype models; Nos. D1, D2, and D3 as flight models.

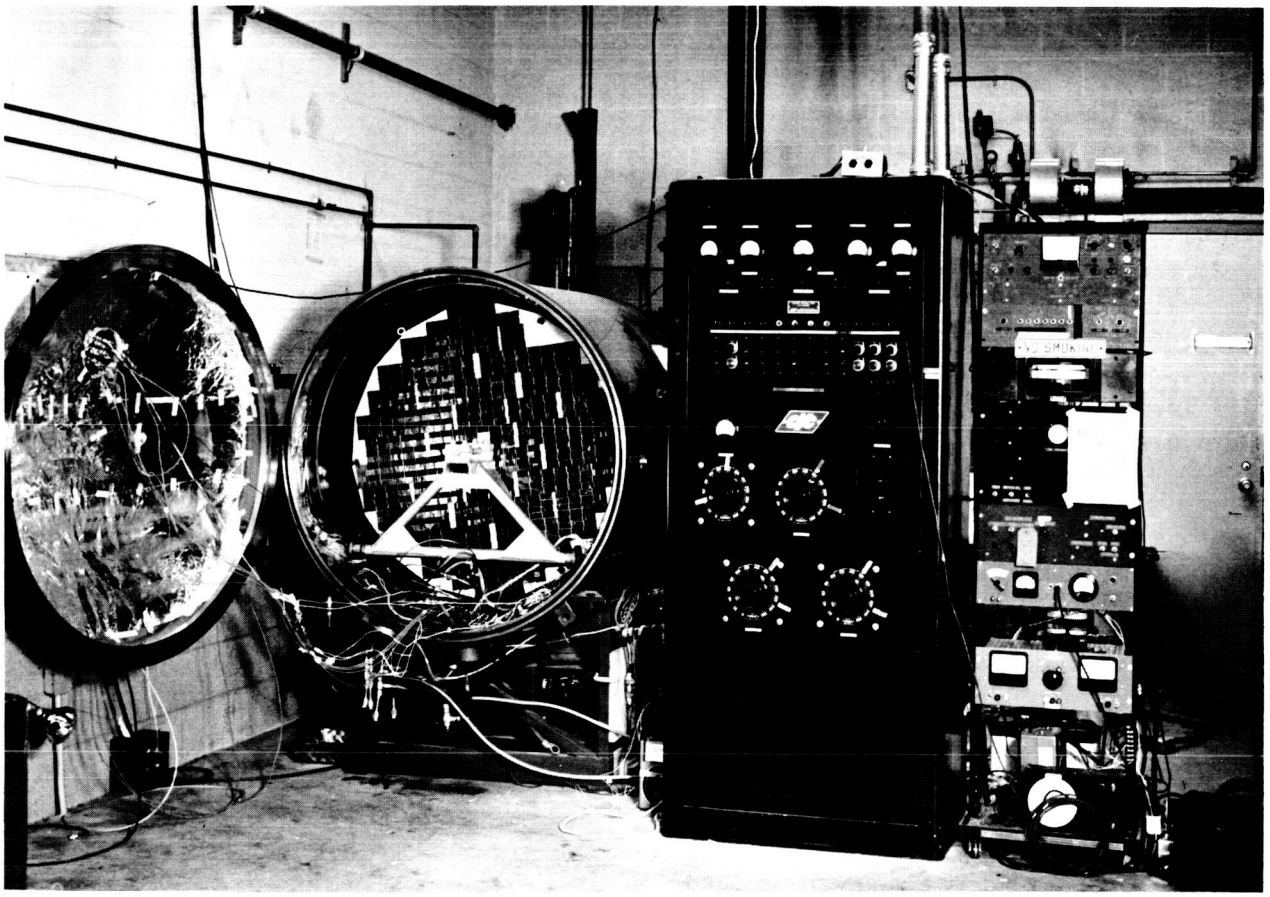

FIGURE 41.—The 48-inch-diameter thermal-vacuum test chamber.

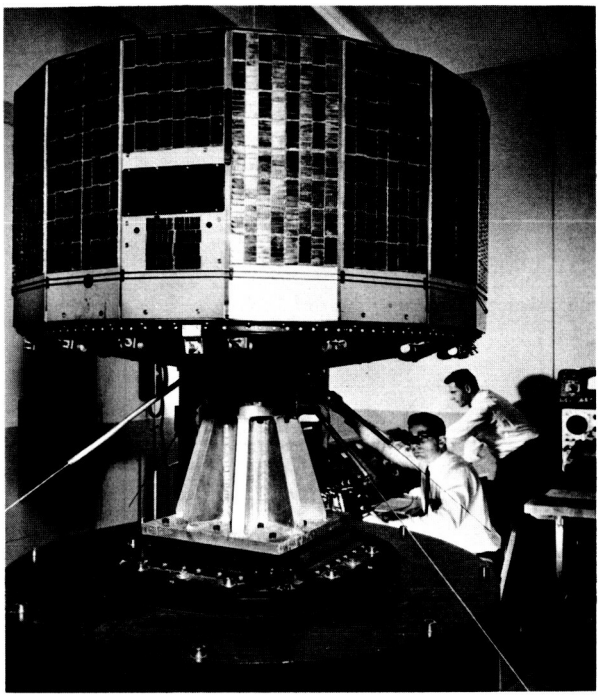

FIGURE 42.—The TIROS I satellite undergoing vibration tests.

of the four cases, a filamentary tube ceased to operate. "Insufficient testing and inspection of subassemblies" (that is circuits and instruments in their own "black box," such as a transmitter or tape recorder) is an important item. This group of failures also includes wiring mistakes, erroneously-placed components and faulty solder joints. It proves the necessity of thorough testing of flight models. Satellites are far from being mass produced items; each unit is "handmade." Each model has its own individuality, no matter how strong the attempt is to make them equal to the prototype.

The fact that design failures were discovered on flight models is partly the result of working on a very stringent schedule. Part of the flight model test overlapped prototype testing, which is obviously not desirable.

Last, but certainly not least; a fair number of malfunctions turned out to be mistakes and accidents caused by the human operator and his test equipment. The reported number of incidents in this category is probable even higher than that indicated, since only those which occurred during the test phase are reported here. The decay of this type of error from "3" in the prototype to "none" in the third flight model shows quite clearly the importance of training personnel on prototype before flight models are given over to their, sometimes, quite heavy hands.

The engineers who designed TIROS I; the group engaged in the test program; and the Environmental Committee take pride in the fact that all of the shortcomings which are quite natural for such a complex instrument were eliminated in time by a strong and thorough environmental test program. The successful mission was the reward for the many months of hard and sometimes frustrating test work.

Satellite redesign during environmental tests.—As a result of initial environment tests, significant redesign in two general areas was found to be necessary to "qualify" the satellites.

During the prototype vibration test on satellite No. T–2, fractures occurred in the sheet metal chassis of several units. These fractures, which showed up after the random noise test at 14 g rms from 20 to 2,000 cps, were observed in the bases of several units which had high ratio of height to base mounting area. To further clarify the cause of these failures, a survey was conducted to determine the "Q" at the upper end of all units in the vehicle when the baseplate was driven along the thrust axis.

In order to correct the observed failures, a two-phase redesign was incorporated. First, the individual chassis in question were replaced with chassis strengthened by adding doubler plates to their bases and stiffening gussets between the base and vertical numbers. Second, after these strengthened units were remounted on the baseplate, "bridging" brackets were added to couple the tops of adjacent units to provide mutual stiffening for these units and reduce their "Q" as well as to insure against detrimental effects on the batteries due to excesive vibration. These may be seen in the view of the baseplate shown in Figure 35. After this two-phase redesign had been incorporated, the T–2 satellite was subjected to a random noise test of 21 g rms from 20 to 2,000 cps. After this test, a careful inspection of the reworked chassis failed to reveal any sign of fracture.

During electrical integration and environmental testing of the satellite, only one major problem occurred that required a redesign. While the sat-

ellite was in vacuum-thermal test, a high charging rate produced internal gas pressure which bulged the battery cases. This, in turn, ruptured the heat sink, causing eventual internal shorting of the cell. As a result, current regulators were added to control the charging rates and the battery case was redesigned to prevent bulging from destroying the heat sink. The modified batteries are shown in Figure 43.

Final calibration measurements.—At the conclusion of the environmental test program, each satellite was given a rigorous examination in preparation for shipment to Cape Canaveral for the launching. This examination was done from both a mechanical and an electrical viewpoint. Final alingnment and balancing were performed at the completion of this test and this was followed by repeating the standard calibration test as a final check before shipment.

The final mechanical inspection was performed to insure that the required quality control had been achieved. In this inspection, the tightness of every screw and nut was checked, electrical connections were inspected, and the satellite was examined for dust, dirt, and foreign materials.

The final electrical calibration was a standard calibration test with a few extra checks added. Each adjustable component was checked for proper setting and sealed. Particular attention was given the camera sensitivities by using a calibrated light source as opposed to a standard TV test pattern and light meter. Camera focus was checked. Sensor alignment was rechecked. At the completion of these electrical tests and alignments, the satellite was balanced and again subject to another electrical check. At this time the satellite was sealed, and considered ready for shipment to the launch site.

Alignment tests.—During the alignment phase of the qualification test program, the alignment of four subsystems was checked with respect to the satellite reference system; i.e., the vehicle spin axis and the baseplate "north" or "zero" reference. Briefly, the procedure for these alignment tests was as follows:

Camera systems.—The alignment requirement for the two camera systems states that the optical axes of their lens systems must be parallel to the satellite's spin axis within ±1 degree. The procedure for meeting this requirement was as follows.

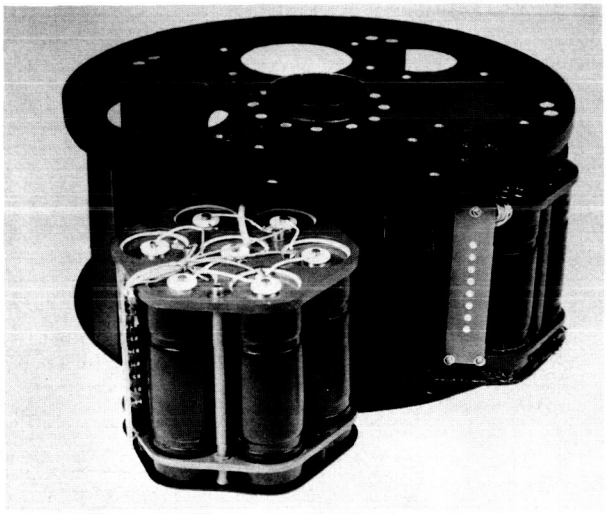

FIGURE 43.—Redesigned batteries for the TIROS I power supply.

Front surface mirrors with inscribed crosshairs were mounted on the end of the mechanical balancing shaft and at the front lens element of each camera such that the intersection of the crosshairs was aligned with the spin axis and the optical center of the respective lenses. The satellite was oriented so that its spin axis was coincident with the line of sight of a collimating telescope which was mounted on a lathe bed with its line of sight perpendicular to the bed's axis. By rotating the vehicle and moving the telescope along the axis of the lathe bed, the alignment reticle in the telescope was superimposed on the collimating mirror crosshairs mounted at the front lens element of each camera in turn. With the telescope so aligned, the parallelism between the spin axis and the camera's optical axis was checked by auto-collimation. The test-fixture components are shown in Figure 44a.

Without upsetting the telescope alignment with the camera, a polar coordinate distortion chart, shown in Figure 44b, was placed on the target plate, which was in turn mounted perpendicular to the barrel of the telescope. This target was so positioned that its center was coincident with the line of sight of the telescope. The collimating mirror was removed from the camera lens and a vidicon picture was taken of the polar chart. A copy of this picture was obtained on 35-mm film

by photographing the ground station monitor display. This picture provides distortion data as well as a measurement of the "offset" between the fiducial marks on the vidicon and the optical axis of the lens system. This distortion check was repeated using a rectangular grid rather than a polar chart. Negatives of the polar and rectangular distortion chart pictures were provided in the alignment and calibration booklets supplied for each satellite.[44] This booklet also contains the parallelism deviation and vidicon fiducial mark offset for each camera.

Results of the alignment measurements are typified by the data in Table 5, recorded for Cameras No. 1 and No. 2 of the D–3 satellite (the one orbited). Angles are measured in a counter-

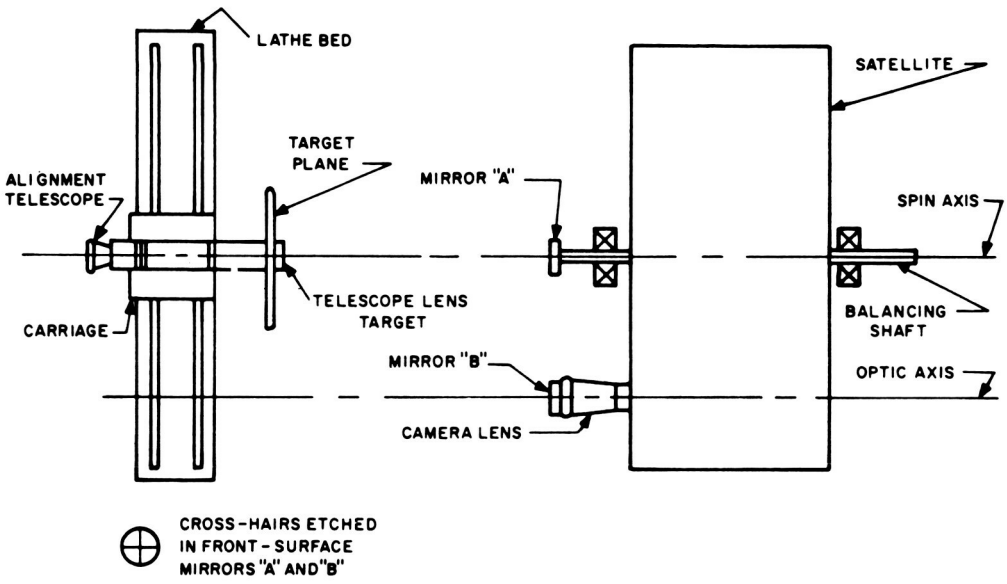

(a)

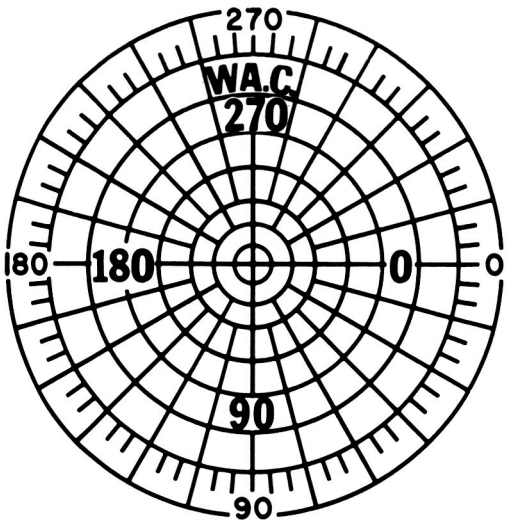

Target Line Width	0.200 inches
Radial Increments	15 degrees
Concentric Circle Increments ($\frac{\theta}{2}$)	5 degrees*
Radius of Largest Circle	11.903 inches
Angular Increment of Largest Circle ($\frac{\theta}{2}$)	35 degrees

*Except smallest circle, which is 3 degrees and the next, which is 6 degrees and 19 minutes.

(b)

FIGURE 44.—(a) TV camera alignment fixture; (b) polar-chart target for camera No. 2.

TABLE 5.—CAMERA SYSTEM ALIGNMENT TEST DATA

Parameter	Camera No. 1 (Narrow Angle)	Camera No. 2 (Wide Angle)
Total deviation of line of optical axis from line of spin axis	44′0″	27′32″
Displacement of vidicon cross-hairs from center of target	43′0″	7°0″
Displacement of optical axis from zero reference line	290°	170°

clockwise direction (viewing the bottom of the satellite) from zero reference line engraved on the satellite baseplate.

North indicator system.—The sensitive axis of the reference sensor had to lie in the vertical plane which passes through the spin axis and the 340° reference line on the satellite baseplate. The sensitive axes of the remaining eight sensors had to be evenly spaced around the periphery of the vehicle such that the angular displacement of each axis was a multiple of 40°+45′ when referred to the 340° sensor. The procedure for meeting these requirements was as follows.

By means of the collimating telescope and lathe bed arrangement employed during the camera alignment check, the satellite was oriented such that its spin axis was parallel to the axis of the lathe and perpendicular to the line of sight of the telescope. The satellite spin axis and the horizontal line of sight of the scope both lay in the same horizontal plane. The satellite was rotated about its spin axis until the 340° scribe mark on the baseplate lay in the same horizontal plane with the line of sight of the telescope. The telescope was then moved along the lathe bed to a position where its field of view included the aperture plate of the 340° sensor. With the telescope so positioned, a fine rotational adjustment of the satellite was made such that the horizontal alignment reticle of the telescope was superimposed on the leading edge of the aperture slit and the sensitive edge of the sun cell inside the sensor housing. (The leading edge of the slit and the edge of the sun cell define the sensitive axis of the sensor.)

The vertical offset between the 340° scribe mark on the baseplate and the sensitive axis of the 340° (nominal) sensor was measured in the plane of the sensor's aperture plate. This offset distance combined with the radial distance from the spin axis to the plane of the sensor's aperture plate was used to calculate the true angular "look axis" of the 340° (nominal) sensor.

For the No. D–3 satellite this "look axis" was 340°10′. The apparent displacement from the physical location because of finite transmission time in the electronic circuitry is 20 (angular) minutes. The sun angle computer at each Command and Data Acquisition Station supplied, on punched tape, a "sun angle" relative to the 340-degree sensor. This value was transmitted to the NASA Space Computing Center at Washington, D.C., and there was converted to the angle referenced to the zero calibration on the satellite by the algebraic addition of the total displacement: −19 degrees 30 minutes.

With the accurate angular location of the reference sensor (340°) established, the relative location of the eight remaining sensors can be checked by recording the nine sequential north indication pulses on a high speed paper tape. Then, by using the leading edge of the 340° pulse or a reference, the "tape distance" is measured to the leading edge of the other eight sequential pulses. If these measured distances are even multiples of the "tape distance" equivalent of 40°± 15′ of satellite rotation the specified requirement is satisfied.

Horizon scanner.—The sensitive axis of the IR horizon scanner had to lie in a plane which intersects the satellite spin axis at an angle of 90°± 15′. This axis should also be oriented radially with respect to the spin axis although this need only be accurate to several degrees to insure that the scanner lens is inside the boundaries of the "window" provided in the side of the satellite. The procedure for meeting these requirements was as follows.

With the satellite positioned with its spin axis parallel to the axis of the lathe bed and perpendicular to the line of sight to the telescope, the satellite was rotated and the telescope moved along the lathe until the alignment cross-hairs in the telescope were centered on the front lens element of the scanner's optical system. A vertically oriented aperture slit was then positioned between the telescope and the sensor such that its center

lay on the line of sight of the telescope. The horizontal position of the slit was measured with respect to a fixed reference. A blackbody source of sufficient size to fill the scanner's field of view was then introduced behind the slit (between the slit and the scope). This vertically-oriented slit was then moved back and forth horizontally in a plane normal to the scope line of sight until it cut the center of the scanner field of view as determined by monitoring the output of the sensor. The horizontal position of the slit was again measured from the fixed reference.

The horizontal distance from the telescope line of sight to the center of the scanner field of view was then obtained from the two measured slit positions. This horizontal offset combined with the measured distance from the front lens element to the plane of the aperture slit determines the angular deviation of the sensor axis from a plane which passes though the center of the sensor optics and is normal to the vehicle spin axis. This "normalcy" error is given in the alignment and calibration booklet.[44] For the No. D-2 satellite this normalcy error was $+0° - 3'$.

Balancing.—The satellites were required to be dynamically balanced within 6 oz-in. The final balance came to within 2 oz-in.

Dynamic balance was accomplished by placing balance weights in two planes; one was located beneath the baseplate, and the other was the top of the vehicle. The satellite was designed to receive a 1-inch O.D. steel shaft completely through it, with collars for locking the shift. This allowed handling of the satellite in a horizontal position.

The balance machine was fabricated at RCA. With the spin axis horizontal, the satellite was driven through a flexible shaft from an electric motor with a pulley speed reducer to give the operating speed of 150 rpm. The two support bearings were hung by thin steel straps so that the bearings had a low resistance to deflection in a direction normal to the spinning axis. Each bearing was attached to the core of a linear differential transformer which was used in a CEC amplifier System "D," consisting of a 3-kc oscillator, a power supply, and a linear integrating amplifier. The movement of the core produced a linear output voltage at the amplifier and therefore this voltage (read from a voltmeter) was a direct function of bearing displacement.

The method of locating the angular position of the unbalance in one balance plane was to place a known unbalance in that plane in each of three positions, 120 degrees apart and recording the amount of unbalance. Knowing the initial unbalance, a vector diagram was drawn and the remaining unbalance (amount and location) was graphically determined. This process was repeated for each balance plane until the remaining unbalance was less than 2 ounce-inches.

The preliminary balance weights (brass plates) were placed within the vehicle. The final balance weights were secured to the outside of the vehicle by bolting those at baseplate locations and using epoxy adhesive to secure those required on top of the satellite.

THE GROUND COMPLEX

The Command and Data-Acquisition (CDA) stations.—The Command and Data-Acquisition stations were all essentially alike, although exigencies of the geographical locations required different groupings of equipment and minor changes in the station make-up. Each includes the following subsystems: program and command, video data reception, display and film recording, accessory picture data, magnetic recording, attitude and telemetry data processing, and calibration.

The two primary stations were located, respectively, at the Evans Signal Laboratory area of Fort Monmouth, New Jersey, and at Kaena Point, Hawaii. At Fort Monmouth, the command transmitters were located in the tower which supported the antenna, and were controlled remotely from a control panel located in the (AWA) building which housed the major equipment racks. The 108-Mc converters for the telemetry receivers were installed in the antenna feed pod, and the 14-Mc output cables were dropped down inside the tower. At Kaena Point, all of the equipment was installed in vans. However, no antenna programmers were supplied with the TIROS equipment, since these existed independently.

The secondary station comprised the prototype equipment developed for the ground station. This was installed principally within the main building of the Astro-Electronics Division of RCA, near Princeton, New Jersey, as a backup station for the Fort Monmouth installation, and as an experi-

mental station for obtaining evaluation data on the operation of the satellite. The RF equipment was located in a van adjacent to a new-type tracking antenna, about 1,000 feet north of the AED building.

The RF equipment in the van is similar to that at other stations except for the RF tracking receiver system. This uses three (Tapetone) 108–Mc converters, three R–390 receivers, and auxiliary IF amplifier phase detector units to drive the antenna servo amplifier. The "sun" receiver of the three 108 Mc units also is used to feed telemetry signals to the ground station telemetry recorder. The recording and control equipment is essentially identical to that used in the primary stations.

The tracking antenna, built by the General Bronze Corp., was mounted on a 20-foot pedestal and consisted of 13 "slow-wave" structure arrays for coverage of the three frequency bands used by TIROS. Eight elements provided 22 db gain in the 108–Mc beacon band and were also combined in a hybrid to provide azimuth-elevation error signals for automatic tracking. The single-element array provided 12 db gain in the 150–Mc band for the command transmitter. The servo system is capable of tracking to approximately ± 0.75 degrees.

The equipment rack installation at Fort Monmouth is shown in Figure 45. The 60-foot TLM–18 antenna at that station is pictured in Figure 46; the General Bronze antenna is pictured in Figure 47.

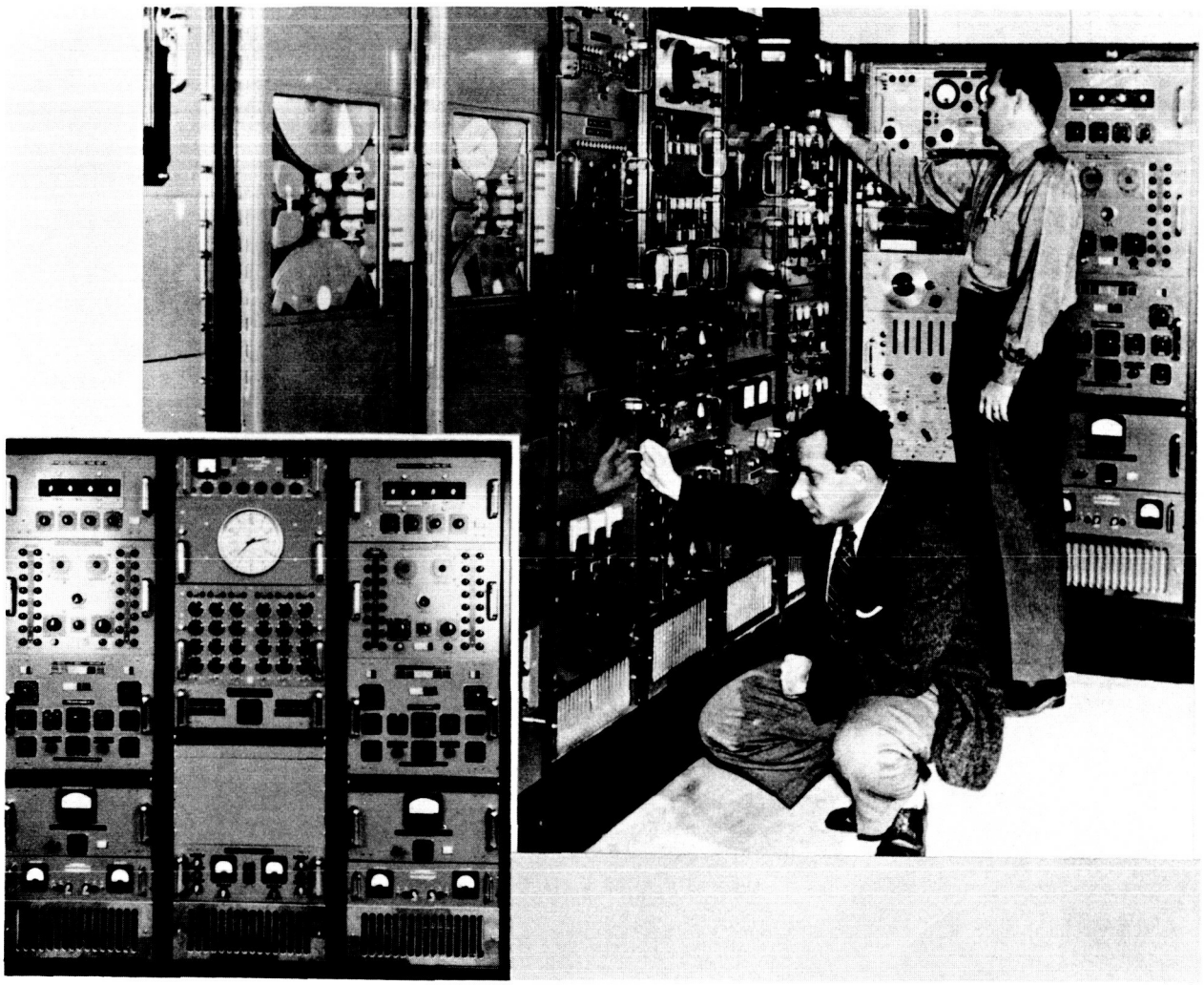

FIGURE 45.—The TIROS I command and data-acquisition station at Fort Monmouth, N.J., and (insert) the satellite programming racks, which are cut off at the right of the main picture.

Satellite programming and command subsystem.—Satellite-instrumentation functions were controlled from the CDA station by means of combinations of eight audio signals which amplitude-modulated the ground-based command transmitter's carrier. A program and command sequence could be set-up for automatic transmission from the ground for as long as 19 minutes. (The maximum time of contact with the satellite was 14 minutes; a chart showing the contact time per orbit appears in Figure 48.) The generation of these signals was controlled by the programmer, which afforded three modes of operation. In the "manual operate" mode (used only for test or emergency) each "tone" would be keyed "on" by manually depressing a push button. In the "manual start" mode, three sequences of events could be initiated in turn, each by depressing a single "alarm" pushbutton. Alarm I turned on the command transmitter carrier and could command direct pictures from either or both of the satellite cameras as selected. Alarm II commanded playback of either or both satellite tape recorders and also initiated the automatic setting of either or both vehicle clocks. Following tape playback, a second sequence of direct pictures could be commanded. Alarm III caused the clock-start command to be transmitted. In the auto-start mode, the above three "alarms" were automatically generated at preselected times determined by a master clock. A block diagram of the Programming and Command subsystem is shown in Figure 49.

Four decade counters were used to count the number of clock-set pulses transmitted to the

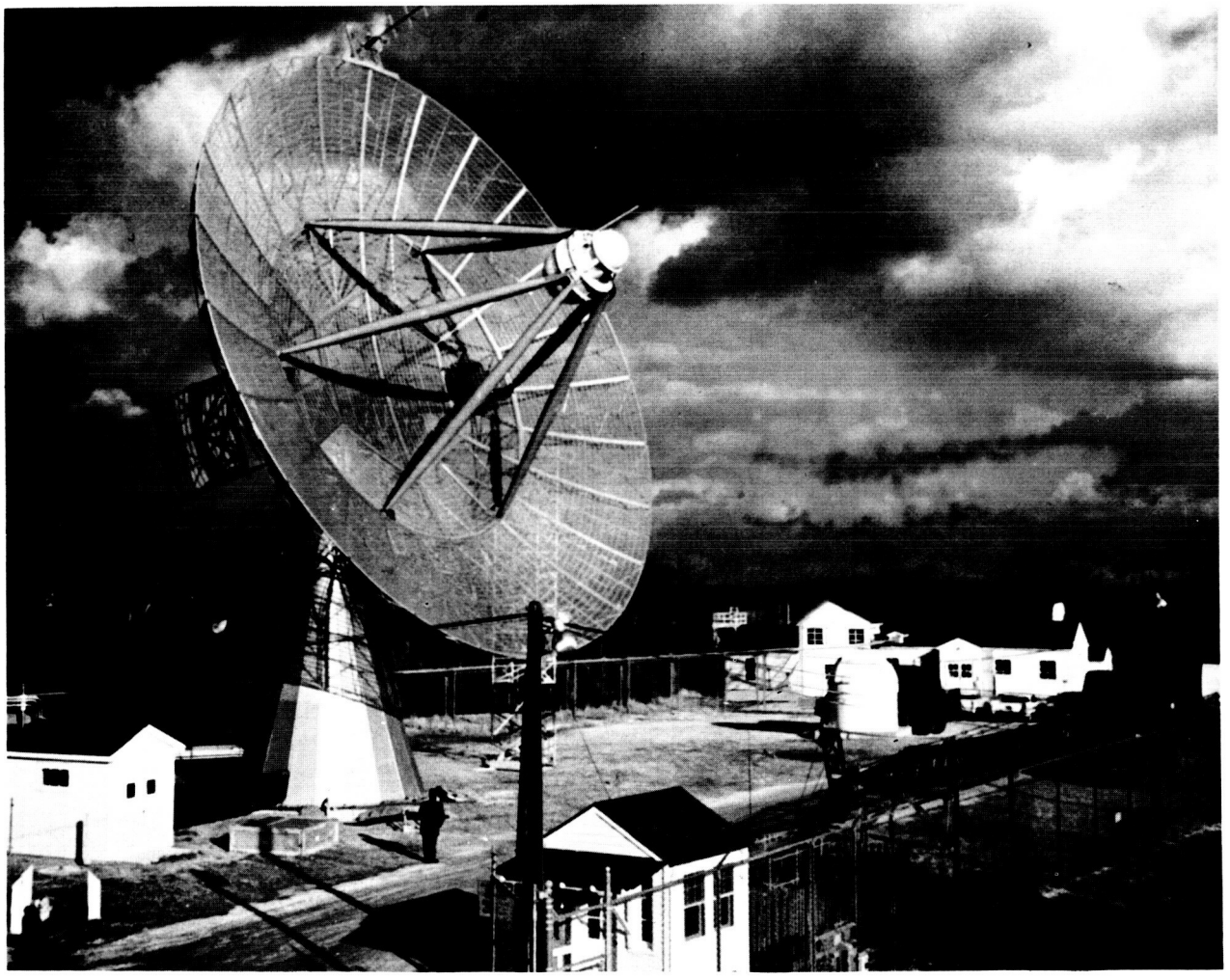

FIGURE 46.—The TLM-18 antenna at Fort Monmouth, N.J.

satellite and to terminate the pulse train when the previously selected number had been sent.

To provide greater reliability and versatility, two identical programmers were used. These could be set up for the same or alternate programs and either unit used to modulate the command transmitter in use. Two command transmitters (Collins 242F2) were installed for reliability and

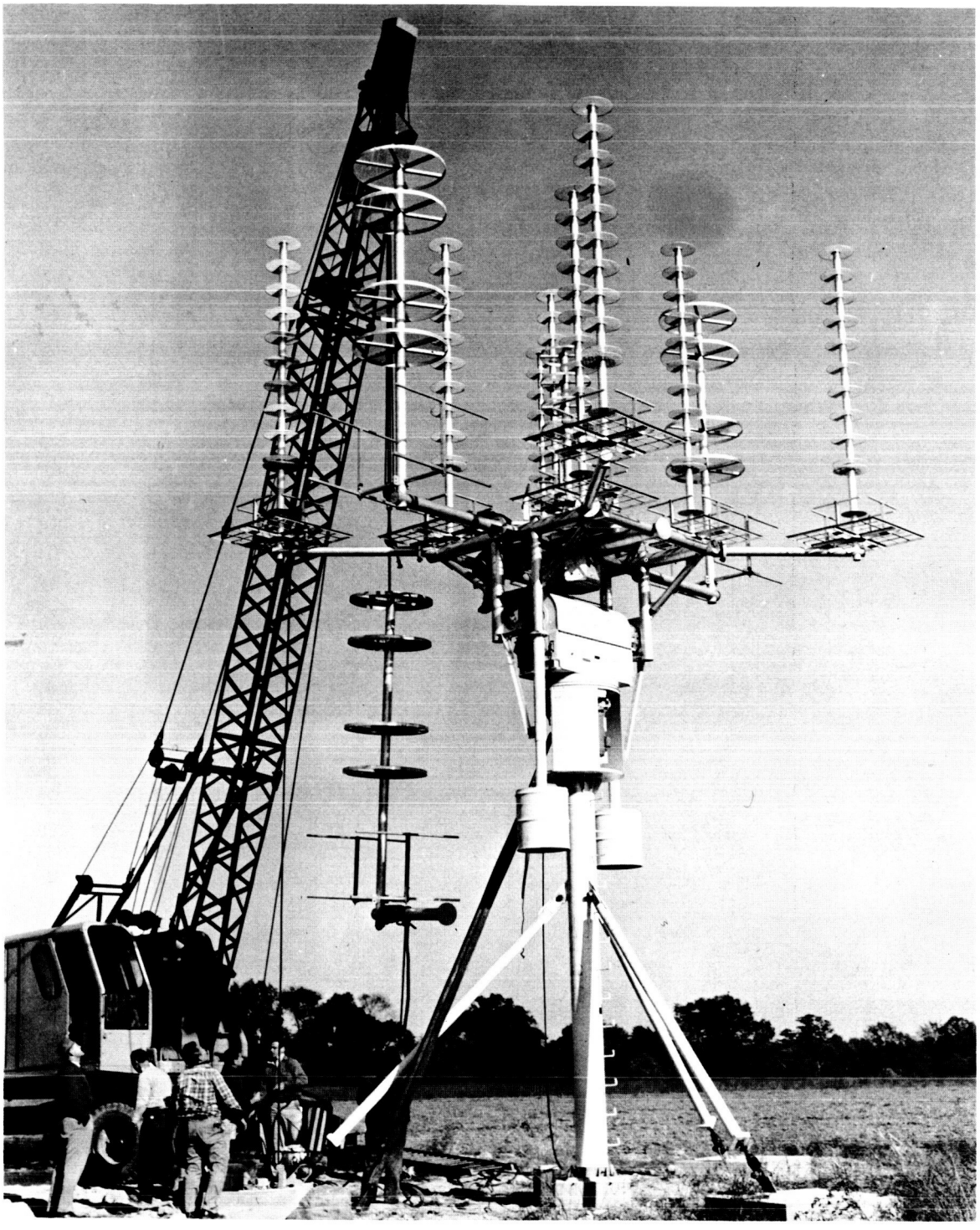

FIGURE 47.—Tracking antenna at RCA–AED, Princeton, N.J.

either could be selected to drive the helix transmitting antenna.

Video data reception.—The signal from the satellite TV transmitters was received by the TLM-18 antenna at each of the primary TIROS I ground stations. Separate probes gathered the vertically and horizontally polarized components of the signal and, after preamplification, these were connected to the inputs of two Nems-Clarke Model 1411 FM receivers. The receiver signal outputs were added together in a diversity combiner which proportioned the signals according to the relative receiver AGC voltage to achieve an output with high signal-to-noise ratio and an absence of nulls. The combiner output consisted of an 85-kc FM subcarrier with the video information and bursts of 10-kc subcarrier (sun pulses) for the north indicator subsystem. These two signals were separated by filters. The 85-kc subcarrier was next applied to a circuit which derived a gate signal for the camera shutter and a vertical sync pulse and was also applied to a demodulator circuit. The demodulator, recovered the video from the subcarrier by generating a pulse of fixed amplitude and duration at every zero crossing of the subcarrier and filtering the pulse train to obtain a smoothed voltage proportional to the momentary subcarrier frequency. The video was amplified and displayed on a kinescope. Synchronization of the kinescope sweep at the 250 cps line repetition

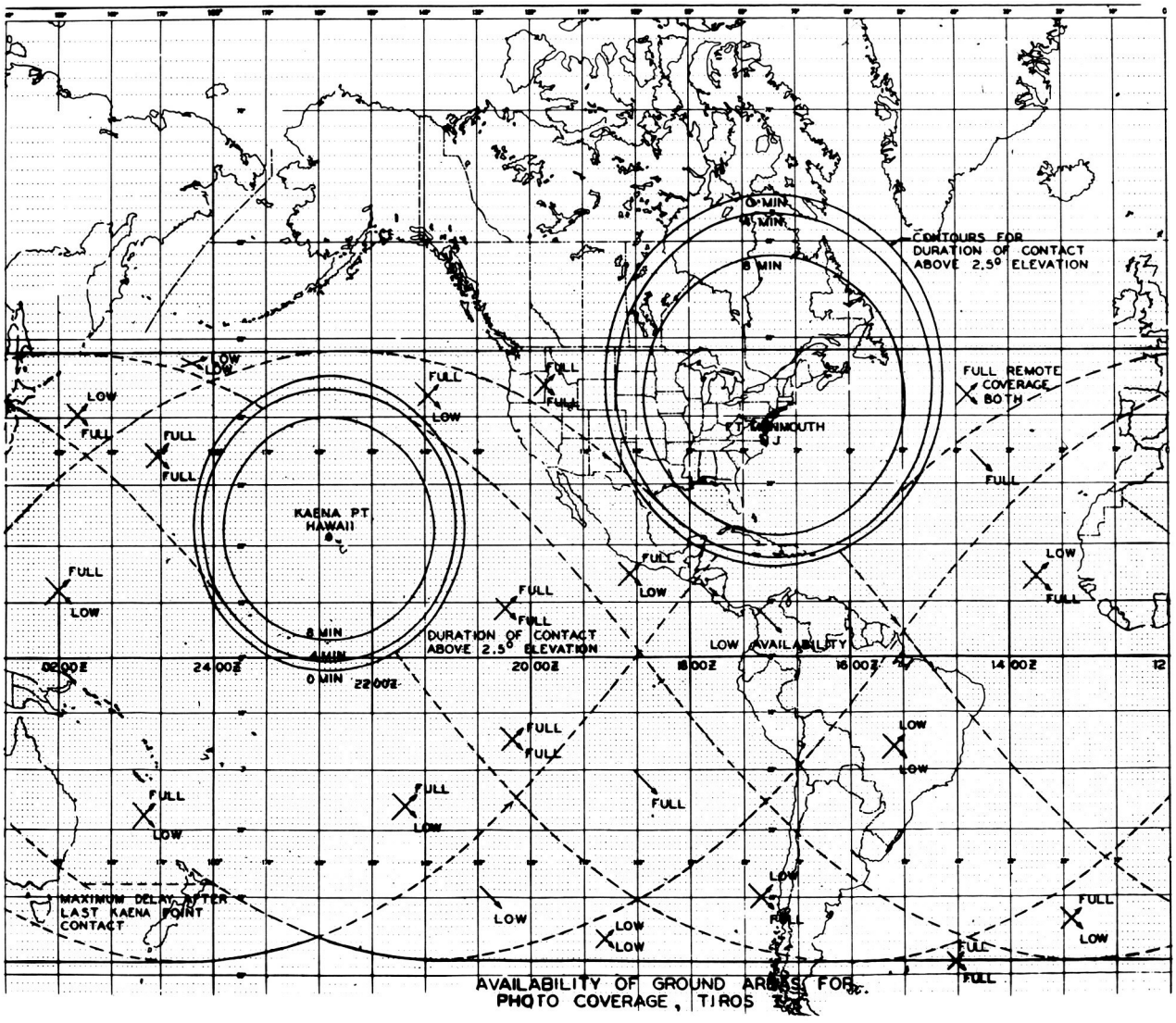

FIGURE 48.—TIROS I line-of-sight reception for Fort Monmouth, N.J., and Kaena Point, Hawaii.

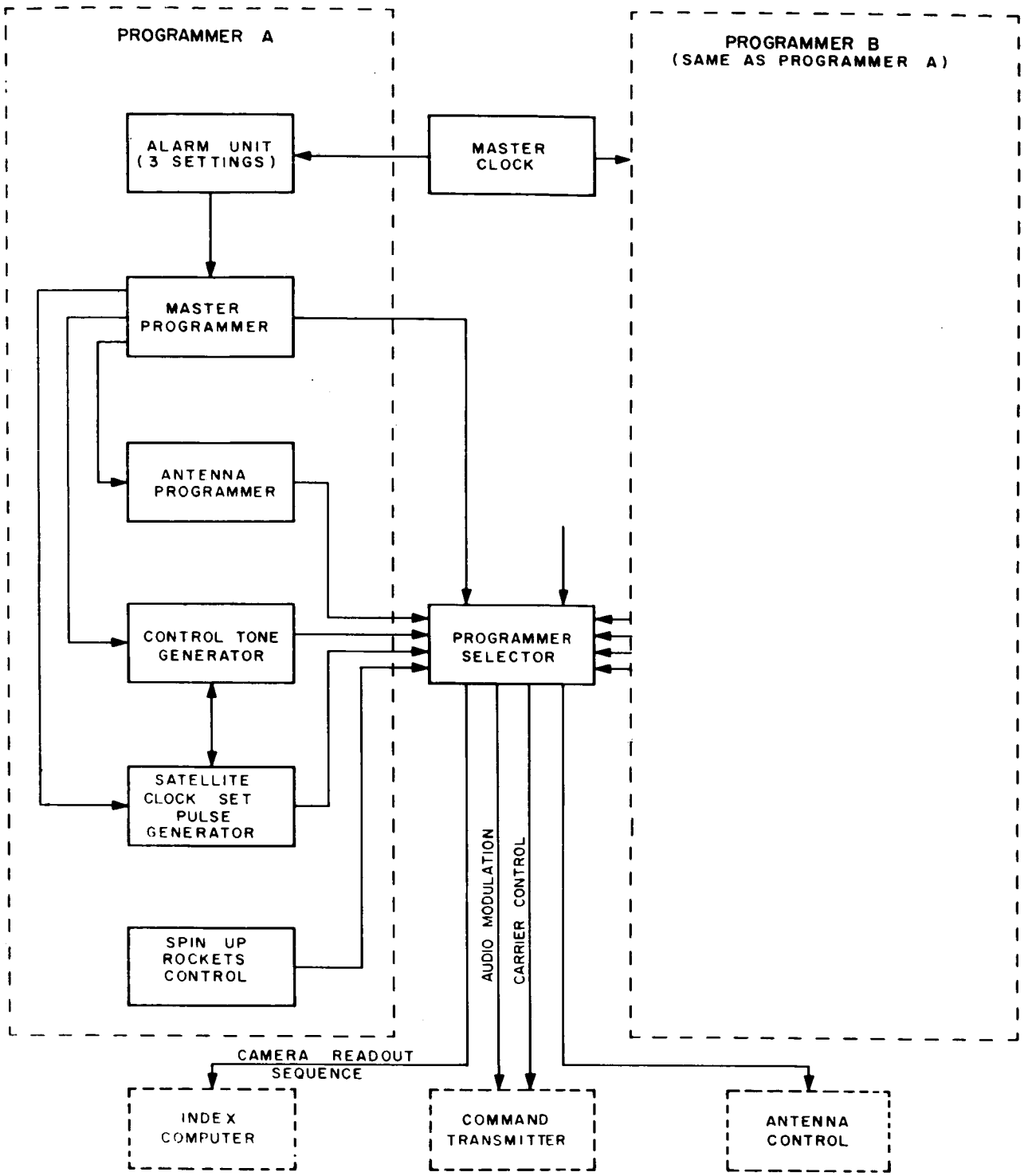

FIGURE 49.—Ground station programming and command subsystem.

rate was accomplished by a "flywheel" sync circuit which was free-running at about 250 cps, and an error sensing loop which corrected the frequency in proportion to the phase error.

The sun angle number, similarly recorded with each picture, was computed by digital circuitry from the timing of the 10-kc "sun pulse" subcarrier bursts relative to the 85-kc video subcarrier. This computation was also affected by whether the pictures were in the direct or tape mode. The length of each sun pulse was measured to identify it as a short, medium, or long type. The coding formed by successive sun pulses uniquely identified the activated sensor, in terms of its angular distance from a baseplate reference point. The refinement of the measurement to $\frac{1}{16}$ degree was done by dividing the time interval between the leading edge of the subcarrier and the leading edge of the first sun pulse (t_a) by the time interval between the leading edge of two successive sun pulses (t_b) and multiplying by 40 degrees.

Video display and film recording.—The specially-developed, ruggedized, kinescope used to to display the video was mounted at the front of the display unit so that the face of the tube was visible through a viewing hood. A panel was mounted on each side of the kinescope with illuminated legends and numbers to indicate station identification orbit number, camera number, direct or tape, index number, and sun angle. This arrangement is shown in Figure 50. A dichroic mirror at a 45 degree angle mounted between the kinescope and viewing hood reflected a portion of the light upward to the camera. A conventional photographic objective lens and solenoid-activated shutter photographed the kinescope and associated display on 35-mm film, 100 feet of which were contained in a motor-driven magazine.

Accessory picture data processing.—The picture source and index number information photographed and recorded on magnetic tape were controlled by digital circuitry, as was the sun angle information similarly presented. The source information was derived from outputs of the command programmer which indicated in which mode the vehicle was being commanded to transmit pictures. These source signals were delayed by about 25 seconds to allow for the warmup and hold on delays of the vehicle control circuitry. The index number was generated by a binary counter

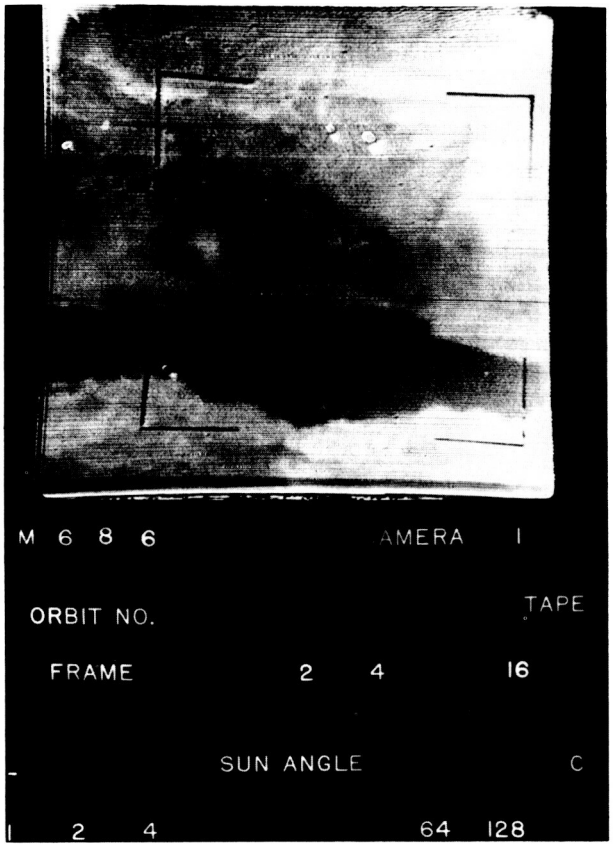

FIGURE 50.—TIROS I video monitor display with photograph.

which was triggered by a pulse derived from the vertical sync pulse at the beginning of each 2-second sweep. The 6-binary-bit index number and the three bits indicating mode and camera were stored in a 9-bit shift register from which parallel outputs drove the lamps to be photographed with the kinescope display, and a serial output keyed a pair of subcarrier oscillators to record the source and index on magnetic tape.

Magnetic recording.—Two Ampex Model FR104 tape recorders were used to record the pictures transmitted from the satellite and the accessory information. One-half-inch-wide tape was used at a running speed of 60 inches per second. Each machine had record and reproduce heads for four-track operation. The first channel of both machines recorded video subcarrier with direct electronics. The second channel of both machines recorded the index-number tone bursts with direct electronics. The third channel of one machine recorded the result of the sun-

angle computation in encoded tone bursts, while the same channel of the other machine recorded the bursts of 10-kc subcarrier carrying the "raw" north indicator of sun-angle data. Both of these used "direct" electronics. (The fourth channel of each machine was provided with FM electronics, but was not utilized for TIROS I.) The tape recorders were remotely controlled to start automatically on a signal from the command programmer equipment at the beginning of the programmed interrogation of the satellite.

Attitude and telemetry reception.—The signals from the satellite beacon transmitters were received on the ground by separate horizontal and vertical antenna probes for polarization diversity and heterodyned down to about 14 Mc by two Tapetone frequency converters. Each of the converters fed two R390 receivers, one converter for each beacon frequency. The two receivers on the same frequency had their AGC and signal circuits interconnected to provide diversity combination. The receiver outputs were used for recording both telemetry and attitude data.

The telemetry data, when present, consisted of a subcarrier tone on each beacon channel frequency modulated between 1,200 cps and 1,400 cps. The tones were demodulated by FM preamplifiers driving a two-channel Sanborn paper-chart recorder. The attitude data was comprised of 3-kc subcarrier bursts of about 100 milliseconds' duration. The data was embodied in the elapsed time between successive subcarrier bursts, and was amplified, filtered, demodulated, squared, and used to generate a single attitude pulse for each subcarrier burst.

Three digital decade counters, each with a capacity of 10^4 counts, were used to count a 1-kc clock frequency. Each attitude pulse caused the clock count to transfer from one counter to the next and initiated a readout of the counter just stopped. The number contained therein was equal to the number of milliseconds between pulses. The binary-decimal numbers were converted to teletype code and punched onto paper tape for transmission via standard teletype equipment.

Events recording.—The proper functioning of the two command programmers was verified and the identification of received pictures facilitated by a 20-channel strip-chart pen recorder. Individual channels were connected to record the presence of each command signal as well as the camera shutter pulse and a ten-second time marker.

Calibration.—Equipment installed at each primary CDA station to enable checkout and adjustment of the TIROS I ground equipment included an FM signal generator, video test-pattern generator and subcarrier oscillator, audio oscillator, frequency counter, interconnecting patch-panel, dummy RF load, reflectometer, and video monitor oscilloscope. Additional portable trouble-shooting equipment was provided.

The satellite tracking system.

The TLM–18 tracking antenna.—Automatic tracking of TIROS meteorological satellites required a high-speed antenna with gain, acquisition ability and wide bandwidths for handling large quantities of video and telemetry data over long distances.[45]

On the 5,000-mile Atlantic missile range, polarization characteristics of a missile's carrier signal change rapidly as flight path changes and distance increases. Also, blind spots in telemetry coverage occur at various locations when the missile grazes the horizon. To solve both of these problems and still maintain good data recovery over the entire range, an auto-track feed was developed for the Radiation, Inc., TLM–18 high-gain circularly polarized antenna. The TLM–18 antenna at Fort Monmouth, N.J., is shown in Figure 46.

The new antenna system was designed to lock on its target and track without manual assistance, using the satellite's carrier wave signal. Data readout on the 216–Mc to 260–Mc video data band and monitoring at the 108–Mc telemetry band was a primary function of the system. Polarization selection was possible from a remote control console, with polarization diversity combining included. Sixteen data outputs were thereby made available.

Even though a satellite is equipped with a so-called circularly polarized radiator, signals received by a tracking station may not be circularly polarized, but may vary from circular right, through linear to circular left sense. This is often caused by the signal grazing the horizon and being changed by its proximity to the ground. A single terminal, circularly-polarized antenna will reject circular polarization opposite to that for which it is designed—a right hand helix will reject a left hand signal to the extent of 40 to 50 db.

646–770 O—64——5

To prevent polarization modulation to the extent that the antenna output signals are below receiver threshold for too long a period, causing loss of target, polarization diversity was desired. The antenna has output terminals so that either linear or circular polarization is available. These terminals are then utilized for a polarization diversity system, and information is made available for automatic tracking by modulating the target's carrier signal.

The method used to produce circular polarization is to orient two equal linear components at right angles to each other and introduce 90 degrees of phase shift between them. Two orthogonal probes, mounted in the skin of a waveguide, excite the circular waveguide cavity to generate two TE modes. Horizontal and vertical wave components are separately derived by this arrangement. The basic feed structure and circuitry are shown in Figure 51. Typical secondary patterns of the video data feed are shown in Figure 52 (made with a 1/12 scale model).

A unique method of producing a conically scanning main beam was employed. Conventional methods use eccentric rotation of all part of the antenna to deflect the beam off-center. The auto-track feed employs instead a hemispheric dielectric lens spinning at 600 rpm in front of a section of circular waveguide mounted in an assembly five feet in diameter. It is supported at the parabola's focal point by six fiberglass spars transparent to radio waves of the telemetry frequency.

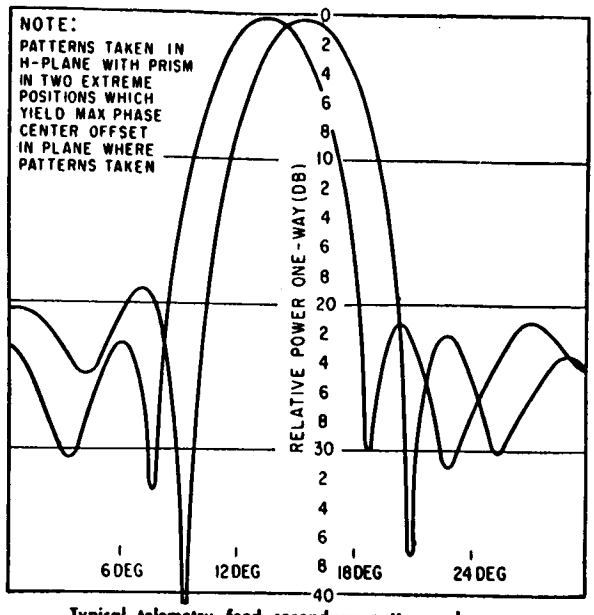

Typical telemetry feed secondary patterns show crossover depth of 1 db, maximum side lobes approximately 19 db down

FIGURE 52.—Secondary patterns of typical feed of the TLM-18 antenna.

The system obtains automatic tracking information through position amplitude modulation of the target's carrier signal. This provides satellite location and an error signal for giving off-track angles of properly referenced phase to drive the antenna-pointing servo motors. These controlling servos obtain this information from the rotating lens which conically scans the antenna pattern's main lobe. Main-lobe scanning provides a linearly increasing error signal for increasing angles from the crossover axis. Gain at

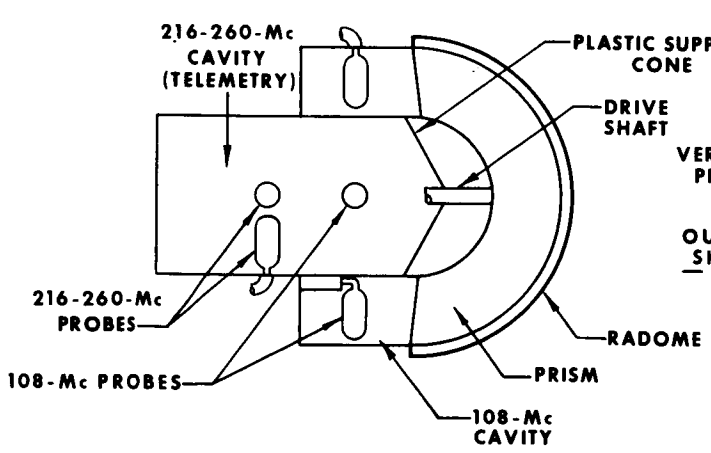

(a) Cross-section of the TLM-18 antenna basic feed structure.

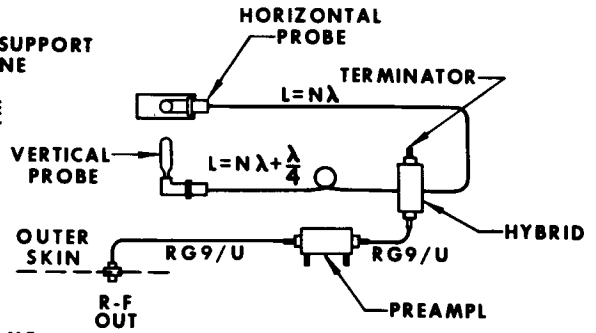

(b) Schematic diagram of the antenna feed.

FIGURE 51

the crossover point is high, with crossover level of 1 db from main lobe maximum quite adequate for the servo system.

The lens, rotating at 600 rpm, supplies a 10-cps error signal whenever the antenna is off-target. A comparison is made between the 10-cps signal created by scanning the target, and a pair of signals of the same frequency but in quadrature with each other created by a reference generator attached to the rear of the lens shaft. Magnitude and phase of the target signal are compared to these reference signals in a demodulator to produce two independent dc voltages, one for azimuth control and one for elevation control. Polarity and magnitude of these voltages are such that the correct torques are developed for returning the antenna to the target.

System data flow is indicated in Figure 53. The signal received by the antenna is divided by the hybrid into two preamplifier channels. The i-f amplifiers in the tracking loops have high AGC gain, so that amplitude variations due to signal fading do not cause significant variation in the tracking error. This i-f amplifier detected output will not vary more than 3 db when there is a 60-db variation input signal, when constant modulation index is used. The phase demodulator synchronously detects the azimuth and elevation error signals, using the scan reference voltages for comparison. When the system is in the automatic track mode, secant correction is employed in the azimuth servo control loop, since error signal sensitivity varies directly as the cosine of the elevation angle.

To improve response characteristics of the power drive equipment, an inner loop feedback (shown as tachometer feedback) is used.

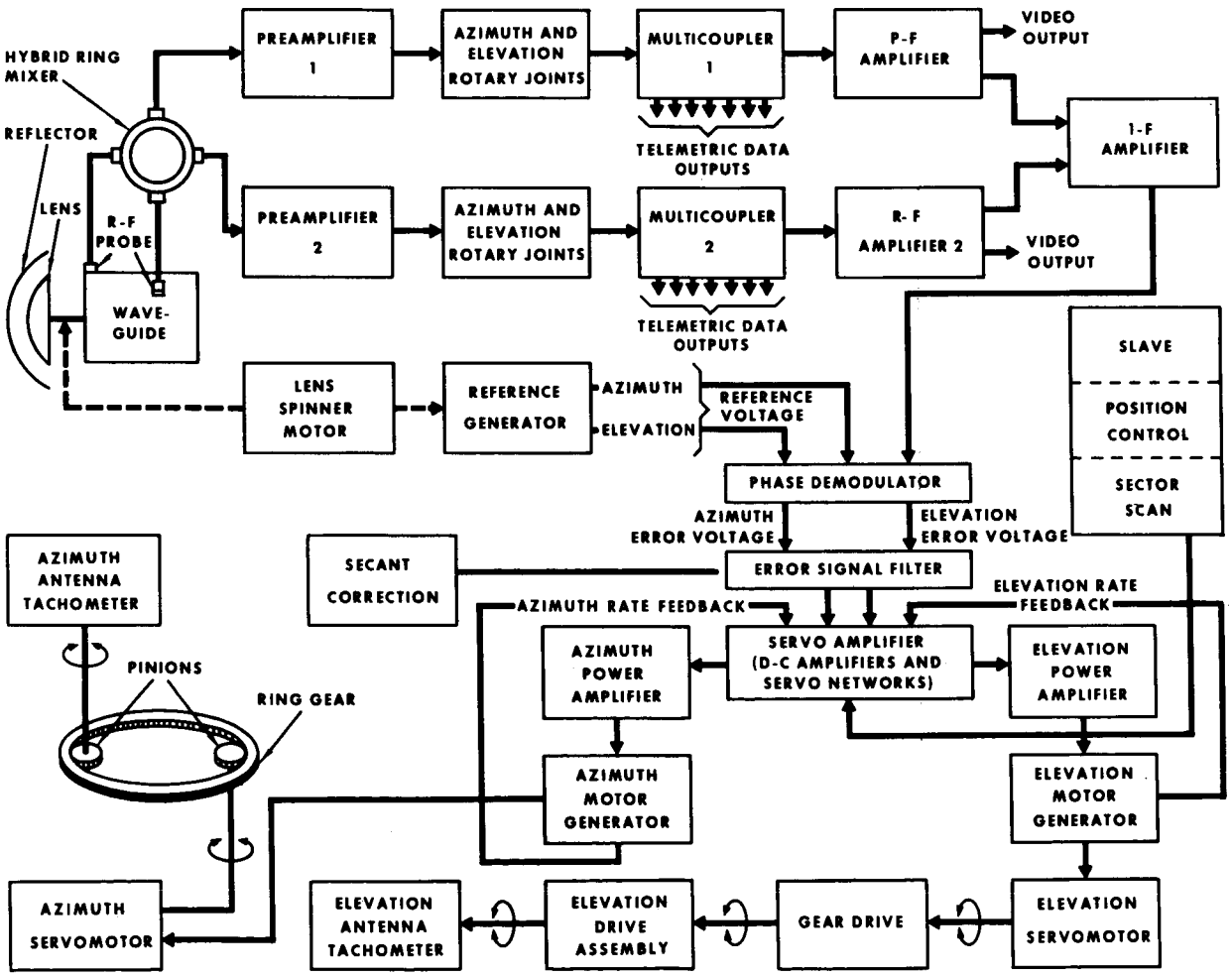

FIGURE 53.—The TLM-18 antenna system data-flow diagram.

Figure 53 shows only a single servo channel. Both servo systems are identical, except for secant correction on the azimuth channel. A Type-1 system, the servo drive motor has a transfer function representing a single integration.

Torque limiting is provided by a voltage derived from motor armature current, and prevents the system from requiring excessive motor torques.

A summary of the electrical characteristics of the TLM-18 antenna is given in Table 6.

The Minitrack network.—The NASA Minitrack network is the primary tracking system for scientific satellites for the United States.[46] It includes 10 primary stations extending around the world (3 in the United States, 1 in the British West Indies, 4 in South America, 1 in Australia, and 1 in South Africa). A complete, full-time teletype communications network connects these stations with the NASA Space Operations Control Center and the NASA Space Computing Center, Goddard Space Flight Center. All stations utilize Mini-

TABLE 6

TLM-18 Antenna Characteristics

Parameter	Value
Reflector Diameter	60 feet.
Frequency Ranges	106 to 110 Mc; 216 to 260 Mc.
Gain Above Isotropic.	22 db min at 108 Mc; 28 db min at 216 to 260 Mc.
Polarization	Horizontal, vertical, right-circular, and left-circular. Available for both frequency ranges and remotely selected 216 to 260 Mc.
Circularity-Axial Ratio.	1.26 or less.
Scan Frequency	10 cps.
Beam Width, 3-db Points.	10.5 degrees at 108 Mc; 4.6 degrees at 216 to 260 Mc.
Scanned Cone, 3-db Points.	12 degrees at 108 Mc; 6 degrees at 216 to 260 Mc.
Side Lobes	18 db.

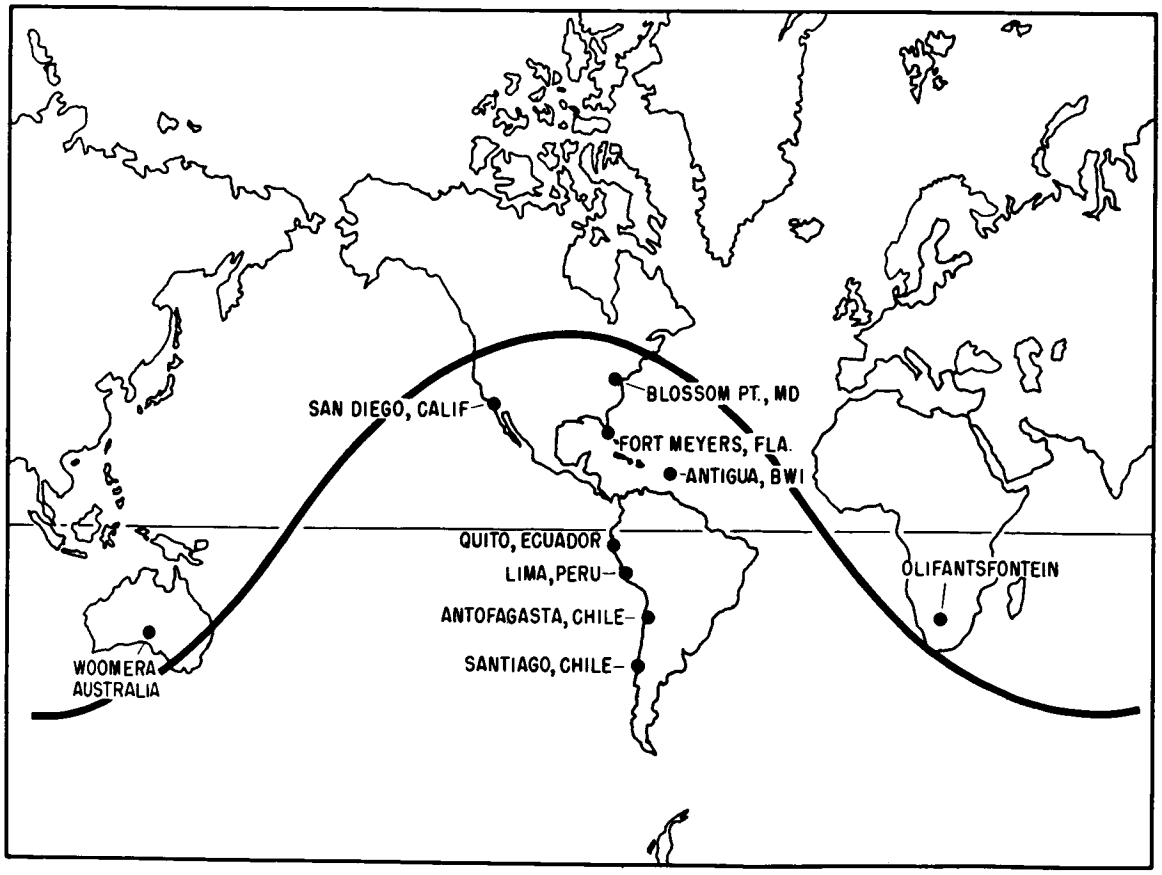

FIGURE 54.—The world-wide Minitrack network (showing TIROS I orbit).

track radio-interferometer tracking equipment, Telemetry receiving and recording equipment, and communications equipment. By virtue of the Minitrack equipment, each station is self-acquiring, and needs no precise station predictions to enable it to operate. Supplemental equipment to allow tracking of foreign or other non-standard satellites emitting radio signals, is included at each station. A map of the Minitrack locations is shown in Figure 54. This network was initially established during the IGY to track satellites launched southeast from Cape Canaveral at inclinations of about 35°. Station placement was made on this basis from 32.5° South latitude to 38° North latitude, providing maximum coverage for satellites in such orbits. Present-day operations allow satellites to be fired northeast from Cape Canaveral, at inclinations of over 50°, requiring additional stations at higher latitudes to provide adequate coverage.

Various other stations under the direct control of NASA, the Department of Defense, and other U.S. agencies, and the facilities of other countries can be added to the total capabilities of the NASA Minitrack Network.

The Minitrack system is designed to acquire and track earth-orbiting satellites which contain a beacon transmitter radiating sufficient power at frequencies between 107.910 and 108.090 Mc. The basic system accuracy is 20 seconds of arc and one millisecond of time. Low satellite power, and the relatively unknown effects of natural phenomena such as ionosphere, atmospheric density, the earth's exact size and shape, perturbations caused by natural heavenly bodies, etc., have prevented reaching the 20 seconds of arc as yet. As the effects of natural phenomena are formulated and satellites with greater power are placed in orbit, operational tracking can be fully expected to reach the system accuracy. Operational tracking

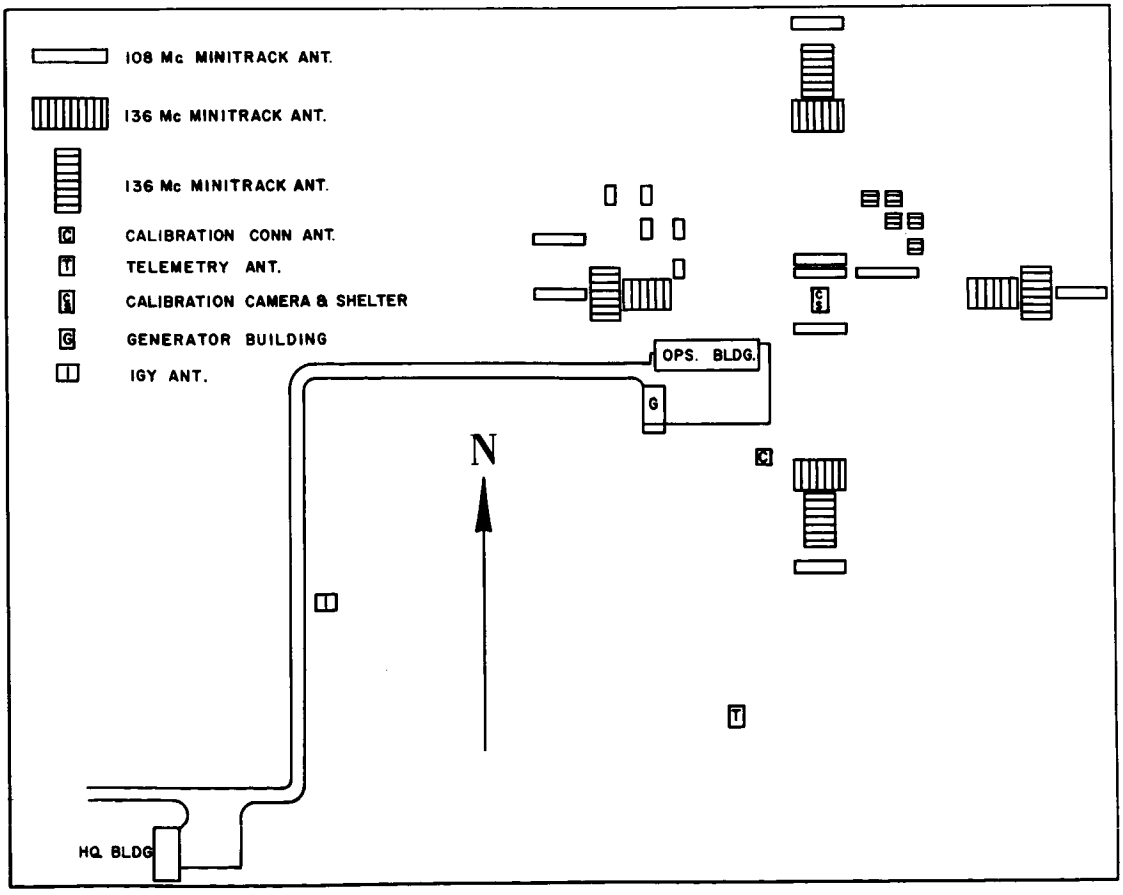

FIGURE 55.—Layout of a typical Minitrack station (Blossom Point, Md.).

accuracy under present conditions is 150 to 200 seconds of arc. A typical station layout at Blossom Point, Maryland, is shown in Figure 55.

The Minitrack stations throughout the world and the NASA Space Operations Control Center (SpaceConn) are linked by a communications system which has as its function the transmission of tracking and telemetry data, operational and administrative traffic, and technical information required in the exploration of space. From NASA SpaceConn, the communications network is extended to link the Space Computing Center, the U.S. missile launching ranges, the DOD space operations agencies (Spacetrack, Space Surveillance, BRL), the military teletype systems, and other agencies and organizations engaged in cooperative efforts with the NASA.

In connection with Project TIROS, the NASA communications network was expanded by the addition of two full duplex teletype circuits from NASA SpaceConn to Kaena Point, Hawaii, one of which is routed by way of AFMD, Palo Alto, Calif. A half-duplex teletype circuit was connected directly to the U.S. Weather Bureau's Meteorological Satellite Laboratory, Suitland, Maryland, and a half-duplex teletype circuit to the primary data-readout control station at Fort Monmouth, New Jersey, with a drop-off to the secondary data readout and control station near Princeton, New Jersey.

THE TIROS I LAUNCHING VEHICLE

The TIROS I launch vehicle (Thor-Able) was a combination of three stages. The first stage consisted of a standard Thor without the AC Spark Plug guidance system. The second stage consisted of an Aerojet-General AJ10–42 propulsion system, a forward-located equipment compartment housing a Bell Telephone Laboratories radio guidance system, a flight controller, instrumentation, power supplies, and a spin table for the third stage. The third stage consisted of an Allegany Ballistics Laboratory (ABL) X248–A7 solid propellant rocket engine and the satellite payload. The third stage was enclosed by a fairing, attached to the second stage, which was jettisoned during second-stage powered flight. An outline drawing of the assembled rocket and satellite is shown in Figure 56.

The first-stage rocket.—The standard Thor SM–75 missile airframe was modified structurally to incorporate additional stages and to remove the standard missile guidance equipment and the re-

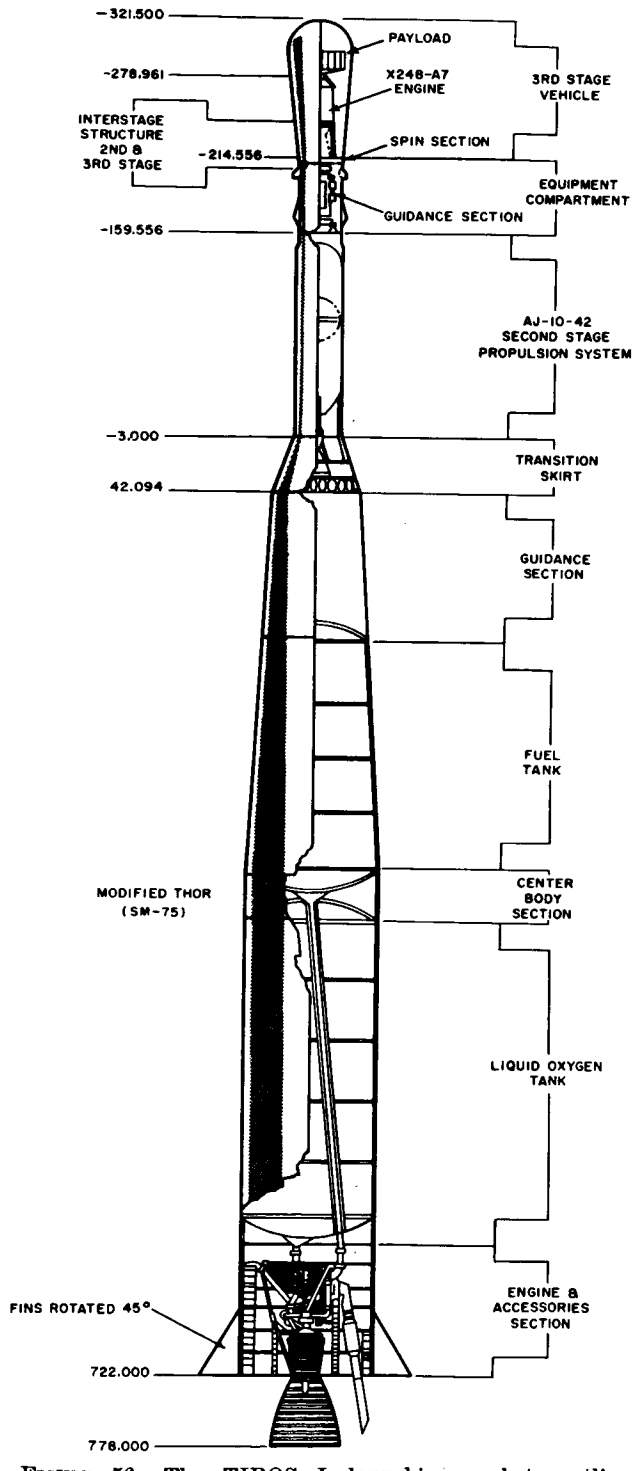

FIGURE 56.—The TIROS I launching rocket, outline drawing.

entry vehicle. A transition skirt was added to the forward section to accommodate the second stage vehicle. Flight control of the first stage was accomplished by a conventional flight controller (CEA) and the BTL guidance system located in the second stage; gain and shaping network modifications were added to compensate for the changes in airframe dynamic characteristics caused by the addition of the upper stages. The pitch and roll programs of the standard flight controller were modified to meet the requirements of the mission; programming was accomplished in the conventional manner. The control reference gyros were identical to those of the standard missile.

First-stage propulsion.—The first-stage propulsion system was the Thor SM–75 liquid bi-propellant (liquid oxygen and RP–1) missile system, and consisted of the gimbal-mounted R/NAA MB–3 main engine, two vernier engines, pressurization system, missile tanks, and associated plumbing.[47] See Figure 57.

The specified characteristics for this Thor system are: sea-level thrust main engine (approx.), 150,000 lb; main-stage burning time (approx.), 160 sec; vernier-engine thrust, each (approx.), 1,000 lb; total first stage weight (approx.), 106,000 lb.

First-stage telemetry.—One pulse-duration-modification/frequency-modulated (PDM/FM) telemetry set was installed in the first-stage vehicle. This set provided 28 channels of data with 2 channels for synchronization. The system samples data sequentially at a rate of 30 times per second and transmits the information to ground receiving stations by means of a frequency-modulated (FM) signal. The major items of information transmitted by the telemetry system have been given in detail elsewhere.[48]

The second-stage rocket.—The second stage consisted of an equipment compartment added to its forward end, and a transition skirt added to the aft end of the Aerojet-General Corporation propulsion unit. In addition, a jettisonable aerodynamic nose fairing extended forward from this stage to cover the third stage and payload. The equipment compartment contained the guidance and control systems, instrumentation and telemetry equipment, and electrical power supplies.

Second-stage propulsion.—The Aerojet-General Model AJ10–42 propulsion system was used on the second stage.[49] This system employed inhibited white fuming nitric acid (IWFNA) and unsymmetrical dimethyl-hydrazine (UDMH) as hypergolic propellants. Shutdown is initiated by a signal from the guidance system. The principal second-stage system specification values are: thrust (vacuum), approx. 7,800 lb; burning time, approx. 115 sec; total second stage weight, approx. 4,800 lb.

The Model AJ10–42 rocket propulsion system consists of a regeneratively-cooled rocket thrust chamber assembly mounted on a gimbal, propellant systems, helium pressurization system, interconnecting plumbing, gimbal actuation system, roll

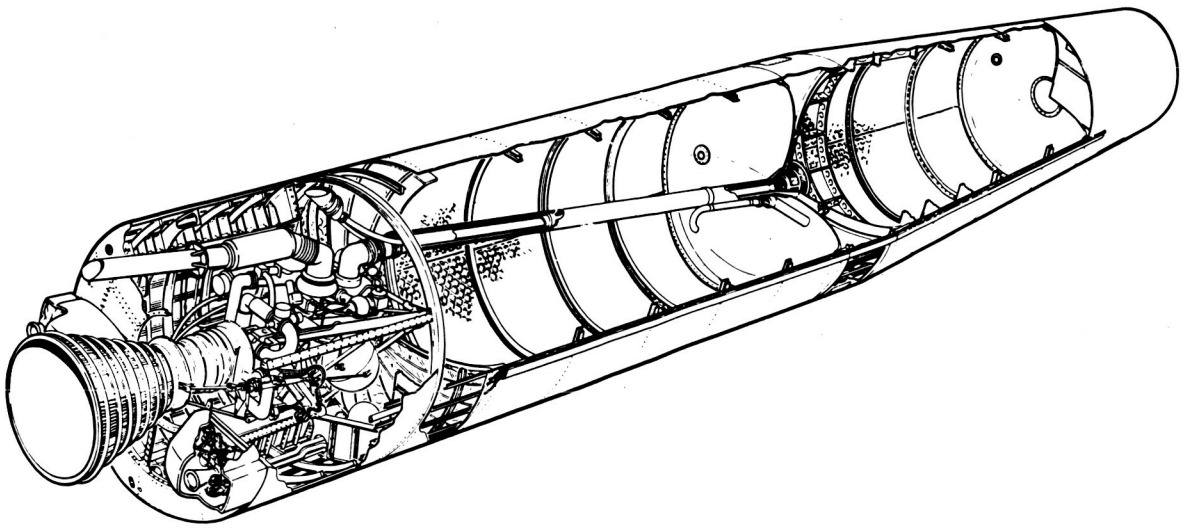

FIGURE 57.—The Thor rocket Model SM–75 (modified) first stage.

control system, aft transition section, destruct system and necessary airframe structures. See Figure 58. Ignition occurred when the propellants were injected into the thrust chamber by a helium pressurization transfer system. Shutdown was initiated by a signal from the guidance system.

Second-stage control.—Flight control of the second stage was by means of a modified SM–75 con-

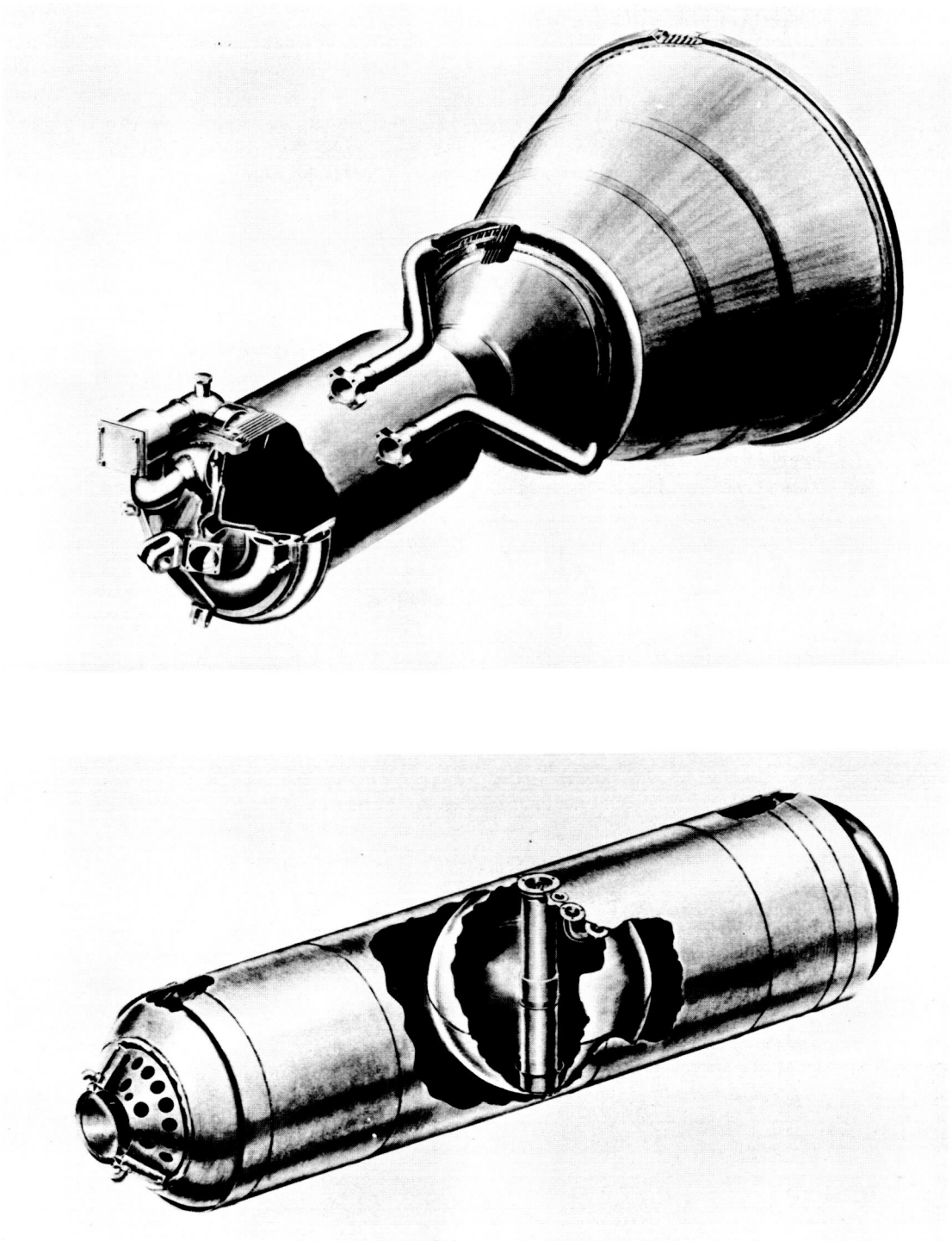

FIGURE 58.—The Aerojet-General rocket Model AJ10–42 second stage.

trol electronics assembly with pulse torquing of the control gyros by the guidance system. Pitch and yaw control was achieved by gimbaling the second stage thrust chamber with hydraulic valve actuator assemblies. Roll control was obtained by discharging helium from a pressurization tank through four roll jets located at the periphery of the spin table.

Second-stage telemetry.—The telemetry system on the second stage consisted of a PDM/FM set identical to the one employed on the first stage.

Stage II/III interstage and spin table.—A spin table was attached to the forward end of the equipment compartment of the second stage. This table consisted of a support structure, a ball bearing, and a monocoque magnesium cone. A frame around the bearing insures adequate hoop stiffness and provides a seat for the cone. A structural ring attaches the bearing to the forward end of the equipment compartment of the second stage. This structure also supports the third stage/payload fairing.

The monocoque cone is divided into four segments to provide a four petal structure similar to the first/second stage transition skirt. Each petal is hinge-mounted at the aft end of the bearing frame which rotates about the missile spin axis. The forward end of each petal is designed to accept the third stage engine. The four petals which engage the third stage engine are retained by a tension strap consisting of two semi-circular segments held together by two diametrically opposed explosive bolts which are released, on command, to allow separation of the third stage vehicle. See Figure 59.

The third stage motor and payload are spin-stabilized. Spin is accomplished by rockets attached to the spin table. The four petal, conical structure is opened by centrifugal force of the spin table, thereby permitting wide angle clearance for third stage separation. Provisions are incorporated to provide torque restraints on the spin table prior to spin-up.

Six Atlantic Research Corporation 0.6 KS–40 rockets and two 1.0 KS–40 rockets are mounted on the spin table. These are ignited by the BTL discrete command two seconds before SECO. These rockets impart a spin rate to the spin table (about 120 rpm) for stabilization of the third stage and payload after separation. Just prior to SECO, a set of rockets was fired to spin-up the spin table joining the third-stage engine to the second stage. This spin table consisted of a support structure, a ball bearing, and a monocoque

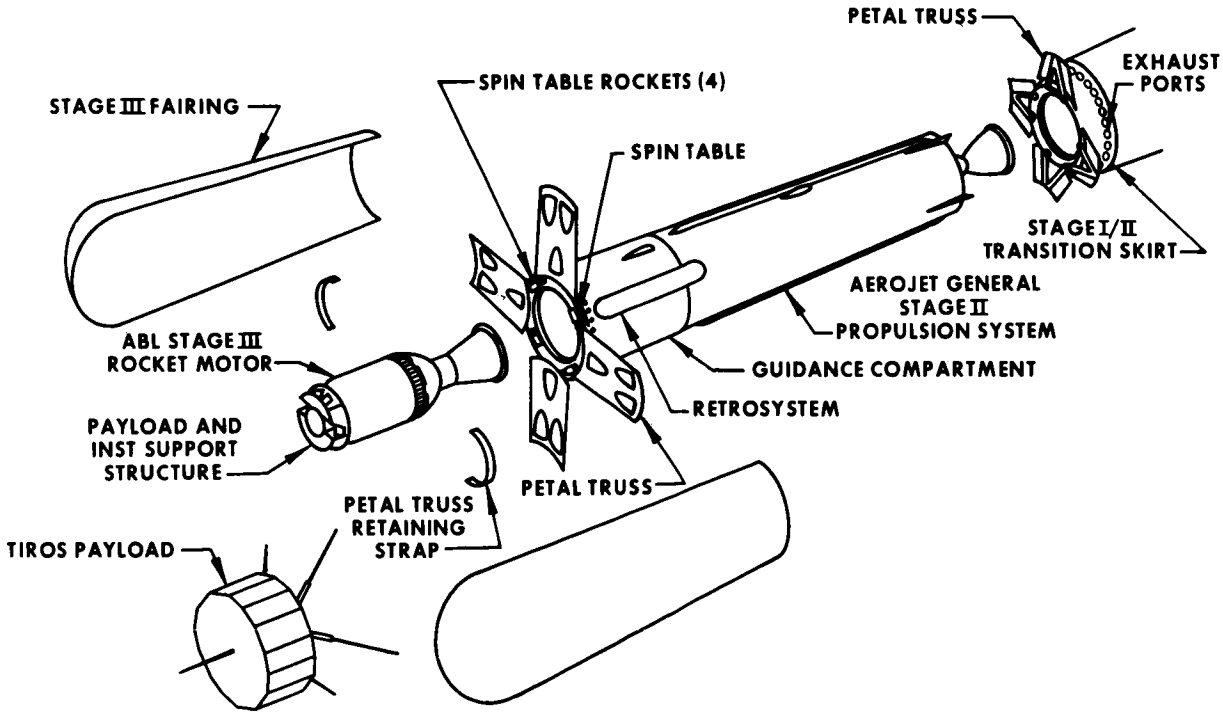

FIGURE 59.—Second and third rocket stages and payload, exploded view.

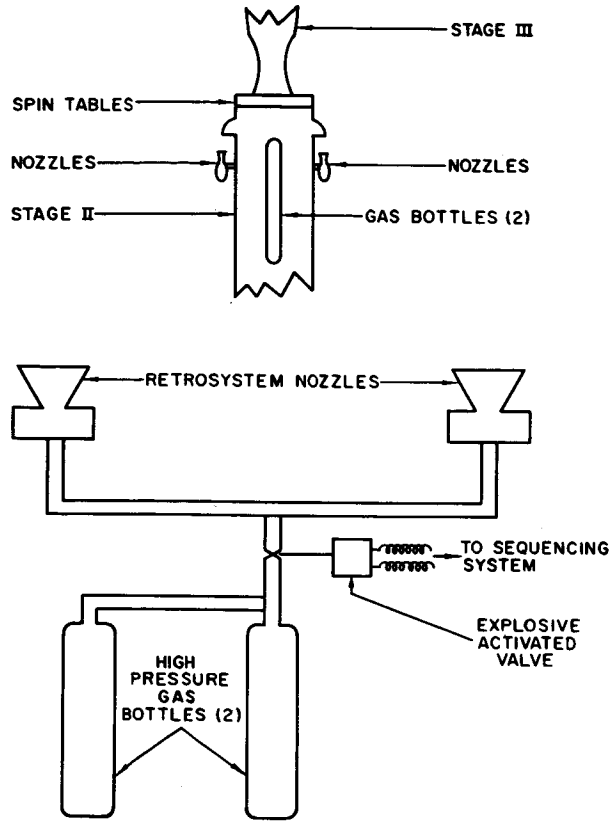

FIGURE 60.—Second-stage retrosystem.

magnesium cone. The monocoque magnesium cone was divided into four segments to provide a four-petal structure. The forward end of the cone was retained around the third-stage engine. The four petals were retained around the third-stage engine by a tension strap consisting of two semicircular segments held together by explosive bolts which were released, upon command, to permit separation. Centrifugal forces resulting from the spin caused the four petals to open, permitting wide-angle clearance for separation.

Second-stage retro system.—In order to prevent the second stage from bumping the third-stage and payload during the coast phase, it was necessary to add a retro system to cancel residual thrust of the second-stage shutdown. The retro system was required to furnish, on appropriate command, a reverse impulse of 300 lb-sec minimum and a reverse thrust of at least 20 $e^{-t/20}$ pounds (where t is the elapsed time of burning).

The retrosystem consists of two reverse thrust nozzles mounted on the Stage II forward guidance section. Nitrogen gas from two high-pressure bottles was admitted to the nozzles through an explosive-actuated valve at the time of State II/III separation (see Figure 60).

BTL guidance system.—The Bell Telephone Laboratories radio-inertial guidance system consists of two main subsystems: the ground and the missile-borne system as shown in Figures 61 and 62. The ground-based radar transmitter sends out interrogation pulses to the beacon receiver in the missile which are fed to the decoder in the missile. The beacon transmitter is then triggered. Its signal is received by the ground-based radar receiver, and the range (R), elevation angle (E), and azimuth angle (A) of the missile are measured. These measurements are digitized and transferred to the digital computer. The digital computer operates on these data to produce steering orders and discrete commands for the missile. They are further converted in the radar to a four-pulse code which is then modulated by shifting the position of the second pair. The pulses are received by the beacon receiver, decoded by the beacon decoder, and used to command the steering and cutoff channels of the missile. The steering signals are sent to the missile autopilot which directs the rocket exhaust nozzle to move and thereby steer the missile into the desired orbit.

The third-stage rocket.—The third stage consisted of the jettisonable aerodynamic fairing covering the ABL propulsion unit, a Millstone tracking

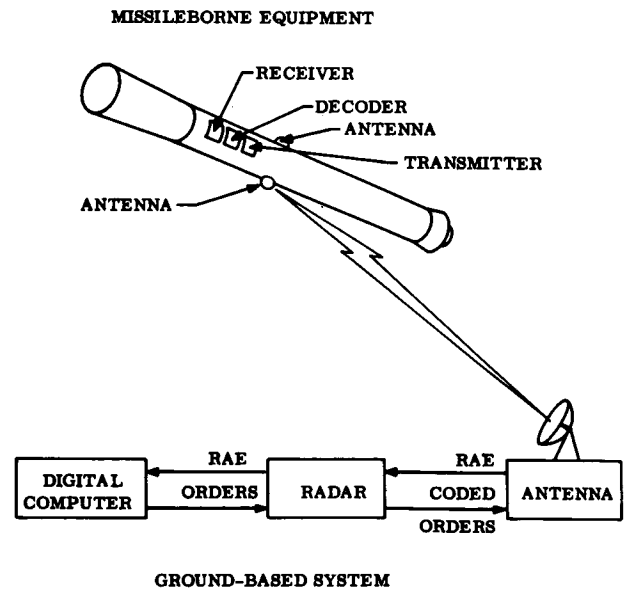

FIGURE 61.—Bell Telephone Laboratories radio-inertial guidance system.

beacon, separation timers, and the payload. The propulsion unit and payload were attached to the spin table which was joined to the second stage. No control or guidance system was employed; stabilization was provided by the spin imparted prior to separation.

Third-stage propulsion.—The third-stage propulsion unit was the Allegany Ballistic Laboratory (ABL) Model X248 A7 solid propellant rocket engine. System specification characteristics were: thrust (at altitude), approx. 3,000 lb; burning time, approx. 40.0 sec; total third-stage weight, approx. 540 lb.

This rocket is a modified version of the Rocket Motor X248 A2, which was originally developed at ABL as the third-stage propulsion system for the Vanguard launching vehicle. The modifications to the X248 A2 were external and provided for payload and spin-table attachment as required for the vehicle. Photographs of the rocket structure and its propulsion system are shown in Figures 63 and 64.

The X248 A7 provided 116,500 pound-seconds of total impulse over a nominal operating time of 38 seconds. Total weight of the rocket motor at ignition was 513 pounds; the weight at burnout, 49 pounds. The rocket mass ratio based on initial and final weights was 0.91.

Third-stage construction.—Rocket Motor X248 A7 utilized a lightweight, high-strength plastic as the primary structural material. The chamber structure was comprised of helically wound con-

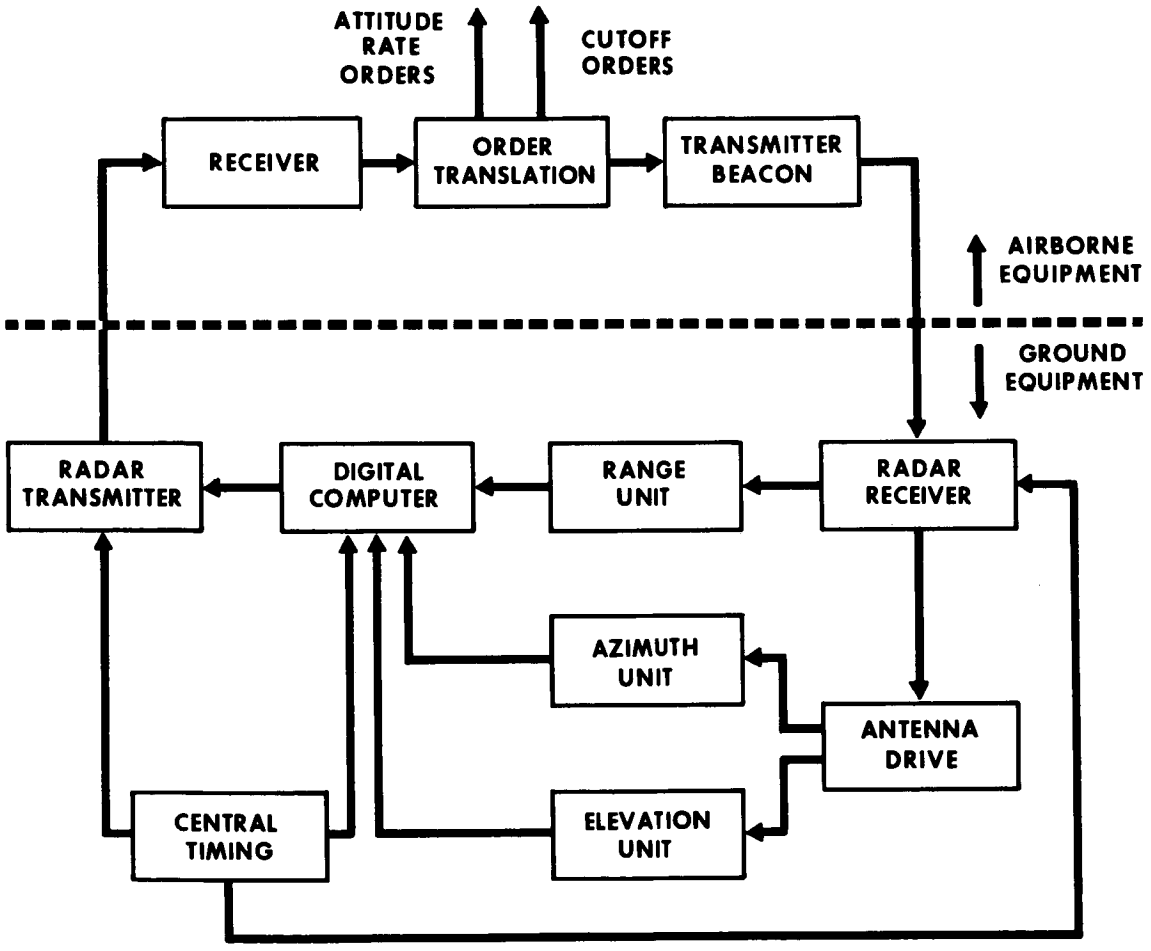

FIGURE 62.—Radio-inertial guidance airborne and ground equipment.

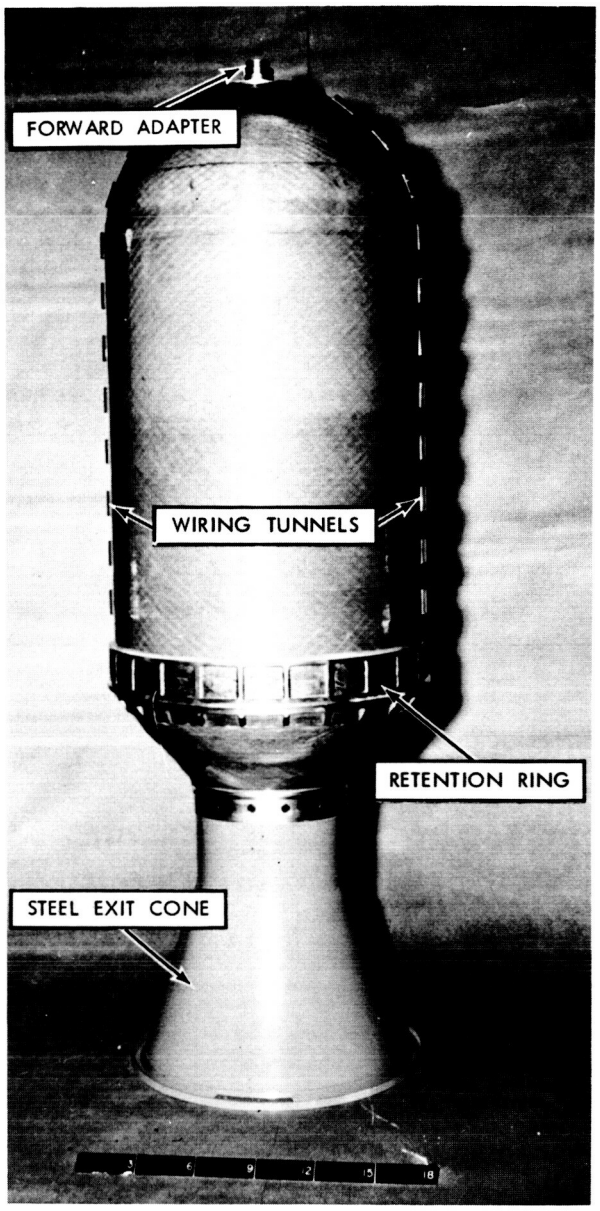

FIGURE 63.—Allegany Ballistic Laboratory rocket Model X248 A7 third stage.

tinuous glass-fiber filaments impregnated with an epoxy resin binder. The chamber was cylindrical with hemispherical ends, and both the forward and aft ends contain aluminum adapters which were wound integrally into the chamber at the time of manufacture. The over-all rocket motor length was 59.3 inches of which the chamber itself comprised 44.2 inches. The propellant, a cast-double-base formulation, was cast directly into and bonded to the chamber interior.

Modifications made to the third-stage rocket motor to comply with the TIROS vehicle requirements consisted of appropriate machining to the forward adapter for payload attachment, the incorporation of wiring tunnels along the chamber cylinder, a magnesium retention ring bonded to the chamber aft dome with an epoxy adhesive, and the use of a spun steel exit cone in the nozzle.

The power source for actuation of the third-stage igniter was packaged around the nozzle attachment area. This package also initiated a timer in the payload which is mounted on the forward adapter. At the termination of the coast period, the motor was ignited by an electrical pulse from the power supply situated around the third-stage nozzle attachment area. Simultaneously, a timer in the payload section was also actuated. The payload timer activated the satellite separation device approximately 7 seconds after third-stage burnout. A diagram of the third stage and satellite configuration, inside the fairing, is shown in Figure 65.

The range safety system.—Missiles flown on the Atlantic Missile Range (AMR) must contain equipment for use in the emergency termination of flight. Flight termination equipment was carried on both stages of the vehicle as follows:

First stage.—Two separate and independent methods of terminating flight were carried by the vehicle for use during first stage powered flight. Flight termination was provided by use of UHF radio command systems which were compatible with the standard AFMTC flight termination system. This requirement was met by the installation of one flight termination system on the first stage and one system on the second stage. Each flight termination system consisted of a UHF command receiver and decoder, antenna system, safety and arming mechanism, detonating cord strands to rupture propellant tanks, and a power supply independent of missile power.

Second stage.—The second stage was too small to skin track by radar; therefore, a C-band beacon was installed to permit tracking. A receiver, detonating network, and explosives all were installed in the second stage to permit the Range Safety Officer to destroy the rocket. Adequate UHF radio command coverage was provided until the end of second stage cut-off.

Impact prediction.—Adequate information on the missile position and flight path must be available to the range during powered flight, otherwise the missile will be assumed to have malfunctioned and will be destroyed. Two independent sources of flight path information are provided. One source was the telemetry ELSSE system which operated by use of radiation from the second stage telemetry system. The second (and primary) source of flight path information was a tracking system which operated in conjunction with an IBM–709 computer to provide instantaneous impact prediction (IIP) information.

The first stage carried a coherent carrier AZUSA transponder which is interrogated by the AZUSA FRW–1 station at CCMTA (Cape Canaveral Missile Test Annex). The second stage carried a transponder which will be interrogated by the FPS–16 radar at CCMTA, and was capable of satisfactory operation until completion of the second stage thrust (beginning of coast phase).

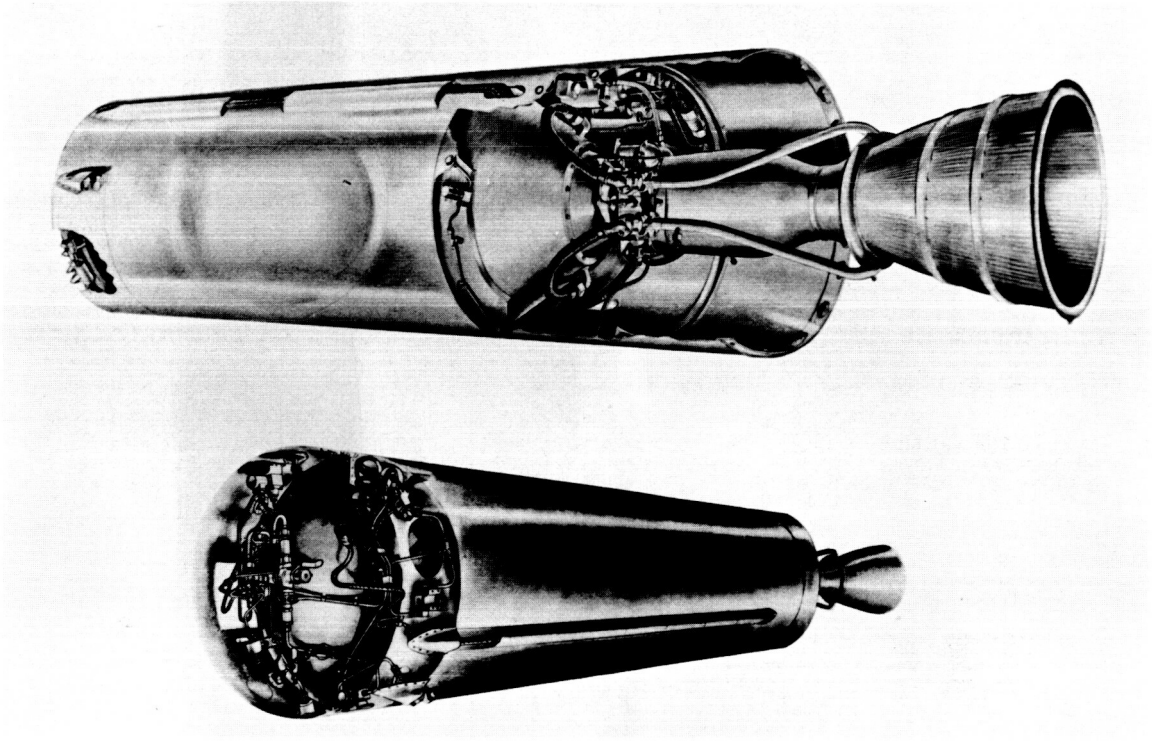

FIGURE 64.—Second-stage rocket propulsion system.

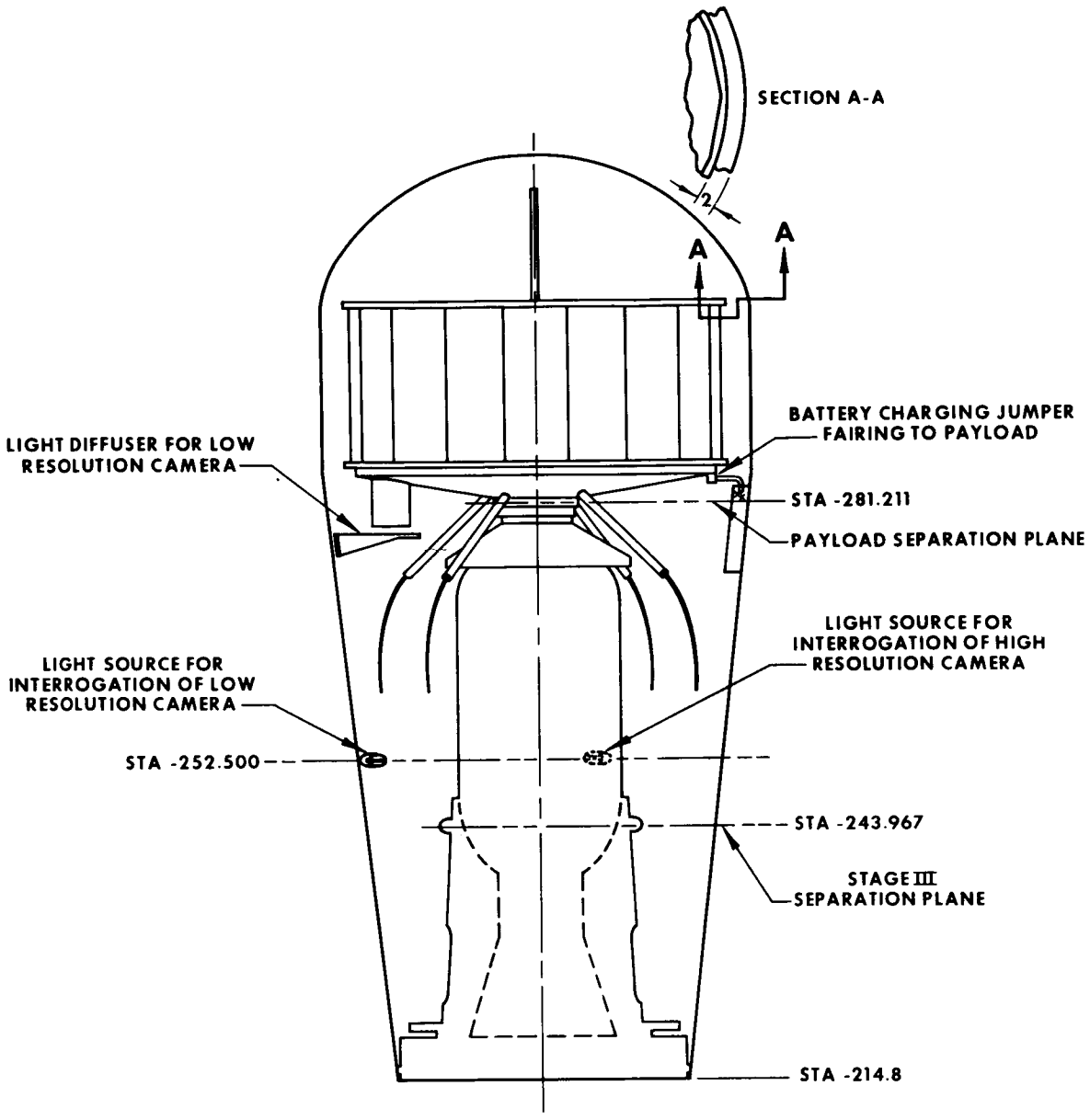

FIGURE 65.—Third stage and satellite assembly.

CHAPTER 3

THE TIROS I OPERATION PLAN

GENERAL

The TIROS I Operation Plan [50] coordinates the efforts of the many agencies involved in the program to effectively meet the objectives of the TIROS meteorological experiment. The primary objectives are (1) to launch the satellite into orbit, (2) to acquire the collected data from the satellite, and (3) to process the data to obtain meteorologically useful information. The secondary objectives are (1) to monitor the thermal conditions in the satellite, (2) to demonstrate the performance of the satellite's subsystems, and (3) to determine the dynamic stability of the satellite.

The data related to the primary objectives are video and attitude reference information obtained by direct-link television, or by readout of magnetic storage devices. That related to the secondary objectives is telemetry data from, respectively, the satellite's temperature sensors, the various electrical performance sensors, and the attitude sensors.

In order to accomplish the primary and secondary objectives of the TIROS I program, the organization chart, as shown in Figure 66, was adopted.

LAUNCH OPERATIONS

PARTICIPATING GROUPS

In addition to the Atlantic Missile Range (AMR) staff, and representatives of rocket-component suppliers: Bell Telephone Laboratories, Aerojet-General, and Allegany Ballistic Laboratory, the following were involved in launch activities:

The NASA GSFC Field Project Branch (FPB) was the technical group at AMR, responsible for technical liaison between Goddard and the AMR field representatives of the other participating groups. A TIROS Field Coordinator was assigned from the FPB to coordinate operational details.

The NASA–AMROO was the formal NASA–AMR contact link through which security clearances and other administrative matters requiring formal NASA contacts with AMR were handled.

The U.S. Air Force, Ballistic Missile Division (AFBMD) was in charge of all THOR vehicle range matters. NASA requirements for range support were submitted through AFBMD.

Space Technology Laboratories was the contractor to AFBMD for management of the Thor-Able vehicle. STL acted for NASA through AFBMD in matters involving the first launch vehicle.

The Douglas AMR field group was responsible for the technical conduct of flight test operations, including preparing the over-all vehicle for flight, and performance of the countdown.

A NASA payload group was assigned to TIROS I, headed by a Payload Manager. He was responsible for readying the payload and defining criteria for mission attainment. No change in criteria could be made without the consent of the Payload Manager.

A NASA Minitrack Operations Group provided local payload minitrack services at AMR, and also reported readiness of the world-wide minitrack net to the Payload Manager and the Payload Representative in the blockhouse.

A TIROS Procedures Committee acted as the prime mechanism for coordinating flight preparations. Membership included a payload representative acting jointly for RCA, Signal Corps, NASA and representatives acting for AFBMD, STL, DAC, AGC, and BTL.

THE LAUNCH STAFF

The Project Manager had responsibility and authority for insuring the ultimate success of the project. He monitored the communication inputs to the Test Director and Test Coordinator. While it was expected that in normal circumstances he would have no reason for actively entering the

operation, he had the authority to do so should it become apparent to him that success of the mission was being jeopardized. He was located in the blockhouse.

The Test Director had overall vehicle preparation and launch responsibility. He received inputs from the Test Conductor and the Payload Representative. Within the framework of established mission objectives he had final authority regarding launch decisions. He was located in the blockhouse.

The Test Conductor was the chief technical agent for conduct of the vehicle launch, including countdown, pad safety and BTL guidance inputs. He received all communications inputs in parallel with the Test Director. He was located in the blockhouse.

The Test Controller was the third member of STL–DAC–BMD Project Command team. He represented BMD Project Office Management in controlling the overall conduct of the operation.

The Payload Representative provided inputs to the Test Conductor concerning the payload and Minitrack status. He was located in the blockhouse and represented the Payload Manager and Minitrack Manager who was remotely located.

The Payload Manager received inputs from the payload monitoring activities and made the final decision as to mission readiness for launch.

The Minitrack Manager was in communication with the NASA Space Operations Control Center. He reported world-wide minitrack readiness and the quality of the payload tracking signals to the Payload Manager. He was located at the AMR minitrack station.

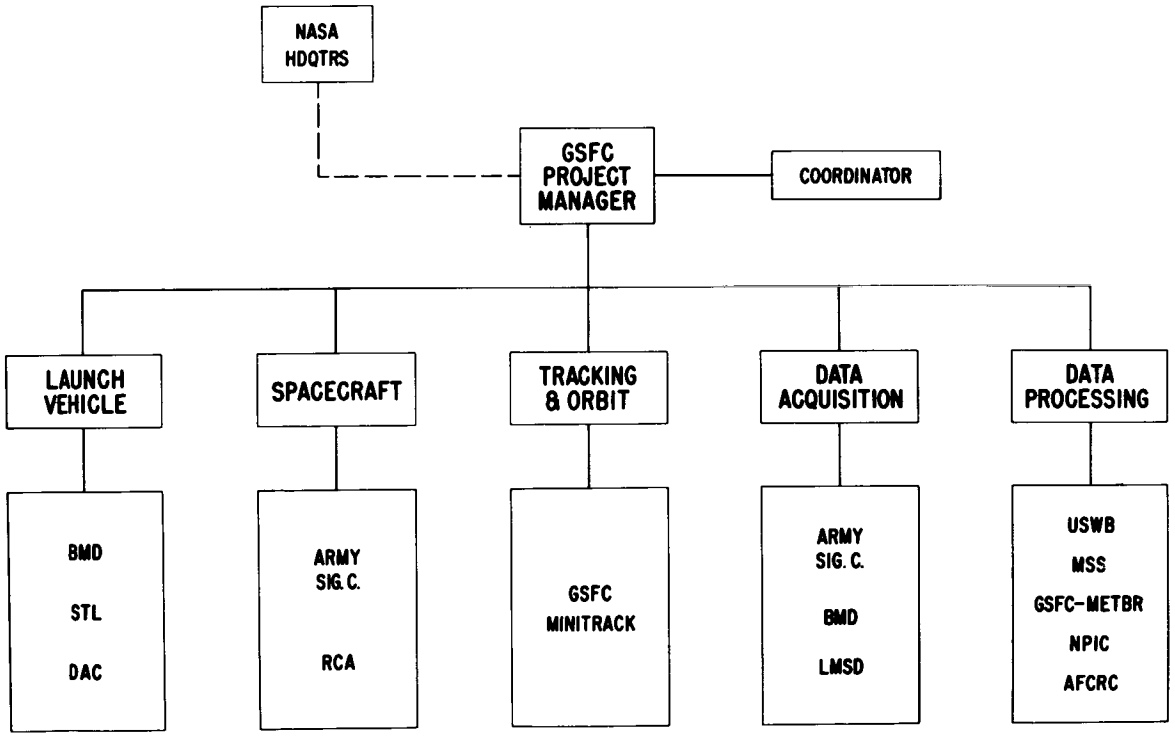

KEY TO ABBREVIATIONS

NASA	National Aeronautics and Space Administration	LMSD	Lockheed Missiles and Space Division
GSFC	Goddard Space Flight Center (NASA)	MSS	U.S. Weather Bureau, Meteorological Satellite Section
BMD	Air Force Ballistic Missile Division	METBR	Meteorological Branch (GSFC)
STL	Space Technology Laboratories	NPIC	Naval Photographic Interpretation Center
DAC	Douglas Aircraft Company	AFCRC	Air Force Cambridge Research Center
SIG. C	U.S. Army Signal Corps		
RCA	Radio Corporation of America, Astro-Electronics Division		

FIGURE 66.—Organization of the TIROS I project.

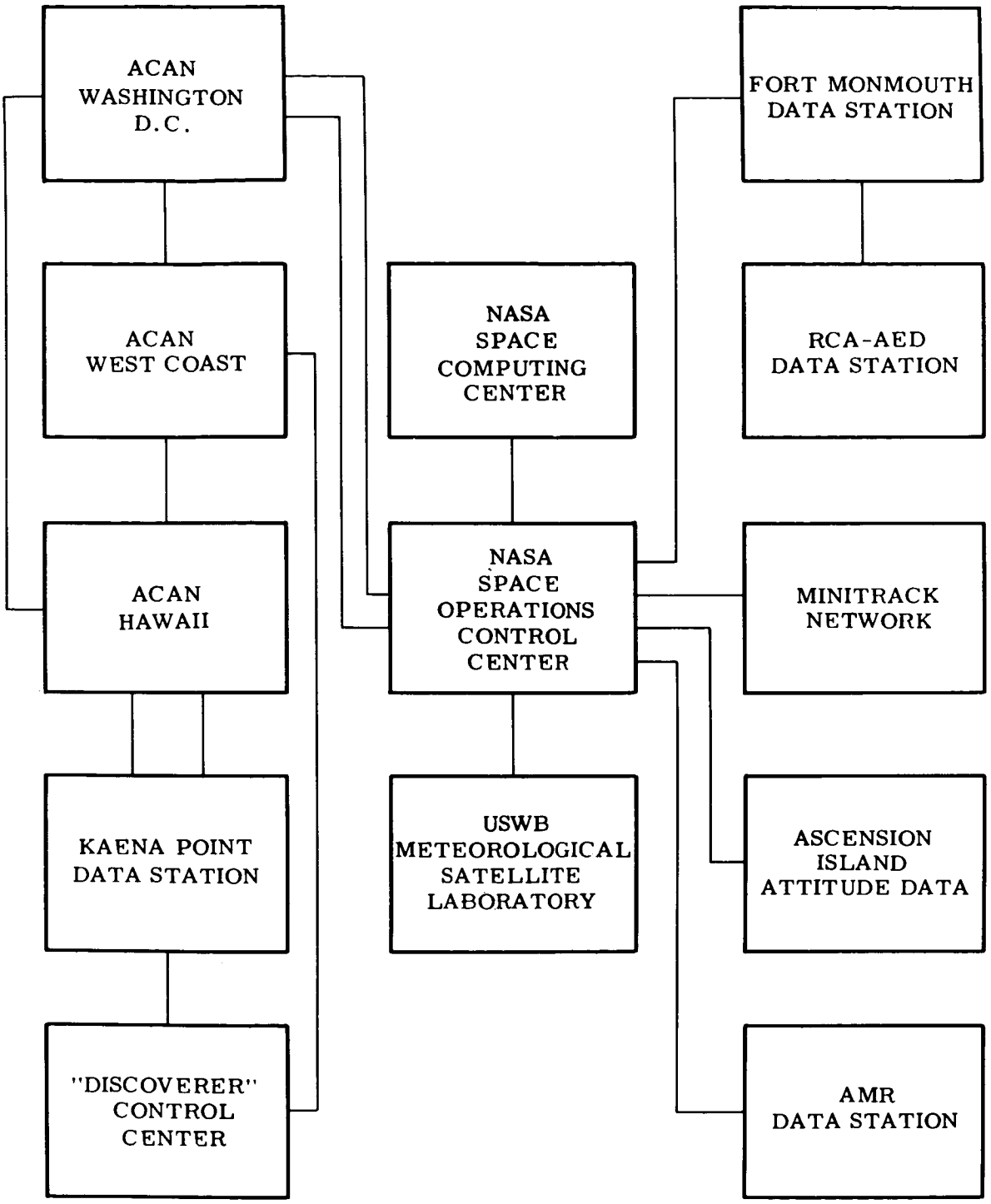

FIGURE 67.—The TIROS I ground-based data communication network.

646-770 O—64——6

LAUNCH AND "COUNTDOWN HOLD" CRITERIA

Criteria to be met by the vehicle prior to launch were established by the Vehicle Manager. These and countdown hold criteria are discussed in Reference 50.

ACQUISITION OF LAUNCH DATA

Several agencies at the Cape Canaveral Missile Test Annex (CCMTA) launch site and various other locations participated in the acquisition of required data. AFBMD/STL project and management officials also were located at both CCMTA and Los Angeles to receive the results and provide a preliminary estimate of the vehicle's performance to NASA and other cognizant agencies. Diagrams of the communication links are shown in Figures 67 and 68.

The focal point of operations at CCMTA for this task was the ACOM communications center in Hangar AA. ACOM accepted all data inputs from the various CCMTA data facilities and transmit data and analysis reports to local base management and non-CMTA organizations. ACOM was composed of the following:

AFBMD/LA Project Representative
STL/LA Project Representative
NASA Project Representative
AFBMD/PAFB Project Representative
STL/PAFB Project Representative
Data Acquisition and Transmission Crew

The AFBMD/STL project representatives had telephone and/or TWX communication with the project representatives at the STL Space Navigation Center (SpaN) at Los Angeles, NASA at Washington, D.C., and MOPS communications with AMR base management.

The NASA project representative had telephone and TWX communications to NASA control and tracking facilities.

The Data Countdown Talker, as head of the Data Acquisition and Transmission Crew, conducted a data acquisition countdown over the communications loops to the participating data organizations, consolidated the data gathered, and

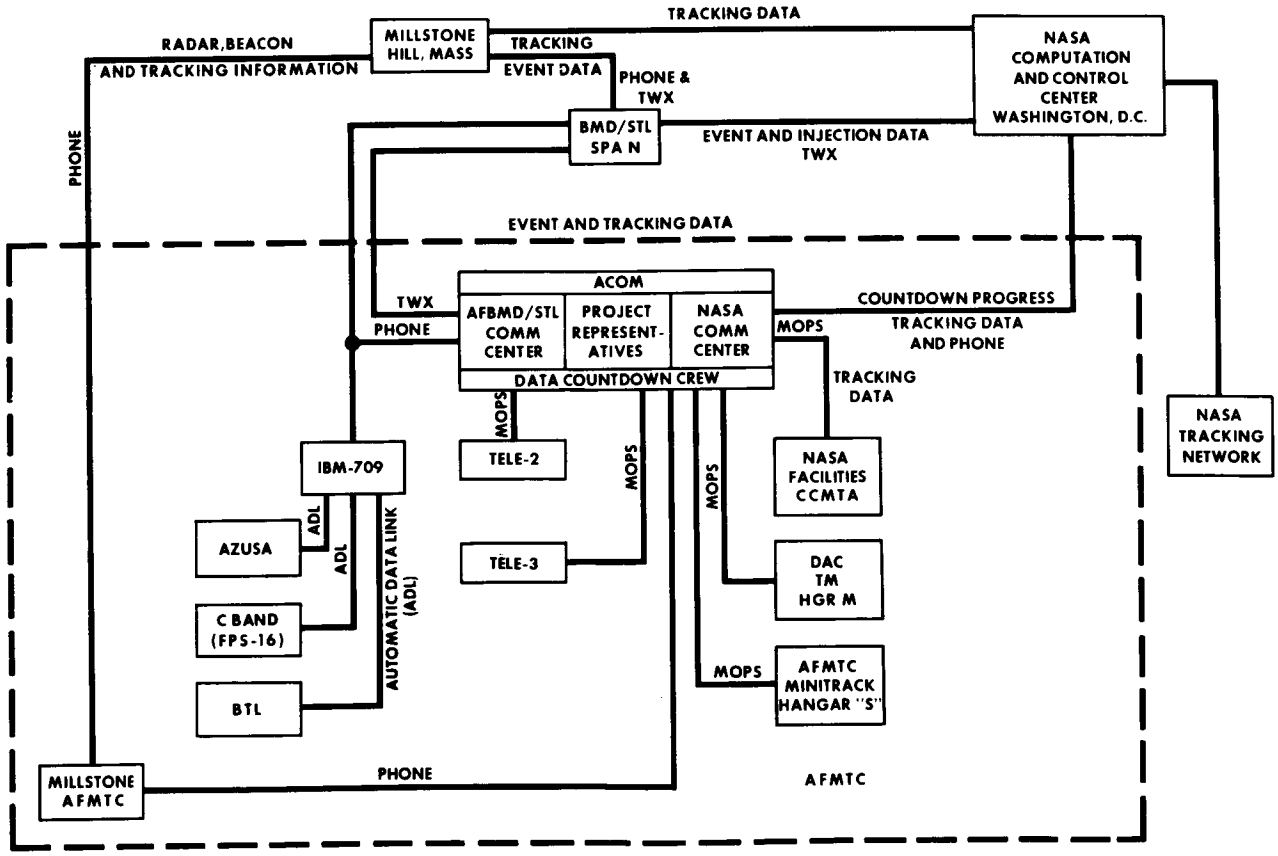

FIGURE 68.—The NASA tracking network.

transmitted the data to the project representatives.

The Data Acquisition and Transmission Crew assisted the Data Countdown Talker by manning communication loops, acquiring and processing data and providing the talker with the desired information.

Launch vehicle event data obtained at CCMTA and required by NASA control and tracking agencies was made available to the NASA representatives at ACOM from the Data Countdown Talker. The NASA representatives were provided with communication loops (TWX and telephone) for transmission of this data to other NASA agencies.

A more detailed discussion, including all of the agencies and locations involved, is given in the official document prepared by the Experimental Space Projects Office of STL.[48]

COMMUNICATIONS

The communication requirements[48] to implement the TIROS I launch are shown in Table 7.

The items headed "station" and "location" define the agency and its location for the initial action in opening a communication loop. The column "By" shows the method of communication. "To" and "Location" refer to the other party in the loop. "At" defines the time the loop must be operational. All times in this item refer to the scheduled missile lift-off time. "Furnished by" denotes the agency responsible for implementing the initiating party's instrument and line requirements.

ROCKET DATA REQUIREMENTS

The data required for determining the rocket injection parameters and estimating vehicle performance in real time are given in Table 8.

In Table 8, the items listed under "Data Item" are data requirements that may or may not be individual measurements. The individual measurements required to provide a data item are detailed in the STL document just referenced.[48] The items listed under "Availability Time" indicate the times when the final data item should be available to the user. This item takes into account the time required for processing measurements to determine the data item. Time required for transmission of the item is assumed to be negligible. The items "From, By and To" show the originating agency for the item, the method of transmitting the information, and the recipient. In cases where several agencies are indicated in each column for one data item, either more than one source is contributing information to determine the item (a data processing function is interposed between the initial originator and the final recipient), or a communication relay exists between the agencies.

The nominal times for the occurrence of the events providing the data item will be found in the DTO.[51] The data gathering countdown specifies the particular time the event should be occurring.

RECEIPT OF METEOROLOGICAL DATA

A ground complex of satellite command and data handling stations was established, centered around the NASA Space Operations Control Center at Washington, D.C., for operation and utilization of the TIROS I system. The major facilities involved are illustrated in Figure 69.

The satellite was tracked by stations of the Minitrack network; the position and attitude data obtained then were forwarded to the NASA Space Computing Center. Future orbits of the satellite then were calculated, and programs for satellite acquisition and tracking sent through the NASA Space Operations Control Center to each command and data-acquisition (CDA) station. A tracking loop and a programming data network are shown in Figures 70 and 71. Areas to be photographed were designated by the U.S. Weather Bureau or cooperating meteorological agencies for transmission through the Control Center to the CDA stations for inclusion in the programming instructions to the satellite.

The launch time was chosen in such a way that illumination conditions were near-optimum for coverage over the Northern Hemisphere during the first two months of operation, with a gradual reduction in coverage beyond that time. The scheduling of the exact launch data was adjusted, with due regard for this pattern, so as to minimize interference between the Discoverer and TIROS projects. To reduce the probable interference on a pass-by-pass basis at Kaena Point, Hawaii, the TIROS exact-launch time could be adjusted by ± 15 minutes with no significant changes in its effectiveness. Similarly, Discoverer launch times could be adjusted, within limits. NASA Space Operations Control Center obtained from the

TABLE 7.—COMMUNICATION REQUIREMENTS FOR THE TIROS I LAUNCHING

Item	Station	Location	By	To	Location	At	Furnished by	Remarks
1	ACOM	Hangar A–A	MOPS	Tele-2	Tele-2	T–35 min	CCMTA	VCL loop.
2	ACOM	Hangar A–A	Phone	Millstone	BH–17	T–60 min	CCMTA	VCL loop.
3	NASA Comm	Hangar A–A	MOPS	Payload	CCMTA	Countdown Start.	CCMTA	Payload loop—STL–2.
4	ACOM	Hangar A–A	Phone	IBM–709 and SpaN.	Azusa Site and Los Angeles.	T–60 min	CCMTA/STL	Call to be placed by SpaN. CCMTA to furnish conference tie-in of ACOM and –709.
5	ACOM	Hangar A–A	MOPS	DAC–TM	Hangar M	T–35 min	CCMTA	VCL loop.
6	ACOM	Hangar A–A	MOPS	Tele-3	Tele-3	T–35 min	CCMTA	VCL loop.
7	ACOM	Hangar A–A	MOPS	IBM–709	Azusa Site	T–35 min	CCMTA	VCL loop.
8	Millstone	BH–17	Phone	Millstone	Massachusetts	T–60 min	CCMTA	
9	NASA Comm	Hangar A–A	Phone	Open	Base and Long Distance.	Countdown Start.	CCMTA	2 Black phones for operational use.
10	ACOM	Hangar A–A	MOPS	Minitrack	Hangar S	T–35 min	CCMTA	VCL loop.
11	SpaN	Los Angeles	Phone	Millstone	Massachusetts	T–35 min	STL	
12	SpaN	Los Angeles	TWX	ACOM	Hangar A–A	T–35 min	STL	Back-up for telephone.
13	SpaN	Los Angeles	TWX	Millstone	Massachusetts	T–35 min	STL	
14	SpaN	Los Angeles	TWX	NASA	Washington	T–35 min	STL	
15	NASA Comm	Hangar A–A	TWX	NASA	Washington	Countdown Start.	CCMTA	

TABLE 8.—REAL-TIME DATA REQUIREMENTS

Item No.	Data Item	Availability Time	From	By	To	Remarks
1	Lift-off		Tele-2	MOPS	ACOM	IBM-709 input for Item 9.
			DAC–TM	MOPS	ACOM	
			ACOM	Phone	SpaN, IBM–709.	
2	Stage II Arm		Tele-2	MOPS	ACOM	
3	Stage I Cut-off (MECO).		Tele-2	MOPS	ACOM	
			ACOM	Phone	SpaN	
4	Stage II Ignition		Tele-2	MOPS	ACOM	
			ACOM	Phone	SpaN	
5	Stage I/II Separation.		Tele-2	MOPS	ACOM	
			AFMTC Minitrack	MOPS	ACOM	
			Millstone, Mass.	Phone	Millstone, AFMTC	Back-up indication from Stage II acceleration data.
			Millstone, AFMTC	Phone	ACOM	
			ACOM	Phone	SpaN	
6	Fairing Jettisoned		Tele-2	MOPS	ACOM	
			ACOM	Phone	SpaN	
7	Spin Start and Spin Rate		Tele-2	MOPS	ACOM	Back-up from Millstone, Mass.
			ACOM	Phone	SpaN	
8	Stage II Cut-off (SECO)		Tele-2	MOPS	ACOM	IBM–709 input for Item 9.
			DAC–TM	MOPS	ACOM	
			ACOM	Phone	SpaN; IBM–709	
9	Stage II Burnout Position and Velocity	10 min. after release of computer by RSO (approx. SECO)	IBM–709	Phone	SpaN and ACOM	Conference telephone line.
10	R, A, and E Raw Data Points					
11	Retrodevice Action		Tele–2	MOPS	ACOM	
			DAC–TM	MOPS	ACOM	
			ACOM	Phone	SpaN	
12	Stage II/III Separation		Tele–2	MOPS	ACOM	
			DAC–TM	MOPS	ACOM	
			ACOM	Phone	SpaN	

TABLE 8.—REAL-TIME DATA REQUIREMENTS—Continued

Item No.	Data Item	Availability Time	From	By	To	Remarks
13	Stage III Start		AFMTC, Minitrack	MOPS	ACOM	
			Millstone, Mass.	Phone	Millstone, AFMTC	
			Millstone, AFMTC	Phone	ACOM	
			ACOM	Phone	SpaN	
14	Stage III Burnout		AFMTC, Minitrack	MOPS	ACOM	
			ACOM	Phone	SpaN	
15	Stage III/Payload Separation		NASA Control	TWX	SpaN	
			SpaN	Phone	ACOM	
16	Millstone Tracking Data.	Approx. 10 min. after launch.	Millstone, Mass.	TWX	SpaN	Data from initial acquisition until loss.
17	Injection Parameters.	1 hour after launch	SpaN	TWX	NASA Control.	
			SpaN	Phone	ACOM	
18	Separation Tracking Data.	10 min. after two orbits (approx. 215 min.)	NASA Control.	TWX	SpaN	Back-up of Item 14. Millstone track of Stage III and Track of Payload desired.

NASA Space Computing Center computations of the long-range coverage pattern and the most probable sequence of early contacts at Kaena Point, in order to reach final agreements with the Discoverer program on scheduling.

Pictures received from the satellite by a primary CDA station were photographed from a TV monitor display, and the exposed film was sent to the Naval Photo-Interpretation Center at Washington, D.C., for the first processing. The original negatives were then stored at the National Weather Research Center, Asheville, N.C., where copies can be obtained by cooperating research and development meteorological agencies. Simultaneously the received picture data was recorded on magnetic tape. The tape was played back to the TV monitor when primary pictures were not being displayed, and a "secondary" film record was made. This film was processed on-site. Meteorologists at the station abstracted cloud information essentially in real time. The resulting nephanalyses were coded and sent by facsimile or teletype to the U.S. Weather Bureau Meteorological Satellite Laboratory at Suitland, Md.[52-56] Many of the analyses were then retransmitted as unscheduled traffic over the operational communication circuits of the U.S. Weather Bureau and the U.S. military weather services. Magnetic tapes and other original records are filed at the Goddard Space Flight Center.

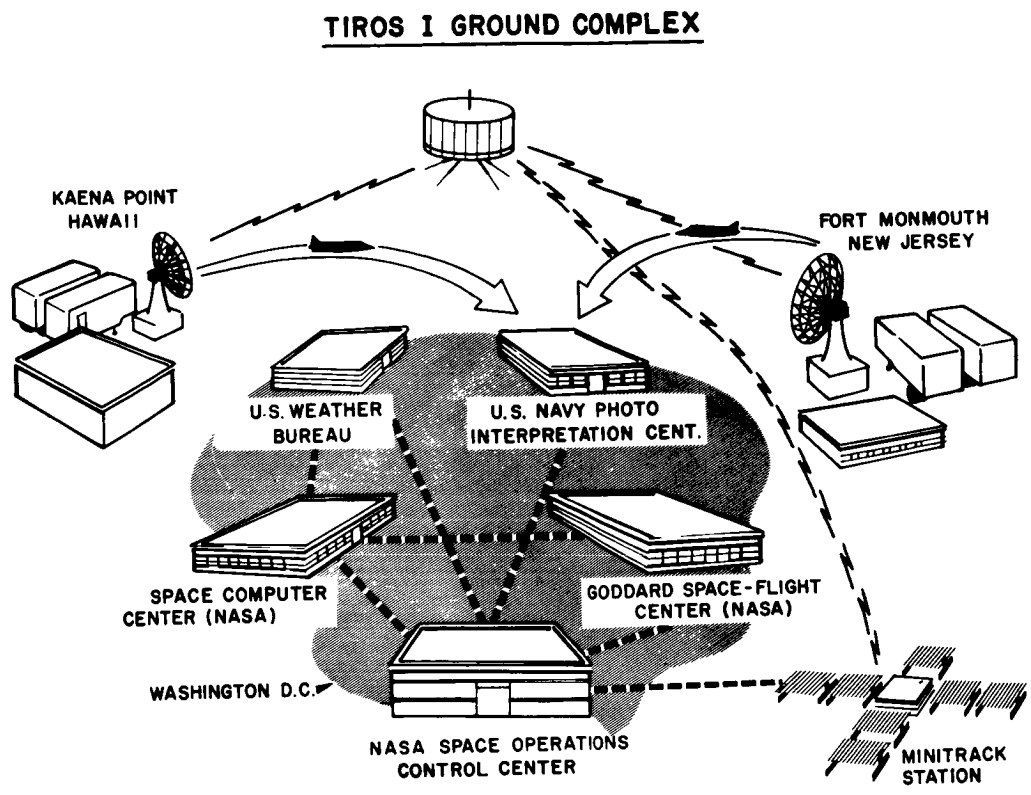

FIGURE 69.—TIROS I operational ground system complex.

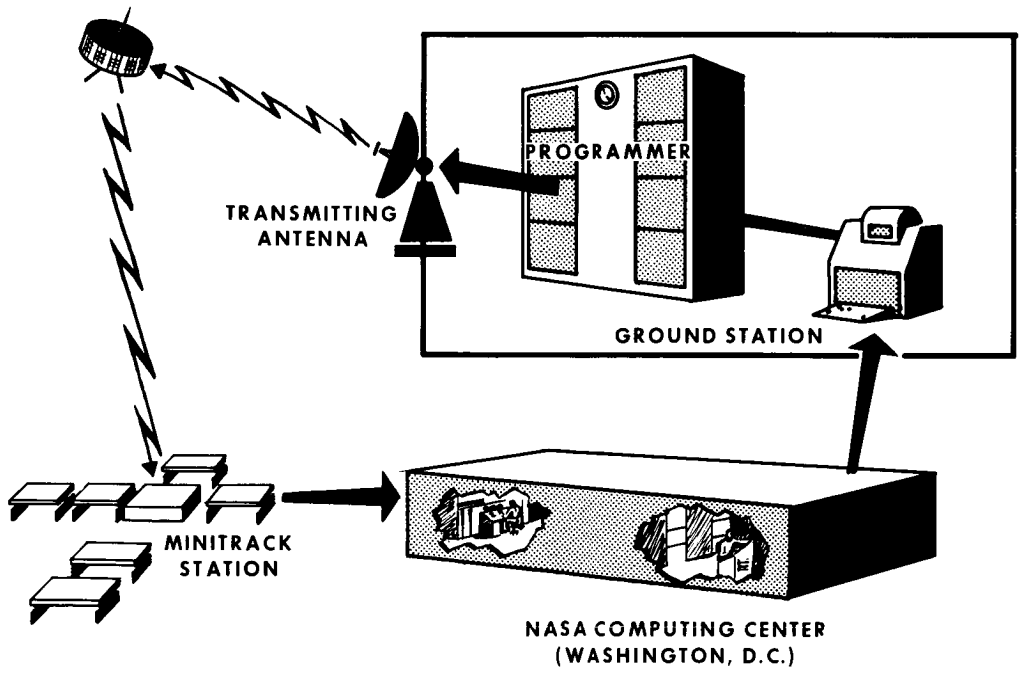

FIGURE 70.—TIROS I satellite tracking network.

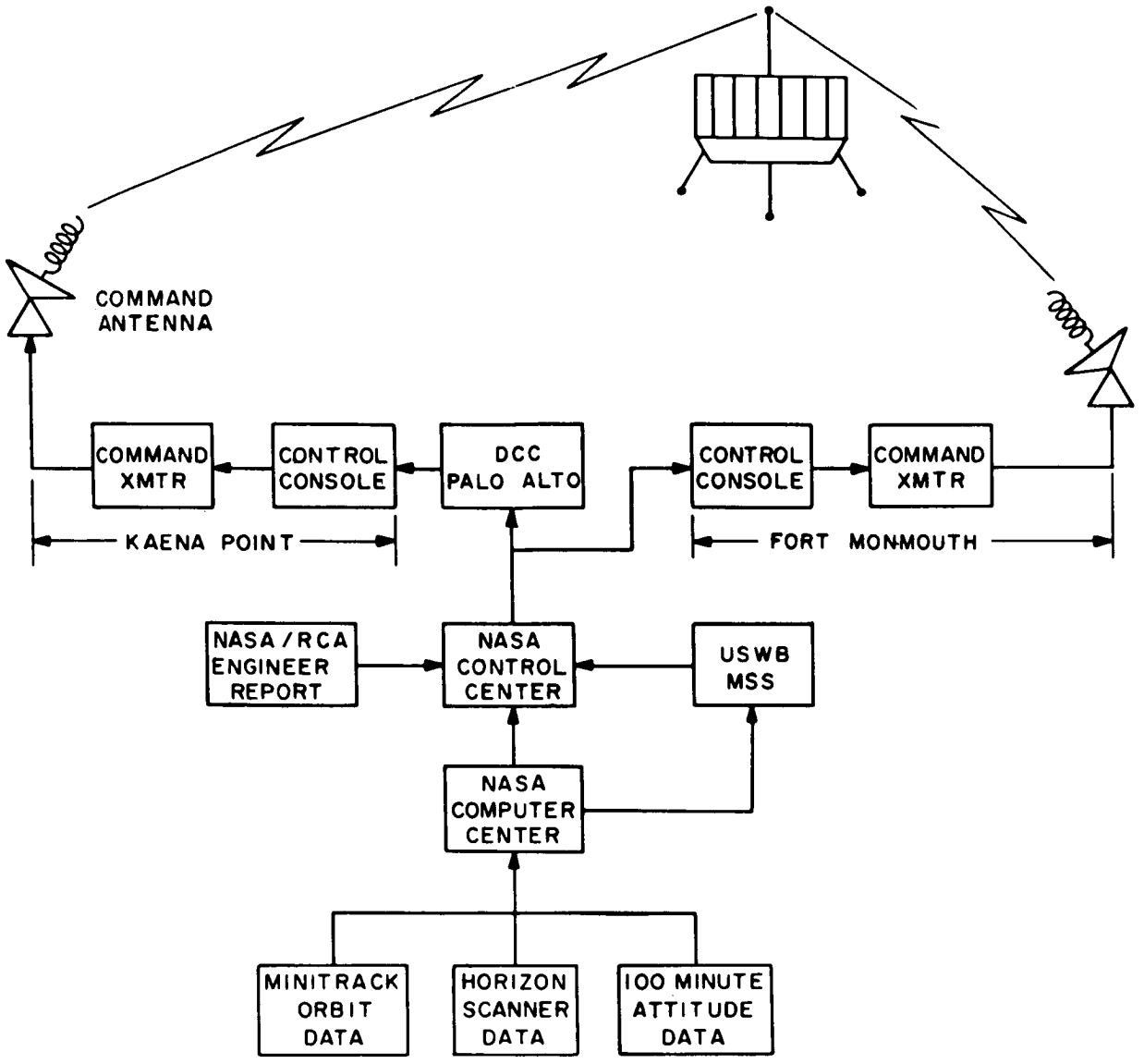

FIGURE 71.—TIROS I programming-data network.

CHAPTER 4

LAUNCH SITE OPERATIONS

EQUIPMENT ARRIVAL AND CHECK-OUT

Three TIROS I satellites were shipped from RCA to the launch site at Cape Canaveral: No. T–2 for training and dry-runs; and Nos. D–1 and D–3 as potential flight models. As each was received, it was housed in Hangar AA for electrical check-out, mechanical inspection, and dust-free storage. Upon satisfactory completion of these tests, the satellite was transferred to Hangar 1366 for mating with the assigned third-stage rocket. The routing of the satellites is shown graphically in Figure 72.

The rocket also was given complete checks before and after assembly (see Figures 73 and 74). All of the satellites were found, upon mating, to be well within the required runout tolerance of 0.082 inch. Figures 75 and 76 show a satellite and third-stage rocket assembly being checked for mechanical alignment and proper clearances.

After mating, the satellite and third-stage rocket assemblies were stored in Hangar 1366. When D–3 was selected as the actual flight unit, this assembly was transferred to the launch complex, and mounted on the second-stage rocket, preparatory

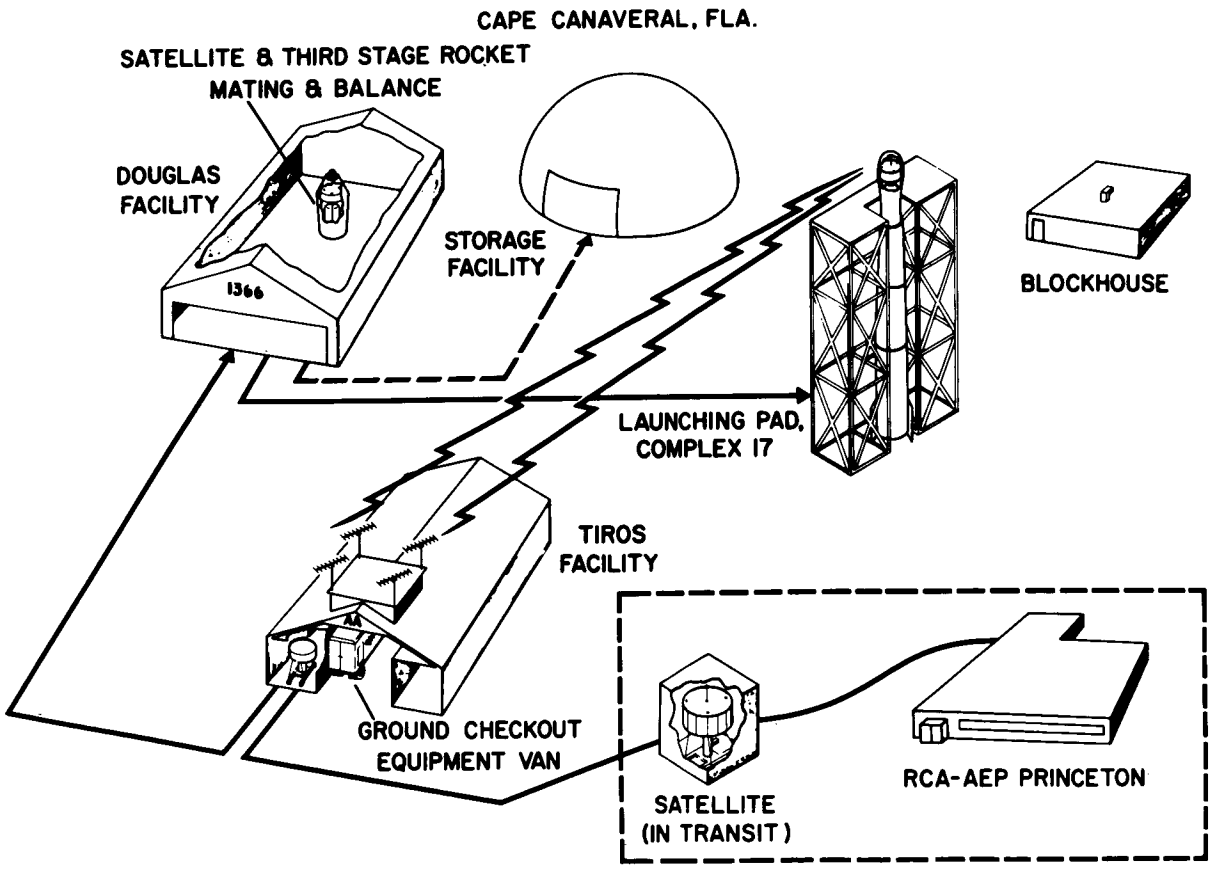

FIGURE 72.—Pre-launch routing of the TIROS I satellite.

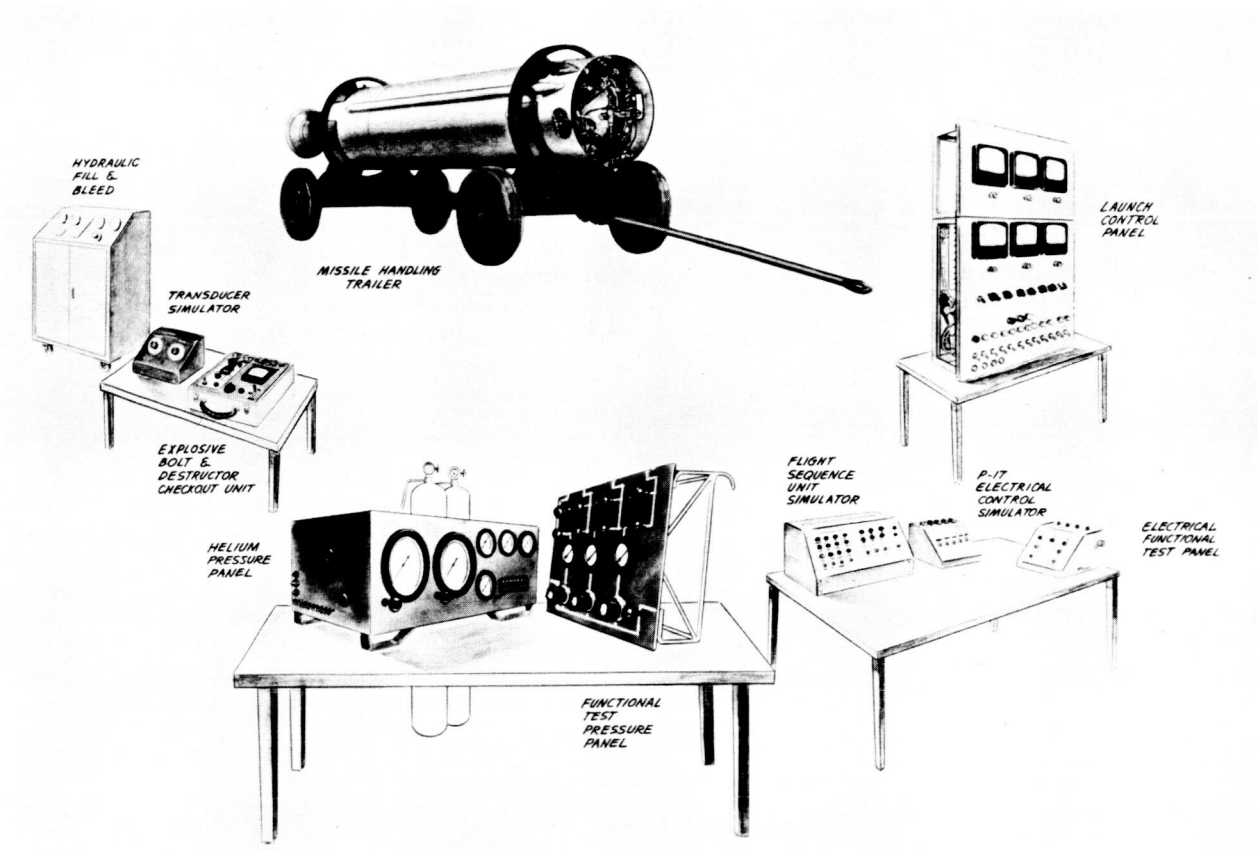

FIGURE 73.—The hangar checkout equipment for the launching rocket.

to launch. During the time following, an air-conditioned tent was installed on the gantry over the assembly to protect it from the weather.

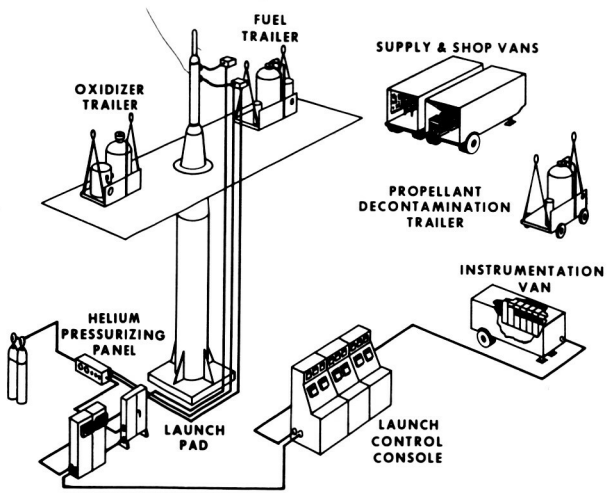

FIGURE 74.—Launch-area support equipment for the launching rocket.

THE SATELLITE CHECK-OUT EQUIPMENT

For satellite testing at the launch site, a special facility was designed at AED. This equipment was essentially a manually-programmed ground station of reduced capability which permitted the conducting of a series of Go, No-Go tests. The main intent of these tests was to check operability of the various satellite functions, rather than to give complete quantitative tests.

The equipment was housed in a laboratory-type van and consisted of the required antennas, transmitters, receivers, video processing equipment, telemetry processing equipment, and the necessary units for control of the satellite functions. Additional units were installed to permit manual operation of a TLM–18 antenna, if the van should be required as a back-up operational ground station.

THE LAUNCH-SITE TEST PROGRAM

The satellite test program at Cape Canaveral consisted of a daily functional check of operation

of each of the payloads with the Go, No-Go equipment (as shown in Task 9 of the TIROS Countdown Manual).[57] When the selected satellite was mounted on the missile and readied for launch, a careful visual check and an operational check were performed each day. Additional interference checks were made as required in the countdown manual during RF systems day and all systems day.

Tests made while the payload was on the missile were carried on by three separate crews: one crew in the Go, No-Go van, a second crew on the gantry, and a man monitoring the blockhouse control panel. The personnel in the Go, No-Go van controlled the satellite and checked the resulting data. The gantry crew operated the auxiliary test equipment to provide the required target sources for the sensors. The man in the blockhouse monitored and recorded battery conditions during test periods. All telemetry data was compared to a master overlay during each test. NASA and USASRDL representatives were present in the Go, No-Go van to monitor all payload checks.

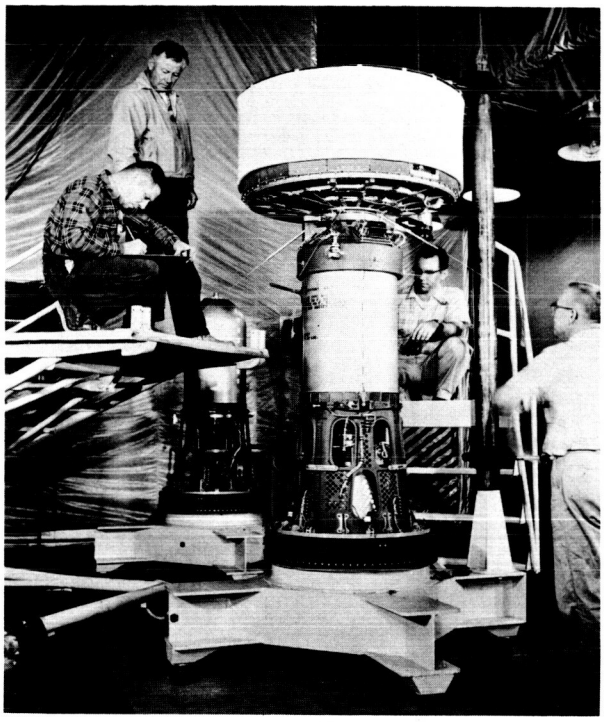

FIGURE 76.—Clearance check of the third stage and satellite assembly.

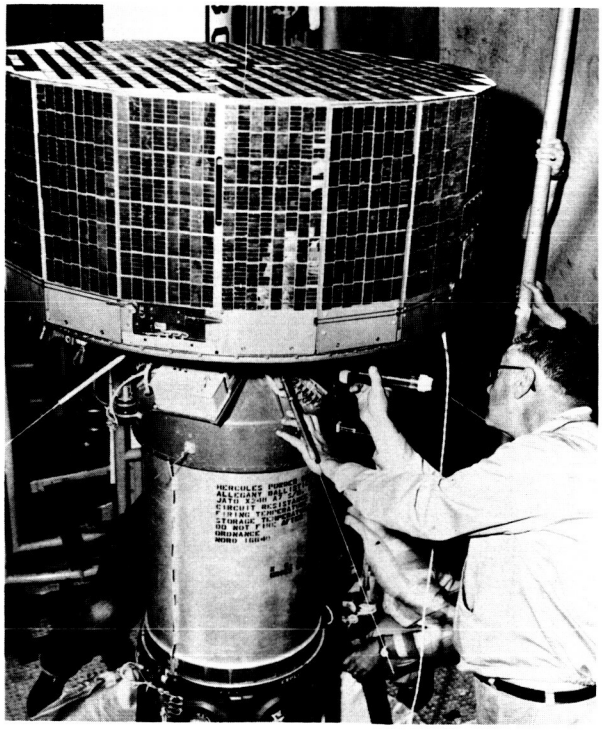

FIGURE 75.—Mechanical alignment check of the third stage and satellite assembly.

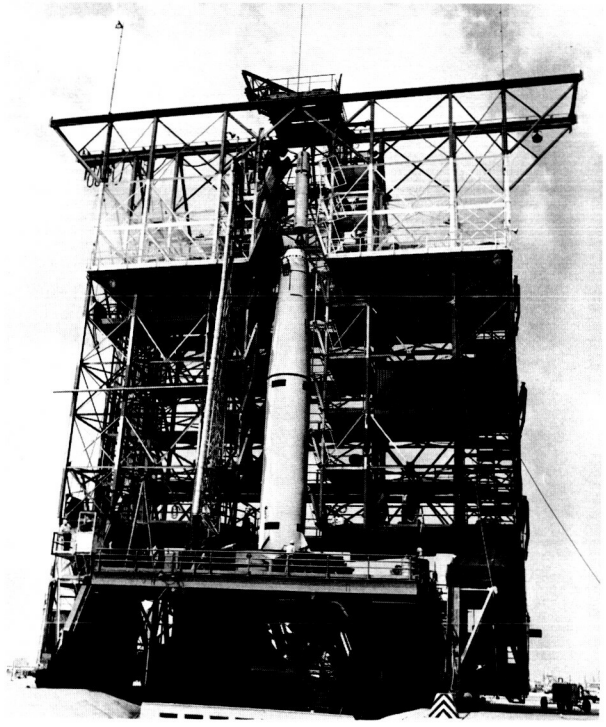

FIGURE 77.—Assembly of second stage to the Thor booster at the gantry.

T–0 DAY OPERATIONS

T–0 day began at 2000 EST on March 31, 1960. The payload checks were made at T–505 minutes (2000 EST), at T–195 minutes, and at T–95 minutes.

The payload check was started at 2030 EST and progressed satisfactorily until the operation of the remote timing function of the satellite was checked. Timing errors were found and ascribed to jamming by a transmitter in the immediate area with a frequency very near the command frequency. No further problems were found after the extra transmitter was taken off the air and the payload check was completed satisfactorily at 2124 EST.

During the next few hours the payload was given a very thorough visual examination and all extraneous material was removed. At the completion of this inspection, the flight fairings were installed and the T–195 checks were made at 0245 EDT, April 1, without incident and the gantry was removed (see Figure 77). The last scheduled check was the T–95 check and this was completed satisfactorily at 0345.

At approximately T–60 minutes, it was discovered that the battery charging leads were open and battery conditions could not be monitored during the remaining countdown time. It was decided that at T–10 minutes a very short payload check would be made to get telemetered information on batteries. At 0535 this was done and the batteries were in good condition. A 1-hour hold at T–2 minutes required that this condition be rechecked at 0631. Everything was found to be satisfactory. The rocket and payload were ready for launch (Figure 78).

FIGURE 78.—The Thor-Able rocket ready for firing.

THE LAUNCHING

The satellite was launched at 064009.2 EST, April 1, 1960. In less than 1 minute from this time, the beacons had been received by both the Fort Monmouth ground station and the Princeton backup station at RCA. About 265 seconds after lift-off, spin-up of the third stage occurred and was noted by the Millstone tracking station to be about 84 rpm. Separation from the third stage occurred at approximately 0652 EST.

IN-FLIGHT SEQUENCE OF EVENTS

The major events that occurred between launch (lift-off) and satellite separation are listed in Table 9. The precalculated time for each event is listed in this tabulation, along with the source or initiating device.

Ten seconds after lift-off the vehicle begins a programmed pitch maneuver to maintain the proper trajectory. The first 90 seconds of flight are controlled by the first stage programmer. The BTL guidance located in the second stage begins steering the vehicle at this time through the first stage control system. The main engine shuts down approximately 159 seconds after lift-off and the second stage start sequence is initiated. The second stage separates from the first stage at about 163 seconds. Shortly thereafter the BTL guidance system begins steering the vehicle. Twenty seconds after second stage start, the nose fairing is jettisoned and BTL completes guidance at 254 seconds. The third stage and payload are spun-up at 269 seconds after lift-off and the second stage engine is cutoff two seconds later. The spinning third stage and payload are separated at this time to begin a coast phase and the second stage retro

TABLE 9.—TIROS I IN-FLIGHT SEQUENCE OF EVENTS

Nominal Expected Time (seconds)	Event	Initiated by
0	Lift-Off	
+2	Roll Program Begins	DAC Programmer.
+9	Roll Program Ends	DAC Programmer.
+10	Pitch Program Initiated	DAC Programmer.
+90	Start BTL Stage I Guidance	BTL Ground Station.
+130	Stage I Pitch Program Comp	DAC Programmer.
+134. 5	Arm Stage I/II Separation	6g Acceleration Switch.
+149	Stop Stage I Guidance	BTL Ground Station.
+158. 53	Main Engine Cutoff (MECO)	Propellant Depletion.
+162. 33	Stage II Fire Signal	3.8 Second Timer.
+162. 73	Stage I/II Separation	Stage II Propulsion.
+172. 3	Start BTL Stage II Guidance	BTL Ground Station.
+182. 3	Jettison Nose Fairing	Fairing Timer.
+253. 93	Stop BTL Guidance	BTL Ground Station.
+255. 53	Stop Pitch Program	BTL Discrete.
+265. 18	Spin Started	
+267. 18	SECO Signal (initiated)	
+268. 64	Start State III Spin-up	BTL Sequential.
+268. 7	Retro Action	
+268. 64	Start Stage III Spin-up	BTL Sequential.
+270. 64	Stage II Engine Cutoff (SECO)	BTL Sequential.
+272. 14	Stage II/III Separation	BTL Sequential.
+662. 89	Stage III Ignition	Coast Timer.
+700. 31	Stage III Burnout	
--------	Loss of Beacon Track	
+2300	Satellite Separation from Stage III	

system is employed. The third stage is ignited 663 seconds after lift-off and burnout occurs 37 seconds later. The expended third stage engine and payload continues in orbit together for 1500 seconds after burnout before the payload is separated from the third stage.

The satellite was injected into an almost circular orbit (having an eccentricity of 0.0042) with an apogee altitude of 465.9 statute miles and an inclination to the equator of 48.36 degrees. The launch trajectory is shown graphically in Figure 79. The plot of the Millstone (Doppler) radar tracking data is shown for comparison in Figure 80. The orbital period was close to 99.19 minutes. The pass over the station at Woomera, Australia, indicated a payload spin rate of 10 rpm showing

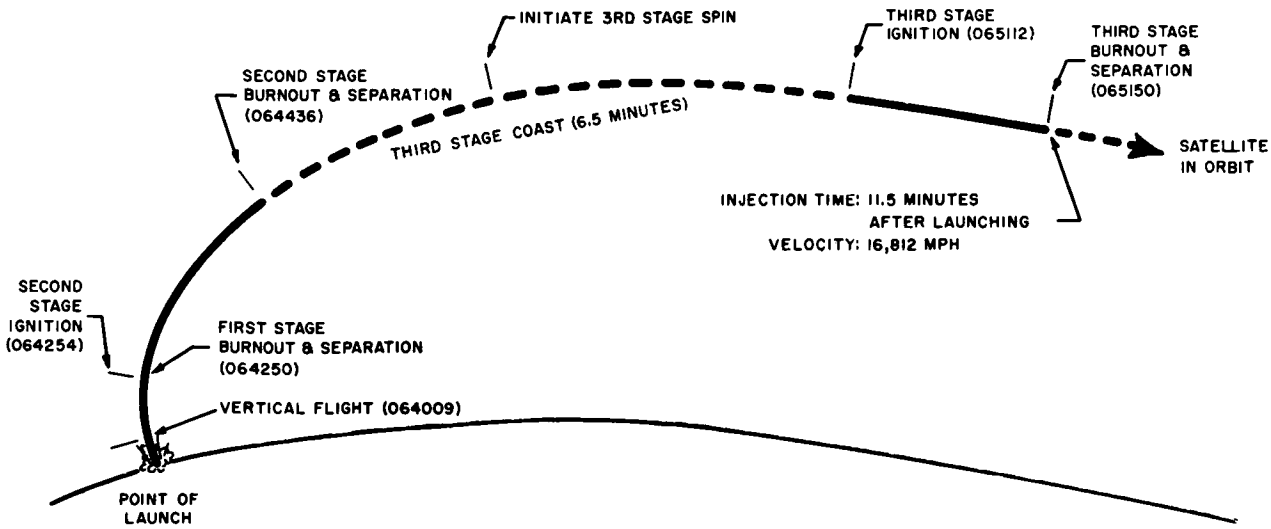

FIGURE 79.—TIROS I launch trajectory

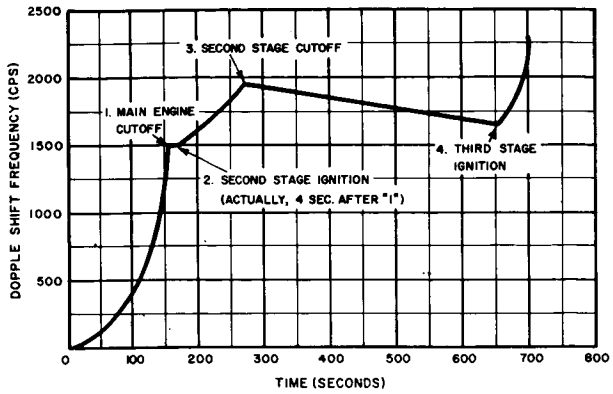

FIGURE 80.—Millstone doppler record of TIROS I launch.

that the despin mechanism of the satellite had operated properly. The first pictures taken were of the Gulf of St. Lawrence and were received at both Fort Monmouth and RCA-Princeton simultaneously. The approximate path of the first four orbits are shown in Figure 81.

LAUNCH VEHICLE PERFORMANCE

First-stage powered flight.—The propulsion system performance was normal throughout flight. The engine start sequence and transition to main stage were satisfactory.

The roll program occurred between 2 and 9 seconds flight time as planned, and rolled the vehicle counterclockwise to a flight azimuth of 49 degrees which was within the expected tolerance.

The pitch program was generated at the correct times and was properly executed to shape the trajectory. The Bell Telephone Laboratories guidance system, located in the second stage, provided steering commands during first-stage opera-

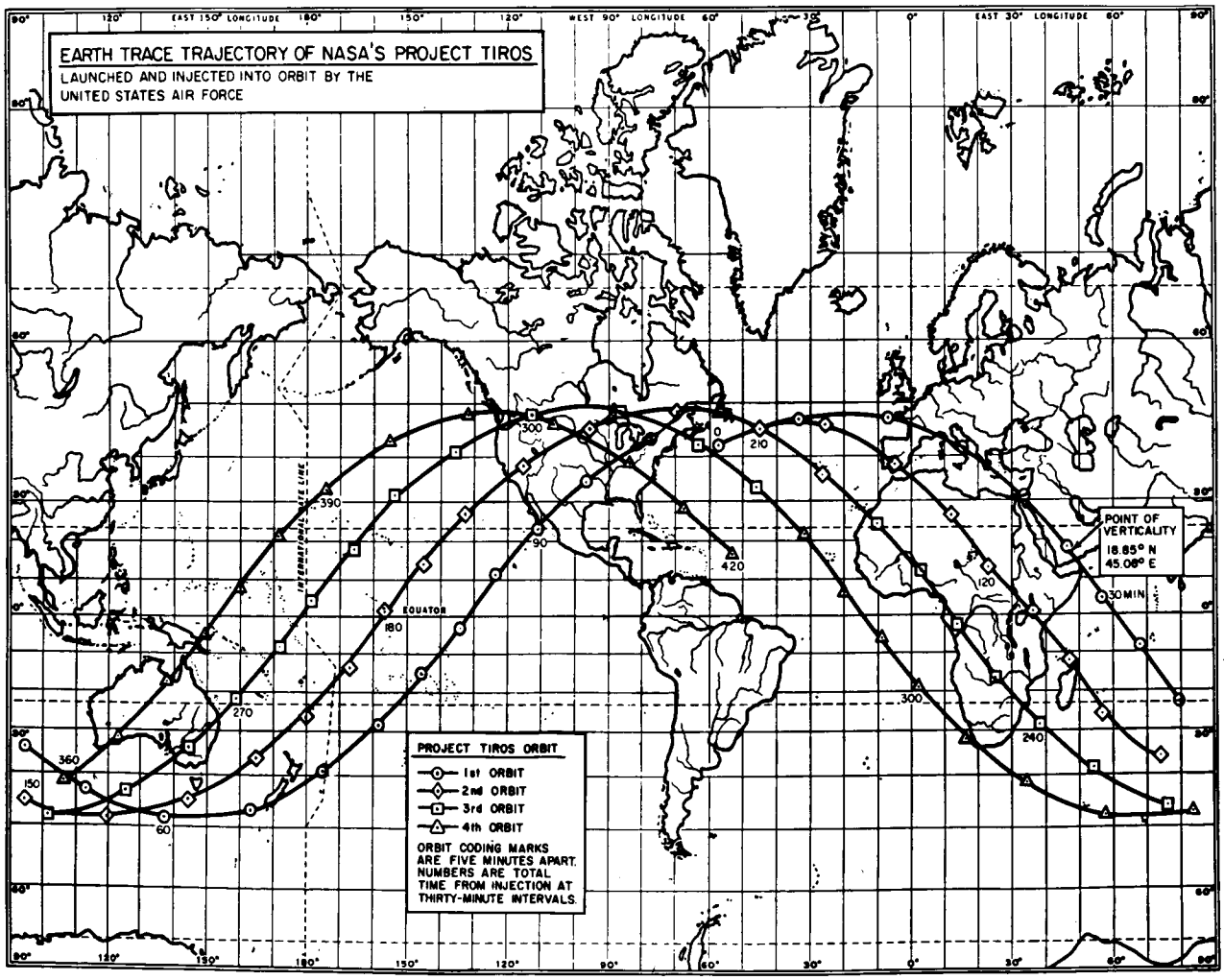

FIGURE 81.—Path of the early TIROS I orbits.

tion. The control system responded properly to these commands.

Main engine cutoff (MECO) was initiated at 160.8 seconds upon propellant depletion. Since no provision had been made for command shutdown of the vernier engines, their operation continued until vernier propellant depletion at 173.8 seconds.

Control signal data correlated with engine position data, gave evidence of satisfactory hydraulic system performance. Performance of the electrical power system was normal throughout flight.

First/second stage staging.—Staging was completely satisfactory. The staging sequence was initiated by the MECO signal as planned at 160.8 seconds. Second-stage ignition occurred 4.0 seconds after MECO.

Second-stage powered flight.—The propulsion system performance was normal throughout flight. The engine operated for 103 seconds. Satisfactory operation of the control system was indicated. The second-stage pitch program began at separation and was completed at 252.8 seconds. Guidance steering commands were transmitted to the vehicle and control system response to these commands was normal. Operation of the gimbal actuation system was satisfactory. Hydraulic pressure was maintained at the proper level throughout flight. Stability was maintained in the roll plane by an on-off roll control system utilizing helium gas which operated for about 1.5 percent of the time from separation to third-stage spin-up.

Second/third stage staging.—Guidance commands initiated third-stage spin-up, second-stage engine cutoff (SECO), and third-stage separation. These were all accomplished within the planned limits. The actual third-stage spin rate obtained was less than the design rate, indicating that all of the spin table rockets did not fire. This apparently did not degrade third-stage performance since the orbit achieved was very close to nominal. The second-stage retro system operated satisfactorily at separation, and the desired change in velocity and attitude was achieved. The vehicle apparently tumbled 8 seconds after the retros were activated as indicated by loss of the guidance track at that time. This was expected.

Third-stage coast period.—Following spin-up and separation, the third stage coasted for a period of approximately 395 seconds to injection altitude. The coast period was controlled by a coast timer. Third-stage ignition occurred at 664 seconds. The 1,500-second payload separation timer apparently started properly at this time.

Third-stage powered flight.—The third-stage engine burned for 38.3 seconds. The velocity increase was slightly greater than required and was partially due to the payload being approximately 6 pounds lighter than predicted. The payload was successfully separated from the third stage.

CHAPTER 5

THE TIROS I POST-LAUNCH PERFORMANCE AND ITS EVALUATION

GENERAL

TIROS I was an exploratory meteorological satellite. It was expected to determine the feasibility of using TV sensors from satellites to photograph the earth's cloud cover for use in weather forecasting as well as to test its design concepts. From the very first picture acquired on April 1, 1960 (Orbit No. 1), the TIROS satellite system demonstrated the capability of television picture-taking techniques that can be utilized as a means of presenting a very large amount of weather data from over a large part of the earth in a very short time—particularly the observation of weather systems that are not observed readily by conventional weather stations. As an experiment, it can be called highly successful, from the viewpoints of both meteorology and space technology. Not only was feasibility demonstrated, but 22,952 cloud pictures synthesized from the video data transmitted by TIROS I have been accumulated, and are being studied to extract the valuable information they might have as an immediate contribution to synoptic weather research. The quality of the cloud pictures exceeded expectations—both the wide angle and the narrow angle views. Implicit in this was proof of the highly satisfactory functioning of the satellite's optical, electrical, and dynamics control subsystems, as well as the complementary subsystems at the ground stations. Pictures stored on tape in the satellite and then played back for transmission were equally as satisfactory, indicating optimum mechanical and electrical functioning of the tape storage equipment.

PERFORMANCE LOG

A summary of the performance of the TIROS I satellite throughout its operational life, referenced to the pertinent orbits and dates, is given in the following tabulation:

Date 1960	*Orbit No.*	*Event*
April 1	001	First wide angle "direct" pictures of cloud cover over the St. Lawrence waterway transmitted to Fort Monmouth, New Jersey, and Princeton (RCA), New Jersey, ground stations. Spin rate 10 rpm.
April 3	022	"Narrow angle" camera clock ceased operation which precluded the transmission of "remote narrow angle" pictures.
April 8	100	100th orbit successfully completed.
April 15	200	200th orbit successfully completed.
April 22	300	300th orbit successfully completed.
April 28	386	Baseplate temperature was +12.2° C.
April 29	400	400th orbit successfully completed.
		"Remote" pictures lost due to a tape recorder "short run" during Orbit 395. Operation of recorder became normal again on Orbit 401. Spin rate down to 9.7 rpm.
May 2	444	Baseplate temperature, side temperature and top temperature reached their maximum of +23° C, +32° C and +48° C, respectively. Attitude sensing system failed. A total of 9,795 pictures taken; 6,495 and 3,300 read out at Fort Monmouth and Kaena Point, respectively.
	457	Attitude sensing system corrected itself and is operating properly.
May 5	500	500th orbit successfully completed.
May 10	562	Unusual programming techniques were tried in an attempt to restore the "narrow angle" camera "remote" operation.
	572	Narrow angle "remote" pictures were received for the first time since Orbit 022 on April 3, 1960.
May 12	600	600th orbit successfully completed.
May 13	604	Spin rate decayed to 9.5 rpm.

Date 1960	Orbit No.	Event
May 19	700	700th orbit successfully completed.
May 23	758–759	An attempt was made to take stereographic pictures from the satellite.
May 26	800	800th orbit successfully completed.
May 27	806	Temperature at top of satellite decreased to −5° C. Spin rate, 9.4 rpm.
	818	An abortive attempt was made to fire one pair of spin rockets.
	819	A second attempt to fire spin-up rockets was successful; increasing spin rate from 9.4 to 12.875 rpm.
June 2	900	900th orbit successfully completed.
June 7	977	The cause of spin axis angular motion has been determined as being mainly due to the interaction of the closed current loop magnetic field along the spin axis of the satellite with the earth's magnetic field. It appears feasible to include a controlled current loop in TIROS II for the purpose of steering the spin axis in space and keeping the sun-spin axis angle within 35 degrees.
June 9	1000	1000th orbit successfully completed.
	1009	One of the two camera (235 Mc) transmitters remained in operation after scheduled shut-down.
	1010	The previously faulty camera transmitter shut down as programmed. Source of difficulty undetermined.
June 13	1067	Erratic operation of wide angle "remote" playback reported.
June 15	1095	The last wide angle pictures read out in this orbit. No telemetry reported.
	1096	One of the two (235 Mc) transmitters failed to shut off at scheduled time. Baseplate temperature is at −9° C, a temperature minimum.
June 16	1100	1100th orbit successfully completed.
	1104, 1105, 1106	No telemetry and no wide angle pictures were received from satellite.
June 17	1119, 1120	No telemetry; no TV carrier received. Interrogation of satellite cancelled until further notice.
June 18	1132	The 108 Mcs beacons were absent for first time.
June 20	1158, 1159, 1160, 1161, 1162, 1163, 1165, 1166, 1167	These orbits were monitored by ground stations. 108-Mc signals received.
June 23	1200	1200th orbit completed.
	1210	The baseplate temperature was 0° C. 108 Mc signal strength appears normal.
June 26	1253	Kaena Point ground station concluded TIROS I operations.
June 28	1276	Satellite was interrogated. No telemetry or wide angle pictures received. Narrow angle pictures received normally.
	1277	Manual programming conducted in an attempt to unlatch suspected "stuck" relay in wide angle camera system.
June 29	1287	Special programming of satellite confirmed sticking of relay, which probably burned out part of wide angle camera circuitry.
	1288	22 "remote" narrow angle pictures read out.
	1289	No "remote" picture received. 108.00-Mc signals received but no 108.03-Mc signals or attitude pulses received.
	1290	7 "remote" narrow angle pictures read out.
	1291	Satellite monitored only; no interrogation.
June 30	1301	An attempt to fire spin-up rockets failed.
	1302	No telemetry or pictures received. Indications of low battery voltages received. A major decision was made to conclude all ground interrogation operations at this time. Minitrack tracking of the 108.00-Mc signals will continue.

THE SATELLITE

THE TV PICTURE SUBSYSTEM

The quality of the pictures from the TV cameras was excellent, exceeding those obtained during evaluation tests. These cameras were optimized for photographing cloud-cover, rather than land areas (see Figures 82a and 82b). Change in electrical or optical focus was not noticed on any of the pictures evaluated. From measurements on the aspect ratio it is seen that during the first several hundred orbits the total aspect ratio remained completely within the design specifications. A comparison of the results and the earlier estimates of the TV signal levels shows good cor-

relation between measured TIROS radiation patterns and the received signal levels. Results from an operational (but not necessarily a meteorological) viewpoint are typified by the companion wide-angle and narrow-angle photographs of the Gulf of California area, shown in Figure 82c. The boxed area in the wide-angle picture was photographed by the narrow-angle camera at approximately 10 times increase in resolution.

THE TELEMETRY AND TRACKING SUBSYSTEM

The TIROS I telemetry subsystem was designed to be simple and reliable, and to give an overall accuracy of 5 percent of full scale on each side of the center of the recorder chart. Transmission of a series of telemetered data was triggered automatically each time the satellite was interrogated. The 40 telemetered parameters were transmitted (and recorded) in about 30 seconds. As each telemetry cycle was recorded, a transparent "standard" overlay chart was laid over the recorder strip chart to determine any extreme or unusual deviations. These quantitative values, plus information on any unusual operating conditions, were teletyped to the NASA TIROS Technical Control Center.

Comparing the telemetered temperature readings from beacon one with beacon two and noting any deviations beyond ±5 percent of full scale (i.e., disagreement of the same sensor as telemetered on the two beacons), it was found that out of 160 temperature readings made at Fort Monmouth, and 104 at Kaena Point, only 3 in each case were beyond ±5 percent. This sampling seems to confirm the expected accuracy of ±5 percent of full scale or ±6.5° C. Regulated battery voltage readings were generally within the 5-percent accuracy of the system. Unregulated battery readings have been less accurately telemetered. To telemeter these voltages in the 28–32 volt range, a 22 volt zener diode was used to "buck out" most of this voltage. A voltage divider then

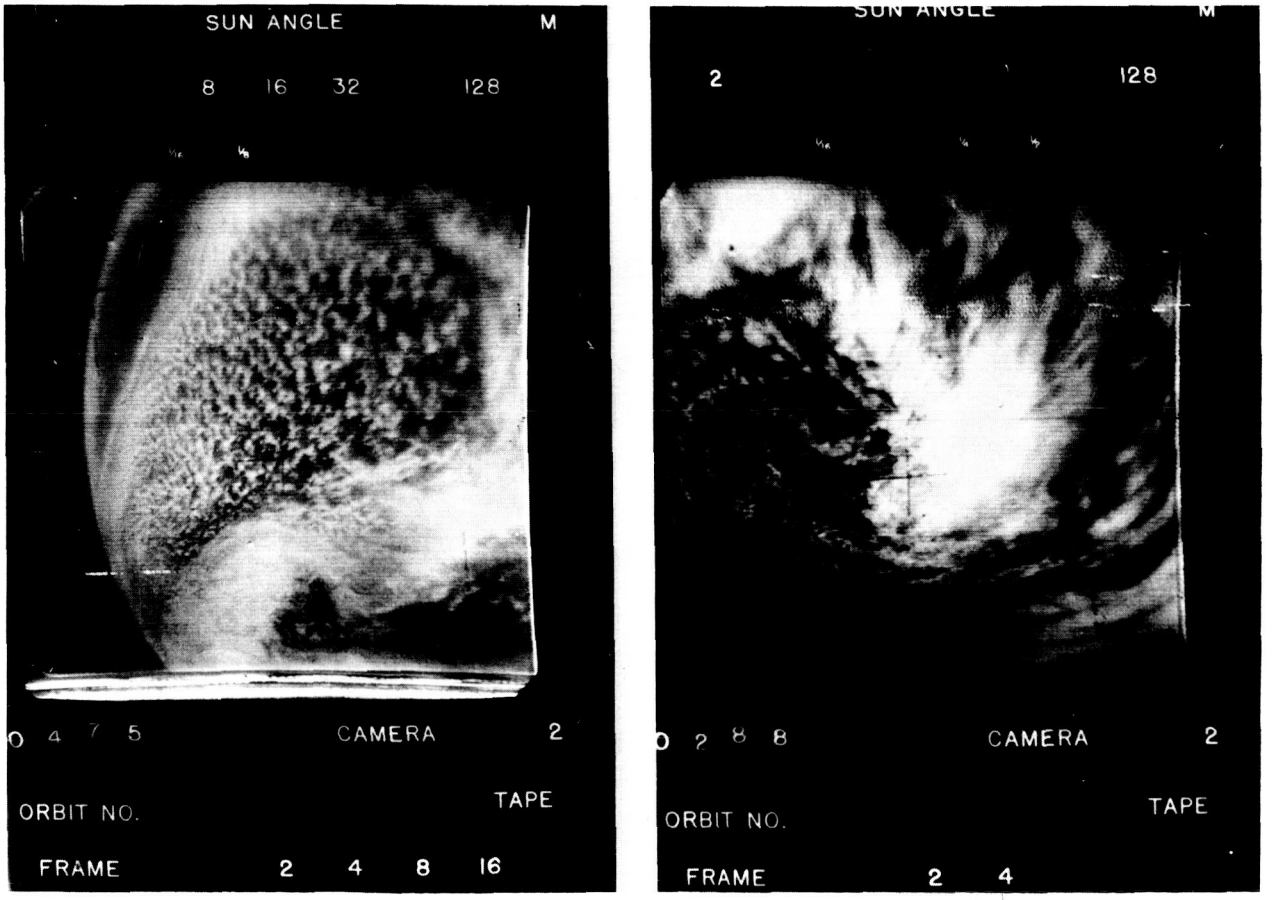

FIGURE 82(a).—Typical TV pictures transmitted by the TIROS I satellite.

sampled the 0 to 10 volt range at 2.5 volts full scale. Thus a 5 percent accuracy should have given a maximum error of ±5 percent × 10 volts, or ½ volt. Larger errors were noted, but these may have been due to temperature effects on the zener diode. The TIROS I telemetry system gave an accuracy of about ±5 percent for most data. Departures from this accuracy were most often due to either sensor variations or non-linearity in the Sanborn recorders. By expanding the scales on some sensors and by better maintenance of calibration on the Sanborn recorders, greater accuracy may be expected.

THE SATELLITE POSITION INDICATOR SUBSYSTEM

The horizon scanner.—The attitude indicator subsystem of the TIROS I satellite was built around an infrared horizon scanner unit, and delivered a pair of spaced pulses indicating the duration of the scan from horizon to horizon of the earth. Some of the characteristics of this subsystem proved to be unsuitable for its intended operation, and it was not possible to use its returned data for satellite attitude measurements. Analysis of the performance of the subsystem has shown that (1) the actual field of the horizon scanner (nominally one degree square) is too large, with insufficiently sharp boundaries, to permit reliable triggering at grazing incidence with the horizon, and (2) the spectral response is such as to permit transitions from earth to clouds to trigger the sensor. Since the recovery time of the associated electronics ranges between 300 and 500 milliseconds, some spurious triggers blocked transmission of succeeding valid pulses.

The wide spectral response caused the sensor to be vulnerable to spurious triggers from reflected solar radiation and changes in radiation intensity as the sensor swept the earth. The sensor field of view was too large and too "fuzzy" to cause a rapid enough change in energy to trigger the electronics for angles of attack of less than 30 degrees.

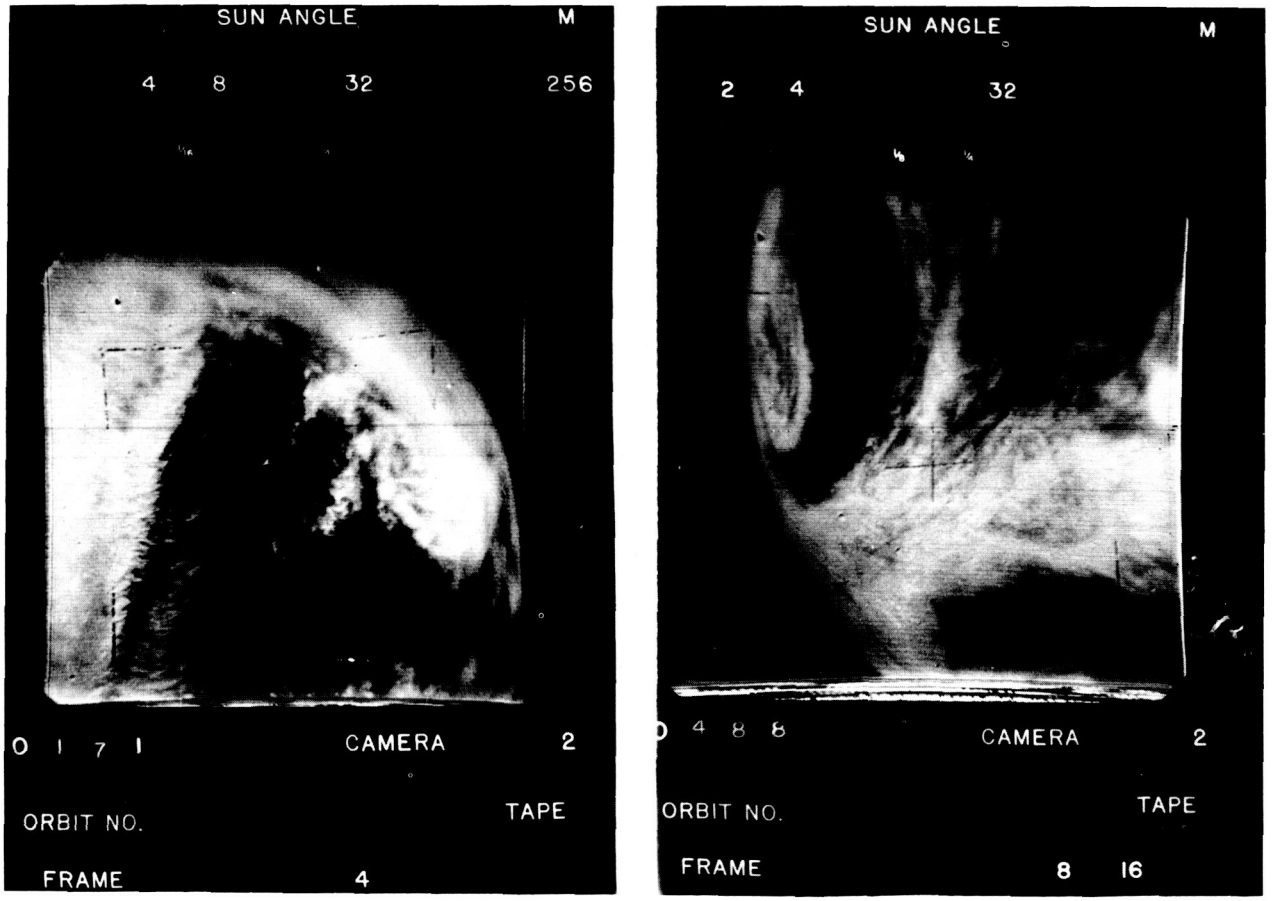

FIGURE 82(b).—Typical TV pictures transmitted by the TIROS I satellite.

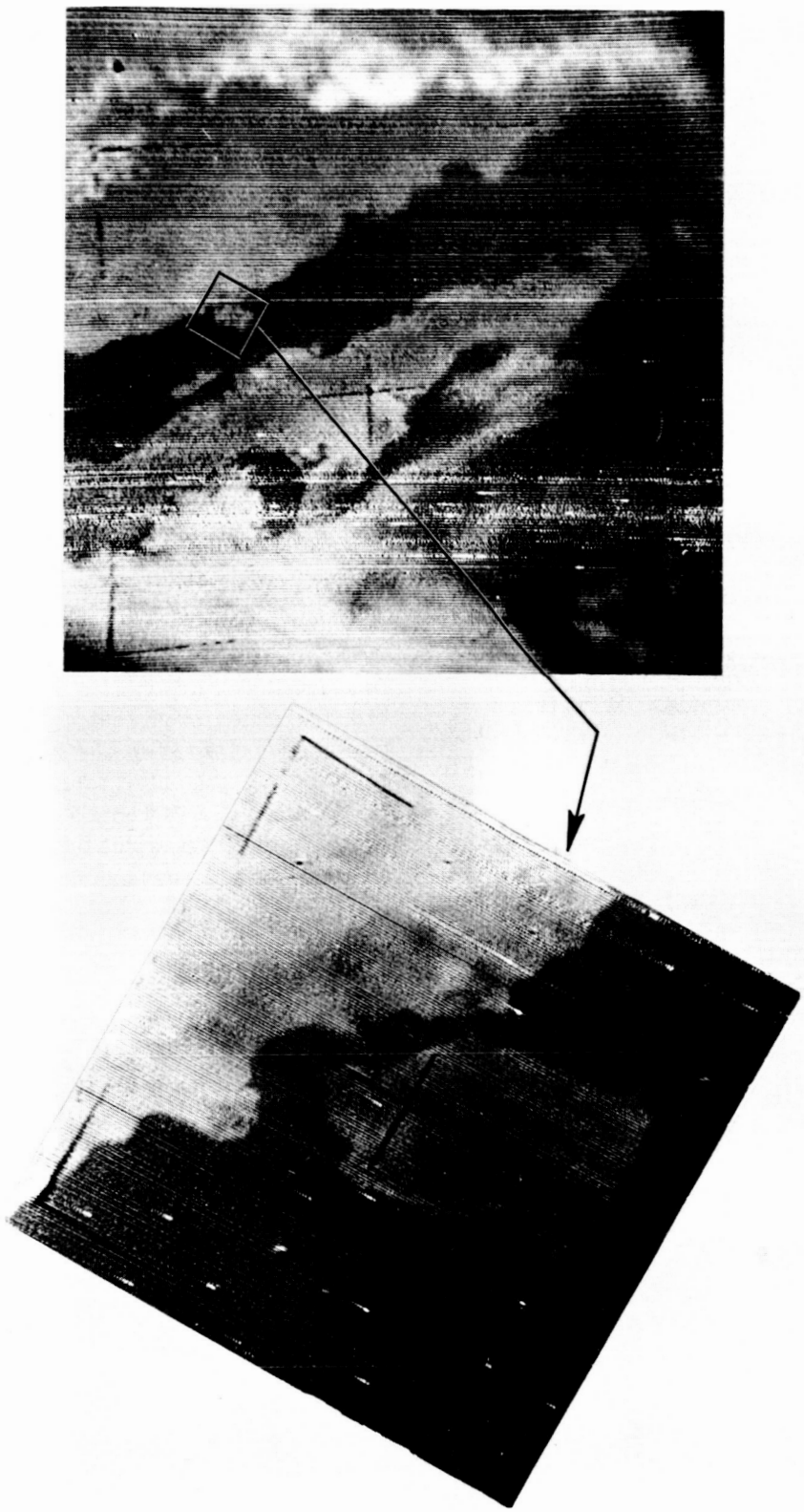

FIGURE 82(c).—Typical TV pictures transmitted by the TIROS I satellite.

The Sun-Angle sensors.—The Sun-Angle sensors and the associated electronic circuitry in the satellite operated satisfactorily, and picture indexing was dependable, except for occasional inconsistencies when noisy signals were received by the ground station.

THE SATELLITE FUNCTION-CONTROL SUBSYSTEM

General.—As evidenced by the full operational capability of the satellite, the function control subsystem with two significant exceptions, performed satisfactorily.

One of the electronic clocks exhibited trouble which disabled the narrow-angle camera channel for a number of orbits. A technique for restoring the clock's operation was discovered and used, and the cause of the malfunction is believed to have been determined.

Toward the end of the scheduled operating life of TIROS I, a control circuit malfunction, believed to be a sticking relay, prevented automatic shut-down of TV transmitter No. 2. This resulted in a steady deterioration of the satellite's performance during its last three weeks of operation.

Clock performance.—The satellite electronic clock and sequencer unit (referred to as the "satellite clock") was supplied by General Time Corporation. Thermal instabilities and transistor breakdowns in the first production necessitated a joint RCA and General Time quality study program, which resulted in the solution of the initial problems. The two clocks in the orbiting satellite (Serial No. D-3) passed the qualification tests at AEP. (However, others required repair or revision of the logic circuits to pass these tests. An improved clock using silicon transistors appears to be the answer to much of the TIROS I difficulties.)

During the D-3 qualification test, it was found that the No. 1 clock could not be set when the temperature was lowered to zero degrees in a vacuum environment. When the temperature was raised to 25 degrees, this difficulty disappeared, and did not reappear again at the lower temperature. The difficulty never reappeared on the ground. An inspection revealed one soldered joint of a questionable nature, which might have caused the trouble. This was resoldered.

During the 22d orbit of TIROS I, the No. 1 system clock failed in a manner similar to that just described. It stayed in this condition until the 572d orbit, when it resumed normal operation as a result of combined mechanical vibrations (from "manual" operation of the telemetry switch) and voltage pulsing (from the clock-set pulses). When the spin-up rockets were fired, the clock again failed briefly, but was restored to normal by the same techniques.

Although the circuit complexity makes it impossible to isolate the exact location of the difficulty, it appears that the remedial technique has been discovered. The operation of the clocks is evaluated indirectly from the telemetered parameters and functional performance of the satellite. Except for the temporary difficulty with the operations of the No. 1 clock, the timing and sequencing components operated satisfactorily within the environmental extremes encountered.

Command circuitry performance.—From April 1st to the middle of June 1960, the command system functioned flawlessly. Between passes 1000 and 1100, suspicion grew that a TV transmitter continued to operate after the time scheduled for its shut-down, going out of range of a ground station. (Indication of a carrier reception on the TV receivers was noted.) During passes 1095 and 1096, on June 16th, continued reception of the transmitter of TV system No. 2 was confirmed (sun-angle pulses were heard and the video carrier was observed on the TV receiver SIGNAL LEVEL meters). It was believed that short-duration "sticking" of a relay in the command circuitry was the cause of this, since battery power still was available on successive orbits, indicating that the battery drain had not been continuous. However, continued deterioration of performance from the TV subsystem led to the decision, on June 17th, to discontinue programming for a number of days to permit a maximum rate of battery recharging.

During pass 1276, on June 28th, the satellite was programmed, but only a few pictures were received. No telemetry was received, which was believed due to TV transmitter No. 2 control circuitry lockout of the telemetry. On pass 1277, special manually-initiated commands were given, designed to exercise the affected relay. However, there was no recovery apparent.

From a careful evaluation of the past history of the satellite during environmental test and the symptoms in orbit it was fairly clear that a contact of command circuit relay K_{2b} (identified in RCA–AED Drawing No. 1176183) was not opening properly at the end of the 26-second timing interval.

At this time, a test was proposed to definitely establish that the K_{2b} relay contact was actually frozen. This test was based on the fact that "clock set" in a normally functioning command system can be accomplished only when the satellite control circuitry first is enabled by other commands. If it were possible to overset the clock (as verified by clock-generated real time pictures) without a "30-second" command, this would prove that the K_{2b} contact was "frozen," since this contact enables the clock-set circuits. During the test, performed during pass 1287 on June 29th, the clock was overset merely by transmitting "set" pulses, which clearly proved the frozen-contact failure theory. With a continuous TV transmitter and camera load, the batteries would drain faster than the solar-cells could recharge them, and the instrumentation operating capability would soon vanish completely.

During pass 1301, on June 30th, the satellite was interrogated, but video response was only momentary. An attempt was made to fire a pair of spin-up rockets, hopefully to shock the relay back to normal operation, but the rockets did not fire.

After pass 1302, about midnight, June 29, 1960, it was decided to discontinue formal operations. At this time, the telemetry still was functioning.

During the period between July 1st and August 19th, 1960, the TIROS I satellite was intermittently monitored. Beacon signals were received, and sun-pulses were detected on the video data carrier. It was estimated that the power supply voltage was between 17 and 22 volts.

On August 18th, a command for firing of the remaining pair of spin-up rockets was transmitted. It was desired to determine if this function was still operative; if the rockets would actually fire; and also to stabilize the satellite orbit to prevent excessive exposure to the sun. The first command sent was ineffective. A second command, sent for a longer interval, was effective. The TIROS I spin rate increased 1.713 rpm.

THE SATELLITE ELECTRICAL POWER SUBSYSTEM

Prior to the TIROS I launching, the energy available to the instrumentation was calculated for each day of the initial three months of satellite life. The equations employed to perform these calculations required use of the time variation of the angle alpha (angle between the sun vector and the satellite spin axis) and the solar-cell temperatures throughout the period of interest. These quantities had been calculated for a specific launch time of April 1, and were based upon the spin axis remaining fixed in inertial space upon achieving orbit.

The 1-hour delay in launch time invalidated these calculations. Furthermore, revised calculations could not be initiated because of the lack of accurate attitude data. A permissible programming load range was determined on the basis of early telemetered solar-cell temperatures and estimates of the angle alpha. It restricted the total load requirements to the range of 23,000 to 30,000 watt-minutes per day or 16.0 to 20.8 watts average.

About 2 months after launch, calculations were carried out which derived the alpha variation with time based on the interaction of the earth's magnetic field and the magnetic dipole characterizing the TIROS satellite. The alpha angle derived from solar-cell telemetry compares closely with these calculations.

Because there was a lack of data concerning variations of the angle alpha, the solar-cell telemetered voltage and temperature were employed to determine alpha. Thus, alpha was not used as a means to find a result, but was calculated from the telemetered data. Figure 83 is a plot of the angle alpha for the first 75 days after launch—the greater part of the operational life of TIROS I. The alpha values shown are average values of 6 to 16 telemetered data points each day. Throughout the 75-day period, the alpha variation calculated from solar-cell telemetry differs by no more than 3 to 5 degrees from that predicted by magnetic-dipole analysis.

In general, the total battery voltages remained in a region of 26 to 31 volts which was the design range. A maximum measurement error of 1.3 volts could have occurred, but this would have been masked by the tolerance in battery voltage.

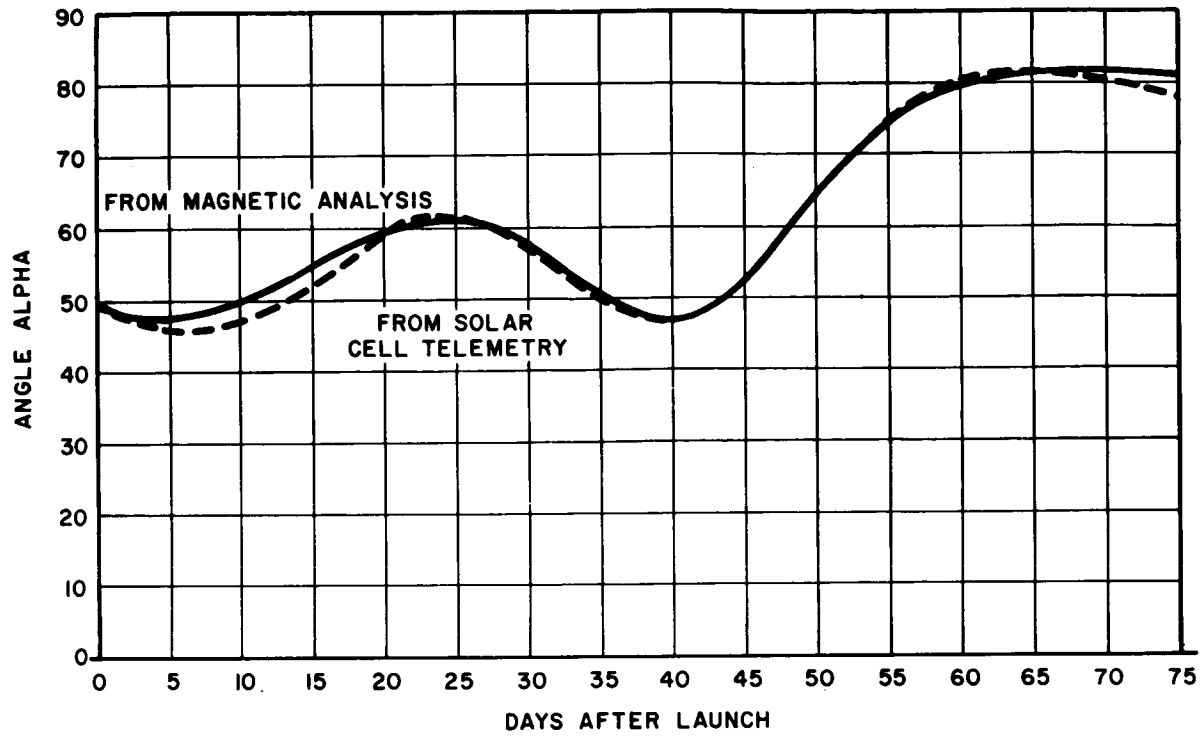

FIGURE 83.—Alpha angle for 75 days after launch.

THERMAL DESIGN

The approach to the temperature control problem for TIROS I comprised three main areas: (1) analysis of the heat-flow problem, (2) development of suitable surfaces and surface coatings for application to the satellite, and (3) experimental verification of the thermal design.

When the constraints on thermal design were established, it was found that the only significant parameters available for thermal control were (1) the surface radiative properties, (2) the hour of launch, and (3) the degree of thermal communication among the mass elements of the satellite.

The temperature-time distributions for TIROS I in orbit as obtained from the telemetry data from the eight temperature sensors (thermistors), has indicated excellent agreement with the predicted thermal responses. Compensation for the known temperature gradient between the baseplate and the average component temperature was required to obtain an exact fit between the telemetered data and the temperature prediction curves, since they refer to different thermal elements.

It was noted with some consternation in the first few days after launch that the satellite temperatures were not following the predicted pattern, shown in the lower curves of Figure 84. This prediction was based on the evolution of alpha angle for the case of an unperturbed spin axis. A plot of the alpha angle vs time curve, using the temperatures obtained from TIROS I telemetry data (Figure 85), compared with the pattern of Figure 84, indicated that the spin-axis was far from remaining stationary in inertial space. This situation soon was confirmed from the reduction of the pictorial data obtained from TIROS. This analysis indicated a precessing spin axis whose resultant angle with the solar flux vector was in excellent agreement with that obtained from pictorial data reduction for the entire life of TIROS to date. It thus afforded a basis for predicting the wanderings of the spin axis for the remaining life of TIROS I.

Figure 86 shows the calculated time-history of the component temperature, based on the actual spin-axis orientation, and the telemetered baseplate temperature as received from TIROS I in orbit. Since only average values of the telemetered temperatures need be employed in this comparison, the random errors in the telemetry

system and readout are necessarily removed by the averaging process. On the date of launch, the two curves differ by 1° C, whereas the component-to-baseplate temperature gradient does not reach its maximum (12° C) until the tenth day after launch. The influence of initial temperature and thermal inertia would reasonably explain the lack of a temperature gradient on the date of launch. The reduction of the component-to-baseplate gradient during the 25th to 28th day is also understandable in terms of both the large α angle and Ψ that existed at this time. From the thermal test it was ascertained that a 9° C gradient existed between component and baseplate temperature for the α=zero, Ψ=1.0 conditions.*

THE SATELLITE DYNAMICS CONTROL SUBSYSTEM

Control devices.—The three devices which were aboard TIROS I to control the satellite dynamics: (1) the tuned energy absorption mass (TEAM) precession damper, (2) the despin (Yo-Yo) mechanism, and (3) two pairs of spin-up rocket motors all went into operation satisfactorily.

The precession damper operated as predicted. The clarity of the cloud pictures received from the first orbit confirmed the effectiveness of this mechanism immediately after satellite separation. After the firing of the spin-up rockets on May 27, 1960, this was corroborated. Variations in the spin rate at that time were noted by measurements made with the aid of the horizon scanner. It was noted that the horizon scanners were receiving pulses from the sun once per revolution. Slight modulation was noted in this period. An analysis was made to show that precession could account for this variation. The calculations further show that the angle that the spin axis made with final angular momentum factor was less than ½ degree, actually something in the region of ¼ degree, and this figure was being reduced over a period of several days.

The Yo-Yo spin-down mechanism was actuated after separation as predicted. The initial speed prior to spin-down was established as 84 rpm by several measurements. The final speed was 10 rpm. The mechanism was designed for a 10-to-1 spin reduction, but the lower ratio, confirmed by the actual operation, was observed on ground tests. The variation between actual operation and design was allowed to stand because supporting computations had been made which indicated that the discrepancy could be accounted for by windage

*Ψ is the fraction of the total orbit time that the satellite is illuminated by the sun.

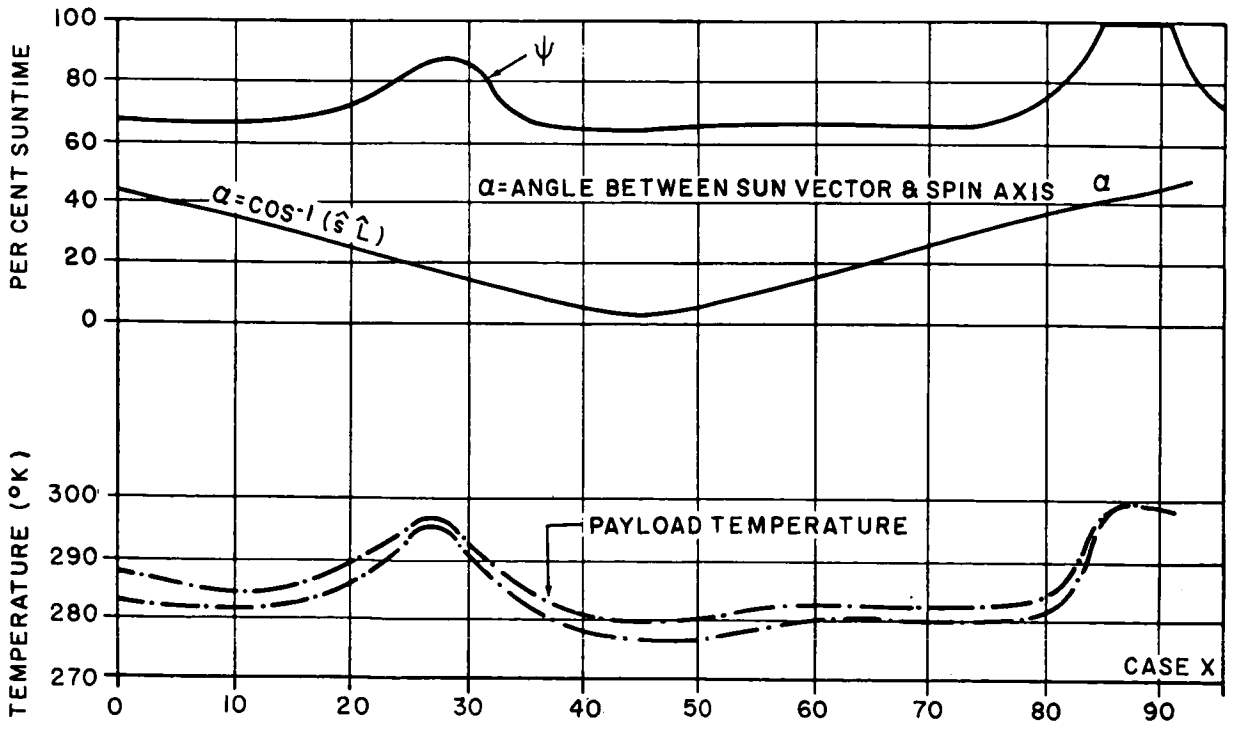

FIGURE 84.—Predicted satellite temperatures for an unperturbed orbit as a function of time after launch.

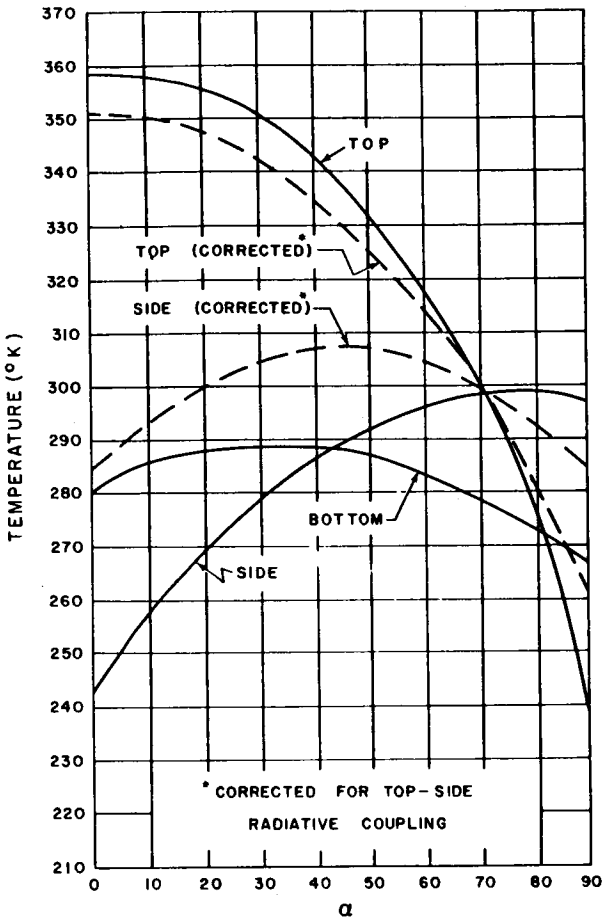

FIGURE 85.—Calculated and measured temperatures as a function of angle alpha.

losses in the ground environment. It should be kept in mind that the 1.6 rpm error amounts to a momentum error of about 1.8 percent. Further work was directed toward determining the source of this momentum discrepancy. Two areas investigated were the release-hook friction and the angle that the cable made with the radial line at the time of release from the hook. However, no conclusive results were obtained. Sufficient empirical data was, nevertheless, available to that a correction factor could be applied to the despin weights, which will give the speed-reduction ratio desired with a considerably smaller error in the future.

The spin-rate attrition of TIROS I was less than had been expected, but approximately 7 weeks after launch it was decided to fire a pair of spin-up rockets to attempt to improve the spin-axis stability, as well as to test the control circuitry. On May 27, 1960, during the 819th orbit, a pair of rockets was fired. The TIROS I spin rate increased from 9.4 rpm to 12.88 rpm (the design increase value was 3 rpm). This is the first know demonstration of a rocket motor on any satellite being fired successfully after such a long period in the space environment.

Spin-axis motion.—A performance anomaly relating to the satellite's spin-axis attitude was both a major annoyance and a potential "dividend." The attitude of the satellite changed in a fashion much different and to a greater extent than was anticipated. Great care was taken to insure that all sources of external torques had been considered before approving a satellite design with no attitude correction system. Five major external torques that could affect the satellite were known. These are: differential gravity, magnetic field interaction with eddy current moments, magnetic field interaction with ferromagnetic materials, drag due to air and/or microscopic dust, and solar radiation pressure. The first two and the last were handled passively in the satellite design. The magnetic materials problem was more difficult because of the nonlinearity of the system, and the air dust drag problem was almost impossible to

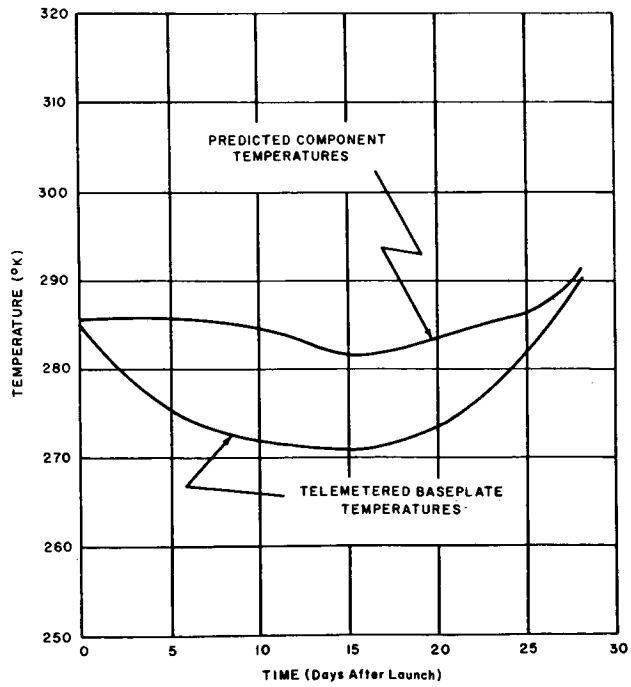

FIGURE 86.—Predicted and measured satellite temperatures as a function of time after launch.

combat because of the lack of information about the distribution at the altitudes in question.

The analysis of this problem was hampered by two other factors in component design. One is that the spectral response of the infra-red horizon scanner was not optimum, so that the data transmitted was extremely noisy and the computer program written beforehand was unable to produce consistent determinations of the axis orientation. The second factor is that the lens of the wide-angle camera was chosen primarily to meet a 104 degrees coverage-angle requirement, and certain of its distortion characteristics made attitude determination by photo-interpretation cumbersome and not too precise. (Methods were later developed for optimum use of both the horizon scanner data and the pictures in making rapid and reasonably good attitude determinations on a day-to-day basis.)

However, using the information available at the time, a study and analysis of the spin-axis motion lead to the discovery of its major causes.[58] The investigation was pursued along the following lines:

The time of injection and the trajectory of the launch vehicle determined that the coordinates of the satellite spin vector on the celestial sphere should have been the following: declination (δ), +19.8 degrees; right ascension (RA), +58.6 degrees (see Figure 87).

After several days of picture taking, it became apparent from analyses of photographs showing the horizon or indentifiable landmarks that the direction of the spin vector (and, hence, the camera axes) was not fixed but was moving southward by as much as 3 to 5 degrees per day (see Figure 88). On April 23, an analysis of photographs indicated that the spin axis had reached its southernmost declination, namely, −30 degrees. At this time its RA had increased to +69.0 degrees. Several days later it was determined from photographs that the spin vector was moving northward again and its RA increasing (eastward) at a greater rate than previously.

Due to a torque exerted on the orbit by the earth's bulge, the orbit regressed (westward) around the equator 4.547 degrees per day. It is apparent from Figure 87 that if the spin vector were to remain fixed in space, the westward motion of the orbit would cause an angle to develop

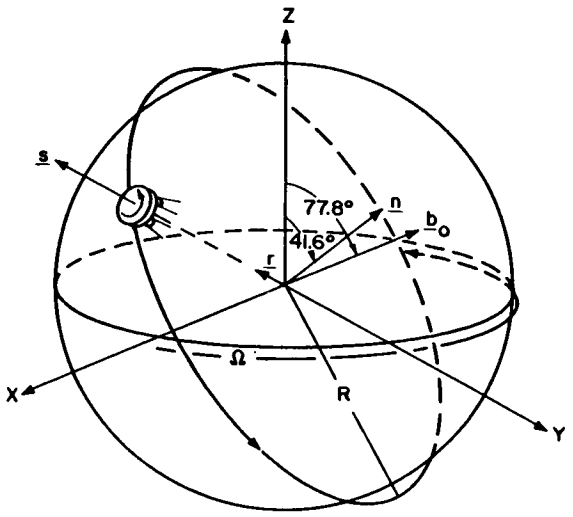

FIGURE 87.—Coordinates of the satellite spin vector on the celestial sphere.

TIROS I at time of injection, 1152 GMT April 1, 1960. X, Y, and Z are space coordinates with origin at the center of the earth and with the X–Y plane in the equatorial plane of the earth; s is the unit spin vector of the satellite. The astronomical coordinates of $\underline{s}$ are: declination 19.8 degrees, right ascension 58.6 degrees; Ω is the angle from the X axis to the orbital ascending node. The orbital nodes regress at the rate of −4.547 degrees per day westward; n is the unit vector normal to the orbit, $\underline{b_o}$ is the mean normalized magnetic dipole field vector appearing to the satellite in one orbit, $\underline{r}$ is the unit vector from the center of the earth toward the satellite, and R is the orbital radius.

between the orbital plane and the spin axis. Since TIROS I has the shape of a short cylinder (19 inches high and 42 inches in diameter), the moment of inertia about its spin axis is larger than the other principal moments of inertia. Hence, when the angle between the orbital plane and the spin axis is greater than zero and less than 90 degrees, a torque due to differential gravity (similar to that exerted by the sun and moon on the earth causing its precession) will be exerted on the satellite. The nature of this torque was investigated but was rejected as the primary torque causing the observed forced precession because it would have caused the spin vector to move northward instead of in the observed southerly direction.

The minimum spin vector declination of −30 degrees was reached about April 23. At this time the orbit had regressed 100 degrees and the unit vector $\vec{n}$, normal to the orbital plane, lay in the same meridional plane as the unit vector $\vec{s}$ along the satellite spin axis. Shortly thereafter, when

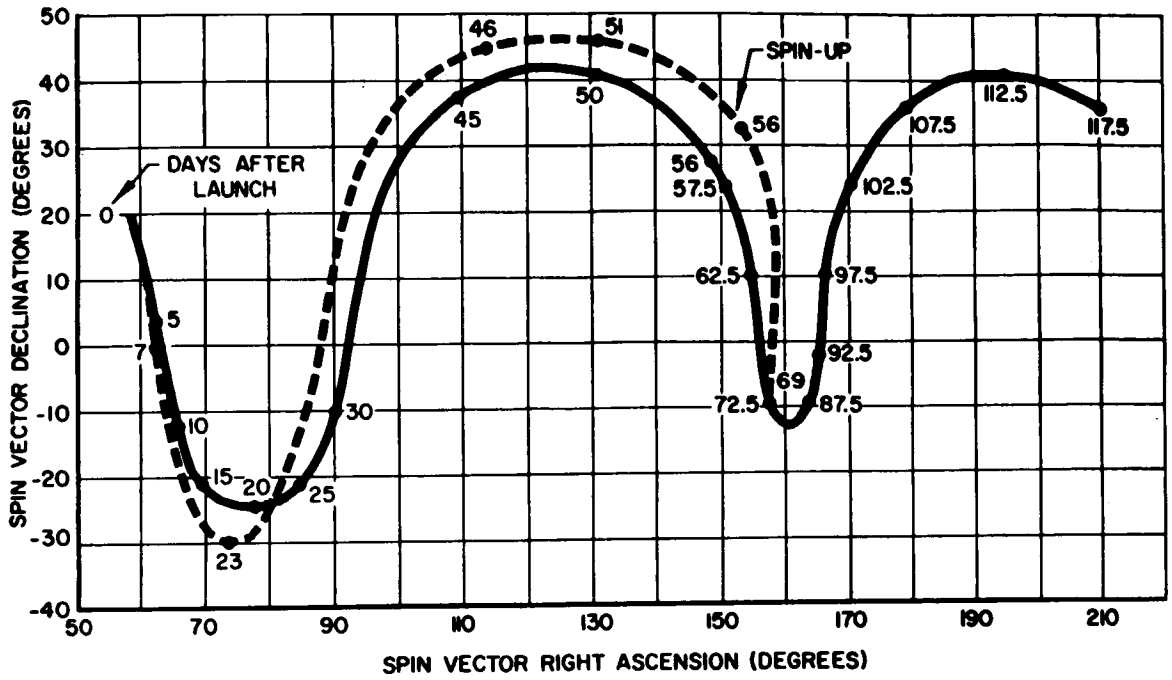

FIGURE 88.—Observed motion of the TIROS I spin vector based on an analysis of photographs (dashed line) compared with the theoretical motion based on the effects of a magnetic dipole moment along the spin axis and differential gravity (solid line). Declination is (+) north and (−) south of the celestial equator; right ascension is (+) east of the vernal equinox along the celestial equator. Increased stability of both the theoretical and observed motion is seen after spin-up on May 27 (56 days after launch). The last picture with clearly identifiable landmarks was received on June 9 (69 days after launch).

$\vec{n}$ developed a westerly component with respect to $\vec{s}$ and the satellite spin axis declination was observed moving northward, the possibility of a magnetic couple being the primary force became apparent and it became the focal point of investigation.

A computer program was undertaken using the initial injection conditions of TIROS I on April 1, 1152 GMT. The results are plotted together with the observed motion of the spin axis in Figure 88, and show excellent agreement. In this computer run a time function for the spin rate was introduced reflecting its observed decrement from 10.0 rpm on April 1 to 9.4 rpm on May 27. (The decay in spin is due to a very small torque caused by eddy currents generated in the spinning satellite by the earth's magnetic field.) On May 27 a pair of spin-up rockets was fired at 2133 GMT, increasing the spin rate to 12.875 rpm. Greater stability was effected at higher values of the spin rate, and this increased stability can be seen in the plot after spin-up.

The outcome of this investigation has indicated that the angular motion of the spin axis of TIROS I can be explained quite well by considering two torques, to wit:

1. A primary torque caused by the interaction of a magnetic dipole along the satellite spin axis (caused by residual permanent magnetism of ferromagnetic materials or by closed current loops in the instrumentation or by a combination of the two) with the earth's magnetic field, and

2. A secondary torque caused by differential gravity in the earth's gravitational field.

Two drawings developed during the course of this investigation to illustrate the physical concepts involved are reproduced here. Figure 89 is a celestial representation of the travel of TIROS I, showing the spin-axis vector projected on the celestial sphere. Figure 90 represents a view from the sun of the satellite at selected times, showing the spin axis and orbital orientations.

THE COMMAND AND DATA-ACQUISITION STATIONS

The three Command and Data-Acquisition stations in operation for the post-launch phase of TIROS I operations were located, respectively, at

Fort Monmouth, N.J.; Kaena Point, Hawaii; and Princeton, N.J. The first two were the primary operational stations, and the third was maintained in the operational network for backup purposes. Essentially, all three stations performed in accordance with their design objectives, although some minor and temporary malfunctions as well as a few difficulties in operating procedures revealed significant information useful in stabilizing and improving their future performance.

THE FORT MONMOUTH STATION

The TIROS I ground station at Fort Monmouth was operational for all but five passes of the satellite for which operation at this location was programmed. The "down time" was due mainly to malfunctions in the antenna and associated circuitry. Other difficulties which developed did not significantly affect or degrade operation of the overall system. An evaluation of the advantages, disadvantages, and specific performance of pertinent components is discussed here.*

Antenna subsystem equipment.—During the first week of operation, considerable trouble was encountered with one of the 235-Mc preamplifiers. This situation was corrected. In another instance, erratic tracking was caused by an intermittent phase demodulator tube. In general, the performance of the system has been satisfactory. The performance of the Antenna Programmer was satisfactory, once the ephemeris had been established. For about the first month of operation, these units were used as back-up for automatic tracking. Later, they were used as the primary tracking means. Use of the programmer permitted delayed operation of the television transmitter. Thus, when commanding 1N or 2N only, it was possible to track the satellite in the absence of 235 Mc carrier until the satellite approached minimum range, in order to acquire data with the best signal-to-noise ratio. In cases where additional telemetry was required, the 235-Mc carrier could be dropped out at any time without loss of tracking capability. The programmers are a desirable and useful part of the station.

Receivers and transmitters.—The Nems-Clarke receivers, the Tapetone converters, the R390 receivers, and the Collins transmitters all operated satisfactorily, and without difficulty.

Command equipment.—A modest amount of maintenance was required to maintain satisfactory operation of the stepping switches in the command programmer. It is felt that some of the difficulties experienced with stepping switches may be

*Other information pertinent to this discussion may be found later in this section under the various subsystem headings.

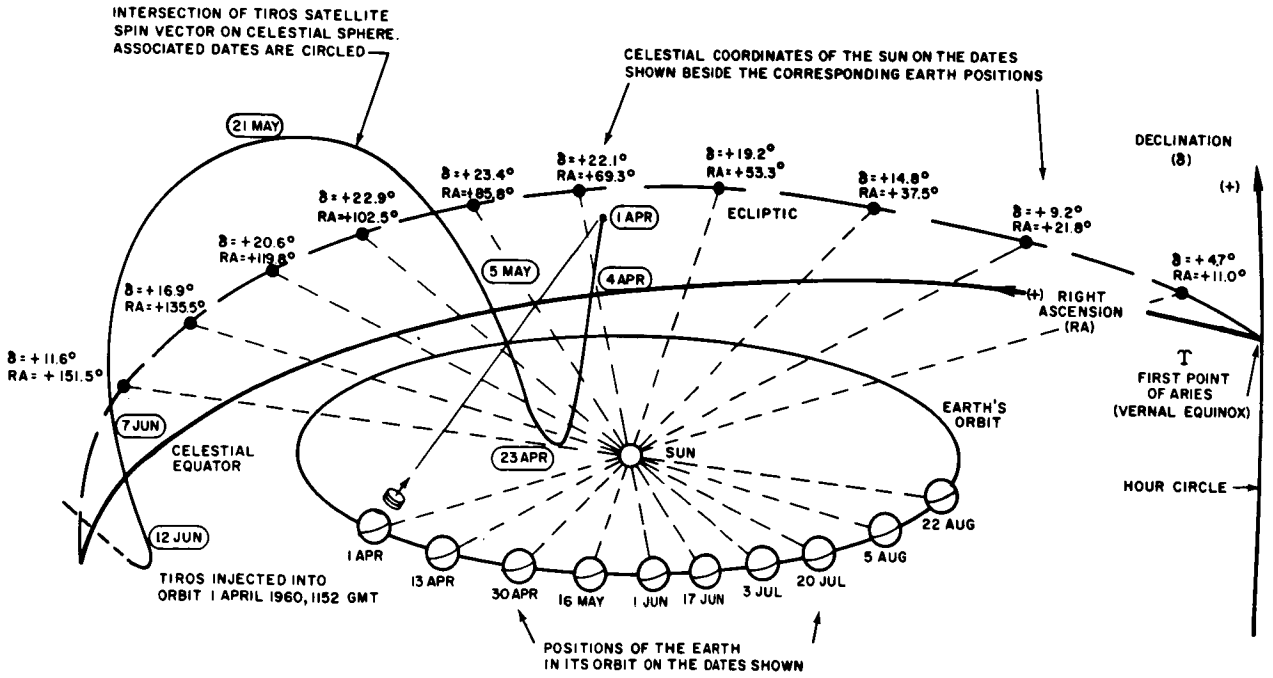

FIGURE 89.—Celestial representation of the travel of TIROS I (showing spin-axis motion).

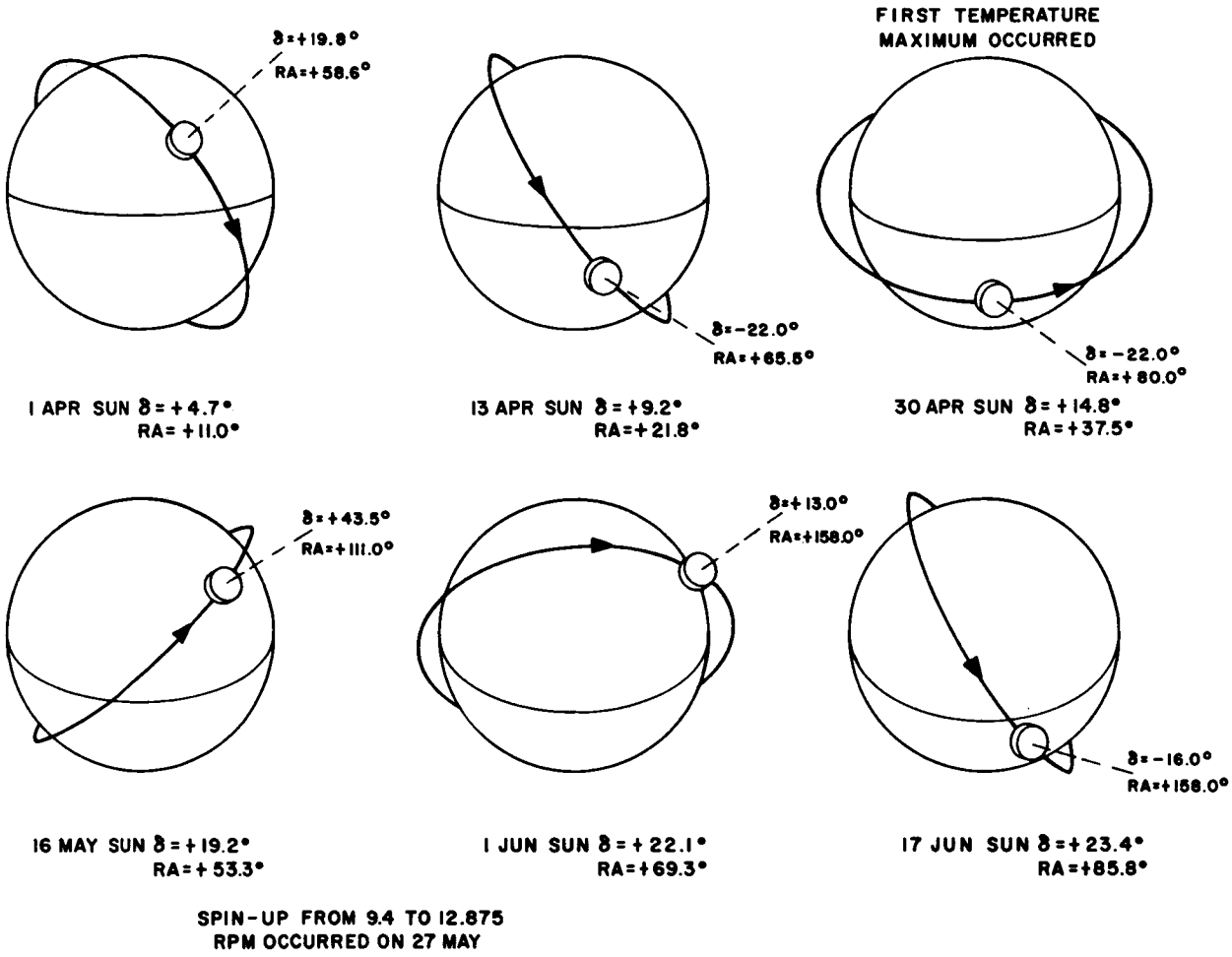

FIGURE 90.—Selected orbits of TIROS I, viewed from the sun (showing change in spin-axis vector).

attributed to a great deal of dust inadvertently brought into the tracking station due to lack of paving in the surrounding area. The use of duplicate programming units is a very desirable feature of the station.

In two instances, the alarm set unit failed to alarm. In one case, alarm three failed and no clock start pulse was sent. This resulted in failure to get playback and subsequent loss of information for one orbit. In another instance, alarm two failed, resulting in loss of command for playback. All stepping switches were cleaned and readjusted by General Time Company, and subsequent operation was satisfactory. Constant monitoring of the Burroughs counters used in the Remote Picture Time-Set unit was required. These devices will occasionally skip a count and, depending on which decade it occurs, a gross error can occur. Checkout of both sets of counters prior to each orbit has prevented such gross errors in set pulses. The problem of the reliability of these units and the circuitry which drives them has not yet been completely resolved. The manufacturer's representative has examined the circuitry and performed tests at both the Princeton and Monmouth locations with no enlightening recommendations.

Further investigation of this type as well as other types of counters is recommended. The Clock-Set Pulse Demodulator recovers the clock-set pulses from the detected RF output of the command transmitter. Operation of this unit has been reliable and satisfactory. The test equipment available for reading these demodulated pulses consists of a Berkely counter (primary) and a Hewlett-Packard counter (back-up).

Three failures have occurred in the Berkely counter. One was in the power supply due to failure of a Zener diode and the others were tube failures within the counter units. In spite of this, the Berkely counter gives a more reliable indication than does the Hewlett-Packard. The latter, because of its higher sensitivity, requires careful monitoring of input level as well as careful input shielding to prevent external noise from introducing as extra count.

TV picture equipment.—Operation of the FM demodulator was satisfactory. Improvements in transient response against tape drop outs would be desirable. Some degree of care is necessary for proper operation of the "killer" circuit. This is largely due to the characteristics of the sun angle and indexing computer rather than a requirement for camera or tape recorder operation. One transistor failure occurred in the deflection amplifier. Operation of the amplifier has been generally satisfactory. Stability against size and centering shifts has been good. Size and centering were constantly monitored, and adjustments were required no more often than once a week. The Sync Separator system gave consistent satisfactory results.

Operation of the Video Display was satisfactory. After about 3 weeks of operation, the kinescope broke at the junction of bulb and neck. This was believed to be due to an unrelieved strain. A week later a second tube broke in the same manner. The tube mounting arrangement was modified and there were no further failures.

The Beattie-Coleman camera and magazine system has given more trouble and required more maintenance than normally would be expected. Several factors have contributed to this situation. Initially, inexperience in loading of the magazines, lack of inspection and cleaning prior to reloading and bent film spools were contributing causes. However, sticking shutters, broken springs, and two defective magazine motors are indicative of marginal design. Since a better double-frame camera has not yet been found, rework of these cameras, with the assistance of the manufacturer, is recommended.

Tape recorders.—In general, the behavior of the tape recorders was satisfactory. Two major failures occurred in the No. 1 tape unit. These were eventually traced to the fact that this machine was used for putting metallic leader on the tape. During this operation, an automatic end of tape circuit was overloaded. When this condition persisted for long periods of time, as was the case when many rolls of tape are being processed, failure of this circuit was liable to occur. Ampex provided the machine with an auxiliary switch which disabled this circuit when the machine was used for putting metallic leader on tape.

Position reference equipment.—The Sun-Angle Computer proved to be susceptible to noise both in the indexing and sun-angle computer sections. A modification was made in the vertical synchronizing generating circuit to prevent noise from affecting the indexing and readout pulse. A fairly critical "killer" circuit should clear up this disadvantage. Also, effectively narrow bandwidths should be used to pass both the sun pulse bursts and subcarrier signal.

The sun angle computer has had several transistor failures within the various subassemblies. These subassemblies are readily repaired; the time consuming portion of the job is diagnosis of the source of trouble.

It should be noted that down time on this computer probably is no greater than that of any other computer having no self-checking features. Its susceptibility to noise is, however, a disadvantage which should be eliminated.

A number of difficulties were encountered in the attitude recorder equipment: Two defective modules were found during operation of the elapsed time computer. One was due to a hairline crack in the printed circuitry and the other was a defective transistor.

The clutch mechanism in the Friden Tape Punch became intermittent in its operation and finally failed after 6 weeks' operation. This has been repaired by the manufacturer. No loss of data resulted.

The Read-out relays are the mercury-wetted type. In two instances, since operation started, one of these relays "hung up." In one case, the diagnosis indicated loss of capillary action and in the other, a shorted contact (perhaps due to impurities in the mercury). An investigation should be started to determine the need for arc-suppressing circuitry. Overloading of the Tape Punch Relay Supply occurred in two instances due to operation of the tape feed for too long a period.

An investigation is underway to determine whether or not double pulsing occurs as a result of a probable defect in the Attitude Pulse Demodulator. Human error in noting the time of the WWV start pulse caused inaccuracies in the time of starting of the Attitude Recorder. The procedure was revised so that an auxiliary clock having a large sweep second hand was operated in parallel with the master clock from the frequency standard. The use of an electronic clock would permit automatic start as well as eliminate the annoying fading conditions of the WWV signal.

Telemetry equipment.—Considerable difficulty was experienced prior to the start of the operation due to a non-linearity in channel B of the Sanborn recorder. This was finally traced to a defective pen system in the recorder.

Summation.—Overall performance of the Fort Monmouth Command and Data Acquisition station has been satisfactory. Components not mentioned in the preceding discussion operated, in the main, satisfactorily and according to design expectations. A few showed minor deviations which did not detract from the successful operation of the station, and which are easily correctable. It is recommended that work be devoted to improving the following characteristics:

Reduction of hum in video components.
Operation of the sun-angle computer in the presence of noise.
Operation of the demodulator and "killer" circuits.
Reliability of photographic camera operation.
Reliability of remote picture time-set operation.

The quality of the developed film from the ground stations as regards uniform picture density range suffers to some degree in comparison with the pictures from the Princess station. The difference lies essentially in the method of operation. Princeton uses an "image enhancement" technique which amounts to manually adjusting the video signal level in the white direction to compensate for shifts in d-c level due to differences between the two camera systems and between direct camera and playback.

The operational (Fort Monmouth and Kaena Point) stations use a definite setting of controls referenced to a standard density wedge. This method reduces the requirement for operator judgment and permits a standard procedure for pre-orbit checkout. Also, the sun density wedge is indicative of the densities to be expected in the television pictures.

It is suggested that the advantages and disadvantages of the two techniques be reevaluated in the light of the results obtained.

THE KAENA POINT STATION

The TIROS I ground station at Kaena Point was successful in achieving all of the primary objectives of the program and in so doing demonstrating a high degree of efficiency and reliability. The station was operational on all passes of the satellite for which such operation was programmed and only rarely did a malfunction or other situation cause notable degradation of data or other failure.

Of the approximately six orbits per day within range of Kaena Point, an average of three to four a day were active. Inactive passes resulted from one or more of the following: schedule conflicts with other programs using Kaena Point tracking station facilities, ground contact time insufficient for useful coverage, no contact programmed for reasons concerning the satellite (battery budget, camera coverage, etc.).

During the periods of active operation, about 150 remotely recorded TV pictures from the wide angle satellite camera were received every day and (when system one was functioning) an equal number from the narrow angle camera. Most passes resulted in one and in a few cases two readouts of telemetry data from the satellite. Attitude data were punched on almost every pass and this data and the telemetry summary were transmitted by teletype to NASA TIROS Technical Control in Washington, D.C., after each pass. The events recorder strip-chart was used by the local meteorologists to help interpret the positive film-strip pictures and afterwards was filed with the other data. All hard-copy data was controlled by the NASA representatives at Kaena Point and under this direction the magnetic tapes, negative film, events records, telemetry records, etc., were periodically mailed to RCA–AEP, NPIC, etc., as required. The operation of some sub-systems and components is worth noting here in more detail.

Antenna system equipment.—Signal acquisition and tracking at Kaena Point for TIROS I was

essentially the same as for other satellite programs which had used the station and so benefited from the experience of the operating personnel. The satellite beacon frequency was always acquired first and manually tracked. When the satellite TV transmitter was turned on, the antenna was usually placed in the autotrack mode at this frequency. Programs which caused dropouts of the TV carrier for more than a few seconds sometimes caused loss of track. Also, on a few occasions, the signal was erroneously tracked on a minor lobe of the antenna pattern, but this situation would be rectified in a minute or two. A more serious difficulty was the strong prevailing wind at Kaena Point which many times made it too dangerous to unstow the TLM–18 tracking antenna. On those passes, the TV signal was received by a "tri-helix" antenna at a much poorer signal-to-noise ratio than with the big dish, and the beacon signal was not received. The usual TV signal from the TLM–18 registered from about 100 microvolts to over 1,000 microvolts at the receivers. The gains of the antenna mounted preamplifiers, etc., were nominally about 40 db, but an undetermined discrepancy caused the vertical and horizontal channels to differ by several db. Under some conditions of weak signal, this inequality may have degraded the resultant signal by causing non-optimum operation of the diversity combiner unit.

Command equipment.—With the exception of a few malfunctions, the TIROS I command subsystem at Kaena Point performed as designed. Proper timing, modulation, and amplitude of the transmission was evidenced by proper response from the satellite. Exceptions to this occurred during schedule conflicts with other satellite tracking operations when it was necessary to remove the command transmitter helix from the radar antenna. The signal from this antenna was marginal and usually caused extra pictures to be transmitted because short fades had the effect on the bird of command tone drop-outs. Command failure on one occasion, when using the helix antenna, was caused by jamming of a slack-adjusting mechanism for the antenna feed cable. Motion of the antenna then caused the cable to part.

The only unreliability experienced with the command programmers was in the remote picture time set units. Several times the Burroughs decade counters in these units failed unpredictably and caused an incorrect number of clock-set pulses to be transmitted.

TV picture equipment.—Although the quality of the pictures produced by the TV subsystem was good, certain difficulties were encountered and in some respects there was need for improvement. Chief of these was the vertical sweep circuitry which had a small amount of drift and hum. The drift made it necessary to check the centering immediately before each pass. Before this practice was instituted, several pictures were produced with about five percent of the image hidden by the kinescope mask. The hum modulation of the sweep voltage produced a grouping of lines which was very noticeable on the early orbits. Replacement of a marginal tube and additional filtering of a critical screen voltage reduced the peak hum displacement of the line position to about half the line spacing.

On the early orbits, the brightness settings were based on calibration runs with nominal video level. Later experience established that the "black level" in the received and demodulated video subcarrier varied considerably from beginning to end of tape playback and from playback to direct camera operation. Nominal brightness settings were revised once for the negative film and several times for the rerun positive films to correct the picture density.

Some trouble was encountered with the electrically operated Beattie-Coleman camera and film magazines. A change in the tension of the return spring of the solenoid actuated shutter was required to assure rapid and reliable closing after each frame. The film magazines required replacement of one motor, repair of one motor lead, readjustment of several microswitches, and addition of a washer under a cover attachment screw to prevent mechanical binding.

Position reference equipment.—The index number count recorded on film and magnetic tape was found in the beginning, to be inconsistent, especially on passes with noisy signal. This condition was shortly corrected by addition of filtering to remove transients from the index generator input and by deriving the index count from the relay closure which also tripped the camera shutter.

646–770 O—64——8

On most passes with good signal strength, the sun angles displayed by the sun angle computer agreed well with the position of the horizon in the corresponding pictures. Further verification of correct computer operation was not obtained, however, since the information locating the picture principal points or subsatellite points was not complete enough to allow the meteorologists to use the sun angle for picture orientation in their immediate analyses. The events recorder strip chart was useful to the meteorologists in determining the time of direct pictures, but in one or two instances uncertainty was caused by the lack of an indication of which of the two programmers was actually in use.

Telemetry equipment.—The telemetry signal was received and recorded with no difficulty on most passes. On one or two occasions, both pairs of receivers were inadvertently tuned to the same frequency, or both channels of the Sanborn recorder were switched to the same receiver output resulting in the loss of data for one channel. On a few passes the signal was noisy enough to affect the recording. The telemetry equipment performed within its rated accuracy; but the cumulative effect of calibration error, drift, pen nonlinearity, overlay inaccuracy, reading error, and quantizing to the nearest 0.05 volt (0.5 mm) resulted in errors of up to perhaps 0.2 volt. An attempt was made to minimize these errors by placing a reference 3-point calibration on the strip chart at the beginning and end of the pass and use of a revised overlay to compensate for pen nonlinearity.

THE PRINCETON STATION

Experience in operation of the Princeton Ground station confirmed to a large extent the evaluation of this portion of the TIROS I equipment as gleaned from observations of and assistance in the operation of the other two stations. Also, since the TIROS I system was exploratory, or experimental, in nature, the Princeton station was valuable as a facility for experimentation with the equipment. At Kaena Point, by contrast, the TIROS I station was under the cognizance of a separate organization, whose responsibilities were considered to be primarily operational. This limited considerably the possibility of experiment, and the times at which RCA–AEP design-engineering personnel had access to the station. At Fort Monmouth, the conditions were considerably more flexible, with experimental as well as operational procedures being freely conducted.

CHAPTER 6

ACKNOWLEDGMENTS

The issuance of this report would have been infinitely more difficult had it not been for the cooperation of the staffs of organizations and periodicals which had published information pertinent to TIROS I and related meteorological events. Permission to reproduce such material in this report is gratefully acknowledged. Material which first appeared in many U.S. Government publications also has been used. The editors hereby express their appreciation to:

Aerojet-General Corporation
Allegany Ballistics Laboratory
ARS Journal (formerly, Jet Propulsion)
Astronautics
Douglas Aircraft Company
Electronics
General Electric Company
General Time Corporation
IGY Bulletin, and Annals of the IGY
Journal of Geophysical Research
Monthly Weather Review
Radiation, Incorporated
Radio Corporation of America
Space Technology Laboratories, Inc.
Stanford Research Institute Journal
U.S. Naval Research Laboratory
U.S. Weather Bureau
World Meteorological Organization
Institute of Radio Engineers, Transactions

Special textual assistance was provided by the Astro-Electronics Division, Radio Corporation of America. Many of the photographs and drawings appear through the courtesy of: The U.S. Air Force, the U.S. Navy, and the U.S. Army Signal Research and Development Laboratories.

LEWIS J. ALLISON,
ERNEST A. NEIL,
Goddard Space Flight Center.

CHAPTER 7

REFERENCES AND BIBLIOGRAPHY

TEXT REFERENCES

1. Tepper, M., "Meteorological Satellites," in: NASA Authorization for Fiscal Year 1961 (Hearings before the NASA Authorization Subcommittee of the Committee on Aeronautical and Space Sciences, U.S. Senate, 86th Congress, 2d Session, on H.R. 10809, June 30, 1960), Pt. 2: Scientific and Technical Aspects of NASA Program, Washington: Govt. Print. Off., 1960, pp. 643–668.
2. Robinson, E., "Meteorology—Newest Region of Exploration," SRI J. 3(2) : 37–40, 1959.
3. Holliday, C. T., "Preliminary Report on High Altitude Photography," Photogr. Engin. 1(1) : 16–26, January 1950.
4. Baumann, R. C., and Winkler, L. "Proposal for Photography from a High Altitude Probe." Vanguard Division, National Aeronautics and Space Administration, February 1959.
5. Bergstralh, T. A., "Photography from the V–2 Rocket at Altitudes Ranging Up to 160 Kilometers," U.S. Naval Research Laboratory Report 3083, April 1947.
6. Crowson, D. L., "Cloud Observations from Rockets," Bull. Amer. Meteorol. Soc. 30(1) : 17–22, January 1949.
7. Baumann, R. C., and Winkler, L., "Photography from the Viking II Rocket at Altitudes Ranging Up to 158 miles," U.S. Naval Research Laboratory Report 4489, February 1, 1955.
8. Baumann, R. C., and Winkler, L., "Photography from the Viking 12 Rocket at Altitudes Ranging up to 143.5 Miles," U.S. Naval Research Laboratory Report 5273, 22 April 1959.
9. Hubert, L. F., and Berg, O., "A Rocket Portrait of a Tropical Storm," Monthly Weather Rev. 83(6) : 119–124, June 1955.
10. "Frontal Cloud System Pictures Obtained by Rocket," Science 129(3343) : 198–200, January 1959.
11. Hubert, L. F., "Analysis of Project Hugo Test Firing, December 5, 1958," U.S. Weather Bureau, MSL Report No. 2, August 1960.
12. Vachon, D. N., and King, J. I. F., "High Altitude Cloud Photography from Ballistic Missiles," Aerosciences Lab., Gen. Electric Co., Techn. Inf. Ser. R59SD471, Contract AF 04(647)269, December 1959.
13. Conover, J. H., and Sadler, J. C., "Cloud Patterns as Seen from Altitudes of 250 to 850 Miles—Preliminary Results," Bull. Am. Meteorol. Soc. 41(6) : 291–297, June 1960.
14. Bull. World Meteorol. Org. 9(1), January 1960.
15. Evans, H. E., Baumann, R. C., and Andryshak, R. J., "The Arctic Meteorology Photo Probe," NASA Technical Note D–706, in press, 1962.
16. Greenfield, S. M., and Kellogg, W. W., "Inquiry into the Feasibility of Weather Reconnaissance from a Satellite Vehicle," Rand Corp. Report R–365, August 1960.
17. Wexler, H., "Observing the Weather from a Satellite Vehicle," J. Brit. Interplanetary Soc. 13(5) : 269–276, September 1954.
18. Wexler, H., "The Satellite and Meteorology," J. Astronautics 4(1) : 1–5, 8, January 1957.
19. Singer, S. F., "Meteorological Measurements from a Minimum Satellite Vehicle," Trans. Amer. Geophys. Union 38(4) : 469–482, August 1957.
20. Singer, S. F., and Wentworth, R. C., "A Method for the Determination of the Vertical Ozone Distribution from a Satellite," J. Geophys. Res. 62(2) : 299–308, June 1957.
21. Hanel, R. A., Licht, J., Nordberg, W., Stampfl, R. A., and Stroud, W. G., "The Satellite Vanguard II: Cloud Cover Experiment," IRE Trans. on Military Electronics, Vol. MIL–4(2–3) : 245–247, April–July 1960.
22. Stroud, W. G., Hanel, R. A., Nordberg, W., and Stampfl, R. A., "Meteorological Measurements from an Earth Satellite," in: Annals of the International Geophysical Year, London: Pergamon Press, 1958, Vol. 6, Pt. 3, pp. 340–345.
23. Hanel, R. A., and Stampfl, R. A., "An Earth Satellite Instrumentation for Cloud Measurements," in: IRE National Convention Record, New York: Institute of Radio Engineers, 1958, Pt. 5, pp. 136–141.
24. Hanel, R. A., Stampfl, R. A., Cressey, J., Licht, J., and Rich, E., "Tracking Earth's Weather with Cloud-Cover Satellites," Electronics 32(18) : 44–49, May 1, 1959.
25. "1958 NASA/USAF Space Probe (Able-1) Final Report," Vol. 2: "Payload and Experiments," National Aeronautics and Space Administration Memo 5–25–59W, Vol. 2, June 1959.
26. Baker, S. C., "Television System Final Report (Pioneer II)," Space Technology Laboratories GM–00–4110–00549, December 10, 1958.
27. "Project Able-3, Final Mission Report," Vol. 2, Space Technology Laboratories, TR–59–V002–02903 (AF BMD TR–60–154, Vol. 2) August 1960.
28. 'IGY Satellite 1959 Iota," Trans. Amer. Geophys. Union 40(4) : 401–405, December 1959.

29. Suomi, V. E., "University of Wisconsin Proposal for Measuring Radiation Budget of the Earth from an Earth Satellite," U.S. National Committee for the IGY, Project 32.11, 1956.
30. Suomi, V. E., and Parent, R. J., "Satellite Instrumentation for Measurement of the Thermal Radiation Budget of the Earth," in: Proc. National Telemetering Confernece, Baltimore, June 1958, New York: Inst. Aero. Sci., 1958, pp. 186–190.
31. Parent, R. J., Miller, H. H., Suomi, V. E., and Swift, W. B., "Instrumentation for a Thermal Radiation Budget Satellite," in: Proc. National Electronics Conference, Chicago, October 1959, Chicago: National Electronics Conference, Inc., 1960, Vol. 15, pp. 824–839.
32. Suomi, V. E., "The Thermal Radiation Balance Experiment on Board Explorer VII," University of Wisconsin, 1960.
33. Wexler, H., "Radiation Balance of the Earth as a Factor in Climatic Change," in: Climatic Change: Evidence, Causes, and Effects, ed. by H. Shapley, Cambridge: Harvard University Press, 1953, pp. 73–105.
34. Davies, M. E., "Are the Lunik III Photos Fakes?" Astronautics 5(6): 46, 48–49, June 1960.
35. Whitney, L. F., ed., "Cloud Conference Summary," U.S. Weather Bureau, MSL Report No. 1, July 1960.
36. Butler, H. I., and Sternberg, S., "Tiros—The System and Its Evolution," IRE Trans. on Military Electronics Vol. MIL–4(2–3): 248–256, April–July 1960.
37. Henry, I. G., "Lifetimes or Artificial Satellites of the Earth," Jet Propulsion 27(1): 21–24, 27, January 1957.
38. Newton, R. R., "Lifetimes of Artificial Satellites," Jet Propulsion 28(5): 331–333, May 1958.
39. Glaser, A. H., "Meteorological Utilization of Images of the Earth's Surface Transmitted from a Satellite Vehicle," Blue Hill Meteorological Observatory, Harvard University, AFCRC–TR–57–241, October 31, 1957.
40. Mesner, M. H., and Staniszewski, J. R., "Television Cameras for Space Exploration," Astronautics 5(5): 36–37, 126–130, May 1960.
41. Katz, A. H., "Observation Satellites: Problems and Prospects," Astronautics 5(4): 26–29, 74–80, April 1960.
42. "TIROS I Meteorological Satellite System; Final Operational Report on Phase I," Astro-Electronics Products Division, Radio Corporation of America, October 1, 1960.
43. Freeman, J. D., "The Tiros I Timer," Astronautics 5(6): 35, 78–79, June 1960.
44. "Sensor Alignment and Calibration Data for the TIROS I Meteorological Satellite No. D–3." Astro-Electronics Division, Radio Corporation of America, April 10, 1960 (CONFIDENTIAL).
45. O'Kelley, H. E., "Tracking Radar for Tiros Weather Satellite," Electronics 33(16): 57–60, 15 April 1960.
46. "NASA Worldwide Tracking and Telemetry Operation," Goddard Space Flight Center, National Aeronautics and Space Administration (undated).
47. "Model Specification MB–3 Rocket Propulsion System for WS–315A," Rocketdyne Division, North American Aviation Co., R–633S, May 20, 1957.
48. "Real Time Vehicle Evaluation and Orbit Injection Determination for Project TIROS," Space Technology Laboratories, TR–59–0000–61932, February 1960.
49. Booth, Frank M., "Model Specification, Rocket Propulsion System, Liquid Propellant AGC Model No. AJ10–42," Aerojet-General Corp. ATS–L4.184, May 29, 1958.
50. "Operation Plan, Project TIROS," Meteorology Branch, Goddard Space Flight Center, National Aeronautics and Space Administration, Rev. December 1959.
51. "Detailed Testing Objectives for Tiros I," Space Technology Laboratories, TR–59–0000–00750, Los Angeles, California, March 15, 1960.
52. Glaser, A. H., "A System for the Meteorological Use of Satellite Television Observations," in: Contributions to Satellite Meteorology, U.S. Air Force Cambridge Res. Ctr., GRD Research Note No. 36 (AFCRC–TN–60–427), ed. by W. K. Widger, Jr., June 1960, pp. 63–91.
53. Widger, W. K., Jr., "Examples of Project Tiros Data and their Practical Meteorological Use," U.S. Air Force Cambridge Res. Lab., GRD Research Note No. 38 (AFCRL TN–60–470), July 1960.
54. "Weather Analysis from Satellite Observations," U.S. Navy Weather Research Facility, NWRF 33–1260–039, December 1960.
55. "Depiction of Satellite Cloud Observations for Facsimile Transmission," U.S. Weather Bureau, Forecast Development Report No. 1, December 1960.
56. Glaser, A. H., "TIROS I: An Operation Evaluation of a New Meteorological Tool," in: Contributions to Satellite Meteorology, Vol. II, U.S. Air Force Cambridge Res. Ctr., GRD Research Note No. 36 (AFCRL 438), ed. by F. R. Valovcin, April 1961, pp. 1–138.
57. "TIROS Countdown Manual," Douglas Aircraft Co., Santa Monica, California, February 1960.
58. Bandeen, W. R., and Manger, W. P., "Angular Motion of the Spin Axis of the Tiros I Meteorological Satellite Due to Magnetic and Gravitational Torques," J. Geophys. Res. 65(9): 2992–2995, September 1960.

BIBLIOGRAPHY OF SATELLITE METEOROLOGY

1. Bjerknes, J., "Detailed Analysis of Synoptic Weather as Observed from Photographs Taken on Two Rocket Flights over White Sands, N. Mex., July 26. 1948," Rand Corp. Paper P–887, April 1951.
2. Conover, J. H., "Cloud Patterns and Related Air Motions Derived by Photography," Final Report on Contract AF 19(604)–1589, Blue Hill Meteorological Observatory, Harvard University, AFCRC–TR–59–246, June 1959.

3. Dryden, W. A., and Prosser, N. E., "Optimum Utilization of Satellite Observations in Weather Analysis and Forecasting," Florida, State Univ. Dept. of Meteor. Final Report on Contract AF 19 (604)–1754, 1 February 1959.
4. Fritz, S., "On Observing the Atmosphere from Satellites, Pt. I, Cloud Observations," Weatherwise 12(4) : 139–144, 163–165, August 1959.
5. Fritz, S., "Meteorological Uses of Satellites," in: McGraw-Hill Encyclopedia of Science and Technology, New York: McGraw-Hill 1960, Vol. 8, pp. 322–323.
6. Greenfield, S. M., "Synoptic Weather Observations from Extreme Altitudes," Rand Corporation Paper P–761, 15 February 1956.
7. Greenfield, S. M., and Kellogg, W. W., "Satellite Weather Reconnaissance," Rand Corporation Paper P–1402, 12 June 1958.
8. Greenfield, S. M., and Kellogg, W. W., "Weather Reconnaissance by Satellites," Astronautics 4(1) : 32–33, 77–78, January 1959.
9. Greenfield, S. M., and Kellogg, W. W., "Calculations of Atmospheric Infrared Radiation as seen from a Meteorological Satellite," J. Meteorol. 17(3) : 283–290, June 1960.
10. Hanel, R. A., "Low Resolution Unchopped Radiometer for Satellites," ARS J. 31(2) : 246–250, February 1961; also NASA Technical Note D–485, January 1961.
11. Hubert, L. F., Fritz, S., and Wexler, H., "Pictures of the Earth from High Altitudes and their Meteorological Significance," in: Space Research; Proc. 1st Internatl. Space Sci. Sympos., Nice, January 1960, ed. by H. K. Bijl, Amsterdam: North-Holland Publ. Co., 1960, pp. 3–7.
12. Johnson, D. S., "Image Sensing as Applied to Meteorological Satellites," J. Soc. Motion Pict. Telev. Engin. 69(1) : 14–18, January 1960.
13. Kuhn, P. M., and Suomi, V. E., "Infrared Radiometer Soundings on a Synoptic Scale," J. Geophys. Res. 65(11) : 3669–3677, November 1960.
14. Ludwig, F. L., and Nagle, R. E., "Cloud Shield and Radar Precipitation Echo Relationships with Satellite Applications," Stanford Research Institute, Scientific Report 1 (AFCRC–TN–60–478), April 1960.
15. Merrill, H. J., "Cloud-Cover Observation and Radiative Measurements From a Satellite," Trans. New York Acad. Sciences Ser. 2, 21(2) : 153–158, December 1958.
16. Kiss, E., "Bibliography on the Use of Satellites in Meteorology," Meteorol. and Geophys. Abstracts 11(10) : 1683–1729, October 1960.
17. Mook, C. P., and Johnson, D. S., "A Proposed Weather Radar and Beacon System for Use with Meteorological Earth Satellites," in: Conf. Proc. 3rd Nat. Convention on Military Electronics, Washington, June–July 1959, IRE Professional Group on Military Electronics, pp. 206–209.
18. "NASA Authorization for Fiscal Year 1961; Hearings before the NASA Authorization Subcommittee of the Committee on Aeronautical and Space Sciences," U.S. Senate, 86th Congress, 2d Session, on H.R. 10809, June 30, 1960, Pt. 2: "Scientific and Technical Aspects of NASA Program," Washington: U.S. Govt. Print. Off., 1960.
19. "Space Handbook: Astronautics and its Applications; Staff Report of the Select Committee on Astronautics and Space Exploration," 86th Congress, 1st Session, Washington: U.S. Govt. Print. Off., 1959.
20. Stroud, W. G., and Nordberg, W., "Meteorological Measurements from a Satellite Vehicle," in: Scientific Uses of Earth Satellites, ed. by J. A. Van Allen, Ann Arbor: Univ. of Michigan Press, 1956, p. 119–132.
21. Suomi, V. E., "The Radiation Balance of the Earth from a Satellite," in: Annals of the International Geophysical Year, London: Pergamon Press, 1958, Vol. 6, Pt. 3, pp. 331–340.
22. "Operational Use of Weather Satellites," U.S. Navy Weather Res. Facility, NWRF 33—0360–029, March 1960.
23. Van Allen, J. A., "Scientific Instrumentation of Satellites," Am. Geophys. Union. Geophys. Monographs No. 2 : 142–146, 1958.
24. Von Braun, W., "The Explorers," in: Proc. 9th International Astronautical Congress, Amsterdam, August 1958, Vienna: Springer-Verlag, 1959, Vol. 2, pp. 914–931; also in: Astronautica Acta 5(2) : 126–143, 1959.
25. Townsend, J. W., Jr., "Experimental Research Program in the Space Sicences," J. Geophys. Res. 64(11) : 1779–1787, November 1959.
26. Wark, D. Q., "On Indirect Temperature Soundings of the Stratosphere from Satellites," J. Geophys. Res. 66(1) : 77–82, January 1961.
27. Wexler, H., "Satellites and Meteorology: A Report to the World Meterological Organization," Washington, March 31, 1959 (Mimeo).
28. Wexler, H., "Satellites and Meteorology," Bull. World Meteorol. Organ. 9(1) : 2–7, January 1960.
29. Wexler, R., "Detection of Ozone Amounts from Satellite Measurements," in: Contributions to Satellite Meteorology, Air Force Cambridge Res. Ctr., GRD Research Note No. 36 (AFCRC–TN–60–427), ed. by W. K. Widger, Jr., June 1960, pp. 181–189.
30. Wexler, R., "Meteorology," in: Science in Space, ed. by L. V. Berkner and H. Odishaw, New York: McGraw-Hill, 1961, pp. 139–155.
31. Widger, W. K., and Touart, C. N., "Utilization of Satellite Observations in Weather Analysis and Forecasting," Bull. Am. Meteorol. Soc. 38(9) : 521–533, November 1957.
32. Widger, W. K., Jr. (ed.), "Contributions to Satellite Meteorology," U.S. Air Force Cambridge Res. Ctr., GRD Research Note No. 36 (AFCRC–TN–60–427), June 1960.

TIROS I BIBLIOGRAPHY

1. Baroni, A., "II Satellite Meteorologico 'TIROS I'," Rivista di Meteorologia Aeronautica 20(3) : 21–30, July–September 1960.
2. Bristor, C. L., and Ruzecki, M. A., "TIROS I Photographs of the Midwest Storm of April 1, 1960," Monthly Weather Review 88(/12) : 315–326, September/December 1960.
3. "Detailed Test Objectives Project TIROS," Space Technology Laboratories TR–59–0000–00750, rev. November 27, 1959. (CONFIDENTIAL)
4. Faust, H., "Wettersatellite TIROS I," Naturwissenschaftl Rundschau 13(6) : 227–228, June 1960.
5. "TIROS I Meteorological Satellite System ; Final Operational Report on Phase I," Astro-Electronics Products Division, Radio Corp. Am., October 1, 1960.
6. "TIROS I Meteorological Satellite System; Final Comprehensive Technical Report," Astro-Electronics Division, Radio Corp. Am. AED–339, July 1, 1961. 3 Vol.
7. "TIROS I Test Report," Test Vehicles S/N 148–2002–3002, "Douglas Aircraft Corp. Report SM–37842", May 1960. (SECRET)
8. Fritz, S. and Wexler, H., "Cloud Pictures from Satellite TIROS I," Monthly Weather Rev. 88(3) : 79–87, March 1960.
9. Fritz, S., " 'Cyclone-Prints' from Satellite (TIROS I)," Interavia 15(11) : 1384–1385, November 1960.
10. Hanel, R. A., and Stroud, W. G., "Infrared Imaging from Satellites," J. Soc. Motion Picture Telev. Engin. 69(1) : 25–26, January 1960.
11. "Instruction and Operating Handbook, TIROS I Meteorological Satellite System," Astro-Electronics Products Division, Radio Corp. Amer., September 15, 1959 (CONFIDENTIAL).
12. Krueger, A. F., and Fritz, S., "Cellular Cloud Patterns Revealed by TIROS I," Tellus 13(1) : 1–7, February 1961.
13. Stager, D. N, "Stage Two and Stage Three Electrical System, Projects TRANSIT IA and TIROS," Space Technology Laboratories TR–59–0000–00734, June 30, 1959.
14. Sternberg, S., "The Post-Launch Performance of the TIROS I Satellite," in: 11th International Astronautical Congress, Stockholm, August 1960, Vienna : Springer-Verlag, 1961, Vol. 1, pp. 330–340.
15. Sternberg, S., and Stroud, W. G., "TIROS I—Meteorological Satellite," Astronautics 5(6) : 32–34, 84–86, June 1960.
16. Sternberg, S., and Schnapf, A., "Performance and Evaluation of Satellites TIROS I and TIROS II," ARS J. 31(11) : 1495–1505. November 1961.
17. Stroud, W. G., "Initial Results of the TIROS I Meteorological Satellite," J. Geophys. Res. 65(5) : 1643–1644, May 1960.
18. Stroud, W. G., "Our Earth as a Satellite Sees It," Nat. Geogr. Mag. 118(2) : 292–302, August 1960.
19. "This is TIROS; A Reference Handbook for the TIROS I Meteorological Satellite System," Astro-Electronics Products Division, Radio Corp. Am., November 20, 1959.
20. "TIROS and TRANSIT Program Requirements at AFMTC," Space Technology Laboratories TR 59–0000–00634, rev. June 4, 1959 (CONFIDENTIAL).
21. "TIROS I Concludes Mission; TIROS II Readied," Weatherwise 13(4) : 159–161, 180, August 1960.
22. Wark, D. Q., and Popham, R. W., "TIROS I Observations of Ice in the Gulf of St. Lawrence," Monthly Weather Rev. 88(5) : 182–186, May 1960.
23. Wexler, H., and Fritz, S., "TIROS Reveals Cloud Formations," Science 131(3415) : 1708–1710, 10 June 1960.
24. Whitney, L. F., and Fritz, S., "A Tornado-Producing Cloud Pattern Seen from TIROS I," Bull. Amer. Meteorol. Soc. 42(9) : 603–614, September 1961.
25. Widger, W. K., Jr., "Some Samples from TIROS I," in: Proc. Eighth Weather Radar Conference, San Francisco, April 1960, pp. 531–542.
26. Widger, W. K., "Satellite Meteorology—Fancy and Fact," Weather 16(2) : 47–55, February 1961.
27. Winston, J. S., "Satellite Pictures of a Cut-Off Cyclone over the Eastern Pacific," Monthly Weather Rev. 88(9/12) : 295–314, September/December 1960.
28. Winston, J. S., and Tourville, L., "Cloud Structure of an Occluded Cyclone Over the Gulf of Alaska as Viewed by TIROS I," Bull. Amer. Meteorol. Soc. 42(3) : 151–165, March 1961.

PART II

by

STAFF

Meteorological Satellite Laboratory
U.S. Department of Commerce
Weather Bureau

CHAPTER 8

INTRODUCTION TO PART II

by

SIGMUND FRITZ

The meteorological satellite TIROS I was launched on April 1, 1960, and obtained cloud pictures of excellent quality with both its narrow-angle and wide-angle cameras. In every instantaneous exposure, each of the wide-angle cloud pictures revealed phenomena covering hundreds of miles; and composites of such "snapshots" captured synoptic meteorological systems, covering thousands of miles, in resplendent detail. Although TIROS I did not yield the sought-after daily world-wide coverage, it photographed many kinds of terrain and climes stretching from about latitudes 55° N to 55° S. It saw and reported cloud systems in the tropics and in mid-latitudes; it saw ice in Canada and the hot land in Africa; it televised pictures of oceanic and desert regions, and mountainous and coastal areas. The photographed cloud patterns ranged in size from the large-scale vortex to the mesoscale local severe storm and the small-scale cumulus cloud.

In general, moist air in the presence of adequate upward vertical motions in the atmosphere will result in cloud formations. But whether large-scale cloudiness or clouds of a more local nature are formed, or whether stratiform or cumuliform clouds are produced, depends on several factors including the three-dimensional temperature, moisture, and wind structure of the atmosphere. Thus it should be possible to examine the photographs and cull from them significant meteorological information about the state of the atmosphere associated with the particular cloud patterns under study. Moreover, in some special cases the cloud systems seen in the pictures resemble phenomena which have been studied in theoretical and laboratory investigations; in those cases it will be valuable to compare the state of the atmosphere which produced the pictured clouds with the theory and with the laboratory results. Where the TIROS results do not agree with previous investigations, further research into the basic fluid mechanics of the situation will be needed before the processes which produced the clouds can be adequately understood.

It is the purpose of Part II of this volume to present examples of several meteorological phenomena which TIROS I observed, and to explore the cloud forms in the pictures for their meteorological significance. Among the most striking cloud patterns seen in TIROS pictures are the large scale cyclonic vortices, whose spiral bands sometimes exceed a thousand miles in diameter. Vortices often have common characteristics, yet they are all different. It is as though each cyclone which spawned the cloud vortex has its own "cyclone-print," just as each person has his own fingerprints; in both types of prints there are similarities, yet each has its own identifying characteristics. Figure 91 shows examples of Northern Hemisphere vortices, while Figure 92* shows some in the Southern Hemisphere. Each example is identified by number to facilitate identification in Figure 93, which shows the location of each vortex, together with the approximate time at which it was photographed.

It might have been possible to surmise the existence of vortices in the large-scale cloud pictures before the advent of TIROS I. But who could have visualized the fascinating pattern of picture 6 in Figure 91, or have foreseen the interesting differences between the patterns of pictures 3 and 4? This ability of TIROS to capture instantaneous patterns, to abstract the gross features and to probe the details, to reveal the cyclonic vortex and to expose its component parts—this novel pattern-revealing capability—has added a new dimension to meteorological observations.

*These figures appeared in Weatherwise 13: 158–180, August 1960.

In a later chapter of this report the clouds in Figure 91, pictures 2, 3, 4, and 6, are discussed in detail. The presence of moist or dry air, the relation of the spiral bands to the wind flow and to the "jet stream," the existence of weak or strong frontal zones—these and other meteorological phenomena will be related to the cloud pictures in Chapters 9 through 12.

Wide bands of cloudiness are fairly frequent phenomena in the atmosphere. A broad band of cloudiness over the subtropical ocean is analyzed in Chapter 13; another band associated with a frontal zone between two cyclones in the North Pacific Ocean is discussed in Chapter 14. In the oceanic areas, especially in the tropical and subtropical oceans, conventional data are scarce; and these reports show how satellite pictures can contribute to an understanding of the atmospheric processes in these areas.

There are, as was noted earlier, TIROS pictures which *look like* phenomena studied in the laboratory. The Bénard cell pattern produced in the laboratory resembles some cloud patterns observed by TIROS. The similarities and differences are discussed in Chapter 15. Cloud "streets," or long narrow lines of clouds, have been studied theoretically; comparisons between TIROS cloud street pictures and theoretical results are discussed in Chapter 16.

Satellite pictures have greatest applicability to large-scale phenomena because of their unique ability to depict large areas at one time, yet the satellite can also contribute to the detection and study of small-scale phenomena, even in dense data networks; for the satellite certainly presents a different view of the associated cloud system, and includes besides pictures of related nearby phenomena. Thunderstorms are examples of severe local storms which can be detected from high level photographs; these storms are often imbedded in meteorological systems which cover much larger areas. An example of a cloud area which contained thunderstorms when it was photographed, and 2 hours later produced hail and tornadoes, is discussed in Chapter 17.

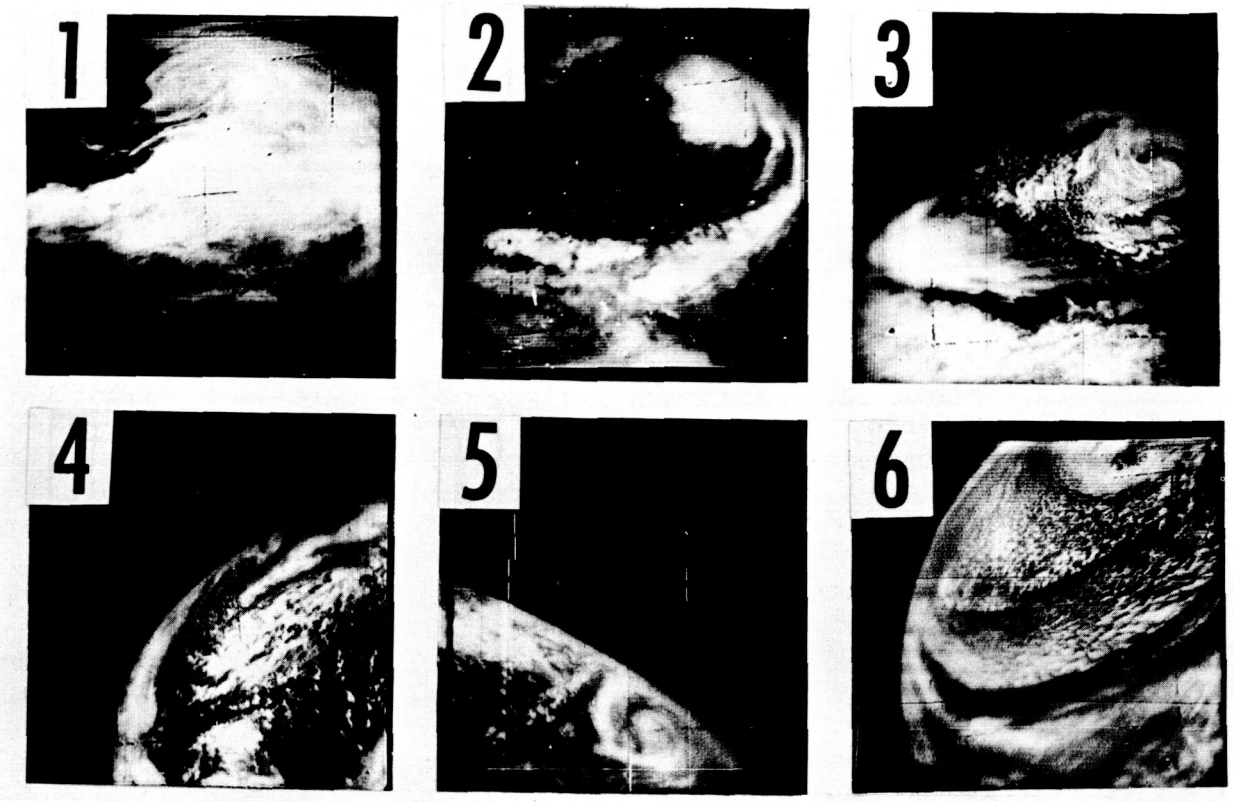

FIGURE 91.—Six vortices photographed in the Northern Hemisphere (see Figure 93 for locations).

Finally, many interesting cloud pictures were obtained from TIROS I which will be valuable for special studies; a few of these are presented in Chapter 18 without detailed analyses, to demonstrate the great versatility and potential of the satellite television system. Orographic clouds produced in mountain areas take on many shapes, and some examples are included. Snow-covered mountain peaks are also shown. It has been suggested that the patterns of sun glitter from the ocean may be used to compute wind speed. In some cases, ice can be detected. A relation between cloud forms and the Gulf Stream is suggested in some pictures. Examples of each of these are presented in Chapter 18.

It will be obvious from the many examples just cited that TIROS could supply much new information, especially in areas where no other information is available. In such areas, the interpretations presented in this report—and even more tentative ones—would be of value to meteorologists in nearby areas. Such regions occur in much of the Southern Hemisphere and Chapter 18 contains a sketch of cloud forms as obtained from TIROS pictures themselves, together with a few cloud pictures that represent what the analyst saw when he made the sketch.

A word should be said about the problems which arise in the utilization of the pictures. The picture quality of the TIROS photographs is excellent. However, there have been some difficulties mainly in locating the picture elements geographically. Location of the clouds requires knowledge of the orientation of the satellite spin axis with respect to some frame of reference at the time the picture was taken. This involves two things: the spatial location of the optical axis of the camera systems, and an accurate estimate of the time when the picture was taken. The problems involved in providing geographic positions for the cloud elements are discussed in Appendix A. In general, the cloud elements described in this report have been located within about 60 miles of their exact locations; where recognizable land features were seen in the pictures, the location was much better.

Finally, a word should be said about the photography. Provided "good" negatives are available

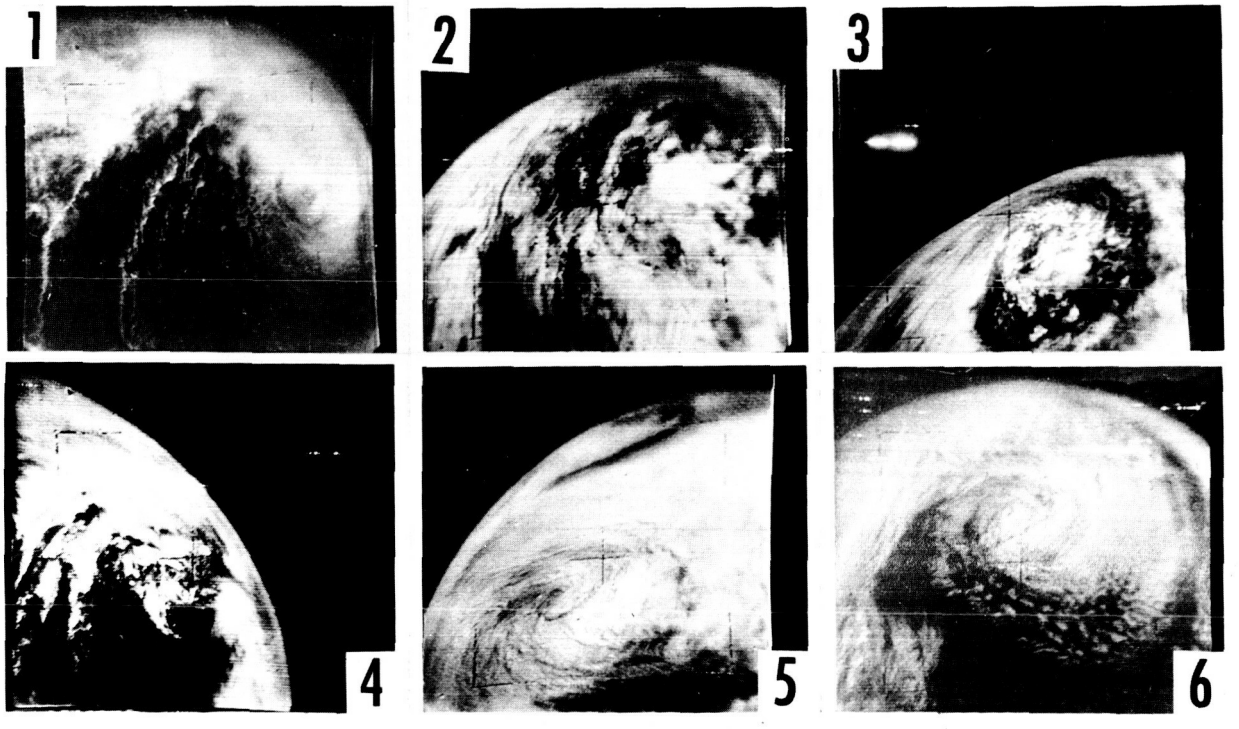

FIGURE 92.—Six vortices photographed in the Southern Hemisphere (see Figure 93 for locations).

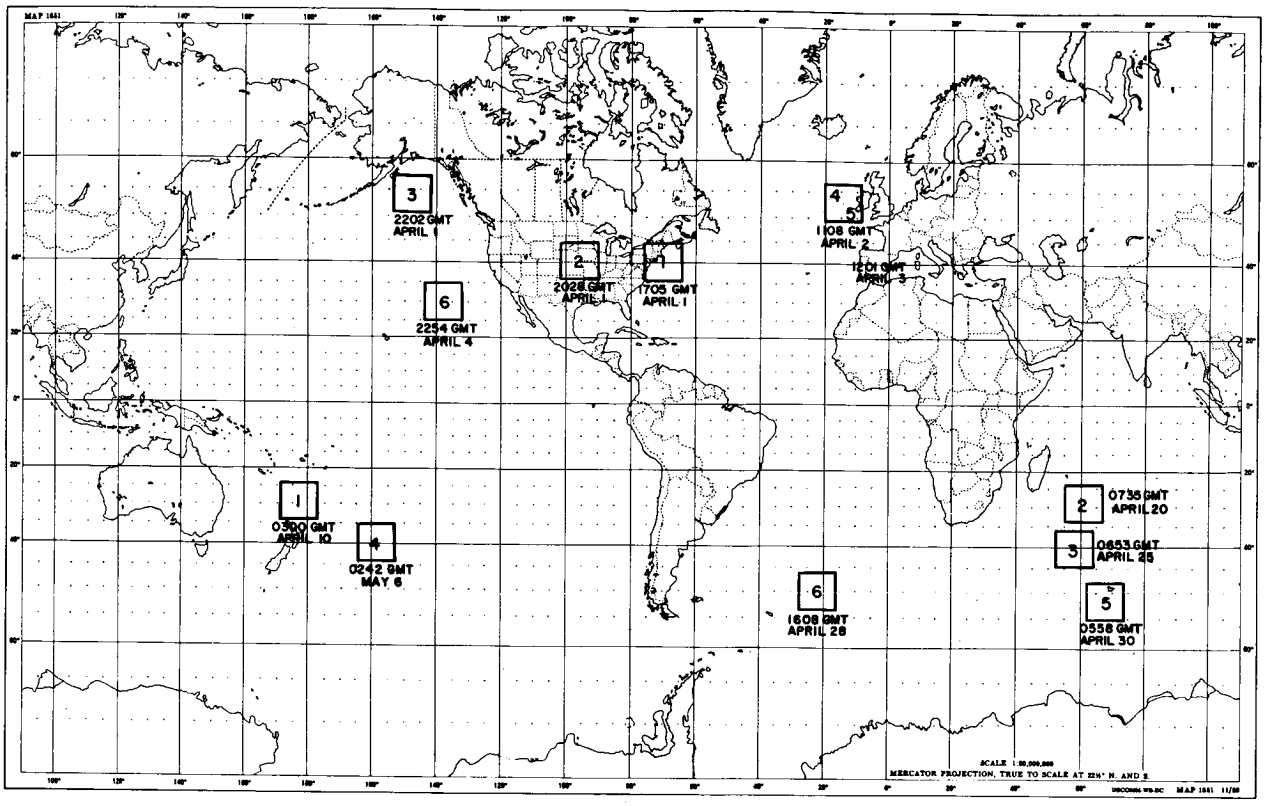

FIGURE 93.—Locations and approximate times of pictures in Figures 91 (Northern Hemisphere) and 92 (Southern Hemisphere).

in the first place, it is possible to produce prints of the pictures with various degrees of contrast. For the most part the prints have been produced so as to bring out the large scale cloud features best; in doing so, some details of smaller or thinner clouds may have been lost. It should therefore be noted that, in general, more detail is available in the original negatives than can be reproduced in this report. None of these "systems" difficulties played a significant role in the final interpretation of the major cloud patterns discussed in this report. The large-scale vortex, the sprawling front, the snow-covered mountain, the tornado breeding cloud—these and other phenomena described in the following chapters are essentially unaffected by the "systems" difficulties.

CHAPTER 9

A CYCLONE OVER THE ATLANTIC OCEAN*

by
SIGMUND FRITZ

INTRODUCTION

On April 2, 1960, during its 14th and 15th orbits, TIROS I photographed the cloud system associated with an old, well-developed cyclonic vortex centered about 400 miles west of Ireland.[1 2] Two composites prepared from these photographs clearly show the cloud pattern. Figure 94a, a composite of several wide-angle frames taken during orbit 14 (at 30-second intervals beginning at about 1106 GMT) best shows the western, northern, and eastern portions of the cloud system. Figure 94b, similarly composed of pictures taken during orbit 15, also shows the pattern in the southern portion well. It is interesting to note the similarity of several cloud features in these two composites in view of the fact that 100 minutes had elapsed between the two sets of photographs.

DESCRIPTION OF THE CYCLONE

The tracks of the 14th and 15th orbits and the major features of the cyclonic vortex have been sketched on a polar-stereographic map (Figure 95). A separate study showed that the major cloud features were located within about 60 miles of their exact locations. This figure shows that the clouds covered an area over a thousand miles in diameter, extending from a point over the Atlantic Ocean eastward to the European continent and covering much of the intervening Atlantic Ocean and the countries bordering the Atlantic.

One of the main features of these cloud pictures is the broad band of stratiform cloud which terminates in the arrowhead-shaped cloud near the center of the vortex. Figures 94b and 95 show that the stratiform cloud is a quasi-circular solid band of cloud. Starting with the protuberance in the wall of the cloud, near 50° N, 30° W, the cloud sweeps southward in a band about 300 miles wide, joining with a widespread cloud mass over western Spain (eastern Spain is nearly cloud-free). The cloud over Spain may in part be enhanced by orographic effects, but it extends also to the south-southwest into the Atlantic Ocean just west of Gibraltar, suggesting the existence of a weak frontal system there. The main stratiform cloud continues over Spain into France, but contains some fairly large holes over the Bay of Biscay region, and continues to circle, passing over England and Ireland. Out over the Atlantic Ocean, it divides into two parts near latitude 55°. One part (or fork) goes into the arrowhead-shaped cloud near the center of the vortex, while the other fork completes the circuit by joining the protuberance just west of the arrowhead. The continuity of the cloud around the northern side of the vortex can be seen even better in individual frames.

The quasi-circular stratiform cloud encircles a swirling galaxy-like mass of more broken, cumuliform clouds lying near the center of the cloud system. In addition, very narrow cloud streets seem to originate in the inner wall of the stratiform cloud, most prominently near the west wall protuberance. These cloud streets, several hundred miles in length, circle south of the arrowhead and sweep into the cumuliform, central cloud mass.

Although 100 minutes elapsed between the two sets of photographs (Figures 94a and 94b), the cloud system had hardly changed at all. The arrowhead and the protruding cloud in the inner west wall of the stratiform cloud remained essentially unchanged. The very narrow cloud streets which appear to issue from the inner west wall protuberance and sweep south of the arrow-

*This article, slightly modified, appears in Quart. J. Roy. Meteorol. Soc. 87(373) : 314–321, July 1961.

head into the cumuliform mass in the center are clearly evident in both parts of Figure 94.

The narrow-angle photographs taken on the 15th orbit are of special interest because the satellite was passing across the center of the cloud system. Figure 96 is a composite of these detailed photographs together with associated wide-angle frames. Actually this composite stretches farther to the west than does the one in Figure 94b; there is evidence that the narrow-angle camera began operating somewhat earlier than did the wide-angle camera. In Figure 96, the rather uniform stratiform clouds on both the western and eastern sides of the cloud pattern are seen to have almost no small-scale detail, but they do contain relatively large patches of dark area denoting thinner clouds or actual holes.* The cumuliform cloud seems to be made up of small elements, especially in the cloud streets; but near the top of the arrowhead and in the galaxy-like cloud, the elements are fairly large and bright and may well have been large cloud elements associated with the scattered shower activity reported in the surface observations.

*The narrow-angle pictures contain a defect which makes the stratiform clouds appear less uniform than they actually are. In Figure 96 the apparent thinning of the cloud occurs in a narrow band across the whole composite, and is especially noticeable in the stratiform cloud. These darker areas along the satellite's path are spurious.

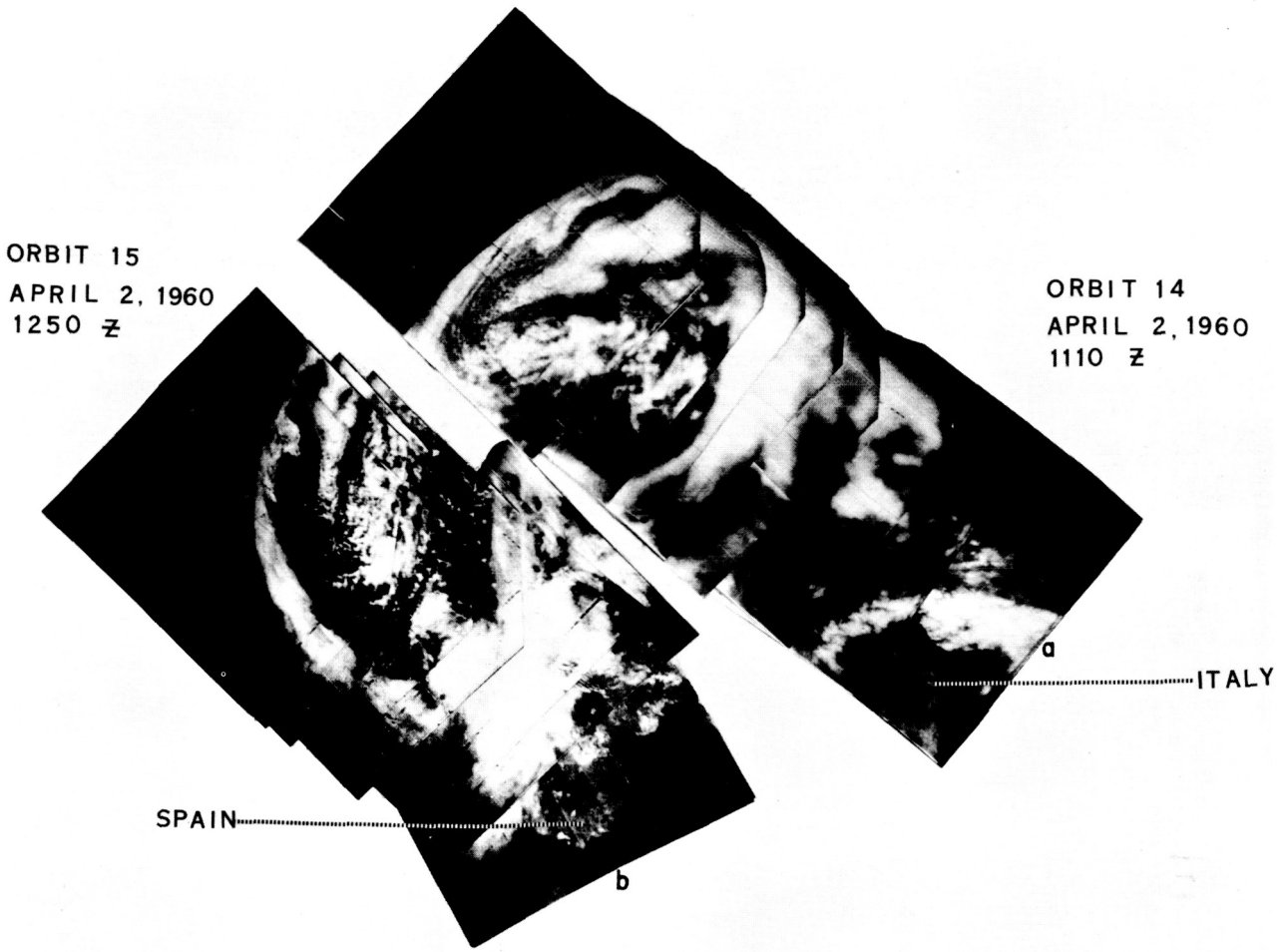

FIGURE 94.—Composites of wide-angle photographs taken by TIROS I on April 2, 1960, on its 14th and 15th orbits, showing an old, well-developed cyclonic vortex centered about 400 miles west of Ireland. The photographs of part (a) began at about 1100 GMT on orbit 14; those of (b) began about 1,250 GMT on orbit 15.

THE METEOROLOGICAL SITUATION

To relate the physical processes in the atmosphere which formed the cloud system seen in these pictures, we need to examine the meteorological state of the atmosphere at the time the pictures were taken. In order to facilitate discussion, meteorological charts are presented here which contain an outline of the stratiform cloud area taken from Figure 95. The surface and 500–mb analyses were prepared independently of the cloud pictures by the National Weather Analysis Center.

SURFACE DATA

At the time the photographs of Figure 94 were taken, a large, mature cyclone was centered about 400 miles west of Ireland. The sea-level pressure chart for 1200 GMT, April 2, 1960 (Figure 97), shows the cyclone with its central pressure of about 974 millibars. The cyclone is characterized by practically circular isobars and strong pressure gradients, which are associated with reported surface winds of up to 50 knots. A weak front along the west coast of Europe sweeps southward and westward across the Azores. Surface observations of the amount and forms of clouds are also shown in Figure 97. Near the frontal zone a band of overcast sky was present in which low and middle cloud (as seen from the surface) predominated. Cirrus cloud forms were also reported over parts of Spain and France. Surrounded by the overcast band, an area of broken clouds predominated over the ocean although scattered

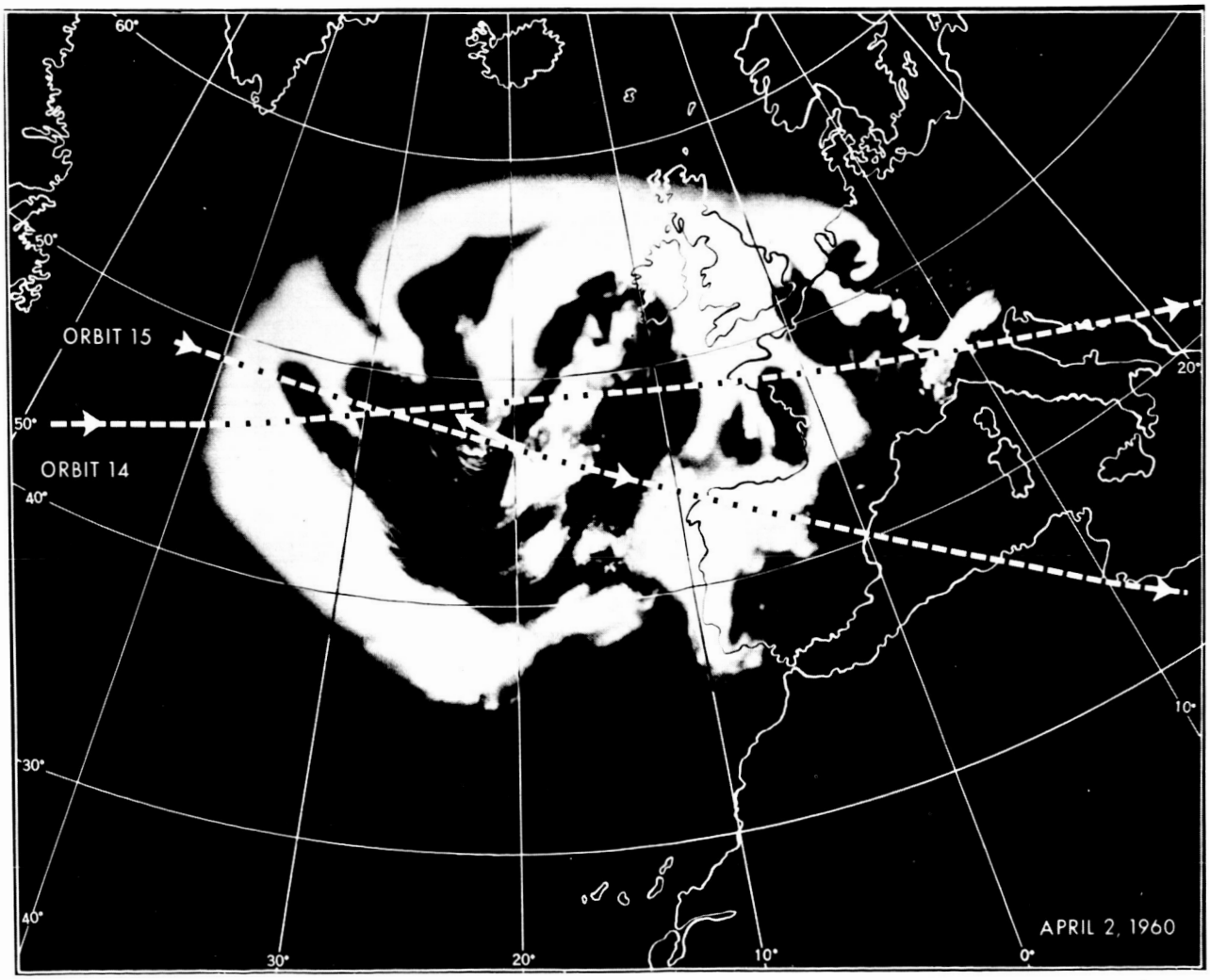

FIGURE 95.—Tracks of the subpoints of TIROS I on its 14th and 15th orbits, April 2, 1960, and the major features of the cyclonic vortex sketched on a polar-stereographic map.

646-770 O—64——9

FIGURE 96.—Composite of narrow-angle photographs together with associated wide-angle photographs of the vortex shown in Figure 94.

clouds were also reported there. The low clouds in this non-overcast area were mainly cumulus clouds in various states of development, and stratocumulus types. Altocumulus and cirrus clouds were also reported. Along the continental edge of the overcast band, cirriform clouds predominated.

Precipitation is reported in only a few locations; more steady rain was reported in the overcast band near the frontal zone, over and near Spain and the British Isles, and in some adjacent ocean areas while a few showers were noted in the central non-overcast region over the ocean.

Although the surface cloud reports were not sufficient to outline the cloud areas completely, even in this rather dense shipping zone, some similarity between the surface reports and the TIROS I picture is apparent.

UPPER AIR DATA

The cyclone was quite symmetrical with height. The "low" center on the 500–mb chart (Figure 98), at a height of about 16,800 feet, was located almost directly above the surface low pressure center (Figure 97).

Figure 98 contains an analysis of the temperature field; the dewpoint temperatures are plotted at the lower left of each reporting radiosonde station. If we denote the center of the cyclone by the position of the lowest height on the 500-mb chart, then we note that a cold, dry mass of air resided close to but somewhat southeast of the center; the exact positions cannot of course be given with the data available. Moreover a warm, moist mass of air circles the center from the Azores, across Spain and England and into the Atlantic. A region of relatively strong winds, up to 60 knots, encircles the southern and eastern sides

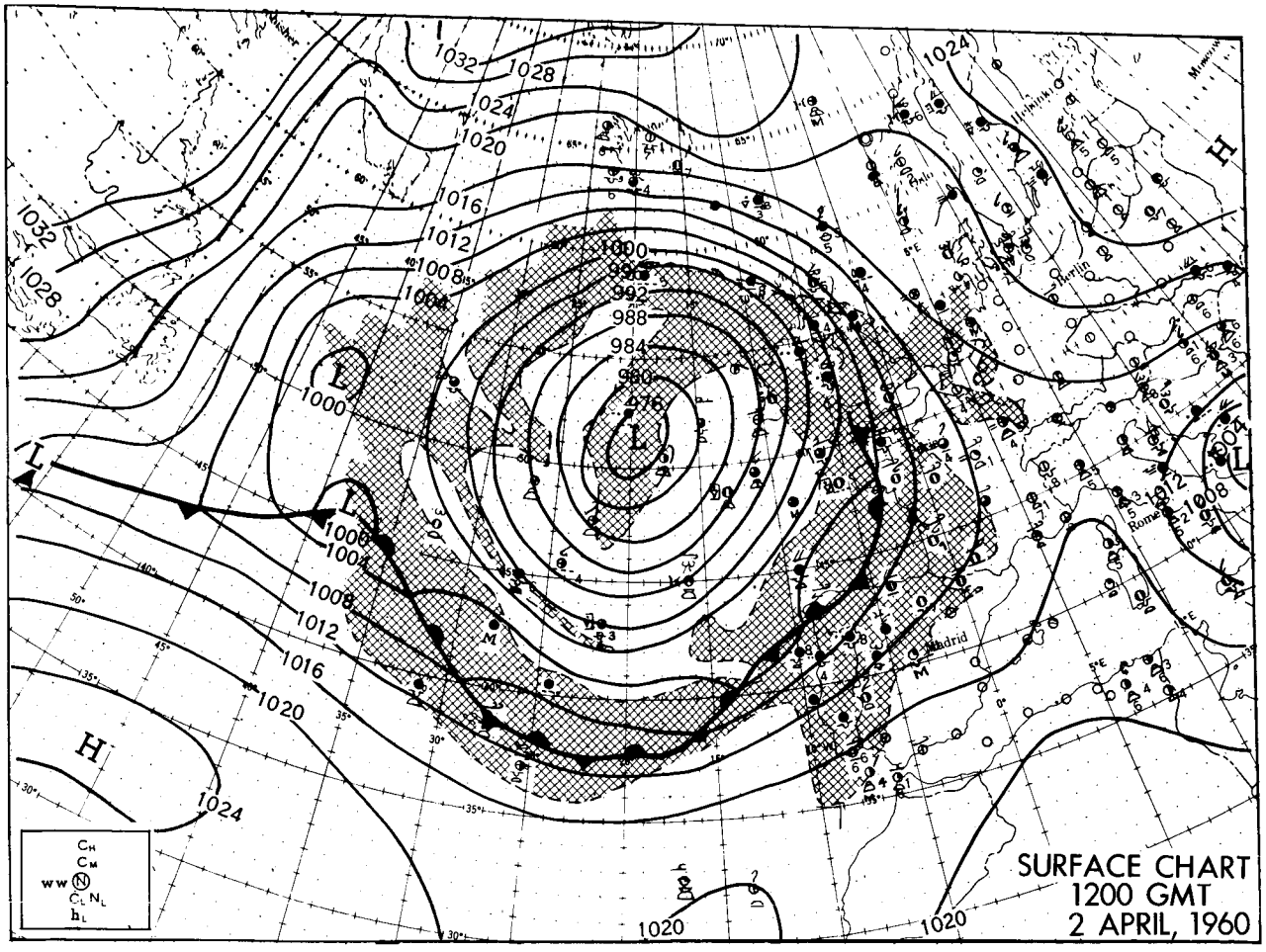

FIGURE 97.—Sea-level chart for 1200 GMT, April 2, 1960, showing the mature cyclone. The outline of the stratiform cloud area shown in Figure 95 is superimposed, and surface cloud observations are shown.

of the 500-mb vortex. This weak "jet stream" lies in or near the inside edge of the semicircular zone of moist warm air.

The flow of the moist air around the cyclone is seen even more clearly on the 300° K isentropic chart shown in Figure 99. This chart represents the surface along which the air would flow if no heat were added to individual air parcels. On this chart, both the relative humidity and the water-vapor mixing ratio are given; and isolines of pressure and of mixing ratio have been analyzed. This isentropic chart reaches a pressure of less than 400 mb in its center, indicating the deep cold air already noted on the 500-mb chart (Figure 98). Moreover, the moist air (high mixing ratio) flows with the winds around the vortex; and the air flows up the isentropic surface, especially on the eastern side of the center. The presence of condensation obscures the real significance of this chart, but the existence of overcast clouds in this region (Figure 95 and 97) attests to the reality of the ascent in this case.

In order to show the vertical extent of the cold, dry air in the vortex center and of the warm, moist air around its periphery, several cross-sections were prepared. One of these, along the line marked A–A in Figure 99, is shown in Figure 100. The cold air is seen to reach from the earth's surface to the tropopause near 300 mb. Relative humidity is shown in Figure 100, since this moisture quantity is readily discussed in relation to clouds. It is clear that, except for the levels near

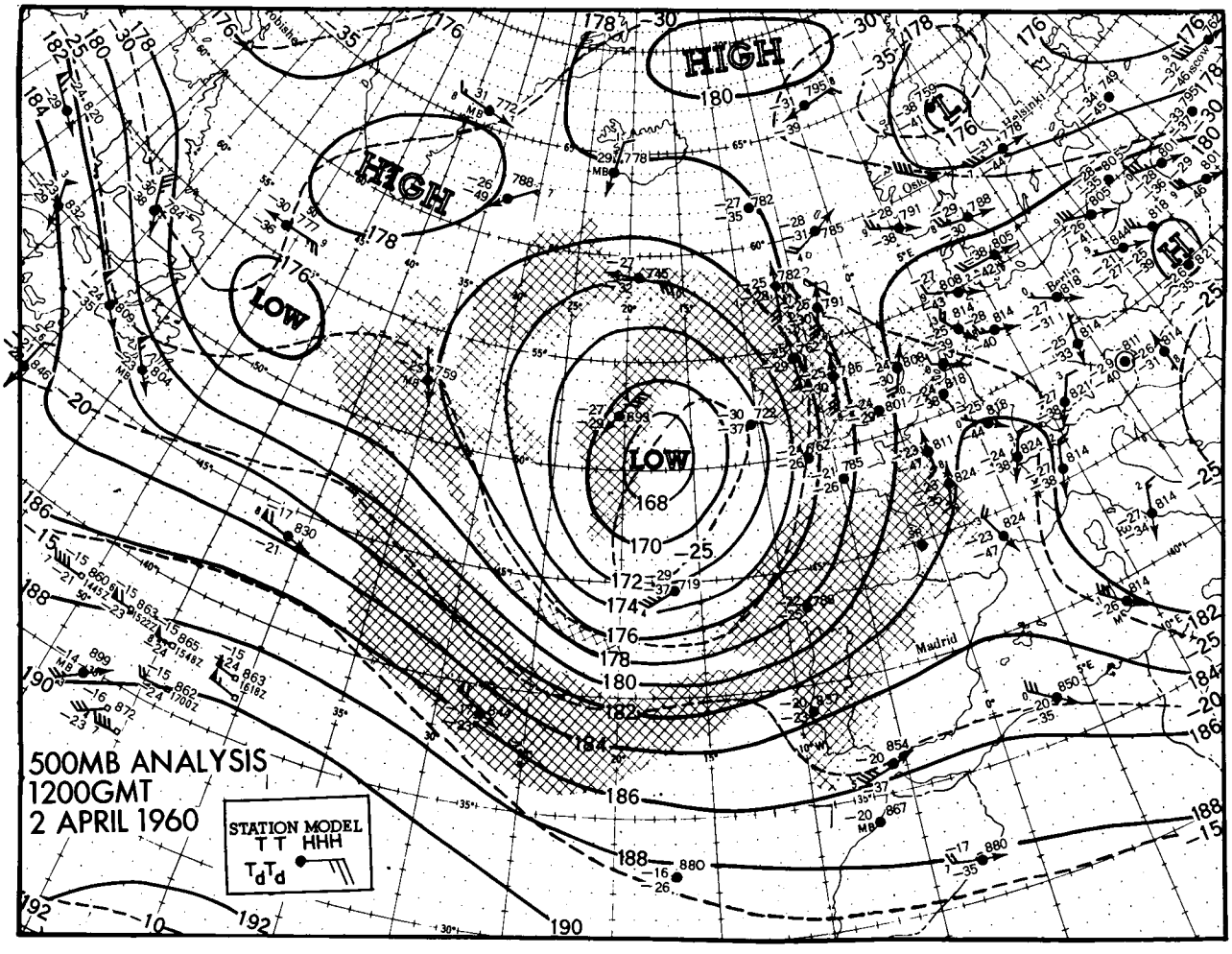

FIGURE 98.—500-mb chart for 1200 GMT, April 2, 1960, showing the mature cyclone. The outline of the stratiform cloud area shown in Figure 95 is superimposed. The solid lines are 200-foot contours, and the dashed lines are isotherms. An analysis of the temperature field is shown; and the dew-point temperatures are given at the lower left of each station.

the ocean surface, the air above ship station K is much drier than the air over ship station J up to 400-mb level. To the south of ship K, over the Azores, the air has about the same relative humidity as that at ship K; small differences do appear but may not be reliable in view of the inaccuracies in humidity measurement.

Commercial plane cloud reports near latitude 56° N indicated that a stratiform cloud top was located at a height of 10,000 to 12,000 feet. This

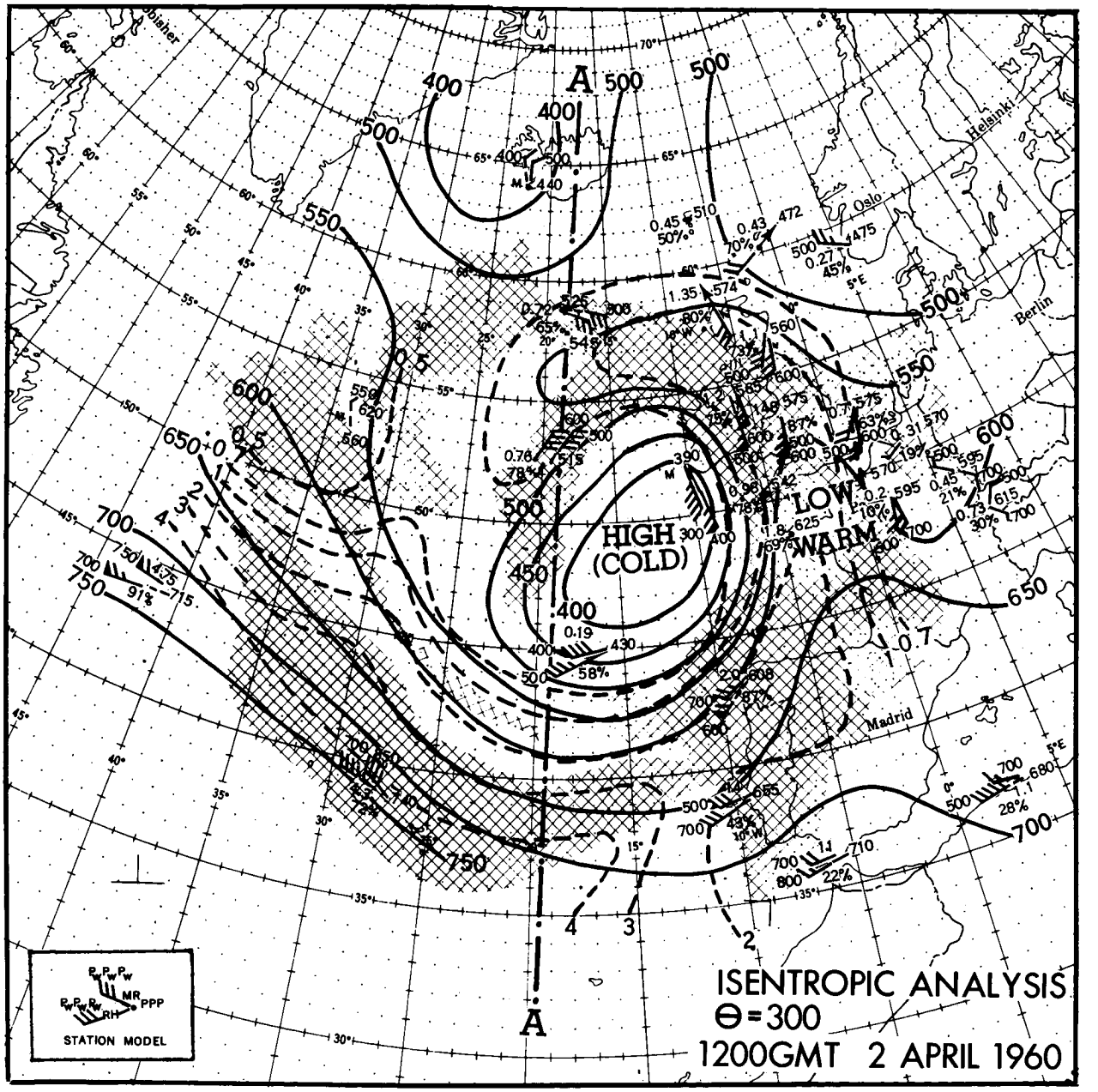

FIGURE 99.—Isentropic chart (θ=300° K), 1200 GMT, April 2, 1960, showing the mature cyclone. The outline of the stratiform cloud area shown in Figure 95 is superimposed. The winds are shown at two pressure levels near the level of the isentropic chart. "High" and "Low" refer to the elevation of the isentropic surface. This chart shows a deep core of cold air with warm moist air flowing around it. The solid lines are isobars on the isentropic surface, and the dashed lines are lines of constant water vapor mixing ratio. Line AA shows the region of the cross-section given in Figure 100.

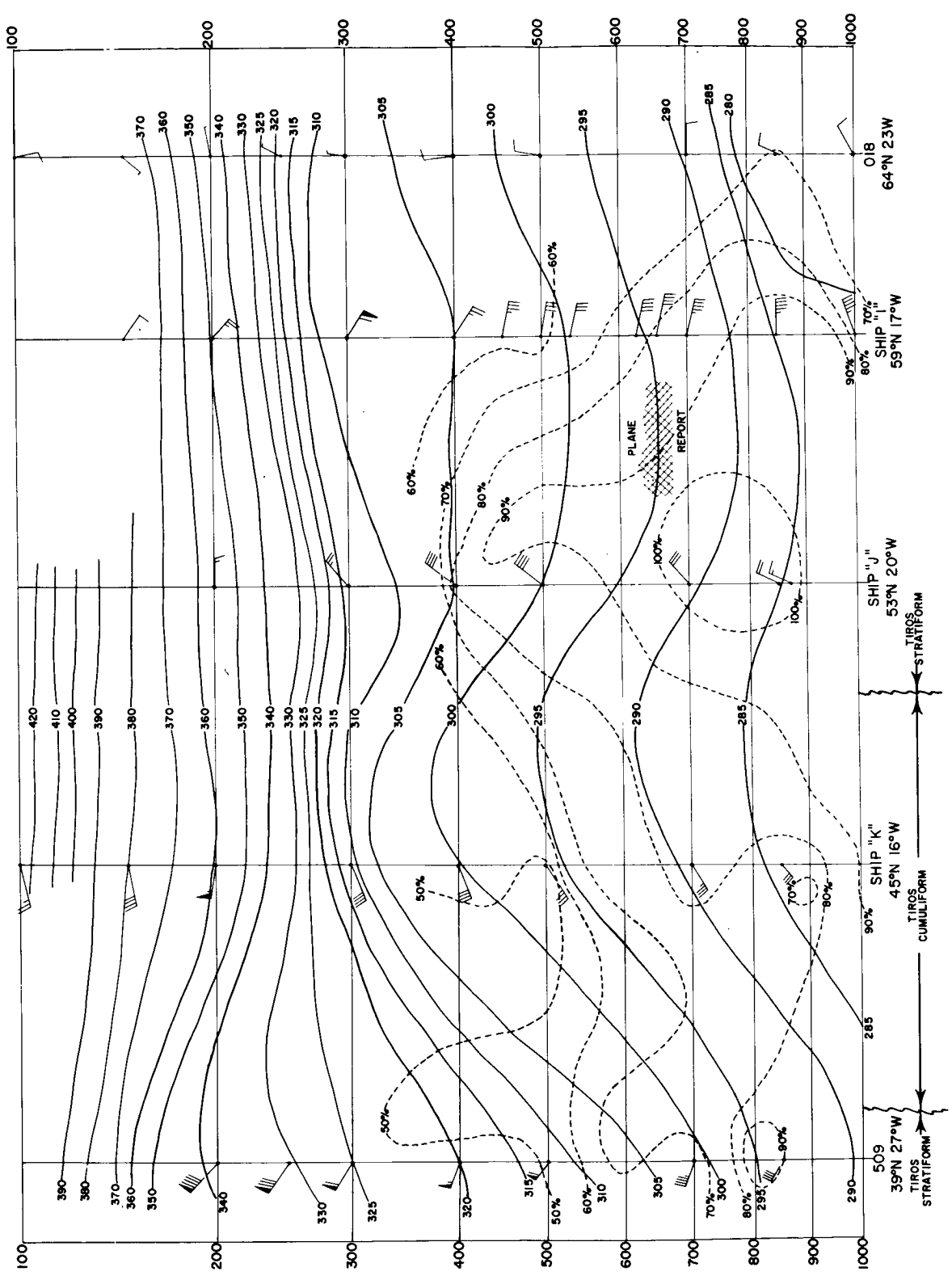

FIGURE 100.—North-South cross-section through the atmosphere along the line AA of Figure 99. The solid lines are lines of constant potential temperature, and the dashed lines constant relative humidity. The inner boundaries of the stratiform cloud shown in Figure 95 are indicated below the diagram.

information is shown in the cross section. The latitude where the cross-section crosses the inner edges of the stratiform cloud, as seen by TIROS (Figure 95), have also been included in Figure 100.

Finally, since the cloud formation is generally associated with vertical motion in the atmosphere, the vertical motion chart for the 600-mb pressure level (deduced by the Joint Numerical Weather Prediction Unit) is shown in Figure 101. The vertical motion is seen to be slightly downward in the center of the cloud pattern. In the overcast cloud region the vertical motion often changes sign, denoting rapid changes from upward to downward motion.

COMPARISON OF CLOUD PICTURES WITH METEOROLOGICAL DATA

From the description of the pictures (Figures 94 through 96) and of the meteorological situation (Figures 97 through 101), it is easy to see the association between the two sets of data. First, the clouds as observed from the surface (Figure 97) agree, as they must, with the TIROS I pictures; the small discrepancies which occur near the edges of the cloud picture patterns may be due to slight mislocations of the cloud elements in Figure 95, or to the fact that the surface observer actually does see past the edge of the overcast. Although it would not be possible from the surface cloud observations alone to delineate the details

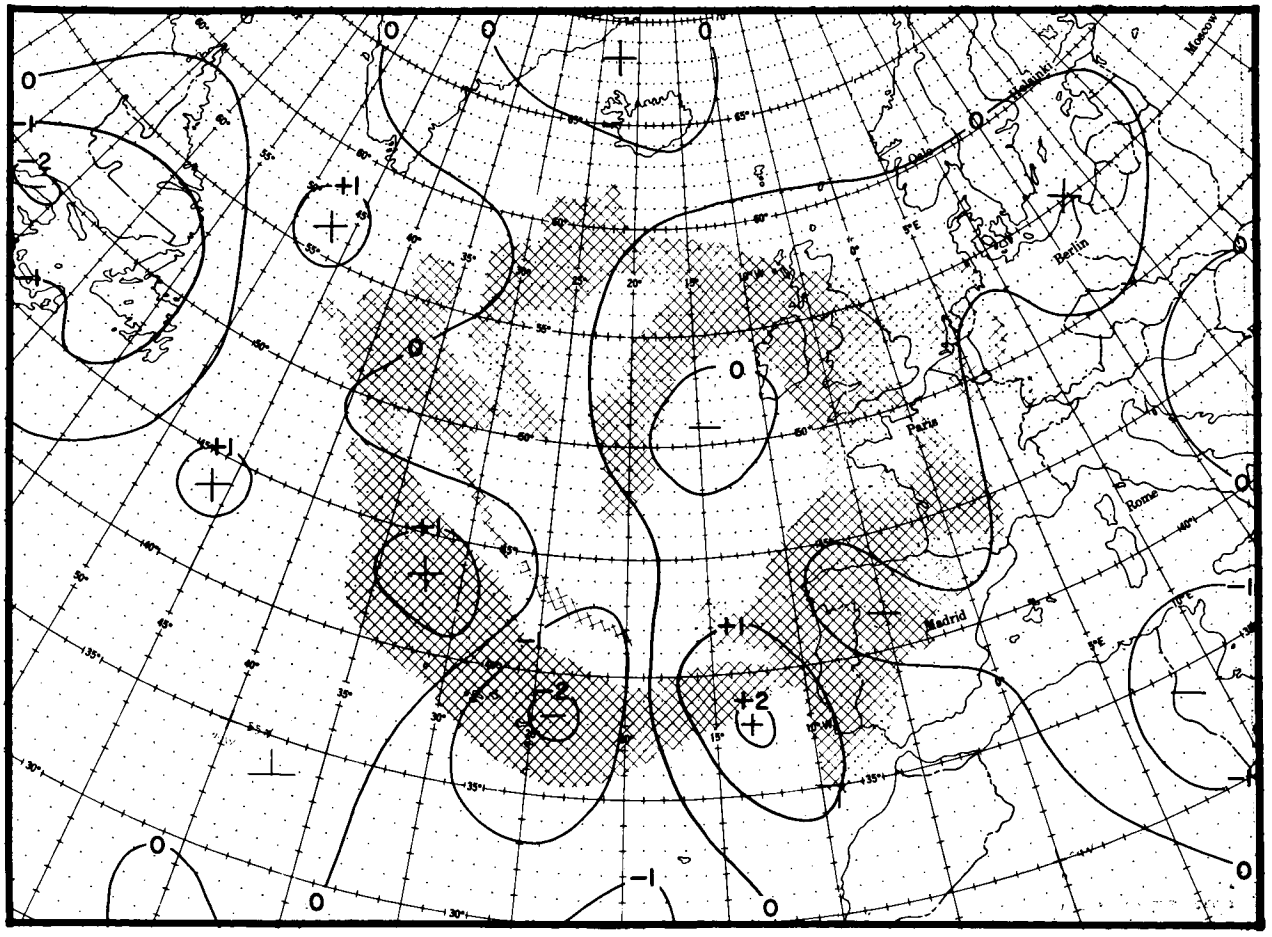

FIGURE 101.—Vertical motion chart for the 600-mb pressure level, computed by the Joint Numerical Weather Prediction Unit. The outline of the stratiform cloud area shown in Figure 95 is superimposed. The units are cm/sec; a plus sign denotes upward motion, and a minus, downward motion.

of the cloud field, the areas of overcast as observed from the surface appear in the solid, stratiform cloud areas of the pictures. Moreover, the area in the center of the cloud vortex, where the non-overcast cumuliform clouds appear in the pictures, corresponds to the broken-to-scattered cloud area in the surface observations. Judging by the surface reports, the cumuliform area also contained some altocumulus and cirrus clouds. Some showers occurred in this region which were doubtless associated with the brighter cloud masses of the photographs (Figure 94).

Now looking at the gross features, it is quite apparent that the stratiform cloud which covers the European coast and then spirals into the arrowhead-shaped cloud is a manifestation of the warm moist "tongue" of air which circles the 500-mb vortex (Figure 98) and appears as an ascending moist tongue in the 300° K isentropic chart (Figure 99).

Furthermore, the broken cloud area in the middle of the cloud vortex coincides perfectly with the deep, cold, dry mass of air (Figure 99). Judging by the continuous cloud in the west side of the vortex, this cold mass of air has been completely cut off from its cold air source further to the west and is now completely encircled by warm moist air.

From the cross-section in Figure 100, it can be ascertained that the stratiform arrowhead-shaped cloud slopes downward towards the north. At ship J, judging by the high relative humidities, the cloud top was about 23,000 feet high (near the 400-mb level). At ship I, the relative humidities are much lower at that level, suggesting a lower cloud level; the airplane reports support the existence of clouds at 12,000 feet.

An area of relatively strong winds (about 60 knots) is present along the inner edge of the stratiform cloud. This is to be expected since the wind will increase with height in the region between the warm and cold air according to the "thermal wind" relation. Thus, strong winds are bound to appear in this region.

Moreover, the cloud streets in the TIROS I photographs lie closely parallel to the contour lines of the 500-mb chart (Figure 98). And since the wind direction was remarkably constant with height (Figure 100), these cloud streets serve as good wind indicators and also suggest (Figure 94) a convergence into the galaxy-like cloud mass, which is itself near the center of low pressure. These cloud streets could not, of course, be discovered from the surface observations alone.

Finally, a word should be said about the vertical motion chart (Figure 101). The slight downward motion in the center of the cloud vortex would agree with the fact that the stratiform cloud did not appear there. It would also suggest that most of the central cumuliform cloud was below 600 mb (about 13,000 feet). This was perhaps truer near the cloud streets near ship K than in the central cloud mass.

In the stratiform cloud area, the computed upward motion agrees with the cloud's existence. The strong downward motions near 37° N, 25° W (Figure 101), seems doubtful. Although there is no proof that upward motion was occurring at that instant, the presence of the cloud casts doubt on the existence of downward motion in the area in the recent past. If the upward vertical motion, which could have been deduced from this stratiform cloud picture, had been used as input to the numerical weather prediction model, rather than the downward motion actually computed, the numerical analysis and forecast made on this date would have been considerably different.

Thus, the cloud pictures may eventually serve as a valuable additional observation to determine the actual state of the three-dimensional motion in the atmosphere as well as of the moisture and temperature structure.

CONCLUSION

The stratiform clouds observed were clearly associated with a warm, moist tongue of air which encircled the cold, relatively dry air in the center of the vortex in the Atlantic Ocean. This cold air, apparently cut off from its source, was associated with the non-overcast, galaxy-like cloud area which was surrounded by the stratiform cloud. The region between the cold and warm air is also the region of maximum jet-like winds, and is therefore to be expected near the inner edge of the stratiform cloud. Cloud streets, which cannot be seen from surface observations, serve to outline the wind flow in the mature storm in which

the wind direction does not change significantly with height.

Finally, a great deal of additional detail is evident in the photographs. The pattern in the form of a nearly closed circle over the European coast near North Germany (Figures 94a and 95) is an interesting example. Is this the counterpart of a meso-scale eddy in the atmosphere? Was the shape of the arrowhead cloud in Figure 94a produced by meso-scale eddies? Looking southward along the "arrow" in Figures 94a and 95, the appearance of the cloud suggests the possibility that a small cyclonic eddy existed on the eastern side near latitude 50° N, and an anticyclonic eddy on the western side of the arrowhead.

It will of course be interesting to examine other cloud patterns which appear like that of Figure 94 to see if similar meteorological conditions are associated with them and to see if generalizations can be formulated.

ACKNOWLEDGMENTS

Thanks are due to Detachment 28, 4th Weather Group of the Air Weather Service for supplying maps of surface cloud information which were used in the preparation of Figure 97. The surface and 500 mb charts (Figures 97 and 98) were used essentially unchanged as prepared by the National Weather Analysis Center, Washington, D.C. Finally, thanks are due to KLM and Alitalia Airlines for recording the cloud information entered on Figure 100 and to the Weather Bureau office at New York International Airport for making those airplane reports available.

REFERENCES

1. Fritz, S., and Wexler, H., "Cloud Pictures from Satellite TIROS I," Monthly Weather Rev. 88(3): 79–87, March 1960.
2. Wexler, H., and Fritz, S., "TIROS Reveals Cloud Formations," Science 13(3415): 1708–1710, June 10, 1960.

CHAPTER 10

A CUT-OFF CYCLONE OVER THE EASTERN PACIFIC*

by

JAY S. WINSTON

INTRODUCTION

On April 4 and 5, 1960, on its 50th and 64th orbits respectively, TIROS I photographed portions of a cut-off cyclone in the eastern Pacific between Hawaii and California. Three photographs taken with the wide-angle camera on April 4, at intervals of 1 minute starting at about 2250 GMT, are shown chronologically in Figures 102 through 104. These pictures were obtained when the satellite was above the points 1, 2, and 3 in Figure 107d, where isobars and fronts of the sea-level analysis for 0000 GMT, April 5, of the National Weather Analysis Center (NAWAC) are also shown. It is evident from the arrows in Figure 107d between the sub-satellite points and the locations of the optical centers (principal points) of the pictures, that Figures 102 through 104 show the cloudiness principally in the storm's western and southern quadrants.

Figure 103 is by now a rather familiar picture since it has already been illustrated several times in the literature [1, 2, 3] and earlier in this report. As was pointed out by Fritz and Wexler,[2] the cloudiness in Figures 102 through 104 is remarkable for its broad, banded structure with narrow, relatively clear bands in between. The forward edges of these bands are generally quite sharp, whereas the rear edges tend to be diffuse. Note that the cloudiness behind lines AA and BB appears to be predominately of the cumuliform type, much of it with very interesting cellular structure (cf. Chapter 15). The broad band behind line DD toward the upper right of Figure 104 appears to have a more stratiform character and very likely represents the altostratus or cirrostratus tops of a cloud system which was rather extensive both horizontally and vertically. However, right along line DD itself, particularly toward the lower left, the clouds have a more cumuliform appearance.

Two photographs of the storm taken with the wide-angle camera on April 5, 1½ minutes apart and ending at 2200 GMT, are shown in Figures 105 and 106. The satellite path, sub-satellite points, principal points of the pictures, and the NAWAC sea-level chart for 0000 GMT, April 6, are illustrated in Figure 107f. Again the pictures are oriented in approximately the same direction and therefore mainly cover the western and southern portions of the cyclone, but there is a better view of the central part of the storm in Figure 106. The broad bands of cloudiness and alternating cloudlessness spiraling into the cyclone center are especially outstanding and resemble strongly the classical cyclonic spiral as observed in the laboratory [4, 5] and as observed by radar in tropical storms.[6] Although a fair degree of cellular structure is still evident in Figures 105 and 106, the areas of cellular cloudiness on the west and south sides of the cyclone center have generally diminished.

SYNOPTIC HISTORY OF THE STORM

The evolution of this major cyclone is illustrated by a series of NAWAC sea-level analyses at 12-hour intervals (Figure 107).

On April 3 at 1200 GMT a broad cyclonic circulation existed over the eastern Pacific from the Gulf of Alaska southward toward about latitudes 30°–35° N. The major low center in this cyclonic complex had just moved northeastward in the previous 24 hours to a position near 48° N., 140° W. The cloud system we are concerned with had its origin in the small perturbation located near 39° N., 155° W. In typical fashion this center and the cold front extending to its west were moving generally southeastward along the periphery

*A revised version of this paper appears in Monthly Weather Rev. 88(9–12): 295–314, September–December 1960.

of the main low center. Available ship reports at 0000 GMT, April 4, indicate that a new center apparently started forming farther southward along the frontal trough at about 34° N, 150° W (Figure 107b).

By 1200 GMT, April 4 (Figure 107c) the system was organizing into a closed cyclonic circulation with pressures increasing to the north. Also a weaker pressure minimum was located to the east along the main polar front near 33° N, 139° W. By 0000 GMT, April 5 (Figure 107d), 1 hour after the photographs in Figures 102 through 104 were taken, an extensive cyclonic circulation had become established owing to both the deepen-

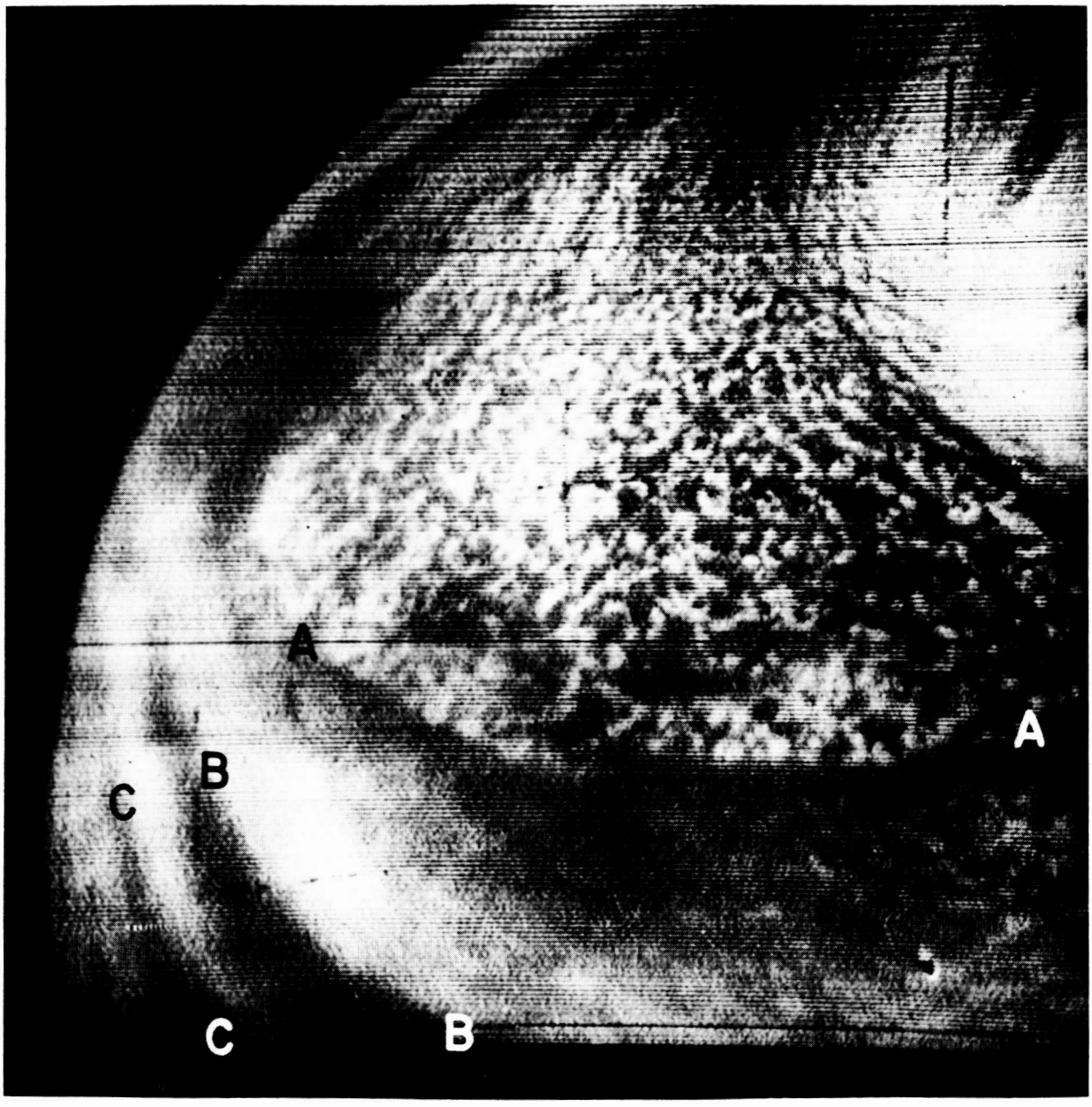

FIGURE 102.—TIROS I photograph of cloudiness west and southwest of a cut-off cyclone in the eastern Pacific, showing principally cellular cumuliform cloudiness with a sharp edge alone line AA. The picture was taken at about 2251 GMT, April 4, 1960, when TIROS I was located above point 1 in Figure 107d.

ing of the new cyclone center and the increases in pressures to the north of the low. Note that the NAWAC frontal analysis on this map had been simplified in that the secondary cold front was dropped and therefore a front no longer extended into the storm center. Twelve hours later, at 1200 GMT, April 5 (Figure 107e), the cyclone reached its lowest central pressure (about 999 mb) and had about the strongest isobaric gradients and hence probably the strongest surface wind field (as viewed on charts plotted at 6-hour intervals). By 0000 GMT, April 6 (2 hours after the photographs shown in Figures 105 and 106 were taken), the storm had begun to fill and surface winds were weakening considerably (Figure 107f). Thus the two sets of pictures show portions of the storm

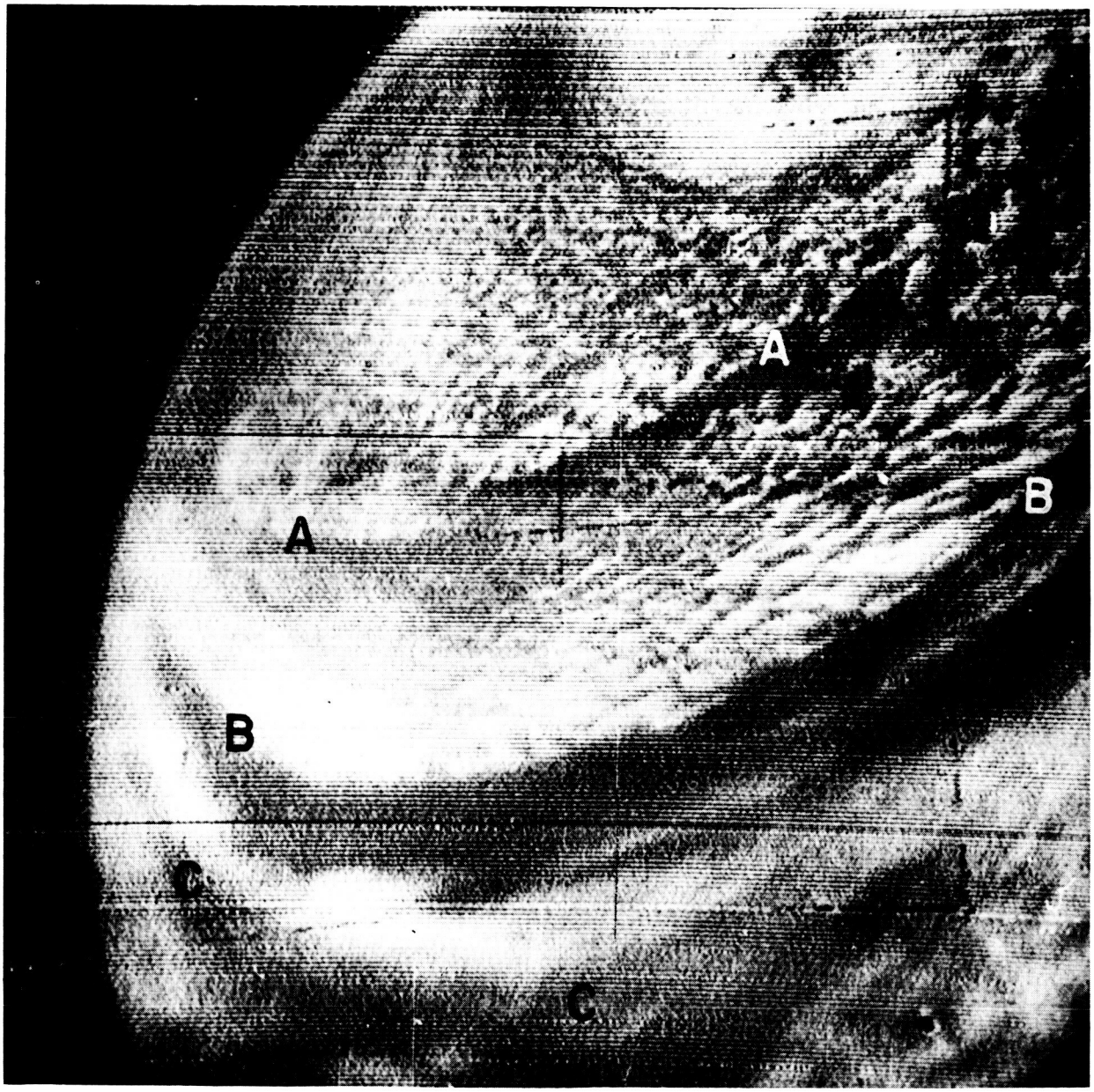

FIGURE 103.—Cloudiness southwest and south of the cyclone, showing pronounced lines, AA and BB, at the forward edges of cumuliform cloud fields. The picture was taken at about 2252 GMT, April 4, 1960, from above point 2 in Figure 107d.

about 12 hours prior to and about 12 hours after its most intense stage.

The history of the storm at upper levels is not especially notable except that a closed upper center was analyzed at 700 and 500 mb as the center deepened. However, the paucity of radiosonde observations in the region left the precise intensity of the upper center somewhat in doubt.

RELATION BETWEEN THE CLOUD PICTURES AND CONVENTIONAL METEOROLOGICAL INFORMATION

Although the TIROS I pictures can be compared visually with the standard synoptic weather data and charts once the satellite's location and general orientation are known, it is not until complete latitude-longitude grids are superimposed

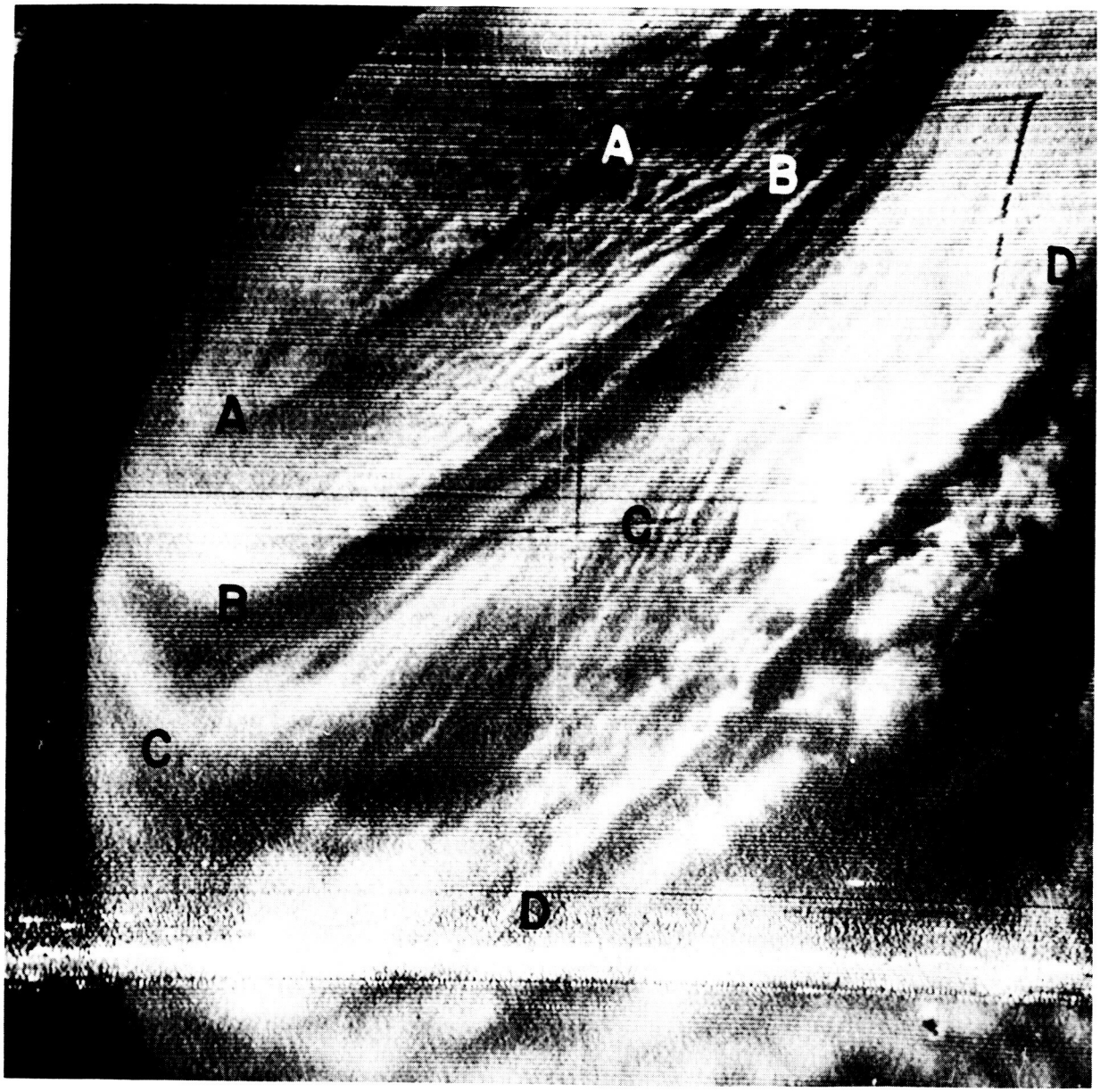

FIGURE 104.—Cloudiness southeast through southwest of the cyclone, showing frontal cloudiness with a sharp forward edge along line DD. Other pronounced lines along forward edges of clouds are those seen more prominently in Figures 102 and 103 (AA and BB), and the one along CC. The picture was taken at about 2253 GMT, April 4, 1960, from above point 3 in Figure 107d.

on the pictures that detailed and moderately accurate comparisons are feasible. Such gridding has been achieved for the pictures in this case by methods described in Appendix A.

CLOUD PICTURES TAKEN ON THE 50TH ORBIT

The pictures taken at about 2250 GMT, April 4, which have already been presented in Figures 102–104, are given again in Figures 108–110 with a two-degree latitude-longitude grid, surface isobars and fronts from the NAWAC analysis, abbreviated surface synoptic reports, and pilot reports of clouds all superimposed. The pictures are shown again in Figures 111–113 with superimposed grid, 700-mb contours, radiosonde reports, pilot reports of winds in the mid-troposphere and vertical motion at 600 mb as computed by the Joint

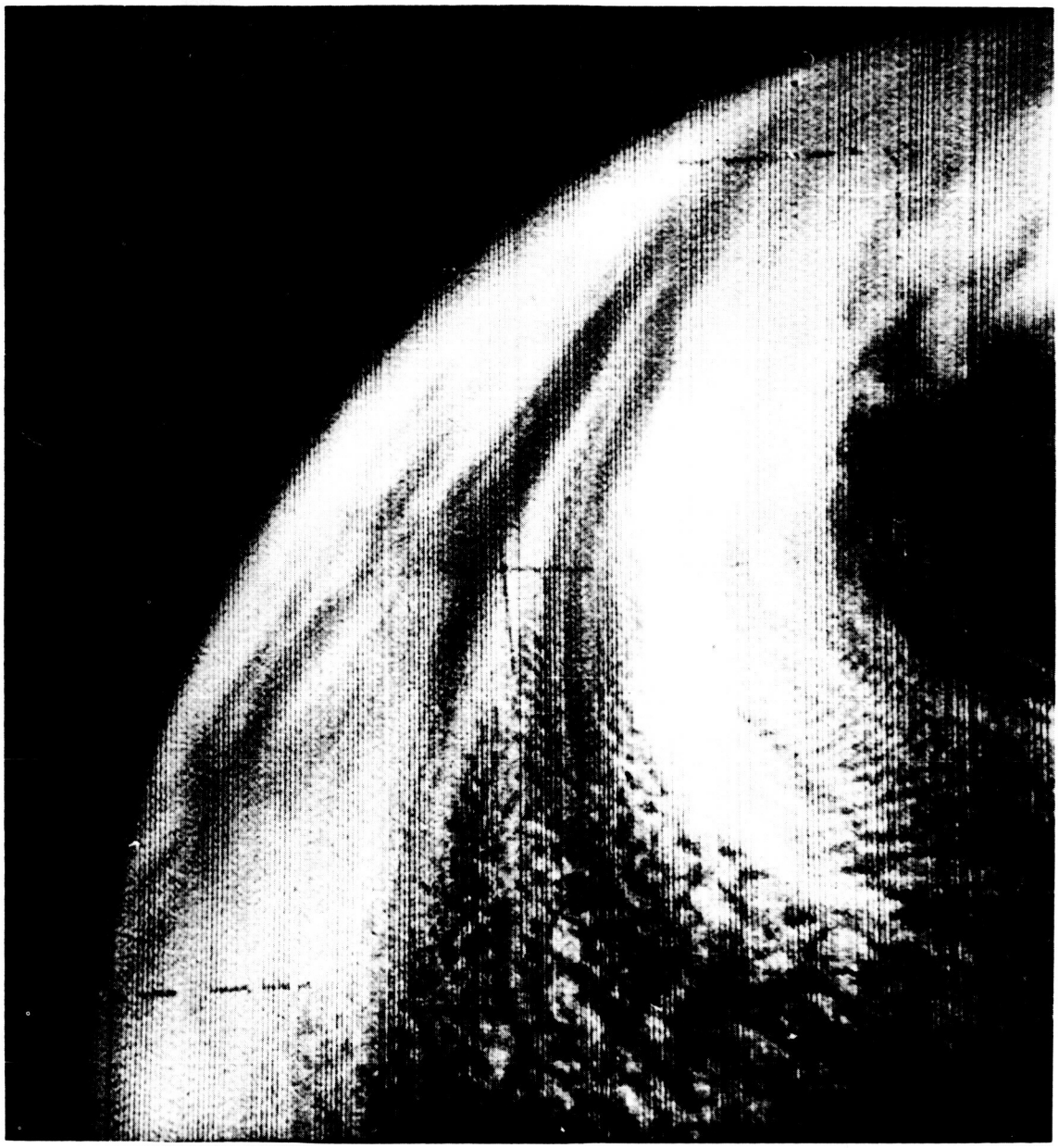

FIGURE 105.—Cloudiness west and southwest of the cyclone on the day following the views in Figures 102–104, showing a broad, cyclonically curved band west of a clear area closer to storm center. The picture was taken at about 2159 GMT, April 5, 1960, from above point 4 in Figure 107f.

Numerical Weather Prediction Unit (JNWP). All data except the pilot reports are from 0000 GMT, April 5.

The most striking thing seen in these figures is that most of the major bands are nearly perpendicular to the surface isobars and 700-mb contours. Only line DD, which is related to the main cold front, and the northeastern end of line BB are closely parallel to the mid-tropospheric flow. It is well known, however, that convergence lines frequently appear in the cold air in the westerly and northwesterly flow to the rear of well-defined cyclones. Such lines appeared frequently in the detailed analyses by members of the Bergen

FIGURE 106.—Cloudiness around the center and southeast through southwest of the cyclone on the day following the views in Figures 102–104, showing pronounced spiral bands near the center and several zones of cumuliform cloudiness well to the south of the center. The picture was taken at about 2200 GMT, April 5, 1960, 1½ minutes after Figure 105, from above point 5 in Figure 107f.

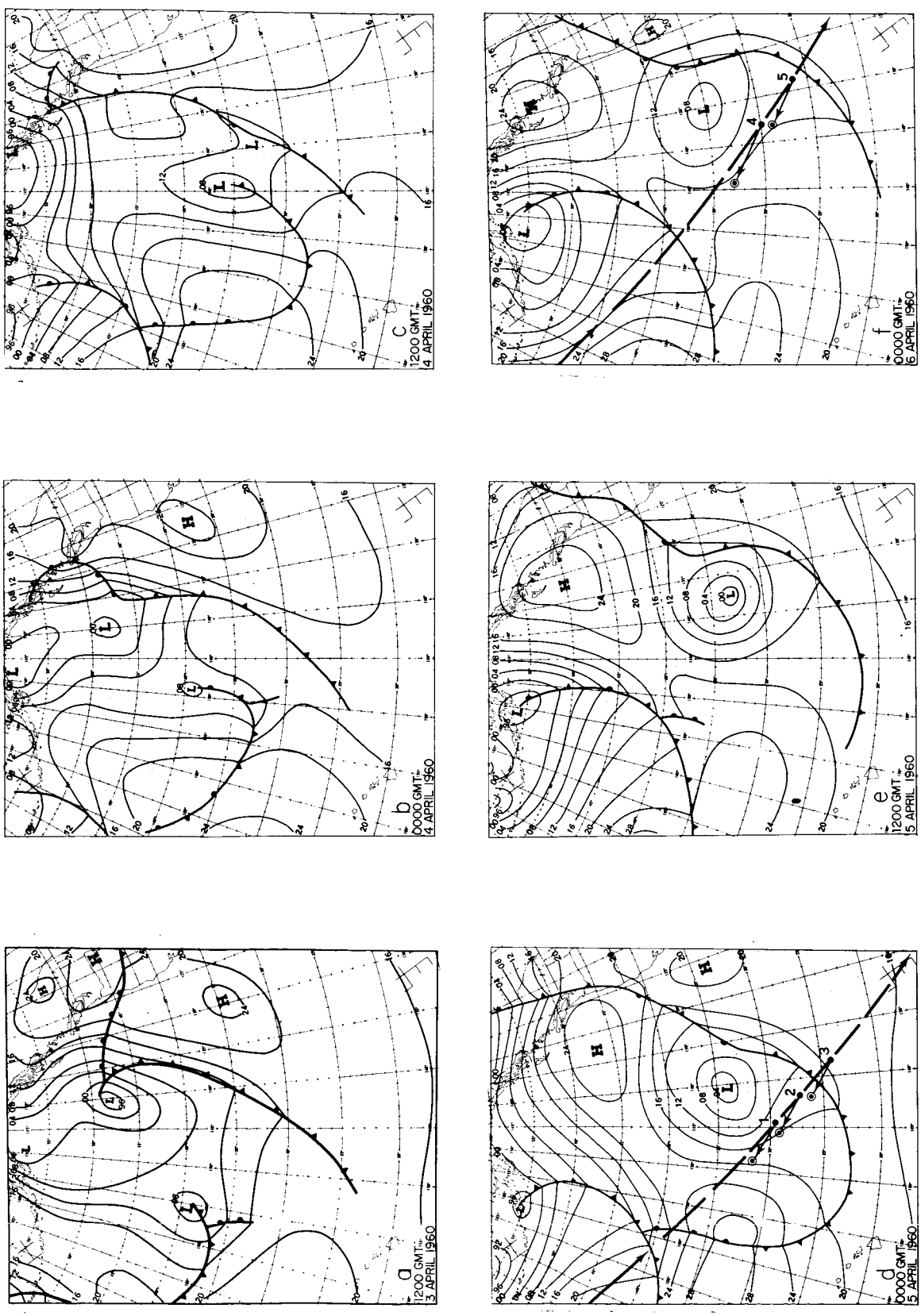

FIGURE 107.—Sequence of NAWAC sea-level analyses of 12-hourly intervals for April 3–6, 1960, showing the evolution of the cut-off cyclone. The paths of TIROS I on April 4–5 are shown in d and f; the sub-satellite points are indicated by dots, principal points of pictures by circled dots, and the horizontal orientation of the camera by arrows. Numbers identify the locations for pictures shown in Figures 102–106.

646–770 O—64——10

school,[7] some of them actually identified as "bent-back" occlusions or secondary cold fronts. In recent years, particularly on maps of a hemisphere scale, there has been a tendency to exclude these more minor systems from the analysis.

In the case under discussion here it appears that lines AA and BB are very likely convergence lines of this type. Close investigation of the position of line BB as compared with the secondary cold front analyzed on preceding NAWAC sea-level

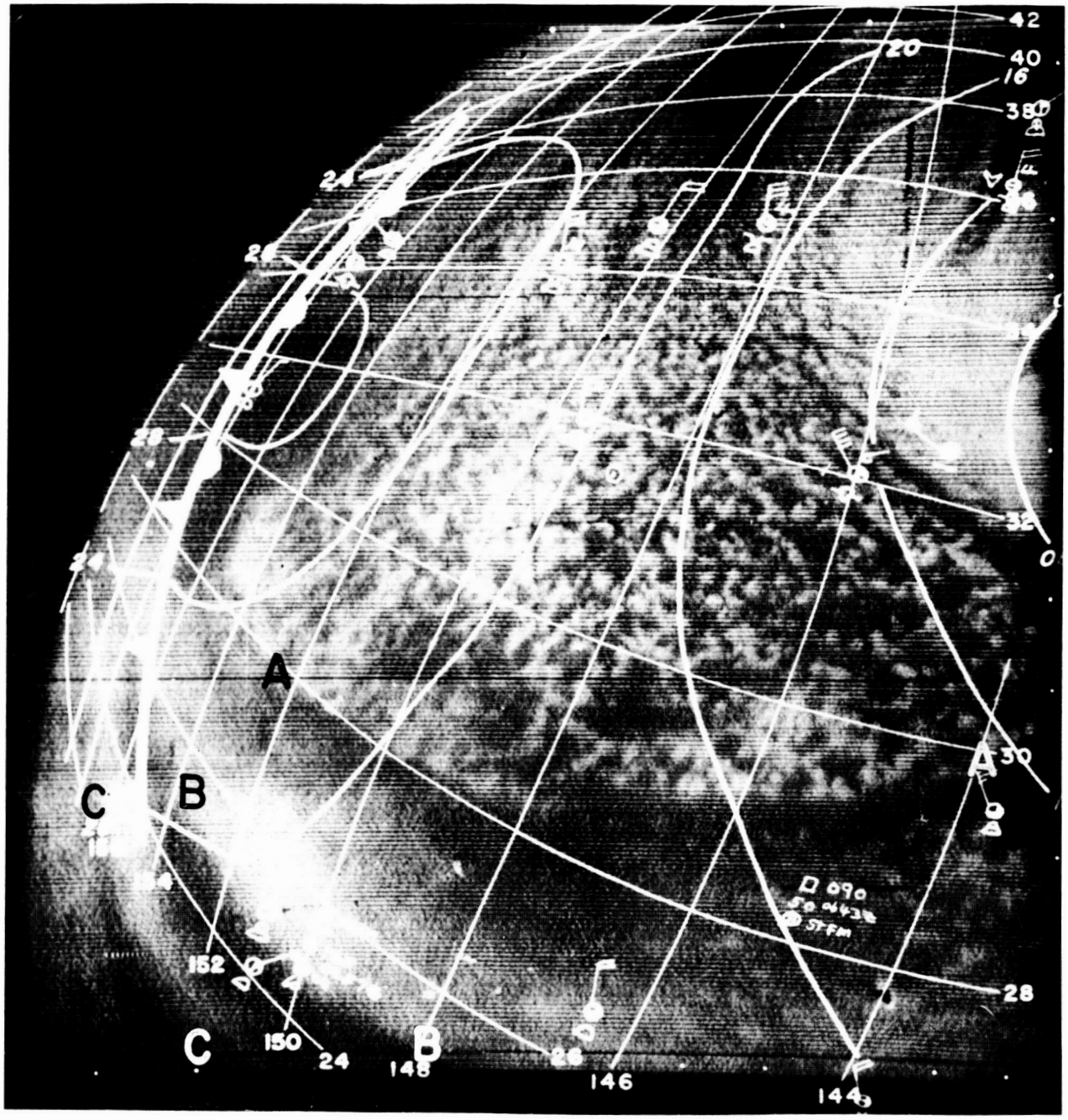

FIGURE 108.—The same photograph as in Figure 102 with superimposed 2° latitude-longitude grid; the principal point of the picture (circled dot); sea-level fronts and isobars at 4-mb intervals; abbreviated surface report showing sky cover, cloud types, present weather, and winds; and pilot reports (squares), for times indicated, of types, amounts, and heights (in hundreds of feet) of bases and/or tops of clouds. The time of the superimposed data, except pilot reports, is 0000 GMT, April 5, 1960.

charts (Figure 107) indicates rather strongly that line BB is indeed associated with this very same surface front. Its rather close fit with previous six-hourly positions of the front as carried on the NAWAC analyses is illustrated in Figure 114. In addition, it is interesting that the surface analysis made by the Weather Bureau Forecast Center at San Francisco (which was consulted after the initial preparation of Figure 114) had retained the second front and its position coincided closely with that shown for line BB in Figure 114.

Inspection of the superimposed 600-mb vertical motion field, which consists of initial vertical velocities computed from a two-level baroclinic model by the JNWP Unit, shows a pattern of large-scale vertical motion which has been found

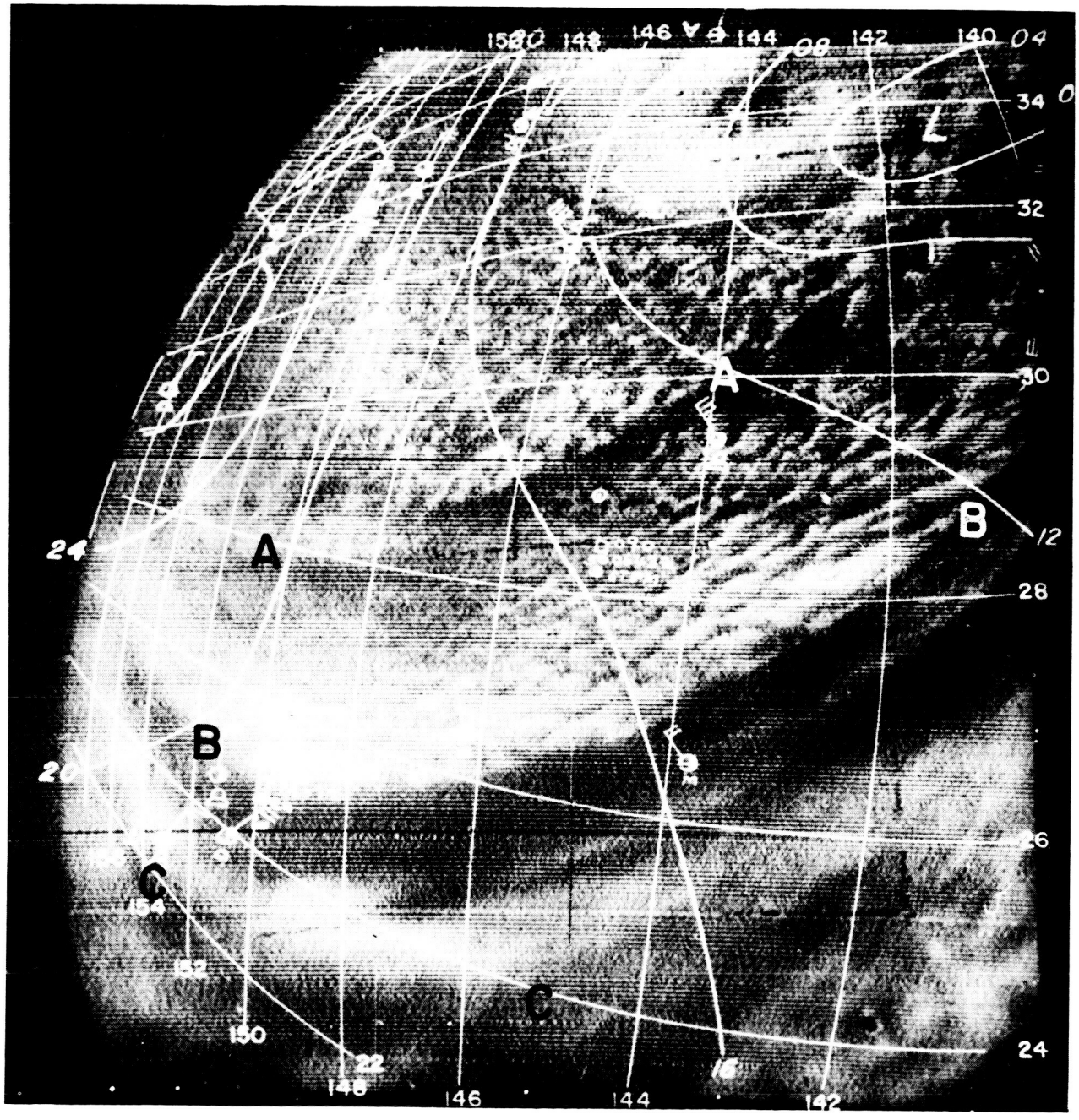

FIGURE 109.—The same photograph as in Figure 103 with superimposed grid and other items as in Figure 108.

typical of trough systems as exemplified by the 700-mb contours in Figures 111–113 (i.e., downward motion to the rear of the trough and upward motion ahead of the trough). It is notable that the area to the rear of line DD (Figure 113), which appears to be a zone of cloudiness extending upward into the middle and upper troposphere, is associated with the main polar front (Figure 110) where slight upward motion was calculated. However, the southwest-northeast orientation of this cloud band, with mostly clear skies to the east of DD, suggests that the axis of

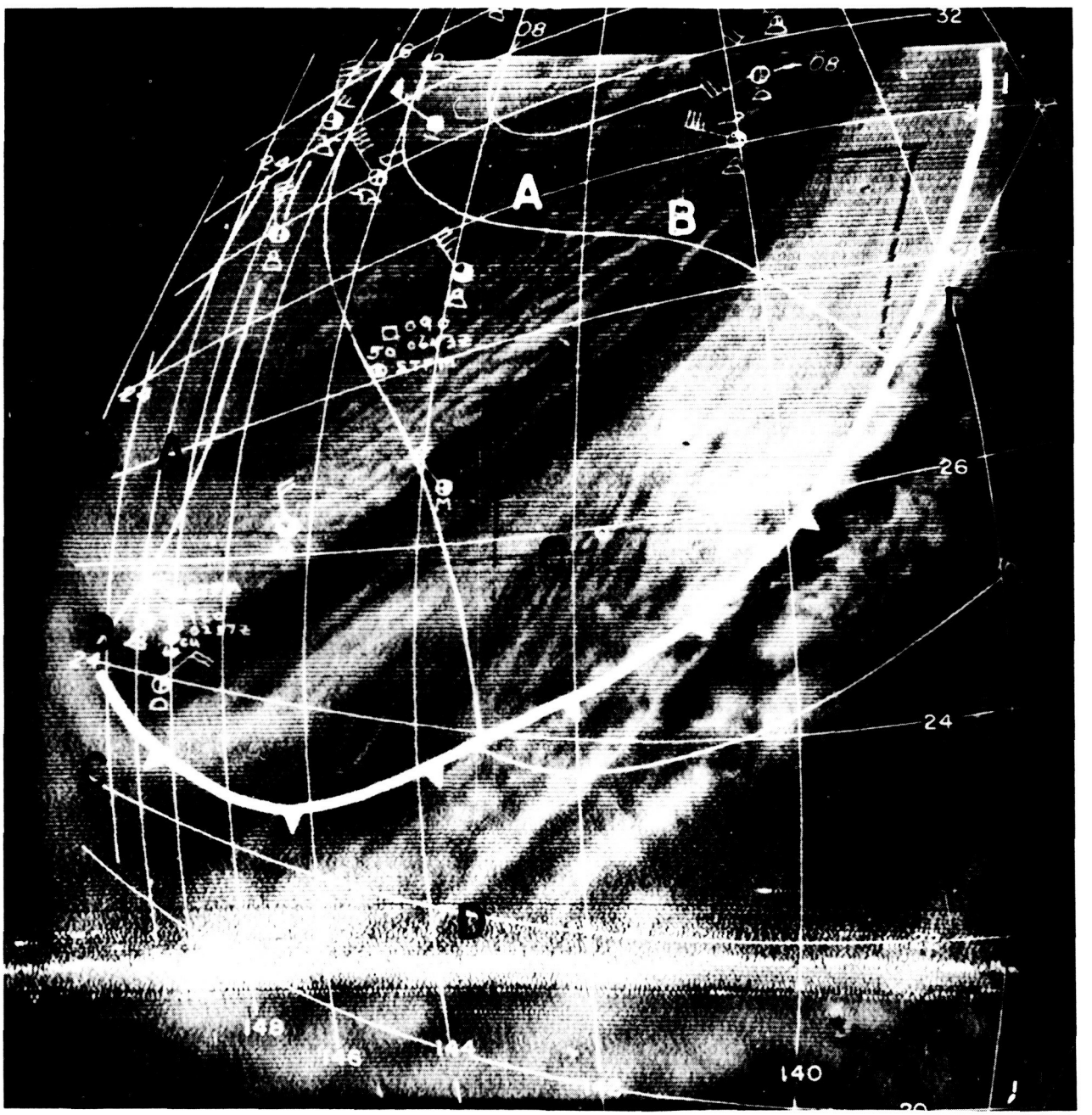

FIGURE 110.—The same photograph as in Figure 104 with superimposed grid and other items as in Figure 108.

maximum upward motion might be elongated southwestward to coincide more closely with this band.

Most of the remaining areas of the pictures, including lines AA, BB, CC, and the cloud areas behind them, are located where downward motion was computed. At first glance it seems surprising that such pronounced zones of cloudiness as those occurring along and to the rear of lines AA and BB should be found where the large-scale

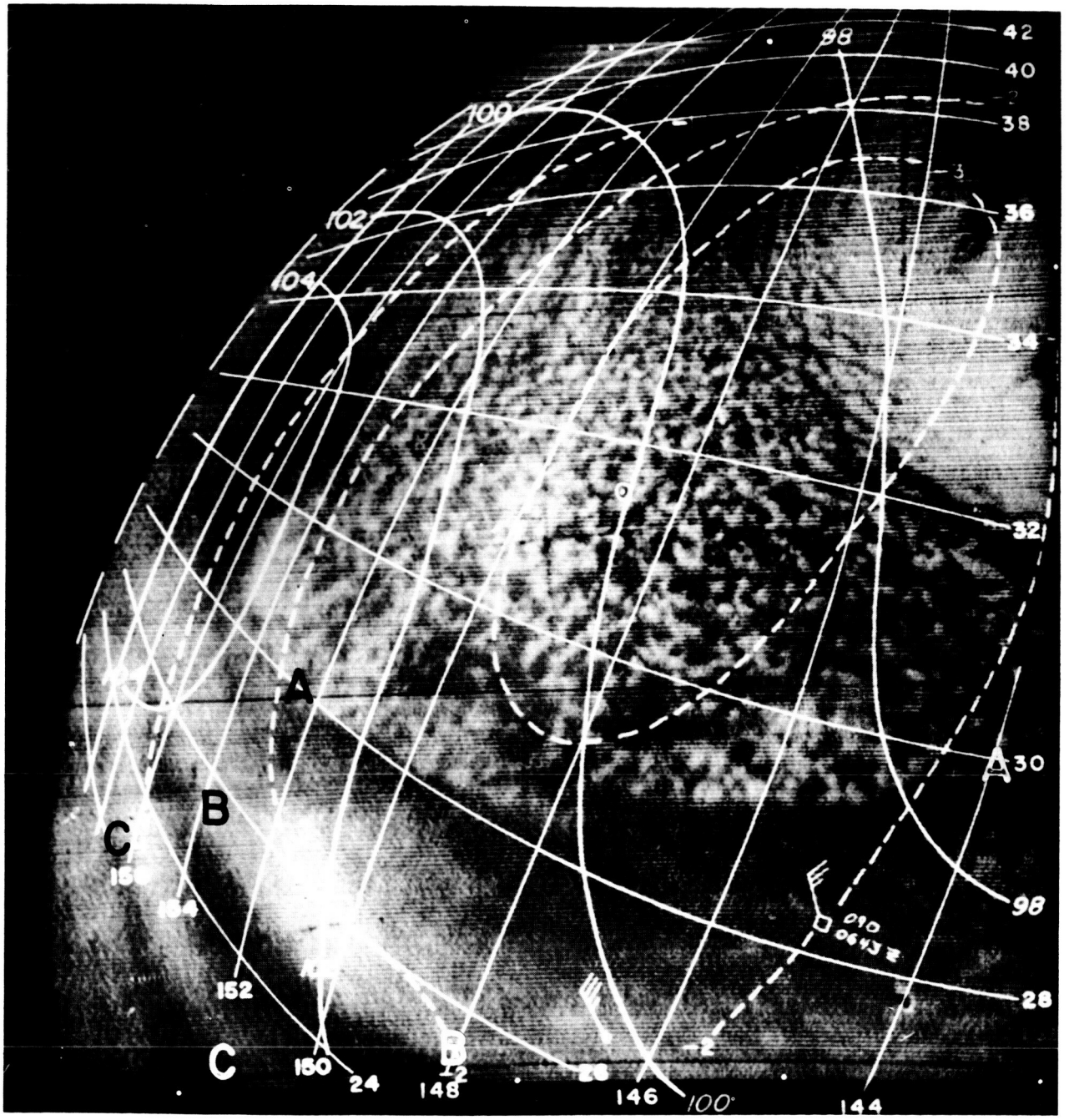

FIGURE 111.—The same photograph as in Figure 102 with superimposed 2° latitude-longitude grid; the principal point of the picture (circled dot); 700-mb contours at 200-ft. intervals; 700-mb winds; winds between 8,000 and 12,000 ft. (from aircraft measurements); and 600-mb vertical motion in cm/sec as computed routinely by the JNWP Unit. The time of the superimposed data, except pilot reports, is 0000 GMT, April 5, 1960.

vertical motion is downward. However, this may indeed be physically correct since most evidence indicates that the cloudiness in these areas is of the cumuliform type which is very likely confined to approximately the lower 5,000 feet. Certainly most of the clouds reported by ships in these areas are cumulus congestus and stratocumulus. A pilot report at 29.5° N, 145° W, about 8 hours after the pictures were taken, indicates broken stratiform (presumably stratocumulus) clouds with tops of 5,000 feet. The soundings at 35° N, 150° W (Figure 115), which is well back in the cellular cloudiness to the rear of line AA, and the sounding at 30° N, 140° W (Figure 116), which is practically on line BB, both reveal a moist, unstable layer of air from the surface to about

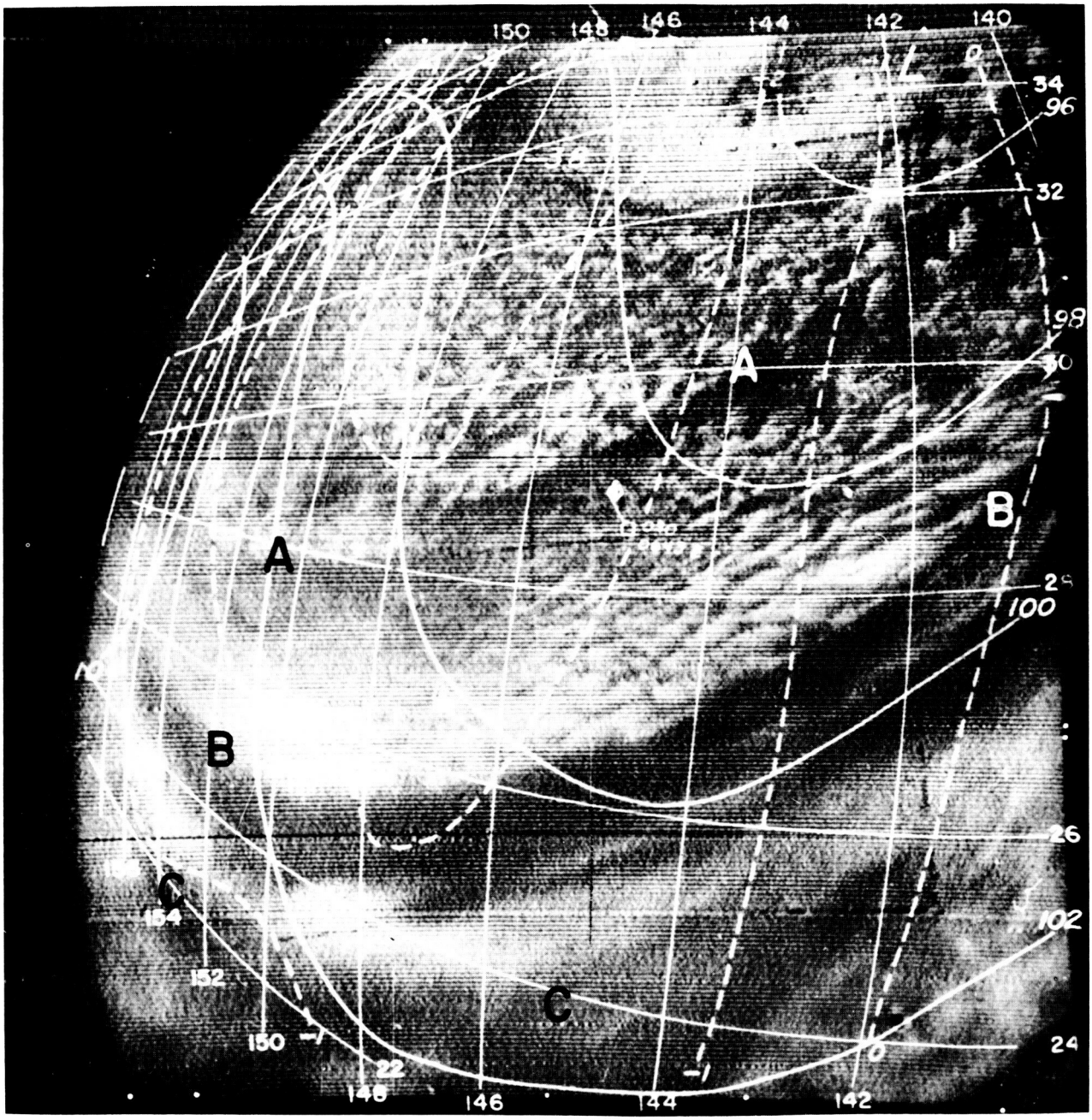

FIGURE 112.—The same photograph as in Figure 103 with superimposed grid and other items as in Figure 111.

850 mb, with a layer of stable, dry air extending from above the pronounced inversion upward to near 600 mb. These soundings certainly suggest that cloudiness in their vicinities would be confined to the instability type in the layer below the inversion. If, therefore, convergence is indeed associated with lines AA and BB, it must be horizontal convergence and upward motion confined to this lower layer.

There is, however, some evidence of middle cloudiness in portions of these areas. Note the altostratus reported by the ship near 35° N, 148° W, just near the western edge of a solid-looking (apparently stratiform) cloud shield (Figure 108). Also, the pilot report at 25° N, 150° W, approximately 4 hours after the picture was taken, shows an overcast of a stratiform type (presumably altostratus or cirrostratus) at an esti-

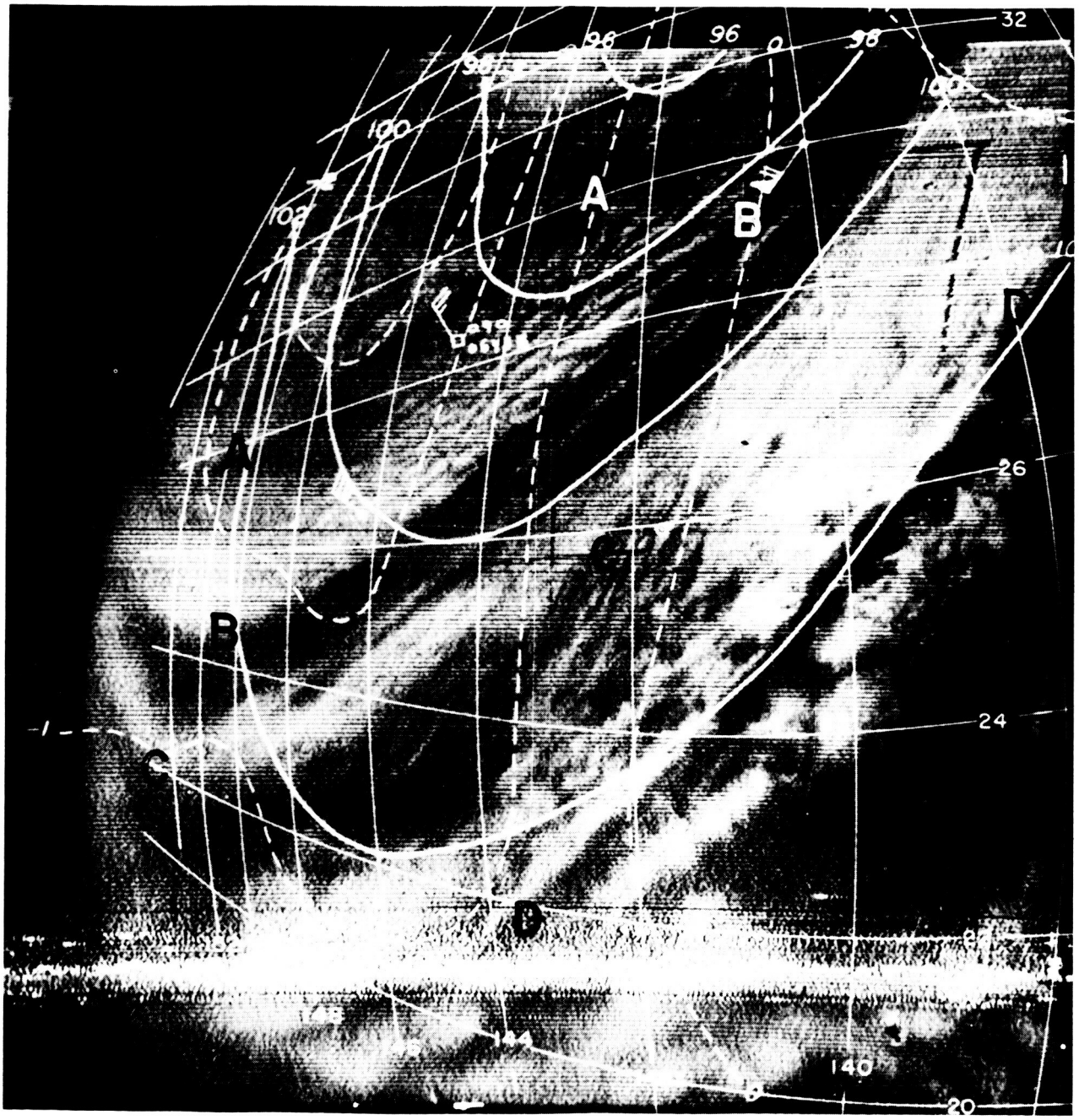

FIGURE 113.—The same photograph as in Figure 104 with superimposed grid and other items as in Figure 111.

mated base of 20,000 feet (Figure 108). This report is also in a region where the cloud appearance suggests stratiform clouds. As the complete pilot report suggests, this upper cloud deck at this point overlies the lower, more extensive cumuliform deck characteristic of the area behind line BB. This presence of middle cloudiness in these areas suggests the likelihood of some large-scale upward motion in mid-troposphere.

Admittedly the relation between cloudiness and upward motion is not as simple as this discussion might suggest, but details of the cloud structure as revealed in these pictures points toward improvements that could be made in the accuracy of the vertical motion pattern around this cyclone.

CLOUD PICTURES TAKEN ON THE 64TH ORBIT

Gridded pictures taken near 2200 GMT, April 5 (previously illustrated in Figures 105 and 106), are shown again in Figures 117 through 120 with superimposed NAWAC surface and 700-mb analyses, abbreviated synoptic surface reports, and 600-mb vertical motion.

It is notable that the broad, banded cloud structure to the west of the cyclone (Figure 117) is closely oriented in the direction of the surface isobars. The ship reports show stratocumulus, cumulus congestus, and low clouds of bad weather in the area under this broad, bright band, and one of these also shows an altostratus-altocumulus layer above the lower clouds. Since the clouds line up so well with the surface flow (and are more perpendicular to the 700-mb flow, as is seen in Figure 119), which has now been coming around from the northern portion of the cyclone for some time, it may be that the middle cloud decks are forming from the tops of the lower cumulus clouds.

The bands spiraling into the center of the storm, as shown in Figure 118, appear to line up with

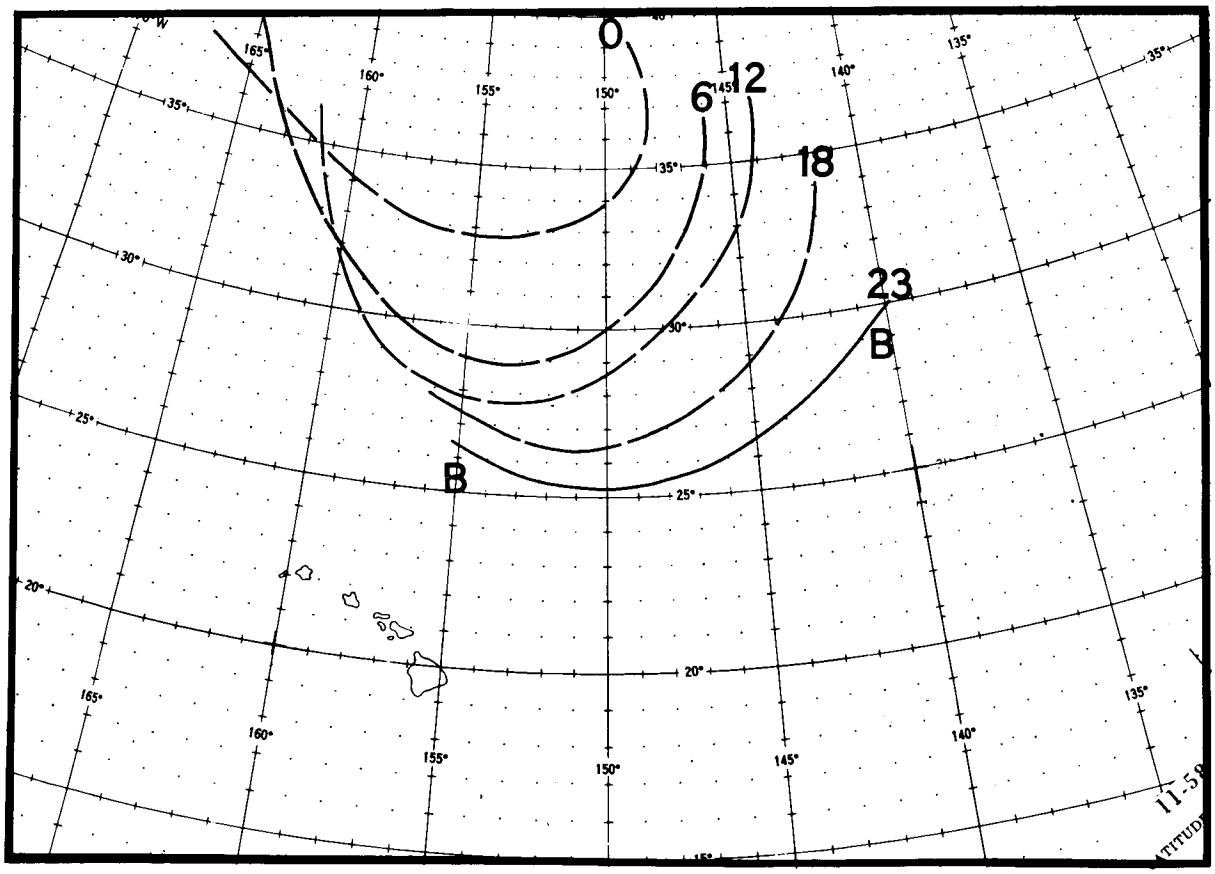

FIGURE 114.—The continuity of the secondary cold front on April 4, 1960. The four positions labeled 0, 6, 12, and 18 are from NAWAC sea-level analyses for 00, 06, 12, and 18 GMT. The position of line BB at 23 GMT was derived from the gridded photograph in Figure 109.

the surface flow north and just east of the low center, although there is some uncertainty of this in view of the center's location toward the edge of the picture, where the accuracy of locating picture elements diminishes. The bands to the south of the cyclone center form a moderate angle of about 30°–45° with the surface isobars near 30° N, 134° W, and this increases to about 90° farther southwestward near 28° N, 138° W. It is probable that the forward edge of the spiral band which emanates from the center and runs approximately through 36° N, 134° W, southeastward to 32° N, 131° W, and thence southwestward through 28° N, 134° W, is the remnant of line BB in the pictures for the previous day (see Figure 109) since its continuity from 24 hours earlier is within reason, although somewhat slower in motion than might have been expected. The primary could front appears to be mainly off the edge of the picture, but the cloud band near the northeastern and southeastern edges of the picture is

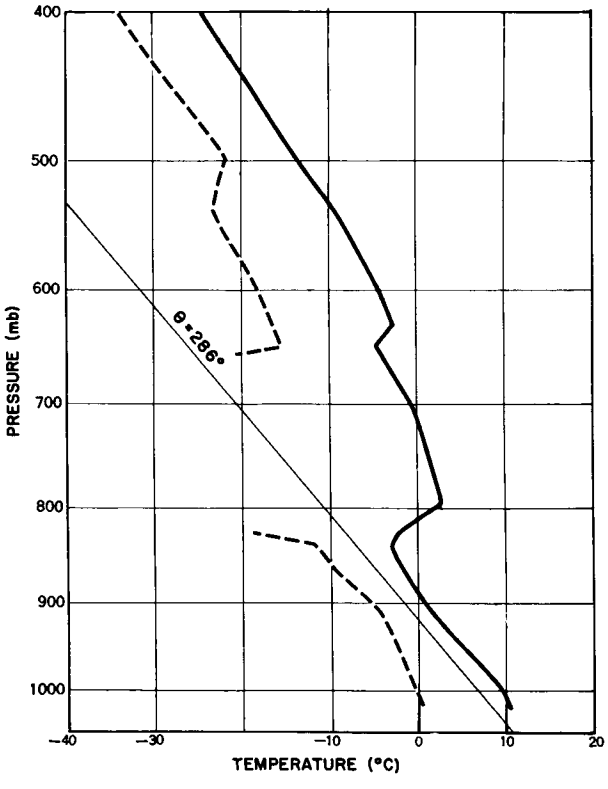

FIGURE 115.—A sounding at Ship NHXN (34.9° N, 150.4° W), 0000 GMT, April 5, 1960. The solid line shows temperature distribution; the dashed line, dewpoint distribution.

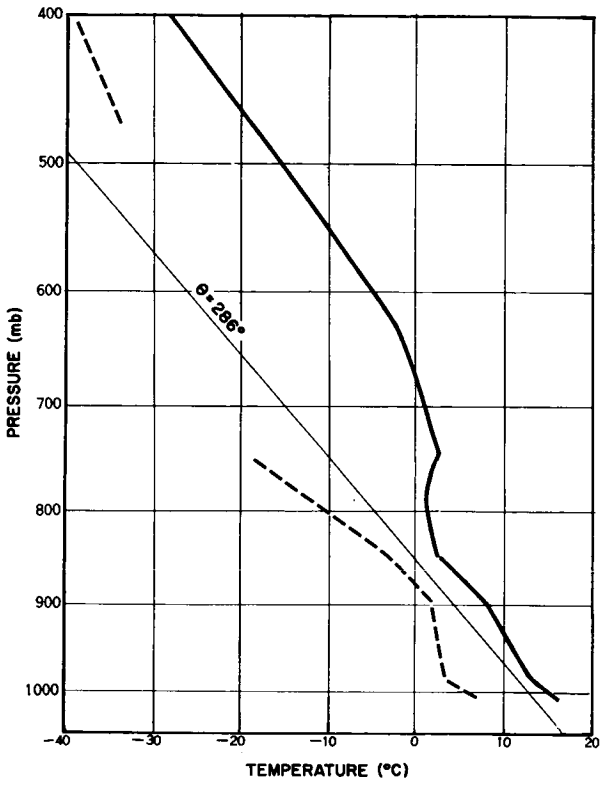

FIGURE 116.—A sounding at Ship 4YN (30.0° N, 140.0° W), 0000 GMT, April 5, 1960. The solid line shows temperature distribution; the dashed line, dewpoint distribution.

very likely part of this frontal system; the suggestion is that the cloudiness and perhaps the front itself have spiraled into the region just north of the surface low center.

The vertical motion fields shown in Figures 119 and 120 again fit in with the general broad-scale distribution expected around the mid-tropospheric trough associated with the cyclone. However, the solid-looking spiral bands and alternating clear areas near the cyclone center suggest that there may be a similar spiraling of the vertical motion pattern in both the lower and middle troposphere. The JNWP vertical motion field is perforce constrained to a simpler pattern because of the general smoothing applied in the numerical calculations and because of the paucity of upper-air observations over this ocean area. It would be interesting to learn whether knowledge of such a spiral arrangement of vertical motion could substantially improve predictions of the further evolution of the cyclone.

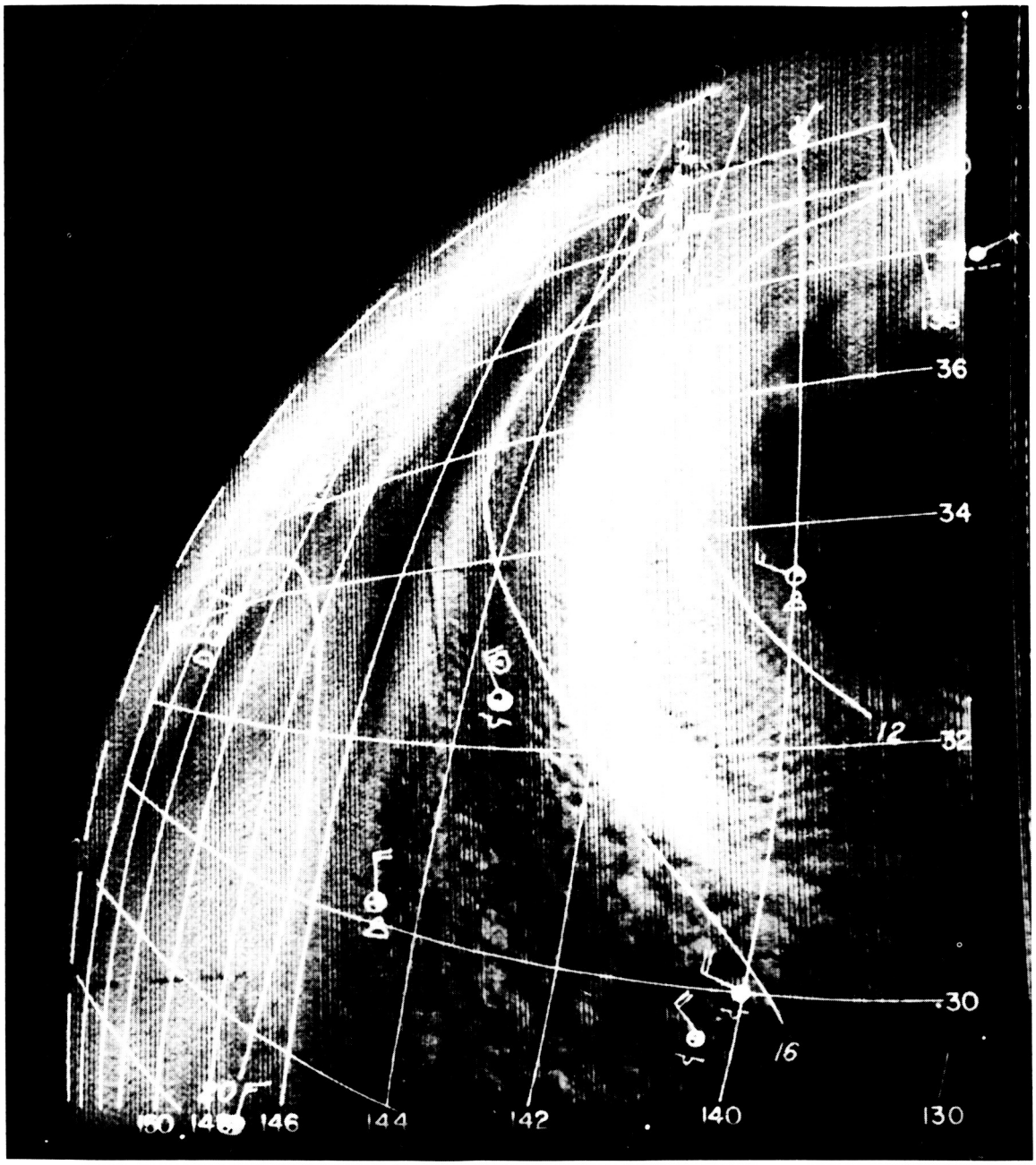

FIGURE 117.—The same photograph as in Figure 105 with superimposed grid and other items (except pilot reports) as in Figure 108, except that the time of the superimposed data is 0000 GMT, April 6, 1960.

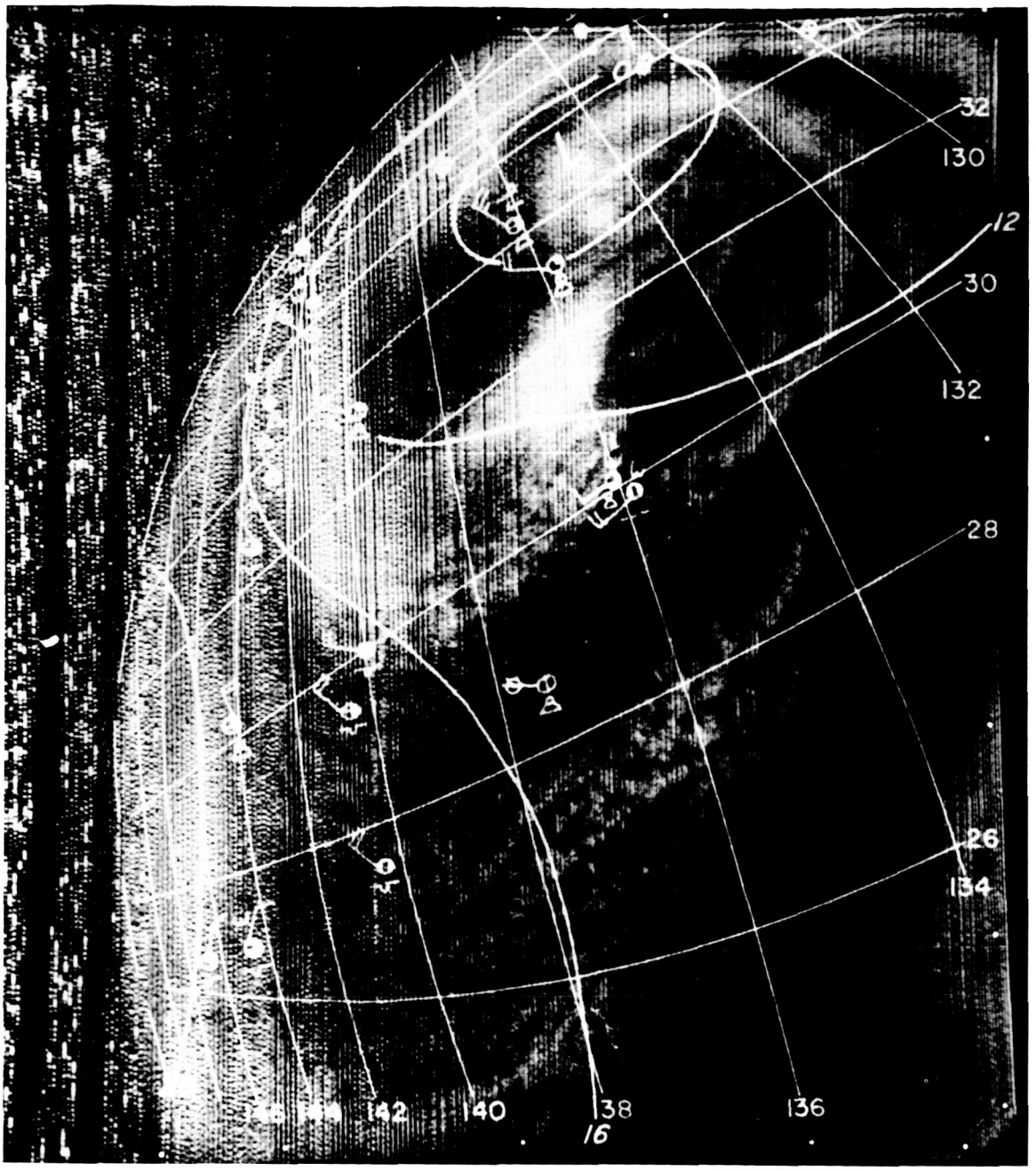

FIGURE 118.—The same photograph as in Figure 106 with superimposed grid and other items (except pilot reports) as in Figure 108, except that the time of the superimposed data is 0000 GMT, April 6, 1960.

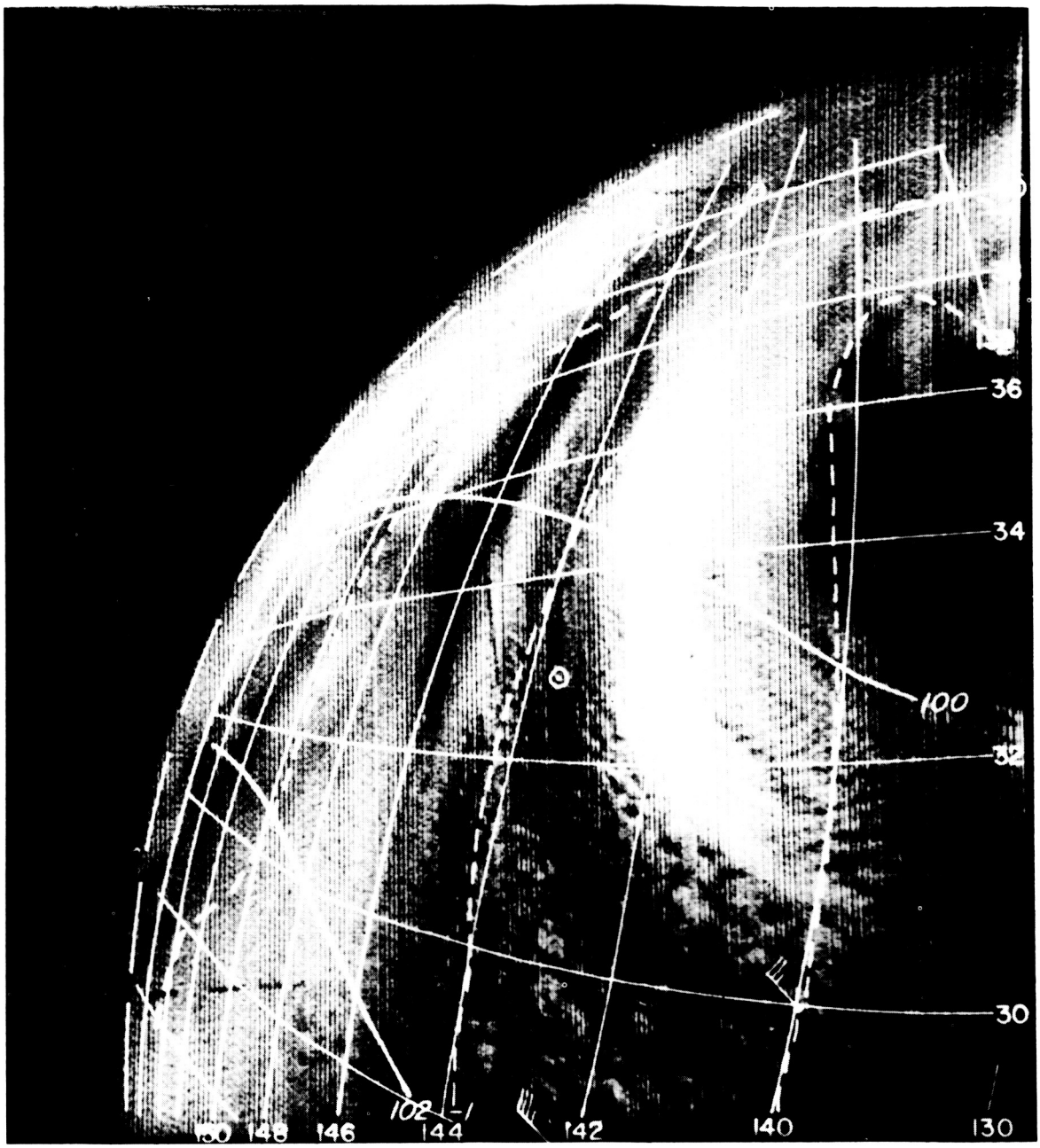

FIGURE 119.—The same photograph as in Figure 105 with superimposed grid and other items as in Figure 111, except that the time of the superimposed data is 0000 GMT, April 6, 1960.

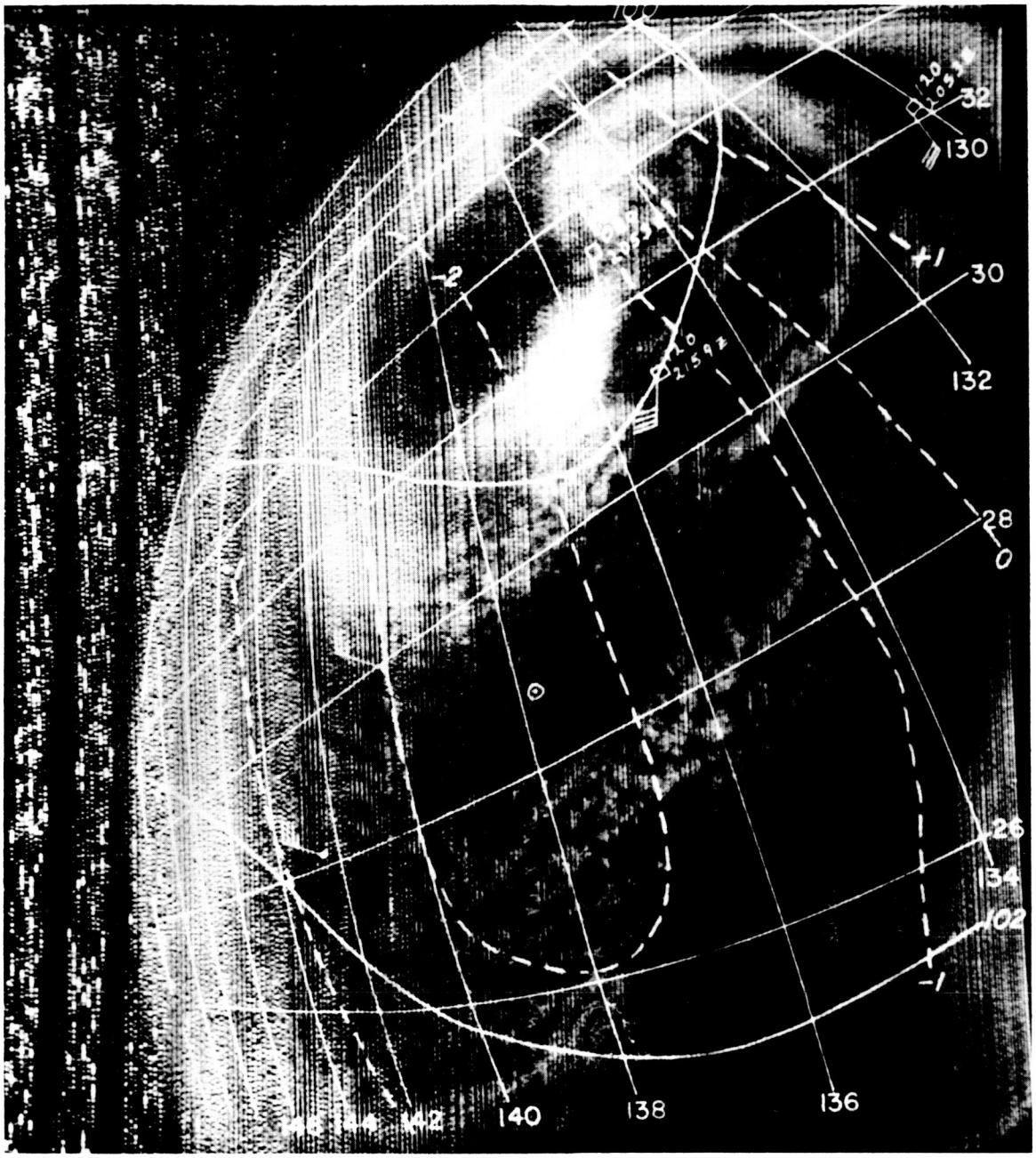

FIGURE 120.—The same photograph as in Figure 106 with superimposed grid and other items as in Figure 111, except that the time of the superimposed data is 0000 GMT, April 6, 1960.

SUMMARY

The TIROS I cloud pictures show the details of the cloud structure around portions of this cut-off cyclone in the eastern Pacific in strikingly clear fashion. It has been shown that some of the major cloud bands in the southwestern portion of this cyclone were nearly perpendicular to the wind direction at both the surface and aloft. Also, one of the most pronounced of these bands was identified as a secondary cold front along which the cyclonic development took place. The cloud patterns viewed by TIROS I suggest possible modifications in estimates of large-scale vertical motion in the lower and middle troposphere. Regular views of entire storm areas, even at intervals of a day, would increase our understanding of the life cycle and structure of such cut-off cyclones.

REFERENCES

1. Stroud, W. G., "Initial Results of the TIROS I Meteorological Satellite," J. Geophys. Res. 65(5): 1643–1644, May 1960.
2. Fritz, S., and Wexler, H., "Cloud Pictures from Satellite TIROS I," Monthly Weather Rev. 88(3): 79–87, March 1960.
3. Wexler, H., and Fritz, S., "TIROS Reveals Cloud Formation," Science 131(3415): 1708–1710, June 10, 1960.
4. Fultz, D., "A Survey of Certain Thermally and Mechanically Driven Systems of Meteorological Interest," in: "Fluid Models in Geophysics"; Washington: Office of Naval Research, 1956, pp. 27–63 (U.S. Government Printing Office).
5. Nakagawa, Y., and Frenzen, P., "A Theoretical and Experimental Study of Cellular Convection in Rotating Fluids," Tellus 7(1): 1–21, February 1955.
6. Wexler, H., "Structure of Hurricanes as Determined by Radar," Ann. New York Acad. Sci. 48 (article 8): 821–844, 1947.
7. Godske, C. L., Bergeron, T., Bjerknes, J. Bundgaard, R. C., "Synoptic Weather Analysis," in: "Dynamic Meteorology and Weather Forecasting," Boston: American Meteorological Society, 1957, pp. 620–722.

CHAPTER 11

AN OCCLUDED CYCLONE OVER THE GULF OF ALASKA*

by

JAY S. WINSTON and LLOYD TOURVILLE

INTRODUCTION

On April 1, 1960, during its 6th orbit, TIROS I photographed portions of an occluded cyclone over the Gulf of Alaska. Wide-angle pictures of this storm and its periphery were obtained on several frames taken at 30-second intervals starting at 2155 GMT. The track of the satellite (from south of the Aleutians southeastward toward Lower California) is shown in Figure 121 superimposed on the sea-level analysis of the National Weather Analysis Center (NAWAC) for 0000 GMT, April 2, 1960 (approximately 2 hours after picture time). Since the satellite passed to the south of the Gulf of Alaska low and its camera was pointing generally backward along the track, the pictures mainly show the cloudiness over the western and southern quadrants of the storm.

As may be seen in the sea-level analysis of Figure 121, this Gulf of Alaska cyclone was a recently occluded cyclone wave of moderate intensity. The center of this storm had moved northeastward into the Gulf of Alaska at an average speed of about 25–30 knots during the previous 24 hours and had very nearly reached its minimum central pressure of about 980 mb at this time. The analysis of Figure 121 also shows that the cold front extending from the cyclone center was nearly stationary south of latitude 38° N, and that a weak frontal wave was indicated near the lower left corner of the map (about 33° N, 160° W).

A composite (Figure 122) of several wide-angle photographs gives an overall view of the cloudiness in the vicinity of this Gulf of Alaska cyclone. (In this and subsequent views the pictures are printed so that north is generally toward the top of the page.) Of particular interest in Figure 122 are several distinctive cloud features: the cloudiness around the center of the major cyclonic vortex (A); broad, solid cloud bands (BC and DE); cellular cloudiness (F); and the probable remnants of an old cyclonic vortex (G).

In order to examine these features in more detail and to relate them to information available from standard meteorological observations, three photographs (Figures 123, 126, and 129) have been selected from the group used in making up Figure 122. These pictures were taken at points 3, 4, and 5, respectively, along the track in Figure 121, where the direction in which the camera was pointed is also shown. Comparison of standard meteorological data and analyses with the pictures has been facilitated by superimposing on the photographs a 2-degree latitude-longitude grid system prepared by the methods of Appendix A. The "gridded pictures" are shown in Figures 124, 127, and 130 with superimposed sea-level data and analyses, and in Figures 125, 128, and 131 with superimposed 700-mb contours, wind reports at 700 mb, and 600-mb vertical motion computed by the JNWP Unit.

CLOUDINESS NEAR THE VORTEX CENTER

The inner core of the cyclone over the Gulf of Alaska is clearly identified by dense cloudiness with pronounced cyclonically-shaped streaks (A in Figure 126). A striking feature of this picture is the pronounced clear "moat" extending outward from near the center of the storm. As may be seen in Figure 129 where more of this clear area is visible, the "moat" appears to be part of a band that spirals into the storm center. Another clear line farther southeastward (Figures 126 and 129) also seems to spiral into the center and to merge with the first clear "moat."

Examination of Figures 127 and 128 shows that the cyclonically-curved streaks in the vortex clouds

*A revised version of this paper appears in Bull. Amer. Meteorol. Soc. 42(3) : 151–165, March 1961.

In NASA. Goddard Space Flight Center Tiros I Meteorol. Satellite System 1962 p 151-165 refer
Submitted for Publication (See N64-17906 10-21) GPO: $2.25

generally parallel the sea-level isobars and most of the reported surface winds. They also parallel the 700-mb flow, since the latter has virtually the same direction as the surface flow, except to the south of the low center where the upper trough is to the west of the surface trough.

The few ships located within the streaky cloud area near the storm center reported stratocumulus clouds in the lower levels with a deck of altostratus clouds above (Figures 127 and 130). There were no reports of cirriform clouds in the area although they could have been present above the deck of altostratus and hence not visible to the ground observer. However, the cloudiness (see Figure 126, where the cloud pattern is not obscured by superimposed data) does not have the

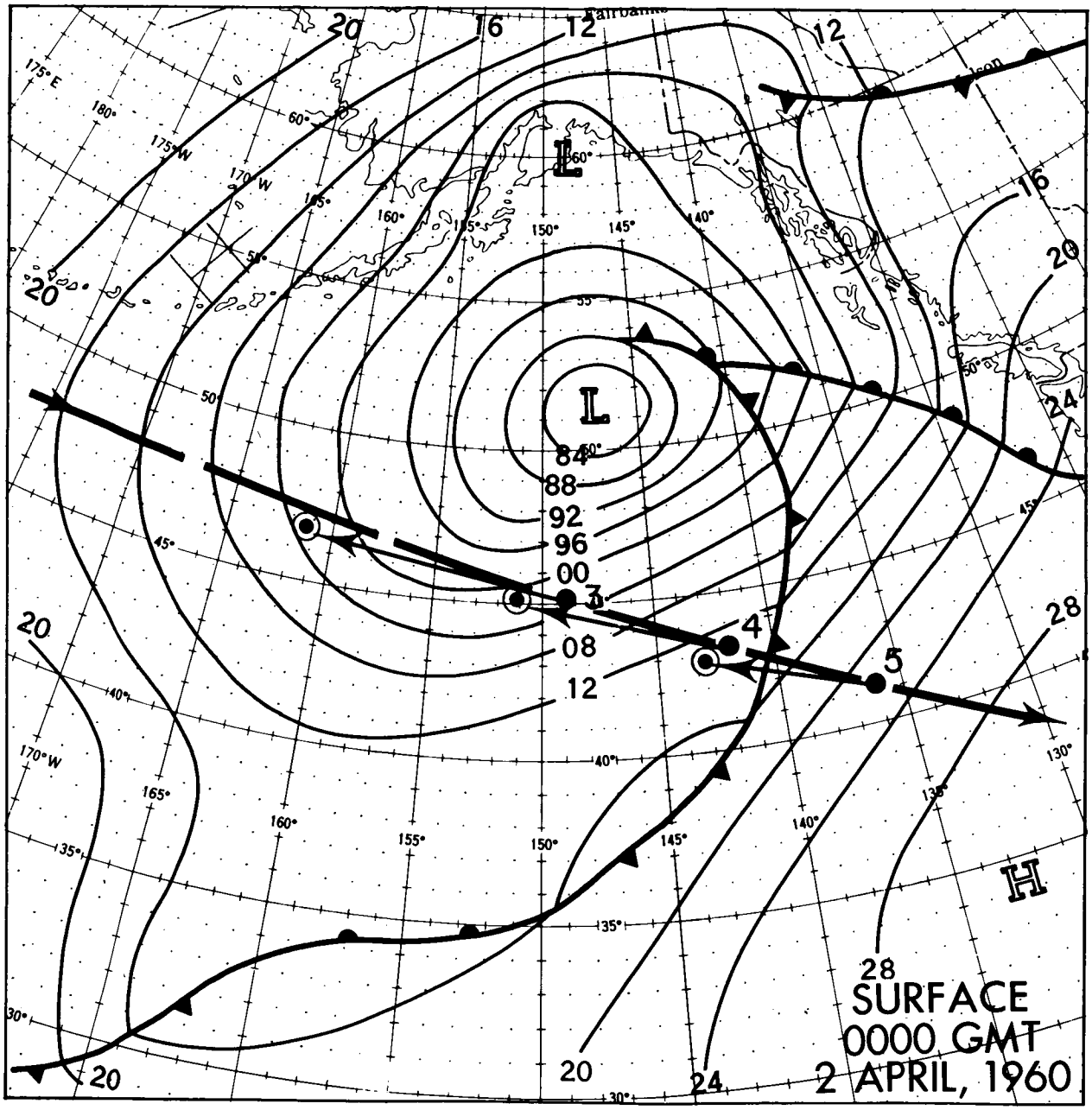

FIGURE 121.—Sea-level analysis for 0000 GMT, April 2, 1960, with the satellite track indicated by the heavy line. Dots and numbers along the path correspond to the pictures shown in Figures 123–131. Circled dots indicate principal points of the pictures, and arrows show the camera orientation for each picture.

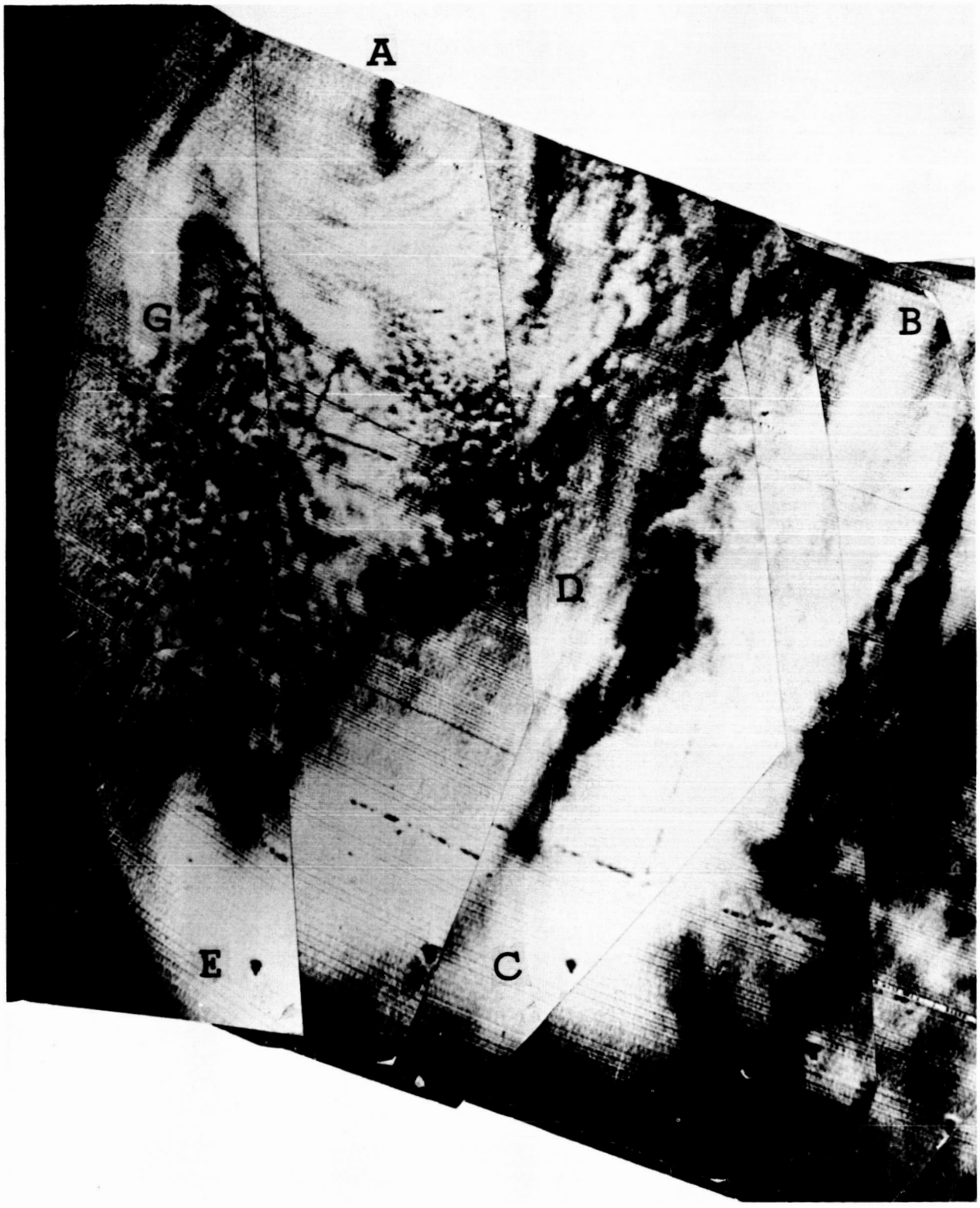

FIGURE 122.—Composite picture of the Gulf of Alaska storm and adjacent synoptic features. The pictures were taken at approximately 2200 GMT, April 1, 1960.

646-770 O—64——11

appearance of a solid cirrostratus overcast. In fact, the streakiness indicates that even the altostratus deck is far from solid, probably broken or very thin.

The only sounding in the vicinity of this cyclone is the one at Ship P (50° N, 145° W), located just southeast of the low center and to the rear of the occlusion (beyond the confines of Figures 126–128, but just barely at the edge of the photograph of Figures 129–131). This sounding (Figure 132), which is very likely typical of most of the cloud area near the center, reveals a lapse rate that is nearly moist-adiabatic all the way up to 400 mb. The dewpoint sounding shows very high relative humidity from the surface up through 700 mb, but somewhat lower humidities (about 50–60 per-

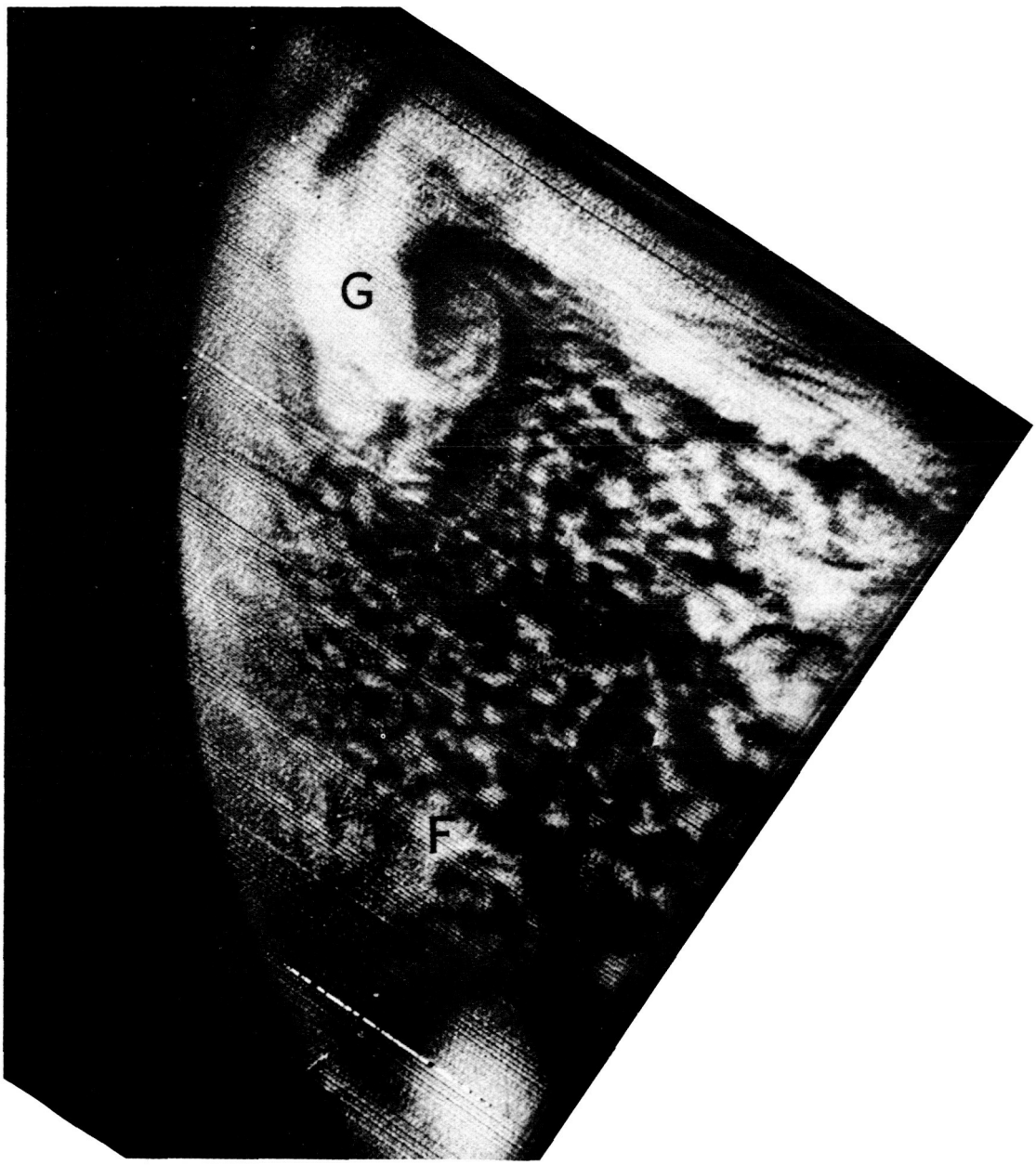

FIGURE 123.—Picture of the clouds west and southwest of the main cyclone in the Gulf of Alaska, showing a probable old cyclonic vortex (G) and cellular cloud structure to the rear of the storm (F).

cent) from 600 mb upward. This indicates that the clouds do not extend beyond middle levels (i.e., about 12,000 feet) and thus corroborates the deduction made from the nature of the cloudiness as viewed in area A (Figure 126). The lack of reports of significant precipitation by ships in area A also lends support to the conclusion that the cloudiness does not extend to high levels.

The vertical motion field in Figure 128 shows a center of weak downward motion in the vicinity

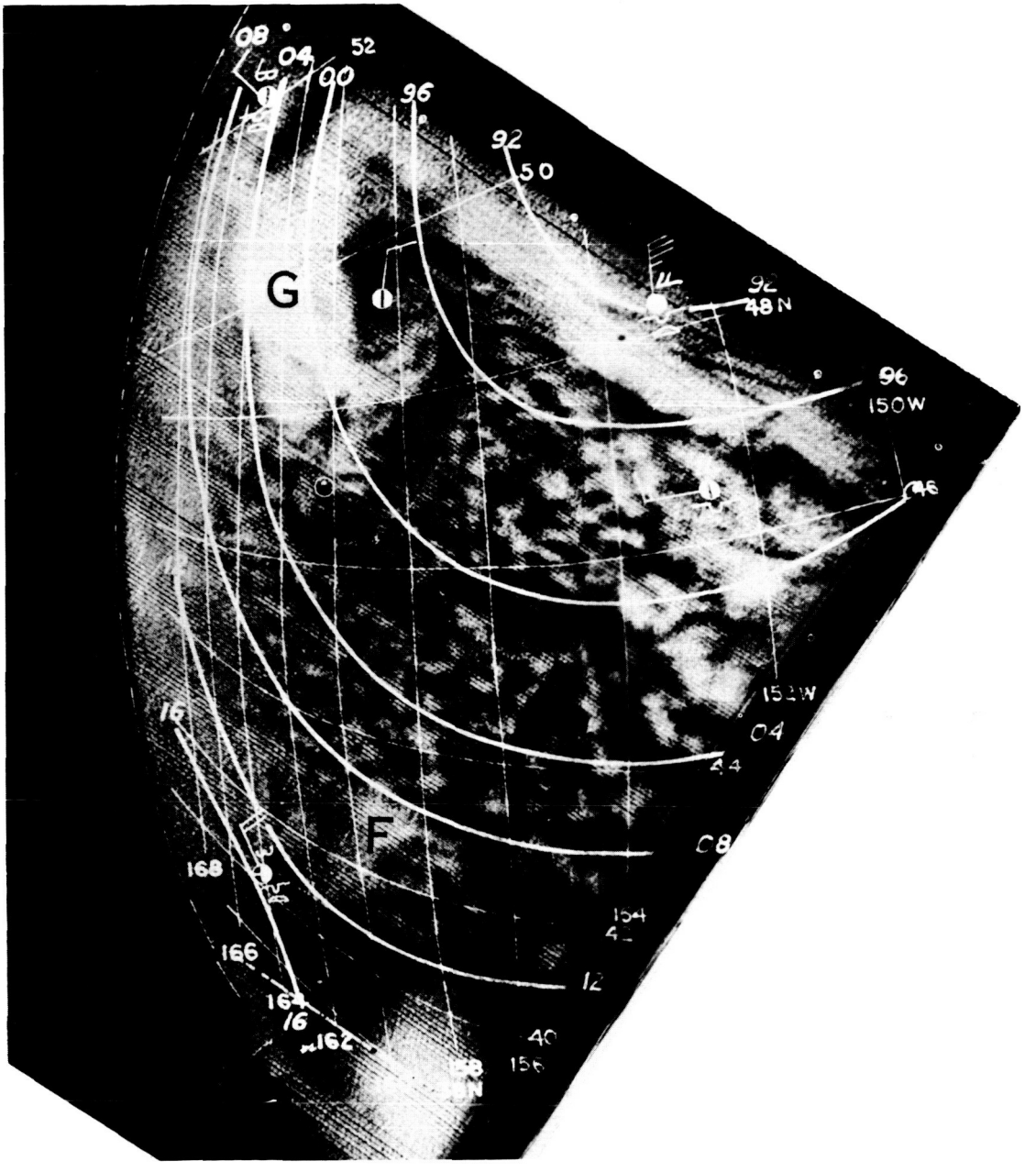

FIGURE 124.—Same picture as in Figure 123 with superimposed 2° latitude-longitude grid; principal point of picture (circled dot); sea-level isobars at 4-mb intervals; and abbreviated surface reports showing sky cover, cloud types, present weather, and winds. Solid white circles denote overcast. Surface data and analyses are for 0000 GMT, April 2, 1960.

of the cloudiness under discussion. If our deductions about the clouds not extending to 600 mb are correct, this computed downward motion for the 600-mb surface may have some validity. However, it is likely, in view of the extensive cloudiness near this low center, that there is some upward motion between 600 mb and the layers near the surface. In any event the downward motion computed by the JNWP model, contrary to the assumption inherent in the model, is very likely not representative of a deep layer of the middle and lower troposphere. Of course, the sparsity of observations in this region, plus some of the other restrictions of the baroclinic model tend to de-

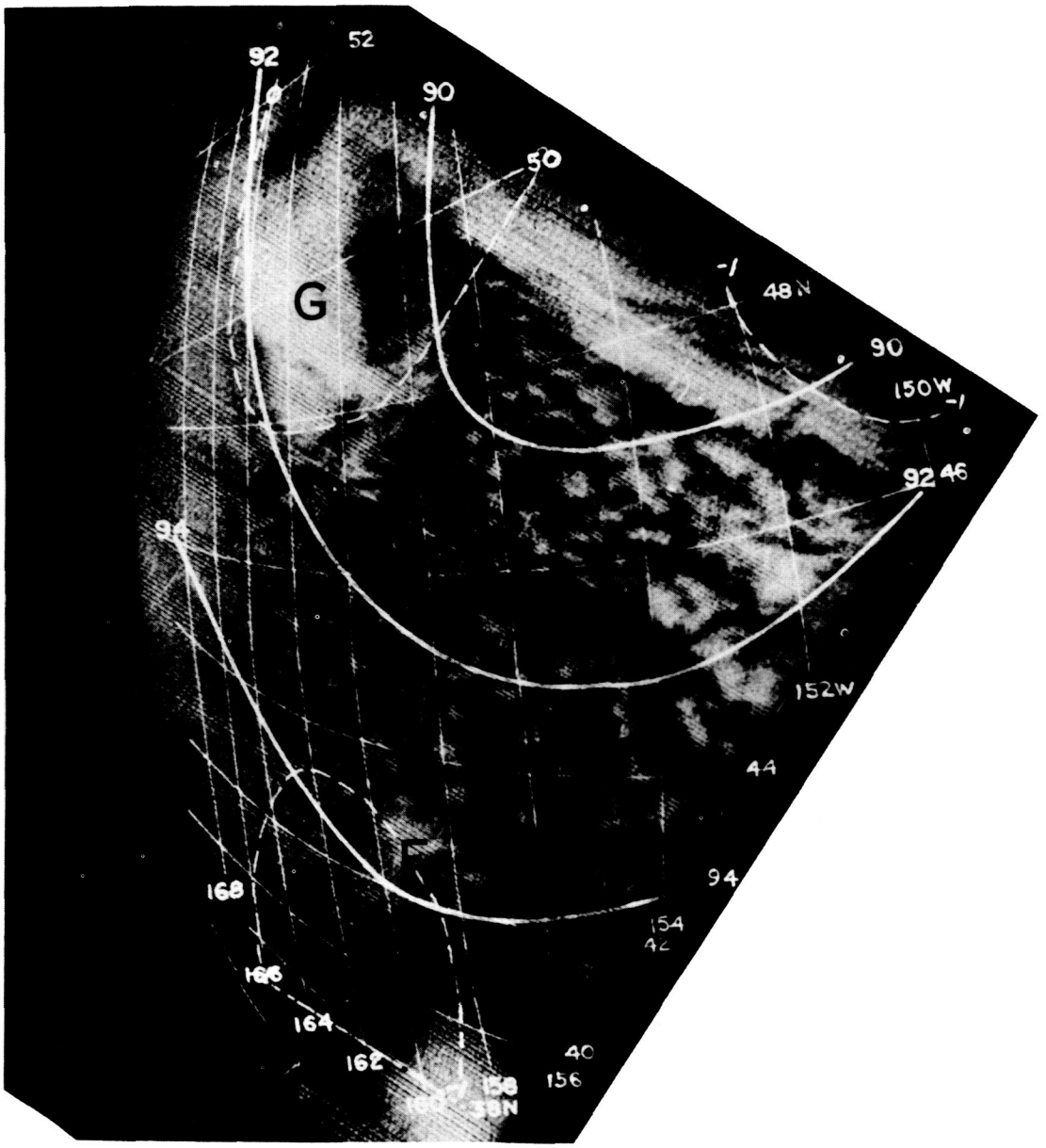

FIGURE 125.—Same picture as in Figure 123 with superimposed grid; 700-mb contours at 200-ft. intervals; and 600-mb vertical motion (dashed) in cm/sec as computed by the JNWP Unit. Superimposed data are for 0000 GMT, April 2, 1960.

grade the accuracy of these computed vertical velocities. The cloudiness revealed in the TIROS I pictures may indeed yield the best estimates, albeit only qualitative, of the predominant vertical motions in the lower and middle troposphere.

Estimates of vertical motion from cloudiness may, of course, be fairly crude since the mere presence of clouds does not necessarily mean that upward motion is instantaneously present. Rather it is the increase or maintenance of cloudiness over a period of time that is indicative of upward motion; this type of comparision has been cited by Panofsky and Dickey.[1] Thus, only when local time sequences of satellite pictures become avail-

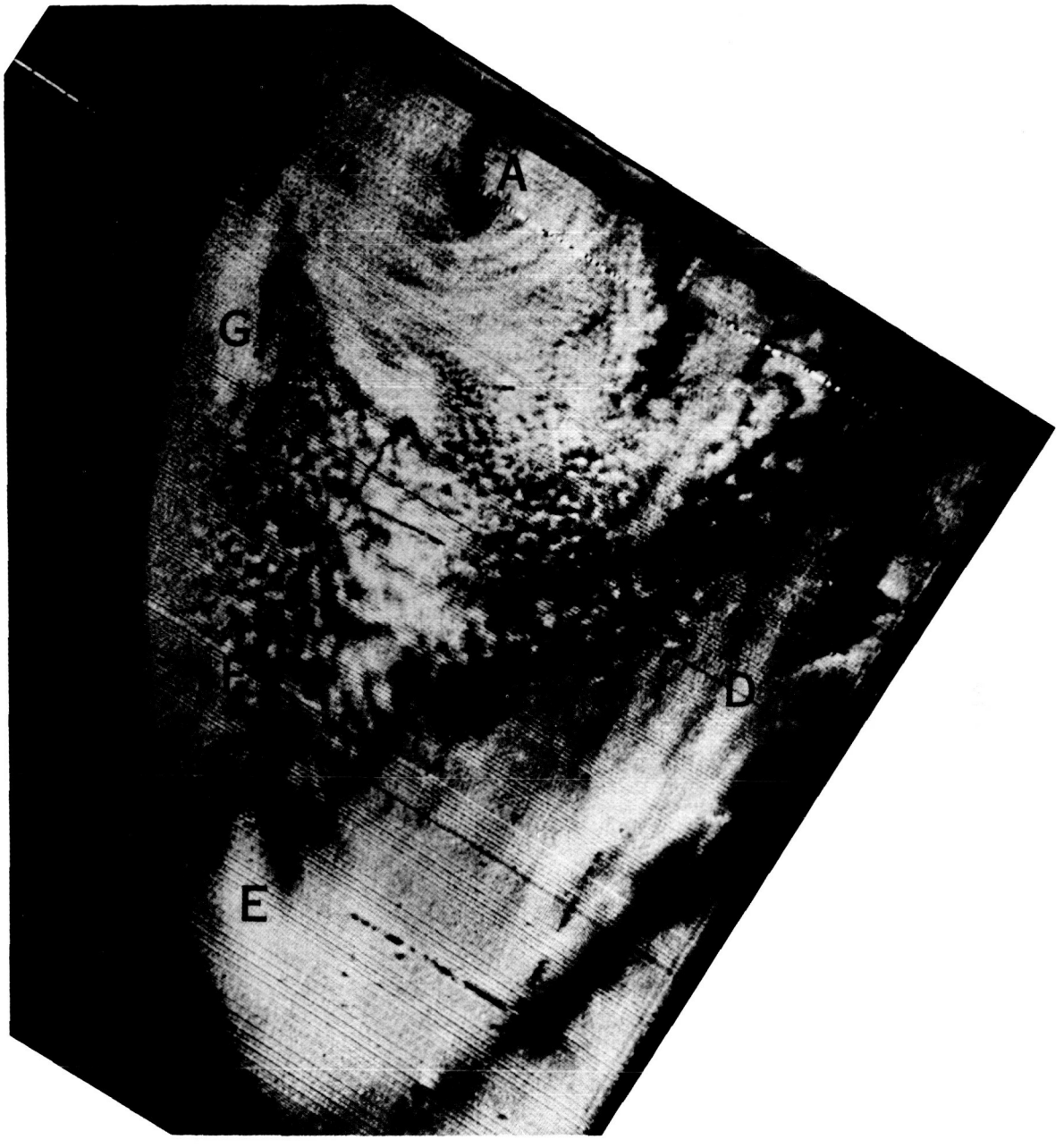

FIGURE 126.—Picture of the cloudiness south and southwest of the Gulf of Alaska cyclone showing cloud structure near the vortex center (A), overrunning cloud system associated with new wave on polar front (DE), cellular cloudiness (F), and probable old cyclonic vortex (G).

able, will the direction of vertical motion be determinable with more precision. However, until better data are available, it may be assumed, as we have in this case, that upward motion is generally occurring in an extensive cloud mass of the size of the one around this cyclone center.

FRONTAL CLOUDINESS

The southern and southeastern fringes of the Gulf of Alaska cyclone are dominated by two wide bands of stratiform cloudiness of a more or less uniform character (BC in Figure 129 and DE in Figures 126 and 129). As may be seen im-

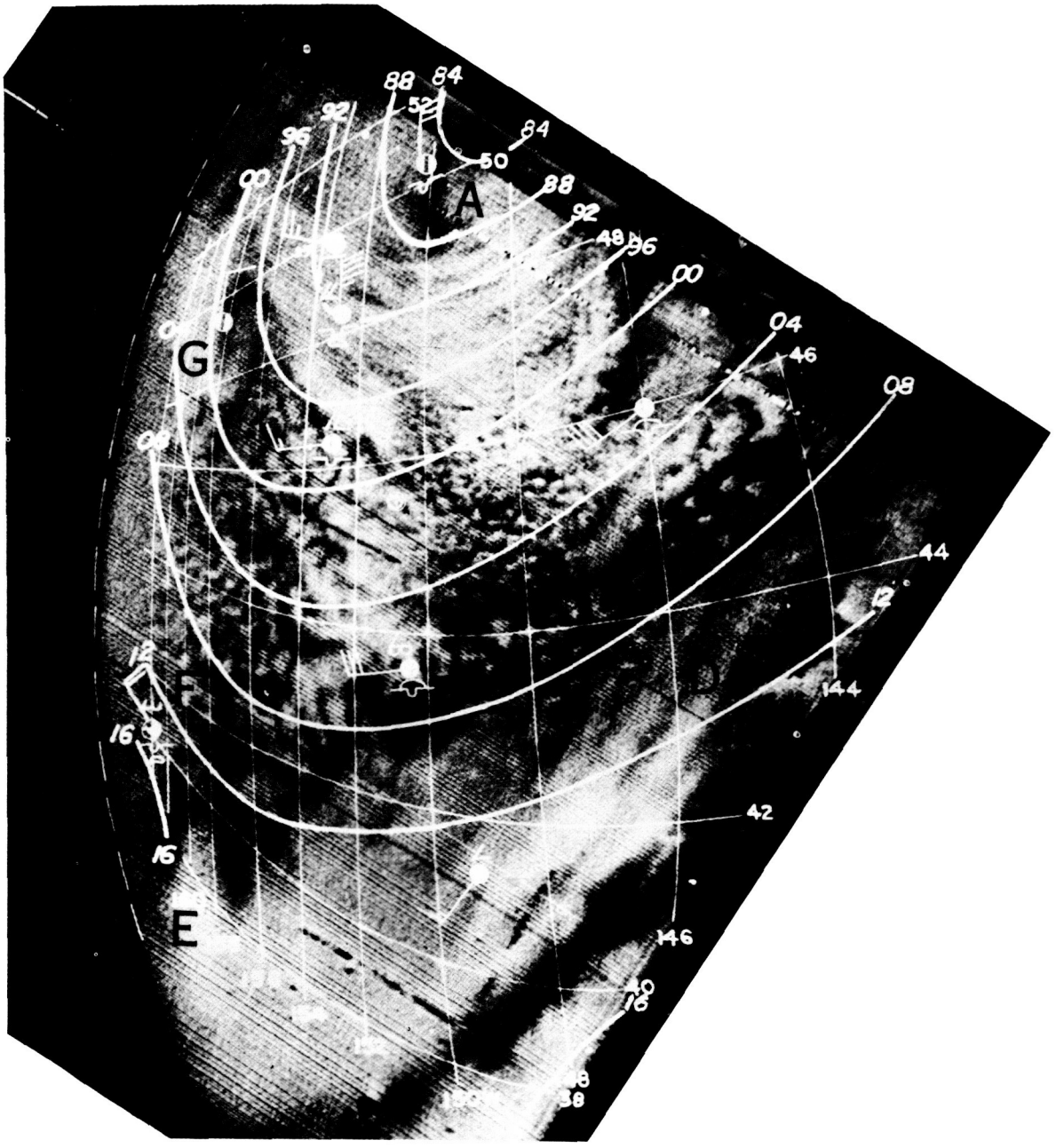

FIGURE 127.—Same picture as in Figure 126 with superimposed grid and other items as in Figure 124.

mediately in Figure 130, band BC generally straddles the major cold front associated with this occluded cyclone. Since the frontal position is fixed rather closely by the ship report at 44° N, 139° W, which requires the front to lie to the west of this location, there is very little doubt that this stratiform cloudiness does occur on both sides on the front in this case. In general this cloudiness is continuous, but there is a suggestion of breaks just east of the front northward from latitude 43° N.

Figure 131 shows that this frontal cloudiness is

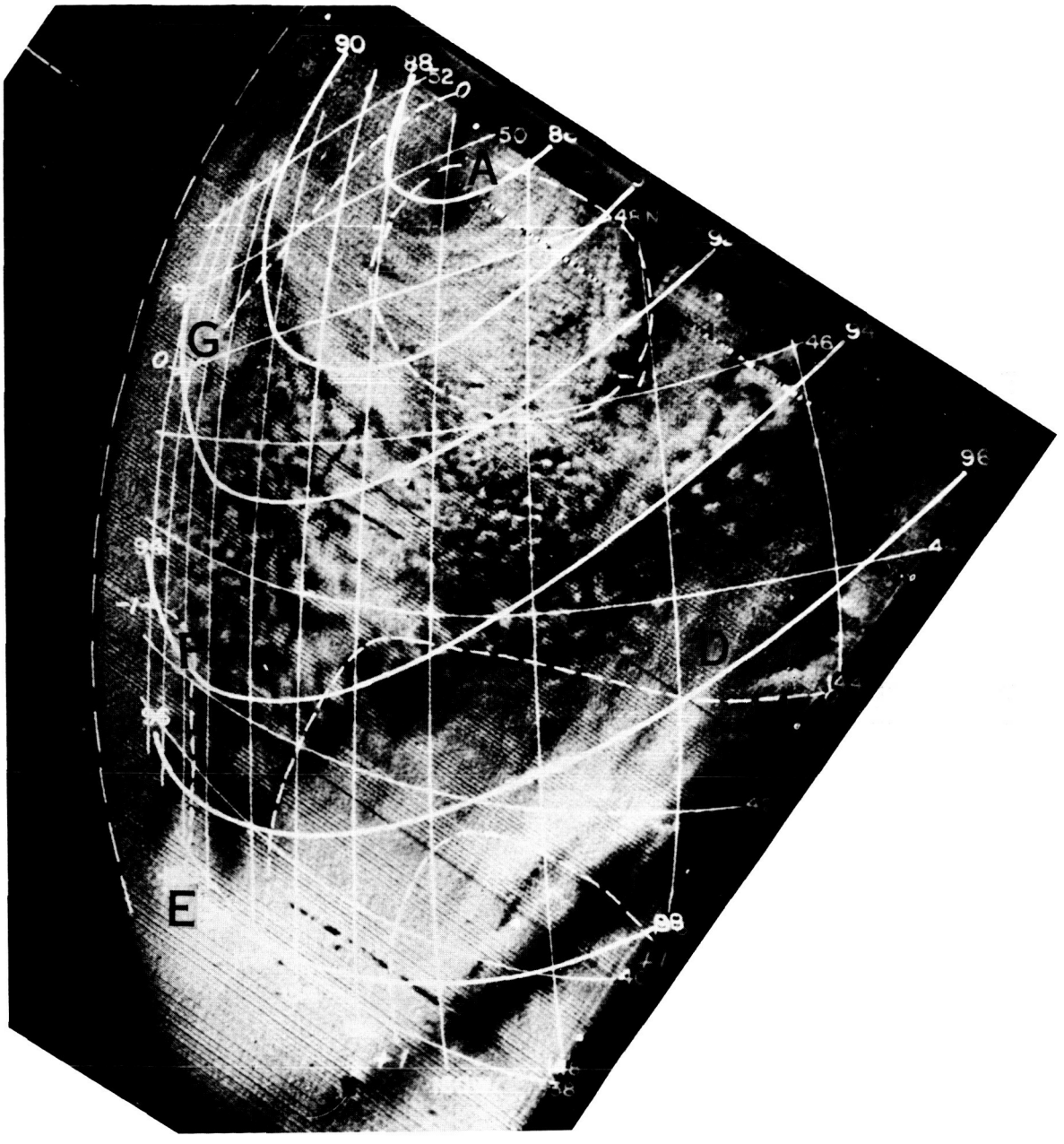

FIGURE 128.—Same picture as in Figure 126 with superimposed grid and other items as in Figure 125.

located in the broad southwesterly current ahead of the trough on the 700-mb chart. The band is elongated at a small angle to the left of the 700-mb contours (looking downstream). Unfortunately, there are no upper-air data within the entire area enclosed by zone BC, but in view of the strength of the cyclonic system at the surface and of the attendant sea-level pressure gradients, there is little doubt that a broad, vigorous southwesterly flow exists aloft in this zone.

Furthermore, it is obvious that this strong flow in the midtroposphere is surmounted by a jet stream (or streams) through this area in the upper troposphere. This is indicated by the flow at 300

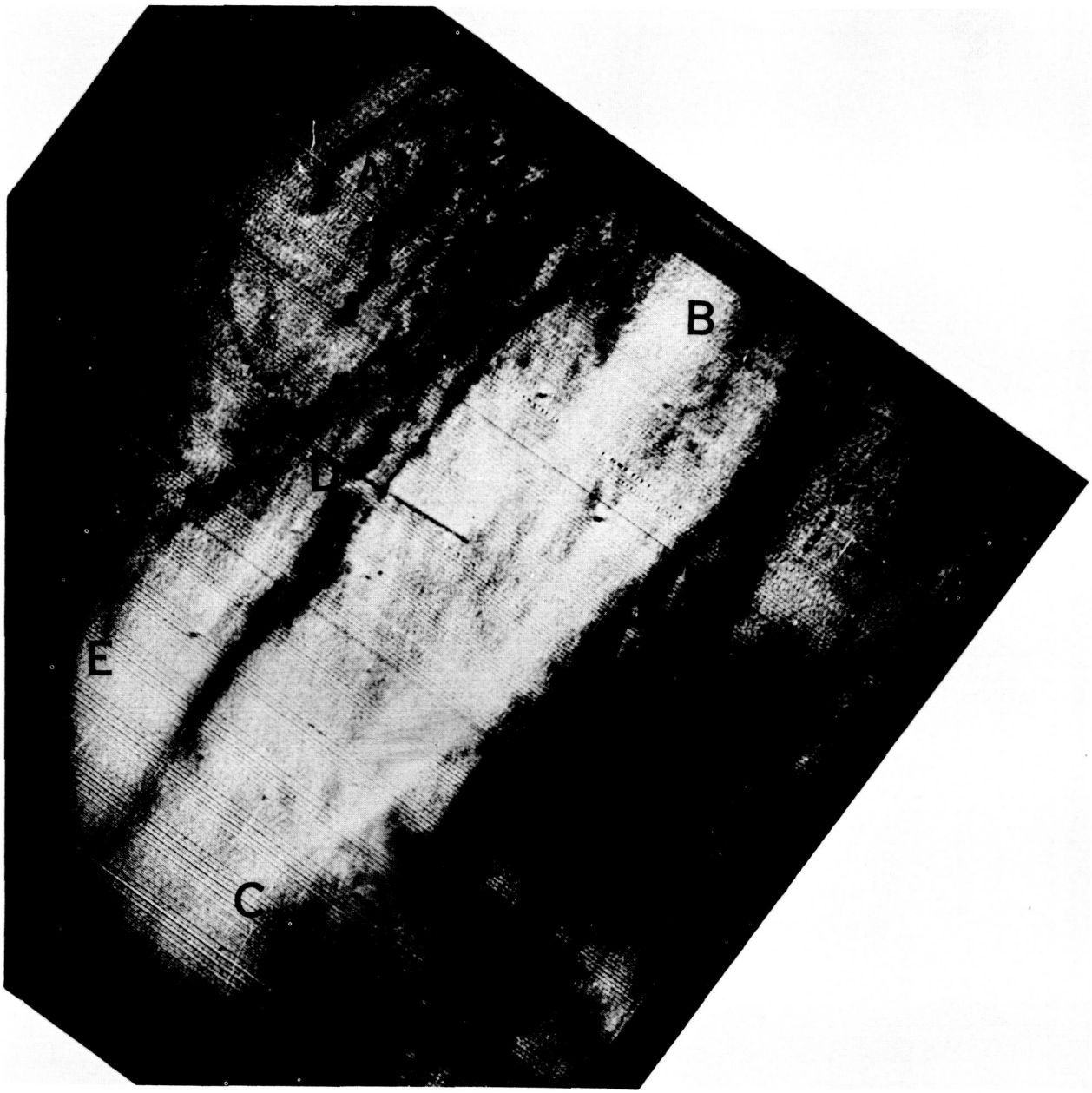

FIGURE 129.—Picture of the cloudiness south and southeast of the Gulf of Alaska cyclone showing zone of frontal clouds (BC), the cloud system associated with a new wave on the polar front (DE), and clouds around the vortex center (A).

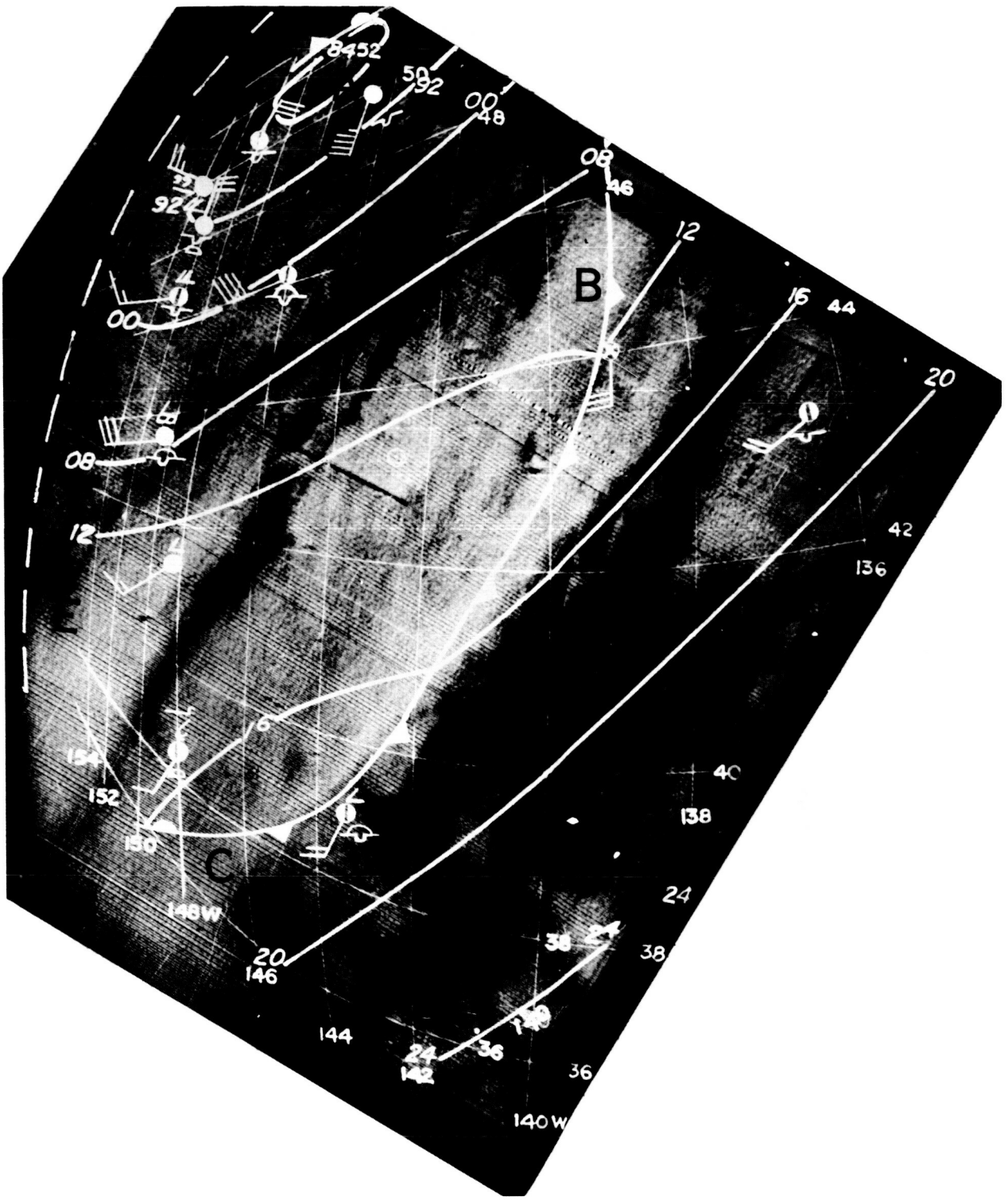

FIGURE 130.—Same picture as in Figure 129 with grid and other items as in Figure 124 except that the isobaric interval is 8 mb for pressures below 1008 mb.

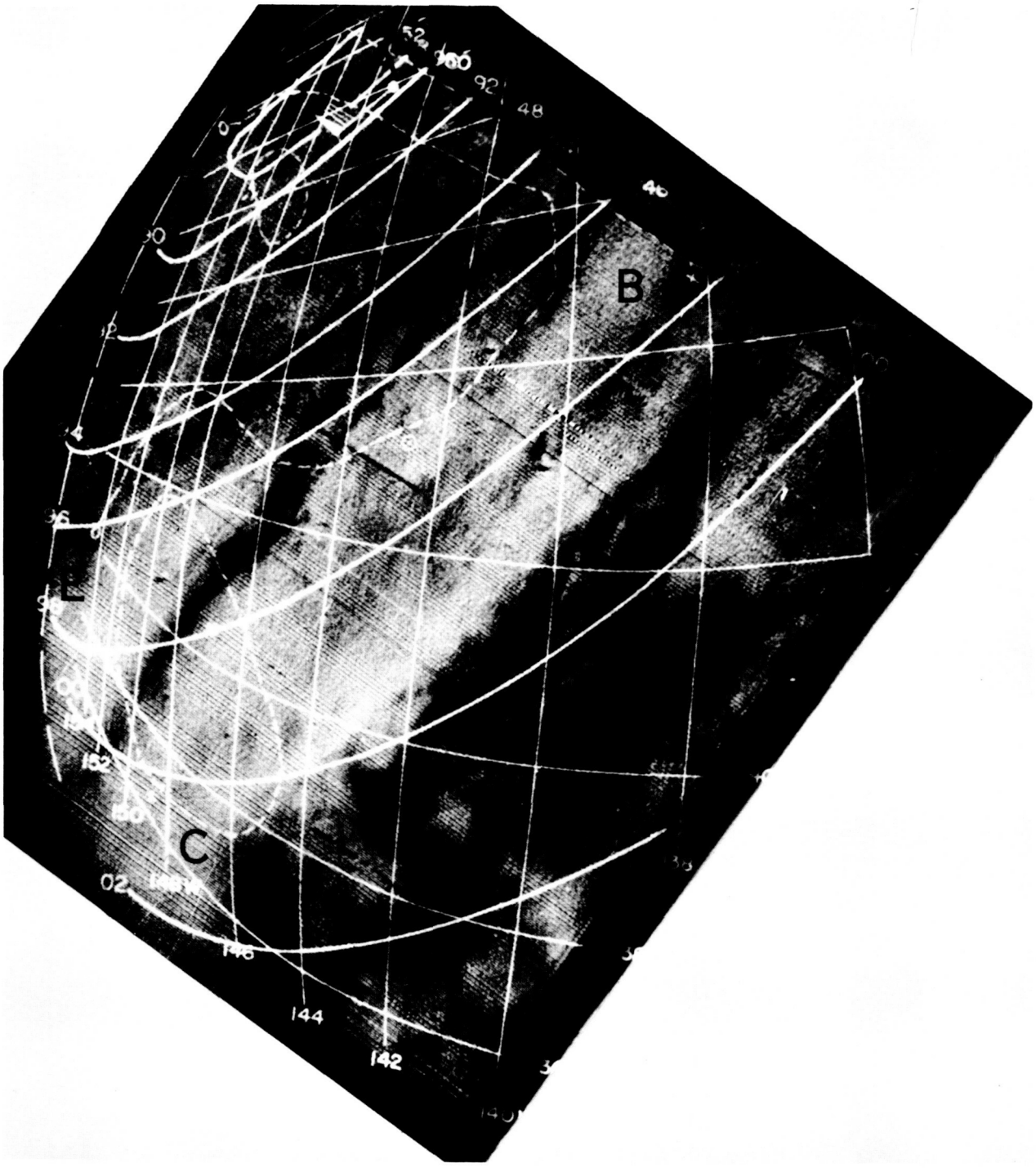

FIGURE 131.—Same picture as in Figure 129 with grid and other items as in Figure 125 except that 700-mb wind at ship P is plotted on this picture.

mb for 0000 GMT, April 2 (Figure 133), where double jet axes are portrayed in the NAWAC analysis. The more southerly of these jets is actually located beyond the northwestern edge of cloud zone BC, but it is not inconsistent with the displacement of up to 5° latitude found between the surface front and the jet stream in typical cases.[2, 3] However, in this case, credence in the precise jet locations can at best be very limited in view of the paucity of upper-air data in this region. (The only report across the entire broad, southwesterly stream is at Ship P, which is on the left edge of the current.) In other words, there may be only one jet axis (or there could even be more than two) and the location(s) in the southwesterly current may be different. If it were known precisely how the jet axis is located relative to the frontal cloudiness, the gridded TIROS I pictures (Figures 130 or 131) would readily fix the position of the jet stream. For example, if Conover's suggestion [4] that the jet axis is located along the northern edge of the frontal cloud shield were accepted, the jet axis would be found at the left edge of zone BC in Figures 129–131.

The other stratiform cloud zone mentioned earlier (DE in Figures 126 and 129) seems to be almost entirely separated from zone BC by a narrow, cloudless channel. The northern fringes of this cloudiness seem to consist of streamers which get progressively thinner toward the north. This suggests the leading edge of a cirrostratus or altostratus overcast (note the ship in Figure 127 which reports an altostratus overcast) which is very likely associated with the wave on the polar front located at about 34° N, 160° W, on the sea-level chart (Figure 121). Subsequent sea-level maps (not shown here) show that this wave moved northeastward and deepened into another major cyclone in the following 24 hours. The more southerly jet axis analyzed in Figure 133 is located very close to the middle of zone DE.

The vertical motion field (Figures 128 and 131) shows upward motion over most of the area occupied by bands BC and DE with a center of maximum upward motion near 39° N, 147° W. Of course, this crude agreement between the vertical motion and these broad cloud areas should be quite satisfactory in view of the data which were available to the JNWP Unit. However, the nature of these cloud areas as seen in the pictures suggests

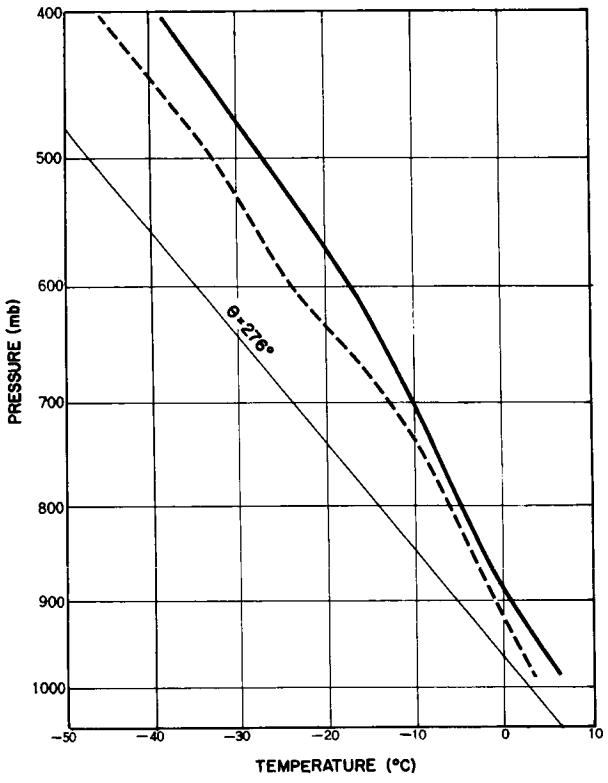

FIGURE 132.—Sounding at Ship P (50° N. 145° W), 0000 GMT, April 2, 1960. The solid line shows temperature distribution; the dashed line, dewpoint distribution.

that the vertical motion field more likely has two axes of maximum upward motion: one in zone DE, where the cloudiness of the incipient wave is spreading northeastward; and the other in zone BC where the cloudiness along the cold front is so extensive. It would be of interest to determine how much improvement could be attained in baroclinic numerical prediction of this situation if the initial vertical motion-divergence fields were altered in this direction.

SECONDARY VORTEX

To the northwest of the main cyclonic vortex is a hook-like cloud (G) which appears to be mainly of a solid, stratiform character (Figures 123 and 126). The shape of this hook-like cloud and the adjacent clear area, as well as the synoptic situation, would permit the deduction that this is a midtropospheric remnant of the circulation around an old cyclonic vortex. Figures 124 and 125 show rather simple northerly or northwesterly flow at both the surface and 700 mb near G. However, the surface data are quite sparse and the

upper-air data nonexistent in this area; thus a center of cyclonic vorticity might still exist near G, at least at the 700-mb level. This could mean that the maximum cyclonic curvature of the 700-mb contours shown at about 1° to 2° latitude southeast of the apparent center of the cloud vortex (Figure 125) actually belongs farther northwest. Inspection of both 500- and 700-mb charts for 24 hours earlier (not shown) indicates that a weak cyclonic vortex existed over the eastern Aleutians, just to the southwest of the Alaskan Peninsula. It is very likely that the cyclonic cloud pattern at G in Figure 123 does mark the remains of this upper-level vortex which is now drifting southward to the rear of the more vigorous cyclone in the Gulf of Alaska. TIROS I

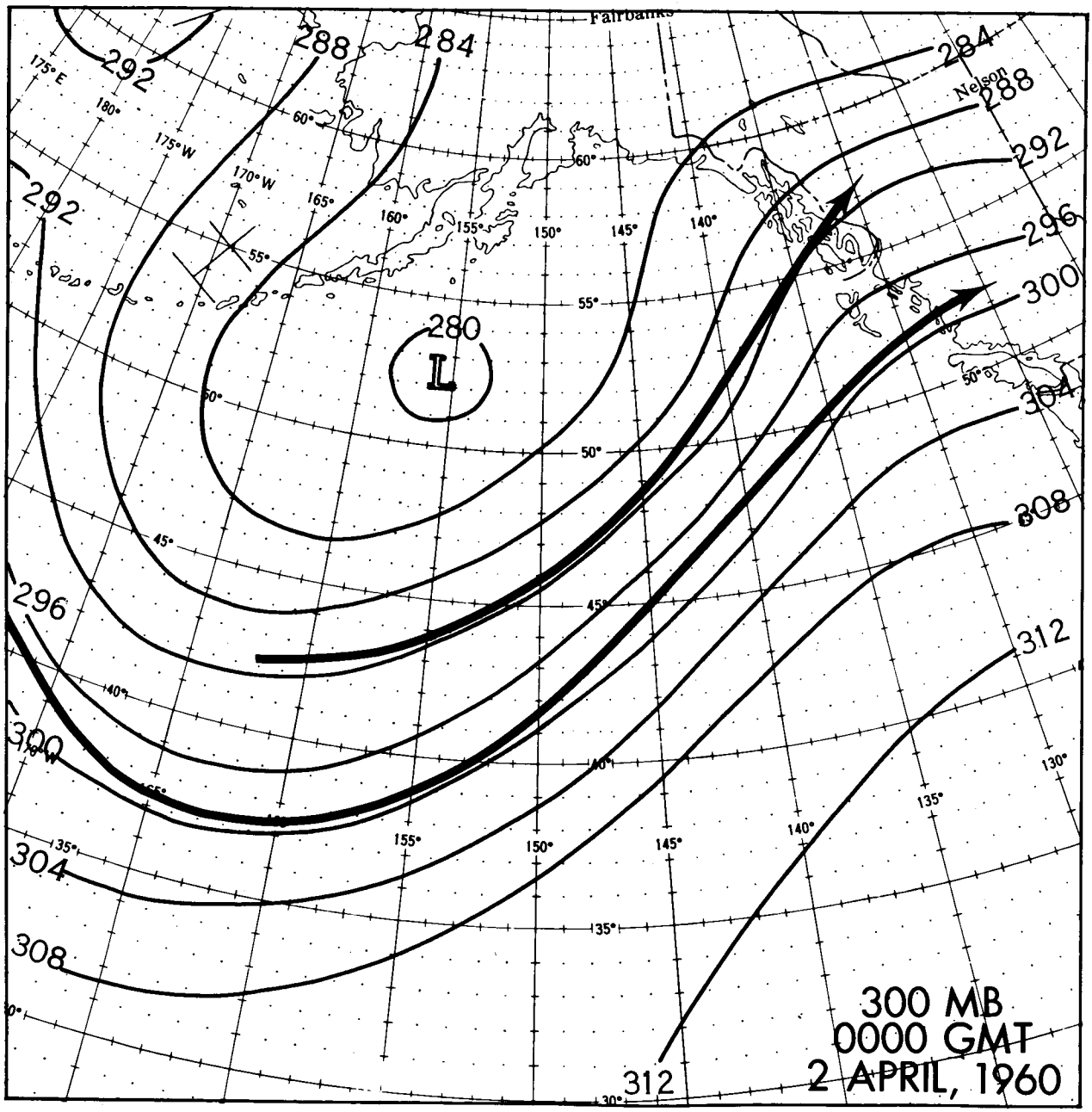

FIGURE 133.—300-mb contours and jet axes (heavy lines) as analyzed by the National Weather Analysis Center for 0000 GMT, April 2, 1960.

pictures in this area on successive days could have provided valuable information in tracing this interesting cloud formation.

It should be noted incidentally that a tongue of positive vertical velocity (Figure 125) seems to extend from the north in rough coincidence with this vortex cloudiness, which probably means that some elements of this vortex circulation were inherent in the midtropospheric analyses at this time.

CELLULAR CLOUDINESS

Much of the region on the western and southwestern side of the Gulf of Alaska cyclone is seen to be occupied by scattered to broken cumuliform cloudiness (area F in Figures 123 and 126). This cloudiness generally has a definite cellular character and is of the type discussed in more detail in Chapter 15. The cloud elements are considerably larger on the right side of Figure 123 which means that they are much larger cumulus clouds and/or represent the spreading of the tops of the cumulus clouds into stratiform, middle, or low clouds.

The sea-level and 700-mb flow patterns in Figures 124–125 and 127–128 show that these clouds are found in the northwesterly and westerly flow beyond the inner core of the cyclone. The vertical motion is generally downward through most of this area, which is probably consistent with the type of cloudiness (presumably of the low-level instability type) observed here.

SUMMARY

The preceding discussion has clearly illustrated how satellite cloud pictures can serve as an invaluable analytical tool in regions where conventional meteorological data are sparse. Details of the cloud structure of the occluded cyclone and its periphery, which could never be determined from the available standard observations, have been clearly revealed in the TIROS I pictures. In particular, the following features have been documented: (1) cyclonically-curved streaks in the dense cloudiness around the inner core of the cyclone; these parallel the surface isobars, (2) a "moat" of clear air spiraling into the center of the cyclone from the northeast, (3) the location and extent of broad bands of stratiform cloudiness associated with the main polar front, (4) the pattern of overrunning cloudiness associated with a nascent wave cyclone, (5) the previously undetected presence of an old cyclonic vortex in the middle troposphere, and (6) the striking cellular arrangement of cumuliform cloudiness in the cyclonic flow to the rear of the storm.

The clearcut orientations and arrangements of the cloudiness tend to corroborate the conventional map analyses and computed vertical motions in many places; this is encouraging for the future interpretation of satellite pictures in areas with even sparser data coverage than the Gulf of Alaska. The cloud pictures suggest that some improvements could be made in these analyses and vertical velocity fields; this emphasizes the complimentary role that satellite pictures can play relative to the more conventional data previously available.

REFERENCES

1. Panofsky, H. A., and Dickey, W. W., "Vertical Motion and Changes of Cloudiness," Bull. Amer. Meteorol. Soc. 27(6): 312–313, June 1946.
2. Riehl, H., Alaka, M. A., Jordan, C. L., and Renard, R. J., "The Jet Stream," Meteorol. Monographs 2(7), August 1954.
3. Vederman, J., "The Life Cycles of Jet Streams and Extratropical Cyclones," Bull. Amer. Meteorol. Soc. 35(6): 239–244, June 1954.
4. Conover, J. H., "Cloud Patterns and Related Air Motions Derived by Photograph," Blue Hill Meteorological Observatory, Massachusetts, Air Force Cambridge Research Center TR–59–246, June 1959.

CHAPTER 12

THE MIDWEST STORM OF APRIL 1, 1960*

by

CHARLES L. BRISTOR and MARY ANN RUZECKI

INTRODUCTION

The Midwest storm of April 1, 1960, developed as a lee disturbance to the east of the Rockies in conjunction with an intrusion of polar maritime air from the west. On its 4th and 5th orbits, TIROS I photographed this storm.

One hundred photographs were taken by the TIROS I wide-angle and narrow-angle cameras during these two orbits. Fortunately, some of these pictures provided an excellent view of the entire storm area. Two composite sketches (Figures 134 and 135) were created from eight photographs to provide a schematic representation of cloud brightness and coverage. The location of the cloud areas was determined by gridding these eight photographs by the methods of Appendix A. Although individual cellular patterns and filament structures are indicated, there has been no attempt to obtain cell-for-cell accuracy. The composite sketch or mosaic on a standard map base is broken into two segments because of the mismatch arising from movement of cloud features during the 100 minutes between the 4th and 5th orbits; the first segment (Figure 134) shows the northern portion of the storm, and the second (Figure 135) the southern portion. The mosaics have been divided into Roman-numbered regions to facilitate the discussion, for it will be convenient to indicate the subregions of the sketches by number.

Figure 136 shows the composite sketches of Figures 134 and 135 superimposed on the sea-level chart for 2100 GMT, April 1, 1960. The radar and sferics reports are also superimposed on this chart. The locations of the individual cloud photographs in this discussion are shown by letter on this chart; capital letters indicate the location of the satellite when the photograph was taken and lowercase letters indicate the optical center of the photograph.

TIROS I CLOUD PHOTOGRAPHS

The wide-angle photographs of Figures 137, 139, and 141 were taken on the 4th orbit about 1843 GMT, April 1, 1960, looking northwestward over the upper Great Plains and the Great Lakes region; the narrow-angle photographs in Figures 138 and 142 show details of Figures 137 and 141, respectively. The locations of the wide-angle photographs were determined by superimposing a computer-produced perspective geographic grid on the photograph. The precision of the gridding procedure and the various difficulties encountered are discussed in Appendix A.

The wide-angle photographs of Figures 143, 144, and 146 were taken on the 5th orbit about 2028 GMT, April 1, 1960, looking back along the orbit as the satellite moved southeastward off the Louisiana coast.

The following comments are designed to point out the main features in the individual photographs and to relate them to the composites in Figures 134 and 135. Also, somewhat in the manner of a cloud atlas, an effort is made to identify the types of clouds being viewed without discussing the weather situation completely. This identification is, however, dependent upon corroborating evidence obtained from the standard meteorological observations of clouds and weather, both from the ground and from airplane reports. The relation of the cloud pictures to circulation patterns and other meteorological mechanisms is discussed later.

Figure 137 is predominantly a view of the extension of the dense overcast area over Kansas

*A revised version of this paper appears as "TIROS Photographs of the Midwest Storm of April 1, 1960," in Monthly Weather Rev. 88(9–12): 315–326, September-December 1960.

In NASA Goddard Space Flight Center Tiros I Meteorol. Satellite System 1962 p 167-181 167
Submitted for Publication (See N64-17906 10-21) GPO: $2.25

AS

and Nebraska (as seen in Figures 143, 144, and 146.) Most of the part shown here, covering the Dakotas, appears equally dense and uniform. These are multilayered, precipitation-bearing clouds. A narrow-angle picture,* viewing the center of the lower half of this frame gives only a faint suggestion of a cellular pattern. Figure 138 is a detailed narrow-angle camera view of the west flank of this large overcast at the point marked on Figure 137. The bright cloud in the lower left evidently contains rows of cumuliform clouds. There also appear to be streaks of thin clouds parallel to the edge of the large overcast. The cloud pattern to the left in Figure 137 is located over Wyoming with the streaks oriented roughly north-south. Some thin cirrus clouds exist here but the brighter portions are rows of towering cumulus clouds in a relatively dry environment. The hook-shaped cloud near the horizon (top, center) extends into Canada beyond Edmonton, Alberta. The clouds near its west edge are cirrus with small cumulus beneath. At the base of the hook-shaped cloud and to the right of the dark spot, low stratus and stratocumulus and drizzle prevail, perhaps with some upper cloud cover. Farther to the right, cirrus and altocumulus clouds are thinner and there are no low clouds. The somewhat square, bright patch farther to the right is apparently a view of the northern portion of Lake Winnipeg with a covering of snow and ice, since only broken upper clouds are reported in that area.

*Unfortunately, strong electronic interference contaminated this photo, making the quality of reproduction marginal.

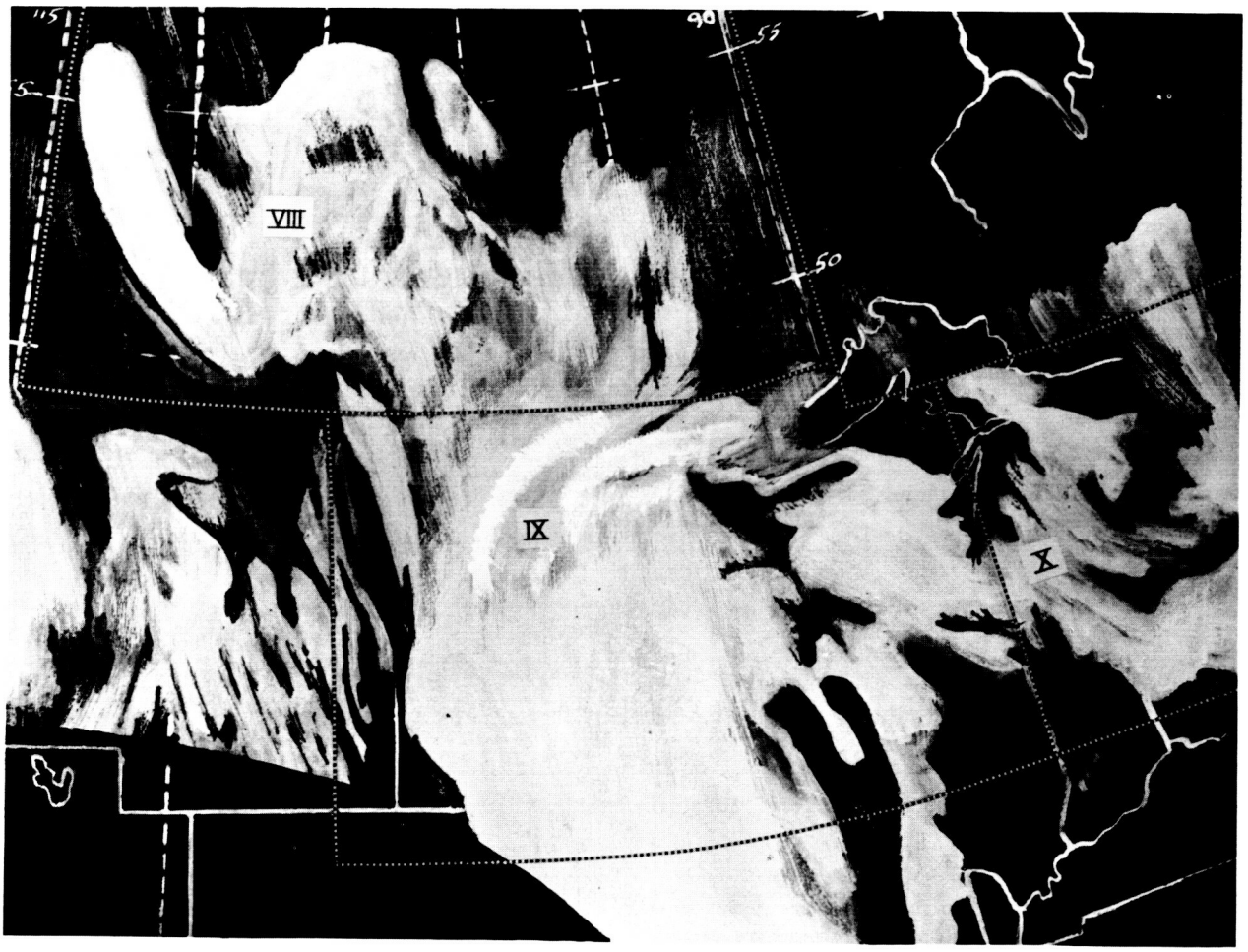

FIGURE 134.—Composite sketch of the cloud area of the April 1, 1960, Midwest U.S. storm. This mosaic was created from wide-angle photographs taken by TIROS I at 1843 GMT, April 1, 1960, and shows the northern part of the storm. The complete cloud pattern is shown on the sea-level chart of Figure 136.

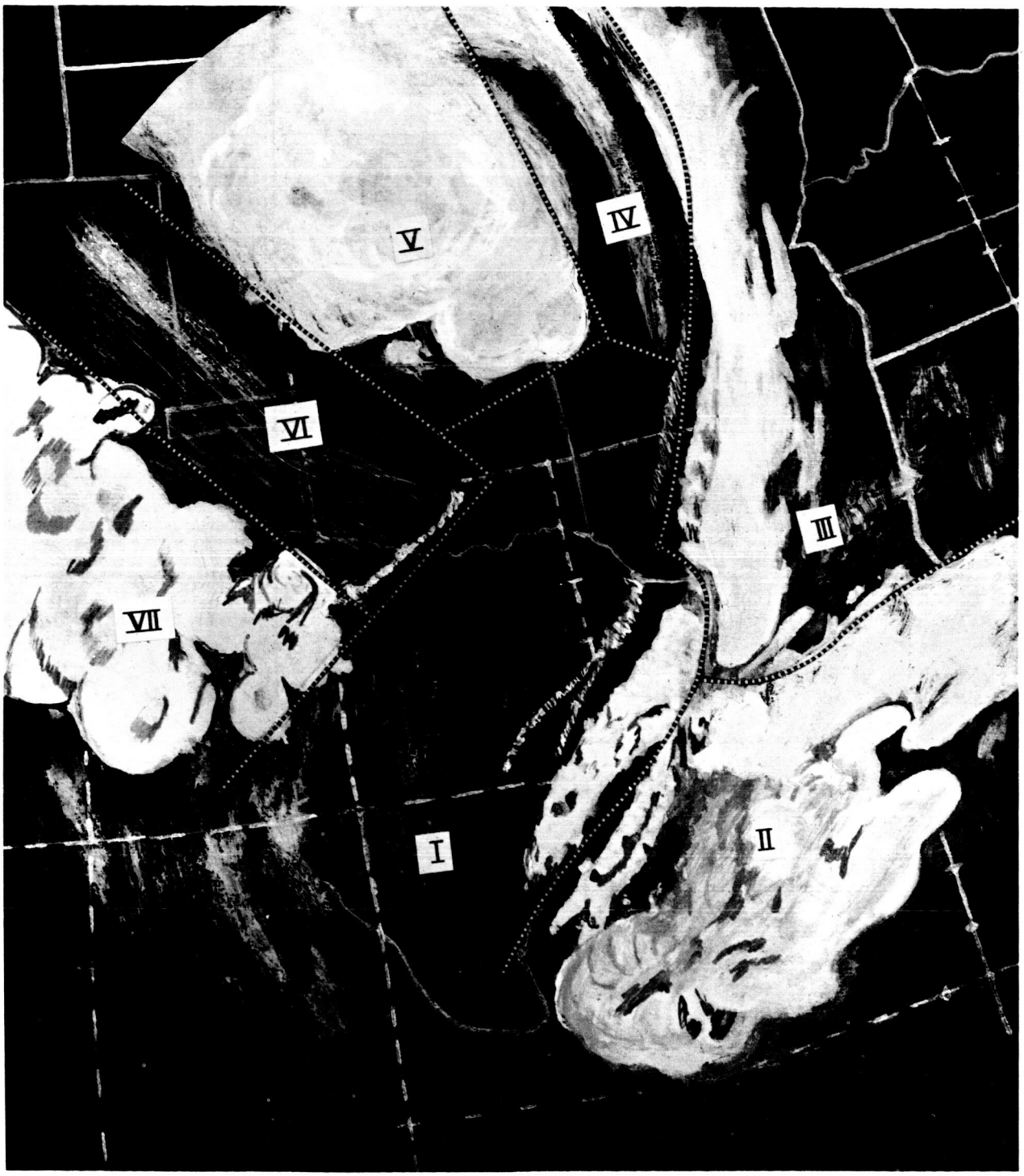

FIGURE 135.—Composite sketch of the cloud area of the April 1, 1960, Midwest U.S. storm. This mosaic was created from wide-angle photographs taken by TIROS I at 2028 GMT, April 1, 1960, and shows the southern part of the storm. The complete cloud pattern is shown on the sea-level chart of Figure 136.

646-770 O—64——12

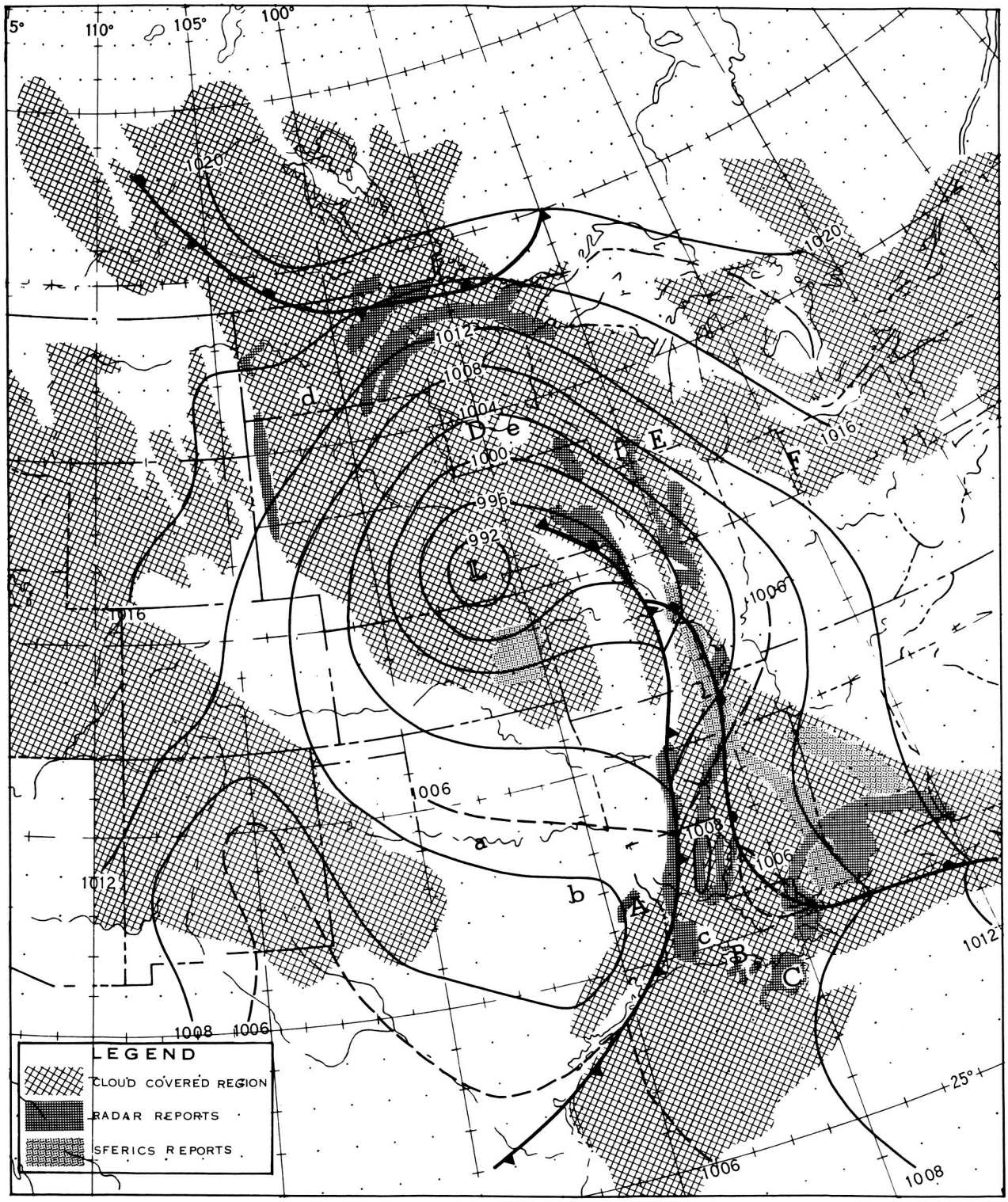

FIGURE 136.—Sea-level chart, 2100 GMT, April 1, 1960, showing the Midwest U.S. storm. The outline of the cloud area shown in Figures 134 and 135 is superimposed. Radar and sferics reports are also shown. The location of the satellite when it photographed Figures 137 through 146 are indicated by capital letters, and the optical centers of the photographs are indicated by the lowercase letters.

Figure 139, taken 1 minute after Figure 137, reveals much detail to the east and northeast of the large overcast region. The slightly brighter parallel cloud bands which appear as arcs to the upper right of the picture center (indicated by thin arrows) are of particular interest. In this area over northern Minnesota, radar echoes (Figure 136) form a remarkably similar pattern of concentric arcs. (An independent diagnosis of this banded structure from the photographs alone would likely be rather difficult because of the lack of contrast in the images.) The bright cloud mass to the lower left extends over eastern Iowa. This is the northern portion of the thundershower structure in the discussion of Figure 144. The partly cloudy darker region from the lower left corner of the frame is the extension of the cloudless wedge also shown in Figure 144. Here, however, much greater detail is available in what appeared 100 minutes later (Figure 144) to be a single cloud band pointing southward into the clear area. In Figure 139, at least two streets of bright shower cloud masses are apparent in this region, along with other isolated groups of cells.

Figure 141, taken 1 minute after Figure 139, contains a gray region to the left of center which is also visible slightly to the right of the center of Figure 139. Figure 142 is a narrow-angle camera view of a portion of the region indicated on Figure 141 and located near La Crosse, Wisconsin. In this narrow-angle photo a few large cumulus clouds appear in the upper left, with multilayer frontal precipitation cloudiness commencing in the lower left. Stratocumulus in various banded arrays appear toward the top and right of the central partly cloudy area. Figure 141 also presents a clear area in the lower right corner which is located along the Ohio Valley. The bright band extending to the right is a mass of low stratus extending eastward along the lower Great Lakes. A cirrus veil covers the stratus and extends northward. No middle cloud exists in this area as indicated by the radiosonde reports.

In the right foreground of Figure 143 (see also Figure 134) is a predominantly clear region extending from east Texas into Missouri. The textured edge of a dense overcast region is visible at the top of the frame over Kansas. The cloud mass to the left has a marked cellular structure

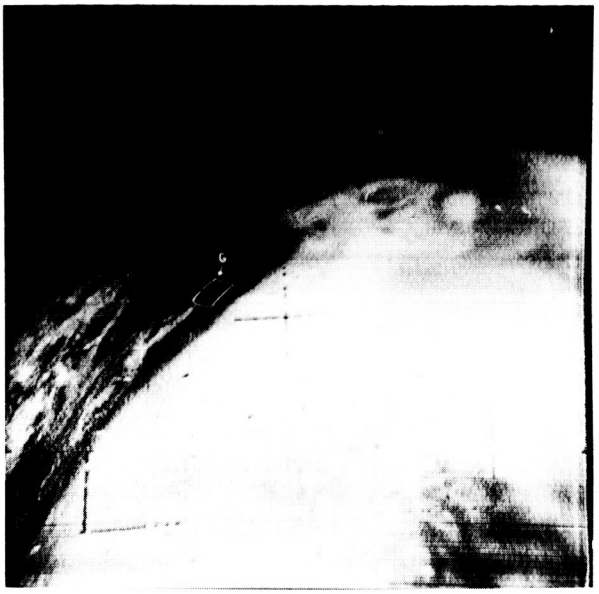

FIGURE 137.—Wide-angle photograph taken at point D of Figure 136.

throughout, with a suggestion of thin upper clouds. The leading clump of cells is near Lubbock, Texas. The main portion of this cloud mass extends over most of New Mexico and northwestward. A filmy veil of clouds appears to emanate from the upper left of the photo (near Denver, Colorado) and terminates in a brighter

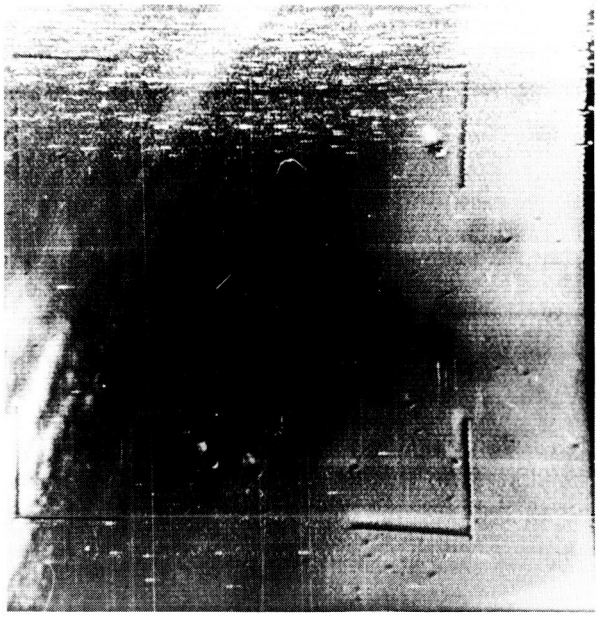

FIGURE 138.—Narrow-angle photograph of area G indicated on Figure 137.

FIGURE 139.—Wide-angle photograph taken at point E of Figure 136.

streak near the center (intersecting the southern Oklahoma border).

Figure 144 was taken 1 minute after Figure 143. The west Texas cloud now appears much foreshortened near the top of the picture. More of the solid overcast region is now visible in the upper right. The overcast extends over much of Nebraska as indicated by the accompanying geographic overlay.

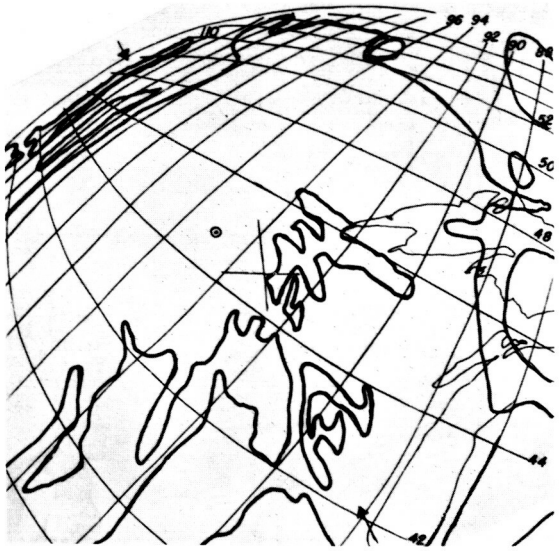

FIGURE 140.—Computer-produced perspective geographic grid overlay for Figure 139.

FIGURE 141.—Wide-angle photograph taken at point F of Figure 136.

A wealth of new detail appears in the foreground. Faint patches of stratocumulus are lined up horizontally along the lower boundary of the clear area. These wisps continue to the right into a brighter wedge of cloud containing cumulonimbus and upper cloud at its junction with the overcast region in the upper right portion of the photo. The features described above are located

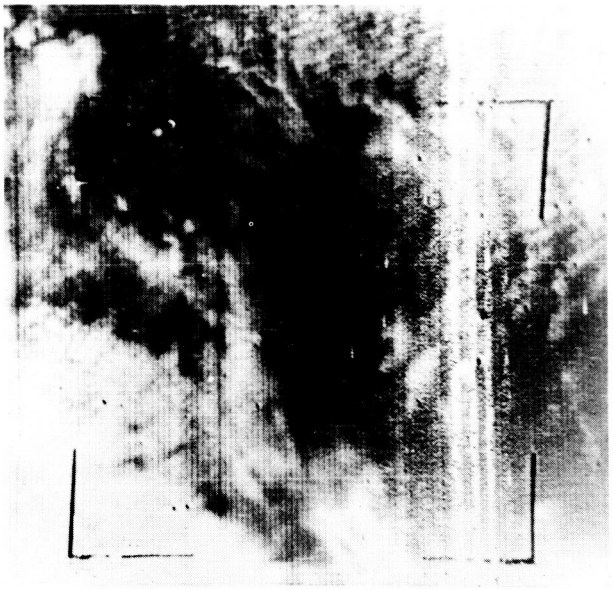

FIGURE 142.—Narrow-angle photograph of area H indicated in Figure 141.

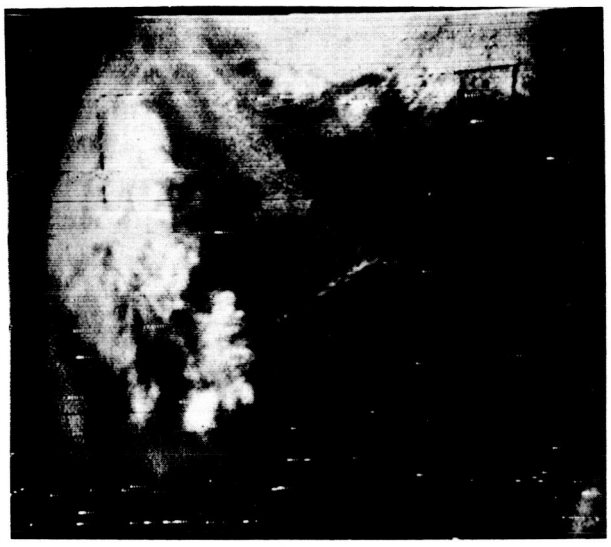

FIGURE 143.—Wide-angle photograph taken at point A of Figure 136.

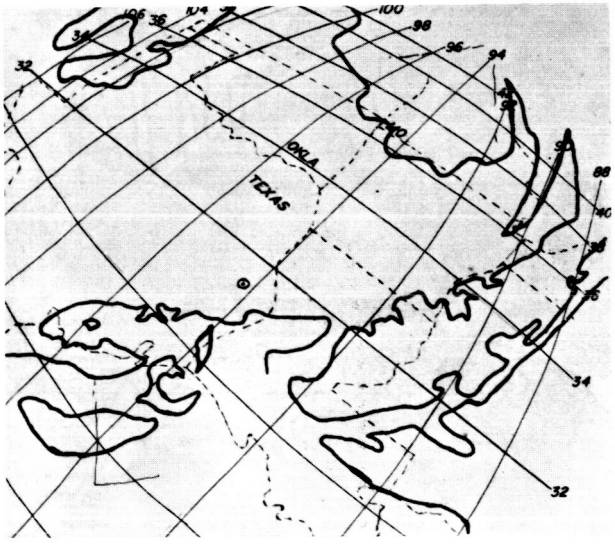

FIGURE 145.—Computer-produced perspective geographic grid for Figure 144.

in the mosaic of Figure 134 along a line through central Arkansas and northward into Iowa. Much brighter clouds of great variety extend across the photo in a broad belt immediately below and paralleling the features just described. Widespread shower activity with cumulus and cumulonimbus clusters, together with middle and high clouds, occupy the band from the upper right down to the bright "finger" in the lower central foreground of the picture. A cloud system, with parts almost as bright, extends on to the left. The brighter portion of this left branch near the center of the photograph is a region of cold frontal shower activity. Two sizeable clear patches appear as black spots farther to the left in a post-cold-frontal region of waning shower activity. The larger, relatively clear, horizontal areas below this cloud region are located over the Gulf of Mexico near the northern portion of the Texas coast.

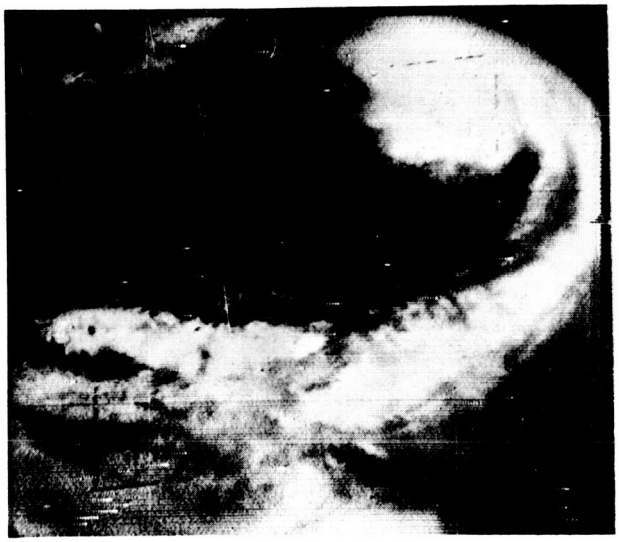

FIGURE 144.—Wide-angle photograph taken at point B of Figure 136.

FIGURE 146.—Wide-angle photograph taken at point C of Figure 136.

Figure 146 was taken 30 seconds after and largely overlaps Figure 144. The important extension of the viewed area is in the foreground. The bright region at the lower edge of Figure 144 is now located near the center of the picture (Figure 146) with a broad, very bright band extending to the lower right. This band, extending from New Orleans eastward along the Gulf coast consists of an almost solid mass of cumulonimbus activity with extensive middle and upper cirriform overcast. The gray area to the lower left extending off the Louisiana coast contains patchy lower clouds with little or no upper cloud cover. The darker region in the lower right, covering parts of central and northern Mississippi and Alabama represents mostly high, broken cloudiness with a few patches of lower, cumulus shower activity.

CLOUD FEATURES AND THE SYNOPTIC WEATHER SITUATION

The foregoing discussion permits geographic location of the various cloud features seen in the

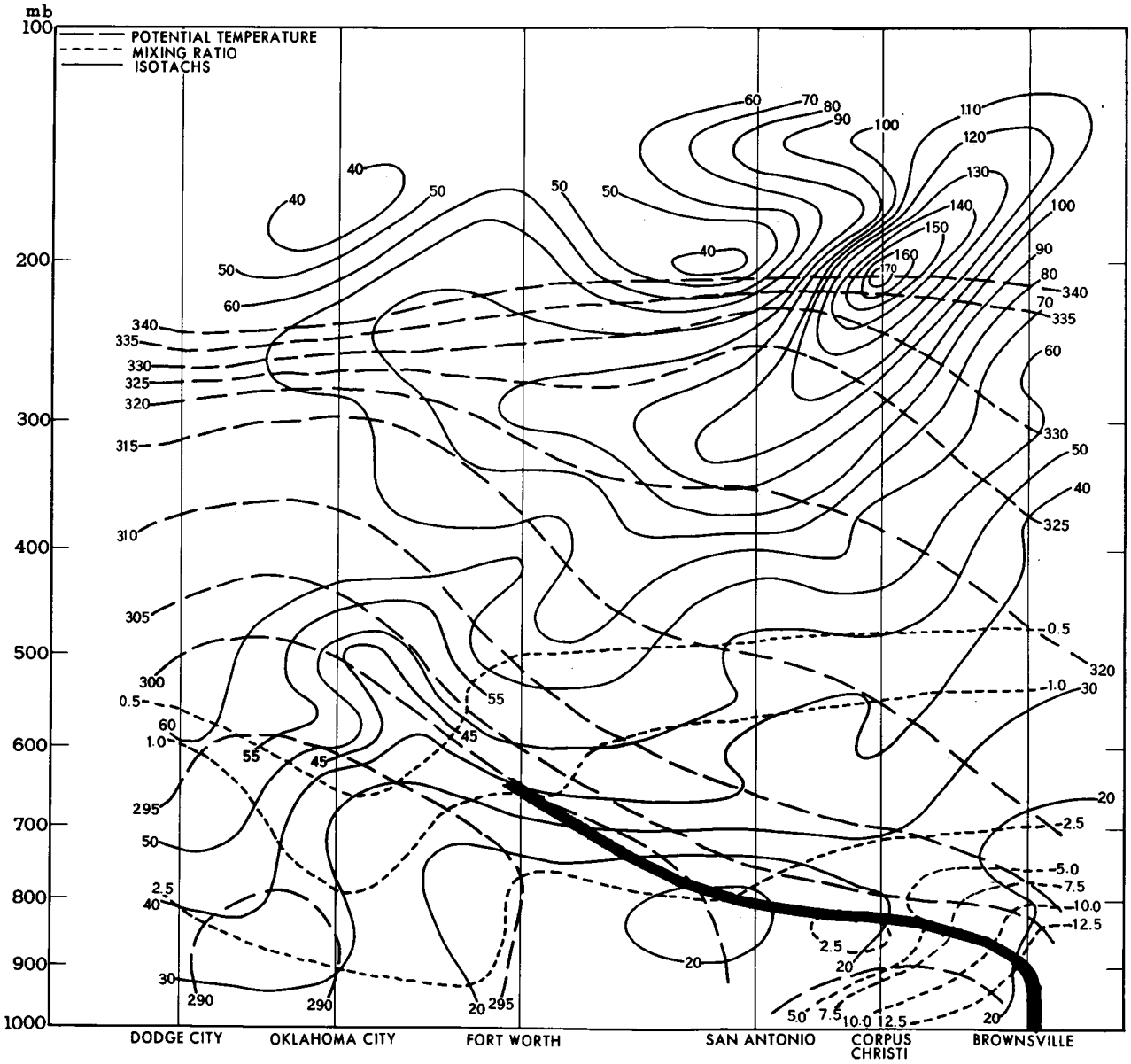

FIGURE 147.—North-south vertical cross-section (isotachs in 10-knot intervals) for 0000 GMT, April 2, 1960. Dashed lines are potential temperatures, dotted lines are mixing ratios, and solid lines are isotachs.

photographs. The two composite cloud representations in Figures 134 and 135 are now to be related to the storm structure.

Region I (Figure 135) is the post-cold-frontal sector of the storm. Considering the fact that the pictures were taken near midafternoon local time, it may seem remarkable that this region is so free of even convective-type clouds. The air was extremely dry, however, as indicated by surface reports (e.g., Fort Worth, Texas, reported a temperature of 72° F and dew point of 28° F). Immediately to the rear of the front along the Texas coast a broad band of clouds, which appears brightest to the northeast and also has some small, distinct clear spots embedded in it. Reports from stations along the Texas coast show that this post-frontal cloud band consists of towering cumulus and stratocumulus types. Reports of any major shower activity in this area, either from surface reports, radar, or sferics were lacking, however. These clouds were very likely entirely within the warm air above the cold front. Figures 147 and 148 show that the cold air was rather shallow for some distance behind the front, so that warm-air cloudiness could have had bases as low as about 5,000 feet. The deeper cold, dry air was not reached until farther west of the front. The faint patches of stratocumulus in Figure 144 may mark the leading edge of the deep cold air.

Region II (Figure 135) is very moist as indicated by the high condensation pressures on the isentropic surface displayed in Figure 149. Clusters of radar echoes shown in Figure 136 marked the frontal thunderstorms from Lake Charles, Louisiana northward toward Little Rock, Arkansas. Heavy clusters of radar echoes and sferics reports blanketed another large thunderstorm area which extended from New Orleans,

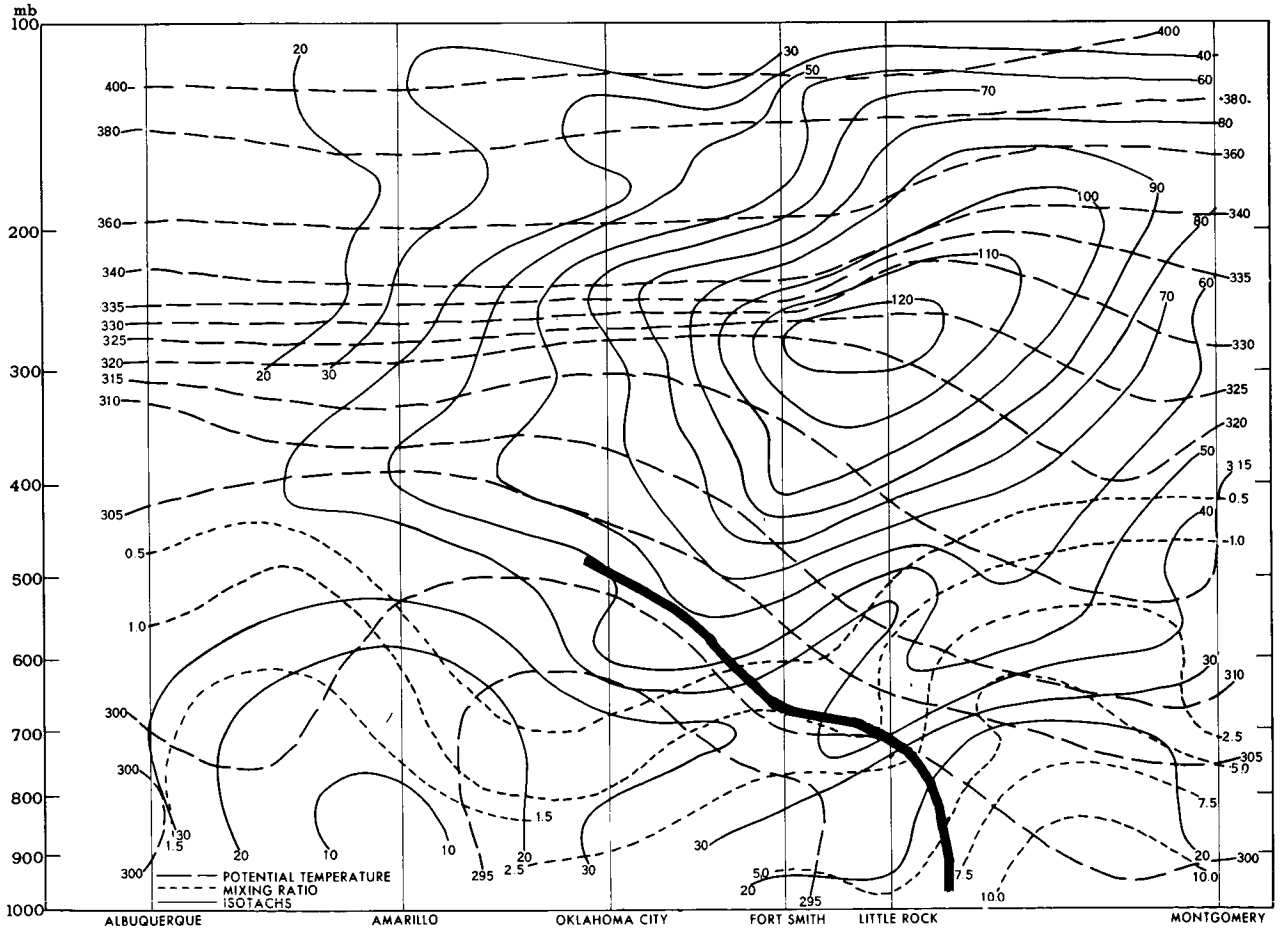

FIGURE 148.—East-west vertical cross-section isotachs in 10-knot intervals for 0000 GMT, April 2, 1960. Dashed lines are potential temperatures, dotted lines are mixing ratios, and solid lines are isotachs.

Louisiana, eastward in the warm-frontal zone along the Gulf coast. Upper-level charts indicated a branch of the jet stream extending from near the Mississippi River Delta toward central Florida. One might thus speculate that the marked contrast in cloudiness and precipitation, indicated in Figure 146 by the bright coastal cloud band and the reduced activity offshore (see also bottom and lower left in Figure 144), may reflect differences in the large-scale vertical motion pattern on either side of the jet axis. Aircraft reports indicated a cirrus overcast between 300 and 400 mb which extended over the thundershower area, but also ended at the Gulf coast.

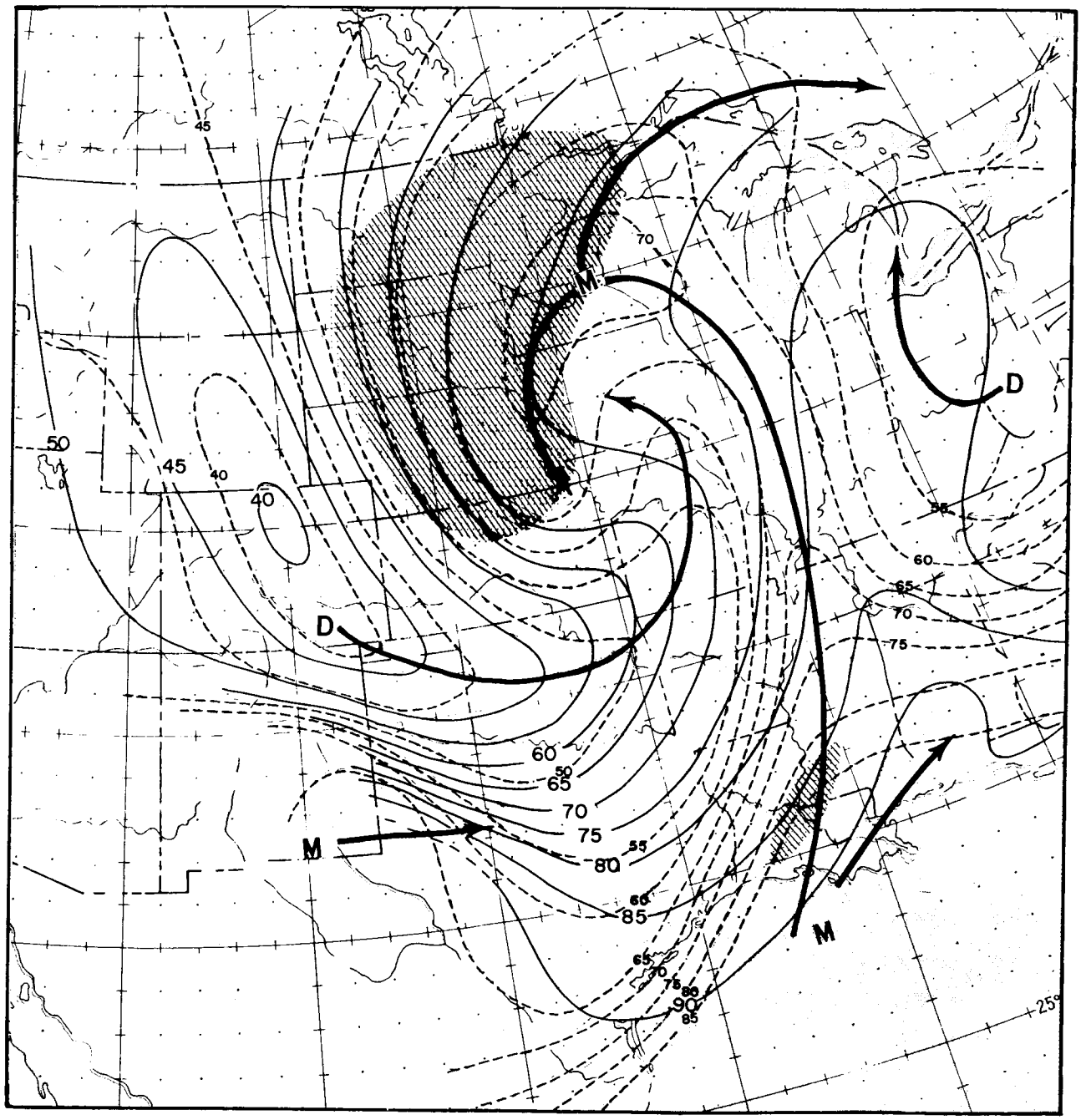

FIGURE 149.—Isotropic chart for 0000 GMT, April 2, 1960. Solid lines are 300° K pressure and dashed lines are condensation pressure.

Region III (Figure 135) includes the warm tongue shower activity which extends in a band northward along the Mississippi River to southeastern Iowa. Although surface reports did not generally indicate high humidity in this band, there was evidence of a well developed moist tongue on the isentropic chart (Figure 149). A line of sferics fixes extended through this band from Jackson, Mississippi, to St. Louis, Missouri. Clusters of radar echoes marked the bright "finger" of cloud in Figure 144 near the southern end of this band and similar echoes marked the equally bright cloud clusters in Figures 139 and 141 to the north.

Region IV (Figure 135) is an extension of the post-frontal and frontal region. Close inspection of Figure 144 suggests a veil of thin upper clouds covering the easternmost dark wedge. Radar and surface reports located thundershowers in the northern portion of the brighter central cloud area and southwesterly upper winds could have carried convectively produced upper clouds into the dark wedge. Surface reports required that the occluded front be placed near Des Moines, Iowa, at 2100 GMT in the central cloud area. Thus, the eastern dark wedge of reduced cloudiness is in the warmer air to the east of the cold front. This is in agreement with observations from stations such as St. Louis which reported partly cloudy skies in the southerly warm flow. To digress slightly, in Region IX (Figure 134), there are similar indications of the frontal position. Surface data at 1800 GMT suggest that the left-most bright appendage in the dark area in the lower left of Figure 139 is associated with the cold front over southwestern Iowa. Stations with partly cloudy skies were located well to the east of the front, but west of the bright shower band in the moist tongue.

Region V (Figure 135) is the southern portion of the area of upslope precipitation. The pattern of ascending, saturated air is indicated on the isentropic surface (Figure 149) by the southwestward curving branch of the moist tongue. Rain and snow had ended in the southeastern portion of this cloud mass and pressures were rising. The rather well defined edge of these clouds suggests the desiccating power of the descending motion pattern around its perimeter.

The thin cloud veil in Region VI (Figure 135) appears to have been generated by shower activity farther to the northwest. The sounding at Lander, Wyoming, indicated extremely unstable showery air up to approximately 16,000 feet. The northwesterly flow at such heights was apparently propagating high clouds from this showery source region southeastward across Oklahoma. Denver and Dodge City soundings indicate a cloud base near 620 mb. The thin texture of this cloud veil, as contrasted with the brighter streaks of cloud over Wyoming (Figure 137), suggests that these clouds may be poor indicators of upward vertical motion. They appear to be barely tolerated by the broad scale vertical motion pattern. The north-south cross section in Figure 147 suggests an explanation for the abrupt cloud streak which appears to terminate the thin cloud veil. (The cross section, Figure 147, is essentially normal to the midtropospheric flow as seen on the 500-mb chart, Figure 151.) Kuettner [1] has discussed observations of similar cloud streaks or bands in association with jet streams. Although the jet stream in this case was far removed from the cloud streak, there is evidence of considerable variation in horizontal wind shear oriented in the same direction as the cloud streak. Close examination of Figure 144 on the original film strip reveals not only the bright cloud lines but a faint resumption of cloud farther to the southeast. There is thus an impression that vertical motions in response to the streaks in the horizontal shear created an undular pattern in the cloud veil—augmenting the cloud in regions of ascending motion and subduing it where sinking motion occurs. The bright streak is located about midway between Oklahoma City and Fort Worth, near the zone of maximum cyclonic shear on the cross section.

In Region VII (Figure 135) the isentropic chart (Figure 149) suggests that a broad-scale ascending motion area existed in the middle troposphere, with air being lifted along the flank of the cold dome. In Figure 148, between Albuquerque and Amarillo, air with slightly higher moisture content is noticeable. Soundings in this sector had extreme instability in the lower layers. Dry adiabatic lapse rates extended upward beyond 700 mb at Albuquerque, New Mexico, and at Amarillo and Midland, Texas. The unstable air terminated at the tropopause near 400

mb. The cellular structure in Figure 143 thus appears to be made up of a cirrus veil above large cumulus groups.

Region VIII (Figure 134) contains a variety of cloud types. Unfortunately, the foreshortened view precludes any serious attempt to distinguish one type from another. The hook-shaped western boundary of the cloud is located in an air mass of Pacific origin where the previously mentioned cirrus and small cumulus clouds were reported. The sharpness of this west edge may reflect an orographic downslope motion to the east of the Canadian Rockies since westerly winds aloft were reported in the Edmonton-Calgary area. Farther east the quasi-stationary front shown in Figure 136 bounded a colder and much drier polar continental air mass. The stratiform clouds along the west limb of the front are probably covered by middle and upper clouds which extend eastward into the partly cloudy area over the colder air mass. No low clouds were reported in the dry polar air—the dull gray patches being thinner areas of middle and high clouds.

Region IX (Figure 134) has been discussed in connection with the overlapping regions to the south. The central portion of the widespread continuous rain and snow area is located in eastern South Dakota. The cloud and radar echo areas, mentioned in connection with Figure 139, appear to be near the perimeter of the frontal upslope activity in the isentropic pattern of Figure 149, and on the very fringe of the region of frontal precipitation as indicated by surface reports. Another isolated line of radar echoes is indicated in Figure 136 near Rapid City, South Dakota.

In contrast to the northern Minnesota cloud arcs which exist in a region having a marked frontal inversion, the sounding at Rapid City, South Dakota, revealed extreme instability in the lower layers. The north-south alignment of the echoes with the flow at lower levels over the western Dakotas suggests a band of convective activity induced from the ground rather than from frontal lifting. It is quite remarkable that all cloud activity ceases rather abruptly at the western edge of the large frontal cloud mass. A combination of factors seem to be involved since the edge appears to coincide at all cloud levels. Reversal of the midtropospheric vertical motion from ascending to descending at the cloud edge may have been the predominant factor. The filmy appearance of the edge of the cloud bands in Figure 138, coupled with the suggestion of downslope motion over the Canadian and Montana Rockies, suggests that lateral mixing of dry air may also have assisted the process of middle and upper cloud decay along this western edge. At lower levels, moist northeasterly trajectories, within the upslope cloud mass—in contrast with drier northwesterly trajectories farther west—may have favored such an abrupt edge within the convective layers.

Region X (Figure 134) presents the situation in the eastern portion of the storm's perimeter. The isentropic chart in Figure 149 indicates an eastward branching moist tongue with a lateral admixture of drier air from Kentucky and Tennessee. No middle clouds were indicated by the soundings, nor by the isentropic chart which intersected above a strong low-level inversion in this area. Presumably a pattern of overrunning motion farther aloft produced clouds, since aircraft reported cirrus in conformity with the filmy white clouds seen throughout the Central and Eastern Lakes region in Figure 141. Soundings at Dayton, Ohio; Flint, Michigan; and Pittsburgh, Pennsylvania, indicated a strong temperature inversion and moisture lapse at 3,000–5,000 feet. Reports of fog accompanying the low clouds in this strong inversion area suggest a rather solid layer of fog, stratus and stratocumulus from the ground up. Such density of low cloud may help to explain the very bright, solid appearance of the band as seen from above.

The foregoing discussion suggests several problems which will arise in using cloud photographs as an analytic tool. For example, the bright cloud band in Figure 141 might be considered a cloud system similar to that in the lower right portion of Figure 146. Careful photographic work and interspersed narrow-angle shots to indicate detail would probably suffice to isolate the cellular showery cloud system from the stratiform system. Certainly brightness alone does not appear to be a dependable indicator of cloud type.

Thin cirrus cloud veils may also present some uncertainties: slight ascending motion in the broad-scale sense might allow clouds such as those in Figure 143 to be transported far from their source region, which contains the marked ascending motion we may wish to identify.

Aspect is another problem in that foreshortened views are desirable in expressing a broad cloud pattern. Certainly Figure 144 is a remarkable photograph, suggesting the classical cloud structure of a cyclone. However, it should be pointed out that foreshortened portions tend, even with cellular texture, to assume a solid stratiform appearance; caution must be used in these areas. Sun glint and land-water undersurface contrasts are other factors which tend to confuse relative brightness of clouds.

The preceding discussion has indicated that, despite such problems, there is a correspondence between distinctive features of the cloud photos

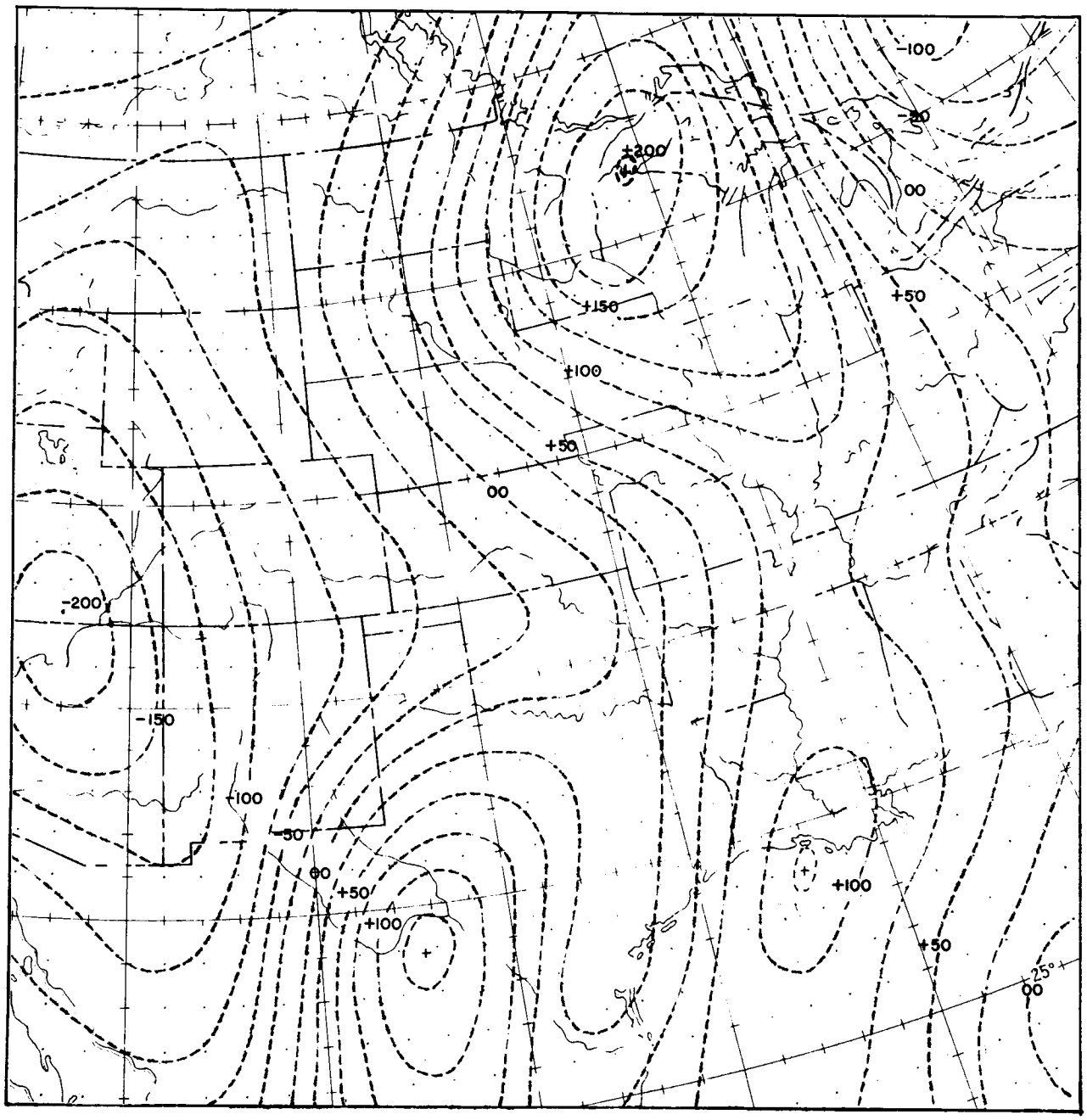

FIGURE 150.—Broad-scale 600-mb vertical motion in arbitrary units at 0000 GMT, April 2, 1960, about 5 hours after the photographs of Figures 137–146 were taken.

and a synoptic weather situation analyzed with standard observational material

CLOUD PHOTOGRAPHS AND OBJECTIVE MAP ANALYSIS

One of the main points in support of cloud observations from meteorological satellites has been their potential use in providing observations over sparse data regions of the earth, especially in oceanic areas. Apart from direct operational application as a warning of the existence of various severe large-scale weather phenomena, such data would also be expected to contribute to our ability to predict the motion and evolution of storms generally. This contribution might best be included

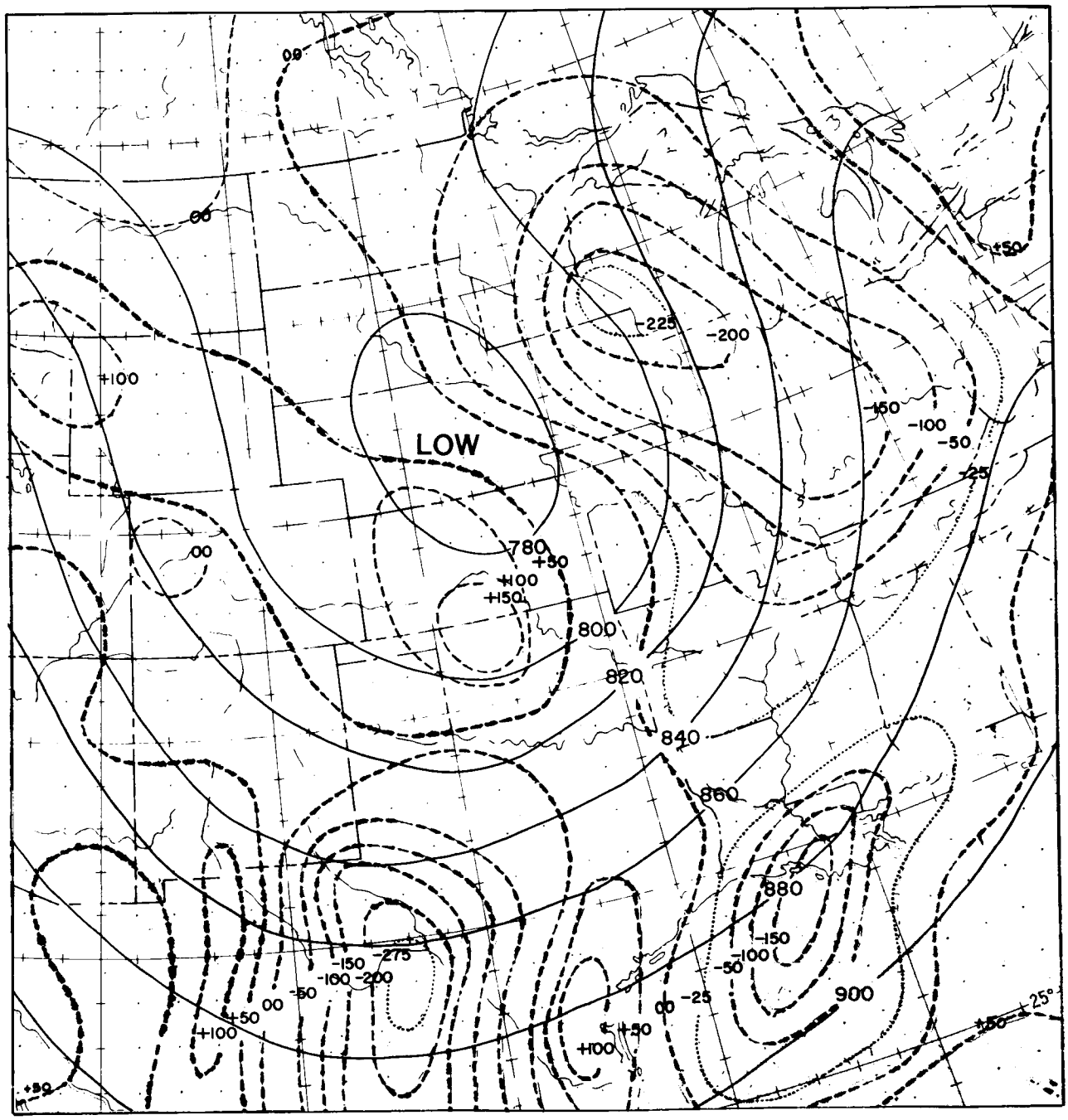

FIGURE 151.—500-mb chart for 0000 GMT, April 2, 1960. Solid lines are 500-mb contours; dashed lines are vorticity advection in arbitrary units.

in an objective fashion in the process of numerical weather prediction. Since modern numerical weather prediction is basically an initial value problem, such added forecast skill could be considered to be a reflection of the degree to which the new information from meteorological satellites can be used to better delineate the three-dimensional state of the atmosphere at a particular time selected as the starting point for a numerical prediction.

The brief discussion which follows is without results but is presented to indicate current efforts in this direction.

If one now admits cloud photographs such as those obtained from TIROS I as the new information in sparse data regions, a new question arises: how does one correct or refine first estimates of the wind field and the field of geopotential obtained from wind and pressure data—the common input information for numerical weather prediction—through the addition of cloud photos observations? The suggestion involves using the cloud photos as indications of broad-scale vertical motion patterns. Figure 150 is an expression of the broad-scale vertical motion at 600 mb over the Midwest about 5 hours after the TIROS I cloud photos of Figures 137 through 146. (The units are arbitrary with plus areas signifying ascending motion.) In general, there is good agreement between the vertical motion chart and the cloud analysis—the principal region of ascending motion corresponding to the frontal activity and moist tongue, with a secondary maximum of ascending motion near the Louisiana coast. The vertical motion patterns in turn are, of course, related to the horizontal fields of wind and geopotential through the divergence patterns specified by these fields. From a simple atmospheric model the divergence at 500 mbs may be approximated by the advection of vorticity at that level. Figure 151 presents the 500-mb chart with vorticity advection. With change of sign this pattern strongly resembles the vertical motion chart in Figure 150. The suggestion thus involves the adjustment of a preliminary analysis of the height of a midtropospheric pressure surface in regions of sparse data so that the pattern of vorticity advection is compatible with the midtropospheric broad scale cloud pattern as revealed by satellite cloud photos. Despite the empiricism involved in deriving divergence from cloud patterns, preliminary comparisons of degraded 500-mb analyses with original analyses over regions of good data are encouraging. Following the work of Cressman[2] and Sasaki,[3] efforts toward production of such a corrective anaylsis procedure by high speed computers are now underway.

CONCLUSION

In the present descriptive study, standard meteorological measurements over a dense data network have been compared to TIROS I cloud photographs for a particular synoptic situation. The utility of such a wealth of photographic information over a broad land expanse has been suggested by these comparisons. It appears likely that a series of such studies can generate semi-empirical relationships which would be of great assistance in making adjustments and corrections to the analysis of upper-air charts over sparse data areas. In a more quantitative vein, a method has been suggested whereby such cloud data could be used in a computer-produced objective map analysis.

ACKNOWLEDGMENTS

Special acknowledgment is given to the Geophysical Research Directorate, U.S. Air Force, and the Stanford Research Institute for their radar information concerning this storm, and also to Detachment 4, 4th Weather Group, U.S. Air Force, and the Severe Storm Center of the U.S. Weather Bureau at Kansas City, Kansas, for their radar and sferics data. Acknowledgment is extended to Detachment 19, 9th Weather Squadron of March Air Force Base and Detachment 11, 26th Weather Squadron, Barksdale Air Force Base, for their nephanalysis and other valuable charts which aided in the preparation of this discussion.

REFERENCES

1. Kuettner, J., "The Band Structure of the Atmosphere," Tellus 11(3): 267–294, August 1959.
2. Cressman, G. P., "An Operational Objective Analysis System," Monthly Weather Rev. 87(10): 367–374, October 1959.
3. Sasaki, Y., "An Objective Analysis Based on the Variational Method," J. Meteorol. Soc. Japan 36(3): 77–88, June 1958.

CHAPTER 13

A SUBTROPICAL CONVERGENCE BAND OF THE SOUTH PACIFIC*

by

LESTER F. HUBERT

INTRODUCTION

The origin, dynamics, and even description of tropical disturbances are incompletely known, but it is generally agreed by tropical meteorologists that lines and areas of convergence lying completely within a homogeneous air mass exist in the lower troposphere. Examples of such systems are the easterly waves studied by Riehl,[1] the equatorial waves described by Palmer,[2] and the intertropical convergence zone (ITC) which has received continued attention ever since polar front enthusiasts attempted to apply the air mass model at the equator.

In addition to the traveling disturbances in the tropics and subtropics, there exists a system variously identified as a convergence line, a shear line, or even a stationary front. Indeed, it is sometimes possible to trace back such a line of convergence to a true polar front from mid-latitudes. Of course, having traveled many days over a warm ocean it no longer represents an air mass boundary.[1] Despite complete frontolysis, a band of cloudiness and frequently an accompanying line of shear retain their identities for several days.

Such systems are significant, since it is clear that they are self-perpetuating long after the potential energy of the cool air mass has been dissipated, thereby posing the interesting question of the dynamics of their maintenance after the potential energy is consumed. Furthermore, since they often become quasi-stationary, these systems may remain undetected for long periods because they do not sweep across reporting stations as do the waves and vortices. For this reason, they have been incompletely described and largely neglected insofar as theoretical study is concerned. The study presented here considers such a quasi-stationary convergence line in the southwestern Pacific.

On May 11 and 12, 1960, during its 574th, 575th, 588th, and 589th orbits, TIROS I photographed the area shown in Figure 152 over the Southwest Pacific east of Australia. The region of favorable picture-taking conditions (camera angle and illumination) was approximately between latitudes 40° S and 20° N as the satellite was moving northeast. Figure 152 also shows the track of the satellite subpoints and the time of each orbit when the satellite passed latitude 25° S. The cameras were viewing back along the track toward the southwest. These pictures were taken by the remote mode of operation, stored on magnetic tape, and read out at a receiving station further along the orbit (see Appendix B for actual orbits). It should be noted that orbits 574 and 575 passed latitude 25° S at 0002 GMT and 0141 GMT on May 11, while orbits 588 and 589 passed latitude 25° S at 2311 GMT on May 11 and 0050 GMT on May 12. Thus, the pictures were taken at the beginning and end of a full day.

Figure 153 gives four composite photographs showing the area picture during the four orbits, while Figures 154 through 161 are individual frames covering a large part of the same area; geographical grids prepared by the methods of Appendix A have been superimposed on the latter. These grids were computed with camera positions and orientation derived from a careful analysis to correct the discrepancy between programmed and actual picture-taking times. Thus, even though no landmarks can be identified on any of these photographs, it is estimated that the location accuracy is about ±50 nautical miles at ranges halfway to the horizon. The outline of the cloud area is superimposed on the surface streamline analyses of Figures 162 and 163.

*This chapter, slightly modified, appeared in J. Geophys. Res. 66(3) : 797–812, March 1961.

In NASA. Goddard Space Flight Center. Tiros I Meteor. Satellite Symposium 1962 pp 183-197
Submitted for Publication (See V64-17906 10-21) GPO: $2.25

CASE STUDY OF A CONVERGENCE LINE

PHOTOGRAPHIC DATA

The outstanding synoptic feature that appears on the satellite photographs is a broad, solid band of clouds (average widtht about 300 nautical miles) which extends from the Solomon Islands nearly 2,000 nautical miles toward the southeast (Figures 162 and 163). It is not possible, in general, to identify cloud genus (e.g., stratocumulus vs. altocumulus) at great distances on the wide-angle pictures; but the narrow-angle pictures, when available are usually adequate to distinguish between cumuliform and stratiform clouds. Comparison of the higher resolution narrow-angle photographs with simultaneous wide-angle photographs shows that separate elements of cumuliform clouds produce a gray, granulated texture on the wide-angle photographs where the size of the cloud elements and the size of the clear spaces between clouds approach the limit of resolution of the television system.* For example, note the area on Figure 156 immediately surrounding the intersection of grid lines 12° S, 170° E, and also

*This matter is discussed in "Identification of Cloudforms From Tiros I Pictures," C.O. Erickson and L. F. Hubert, Meteorological Satellite Laboratory Report to the NASA, MSL Report No. 7, U.S. Weather Bureau, June 1961.

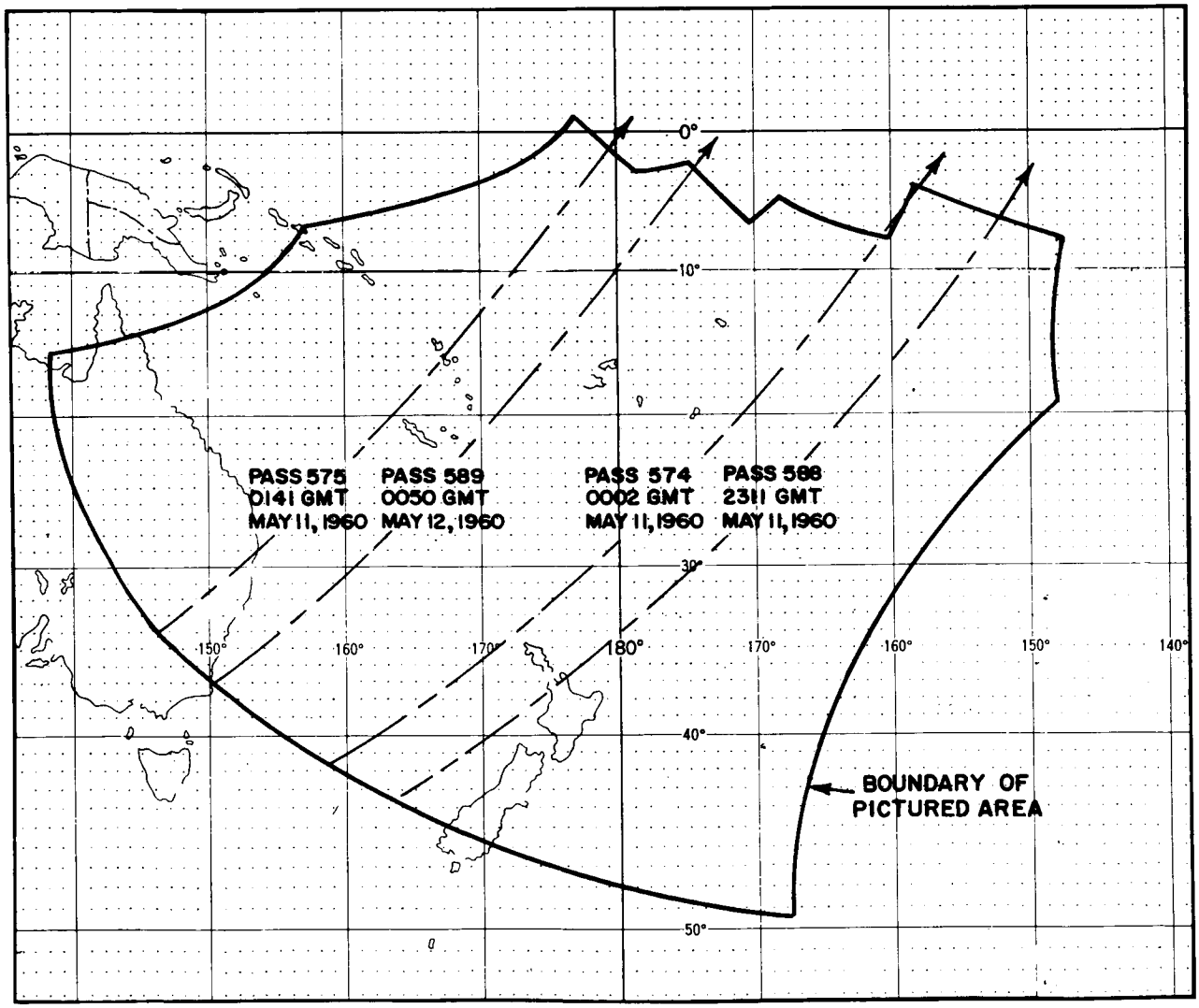

FIGURE 152.—Map of the area over the Southwest Pacific Ocean east of Australia showing the area photographed by TIROS I on its 574th, 575th, 588th, and 589th orbits. The tracks of the satellite subpoints and the time when the satellite passed latitude 25° S are shown for each orbit.

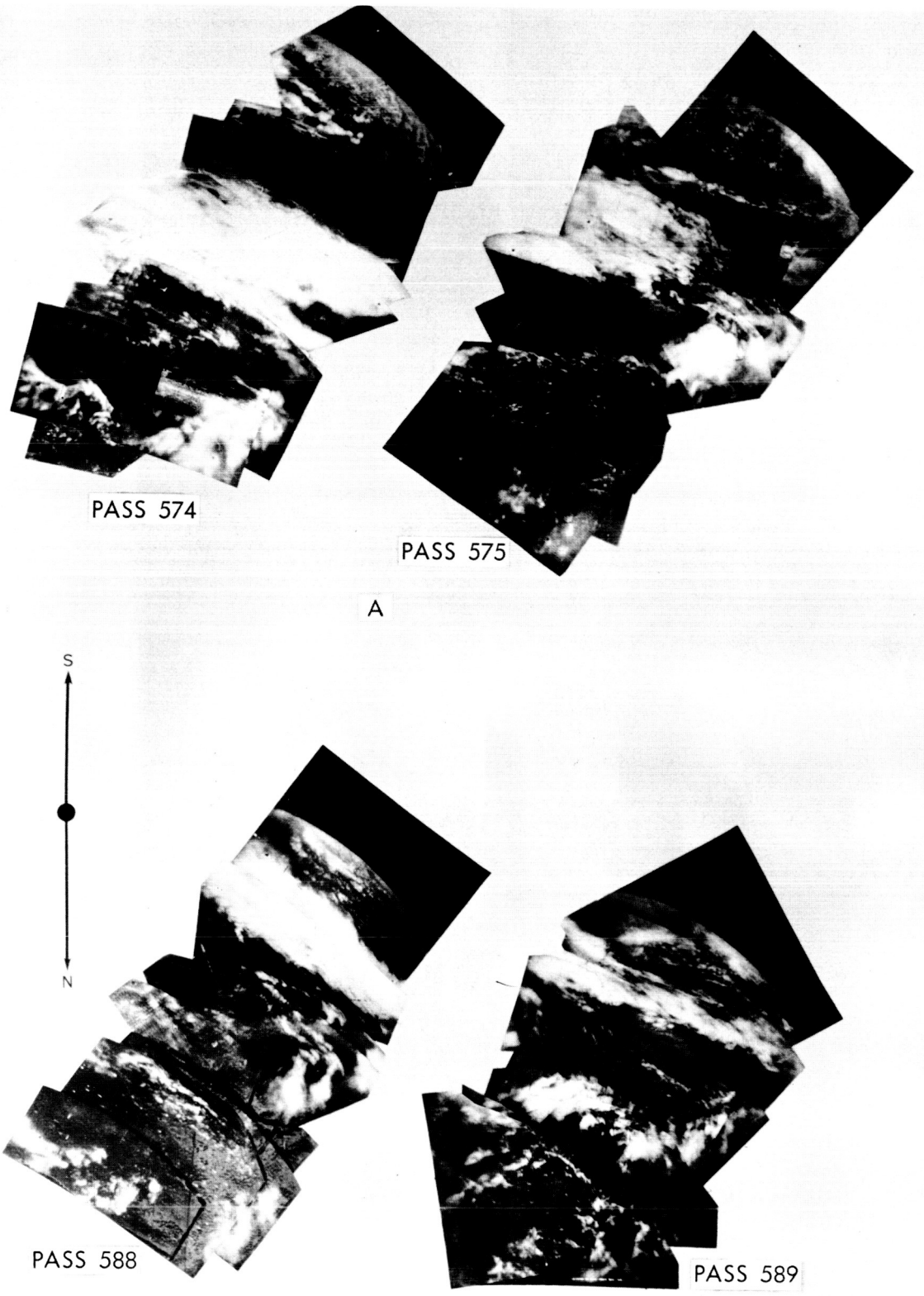

FIGURE 153.—Composites of the wide-angle photographs taken by TIROS I on May 11 and 12, 1960, in the area shown in Figure 152.

the area on Figure 157 enclosed by 22° and 24° S, 160° and 162° E. The pictures, therefore, indicate that the major cloud band is a solid overcast with cumulus clouds on the edges, suggesting that the band is composed of built-up and merged cumulus or multilayered clouds. The surface reports confirm this. It is also clear from surface reports that cirrus clouds existed over parts of the region, but for the most part they cannot be identified from the pictures: for example in Figure 160 at 13° S, 177° W, where cirrus is reported (Figure 162).

Figure 153 shows the clouds at about 0000 GMT on May 11 and at about 0000 GMT on May 12. The compass arrow at the left margin indicates the approximate orientation. The view of the clouds is toward the southwest horizon and the foreground is almost directly beneath the camera. Because of the enormous change of slant range from the foreground (about 390 nautical miles away) to the horizon (1600 nautical miles away), the smaller patches of clouds beneath the camera are exaggerated while the major cloud bands at great distances are minimized.

In order to show the relative sizes and positions of the essential cloud features, the outline of the cloud area is shown by shading on the surface maps (Figures 162 and 163). The shading is intended to depict schematically only the major features; a full appreciation of the cloud details may be gained from Figures 154 through 161, where latitude-longitude grids permit location of cloud patterns relative to the map.

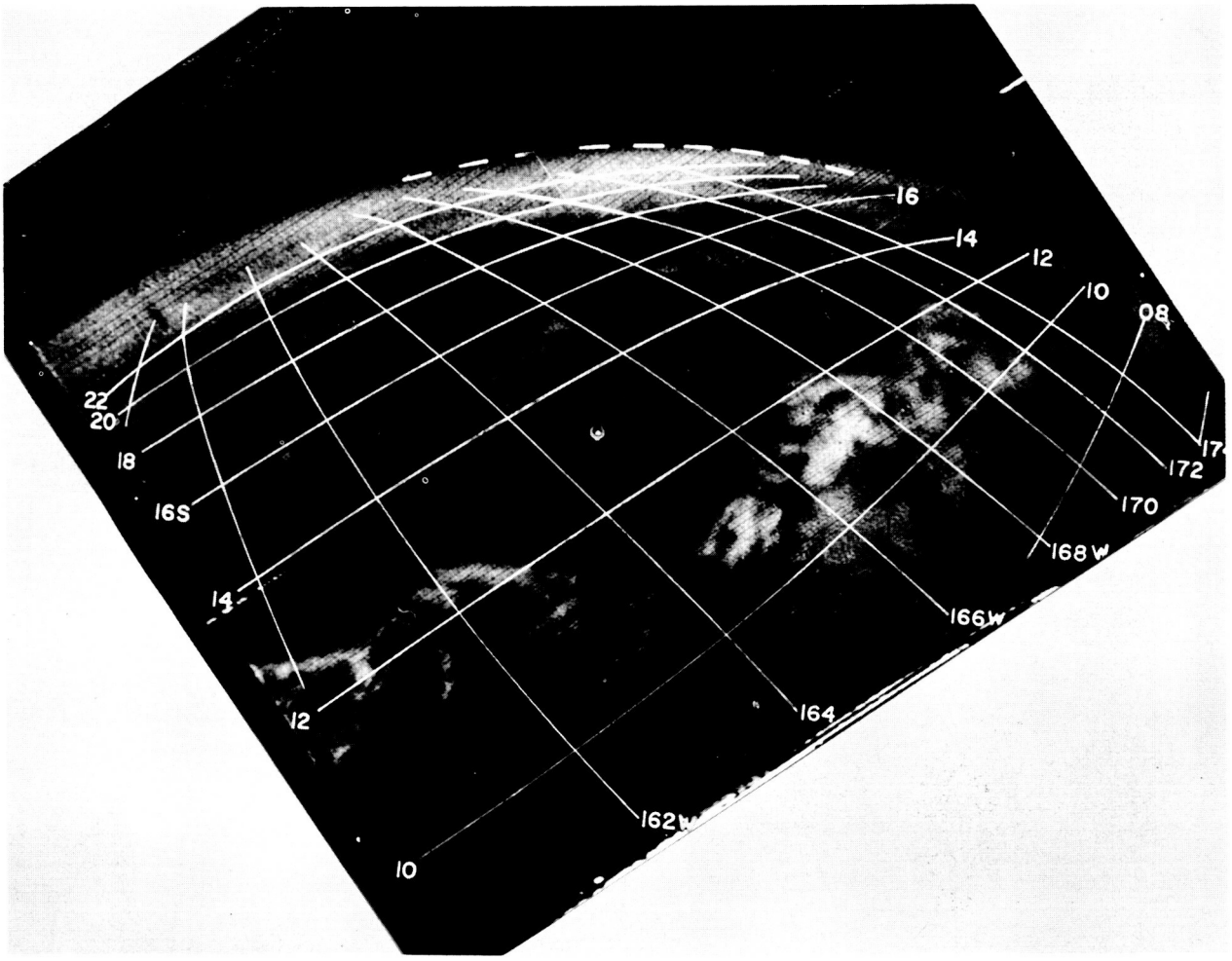

FIGURE 154.—Wide-angle photograph taken during orbit 575 at 0009 GMT on May 11, 1960, showing weak convergence clouds in the tropics and a major cloud band on the horizon. The optical center is shown by the circled dot.

ANALYSIS OF STANDARD DATA

In this part of the South Pacific a great many surface reports are available; but the tropical analyst must be cautious in evaluating the conflicting evidence of individual observations, because the synoptic systems produce subtle changes that are easily masked by local effects and small inaccuracies. For example, significant weather-producing systems are often revealed only by a small change in wind direction and an increased cloudiness and precipitation, but every sizable island has local and diurnal effects that produce changes of equal magnitude.[3] Ship reports, of course, are not affected by terrain, but small wind changes are not efficiently observed from a moving ship. In the tropics the cloud-reporting code is inadequate to differentiate local cumulus and showers from the clouds and showers of a disturbed situation. The clue to synoptic disturbances provided by surface observations is a larger-than-normal amount of middle cloudiness at a group of stations.

In the case at hand, the surface observations do confirm large amounts of middle clouds in the region of the main cloud band; but it is not possible to deduce from those observations that a continuous band existed. Surface pressure analysis by itself is inadequate to delineate synoptic systems before they have reached great intensity, so streamline analyses of the surface wind reports have been made and are shown in Figures 162 and 163.

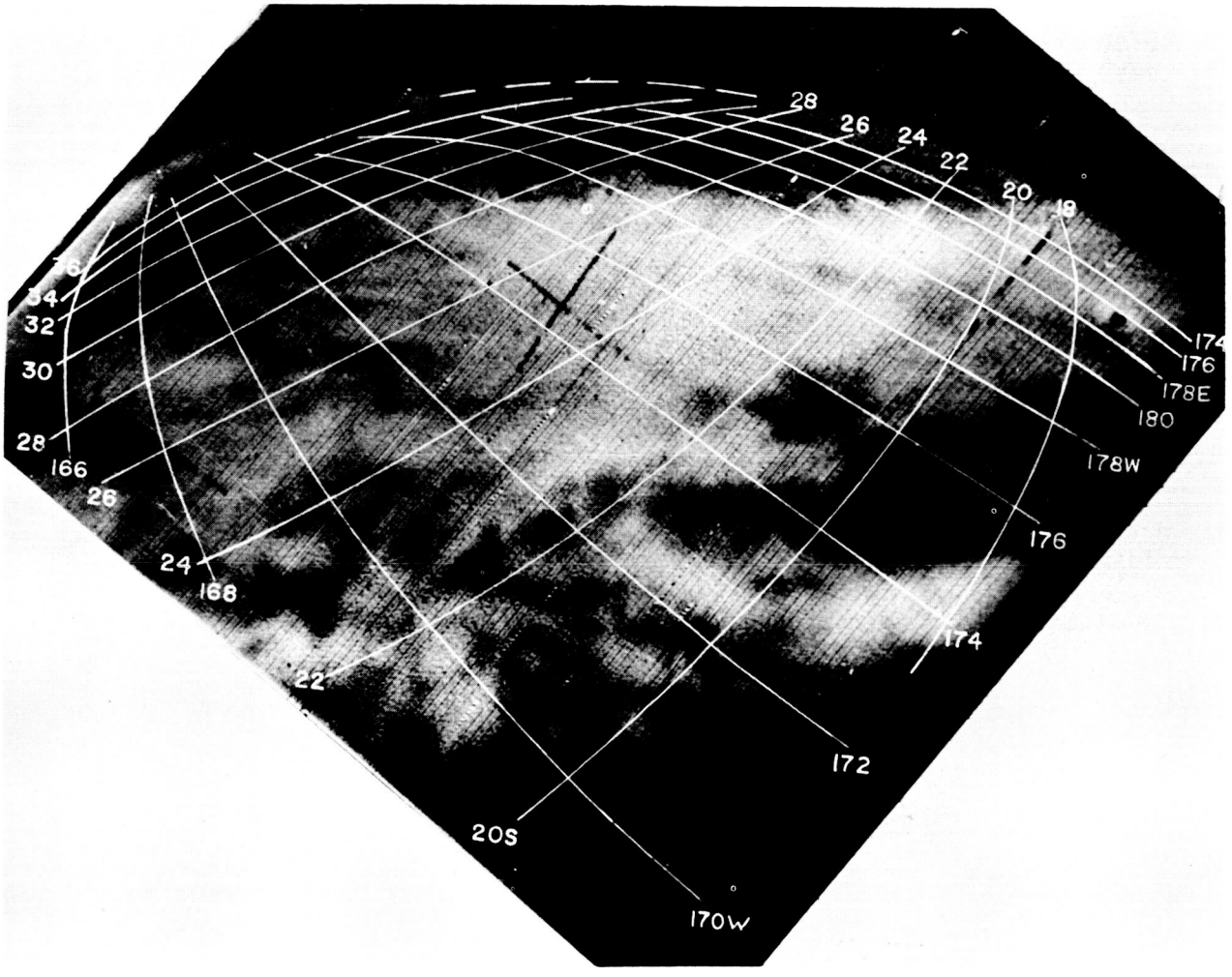

FIGURE 155.—Wide-angle photograph taken during orbit 574 at 0005 GMT on May 11, 1960, showing a cloudless corridor of an anticyclone (19° S, 176° W) cutting into the northern edge of a major cloud band. The optical center is shown by the circled dot.

The analyses of Figures 162 and 163 were made from the data plotted thereon, independently of the photographic data. Six-hourly maps for May 10, 11, and 12, 1960, were analyzed to exploit time continuity, and manuscript maps for this area furnished by the U.S. Weather Bureau Airport Station at Honolulu, Hawaii, were available to show changes over longer periods. Most of the islands in this region are of rugged volcanic character; consequently, all have local effects that create serious problems in surface streamline analysis. It will be noticed that some of the wind reports do not fit the analyses. In every case where a choice has been made between conflicting evidence, it has been done by reviewing the station's location relative to terrain,[4] considering time continuity, and making the most reasonable meteorological choice. For example, the surface west wind reported at Nandi (17.6° S, 177.6° E) appears to be a local wind signifying no large-scale synoptic feature in the low troposphere—an opinion based partially on the fact that this station is downwind from 4,000-foot peaks and partly because the pibal shows easterlies from 2,000 to 9,000 feet at the first map time and light and variable winds up to 7,000 feet at the second map time.

One of the important uses of streamline analysis in the lower troposphere is to indicate areas of divergence and, thereby, vertical motion. Divergence is of course dependent upon speed, as well as directional, divergence. Figures 162 and 163 show no speed field because the data are inadequate to yield a definitive isotach analysis. It has been

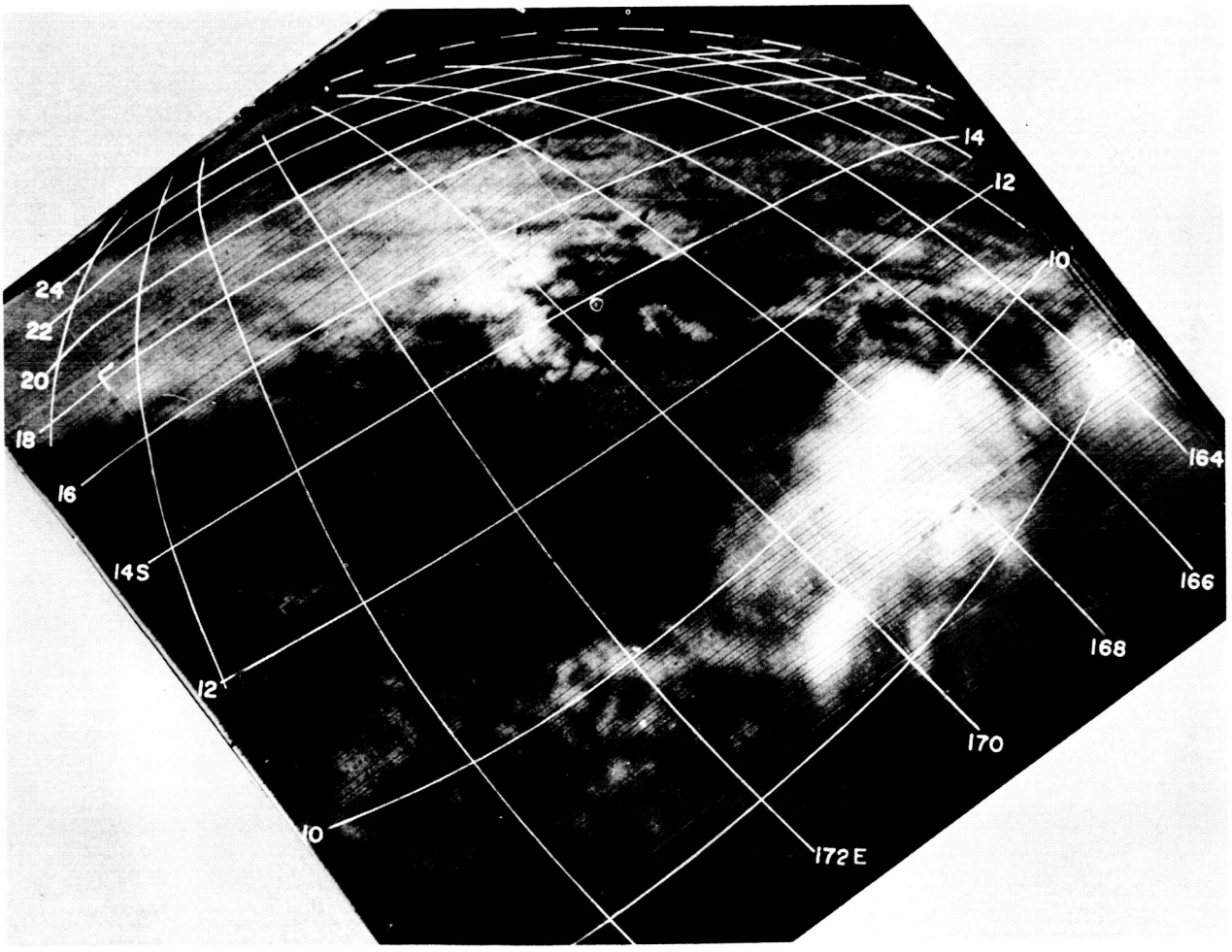

FIGURE 156.—Wide-angle photograph taken during orbit 575 at 0150 GMT on May 11, 1960, showing the western end of a major cloud band and weaker convergence clouds at 10° S. The optical center is shown by the circled dot.

shown, however, that in the tropics there frequently is correlation between directional divergence in the low troposphere and total horozontal divergence [3] so that the streamline pattern is of some use by itself in indicating probable lines of convergence for comparison with the photographed cloud band. Directional convergence is implied by the analysis of Figure 162 along the asymptote emanating from the col at longitude 180°. It can be shown that two principal asymptotes must intersect in a col (neutral point)—one being the locus of converging streamlines, the other the locus of diverging streamlines.[3] The convergent asymptote is indicated by the double-weight streamline through the col near the date line in Figures 162 and 163.

If we now examine the pattern of streamline convergence for correlation with the major cloud band, we can see some agreement. In general, the cloud band follows the convergence asymptotes emanating from the col at longitude 180°. Furthermore, the portion of that asymptote southeast of the col moved poleward during the 24 hours shown and the cloud band in that region also moved south. Meanwhile the asymptote extending toward the northwest showed little displacement and the cloud band here was also stationary.

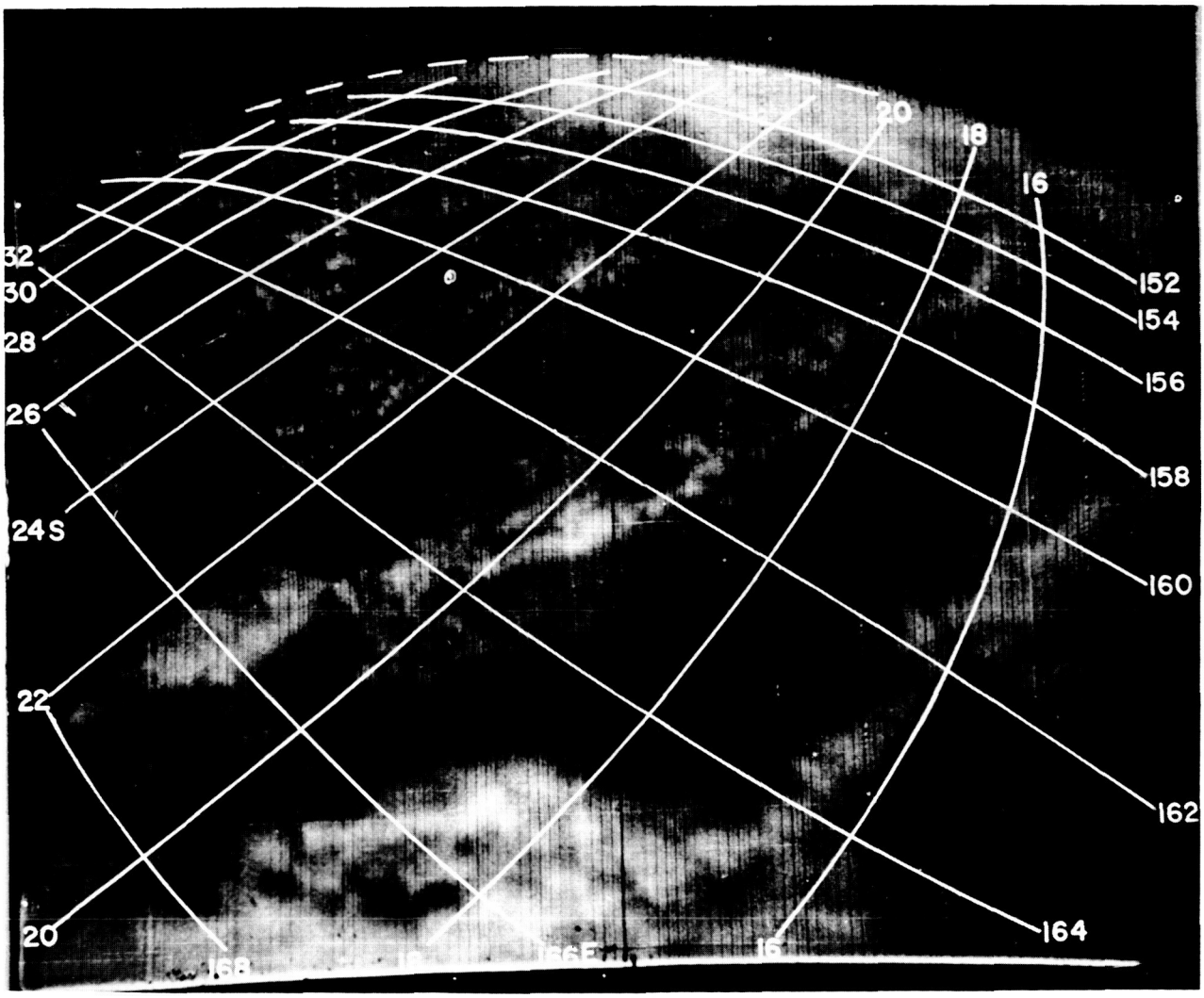

FIGURE 157.—Wide-angle photograph taken during orbit 575 at 0145 GMT on May 11, 1960, showing the cloud pattern in an anticyclone from New Caledonia (left foreground) to Australia (horizon). The optical center is shown by the circled dot.

The small anticyclone that moved from 174° W to 180° in this interval is well documented, so there is little question but that it moved along the cloud band without any great effect on the total cloud cover. Apparently a corridor of little cloudiness extended from the cell center toward the northwest (shown by the shading in Figure 162 and in the foreground of Figure 155), and 24 hours later a break appears in the solid band at 21° S, 178° W, on Figure 160. It is significant that this cell was not the typical subtropical anticyclone, that is, a slow-moving, large-scale high. Rather, it was small and moved downstream in the trades at a speed typical of disturbances in the easterlies (10 to 12 knots). It is therefore likely that this small cell was quite shallow and produced divergence and downward motion only in the low troposphere. If this were the case, it would suppress the low cloudiness with little effect on the middle clouds. Indeed there is a hint of this from the reports in the cell at 0000 GMT on May 11 at 19° and 21° S, and at 0000 GMT on May 12 at 21° S, where only one-tenth to two-tenths of low clouds are reported beneath the

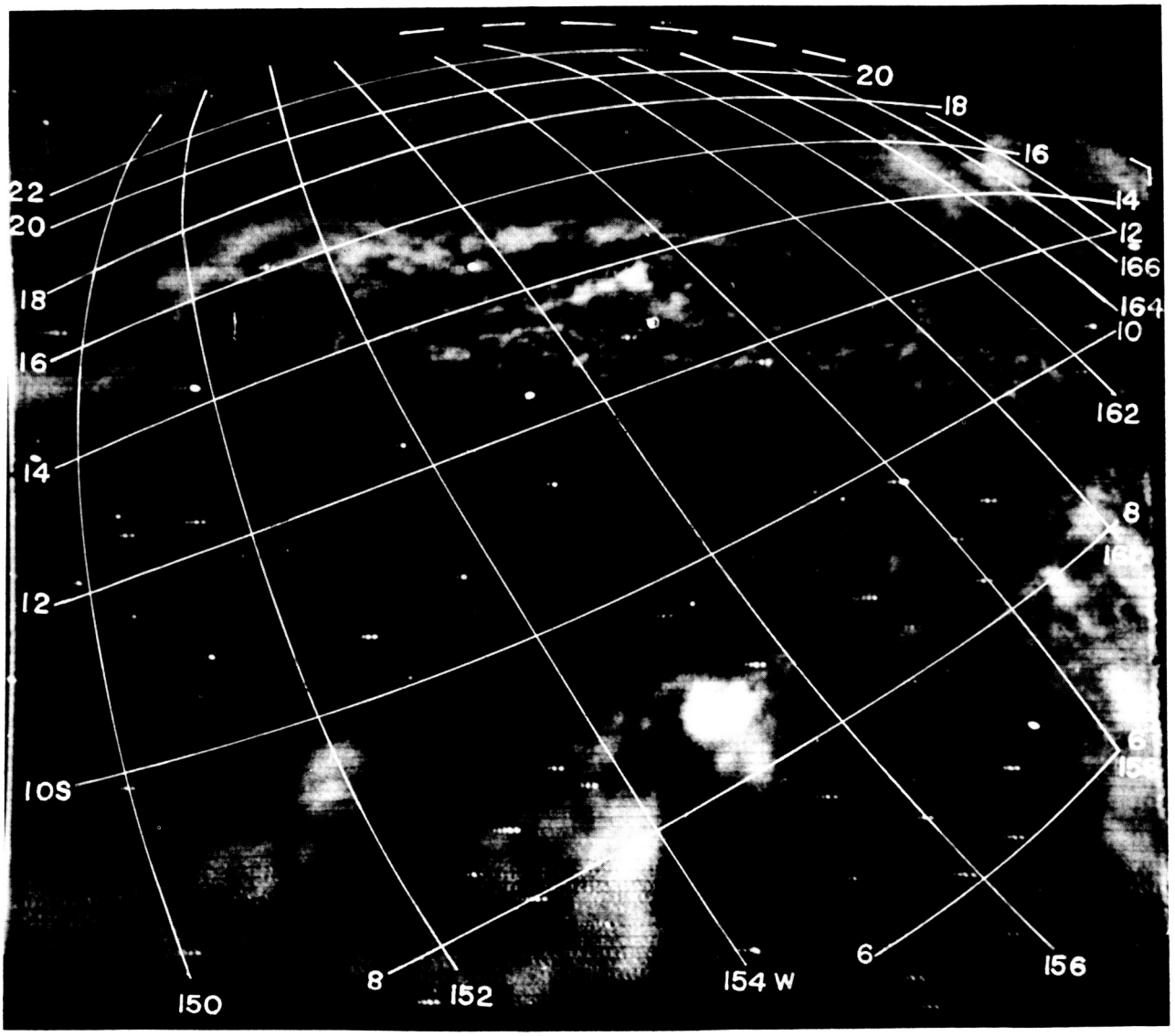

FIGURE 158.—Wide-angle photograph taken during orbit 588 at 2317 GMT on May 11, 1960, showing weak convergence clouds in the tropical south Pacific area. The optical center is shown by the circled dot.

middle clouds. In addition, a pibal located at 21° S, 175° W, at 2300 GMT on May 11 shows the wind backing from southwest, through south and east between the surface and 4,000 feet, strengthening the deduction that the cell was very shallow.

During its evolution, if the cloud band was initially associated with a polar front, it was quite likely a line of cyclonic vorticity because of the shear and sharp cyclonic curvature of the air motion that characterizes frontal zones. The air mass difference across the front decreases and finally disappears during its slow movement over the warm ocean and in the tropical phase frequently only the cyclonic shear remains, thereby giving rise to its identification as a shear line. Finally, even the shear must dissipate; therefore, it seems reasonable to examine the shear along the cloud band (insofar as it is confirmed by surface data), attempting to obtain an estimate of the phase of evolution shown in the photographs from a frontal zone to a shear line to a line of weakening convergence.

Were the isotach field available, the vorticity along the cloud band could be computed with reasonable accuracy. In the absence of an adequate speed field, however, the following procedure was adopted in an effort to examine this feature. The surface pressure field was analyzed at intervals of 1 mb and the pressure gradient measured on either side of the cloud band at intervals of 180 nautical miles along its length (with the exception of the southeastern extremity where no data were available). From the relation between the

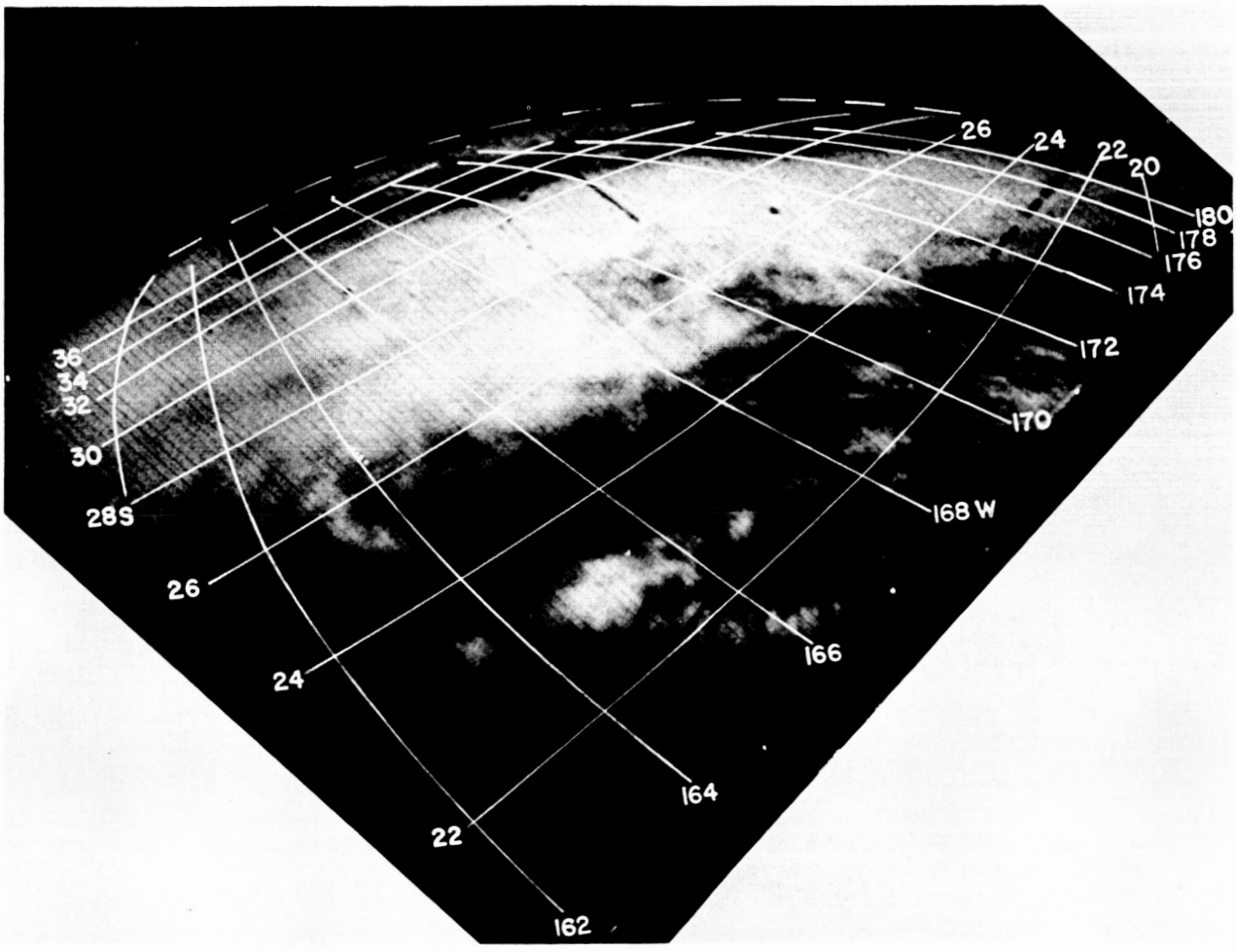

FIGURE 159.—Wide-angle photograph taken during orbit 588 at 2313 GMT on May 11, 1960, showing the western portion of a major cloud band. The optical center is shown by the circled dot.

average geostrophic and average actual wind speed at low latitudes, after Jordan,[5] the shear across the cloud band was computed and the results are shown in Figure 164. Although this computation of the shear above the friction layer must be regarded only as a crude indication, the similarity between the two curves of Figure 164, representing the beginning and end of a 24-hour period, suggests that the sense of the shear may be determined. Figure 164 shows that not only is the cyclonic shear small—even at its maximum of 7 knots per 180 nautical miles (10^{-5}/sec)—but the sign reverses, so that anticyclonic shear extends from the col southeastward.

The point of this is to show there is a suggestion, at least, that this line of convergence retained its vigor for the interval pictured here even though its evolution had passed through the frontal phase and even perhaps, well through the shear line phase. Further, at this stage it appears to follow the motion of the convergent asymptote between subtropical anticyclones—and indication that its future depends critically upon the convergence between flow in the equatorward limb of the anticyclones and the trade wind easterlies.

UPPER AIR OBSERVATIONS

The upper air data coverage is an order of magnitude less dense than the surface data so no upper air analyses have been made, but some comment can be made relative to the upper-air circulation in the vicinity of the few reports available. The

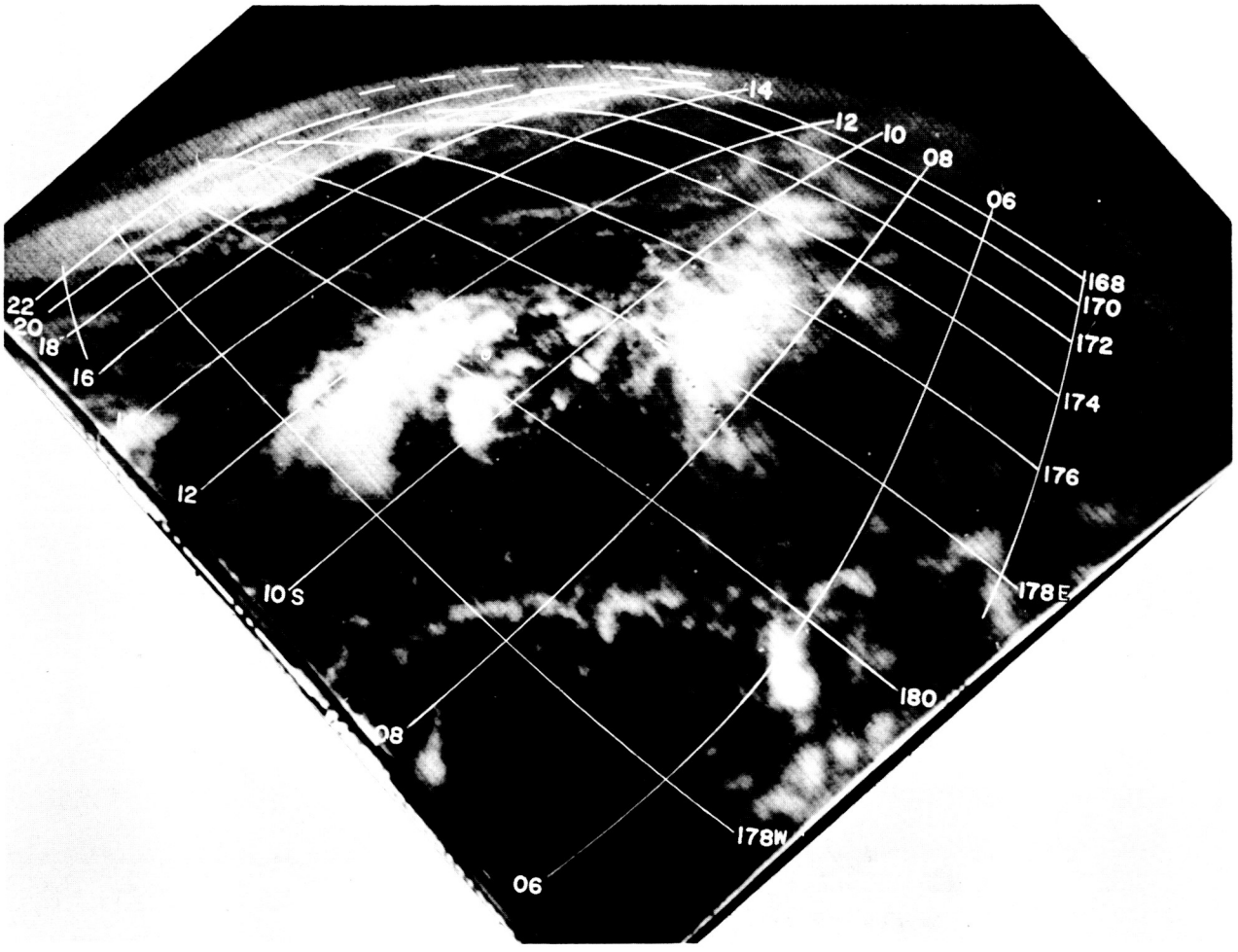

FIGURE 160.—Wide-angle photograph taken during orbit 589 at 0057 GMT on May 12, 1960, showing a tropical convergence line near 10° S and a major cloud band on the horizon. The optical center is shown by the circled dot.

single wind observation near the small high cell has already been mentioned—no radiosonde observation was taken at this station.

Upper-wind observations in the equatorial and tropical regions, at Nauru Island (0.5° S, 167° E), at Guadalcanal (9° S, 160° E), and at Bora Bora (16° S, 152° W), all show typical trade wind flow with easterlies throughout the low and middle troposphere. Of this group only Guadalcanal has a radiosonde and this showed a typical trade wind layer overlain with deep easterlies, and a moist layer from the surface to about 12,000 feet. The great distance between stations leaves ample room for undetected perturbations, and the winds are cited only to point out that the non-perturbed surface flow in the vicinity of those stations is confirmed by the upper air observations.

Two wind reports taken on opposite sides of the major cloud band are interesting because they detect flow, in the layer between the surface and about 7,000 feet, directed toward the cloud band from opposite sides. The pibal taken at 15° S, 167° E, indicates light northeast winds just north of the band, and at 22° S, 166° E, the winds are all south of east. Again, the latitudinal span of 7 degrees between these observations may contain a complicated circulation pattern—one can only point out that the data do not conflict with the convergence asymptote shown on the surface analysis.

The only other upper-air data available in the area of interest are radiosonde and wind observations at Nandi (17.6° S and 177.6° E). It has already been mentioned that the layer from 2,000 to 7,000 feet contained east winds, but the winds changed to westerlies at greater height; at about 10,000 feet at the beginning of this 24-hour period, at 8,000 feet at 1200 GMT, and at 3,000 feet during the last 6 hours of the 11th. Because a trough line extending from higher latitudes moved over Nandi during this 24-hour interval and because the westerlies increased with height, is quite certain that these were mid-latitude westerlies overlying the very shallow easterlies at the surface.

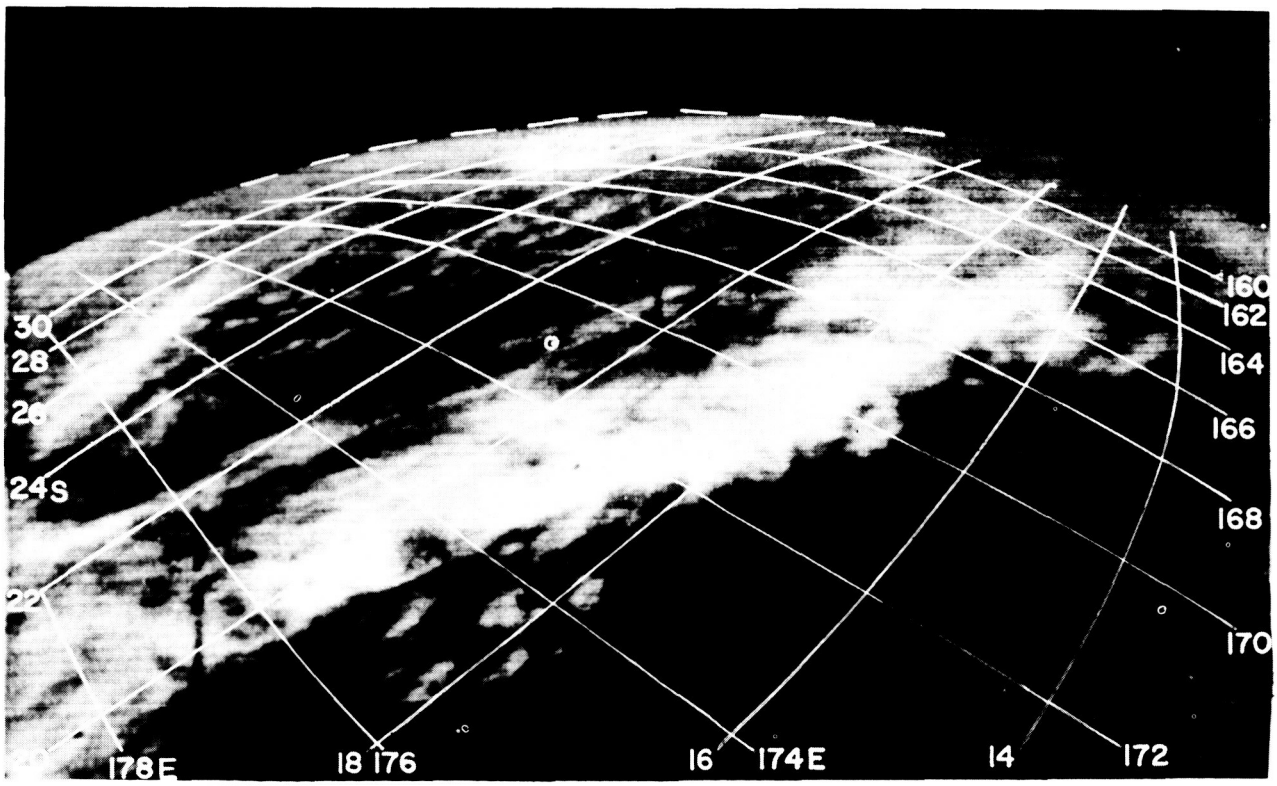

FIGURE 161.—Wide-angle photograph taken during orbit 589 at 0054 GMT on May 12, 1960, showing the western end of a major cloud band and cloud-covered eastern Australia on the horizon. The optical center is shown by the circled dot.

No doubt, clouds were associated with this polar trough, but no good pictures were obtained of the high latitude portion of the trough.

TIROS I PICTURES AS COMPLEMENTARY METEOROLOGICAL DATA

In the pictures presented here there are features not discussed up to this point, which illustrate the potential of satellite data in synoptic analysis. An intermittent zone of increased cloudiness is visible along latitudes 10° S to 12° S indicating a line of weak convergence roughly parallel to the major subtropical band to the south—a feature only vaguely indicated by the surface data (see Figures 154, 156, 158, and 160). The tropical analyst would note this weak convergence at this map time and forecast no extreme weather for the pictured area in the near future.

When any one wind report shows a significant deflection from east in the trade wind region, the tropical analyst must scrutinize all evidence in an attempt to explain it. This evidence consists of the past record, indicating whether the cause might be a sea breeze or other local effect, the reputation of that particular station for reliability, and the previous weather analysis of the upstream area to see if a wave may have been developing unnoticed. In cases like this even the negative information of weather satellite pictures showing no well-developed waves is useful because the "detective work" is enormously eased. An example of this occurred during the analysis of the map series necessary to produce Figures 162 and 163. At 0000 GMT on May 10, the surface wind at Christmas Island (2° N, 158° W) was south at 20 knots and 24 hours later it had returned

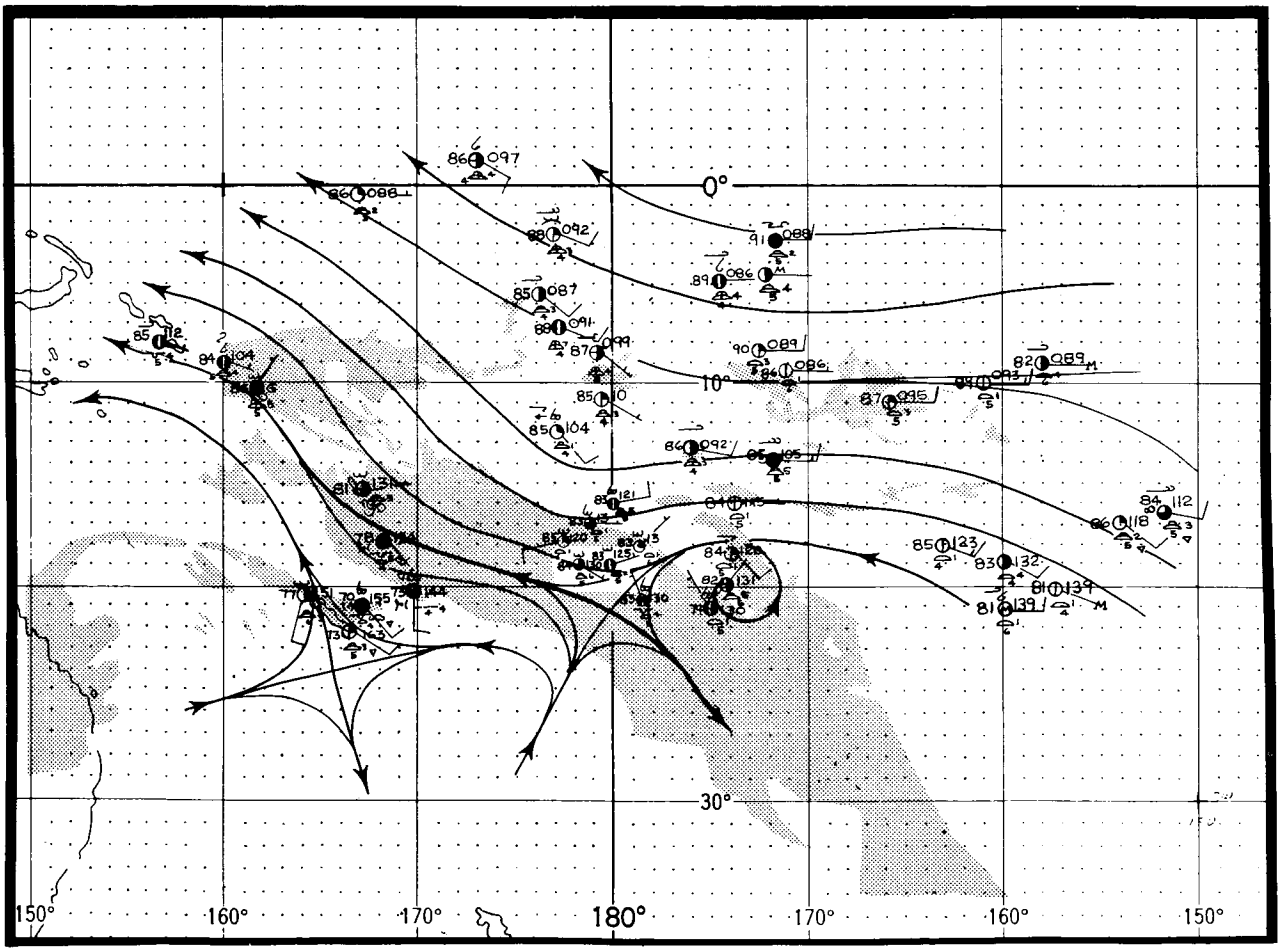

FIGURE 162.—Surface streamline analysis for 0000 GMT, May 11, 1960. The cloud area photographed is shown by shading.

to southeast. Because the map series was being analyzed independently of the TIROS I photographs, considerable time was spent in attempting to account for this wind shift by a strong disturbance extending both north and south of the equator, extrapolating its motion downstream to see if appropriate wind changes at other stations verified a traveling disturbance. Finally, with no other changes occurring downstream, it was concluded that no significant disturbance had moved into the area and Figures 162 and 163 show uniform easterlies in the tropical area west of 170° W. A brief inspection of the TIROS I photographs verified the absence of an intense wave (see Figures 154 and 158). Use of the photographs during the analysis would have eased the analysis chore and lent confidence to the final result.

Because the camera was viewing well above the horizon while the satellite was south of 30° S, photographs taken in the higher latitudes are less satisfactory than photographs taken in the tropical latitudes. Nevertheless some excellent photographs were obtained of the patterns within the subtropical anticyclone. The top of the first composite (Figure 153) and the individual frame in Figure 157 show a curved pattern of clouds spiraling from the left foreground around to the right and to Australia on the horizon. This pattern delineates the northern limb of an anticyclone which is not shown on Figures 162 and 163 because of lack of data, but which was included in the Australian encoded analysis (not shown). According to that source, a high was centered at 30° S, 158° E, at 0500 GMT on May 11.

These pictures of clouds in the anticyclone are of interest because a large number of vortex patterns so prominent in the TIROS I data are associated with cyclones where the low-level conver-

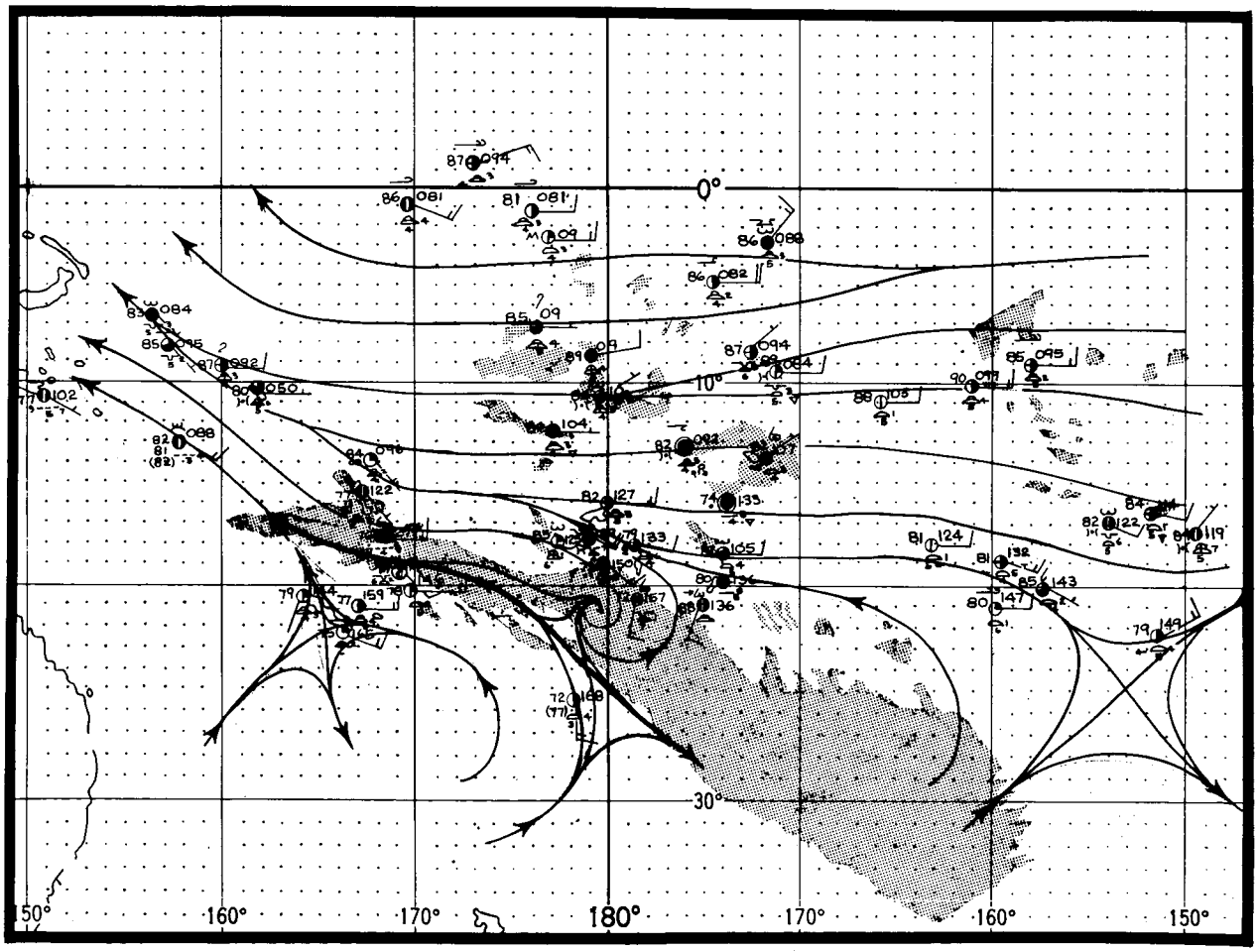

FIGURE 163.—Surface streamline analysis for 0000 GMT, May 12, 1960. The cloud area photographed is shown by shading.

gence produces copious cloudiness which arranges itself in the characteristic spiral patterns. Here, however, is anticyclonic circulation which is undoubtedly producing surface divergence and subsidence, yet there are sufficient clouds (probably no more than a few tenths) to show this curved pattern. Purely from meteorological reasoning we can be moderately confident that the cloudiness is suppressed cumulus limited by an inversion or stable layer.

CONCLUSION

This study has shown that a dense (by tropical standards) network of surface observations provided only a rough indication of lines of convergence in the low troposphere. Based only on surface cloud data the presence of disturbed weather near the major convergence line was suggested, but from surface reports alone it was not possible to delineate a continuous band of clouds or a continuous convergence line. Furthermore, efforts to detect a line of maximum vorticity failed to show a concentration of cyclonic shear along the convergence line. One might therefore conclude that the evolution of the system producing the major cloud band had passed through the frontal stage and even the shear line characteristic was dissipating. In any event, an excellent surface data network in the tropics is not adequate to describe the quasi-stationary type of system studied here because the effect on the field of horizontal motion is so small that it is virtually undetectable. The standard data must be complemented by more complete cloud observations such as those provided by satellite observations. The photographs obtained on the four orbits showed nearly 2,000 miles

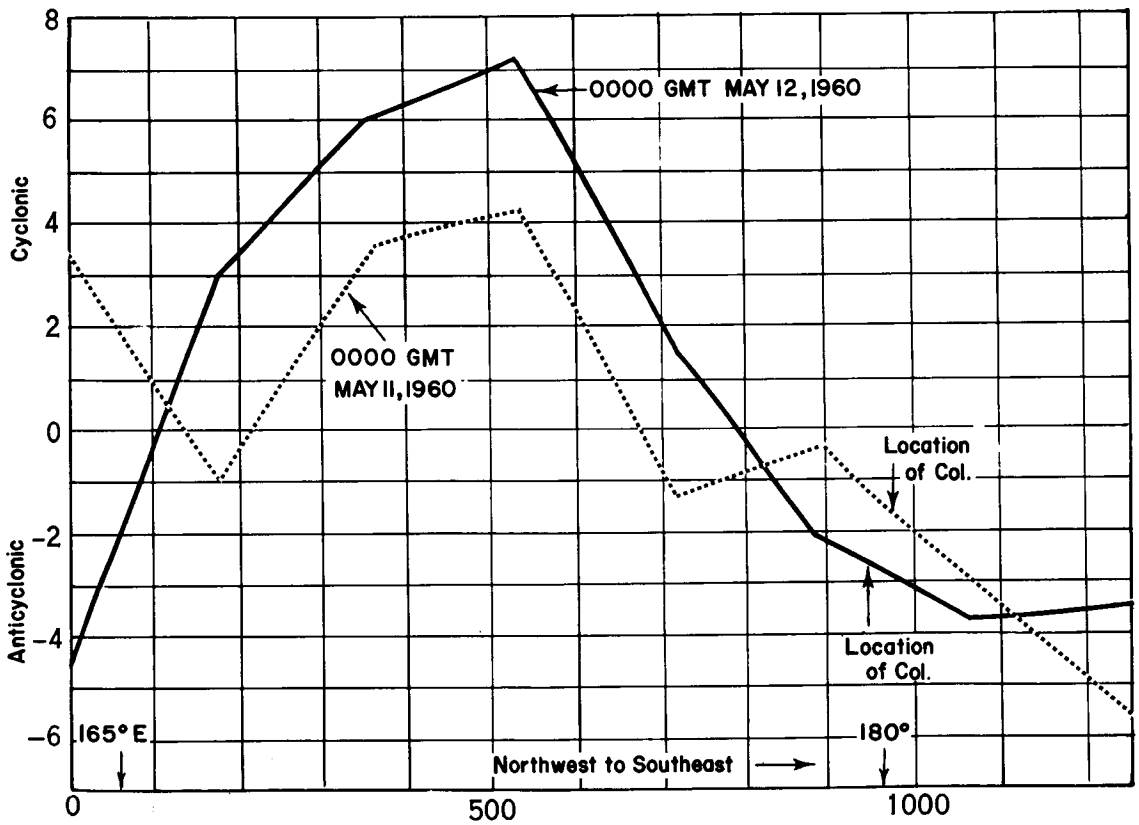

FIGURE 164.—Computed shear across the major cloud band; the locations of the col are shown for the beginning and end of May 11, 1960.

of a vigorous band of middle and low clouds that apparently maintained its position over the main convergence asymptote at the surface—very good pictorial evidence of a persistent line of convergence.

REFERENCES

1. Riehl, H., "Tropical Meteorology," New York: McGraw-Hill, 1954.
2. Palmer, C. E., "Tropical Meteorology," Quart. J. Roy. Meteorol. Soc. 78(336): 126–164, April 1952.
3. Palmer, C., Wise, C. W., Stempson, L. J., and Duncan, G. H., 'The Practical Aspects of Tropical Meteorology," U.S. Air Weather Service Manual 105–48, September 1955.
4. Ramage, C. S., ed., "Notes on the Meteorology of the Tropical Pacific and Southeast Asia," Honolulu, Hawaii Institute of Geophysics, Air Force Surveys in Geophysics No. 126, AFCRC–TN–60–455, June 1960.
5. Jordan, C. L., "A Comparison Between Observed and Geostrophic Winds in Low Altitudes," Quart. J. Roy. Meteorol. Soc. 79(339): 153–156, January 1953.

CHAPTER 14

COMPARISON OF A SATELLITE NEPHANALYSIS WITH A CONVENTIONAL WEATHER ANALYSIS FOR A FAMILY OF PACIFIC FRONTAL STORMS

by

VINCENT J. OLIVER

Meteorologists for many years have known the general nature of storms and their movements, but have lacked a measure of their individuality, a "cyclone print" (See Chapter 8) of the storm. This characteristic of the storm now becomes strikignly clear in the pictures taken by TIROS I of the cloud distribution around storms.

On May 19–20, 1960, on its 704th and 705th orbits, TIROS I obtained a series of excellent pictures over the western United States and the northeastern Pacific.The area contained three quite active frontal systems, all clearly detectable in the cloud distribution shown by the satellite pictures.

Since 30 large-area overlapping pictures were obtained on each of the 2 orbits, it was possible, by combining a few frames from each, to make composite pictures of the area from the Northern Plains States westward to the central North Pacific. These composites are shown as (a) and (b) in Figure 165. A schematic nephanalysis* derived from these pictures has been superimposed on the sea-level frontal and isobaric analysis (Figure 166) and on the 300-mb pattern (Figure 167).

Several features of these pictures clearly show the ability of the satellite to reveal patterns, both large and small in scale, that are rarely if ever detectable from the ground. For example, the spiral cloud band around the cyclonic vortex in the central Pacific, seen in (b) and on the extreme left of (a) in Figure 165, could never have been located or even recognized from surface reports of the type and quantity now available. Also, the extraordinary spatial continuity of the frontal cloud band extending from this storm for more than 2,000 miles into western North America, the parallel rows of oversized cumulus deep in the cold mass near the center of (a) in Figure 165, and the numerous merging bands of clouds and clear areas near the front, could never have been detected from the available surface observations.

Over the area from the west coast to the Continental Divide (the right side of (a) in Figure 165), the clouds become less dense and then break up into cumuliform rows. Large cumulus and cumulonimbus are apparent over the eastern mountain region, with the cells increasing in size the farther southeast they extend from the stratified frontal deck.

Although the satellite cameras have detected many patterns of which meteorologists heretofore were, for the most part, unaware, some of the patterns are familiar from earlier studies of aerological data. In particular the moist and dry tongues of the "isentropic era" of the 1930's have now reappeared in clear pictorial form. For example, it is clear that the cloud patterns of the storm in the central Pacific seen at the left end of (a) strikingly illustrate the branching moist tongue which Namias[1] and others found to be associated with most large storms. The anticyclonic branch of the moist air, south of the axis of the jet stream (b), shows up as an eastward extension of the thick cloud deck of the storm. The anticyclonic curvature of the flow pattern aloft is seen reflected in the band of clouds which extends from the western portion of the Pacific frontal zone northward and then eastward around the clear area seen in (a) and (b), Figure 165. (The relatively bright area in the middle of the clear zone is sun glint.) The cloudless area

*This nephanalysis is based on the original picture rectification made operationally at the readout station. The geographic location of cloud elements was estimated to be accurate to within about 2 degrees of latitude. Work is underway to obtain more accurate latitude-longitude grid for these pictures. See Appendix A.)

In NASA Goddard Space Flight Center Tiros I Meteorol. Satellite System 1962
p 199-203 ref (See N64-17906 10-21) GPO: $2.25

near the center of the vortex and the nearly clear area to the rear of the frontal system along the west coast of North America are both part of the classical picture of the cyclonic tongue of dry air to the rear of the storm.

A closer look at the details of the cloud patterns in various parts of the storm is made possible by the narrow-angle camera. The narrow-angle camera takes a picture approximately in the center of each of the wide-angle pictures. These narrow-angle pictures, taken when the camera is looking vertically down at the earth, are about 80 miles square and afford a view of the individual clouds. Cumulus-type clouds in the unstable, cold air mass over Wyoming and Montana, are seen in (c) and (d) on Figure 165. In the surface observations in this area (Figure 168) cumuliform clouds with showers were reported at each station or within sight. However, the variations in density, size, and spacing of the clouds which show up in the photographs cannot be determined from the surface network.

The differences between the appearance of stratified cloud layers and cumuliform cloudiness are demonstrated by two narrow-angle pictures shown as (e) and (g) in Figure 165. Note the

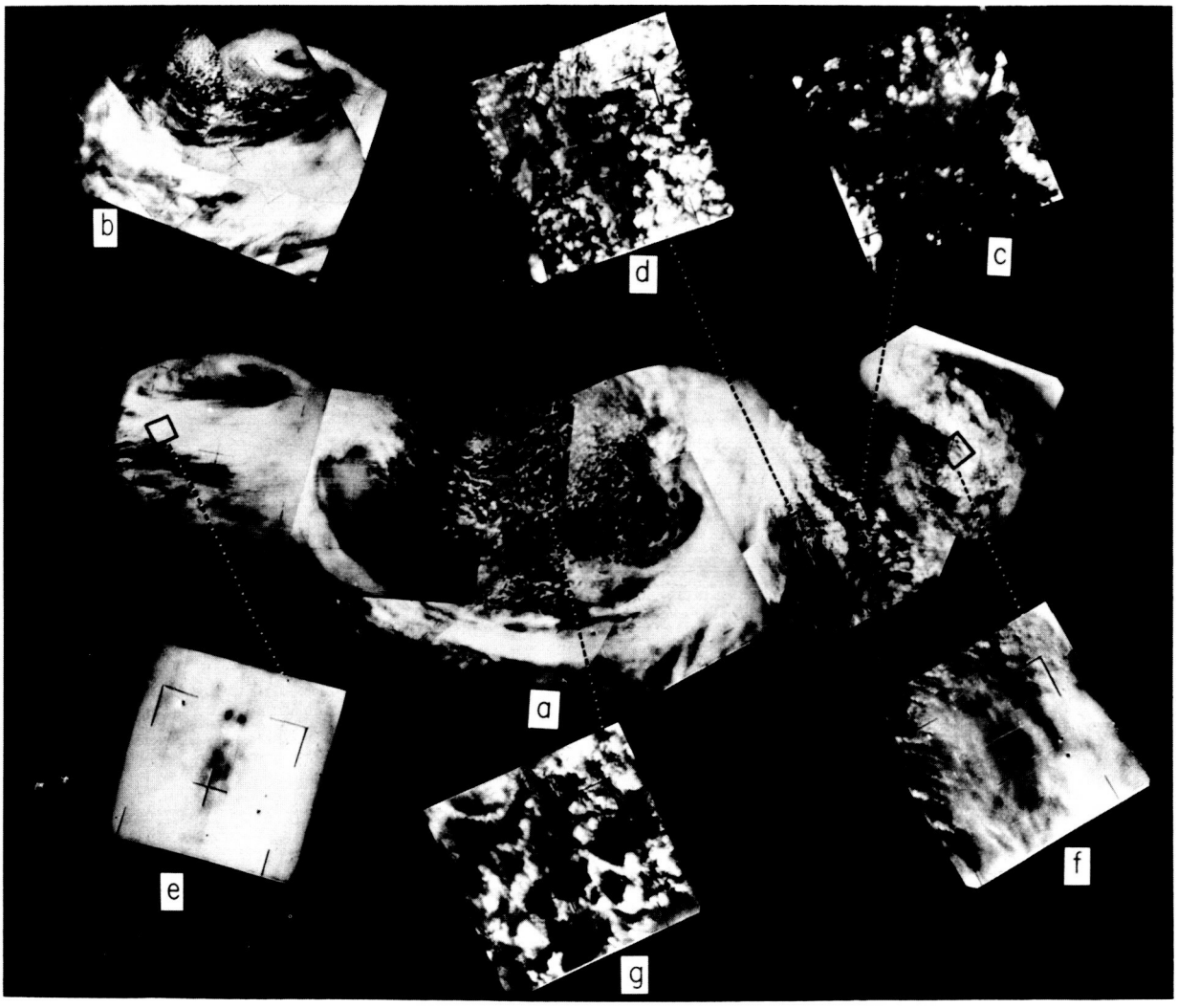

FIGURE 165.—Pictures taken on two TIROS passes at 2300 GMT, May 19, 1960, and 0100 GMT, May 20, 1960, showing wide-angle camera views (a and b) and narrow-angle views (c through g). Composite picture (a) extends from the central North Pacific to the Northern Plain States of the U.S.A. Composite picture (b) shows more detail of the storm in the central Pacific.

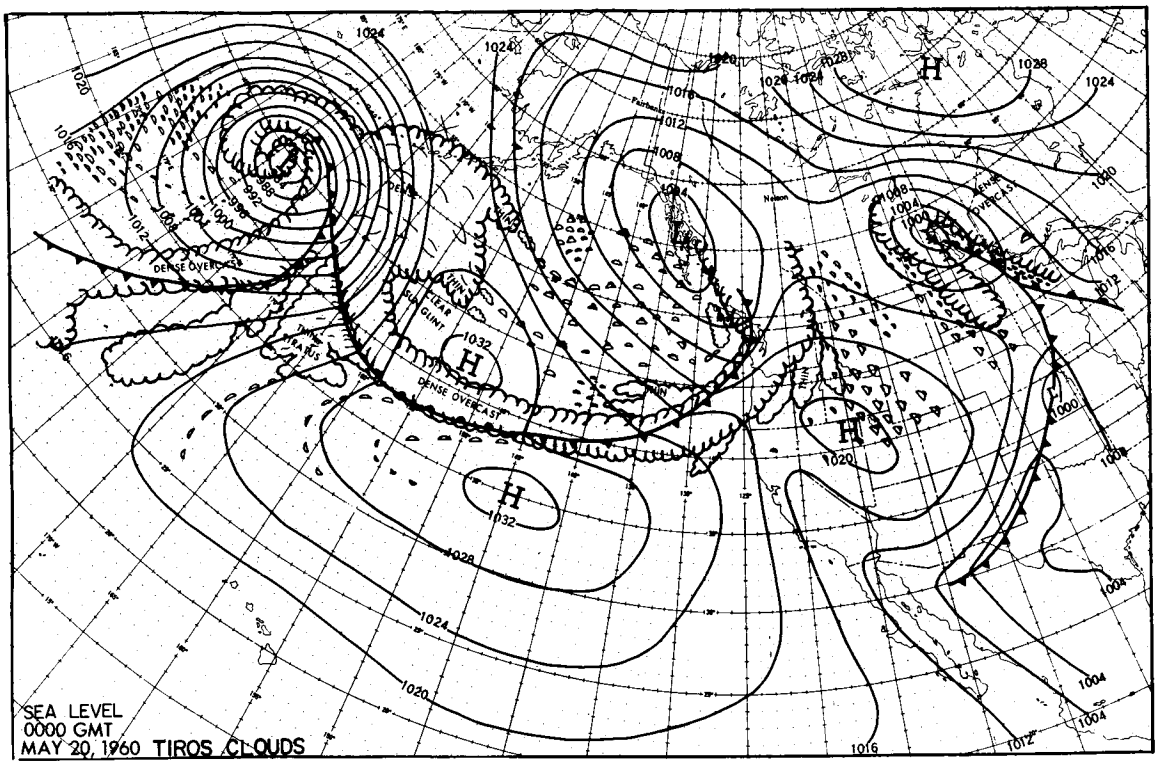

FIGURE 166.—Cloud analysis based on the pictures shown in Figure 165, superimposed on a sea-level chart.

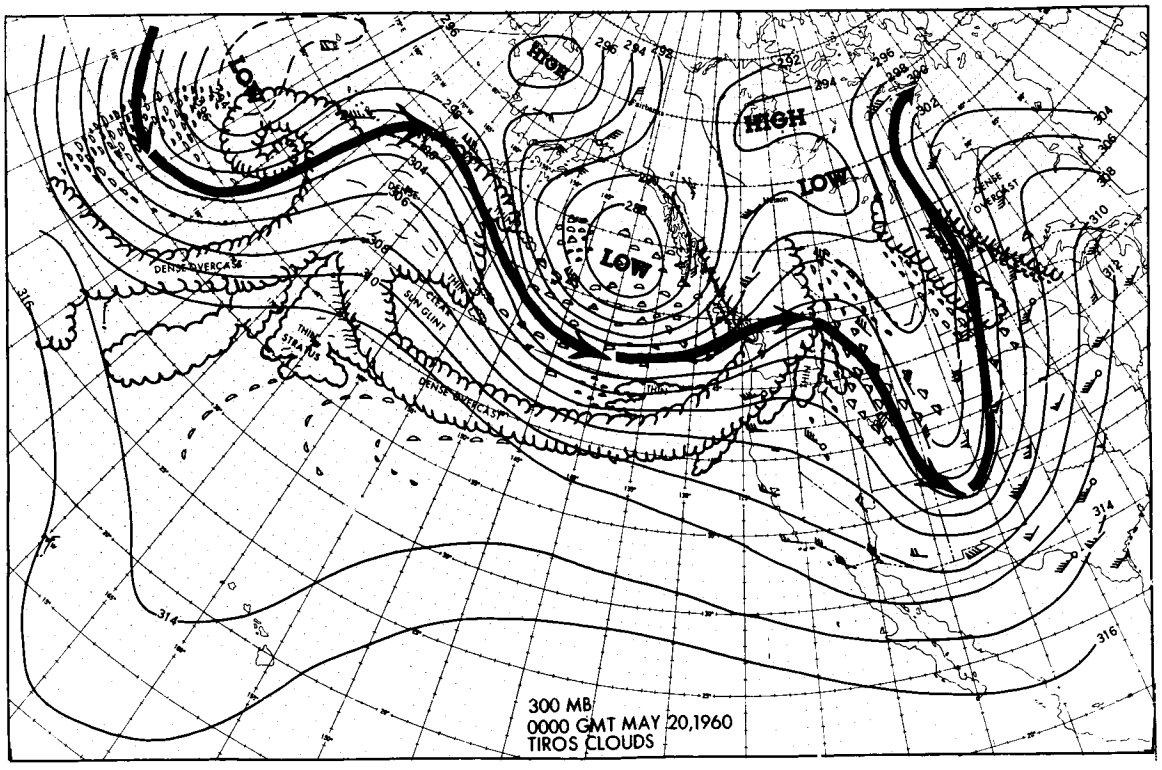

FIGURE 167.—Cloud analysis based on the pictures shown in Figure 165, superimposed on a 300-mb chart.

lack of structure within the frontal stratus zone in (e) in contrast with the sharpness of the cumulus and clear areas deep in the cold air mass in (g).*

The narrow-angle picture (f) taken over the Dakotas shows parallel rows of cumuliform clouds aligned with the surface wind. They appear to have formed, grown, and spread into the large cloud mass which covers the remainder of (f). The narrow-angle picture (g) taken north of the front in the Pacific, shows cumulus of all sizes and shapes, with holes, somewhat circular in shape, between the larger cloud masses. The larger and brighter of these cloud areas are most likely showers or thundershowers, while the smaller elements would be cumulus, stratocumulus, and swelling cumulus.

In summary, it seems quite clear that satellite data make possible, for the first time, the accurate, timely analysis of the "state of the sky" so

*The dark portions near the middle of (e) are caused by a defect in the narrow-angle camera and appear in all pictures taken with this camera.

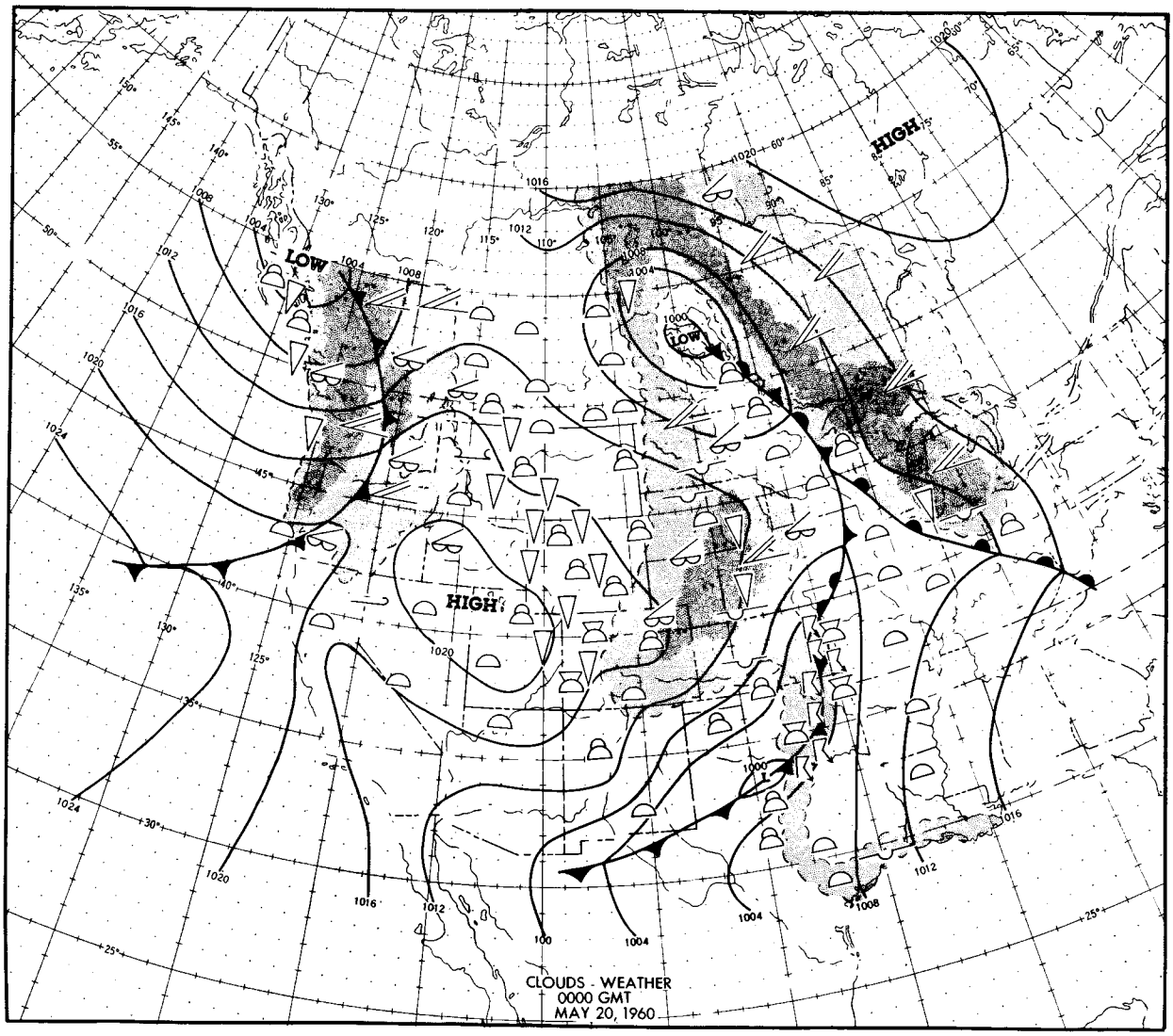

FIGURE 168.—Clouds, weather, frontal and isobaric analysis based entirely on surface reporting network. Light shaded area is overcast, darker area is precipitation.

long sought after.[2, 3, 4] Moreover, on many occasions storm centers, frontal zones, jet streams, and the positions of clear areas can be placed more accurately—especially over the oceans—than ever before. Figure 165 would be a powerful briefing tool to the international aviation forecaster and military strategists planning flights in this area. Many details in the patterns of each storm are unique to the storm and may remain with it from birth to maturity. Continuous satellite pictures of these patterns will finally make available to the forecaster the much needed "cyclone print."

REFERENCES

1. Namias, J., "The Use of Isentropic Analysis in Short-Term Forecasting," J. Aeronaut. Sci. 6(7) : 295–298, May 1939.
2. Schereschewsky, P. L., "Clouds and States of the Sky," in: Handbook of Meteorology (Section XI, 881–926), ed. by F. A. Berry, E. Bollay, and N. R. Beers, New York: McGraw-Hill Book Co., 1945.
3. Godske, C. L., Bergeron, T., Bjerknes, J., and Bundgaard, R. C., "Dynamic Meteorology and Weather Forecasting," Boston: American meteorological Society, 1957, pp. 14, 640–641.
4. Brooks, C. F., "The Use of Clouds in Forecasting," in: Compendium of Meteorology, 1167–1178, Boston: American Meteorological Society, 1951.

CHAPTER 15

A CELLULAR CLOUD PATTERN REVEALED BY TIROS I*

by

ARTHUR F. KRUEGER and SIGMUND FRITZ

INTRODUCTION

One of the cloud features photographed by TIROS I is a cellular pattern having horizontal diameters as large as 30 to 50 nautical miles and consisting of clear centers bounded by ring- or U-shaped cloud elements about 10 to 15 nautical miles wide. Such features are too broad to be recognized by a single observer at the earth's surface, and yet small enough to remain undetected by even the best distribution of standard synoptic reports.

Three examples of such a cellular pattern are the wide-angle photographs shown in Figures 169 and 171. The picture shown in Figure 169 was taken over the Atlantic, 650 nautical miles northeast of Bermuda at 1612 GMT, April 4, 1960; Figure 170 was taken over the north central Pacific, looking northward towards the Aleutians at 2341 GMT, April 1, 1960; and Figure 171 was taken 750 nautical miles northeast of Hawaii at 2250 GMT, April 4, 1960.

The aim of this discussion is to relate this cloud pattern to the available conventional meteorological observations. The emphasis is mainly on the Atlantic case (Figure 169) because more extensive conventional observations were available for this cloud pattern than for the other two. The conventional observations consist of the standard surface reports, radiosondes, pilot balloon observation, and aircraft reports including several dropsondes. The problem of cellular convection, as treated by laboratory and theoretical studies, will also be discussed briefly in relation to these TIROS I observations.

*A revised version of this paper, "Cellular Cloud Patterns Revealed by TIROS I," appeared in Tellus 13(1) : 1–7, February 1961.

FIGURE 169.—Wide-angle photograph taken by TIROS I at 1612 GMT, April 4, 1960, 650 nautical miles northeast of Bermuda.

SYNOPTIC ANALYSES

THE ATLANTIC CASE

Figure 172 shows a latitude-longitude grid, derived by methods described in Appendix A, superimposed on Figure 169 to establish location and scale. It is readily apparent that the cellular cloud pattern in the foreground (Figure 172) occupies a large area, extending in the photograph about 650 nautical miles in a west-east direction and 300 nautical miles in a north-south direction. These cells have diameters ranging from 20 nautical miles near the picture center to about 40 or 50 nautical miles in the lower right portion of the photograph.

The surface weather map corresponding most closely in time with this photograph is for 1800 GMT, April 4, 1960 (Figure 173). This analysis shows an intense anticyclone with a maximum pressure of 1029 mb dominating the picture area. Northwest of this high pressure center, extensive middle and low cloudiness were reported, with rain occurring near Nova Scotia and Newfoundland (Figure 174). This cloudiness, having the

In NASA, Goddard Space Flight Center Tiros I Meteorol. Satellite System 1962 p 205-212
rep Submitted for Publication (See N64-17906 10-21) GPO: $2.25

FIGURE 170.—Wide-angle photograph taken by TIROS I at 2341 GMT, April 1, 1960, over the North Central Pacific Ocean looking northwestward toward the Aleutian Islands.

FIGURE 171.—Wide-angle photograph taken by TIROS I at 2230 GMT, April 4, 1960, 750 nautical miles northeast of Hawaii.

appearance of a stratiform type, is apparent toward the northwestern (upper left) portion of Figure 172. However, in the cellular cloud region of Figure 172, only low clouds, chiefly stratocumulus and cumulus, were reported (Figure 174). These observations were verified by a few aircraft in the vicinity, which estimated these clouds to have bases around 2,000 to 3,000 feet and tops ranging from 4,000 feet in the northern part of the pictured area to 12,000 feet in the southern part (Figure 175).

The buoyancy of these cumuliform clouds arises in part from heating of the air mass at the ocean surface. Ships in this region, for example, reported ocean temperatures averaging about 3° C warmer than the air just above, with the smallest differences on the western side of the high pressure center and the greatest on the east where the surface flow had a northerly component (Figure 174). Radiational cooling at the cloud tops should also contribute to the destabilization of this air mass.

Radiosonde observations for Bermuda and Ship E (35° N, 48° W) for 1200 GMT, as well as dropsondes from reconnaissance aircraft are shown in Figure 176. The sounding closet in time (1800 GMT) to Figure 169 was a dropsonde at 38.4° N, 53.6° W taken near the edge of an altostratus deck (Figures 172 and 174). This sounding showed a marked subsidence inversion at 900 mb (about 3,000 feet) capping a moist layer where the temperature lapse-rate was close to dry-adiabatic. Any convective clouds below this inversion presumably would be shallow, since the condensation level was only 20 mb below the inversion. The presence of a higher cloud deck was indicative by increasing moisure with height above 600 mb.

A similiar low-level structure, but with considerable variation in the height of the inversion and also convective cloud thickness, was indicated by the other soundings. The highest inversion (730 mb or about 9,000 feet) occurred in the southern part of the picture region (32.7° N., 53.8° W), with the thickest clouds also indicated (bases about 2,000 feet, tops about 12,000 feet). This seems to be connected with larger cloud elements and also larger clear spaces in the lower right portion of Figure 172.

The systematic spatial variation in depth of the moist layer is seen in Figure 177, which is an analysis of the topography of the subsidence inversion based on the few soundings available. The average depth of this layer was about 850 mb, or approximately 5,000 feet. Thus, if the cellular pattern is considered to include the entire convective layer rather than just the visible cloud, the horizontal scale is about 30 times the vertical scale.

Upper-wind soundings (Figure 178) were available only for Bermuda (1200 GMT) at the western extremity and Ship E (1800 GMT) at the eastern end of the region. These showed a veering of the wind up to 3,000 feet with a small decrease in

wind speed. Above 3,000 feet the wind speeds increased to about 10 knots at 6,000 feet, while the wind direction remained uniform up to the base of the inversion (4,000 feet at Bermuda, 7,000 to 8,000 feet at Ship E). Above the inversion the winds backed to a northerly direction, indicating cold advection.

THE PACIFIC CASES

The surface map corresponding to the cloud pattern of Figure 170 is shown in Figure 179, and that corresponding to Figure 171 is shown in Figure 180. In both figures the track of the satellite is shown and the area occupied by a cellular cloud pattern is outlined. The synoptic conditions accompanying the cloud pattern of Figure 170 will be discussed first.

As may be seen in Figure 179, the surface flow in the region outlined varied from anticyclonic to cyclonic, in contrast to the anticyclonic flow accompanying Figure 169. But surface reports in

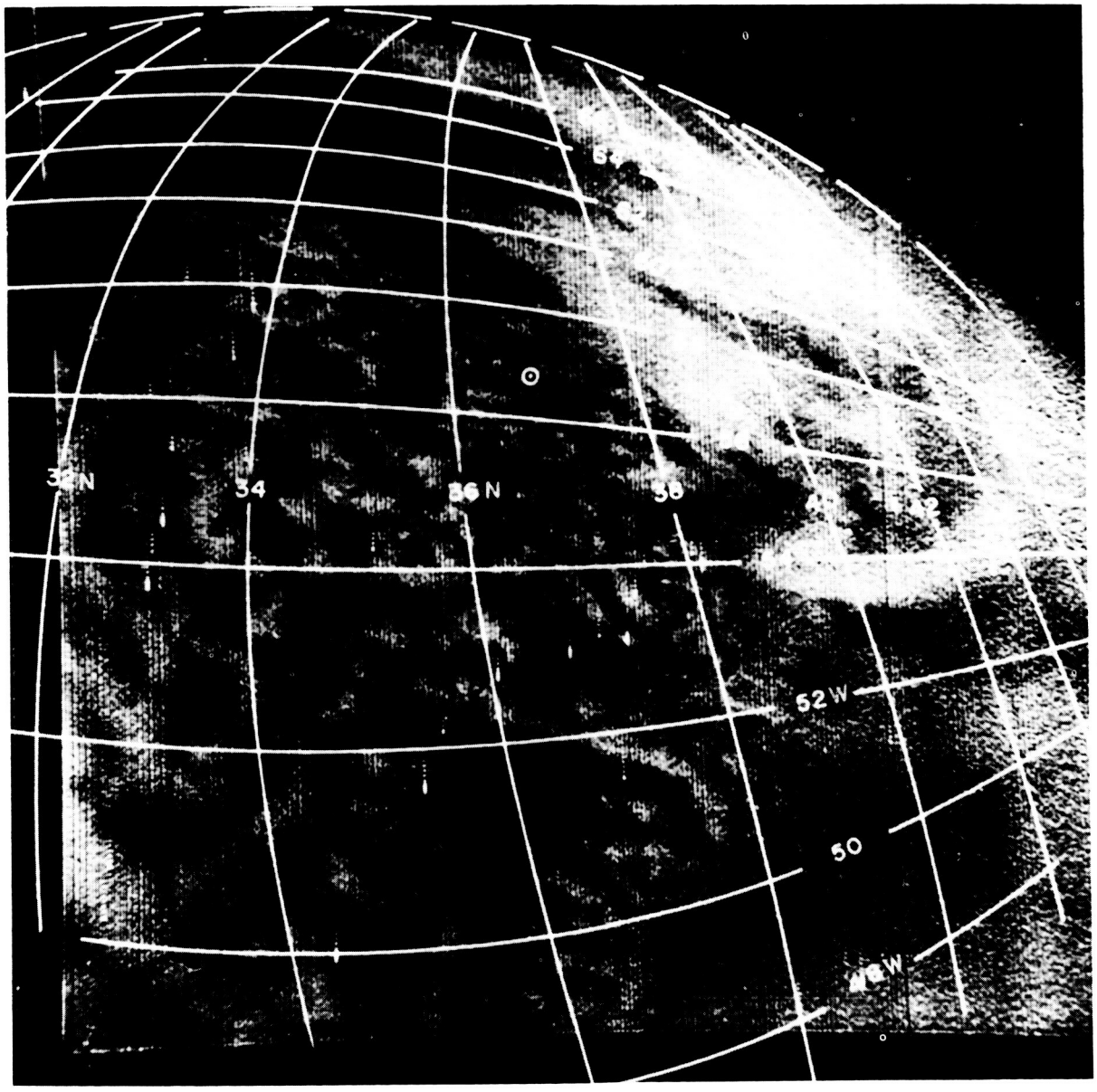

FIGURE 172.—The same photograph as Figure 169 with superimposed 2° latitude-longitude grid prepared by the methods of Appendix A. The principal point, or optical center, of the photograph is shown by the circled dot.

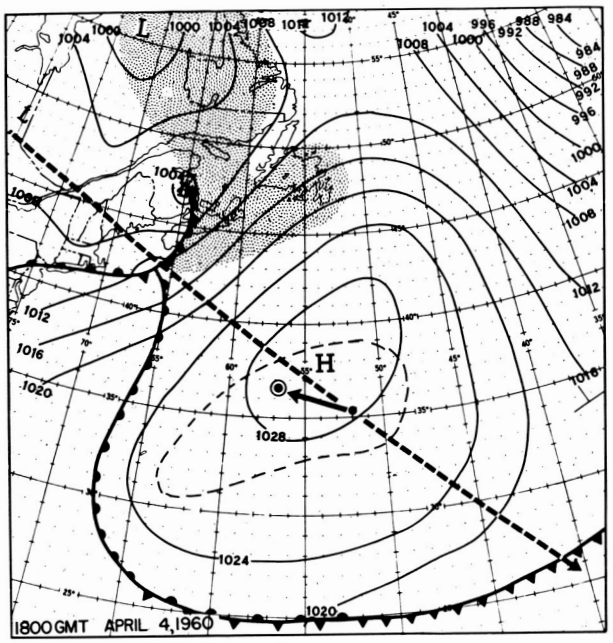

FIGURE 173.—Surface weather map for 1800 GMT, April 4, 1960, showing the satellite's track on its 46th orbit (heavy dashed line); the satellite's location when Figure 169 was taken (dot); the optical center (circled dot); the camera's orientation (arrow); and the area of the cellular cloud pattern of Figure 169 (light dashed line).

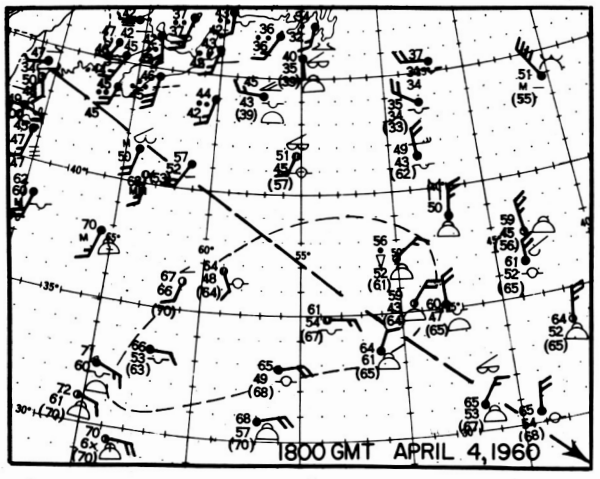

FIGURE 174.—Surface synoptic reports for 1800 GMT, April 4, 1960. The plotting model is abbreviated. The numbers in parenthesis are ocean surface temperatures. The satellite's track on its 46th orbit is shown by a heavy dashed line. A light dashed line encloses the area of the cellular cloud pattern of Figure 169.

the area, except for the Aleutians, were almost nonexistent. These Aleutian reports did, however, indicate considerable amounts of stratocumulus clouds. Such a northerly current from the Bering Sea, as was observed over the area, would also be expected to undergo considerable heating at the ocean surface. The only radiosonde observation available was from Adak, 730 nautical miles to the northwest of the picture center, and was quite similar to those for the Atlantic case. Here the subsidence inversion was at 800 mb (Figure 181). Whether this sounding was representative of conditions in the central part of Figure 170 may be questioned, for it is generally expected that cyclonic flow is more unstable throughout a deeper layer than anticyclonic flow.[1] That this may not be the case here is suggested by the Joint Numerical Weather Prediction Unit vertical motion computations (not shown). The JNWP chart, applicable at 600 mb, showed subsiding motion over the picture area and suggested that an inversion should form at the base of this subsiding layer with the cellular pattern confined to the convective layer below 600 mb. Some indication of greater vertical development, however, is suggested in the immediate foreground of Figure 170, where a blurred appearance may represent anvil tops from cumulonimbus or patches of altostratus.

The second Pacific case (Figure 171) shows the smallest cellular pattern of the three. This pattern is located in northerly flow with the isobar

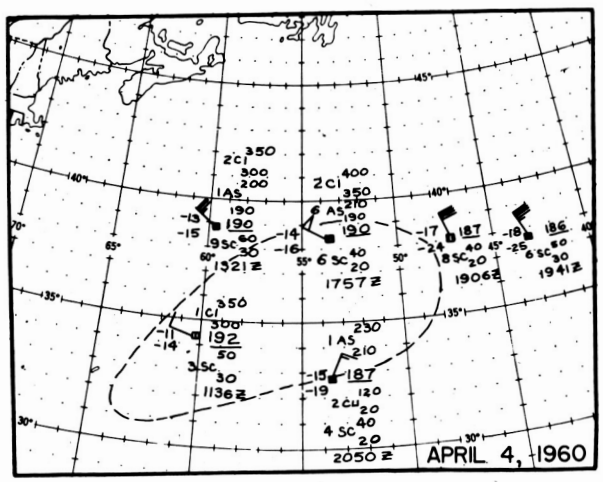

FIGURE 175.—Aircraft reports for the period 1200 GMT to 2300 GMT, April 4, 1960. A dashed line encloses the cellular cloud area of Figure 169.

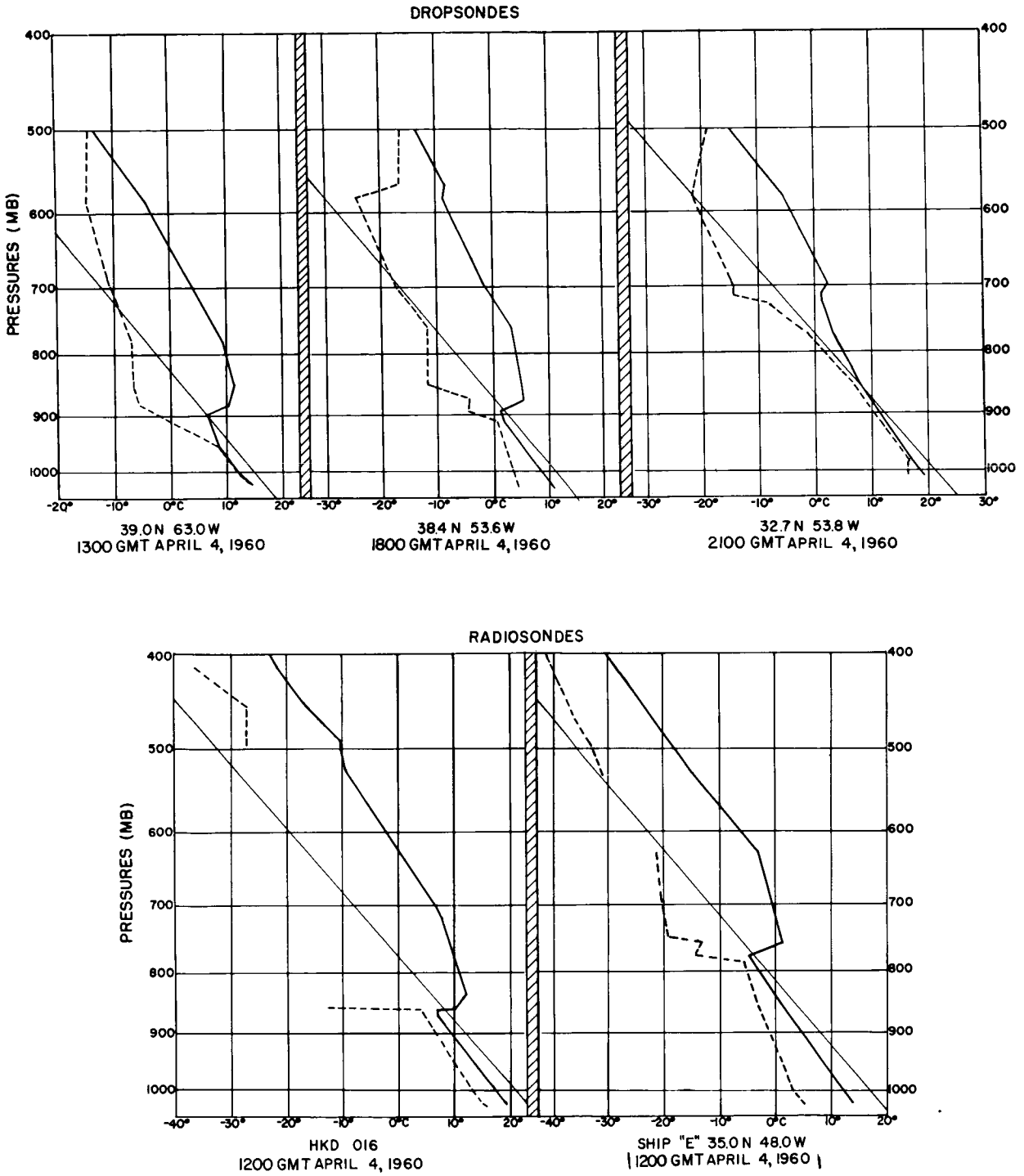

FIGURE 176.—Aircraft dropsonde observations at locations indicated, and radiosonde observations at Bermuda and Ship E between 1200 GMT and 2100 GMT, April 4, 1960. The solid lines show temperature distributions; the dashed lines, dewpoint distributions.

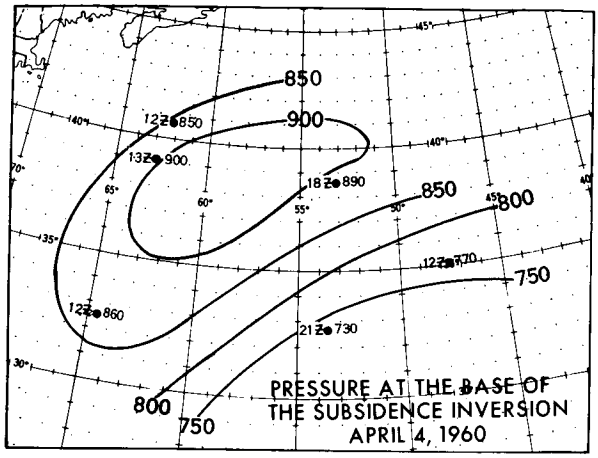

FIGURE 177.—Topography, in intervals of 50 mb, of the pressure at the base of the subsidence inversion April 4, 1960, computed primarily from the data of Figure 176.

curvature varying from anticyclonic to cyclonic across the area and occur to the rear of the cutoff low discussed in Chapter 10. In this area stratocumulus clouds were reported, and surface heating was indicated from the sea-air temperature difference. One radiosonde observation available in the area was quite typical of the others cited earlier (Figure 182). The significant difference of this case from the Atlantic case, however, was in the surface wind velocities: up to 30–35 knots compared with 12–20 knots for the Atlantic. Pilot balloon observations were not available except from a ship about 300 nautical miles to the south, and this indicated little variation in direction or speed up to 5,000 feet.

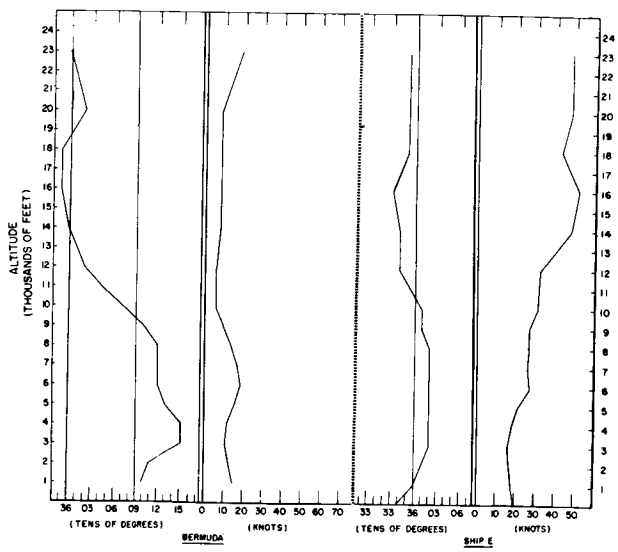

FIGURE 178.—Upper wind soundings for Bermuda at 1200 GMT and Ship E at 1800 GMT, April 4, 1960.

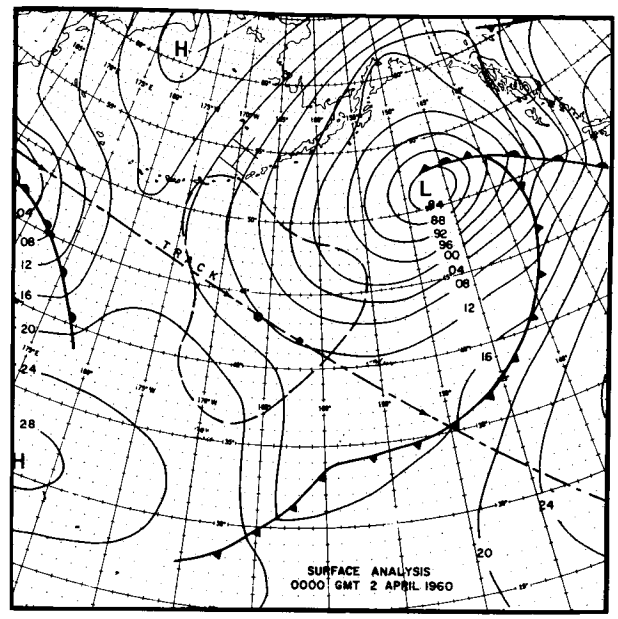

FIGURE 179.—Surface weather map showing sea-level isobars and fronts, 0000 GMT, April 2, 1960, showing the satellite's track on its 7th orbit (broken line); the satellite's location when Figure 170 was taken (dot); the optical center (circled dot); and the cellular cloud area of Figure 170 (dashed line).

SUMMARY

A study of the synoptic observations accompanying the three satellite pictures of cellular cloud formations described in this report indicated that: (1) a layer of moist air about 5,000 feet deep was heated at the ocean surface, resulting in an adiabatic lapse-rate; (2) superimposed over this layer was another of greater stability which served to inhibit the convection; and (3) throughout the convective layer there appeared to be little variation in wind speed and direction above that portion influenced by surface friction.

These distinctive cloud patterns, especially those in Figure 169, have the appearance of Bénard cells. There are, however, many important physical differences between the patterns observed by TIROS I and those observed in the laboratory.

Author

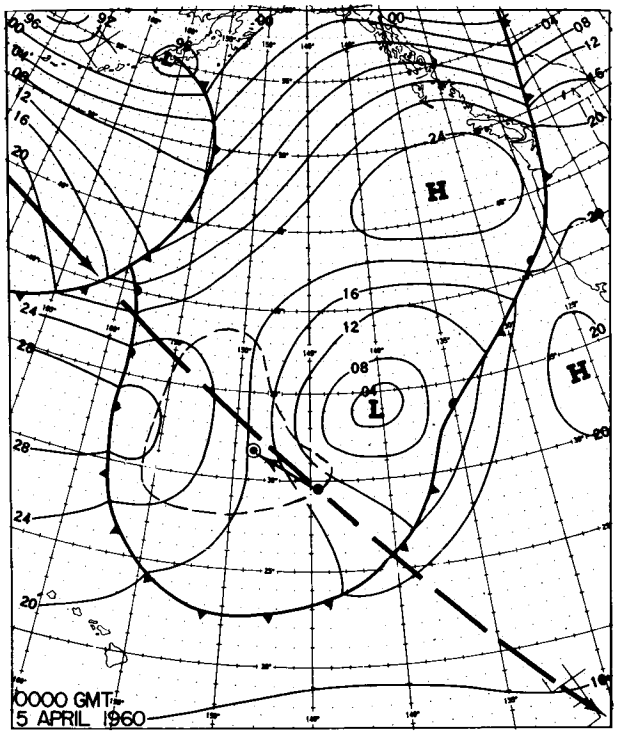

FIGURE 180.—Surface weather map showing sea-level isobars and fronts, 0000 GMT, April 5, 1960, showing the satellite's track on its 50th orbit (heavy dashed line); the satellite's location when Figure 171 was taken (dot); the optical center (circled dot); the camera's orientation (arrow); and the cellular cloud area of Figure 171 (light dashed line).

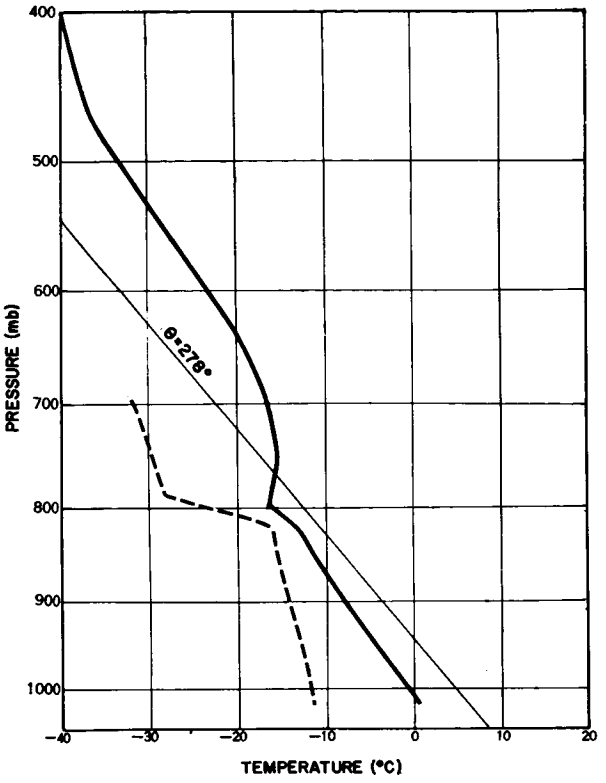

FIGURE 181.—Radiosonde observation at Adak, Alaska, 0000 GMT, April 2, 1960, at 51°53′ N. 176°39′ W. The solid line shows temperature distribution; the dashed line dewpoint distribution.

PHYSICAL NATURE OF CELLULAR CONVECTION

Cellular convection was first studied in detail by Bénard early in the century (cf. D. Brunt[2]). The patterns he observed in unstable liquids consisted of cells with upward motions in the center and descent at the periphery. His findings led him to suggest that certain cloud patterns, such as cirrocumulus, might represent cellular convection. Stimulated by his pioneering, other investigators undertook the study of these Bénard cells and attempted to relate their findings to atmospheric cloud patterns. Theoretical work was originated by Rayleigh[3] who determined the onset criterion. This criterion indicates that Bénard convection will not occur unless the density at the top of a fluid layer exceeds that at the bottom by an amount that varies directly as the molecular heat conductivity and viscosity, and inversely as the cube of the depth of the fluid.

The cloud patterns illustrated in this chapter, presumably with upward motion and cloudiness at the periphery and descent in the clear centers, are more typical in general appearance of cellular patterns obtained from convection experiments with an unstable layer of air.[4, 5] In these experiments smoke-laden air confined within a suitable container is destabilized, usually by heating from below. If no shearing motion in the vertical is present, it is found that the mixture breaks up into a series of polygonal cells that have the intracellular motion just described. The observed polygonal pattern is an unsteady one, displaying a tendency for the cells to join into long rolls, and the rolls in turn breaking up into polygonal cells. Increasing the depth of the chamber—or instead, increasing the vertical temperature gradient—results in an increase in the cellular diameter, but the ratio of this diameter to the depth of the convective layer remains about three to one. This cellular configuration with its characteristic intra-

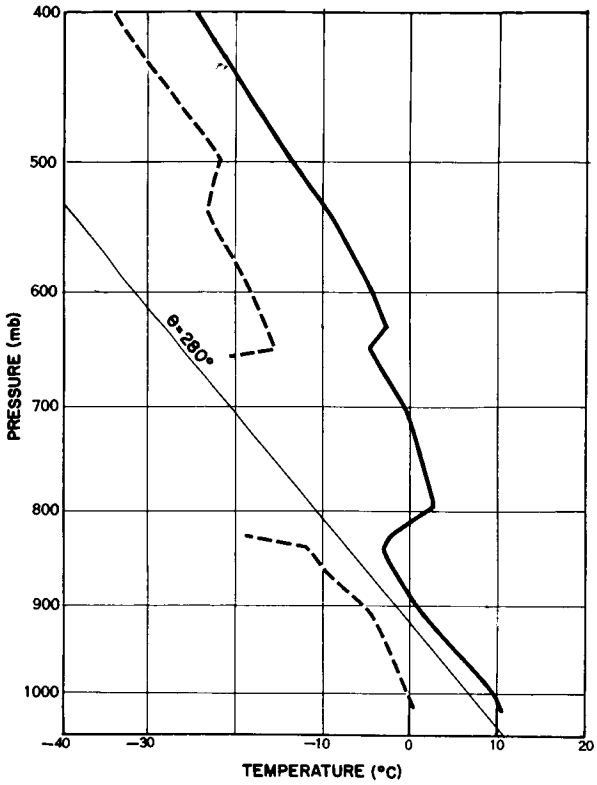

FIGURE 182.—Radiosonde observations at Ship NHXN (34.9° N, 150.4° W), 0000 GMT, April 5, 1960. The solid line shows temperature distribution; the dashed line dewpoint distribution.

cellular circulation has hitherto rarely been observed in natural cloud patterns, and consequently the reverse type, characteristic of cellular convection in liquids, has been the expected one.[2]

Although observations of cellular convection by TIROS I have the appearance of experimental and theoretical studies of Bénard cell convection, significant differences are evident. If the observations presented here are to be compared with Bénard phenomena, then certain problems suggest themselves. One of these is related to scale. For example, in laboratory and theoretical studies a diameter to depth ratio of three to one is obtained.[4, 6] In this study a value 10 times as large was obtained—a ratio that is, interestingly, comparable to that found by Woodcock and Riley [7] from a study of cellular patterns in pond ice. Clearly, further investigation into the physical parameters that determine scale is required.

Another problem is related to the detailed structure of the convection cells. This is apparent from an examination of a narrow angle TIROS I picture corresponding with Figure 169 (not shown here) where it is seen that the cell walls are often made up of individual cloud elements. This is verified by surface observations of stratocumulus in the area (Figure 174). Thus the TIROS cellular cloud pictures indicate several scales of motion, while in contrast the typical Bénard cell as obtained in the laboratory appears to possess a very simple structure and circulation.

Further difficulties involve the treatment of heat conduction and viscosity since, at this scale, the use of eddy coefficients is required, and these vary widely in space and time. Also, the release of latent heat, the compressibility, and perhaps the spatial variation of heating should be considered. Some of these problems have been discussed by Malkus [8] in an interesting review of the convective cloud problem.

The observations presented in this chapter are but a few examples of cellular convection obtained during the lifetime of TIROS I. Many other examples remain to be studied. For, among its many findings, TIROS I has indicated that cellular convection occurs at a larger scale, and over a greater portion of the earth's surface, than has heretofore been realized. These observations should stimulate an increase of interest in this challenging problem.

REFERENCES

1. Petterssen, S., Knighting, E., James, R. W., and Herlofson, N., "Convection in Theory and Practice," Geofysiske Publikasjoner 16(10), 1946.
2. Brunt, D., "Experimental Cloud Formation," in: Compendium of Meteorology, 1255–1262, Boston: American Meteorological Society, 1951.
3. Rayleigh, Lord, "On Convections Currents in a Horizontal Layer of Fluid, When the Higher Temperature Is on the Under Side, "Phil. Mag. 32(192): 529–546, December 1916.
4. Chandra, K., "Instability of Fluids Heated From Below," London, Proc. Roy. Soc. 164–A(917): 231–242, January 21, 1938.
5. Graham, A., "Shear Patterns in an Unstable Layer of Air," Phil. Trans. Roy. Soc. London 232–A: 285–296, April 1934.
6. Nakagawa, Y., and Frenzen, P., "A Theoretical and Experimental Study of Cellular Convection in Rotating Fluids," Tellus 7(1): 1–21, February 1955.
7. Woodcock, A. H., and Riley, G. A., "Patterns in Pond Ice," J. Meteorol. 4(3): 100–101, June 1947.
8. Malkus, J. S., "Recent Advances in the Study of Convective Clouds and their Interaction with the Environment," Tellus 4(2): 71–87, May 1952.

CHAPTER 16

CLOUD STREETS IN THE CARIBBEAN SEA*

by

JOHN SCHUETZ and SIGMUND FRITZ

INTRODUCTION

TIROS I[1] presented an opportunity to view the meso-scale structure of cloud system as well as the large-scale structure.[2, 3, 4, 5] The meso-scale structure is often better shown by the "narrow-angle" camera which, when pointing vertically downward from a height of 380 nautical miles, photographed an area whose diagonal was about 85 nautical miles across. Such detail permits the study of several interesting features of "cloud streets."

Such long, thin lines of clouds occur fairly frequently in the atmosphere. For example, Riehl et al.,[6] in a study of cumulus cloud bands in the tropical Pacific, found that the bands were oriented parallel to the low-level wind flow. Kuettner[7] presented several examples in which cumulus cloud streets were parallel to the wind; he also discussed the meteorological conditions under which such cloud bands will align with the wind. He considered mainly cloud streets formed when cold air flows over warm surfaces, although other types were also mentioned.

The TIROS I narrow-angle camera also photographed some cumulus cloud streets, and the relationship of the flow patterns to the orientation and other aspects of the streets shown in the pictures will be discussed here.

THE SATELLITE PICTURES

Figure 183 is a composite assembled from several narrow-angle pictures taken at 10-second intervals between 2030 GMT and 2033 GMT on April 1, 1960. The satellite was traveling from northwest to southeast (left to right in the composite). The camera axis was oriented slightly back and to the left at this time.

The white areas in Figure 183 are probably all cumuliform clouds. Grand Cayman Island is relatively cloud-free, while the western end of Cuba and the Isle of Pines are more cloud covered. Figure 184 is a schematic representation of the clouds shown in Figure 183.

The composite and the schematic diagram indicate a greater concentration of cumulus clouds over the heated land areas of the Isle of Pines and Cuba than over the adjacent ocean areas. This is perhaps better seen in Figures 185 and 186, which depict the detail of cloud masses over Cuba and over the Isle of Pines, respectively. (The shoreline of the islands is indicated by the white outline.) These figures show much more extensive cumulus activity over the heated islands than over the adjacent ocean areas.

This more extensive convective activity is apparently indicative of the greater instability over the islands. Comparison of the 0000 GMT, April 2, 1960, radiosonde observation (Figure 187) at Havana (considered representative of the heated air over the island of Cuba), with the radiosonde (Figure 188) at Grand Cayman (considered representative of the oceanic air) shows the Grand Cayman sounding to be more stable and drier, particularly in the region from 900 to 800 mb. Differences in heating doubtless account for much of this stability difference. An inspection of the sounding for 0000 GMT, April 2, and for 12 hours earlier (not shown here) at Havana (land influence) and at Grand Cayman (oceanic influence) shows that the lower layer at Havana experienced considerably more warming between early morning and evening than the lower layer did at Grand Cayman.

*A revised version of this paper appears in Monthly Weather Rev. 89(10) : 375–382, October 1961.

In NASA Goddard Space Flight Center Tiros I Meteorol. Satellite System 1962 p 213-220
rep Submitted for Publication (See N64-17906 (0-21) GPO: $2.25

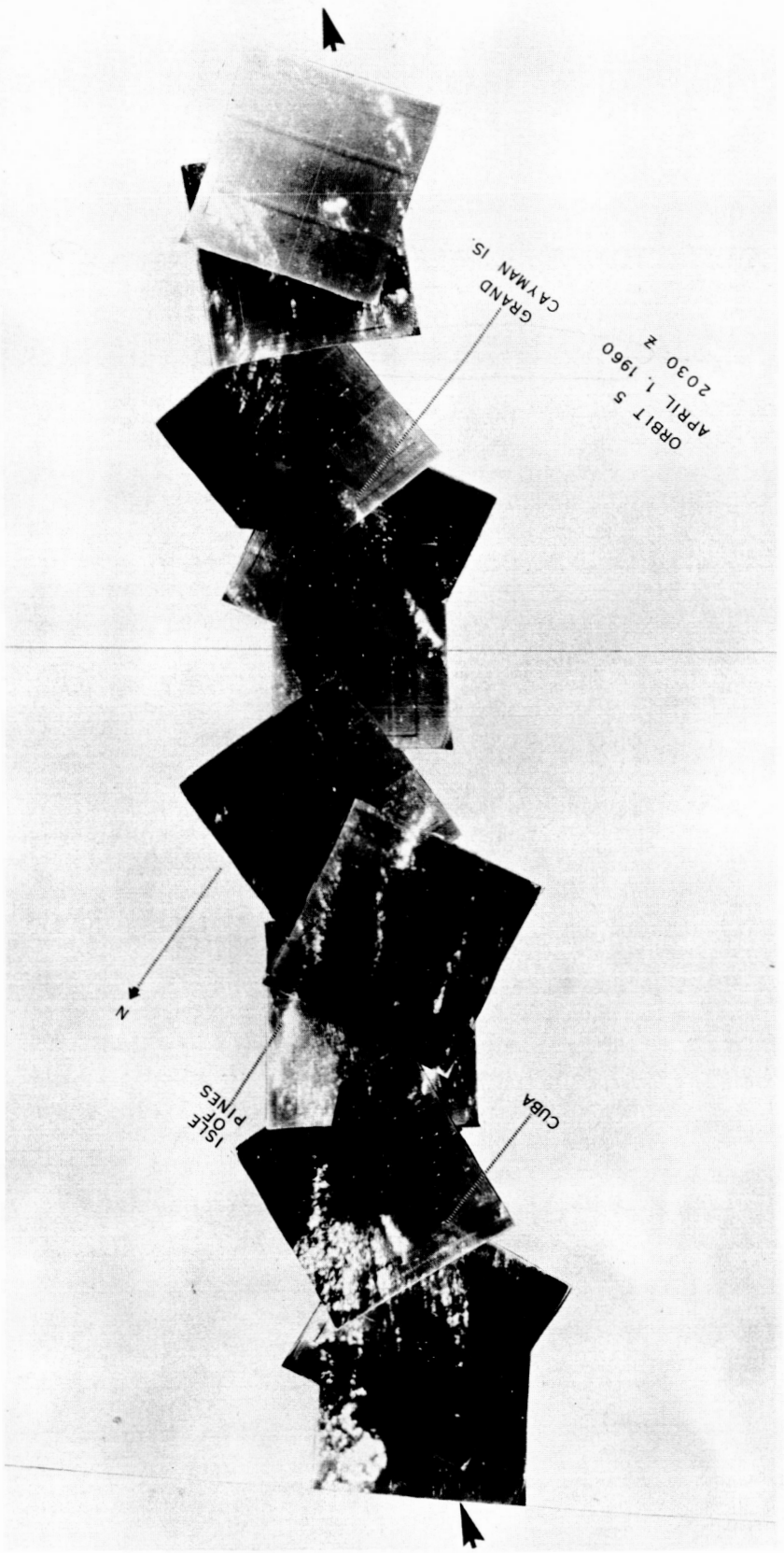

FIGURE 183.—Mosaic of narrow-angle photographs taken by TIROS I at 10-second intervals between 2030 and 2033 GMT, April 1, 1960, on its 5th orbit, showing cloud streets in the Caribbean Sea area.

CLOUD STREETS IN RELATION TO THE WIND FIELD

The tendency for cumulus clouds to line up in bands or streets under certain conditions has been pointed out.[6, 7] Kuettner[7] discusses some conditions required for the convectively formed clouds to align in bands parallel to the wind. In his observation, the wind direction was fairly constant throughout the convective layer; but a wind-speed maximum also existed within the convective layer, giving a negative mean curvature. The important parameter, according to Kuettner,[7] in determining whether such bands will align with the wind is the mean curvature of the vertical profile of the horizontal wind speed within the convective layer. He found typical values of this speed-curvature to be of the order of -10^{-7} cm^{-1} sec^{-1}.

Figures 189 and 190 show the wind direction and speed at Havana and at Grand Cayman as a function of height. (Note: The 0000 GMT April 2 wind record for Havana was missing; therefore the 1200 GMT April 1 wind sounding was used. This difference is probably not serious, since the synoptic situation in this region was generally unchanged in this 12-hour period.) The Grand Cayman wind profile (Figure 190) shows a well defined broad wind-speed maximum in the lower layers, while Havana (Figure 189) shows a poorly defined slight maximum at 10,000 feet. Although the wind maximum may not be significant for Havana, computation of the mean curvature in the first 12,000 feet indicated that the wind profile curvatures at both stations were negative and had values, within an order of magnitude, of 10^{-7} cm^{-1} sec^{-1}.

The cloud mosaic and schematic (Figures 183 and 184) show the cloud bands in the vicinity of the Isle of Pines and Cuba oriented at about 140 degrees and the three cloud bands, just southeast of the Isle of Pines, oriented at 150 to 160 degrees. In Figure 189 it can be seen that the winds at Havana in the first 12,000 feet were within 30 degrees of these orientations. In the layer from 2000 to 12,000 feet, the wind at Grand Cayman was between 120 and 140 degrees. Thus the cloud streets are aligned quite closely with the wind direction in the convective layer at the two stations.

Satellite pictures present an opportunity to observe spacing, shape and other characteristics of cloud bands. For example, the three cloud bands

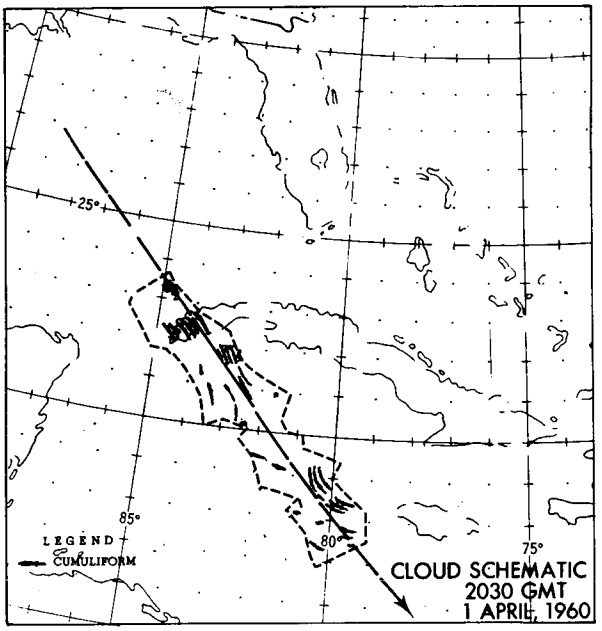

FIGURE 184.—Schematic representation showing the location of the cloud features of Figure 183. The irregular outline delineates the geographic coverage of the mosaic; the dashed line and arrow indicate the track of the satellite.

immediately south and southeast of the Isle of Pines just mentioned (Figure 183) are interesting because their length and of the large distances between them. Figure 191 shows these three bands in greater detail. The distance from the easternmost band in Figure 191 to the middle one is about 20 nautical miles, and from the middle band to the westernmost one is about 30 nautical miles. The length of the middle band (neglecting the brighter portion in the south, which may be part of another cloud band) is about 30 nautical miles, and of the other two about 50 nautical miles.

Noting again Figures 185 and 186, it can be seen that over the heated land masses of the Isle of Pines and Cuba the spacing of the bands is an order of magnitude smaller than the spacing over the ocean. Over Cuba the spacing is about 3 to 4 nautical miles; over the Isle of Pines, about 2 to 3. Moreover, the length of these lines appears to be related to the distance across the island in the direction of the wind flow. For example, the bands (Figure 185) over extreme western Cuba are shorter than those farther east over Cuba; the bands over the very narrow southwestern portion of the Isle of Pines (Figure 186) are much shorter than those over the northeastern portion of the

island. The distances across the islands in the direction of the wind flow vary in a similar manner.

In the extreme southeastern end of the picture swath, some anticyclonically(?) curved bands, which were embedded in the general southeasterly flow, were noted (Figures 183 and 184). These are illustrated more clearly in Figure 192. The radius of curvature of these bands is 60 nautical miles and they are spaced at intervals of 3 to 4 nautical miles. Meteorological observations in this area were too sparse to determine whether a circulation of such a small scale existed. Nevertheless the curvature in the cloud streets suggests that such small undulations in the circulation may have existed.

CONCLUSION

The TIROS narrow-angle camera presents a means of determining such factors as orientation, spacing, and length of cloud streets. In this study the streets were aligned within 30 degrees of the wind direction in the convective layer. The spacing of the streets over heated land was much less than those over the ocean. The length of the

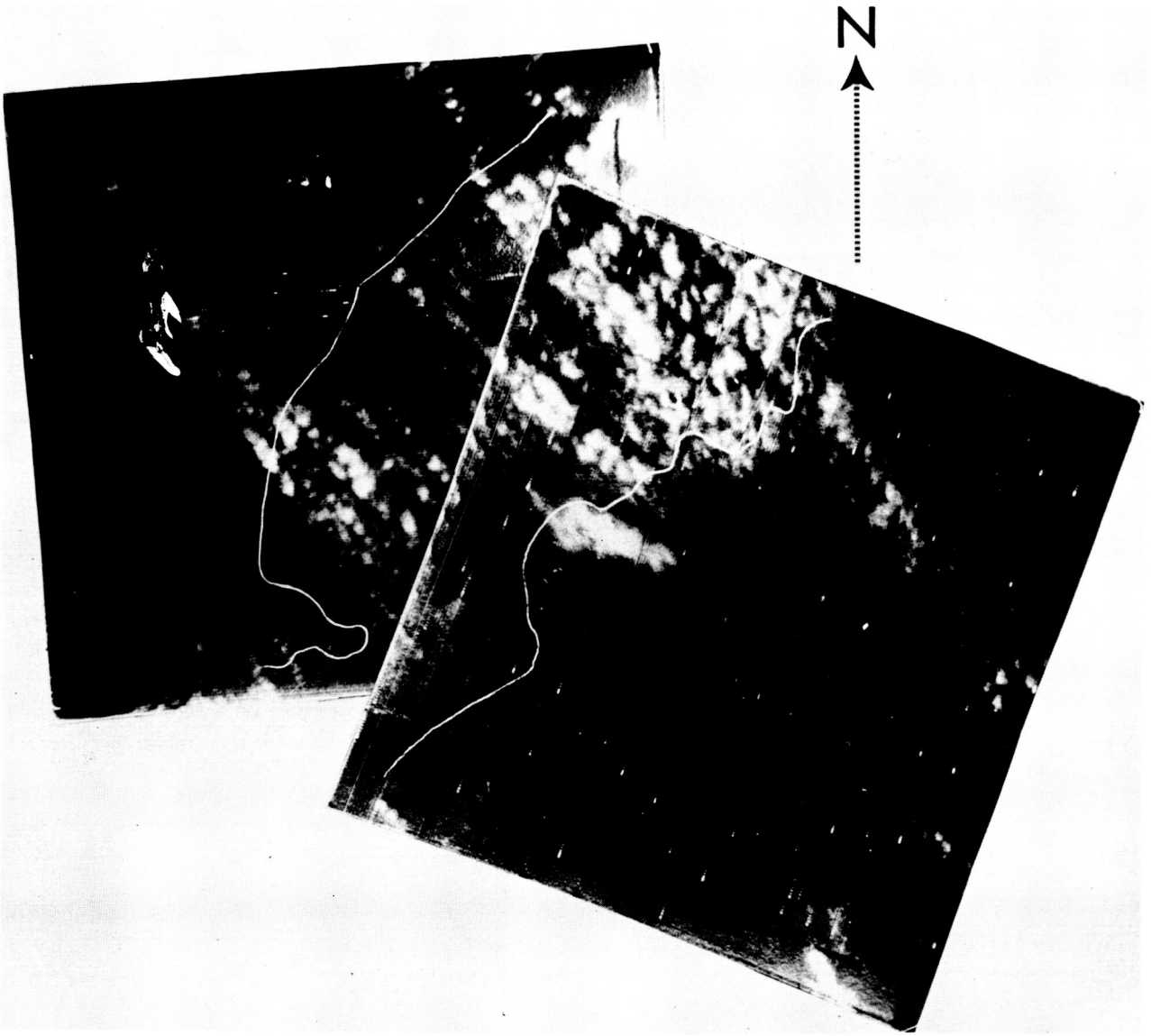

FIGURE 185.—Detailed composite of the portion of the mosaic showing Cuba. The coastline is outlined in white.

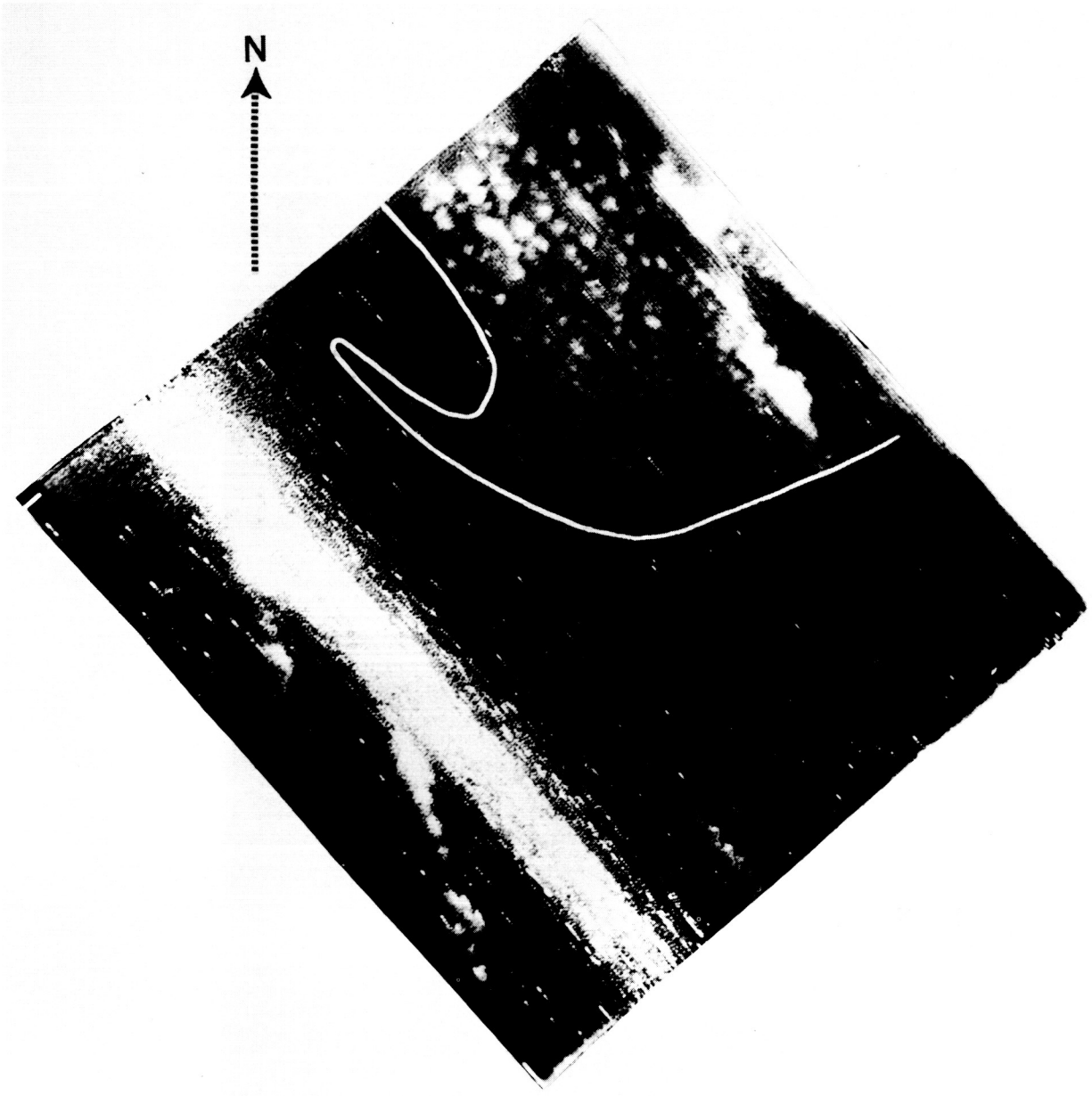

FIGURE 186.—Detailed view of the cloud streets over the Isle of Pines. The coastline is outlined in white.

646-770 O - 64 - 15

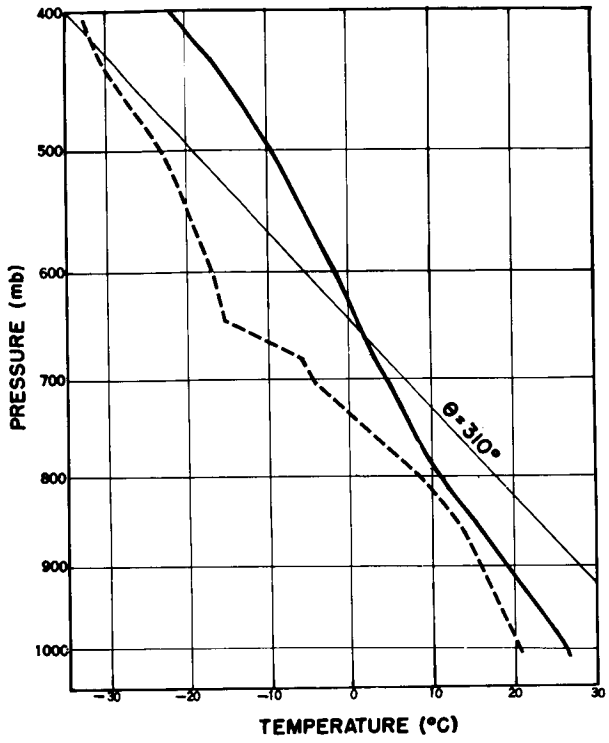

FIGURE 187.—Radiosonde observations at Havana for 0000 GMT, April 2, 1960. The solid line shows the temperature distribution; the dashed line, dewpoint distribution.

streets over the larger islands appeared to be related to the distance across the island in the direction of the wind flow.

REFERENCES

1. Sternberg, S., et al., "Roundup on TIROS I," Astronautics 5(6) : 32–102, 33, June 1960.
2. Fritz, S., and H. Wexler, "Cloud Pictures From Satellite TIROS I," Monthly Weather Rev. 88(3) : 79–87, March 1960.
3. Winston, J. S., and Tourville, L., "Cloud Structure of an Occluded Cyclone Over the Gulf of Alaska as Viewed by TIROS I," Bull. Amer. Meteorol. Soc. 42(3) : 151–165, March 1961.
4. Fritz, S., "Satellite Cloud Pictures of a Cyclone over the Atlantic Ocean," Quart. J. Roy. Meteorol. Soc. 87(373) : 314–321, July 1961.
5. Bristor, C. L., and Ruzecki, M. A., "TIROS I Photographs of the Midwest Storm of April 1, 1960," Monthly Weather Rev. 88 (9–12) : 315–326, September–December 1960.
6. Riehl, H., Gray, W. S., Malkus, J. S., and Ronne, C., "Cloud Structure and Distribution over the Tropical Pacific," Woods Hole Oceanographic Institution, Tech. Report No. 5, January 1959.
7. Kuettner, J., "The Band Structure of the Atmosphere," Tellus 11(3) : 267–294, August 1959.

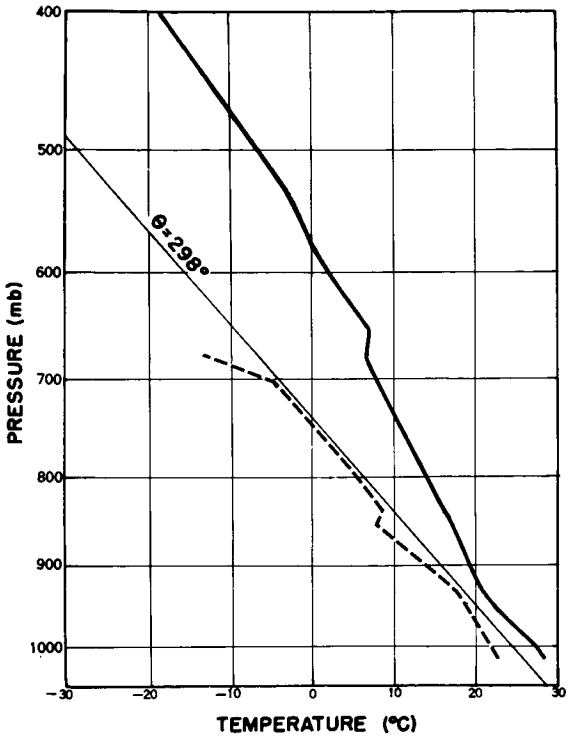

FIGURE 188.—Radiosonde observations at Grand Cayman Island for 0000 GMT, April 2, 1960. The solid line shows the temperature distribution; the dashed line, dewpoint distribution.

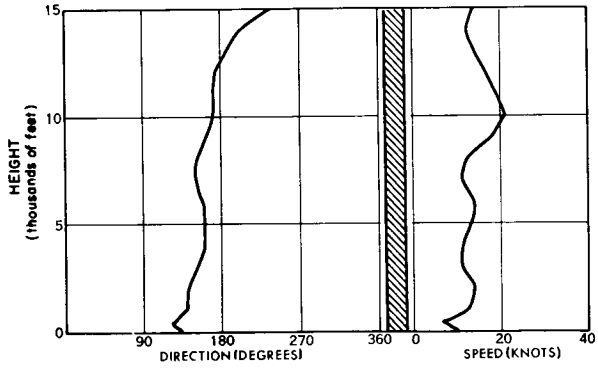

FIGURE 189.—Wind speed and direction as a function of height for Havana at 1200 GMT, April 1, 1960.

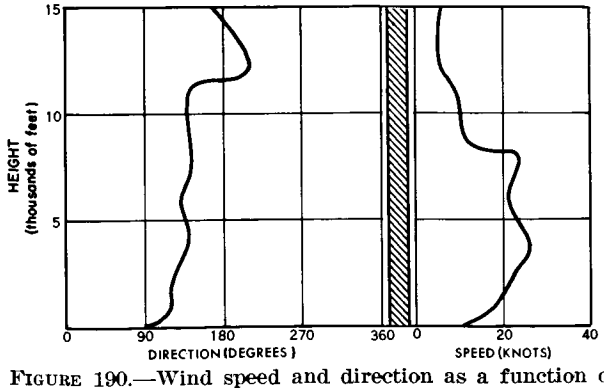

FIGURE 190.—Wind speed and direction as a function of height for Grand Cayman Island at 0000 GMT, April 2, 1960.

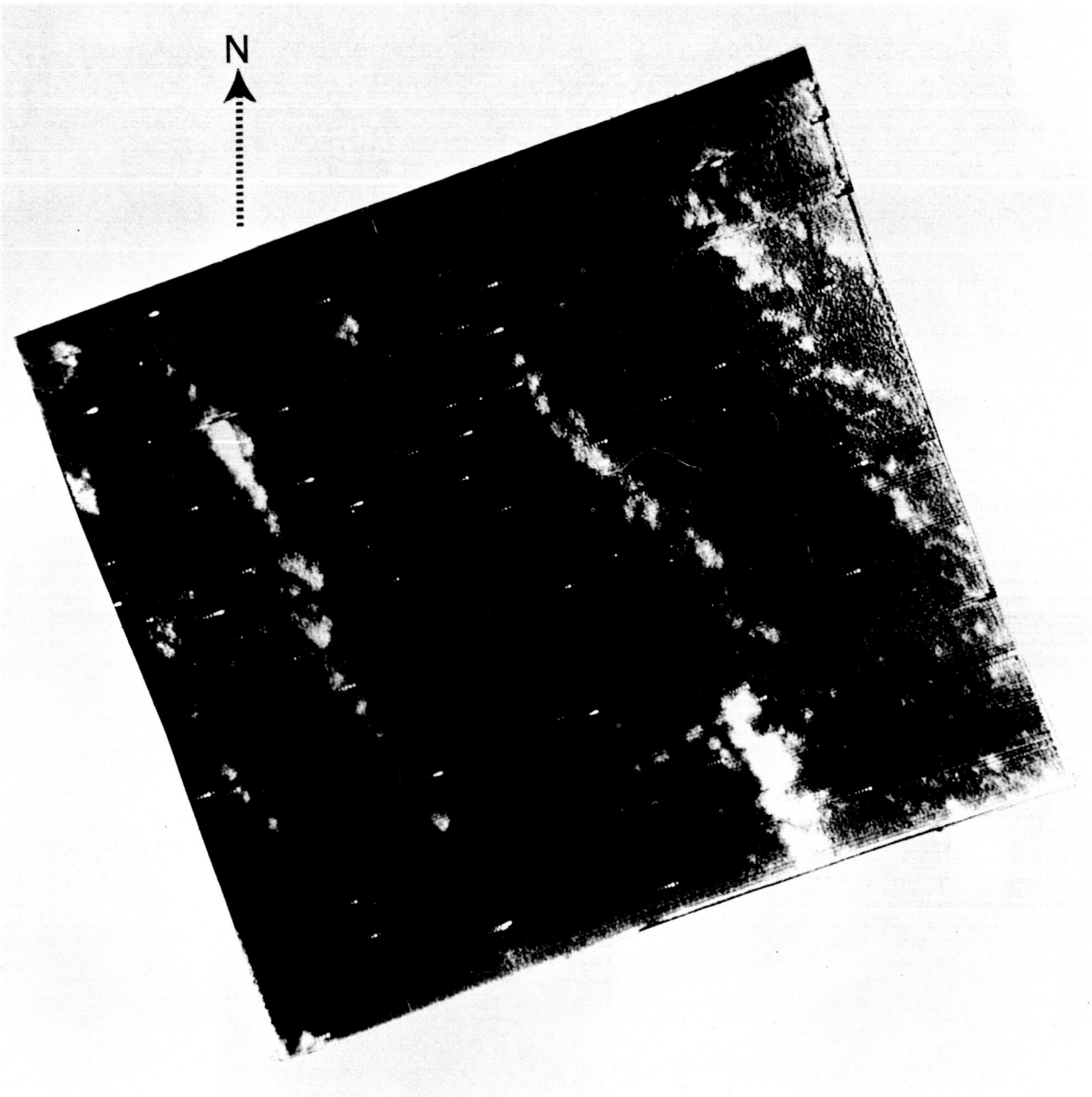

FIGURE 191.—Larger picture of the three oceanic cloud bands shown in Figure 183.

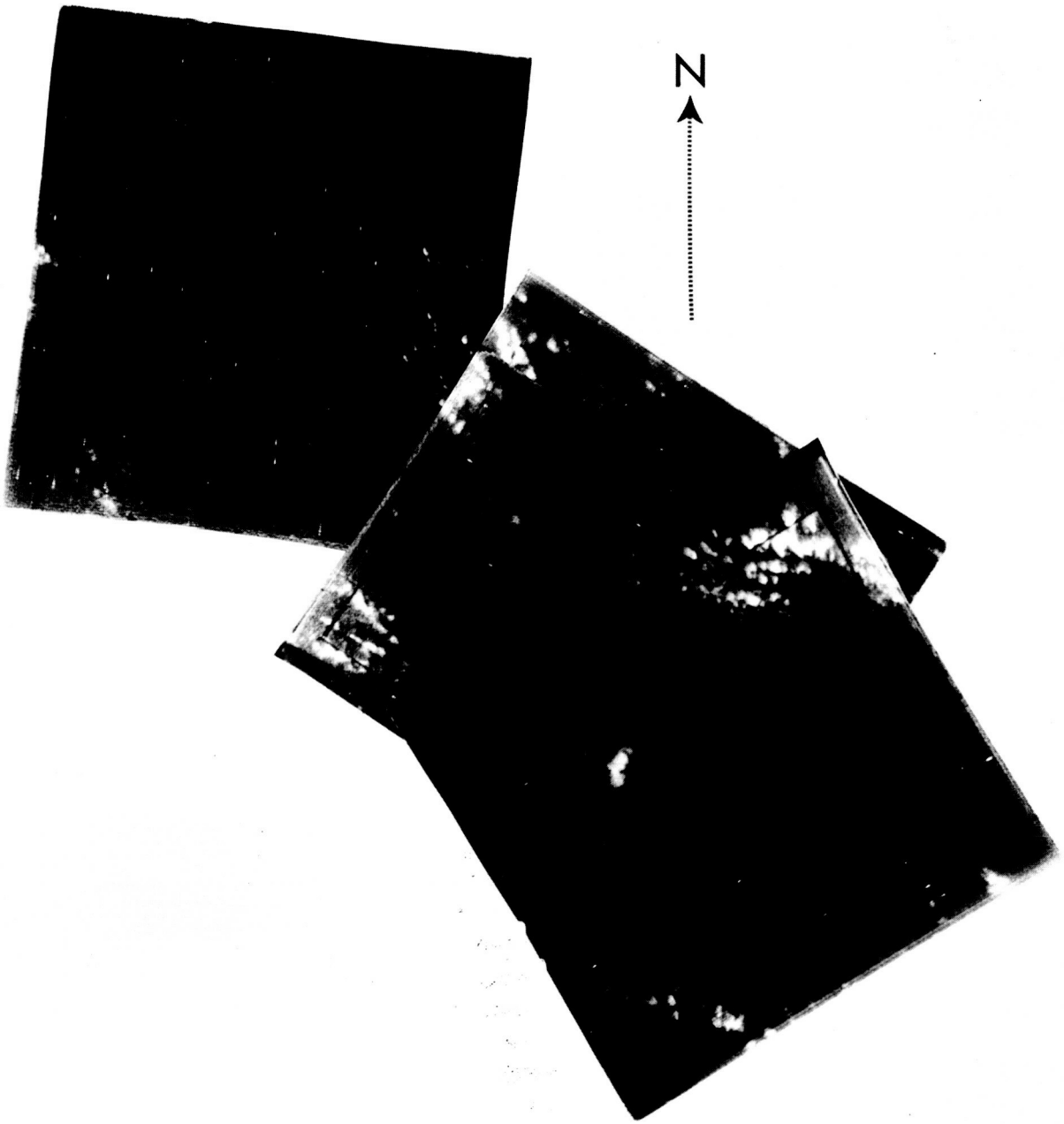

FIGURE 192.—Composite showing the greater detail of the curved bands seen in Figure 183.

CHAPTER 17

A TORNADO-PRODUCING CLOUD MASS SEEN FROM TIROS I*

by

LINWOOD F. WHITNEY, JR., and SIGMUND FRITZ

INTRODUCTION

Several tornadoes were reported in Oklahoma and Kansas during the afternoon of May 19, 1960. On the same afternoon, TIROS I photographed a series of pictures over the central United States. When these pictures were examined for any unusual cloud formations which might be associated with severe local storm activity, one striking and unusual photograph (Figure 193, taken at 2000 GMT) showed a small, isolated cloud which appeared as a very bright square straddling a faint but sharp, smooth line. As Hoecker [1] has pointed out, in many cases at least one side of a tornado cloud is adjacent to a cloudless area. Since it was known that tornadoes and hailstorms had broken out in Oklahoma on a line between Fort Sill and Oklahoma City within 2 hours following the time of the picture, it seemed logical to investigate the possibility that the "square" cloud mass represented the incipient stages of a severe weather system. This report presents the results of the investigation to date.

DISCUSSION AND RECTIFICATION OF THE TIROS I PICTURE

In order to examine the picture in more detail and to compare it with the meteorological analysis, it was necessary that the size and locations of cloud features be determined. This was done with the aid of a latitude-longitude grid prepared by the technique described in Appendix A. A schematic cloud analysis based on the gridded picture is illustrated in Figure 194.

It has been determined that TIROS I was over the extreme southeastern part of Iowa looking obliquely back along its southwest-to-northeast trajectory when the photograph (Figure 193) was taken. Only those portions of the photograph which are discernible and essential to this investigation are shown in the schematic.

The cloud schematic (Figure 194) shows that the bright, isolated cloud, a rhombic configuration about 100 miles on a side, was centered along the Texas-Oklahoma border between Childress and Wichita Falls, Texas. This bright cloud area was superimposed on the faint but sharp line separating clear skies from partly cloudy skies (Figure 193). This line was a synoptic-scale feature, several hundred miles in length, extending south-southwestward from Wichita, Kansas, past San Angelo, Texas.

The southern part of the extensive cloudiness at the top of Figure 193 covered a large area which encompassed much of the states of Colorado, Nebraska, and Kansas. The cloud bands at the bottom right of the picture were oriented east-southeast to west-northwest and lay across eastern Oklahoma and adjoining portions of Missouri, Kansas, and Arkansas. Still other features, such as the relatively dark areas just north and south of the bright, isolated cloud, may be located by comparison of Figures 193 and 194.

METEOROLOGICAL ANALYSIS

Hourly surface charts for the period 1900 through 2200 GMT, May 19, 1960 (Figures 195 through 198), were analyzed for an area bounded by latitudes 30° N and 41° N and by longitudes 90° W and 105° W, and accelerated microbarograph traces in the area of the bright cloud mass were studied. To supplement this surface information, the Wichita Falls, Texas, radar and upper-air information (Figure 199) were briefly investigated. The primary purpose of these

*A revised version of this manuscript appears in Bull. Amer. Meteorol. Soc. 42(9) : 603–613, September 1961.

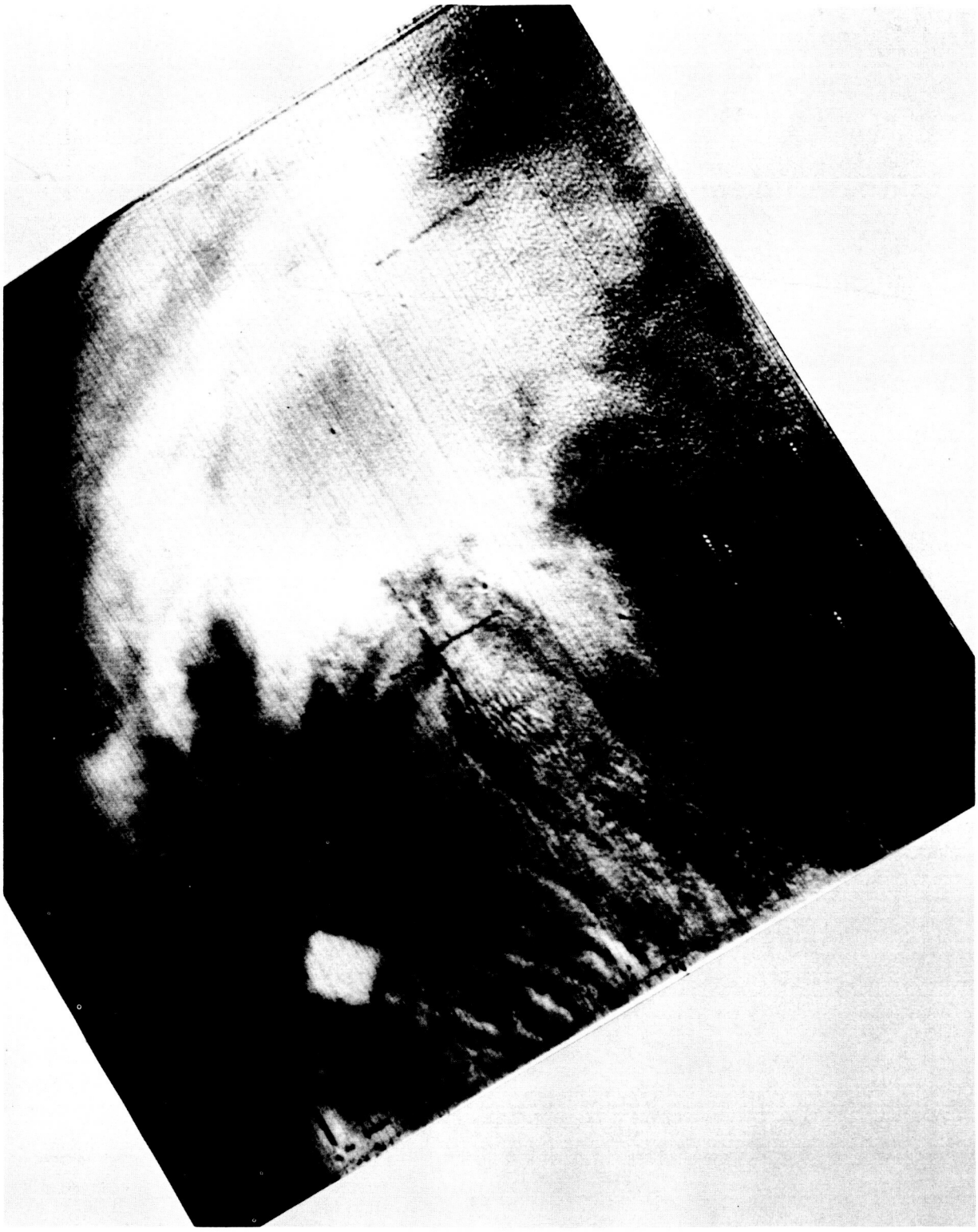

FIGURE 193.—Wide-angle photograph taken by TIROS I at 2000 GMT, May 19, 1960, over the extreme southeastern part of Iowa with the camera aimed obliquely toward the southwest and overlooking much of the Central and Southern Plains. The photograph is so oriented here that north is approximately up. The "square" cloud mass is at the bottom center.

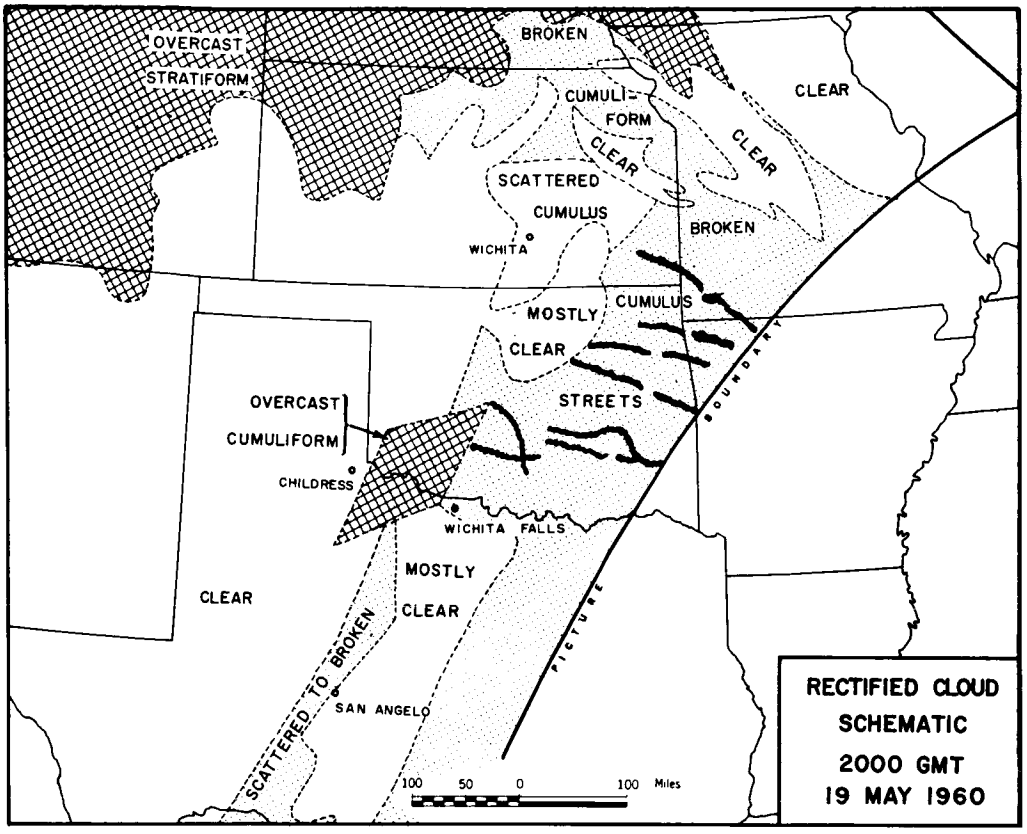

FIGURE 194.—Schematic geographical location of the cloud features appearing in the lower portion of Figure 193. Note that the "square" cloud assumed a rhombic shape after rectification.

analyses was to examine the history of any small-scale convective activity in the area for a period bracketing the time of the picture, and thus to determine tthe connection between the clouds seen in the picture and the physical state of the atmosphere.

The general synoptic situation did not change appreciably over this 3-hour period. A frontal system at the forward edge of a continental polar air mass extended southward from a parent low in central Manitoba, Canada, through a wave in south central Kansas and thence southwestward as a weak cold front across the Texas "Panhandle" into New Mexico. Several minor waves moved along the front in the Panhandle over the period (Figures 195 through 198). A small low persisted in the area of Tucumcari, New Mexico, and Dalhart, Texas. Cloudy skies dominated the cold air over Colorado and western Kansas. A line of sharp moisture gradient extended southward from the cold front near Hobart, Oklahoma, past San Angelo, Texas, separating a hot, dry, southwesterly flow in west Texas from a hot, moist flow in east Texas—the dewpoints being in the 20's to 50's (° F) to the west and upper 60's and lower 70's to the east (Figure 196).

Synoptic reports for 1800 GMT (1200 CST) gave no indication of thunderstorm activity or even heavy cumulus buildups within the area of interest. By 1900 GMT (1300 CST), however, Hobart, Oklahoma, and Childress, Texas, both reported viewing cumulonimbus and towering cumulus activity in the direction of the moisture gradient at the Texas-Oklahoma border (Figure 195). Wichita Falls, Texas, though not reporting heavy cumulus, did record a weak line of radar echoes to the west in the same area (Figure 199). There were no other reports of heavy cumulus activity near the southern Oklahoma border. Overcast skies were primarily restricted to the large cloudy area within the cold air.

At the time (2000 GMT) TIROS I took the photograph of Figure 193, Wichita Falls first reported cumulonimbus clouds to the west (Figure

196), while the line of radar echoes seen the previous hour was closer to the station and more intense (Figure 200). At Hobart, a thunderstorm was observed south of the station, and Childress continued reporting cumulonimbus and towering cumulus to the east—further evidence of a confined region of strong vertical motion along the moisture gradient line at the Oklahoma border. In general, cloudiness had increased appreciably all along the southern border of Oklahoma.

An examination of the two succeeding surface charts (Figures 197 and 198) shows that the convective activity spread from the dewpoint discontinuity northeastward ahead of the cold front, engulfing Fort Sill and Oklahoma City. During the same 2-hour period (2000–2200 GMT), Wichita Falls noted increasingly stronger and larger radar echoes which appeared to be moving northeastward along the echo line (Figure 199, c and d). Hail began between Fort Sill and Oklahoma City shortly before 2200 GMT (Figure 198), and hail and tornadoes occurred thereafter until 2300 GMT. Those tornadoes and hailstorms which occurred within a half hour of 2200 GMT are located in Figure 198. A summary of all severe local storm reports in southwestern Oklahoma up to 2300 GMT appears in Table 1.

The moisture discontinuity mentioned above is a phenomenon frequently observed in the western plains and has been referred to as the dewpoint "front." Fulks [2] has described in detail a mechanism behind the development of this gradient. Briefly, the gradient occurs when the shallow leading edge of maritime polar (mP) air from the Pacific is strongly modified by heating and drying as it moves over the plateau region and the Rockies, and encounters maritime tropical (mT) air in the western plains. The mP air by virtue of the modification becomes essentially a continental tropical (cT) air mass.

Three soundings (Figure 200) taken at 1800 GMT, two in the mT air and the other in cT air, clearly illustrate the air-mass difference across the moisture discontinuity. Fort Worth and Oklahoma City, located in the mT air mass, demonstrate the type of sounding frequently found in mT air; that is, a shallow warm, moist surface layer topped by an inversion. Midland, Texas, on the other hand, was in the cT air mass, and characteristically was warm with no inversion in the troposphere and extremely dry. By comparison, it can be seen that Midland was potentially warmer below 850 mb than was Fort Worth, while above that level there was little difference.

The moisture gradient or dewpoint "front" is of particular interest here since the convective activity appears to have developed on it. This "front," and moisture gradients in general, have been mentioned or implied in the literature as a factor in tornado development in the Plains. Hanks and Neubrand,[3] for instance, found that the tornado producing squall line of April 2, 1956 formed along a dewpoint "front." Provided that all their tornado criteria are fulfilled, Fawbush, Miller, and Starrett [4] state that tornadoes should first develop on the windward border of the moisture wedge. Also Tepper,[5] in presenting the pressure jump theory, stated "a pressure jump

TABLE 1.—SEVERE LOCAL STORM REPORTS FOR SOUTHWESTERN OKLAHOMA DURING THE PERIOD 1800–2300 GMT, MAY 19, 1960

Time	Type	Location	Remarks
Unknown	Hail	Hobart	Up to 90 percent wheat damage southwest of Hobart.
2145 GMT	Hail	Fort Sill	Golf ball size hailstones.
2200 GMT	Two tornadoes	50 miles SW of Oklahoma City	Both tornadoes touched the ground.
2206 GMT	Tornado	235°, 28 miles from Oklahoma City.	Minor tree damage.
2215 GMT	Funnel aloft and hail	18 miles SSW of Oklahoma City	¼-inch hailstones covered the ground.
2225 GMT	Tornado	125°, 7 miles from Oklahoma City	Housetop lifted. Tornado looked like a large dust devil.
2250 GMT	Tornado	70 miles SSW of Oklahoma City	None.
2300 GMT	Unconfirmed tornado	202°, 48 miles from Oklahoma City	From Oklahoma City RAWARC.*

*RAdar WARning Circuit.

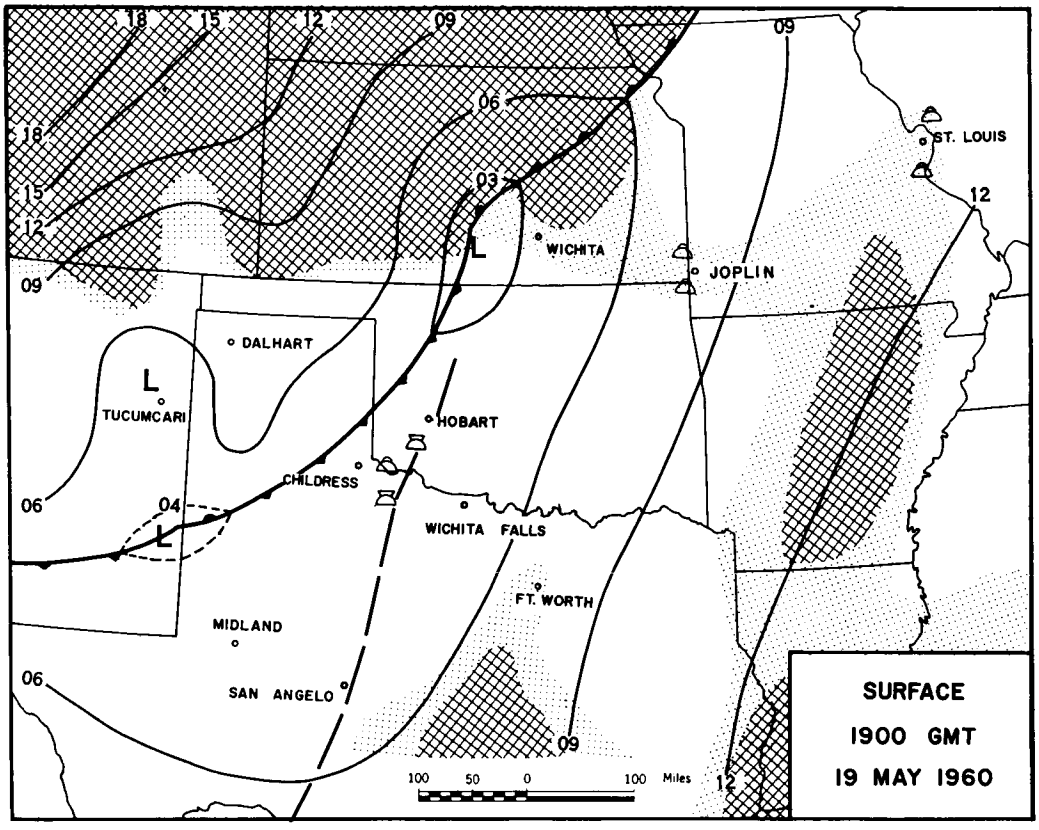

FIGURE 195.—Surface chart for 1900 GMT, May 19, 1960, showing front, sea-level isobars at 3-mb intervals, dewpoint "front" (long dashes), overcast areas from surface observations (heavy crosshatching), broken areas (dotted), and reports of heavy cumulus and/or cumulonimbus clouds (symbols). Clear skies or scattered cloud areas are not shaded.

propagating into a region where the atmosphere is dry may not set off any shower activity; yet if that same jump enters into a region where conditions are more favorable, convective activity may be marked."

No detailed mesoanalysis for May 19, 1960, has yet been performed; however, the accelerated microbarograph traces from the dense Severe Local Storms Research Network in Oklahoma, and in particular, those traces near the bright, cloud mass were studied briefly.

West of the general afternoon position of the dewpoint "front," the pressure traces were very smooth. Quite the opposite situation occurred east of the "front" in Oklahoma and extreme northern Texas. The traces there, though smooth in the morning, became very irregular during the afternoon and night. The first unsteady pressure trace was noted at 1900 GMT at Frederick, Oklahoma (35 miles southwest of Fort Sill), and a second unsteady trace began at Electra, Texas (25 miles west of Wichita Falls), at 1915 GMT. Both locations were beneath the bright cloud mass location of 2000 GMT. During the next few hours, all traces to the east and northeast of Frederick and Electra began showing many short-period pressure fluctuations of varying magnitude.

The first abrupt pressure rise of note also occured at Frederick at 2100 GMT. Thereafter, numerous stations in a "pie shaped" sector northeastward of Frederick recorded strong pressure jumps during at least the following three hours. These stations successively reported the jumps in a manner which indicated the spread of a meso-high northeastward from Frederick. The hail and tornado outbreaks appear to have occurred in close association, both in time and space, with the location of the pressure jump line (leading edge of the mesohigh).

Weighing rain gauge records were also available from some of the network stations. Heavy rainfalls occurred to the northeast of the bright cloud

mass after picture time (2000 GMT) but Frederick, Oklahoma, located very near to the center of the cloud mass, recorded 0.25 inch of rain during a half-hour period which included the time of Figure 193.

Beebe and Bates [6] and Fawbush et al.[4] have discussed the importance of the jet as a factor in the development of tornado activity. In this case, a southwesterly jet maximum at 14,000 feet over Amarillo at 1800 GMT (Figure 201) migrated eastward over Oklahoma City and lowered to 10,000 feet by 0000 GMT (Figure 202).*

Discussion of a high-level jet [6, 7] has been omitted since the very brief sounding taken at Oklahoma City at 0000 GMT did not provide sufficient information for fixing its location. The balloon was forced down by icing conditions after attaining an altitude of only 23,000 feet. It can be stated, though, that the 1800 GMT and 0000 GMT Amarillo radar wind reports (RAWIN) and the 1800 GMT Oklahoma City RAWIN definitely indicated the presence of a high-level jet in the area of interest.

*Cross-sections through Amarillo and Oklahoma City indicated these levels to be most representative of the altitude of the maximum winds, or jet core, for the two times considered. However, it should be mentioned that at 0000 GMT, a second jet core was noted at 7,000 feet immediately beneath the 10,000-foot core over Oklahoma City, Oklahoma.

PICTURE CONTENT AND METEOROLOGY

Identification of the 2000 GMT synoptic elements with the features in the cloud photograph were readily established by direct comparisons, and by means of the locations obtained through use of the cloud schematic (Figure 194). For instance, the extensive cloudiness at the top of the

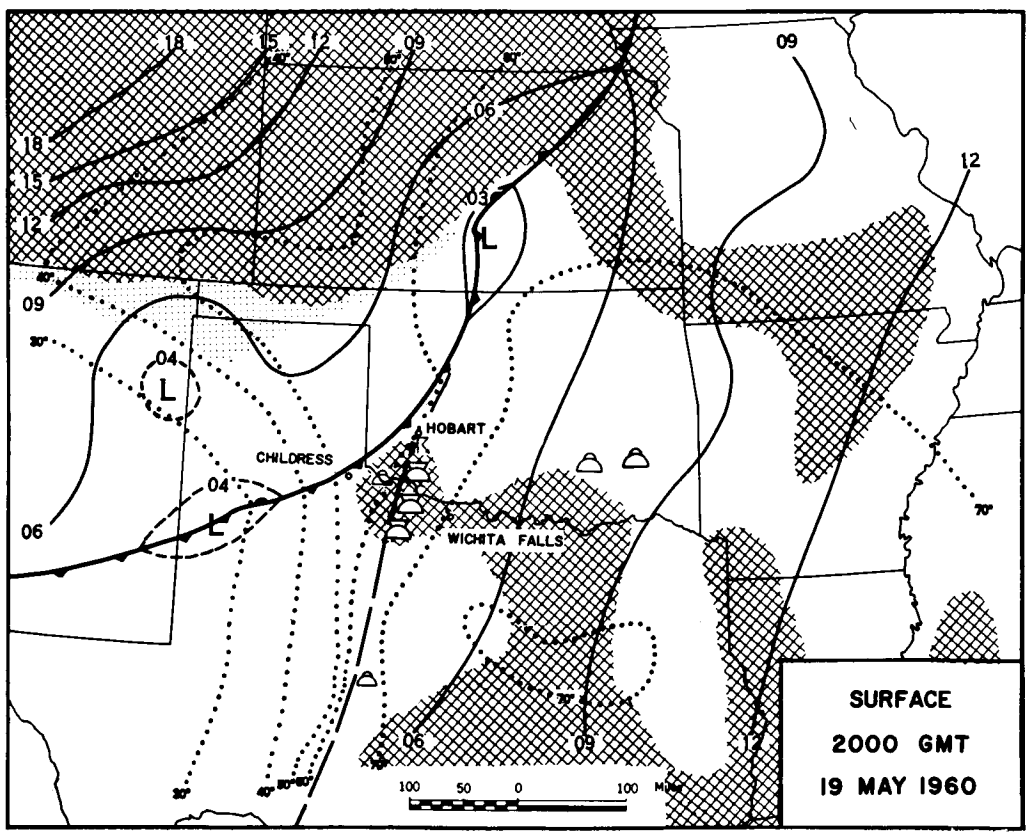

FIGURE 196.—Surface chart for 2000 GMT, May 19, 1960. Dotted lines are isopleths of dewpoint temperature in °F; other information as in Figure 195.

photograph was in part the overcast area over Colorado and western Kansas (Figure 196). The large black areas, one at the right, and the other at the lower left of the photograph were the clear areas over northern Missouri and Iowa, and over New Mexico, western Texas and western Oklahoma, respectively. These identifications may be made by comparison of relative positions, size, and amount of cloud cover of the features in the photograph with the nephanalysis (Figure 196), but they are well corroborated by the rectified schematic within the accuracy limitations (see Appendix A).*

Of special interest, however, is the bright "square" cloud mass and the smooth cloud boundary upon which it was superposed. It is certain that the location of the sharp cloud boundary, as established earlier, coincided mainly with the surface position of the dewpoint "front" which extended southward from the cold front north of Hobart, Oklahoma to the vicinity of San Angelo, Texas (Figure 196). The northern part of the sharp line in Figure 193 may have been associated with the cold front north of Hobart, Oklahoma. The surface reports at 2000 GMT clearly indicated, as does Figure 193, that this boundary separates clear skies to the west from the partly clouded skies (scattered cumulus humilis) to the east.

With this boundary fixed, then it is obvious that the bright "square" cloud mass lay somewhere along the dewpoint "front." In fact, it is evident that this bright cloud represented precisely the concentrated area of heavy convective activity reported by Hobart, Childress, and Wichita Falls

*And the schematic location of the bright "square" cloud mass was within about ±30 miles of the position indicated by surface observations.

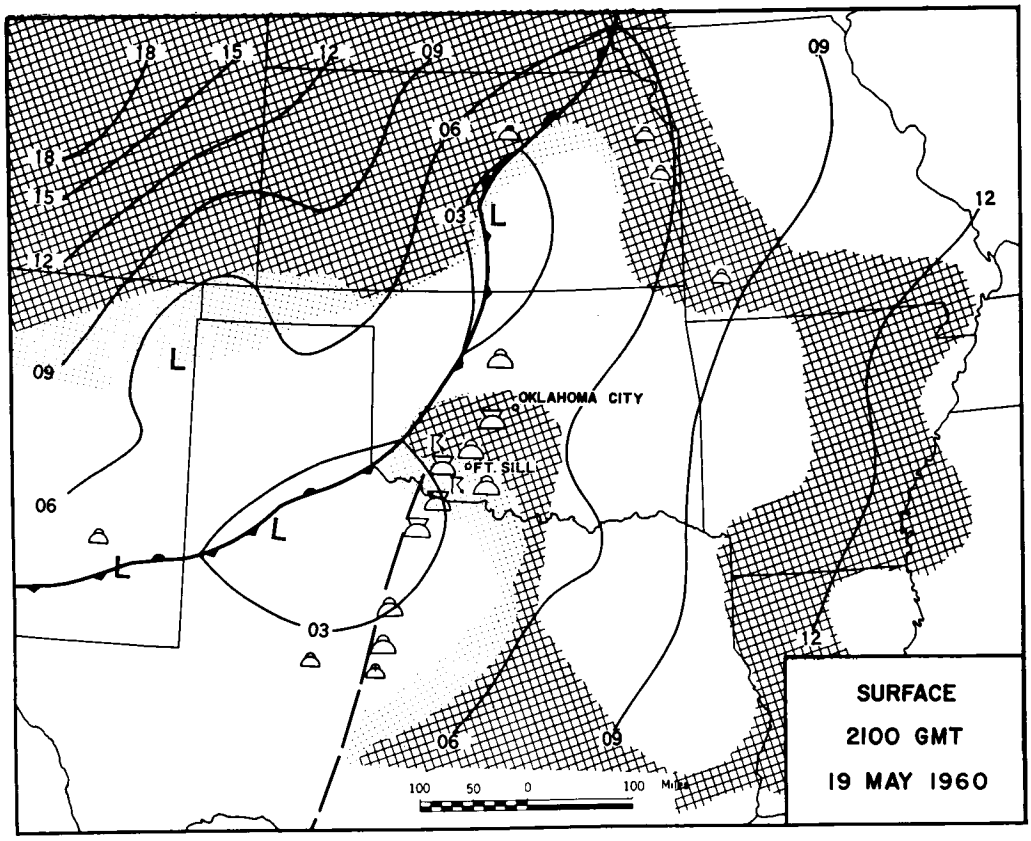

FIGURE 197.—Surface chart for 2100 GMT, May 19, 1960. Information is shown as in Figure 195.

at 2000 GMT. It has been positively shown that rain was falling at the surface in at least one area beneath the bright cloud at picture time.

No well-defined mesohigh could be detected beneath the "square" cloud mass at the time of the photograph, though traces in that area became unsteady during the hour preceding 2000 GMT. A significant pressure rise was first noted at this location 1 hour later. The mesohigh or high associated with this rise spread northeastward expanding and intensifying into a vigorous system preceded by strong pressure jumps.

It is interesting to note from Figures 201 and 202 that the southwest wind direction was more or less perpendicular to the cloud streets in eastern Oklahoma. Moreover, the bright isolated "square" cloud was elongated in the direction of the wind. Perhaps in such situations, the photograph features may offer clues from which one might deduce the wind direction.

The proximity of this cloud and the dewpoint "front" to the wind maximum are reminiscent of the instability released under such conditions.[6] It will be interesting to examine other cases in which isolated bright cloud masses appear near a sharp boundary like the one in Figure 193, to see whether they are associated with regions of wind maxima.

CONCLUSIONS

There is strong evidence that: (1) the first intense cumulus buildups in the Southern Plains on the afternoon of May 19, 1960, were represented

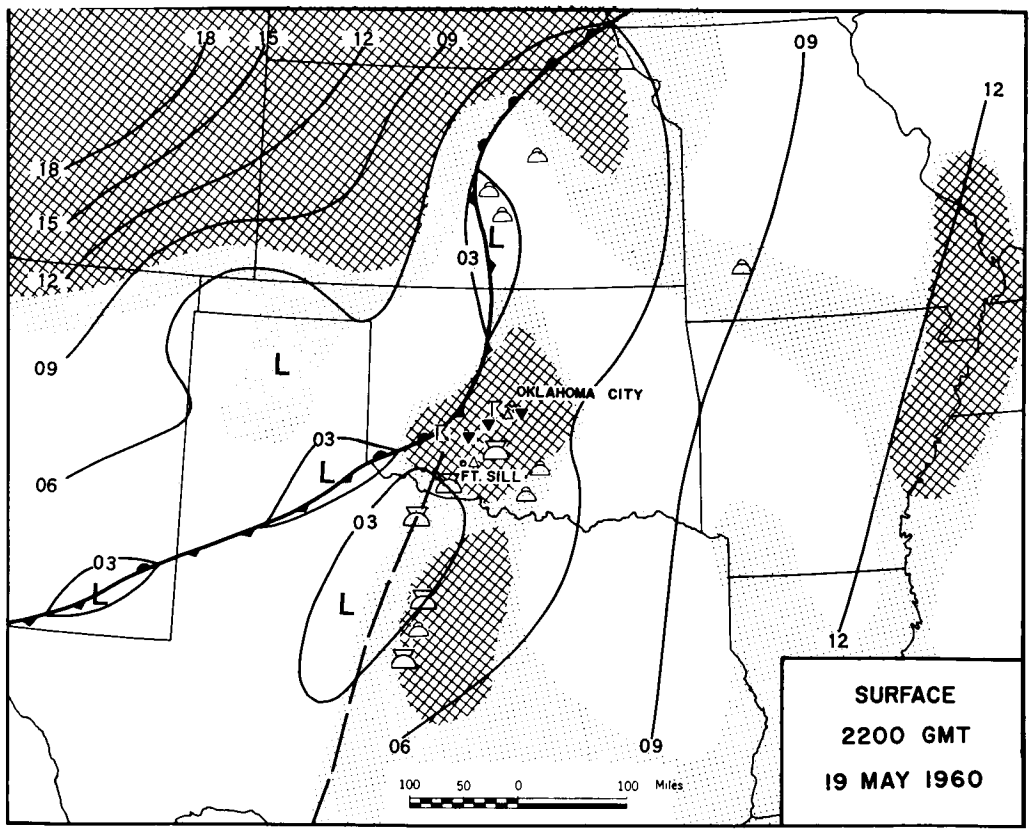

FIGURE 198.—Surface chart for 2200 GMT, May 19, 1960. Tornado locations are shown as black triangles; hail as open triangles; other information as in Figure 195.

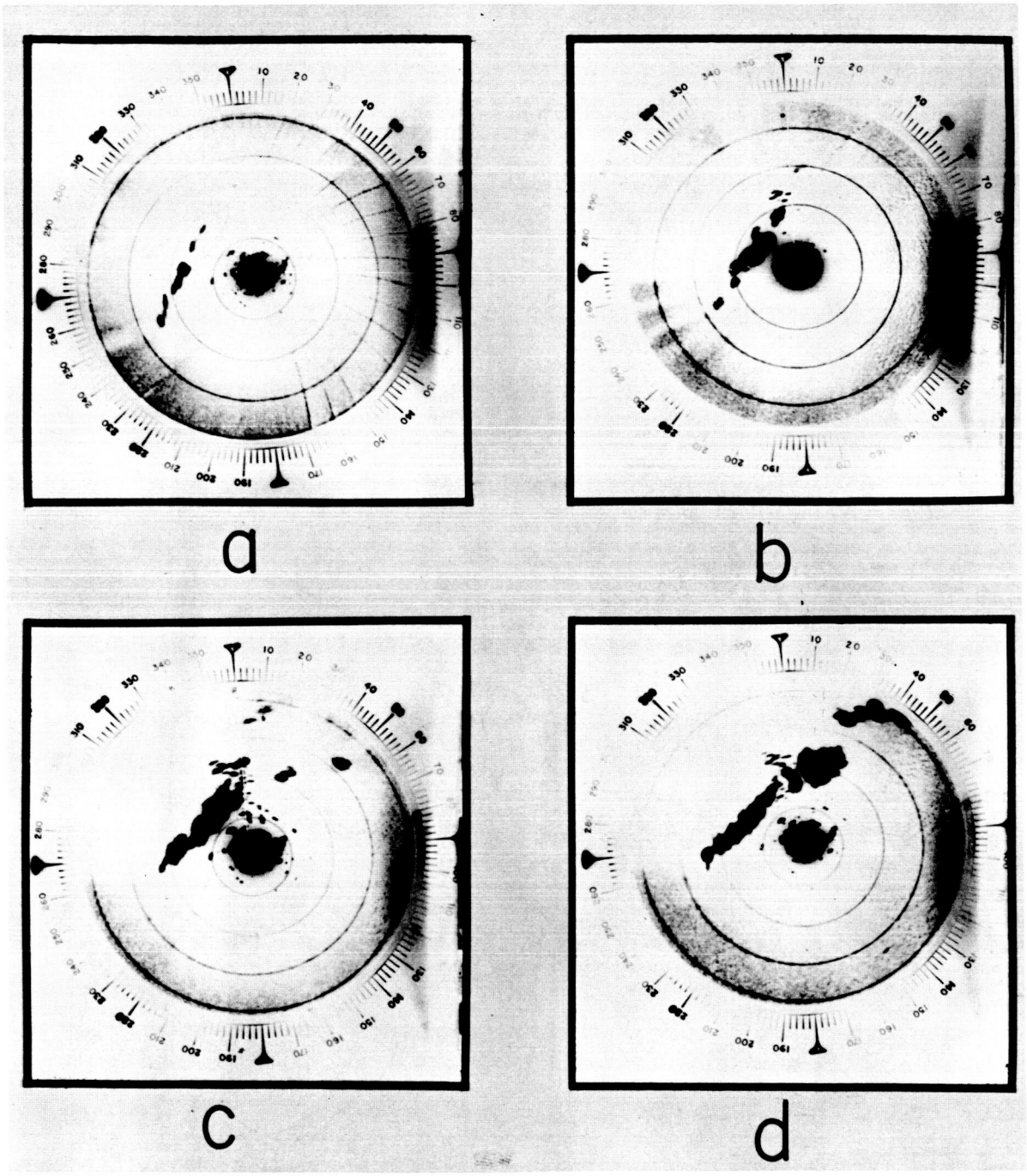

FIGURE 199.—Wichita Falls radarscope photographs for (a) 1900 GMT, (b) 2000 GMT, (c) 2100 GMT, and (d) 2200 GMT, May 19, 1960. Range marks are at 20 nautical miles for all four photographs even though the sweep length was altered in (b), giving a slightly smaller scale size.

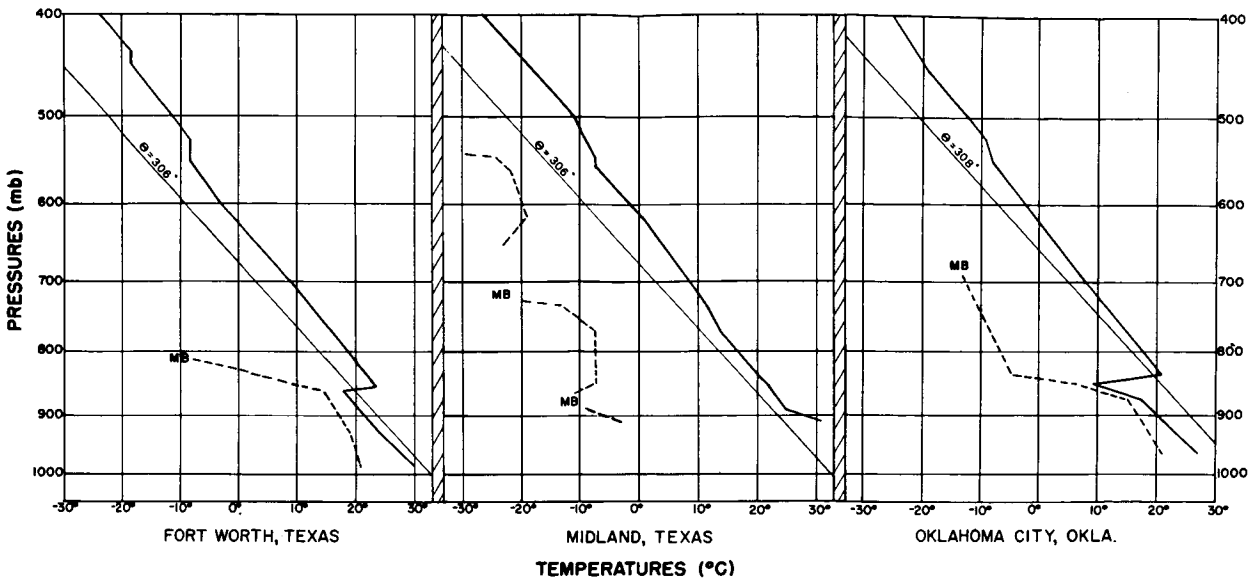

FIGURE 200.—Soundings for 1800 GMT, May 19, 1960. The solid lines show temperature distribution; dashed lines dewpoint distribution.

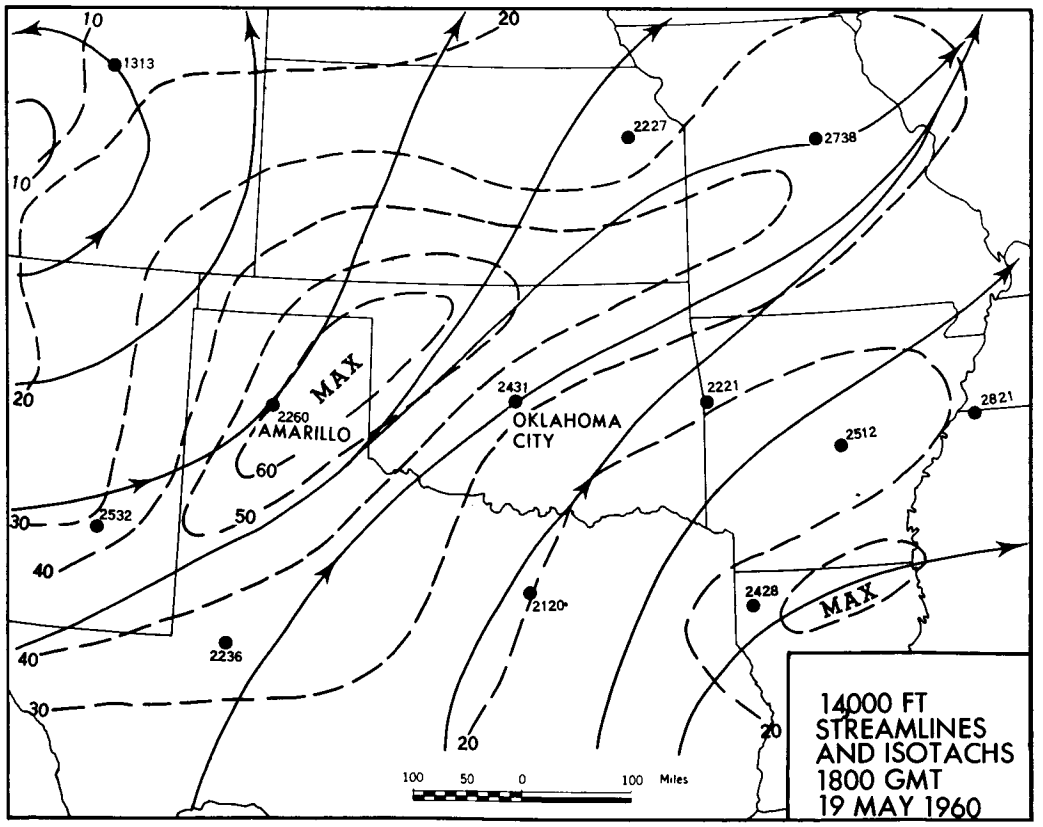

FIGURE 201.—Streamline chart for 14,000 feet at 0000 GMT, May 19, 1960. Solid lines are streamlines; broken lines are isotachs labeled in knots. The plotted data are wind directions and speeds.

by the isolated, "square" cloud mass in Figure 193; (2) the cloud was in an area possessing characteristics commonly found in tornado development; and (3) this cloud mass later expanded and spread northeastward spawning hail and tornadoes in central Oklahoma. The shape of this cloud mass can be considered only as coincidental.

It is not the intent here to imply that every bright isolated cloud mass seen from satellite vehicles will be associated with hail and tornadoes. However, such clouds, or masses of clouds, when considered together with the geographic location, the climatology of the region, and the existing synoptic situation will be subject to close scrutiny as potential producers of severe local storms.

REFERENCES

1. Hoecker, W. H., Jr., "Characteristics Common to Several Tornado Systems," talk given before the 184th Natl. Mtg. of Amer. Meteorol. Soc. held jointly with Amer. Geophys. Union, Washington, D.C., 1960. (Abstract appear in Bull. Amer. Meteorol. Soc. 41, 197.)
2. Fulks, J. R., "The Instability Line," in: Compendium of Meteorology, Boston: American Meteorological Society, 1951, pp. 647–652.
3. Hanks, H. H., Jr., and Neubrand, G. M., "Tornadoes of April 2 and 3, 1956," Mon. Weather Rev. 84(4): 155–162, April 1956.
4. Fawbush, E. J., Miller, R. C., and Starrett, L. G., "An Empirical Method of Forecasting Tornado Development," Bull. Amer. Meteorol. Soc. 32(1): 1–9, January 1951.
5. Tepper, M., "A Proposed Mechanism of Squall Lines, the Pressure Jump Line," J. Meteorol. 7(1): 21–29, February 1950.
6. Beebe, R. C., and Bates, F. C., "A Mechanism for Assisting in the Release of Convective Instability," Mon. Weather Rev. 83(1): 1–9, January 1955.
7. Lee, J. T., and Galway, J. G., "Preliminary Report on the Relationship Between the Jet at the 200-mb Level and Tornado Occurrence," Bull. Amer. Meteorol. Soc. 3(7): 327–332, September 1956.

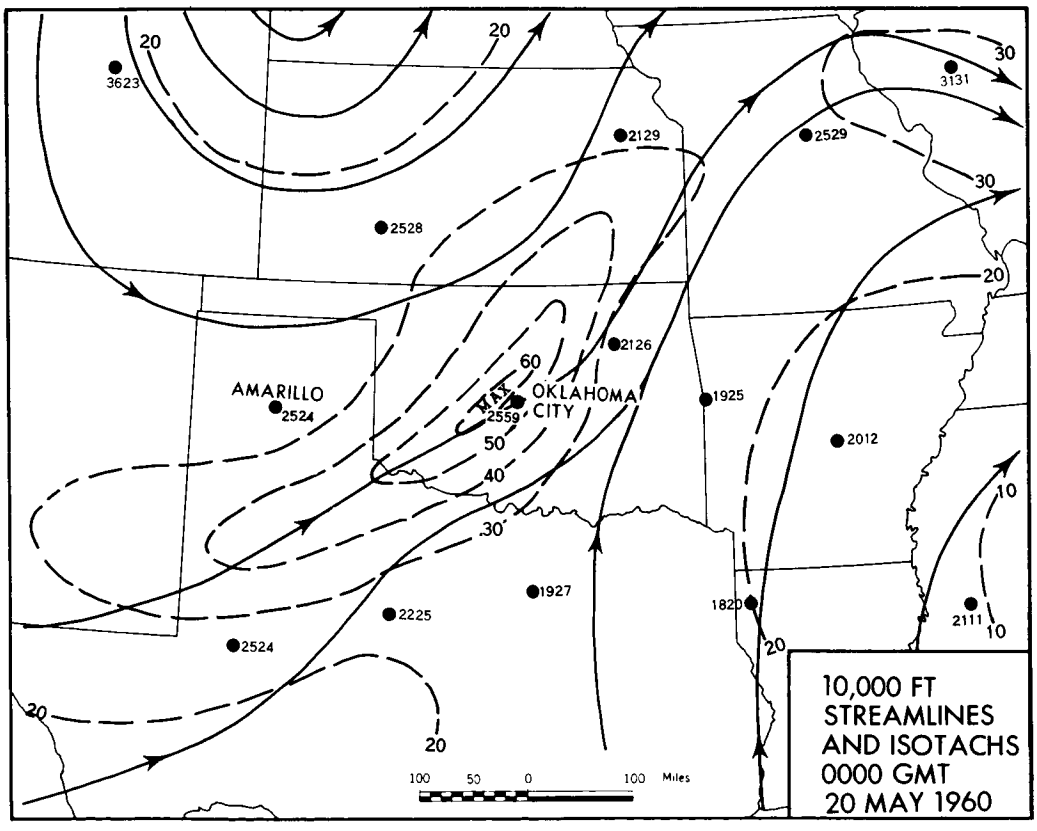

FIGURE 202.—Streamline chart for 10,000 feet at 0000 GMT, May 20, 1960. Solid lines are streamlines; broken lines are isotachs labeled in knots. The plotted data are wind directions and speeds.

CHAPTER 18

MISCELLANEOUS TIROS PICTURES*

by

SIGMUND FRITZ

INTRODUCTION

Many interesting pictures of clouds and of the earth's surface have been obtained by TIROS I in addition to those already discussed in this report. In order to bring them to the attention of the scientific community, several categories of these miscellaneous TIROS I pictures are presented in this chapter without extensive discussion.

MOUNTAIN PHENOMENA

Many investigations have been made of clouds, snow, and other meteorological features in mountainous areas. Clouds are frequently produced over mountains when air is forced up along the slopes. In such cases, clouds and precipitation will generally occur along the slope or near the peak of the mountains. Moreover, when strong winds blow perpendicular to an extended mountain range, waves of clouds with their crests parallel to the ridge may be formed at appreciable distances from the mountain.[1] Snow is of course a common feature on high mountains and quite frequently covers them throughout the summer. Snow is sometimes of special importance to human activities, since it serves as a storage medium, releasing water during the melt season.

Examples of each of these phenomena are shown in Figure 203. In picture 1 of this group, a distinctive white mass lies exactly along the European Alps.† (The northward direction is more or less straight up in picture 1.) It starts as a narrow strip at Monaco on the Mediterranean Sea, curves northward and eastward over the French, Italian, and Swiss Alps, and broadens in the region where the Alps broaden over Italy, Austria, and Yugoslavia. Further to the east, the picture is complicated by clouds which were associated with a weak low pressure area located near Turkey. In general, it may be possible to distinguish between cloud and snow, by viewing the same area many times on different days. If the pattern remains the same from day to day over a considerable period, snow rather than cloud would be suspected as being responsible for the brightness. Picture 1 of Figure 203 was photographed on April 2, 1960, and the same white configuration was photographed on April 3, 5, 6, and 7; in some cases the bright area was identical on different days even as to minor dark lines which represent the Rhone River valley, etc. Thus the bright area over the western Alps mainly represents snow. However, a few minor changes did occur in the bright area from day to day, indicating that a few clouds were also present at times over or near the snow-covered area.

Picture 3 of Figure 203 was taken over the Himalayas; picture 3A is a narrow-angle picture of the area enclosed by the rectangle in picture 3. Certainly a large part of the bright area in picture 3 is snow-cover, in view of the sharp outlines marking the peaks and valleys along the mountain ridges.

Picture 2 of Figure 203 we see what appears to be cirrus cloudiness streaming off the east coast of Argentina into the Atlantic Ocean. The picture also suggests a wave pattern in the sense that the cloud is bright nearer to the horizon, followed to the east (toward the coast) by a relatively dark area in which a rather sharply defined bright area extends from north to south; and following that

*Many of the pictures shown in this paper appear in: Fritz, S., and Wexler, H., "Planet Earth as Seen From Space," Chap. I in "Planets and Satellites," Solar System Vol. III, ed. by G. P. Kuiper and B. M. Middlehurst, Chicago: University of Chicago Press, 1961.

†For more detailed discussion, see "Satellite Pictures of the Snow-Covered Alps During April 1960," to appear in Archiv für met., Geophys., und Bioklimat (1962).

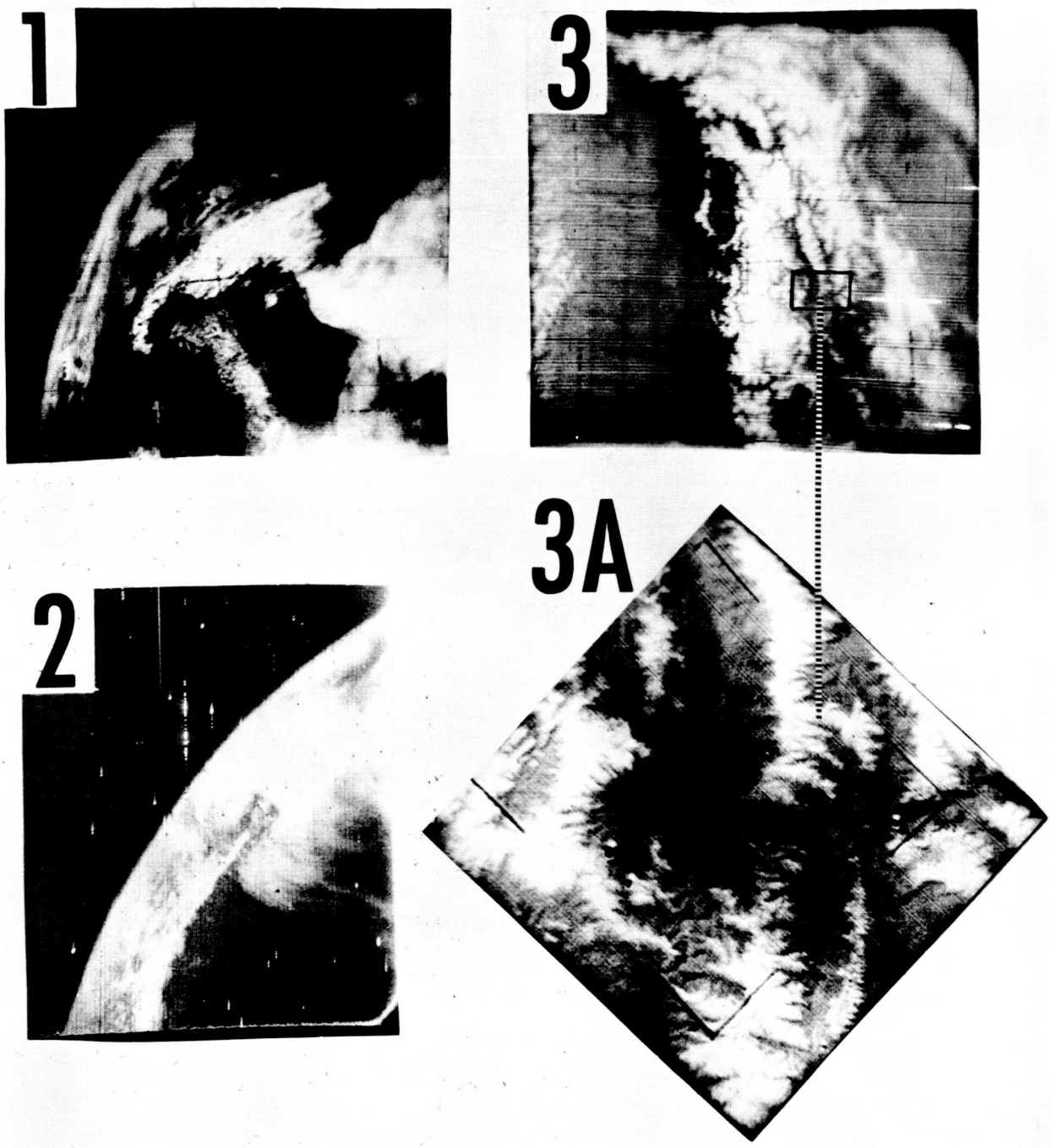

FIGURE 203.—TIROS pictures related to mountainous areas: (1) Snow and a few clouds over the Alps (April 2, 1960); Italy extends southward from the Alps to the lower center of the picture. (2) Clouds streaming off South America (April 29, 1960); (3) Snow and a few clouds over the Himalayas (May 13, 1960); (3A) Narrow-angle camera view of rectangular area shown in (3).

a more dense cloud, which seems then to thin out into a streaky cirrus pattern, extends into the ocean. Whether or not this can be attributed to the mountains further to the west is problematical; but the picture does suggest the type of wave pattern which is found in studies of mountain waves.[1]

An interesting view of the western United States taken on May 19, 1960, is shown in Figure 204a. Here we see the San Francisco Bay area illuminated by strong reflections of sunlight. The bright Sierra Nevada Mountains to the east are snow-capped. Off the coast, over the Pacific Ocean, a cloud system was present. A TIROS I picture of the western mountain area taken 3 days earlier (on May 16) is also shown in Figure 204b. In this picture, the San Francisco coast area is again evident in the lower left part of the picture. The snow-capped Sierra Nevada Mountains are again seen parallel to the coast. But this time, a cloud has formed over the mountains in the southern part of the picture, while complicated cloud patterns, in some cases possibly associated mountain-lee waves, appear in the picture.

ICE

In addition to the snow in mountain areas, it is sometimes possible to detect floating ice. During the first days of the TIROS I satellite's existence, both wide-angle and narrow-angle pictures of the Gulf of St. Lawrence were obtained. Ice in the gulf is a hazard to shipping and reports of the ice from surface observations are made regularly. From an analysis of the surface reports and also from the appearance of the pictures, Wark and Popham have been able to differentiate between ice and clouds in the Gulf of St. Lawrence. An example of this is shown in Figure 205, which is taken from their paper.[2]

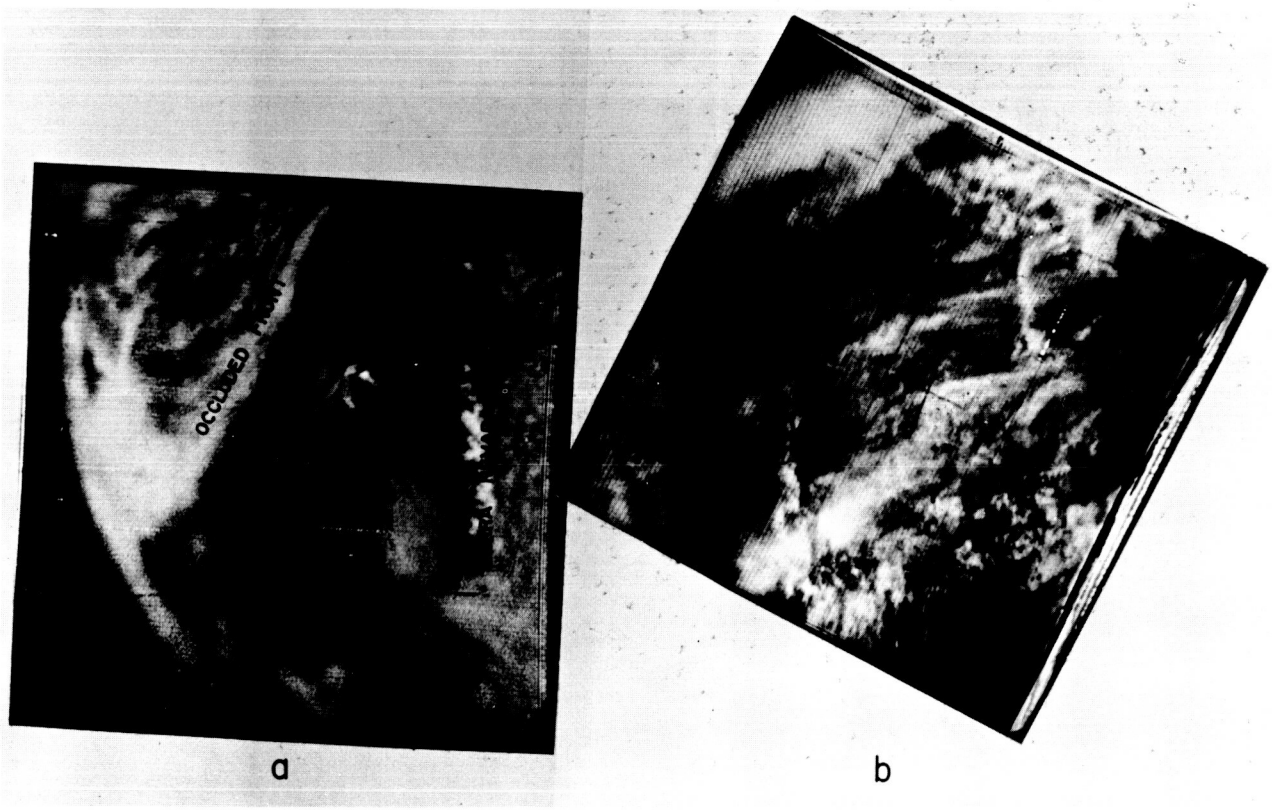

FIGURE 204.—(a) TIROS picture of San Francisco Bay area, and snow-capped Sierra Nevada Mountains (May 19, 1960). (b) TIROS picture of western United States, showing San Francisco Bay area, snow-capped Sierra Nevada Mountains, and complicated cloud patterns over western mountains (May 16, 1960).

SUN GLITTER

Sun "glitter," another phenomenon which is of interest from several standpoints, is the strong reflectivity of the direct sun from the ocean's surface. Cox and Munk [3] have suggested that the pattern and extent of the brightness of the ocean in strongly reflected sunlight is related to the speed of the wind over the ocean at that place. Thus, the sun "glitter" can serve as an estimate of the wind speed. Another value of sun reflection may arise from its utility in determining the orientation of the satellite camera optical axis by use of the fact that the angle of incidence equals the angle of reflection. Since the position of the sun is accurately known, it should be possible, if the location of the sub-satellite point and picture taking time can be determined, to compute the angle at which the television camera was pointing with respect to the vertical. This is especially true if the sun's image occurs near the point in

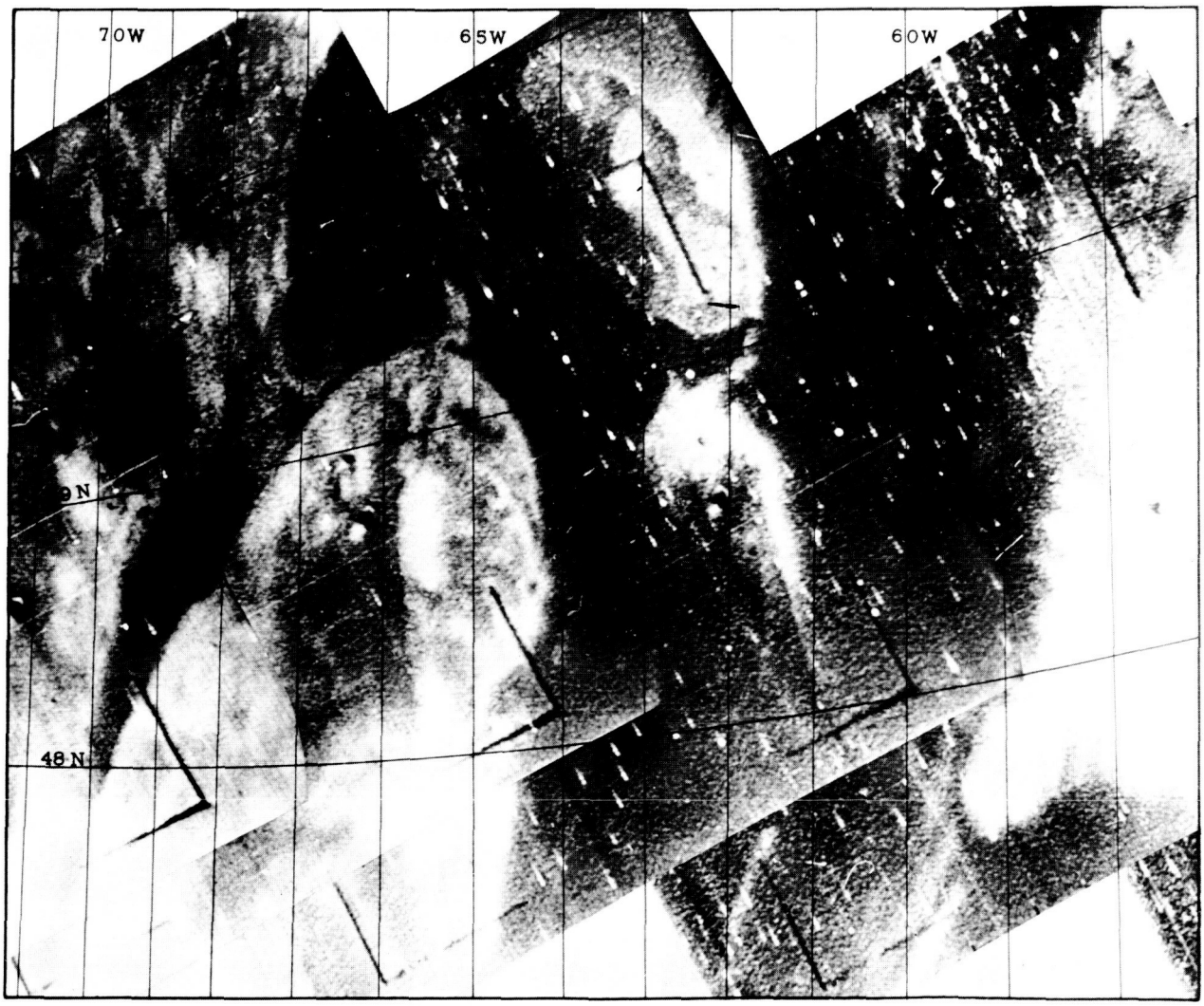

FIGURE 205.—Picture of ice in the Gulf of Saint Lawrence. The rounded land near 49° N, 66° W is the Gaspé Peninsula; Anticosti Island lies to the northeast of it. The whitish areas north of Gaspé are ice areas; the bright areas around Anticosti Island and the one south of the island are also apparently ice.[2]

a

b

FIGURE 206.—(a) Sun "glitter" strongly reflected from the water just west of the west coast of Florida. (b) The Florida Peninsula and the bright coastal water off the Georgia coast. A long, narrow cloud "street" meanders from the southern Florida coast, northeastward, possibly along the edge of the Gulf Stream.

the picture corresponding to the optical axis of the camera. A series of pictures taken as the satellite passed across Florida and along the east coast of the United States was taken on May 16, 1960, and appears in Figure 206a. The pictures clearly show the sun glitter, which is especially well-marked in the region just to the west of the Florida coast in the Gulf of Mexico.

GULF STREAM CLOUD

Sometimes rather odd-looking clouds appear which may be related to particular geophysical phenomena. Such a cloud is shown in Figure 206b. A very narrow cloud, probably about 5 miles wide, stretches for a distance of several hundred miles; and starting close to the southern coast of Florida it diverges from the coast as it

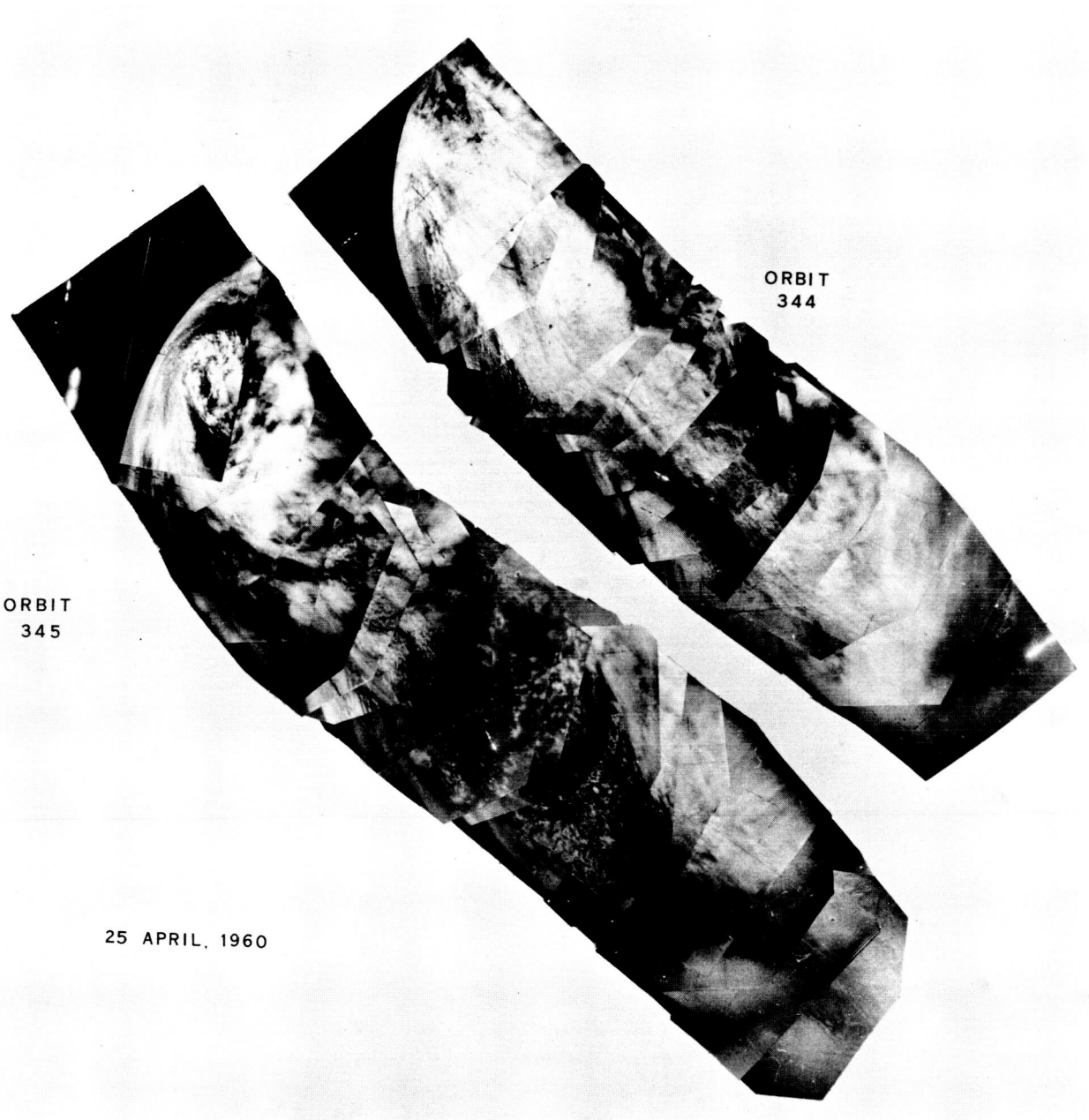

FIGURE 207.—A composite of pictures taken in the Southern Hemisphere (see Figure 208).

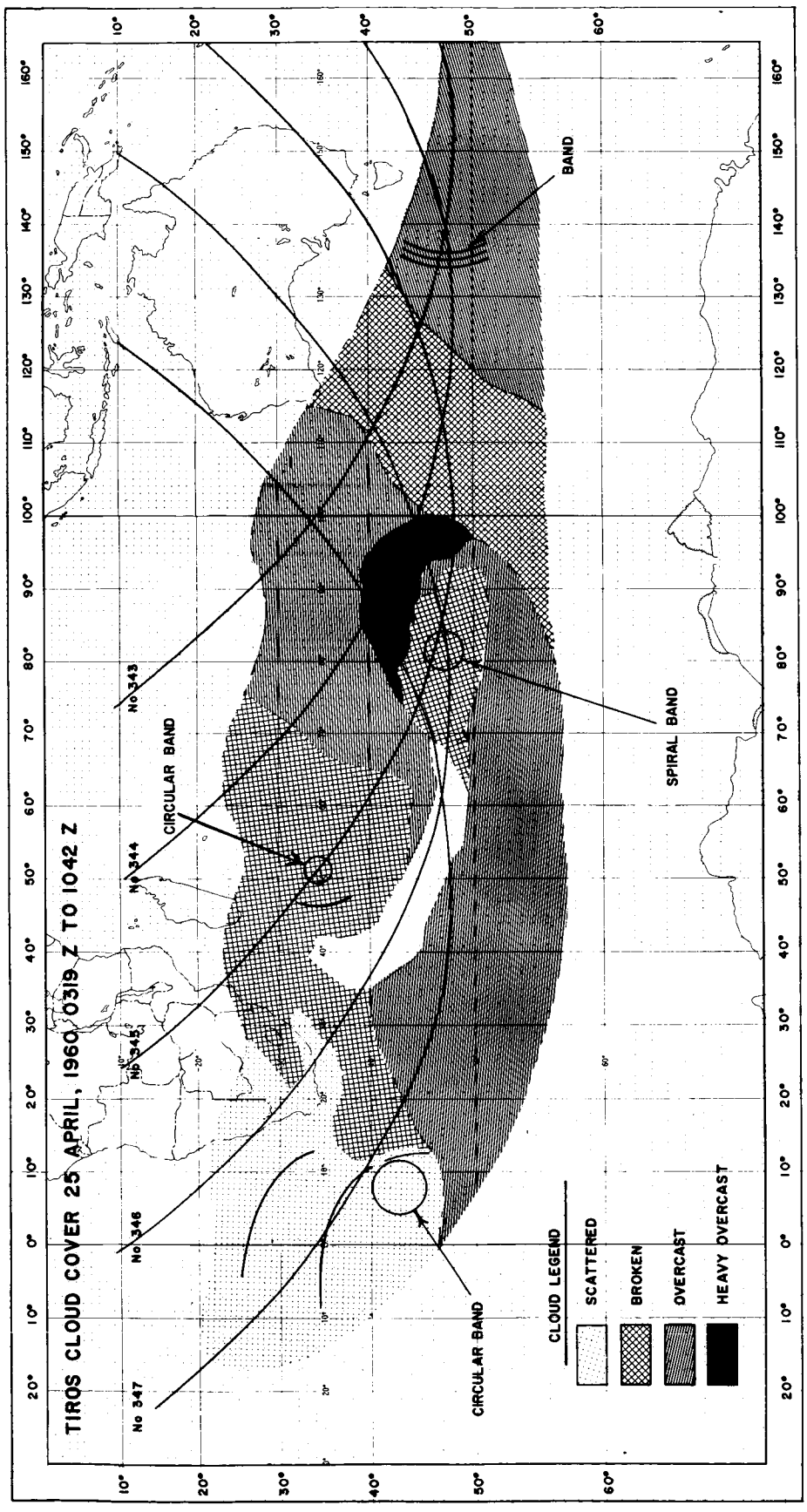

FIGURE 208.—A schematic presentation of cloud amount and pattern for several orbits in the Southern Hemisphere (see Figure 207 for cloud pictures in orbits 344 and 345).

progresses northward. The possibility that this cloud parallels the edge of the Gulf Stream is being investigated.

SOUTHERN HEMISPHERE

Finally, it has been emphasized several times in this report that cloud pictures from regions where meteorological data are sparse would obviously be of considerable importance to meteorologist in nearby land areas. This is the case in many parts of the Southern Hemisphere; therefore a composite of pictures taken during several orbits over the Southern Hemisphere has been assembled (Figure 207).

During the operation of TIROS I, the Belmar, New Jersey, readout station was staffed by meteorologists who scanned the pictures, extracted from them the significant meteorological information, put this into the form of a sketch, and then transmitted the sketch by facsimile to the U.S.W.B. Meteorological Satellite Station in Suitland, Maryland. From Suitland, the information was disseminated to certain civilian and military users. A sketch modified by H. Wexler from the original facsimile transmission is shown in Figure 208. The pictures in Figure 207 correspond to part of the sketch in this figure. Such observations in this data-sparse region of the Southern Hemisphere, reported regularly, would be quite valuable to meteorologists in such places as Australia, South America, and Africa. For example, near the top of orbit 345 (Figure 207) the vortex of bright clouds was associated with a mature cyclone in agreement with the study in Chapter 9 of this report. The cumuliform clouds lower down in that orbit are also arrayed in spiral bands; but these clouds may have been embedded in the cold air behind another frontal system, as suggested in the studies by V. J. Oliver in Chapter 14 and J. S. Winston in Chapter 10.

Additional interesting features have already been noted in the thousands of pictures from TIROS; still more will be found in the near future. This chapter has merely extracted a few of the more striking phenomena which have been noted to the date of this writing.

REFERENCES

1. Alaka, M. A., "Aviation Aspects of Mountain Waves," WMO Technical Note No. 18, 1958.
2. Wark, D. Q., and Popham, R. W., "TIROS I Observations of Ice in the Gulf of St. Lawrence," Mon. Weather Rev. 88(5) : 182–186, May 1960.
3. Cox, C., and Munk, W., "Slopes of the Sea Surface Deduced from Photograph of Sun Glitter," Scripps Inst. of Oceanography Bull. 6(9) : 401–487, 1956.

APPENDIX A

GEOGRAPHIC LOCATION OF CLOUD FEATURES

by

RUSSELL C. DOOLITTLE,* LAURENCE I. MILLER, and IRWIN S. RUFF

INTRODUCTION

With the successful launching and performance of TIROS I an enormous quantity of useful cloud photographs has been received, but the attendant problem of determining the exact geographic location of the individual pictures still remains.

Logically this problem can be considered as comprised of two separate parts; (1) determining the geographic position of an image point on a photograph, and (2) visual graphic representation of the location of meteorological features. The first requires an exact knowledge of the geometrical characteristics of the camera system, and of the position and attitude of the camera at the time of exposure. The second depends primarily on the use to be made of each picture. Once the basic space relationship between the ground and the position of the photographic image has been determined, overlay grids of lines of constant latitude and longitude can be constructed and superimposed on the photograph. Because of the comparatively small ground areas covered by the narrow-angle camera, only wide-angle camera photographs are to be gridded at this time.

PRELAUNCH PHASE

Prelaunch plans for computing the location of cloud features were based on the assumptions that: (1) the camera position would be provided by ground tracking, (2) the camera attitude would be determined from instrumentation in the satellite, and (3) the time at which pictures were taken would be known through ground station commands to clocks which controlled the cameras.

The programmed times for picture taking were based on considerations of meteorology, camera attitude, illumination, and the engineering capability of the satellite. Each sequence of pictures taken in the remote mode of operation was composed of 32 pictures taken at 30-second intervals. The camera position, attitude, and times of exposure, together with the geometrical characteristics of the camera system, provide sufficient information for the gridding of any photograph of meteorological interest.

In addition, the TIROS I operation plan provided for geographic location of pictures by photogrammetry. This work was to be performed by the Naval Photographic Interpretation Center, in collaboration with the U.S.W.B. Meteorological Satellite Laboratory (MSL), to provide an alternative procedure in case of failure of one or more of the other sources of location data. A method was devised on the assumptions that camera positions would be known at exposure times, but that data from the attitude sensors might be lacking, and that the apparent horizon would be well imaged but sufficient ground points for resection, in general, would not. In this procedure, the nadir angle (tilt) and swing are computed from the measured image coordinates of five points of the horizon; the azimuth of the principal plane is then computed from the image position of a recognizable landmark and the position of the satellite at the time of exposure.

POST-LAUNCH EXPERIENCE

Throughout the life of TIROS I the NASA world-wide Minitrack network tracked each orbit of the satellite and forwarded the information to the NASA Space Computing Center at the Goddard Space Flight Center. From these data the orbit was refined and ephemeris predictions were obtained. Subsequently, the exact data for each orbit were recomputed and published as items included in a "world attitude map" together with other quantities which depend on the attitude of the satellite spin axis, to which the optical axes

*U.S. Naval Photographic Interpretation Center, Washington, D.C.

(Figures A1 and A2) of the two television cameras were essentially parallel.

TIROS I was launched into a nearly perfect orbit and the position of the satellite with time was accurately known. However, the horizon sensors failed to operate satisfactorily; also there were uncertainties in the time and therefore position of the camera at a given remote exposure. In addition to possible errors in the satellite clock, a second source of error may have occurred in the preset taking-rate of one frame every 30 seconds. A more important cause of uncertainty arose when less than 32 frames were recorded during readout, with the result that none of the frames could be correlated with the programmed time.

It was initially believed that the orientation of TIROS I would be a slowly changing function of time, remaining essentially constant for a week

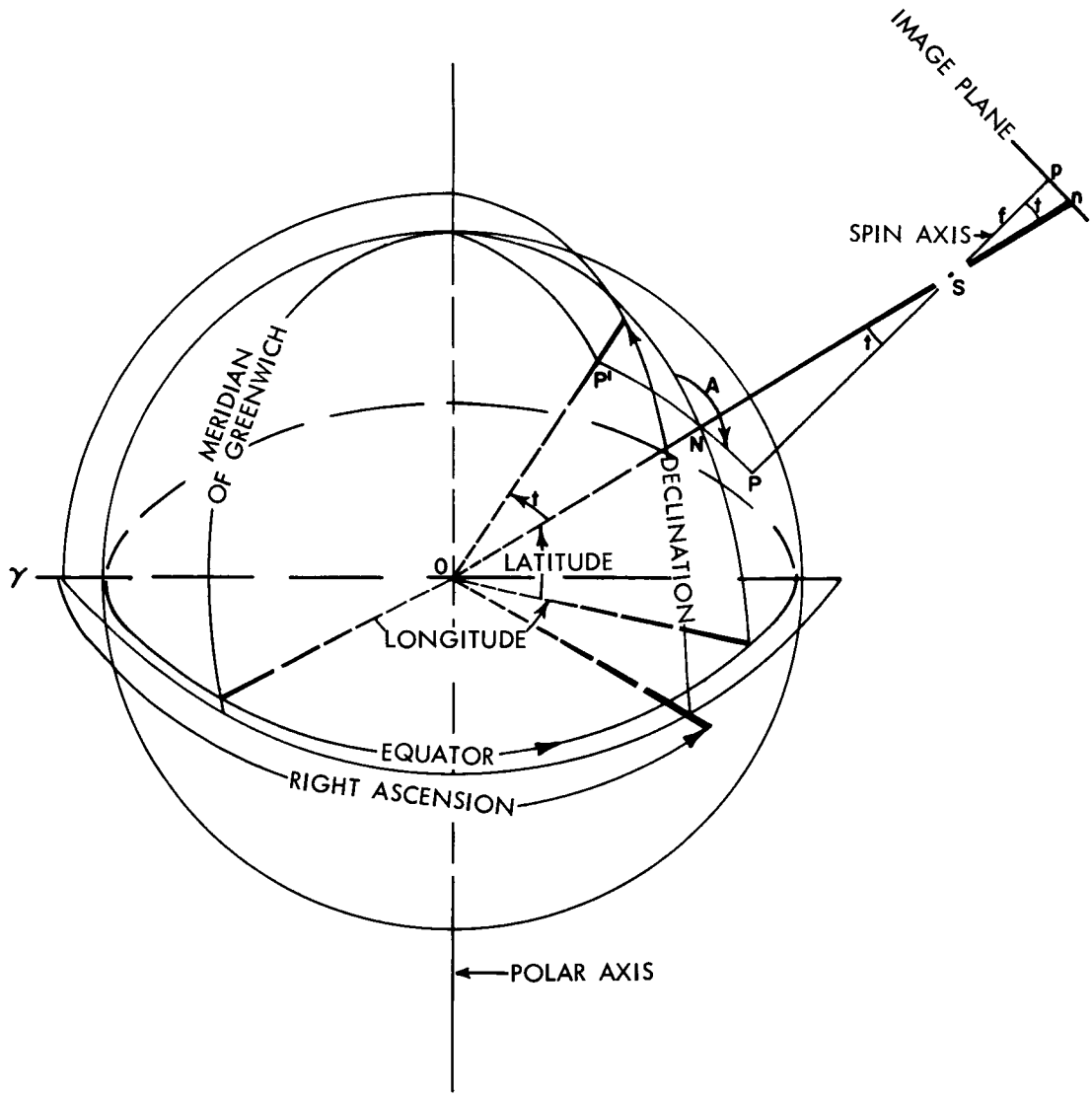

A—Azimuth of principal plane
N—Ground nadir point
P—Ground principal point
p'—Terminus of Geocentric radial parallel to spin axis
S—Satellite (camera) position
f—focal length
n—photo nadir point
p—principal point
t—tilt or nadir angle
γ—vernal equinox

FIGURE A1.—Diagram illustrating relations between geocentric and local geographic angular coordinates used to define spin axis attitude.

or more. The photographs obtained during the first week after launch, however, indicated that this was not the case, and that the orientation was changing rapidly. Because of this, and also because of the failure of the horizon sensors, a quick determination of the orientation of the camera was required for use in the immediate operational phase.

The actual orientation was calculated from subsatellite points obtained from the world-

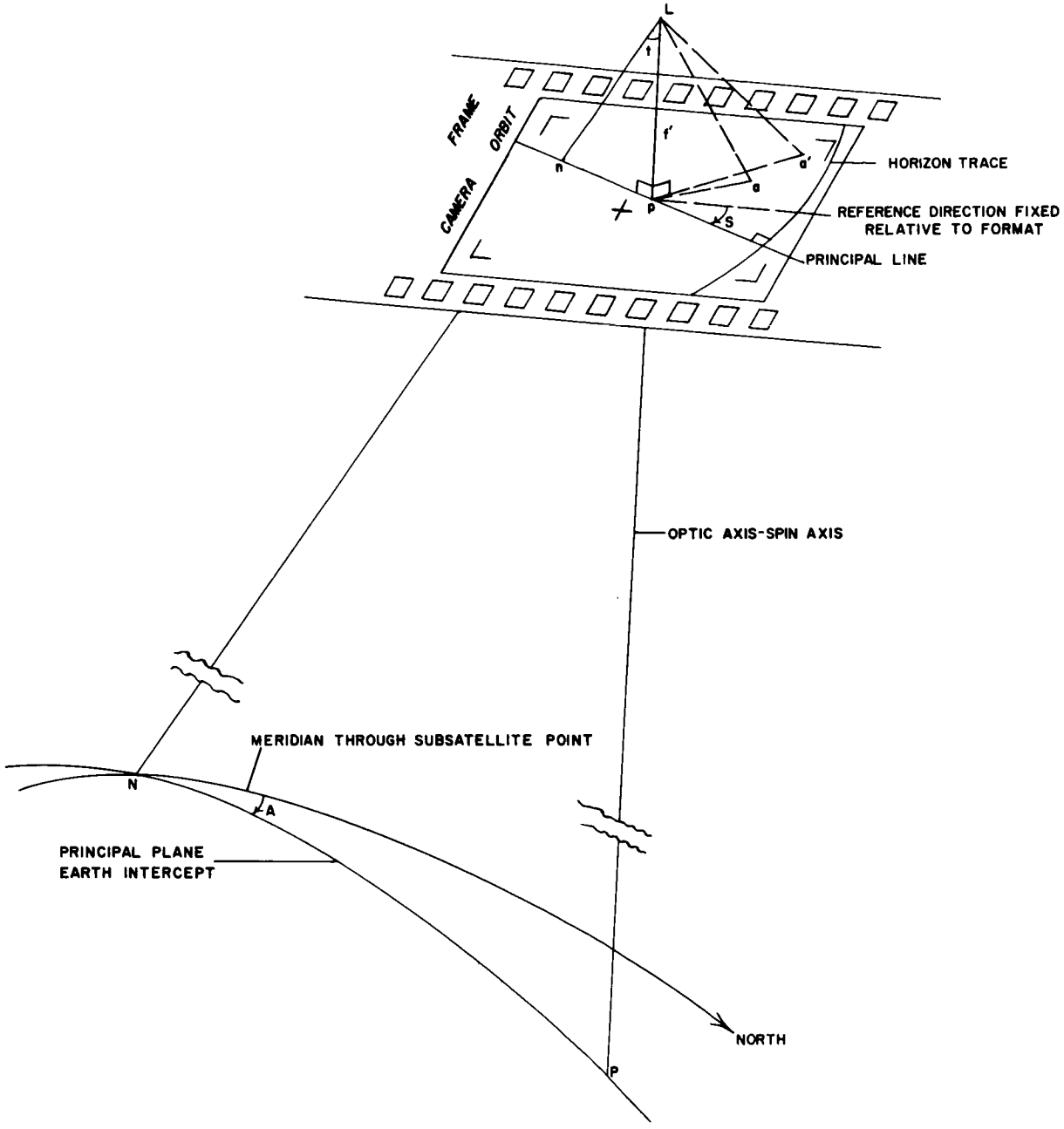

FIGURE A2.—Diagram illustrating relations between image plane and the Earth.

a, a'—image points
f'—principal distance
L—perspective center of photograph
s—swing (rotation angle)

attitude maps and principal points, measured from photographs, and relayed to MSL by the readout stations. The coordinates of the intersection of the spin axis with the celestial sphere (defined by declination and right ascension of the spin axis) were plotted and subjectively extrapolated for purposes of programming the picture taking on succeeding orbits. The method of computing these coordinate angles is quite sensitive to errors in both principal point and subsatellite point. For that reason the spin axis orientation shown in Figure A3 may be in error by several degrees of great circle arc. This would be especially true for the calculations of the earlier orbits because they were based on only one or two photographs. The computed results were therefore not sufficiently accurate to give a precise location of cloud features on individual frames, although they were close enough to the true values for programming purposes, and as a first approximation of the true orientation.

Theoretical investigations[1] indicate that the main cause of the changing orientation was the interaction of a magnetic dipole oriented along the satellite spin axis with the earth's magnetic field. The orientation was also changed by the effects of varying gravitational attraction on different parts of the satellite. Other effects, not considered, may have further affected the orientation, but to a much smaller extent than either the magnetic or gravitational forces.

CALIBRATION OF THE PHOTOGRAPHS

In an ideal camera system, rays from object space (the ground) all intersect at the front nodal point of the lens system (exterior center of per-

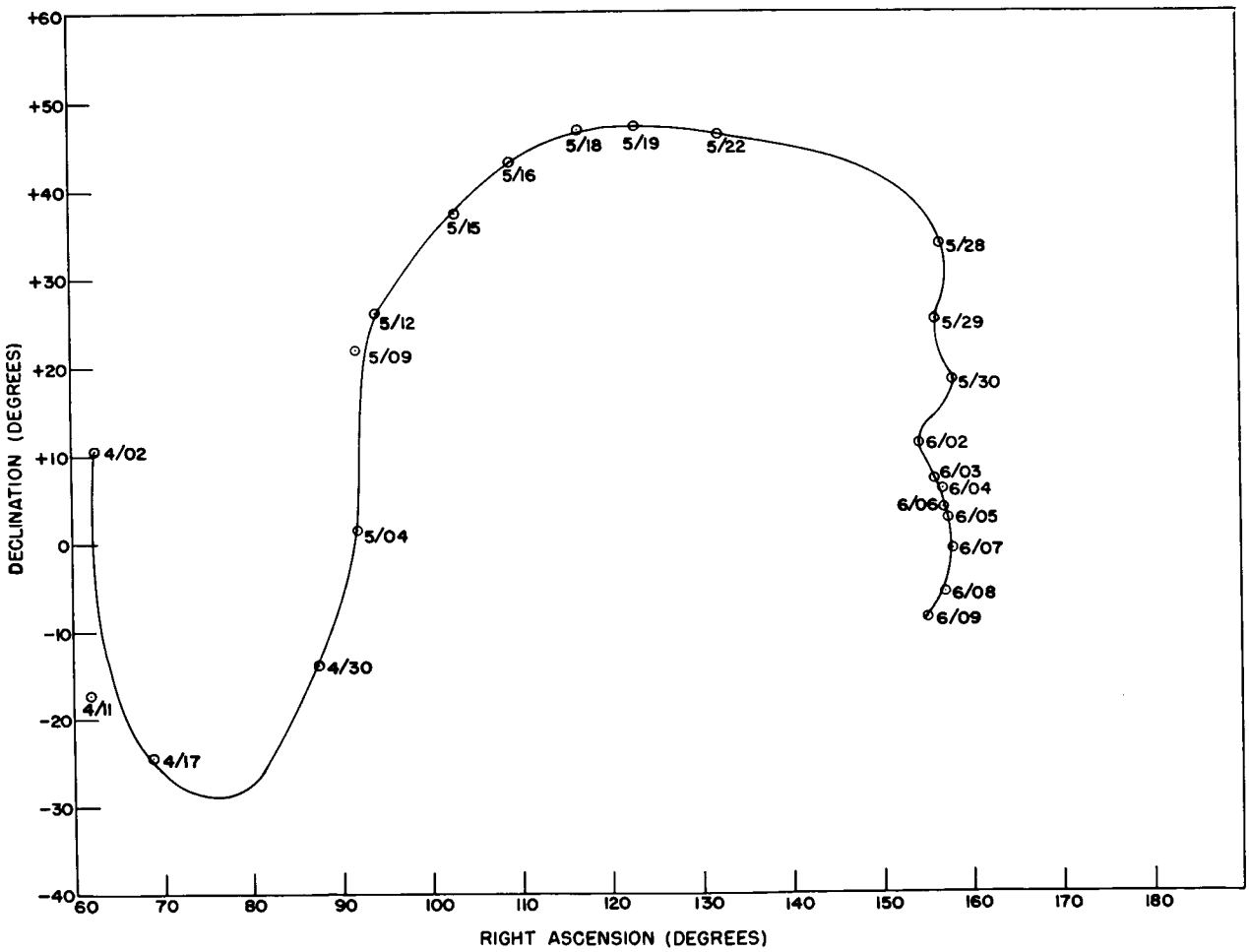

FIGURE A3.—Preliminary graph of optic axis orientation of TIROS I.

spective) and all of the image-forming rays emerge from the rear nodal point (interior center of perspective) with their directions unchanged. Therefore, the angular relationship between rays from the ground to the camera may be deduced from the image positions in the photograph, provided the principal distance, and location of the principal point are known. The principal distance is in effect the z coordinate of the photographic image plane when the origin is at the interior perspective center and the z axis is along the optical axis (Figures A1 and A2). The principal point is the intersection of the optical axis with the image plane and serves as an origin for x and y coordinates of the photographs. In practice, because of imperfections in the camera system, the angles computed from measured image position are not true. Corrections for image distortion are required which will give revised image coordinates such that, when used with the principal distance determined from calibration, the angles computed will be precisely equal to the corresponding angles between rays from the ground to the camera. In the television camera on TIROS I, the wide-angle lens has a calibrated focal length of 5.33 millimeters. With this lens, points are displaced inward toward the principal point by an amount which increases rapidly with the distance of the image from the principal point.

An IBM 704 program written to correct for this lens distortion was incorporated in the photogrammetric computations. In this program, the image area is represented by an arbitrary 520-by-520 square matrix. The center of the matrix represents the principal point which is not indicated directly on the TIROS I photographs but which can be found by its relationship to the center and corner registration marks. This relationship between the principal point and the registration marks was determined from prelaunch calibration photographs [Figure A4 (a and b)] provided by the Radio Corporation of American, which show images of targets of known dimensions televised through the TIROS I system, displayed on a ground station monitor, and copied on 35-mm film. In these photographs the principal point is at the center of the targets.

The correlation between the coordinates of an image on a 35-mm photograph and position in the arbitrary matrix can be obtained by considering the principal distance of the 35-mm photographs and the number of matrix units corresponding to a known object angle.

The semidiagonal of the matrix (368 units) corresponds to an "object" angle of 52 degrees between the optical axis and incident ray. Correction for the lens distortion increases the semidiagonal to 563 units, which would be subtended by an angle of 52 degrees at a principal distance of 440 units.

The principal distance of 35-mm TIROS I photographs can be computed by multiplying the calibrated focal length of the camera lens by the enlargement ratio of the photograph relative to the original image formed in the satellite camera. The ratio of enlargement is the ratio of the distance between registration marks in the photograph to the corresponding distance on the vidicon. The principal distance of the calibration photograph of the polar target was determined in this manner and equated to 440 units to establish the relationship between the units used in measuring image coordinates and the arbitrary matrix.

The IBM 704 program corrects for lens distortion, but neglects electronic distortion.

An alternate determination of the principal distance was made from the calibration photographs in the following manner: The radial distance of every intersection from the principal point was computed. The radial distances corresponding to the same object angles were averaged. The object angles between the optical axis (target center) and the rays from other points on the targets were known from the dimensions of the target and its distance from the lens. The mean radial distance divided by the tangent of the object angle was plotted against the square of the object angle (Figure A5). A straight line was fitted to these points and the y-axis intercept of the line was taken as the principal distance.

It can be shown that the fitted straight line of Figure A5 can be used to derive an image distortion curve which represents the radially symmetric component of image distortion. Because these data have been obtained by employing the entire optical-electronic system, the distortion curve includes both lens and electronic distortions. Comparisons between known object angles and object angles computed from image distances and

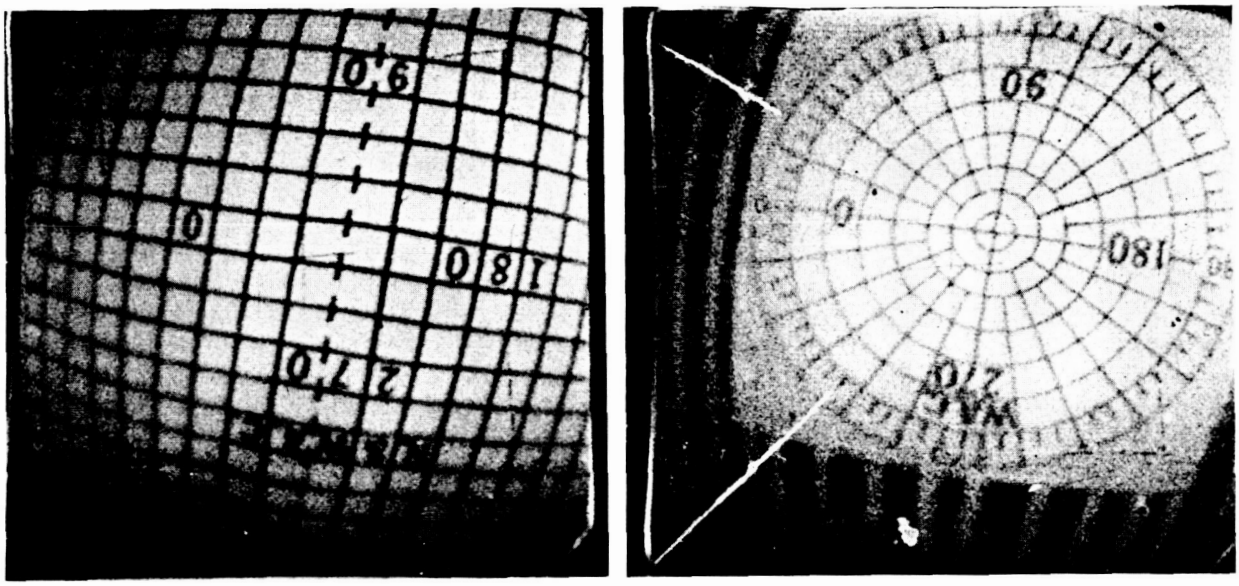

(a) (b)

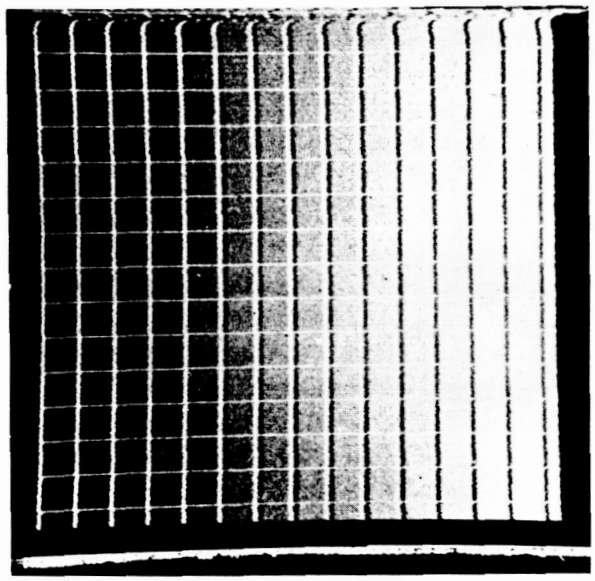

(c)

(a) Rectilinear target taken with wide-angle camera.
(b) Polar target taken with wide-angle camera. (The principal point of the photograph is at the center of the target.)
(c) Ground monitor display calibration pattern.

FIGURE A4.—TIROS I calibration photographs.

this derived distortion curve, indicate that residual errors are reduced to about 10 minutes of arc for *mean* radial image distances. Use of this correction procedure should be superior to that of the program used because it would correct for electronic distortions in the system as well as for the distortion of the lens in the satellite camera. However, this correction procedure has not been applied, because there has not been sufficient time to program this procedure and because it would not correct for the lack of symmetry in the distortion.

Asymmetrical distortion is reflected in the variation of measured radial image distances for the same object angle. Maximum *errors* in computed object angle from these distortions as on the order of 1½ degrees. This asymmetric distortion results in part from the aspect ratio in which vertical image dimensions are compressed relative to horizontal dimensions, and partly from the fact that the optical axis is not displayed at the center of either the ground monitor raster or the satellite vidicon about which the electronic distortion is centered.

A linear correction is made for the vertical compression of the raster, but the portion of the asymmetrical distortions caused by the displacement of the principal point from the raster center is not corrected. In order to correct for this it would be necessary to greatly expand the IBM 704 program now in use. Such a correction will be employed for TIROS II photographs.

The procedure now used to correct for image distortion consists in determining the aspect ratio from the coordinate readings on the center cross and corner registration marks, increasing the y coordinate to compensate for lack of squareness in the raster, and scaling the images to correspond to the size of the calibration photographs. The coordinates of ground landmark images are then referenced to the principal point and the symmetrical correction for lens distortion is applied.

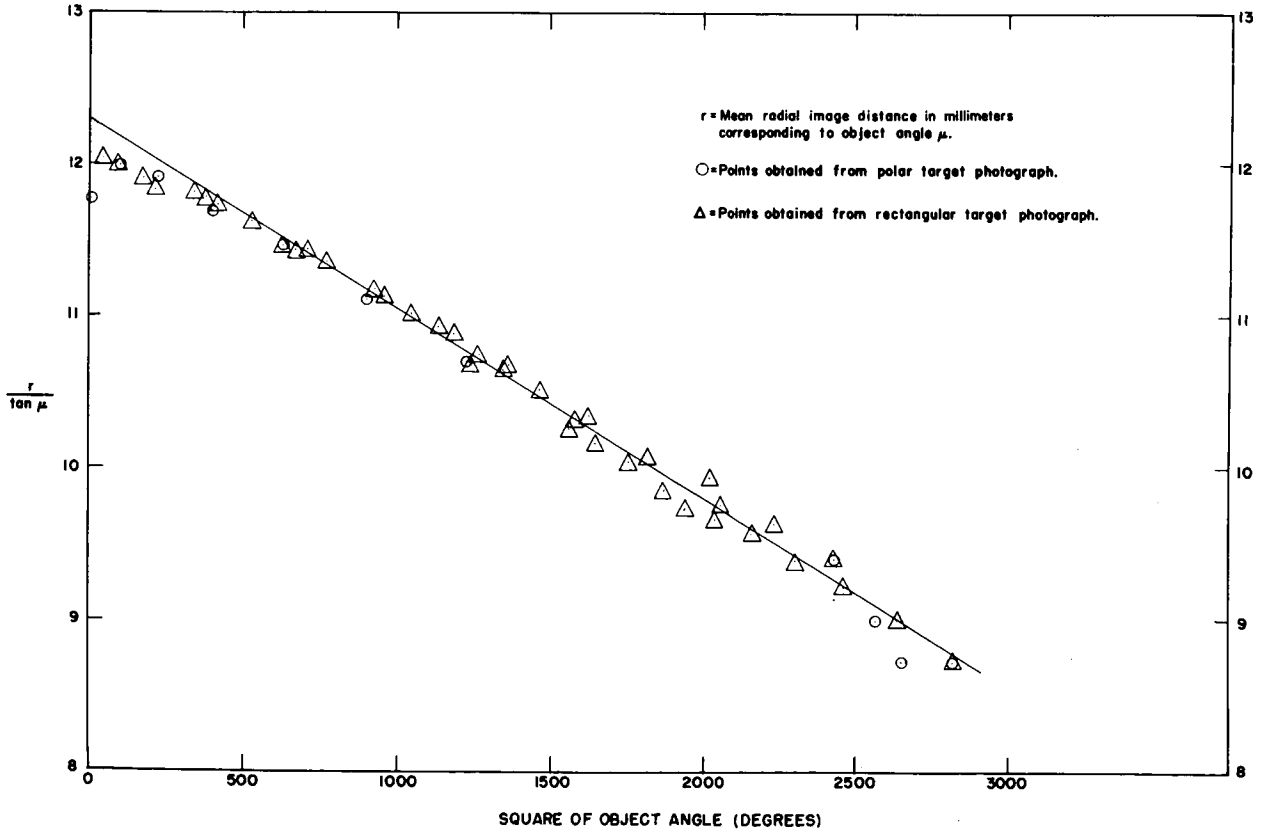

FIGURE A5—Graph of object angle squared plotted against the ratio r/tan μ, where r=mean radial distance (calibration photos), and μ=object angle; used to determine principal distance.

There is a further source of error in this procedure in that variations in the monitor distortion pattern are neglected. Information for making such a correction is provided by monitor calibration photographs of a rectangular pattern taken at every readout (Figure A4c) and when a more elaborate distortion program is written, it should make use of this information. Such a procedure would entail coordinate measurements on a calibration photograph for each orbit used. In any event any variations in image distortion resulting from changes in the physical environment of the television camera in the satellite cannot be corrected.

DETERMINATION OF SPIN AXIS ATTITUDE

Because of the uncertainty of the time of the remote photographs, and therefore of the camera position, the horizon-and-one-landmark procedure is not directly applicable for obtaining values of the spin axis attitude and is being held in abeyance. Fortunately, the image quality of the television picture is sufficiently good that numerous ground points can be identified on individual frames. Several methods are available for resecting camera position from three or more ground points;[2,3] however, these methods depend for their ultimate accuracy on the lack of distortion in the image positions (or the ability to make precise corrections for distortions) for it is a basic premise of photogrammetry that the photograph provides an accurate record of angles formed at the camera station by rays from points in object space. Uncorrected distortions in image positions result in errors in reconstructed angles in object space, and therefore in resected camera positions.

Because of the inability to make a precise correction for the distortion of image positions, a modification of Church's procedure[2] has been devised (Figures A6, A7). With N ground points, $N(N-1)/2$ angles are formed at the lens between rays from different pairs of points. All identifiable ground points up to a maximum of six are used in this method in the attempt to minimize the effect of residual image distortion.

In this modified Church's procedure, the cosines of angles formed at the lens between ground-point rays are computed for a sequence of camera positions corresponding to 1-minute intervals starting 5 minutes before the programmed picture-taking time and continuing to 5 minutes after programmed picture-taking time. Each of these cosines representing an "object space" angle is subtracted from the corresponding "image space" cosine and the differences for each camera position are squared and summed. The position in the orbit closest to the actual position of the camera at time of exposure is that for which the sum of the squares of the cosine differences is a minimum. The search for the actual camera position is then continued by the same procedure for camera positions at the 5-second intervals between the 2 minutes which most nearly agreed with the position of the camera at the exposure time. Once the time of exposure and position are known, the attitude of the optical axis is determined by computing the swing, tilt, and azimuth of principal plane and expressing the orientation as right ascension and declination. All ground points that were used to find camera position (maximum of six) are also used to compute spin axis orientation.

The determination of the attitude of the optical axis from three ground points and the camera position involves the solution of three simultaneous linear equations in three unknowns. An additional equation in the same three unknowns is added for each additional control point. From these equations, three normal equations were formed by the method of least squares.

The method of obtaining image measurements from the 35-mm film is as follows: Control points are initially selected by comparing a 5-times enlargement from the original 35-mm negative with a 1:5,000,000 scale map. Points selected are identified on the print and on the map, and then cataloged together with latitude and longitude from a 1:000,000 World Aeronautical Chart. The image coordinates of the ground points and fiducial marks are then measured on a DILOG film reading system at a magnification of 20×.

The DILOG system's major component's are: the reader, called the Telereadex; the digital recorder, called the Telecordex; and a Friden Flexowriter for typewritten visual record of the data. The Telereadex projects the film and enlarges the image up to 45 diameters on a table viewing surface. The viewing table is the plane of a measuring coordinate system with two movable orthogonal cross wires parallel to the x

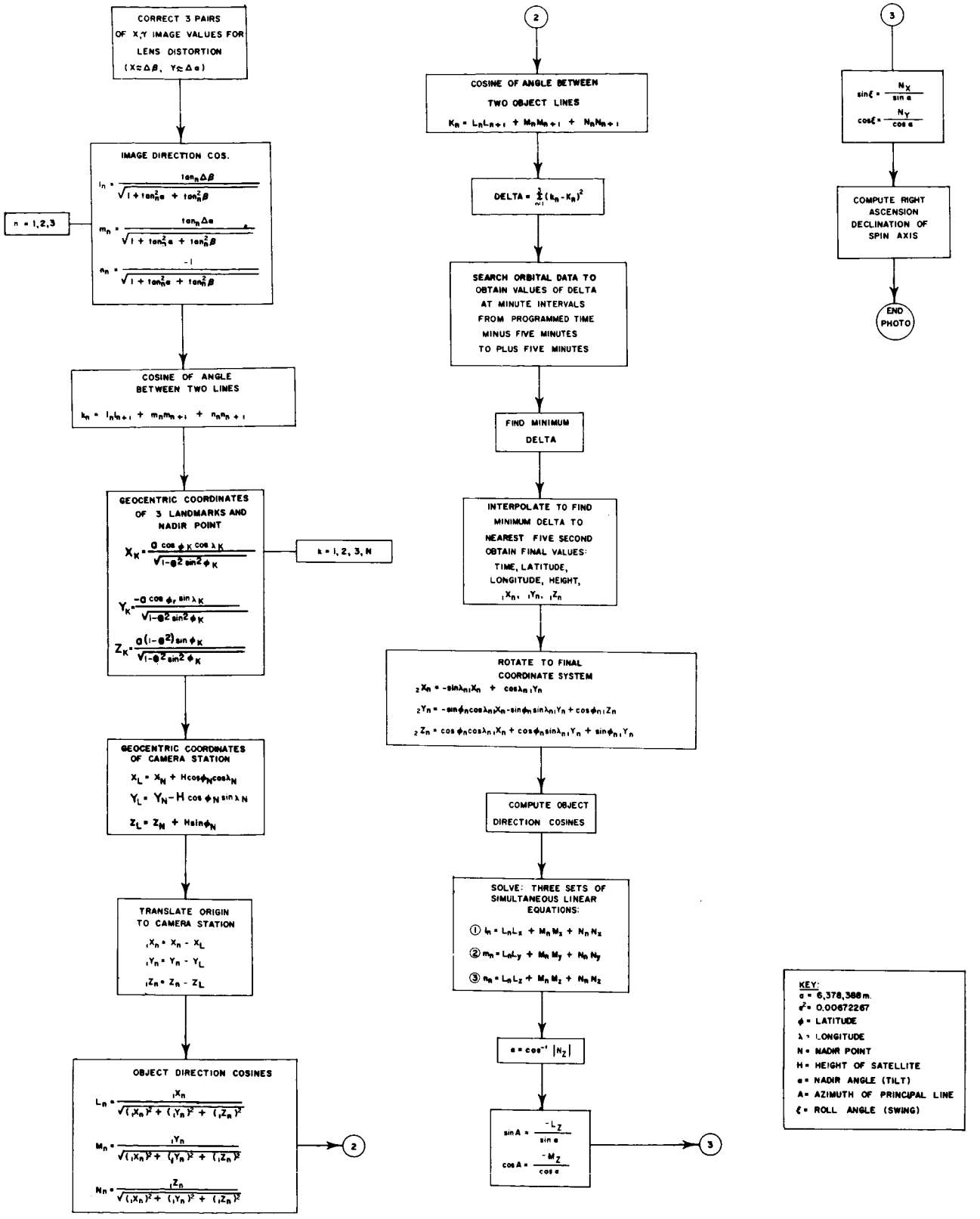

FIGURE A6.—Block diagram illustrating procedure used to obtain camera fixes.

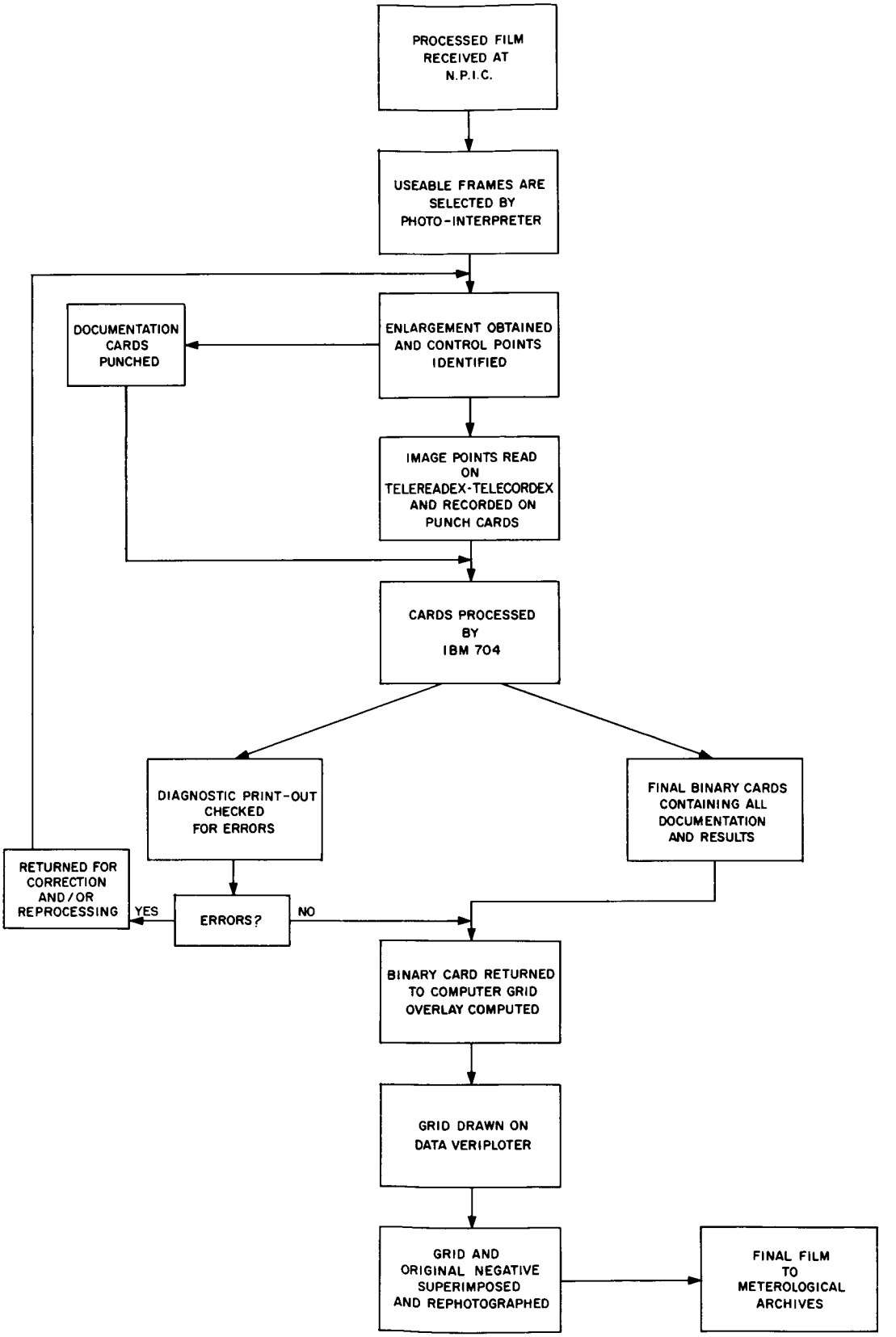

FIGURE A7.—Flow diagram of computational procedure used to determine spin axis attitude.

and y axes. When these are adjusted to intersect on a point, the coordinates can be automatically recorded and fed into a digitizer (Telecordex) which is connected electrically to the film reader. One unit measured by the Telereadex on the enlarged (20 ×) projected image represents approximately 3.7 microns on the original 35-mm film positive. A well-defined point can be repeated within ±1 unit. The image coordinates registered by the Telecordex are punched out automatically on standard IBM cards. These cards, with necessary documentation, are then used directly with the IBM 704 program. The final result of this phase is both a printout of diagnostic information (Figure A8) and a binary card for each picture containing all original documentation and the final attitude and position.*

The results of the spin axis attitude determination by the above procedure are shown in Figure A9, where right ascension and declination of the attitude vector are plotted against time. The partial nature of the result is evidenced by the gap of information between orbits 172 and 538 and by the fact that orbits later than orbit 700 are not represented. The photogrammetry was started on orbits selected from the first 700 before photographs from later orbits were available. The orbits selected were not used in chronological sequence, but were separated into common geographical areas to facilitate the selection of ground points. Work is in process on 35 additional orbits which will fill in the gap and extend the range of the curve.

Two or more frames from each selected orbit were processed to provide a check on the consistency of attitude values obtained. In some orbits all of the values agreed within 1 or 2 degrees and were accepted without further check. In other orbits larger discrepancies occurred and these photographs were reviewed in detail. Sometimes this review indicated mistakes in recording ground point coordinates, or in reading camera positions from the world attitude map, etc. The attitude values for these orbits were recomputed with corrected data, and only the corrected results were plotted on the graph. In other cases no mistakes could be found and the discrepancies were attributed to marginal image quality, to a distribution of ground points on the photograph which was unfavorable for the angles provided for resection, or to uncorrected image distortion. These orbits are responsible for much of the scatter on Figure A9.

It was noted that the most consistent results were obtained where the times at exposure for successive frames were found to be 30 seconds apart. Where the times determined for successive frames were apparently 25 or 35 seconds apart, the computed values of right ascension and declination differed by several degrees. This fact would encourage the use of a 30-second interval between frames to obtain camera positions for other pictures on those orbits on which some positions have been determined.

DIFFICULTY OF MASS GRIDDING

The binary card for each picture produced by the procedure described in the previous section contains all input information required to compute a geographical grid for that particular frame. The binary cards are returned to the IBM 704, and under the direction of a new stored program a grid overlay of latitude and longitude is computed. This grid overlay contains corrections for the symmetrical lens distortions but not for asymmetrical electronic distortions. A new IBM program will be written to contain corrections for some electronic distortion as well as for the lens distortion.

In this pilot work each overlay is hand-drawn and matched to the photograph. Eventually, it is planned to use a newly acquired data plotter to draw the grid lines on the overlays automatically. Finally, a vertical optical printer will be used to obtain 35-mm film strips containing the original picture and the superimposed grids.

Grids of latitude and longitude superimposed on satellite pictures would make satellite weather photographs immediately useful to the meteorological community as a source of data. Although it was not known how many pictures would be obtained by TIROS I, plans were made to grid a large number . . . perhaps of the order of 5000. For this purpose procedures were devised and euipment obtained to mass-produce 35-mm film strip with superimposed grids.

*The computations were performed on a desk calculator to provide a test case for the IBM 704 computer. The hand calculations required about 10 man-days; the machine operation requires about 6 seconds for computation and approximately 30 seconds for printout.

ORBIT NUMBER 000144 PICTURE NUMBER 000008 MONTH000004DAY 000011HOUR 000008MIN. 000036DMIN. 000000DSEC. 000010

SSP LAT.	SSP LON.	HGHT.	ROLL	AZIM.	NADIR	R.A.	DECLIN.	DELTA	NO. CONT.	SUM IMAGE/NO. ANGS.
522045	5244217-	56696	5238153	5329964	5263062	5266077	5214763-	462598	51400	5089799

LX	MX	NX	LY	MY	NY	LZ	MZ	NZ	SUM2X	SUM2Y	SUM2Z
501292	508170	505666	506360-	503466-	507213	507762	504417-	504530	5110052	5110448	5110028

IMAGE ANGLE COSINES

50000 50000 50000 50000 50000 50000 50000 50000 50000 50971 50986 50738 50992 50877 50824

LAT.	LONG.	HGHT.	DELTA	OBJECT ANGLE COSINES													
52207	52440-	56696	47484	50000	50000	50000	50000	50000	50000	50000	50000	50000	50970	50986	50721	50991	50868	50813
52205	52442-	56696	46260	50000	50000	50000	50000	50000	50000	50000	50000	50000	50972	50987	50736	50991	50875	50820
52202	52444-	56696	47171	50000	50000	50000	50000	50000	50000	50000	50000	50000	50974	50988	50749	50992	50881	50828
52200	52446-	56696	47863	50000	50000	50000	50000	50000	50000	50000	50000	50000	50975	50989	50763	50992	50887	50836
52198	52448-	56696	48204	50000	50000	50000	50000	50000	50000	50000	50000	50000	50977	50990	50775	50992	50892	50843
52196	52451-	56696	48365	50000	50000	50000	50000	50000	50000	50000	50000	50000	50978	50991	50787	50993	50898	50850
52193	52453-	56696	48562	50000	50000	50000	50000	50000	50000	50000	50000	50000	50980	50992	50799	50993	50903	50857
52191	52455-	56696	48790	50000	50000	50000	50000	50000	50000	50000	50000	50000	50981	50993	50810	50993	50909	50864
52189	52457-	56696	49104	50000	50000	50000	50000	50000	50000	50000	50000	50000	50982	50994	50820	50993	50914	50870
52187	52459-	56696	49131	50000	50000	50000	50000	50000	50000	50000	50000	50000	50983	50994	50830	50994	50918	50877
52184	52461-	56696	49160	50000	50000	50000	50000	50000	50000	50000	50000	50000	50984	50995	50839	50994	50923	50883
52331	52297-	56700	49815	50000	50000	50000	50000	50000	50000	50000	50000	50000	50980	50983	50949	50993	50993	50978
52308	52328-	56699	49465	50000	50000	50000	50000	50000	50000	50000	50000	50000	50940	50940	50856	50988	50981	50961
52284	52358-	56698	49540	50000	50000	50000	50000	50000	50000	50000	50000	50000	50859	50853	50629	50982	50939	50913
52260	52386-	56697	50109	50000	50000	50000	50000	50000	50000	50000	50000	50000	50856	50865	50456	50979	50851	50807
52234	52413-	56697	49607	50000	50000	50000	50000	50000	50000	50000	50000	50000	50927	50949	50525	50985	50805	50740
52209	52438-	56696	48159	50000	50000	50000	50000	50000	50000	50000	50000	50000	50968	50984	50706	50991	50862	50805
52182	52463-	56696	49190	50000	50000	50000	50000	50000	50000	50000	50000	50000	50985	50995	50848	50994	50927	50888
52156	52487-	56696	49524	50000	50000	50000	50000	50000	50000	50000	50000	50000	50992	50998	50917	50996	50961	50936
52129	52510-	56696	49754	50000	50000	50000	50000	50000	50000	50000	50000	50000	50995	50999	50952	50997	50978	50961
52102	52533-	56696	49889	50000	50000	50000	50000	50000	50000	50000	50000	50000	50996	51100	50969	50998	50986	50974
51740	52555-	56696	49970	50000	50000	50000	50000	50000	50000	50000	50000	50000	50997	51100	50979	50998	50991	50982

FIGURE A8.—Diagnostic print-out from attitude computations.

First row contains documentation and estimate of picture time for camera program. "DMIN." and "DSEC." indicate a time correction based on best fit of image and object angles.

Second and third rows show final values of position and attitude.

Fourth and fifth rows give direction cosines of optical axis relative to local geographic coordinates.

Rows 9–19 show the object angle cosines computed for 5-second intervals.

Rows 20–30 show the object angle cosines computed at minute intervals from 5 minutes before to 5 minutes after programmed time.

Delta is a measure of fit. All numbers are represented by a characteristic to the base 50 (e.g., 52957 equals 95.7, 46630— equals —0.0000630).

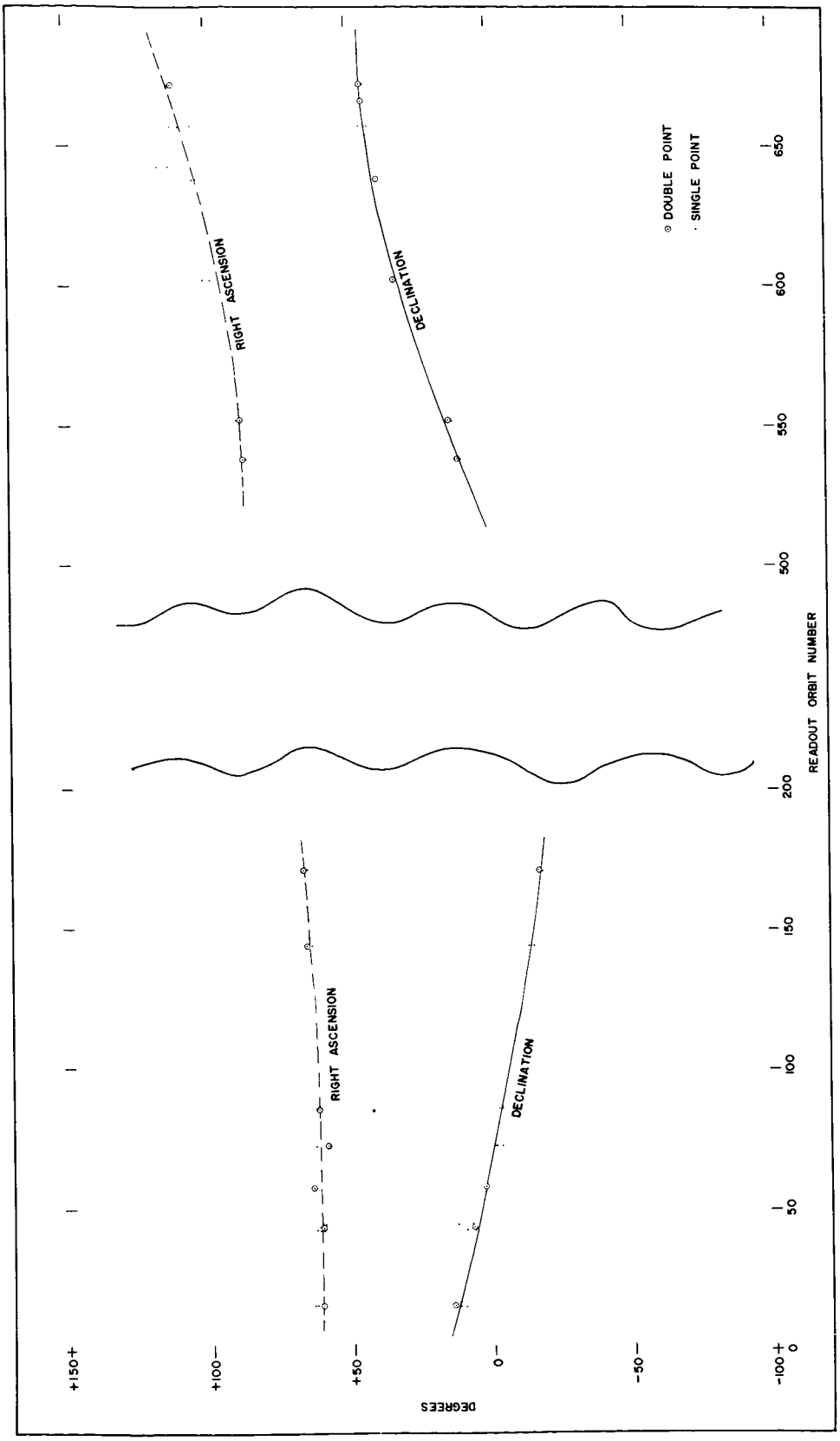

FIGURE A9.—Graphs of spin axis attitude vector right ascension and declination against time.

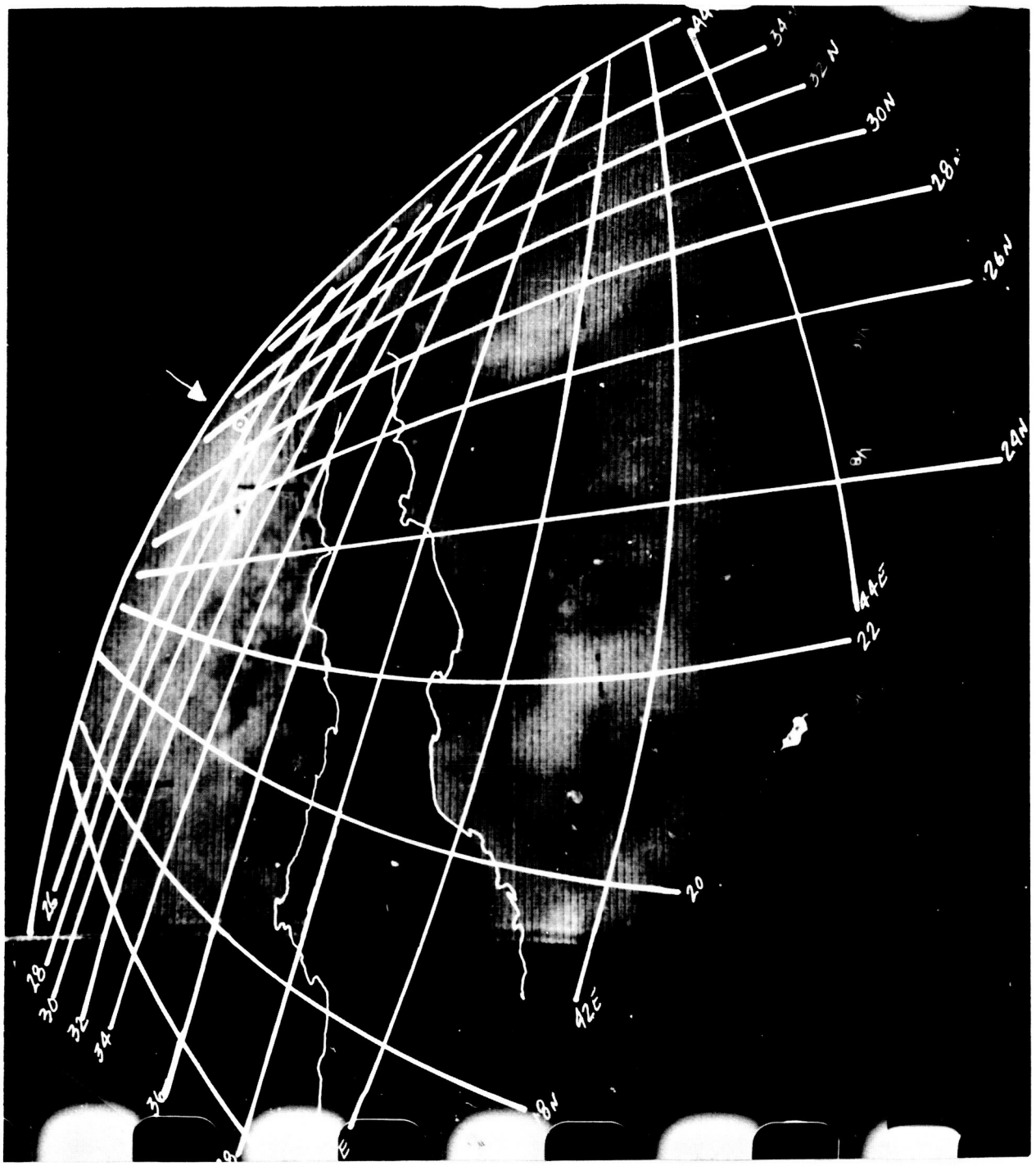

FIGURE A10.—TIROS I picture with superimposed geographic grid. The grid lines were hand drawn from values of latitude and longitude computed for evenly spaced points in the image format.

The combined lack of satisfactory attitude information and the uncertainty of the time at exposure has greatly increased the effort required for location of cloud features in the photographs on any systematic basis. Photogrammetric procedures can be used to determine the camera position and attitude of selected frames that contain suitable landmarks, and it is possible to grid all pictures which contain adequate fiducial marks, at least three recognizable landmarks or one recognizable landmark, and a well-imaged horizon and the exact time of exposure. However, pictures which contain adequate fiducial marks represent a very small fraction of the total number of pictures presently available. Therefore, although the presentation of curves of attitude versus time (Figures A3 and A9) leads to a better understanding of the history of the satellite spin axis orientation and thus the optical axis orientations, this represents only a partical solution to the final problem of mass-production gridding.

In order to locate cloud features on other photographs it will be necessary to accomplish two things. First, it will be necessary to determine the attitude of the camera axis (spin axis) as a continuous function of time, taking into consideration both the physical forces acting on the satellite and attitude fixes obtained from frames containing landmarks. Once this has been accomplished, a revised attitude map can be published. Second, it will be necessary to determine the time at exposure of photographs which contain features of meteorological interest but do not contain landmarks. When these photographs occur in orbits for which time fixes have been obtained on other frames containing landmarks, it may be possible to make use of the 30-second interval between successive frames. However, when these photographs occur in orbits for which no frames contain sufficient landmarks to determine the camera position, it will be necessary to determine the nadir angle from the apparent horizon and to find the time of the exposure by interpolation with respect to the value of nadir angle published in the final world attitude map.

This method of time determination depends critically upon an accurate history of the spin axis orientation. Figures A3 and A9 indicate that the declination and right ascension are not stable, even over very short intervals, and it is not readily apparent whether these fluctuations are inherent in the satellite or in the accuracy of the photogrammetric procedures, or both.

Whatever the cause, grids produced on the bases of camera attitude represented by Figure A9 and of picture-taking times based on the nadir angle analysis may not be satisfactory for superimposition on cloud pictures on a mass-production basis. For that reason satisfactory mass-gridding may not be feasible for TIROS I data. In any event, it has already been demonstrated by the grids used in this report and by Figure A10 that satisfactory gridding can be done when the pictures are handled on an individual basis. Figure A10 is a sample of a calculated grid which has been hand-drawn from a digital printout of the IBM computer. At this writing a delay in check-out of the line drawer (which will produce grids directly from the digital output produced by the IBM 704) has prevented any large-scale on this problem, but mass production gridding will be attempted at an early date to test the feasibility of eliminating individual grid-picture fitting.

GLOSSARY OF TERMS

APPARENT HORIZON: The apparent or visible junction of earth and sky as seen from any specific position.

AZIMUTH: The direction of a line as given by the angle between the meridian and the line, measured in a clockwise direction.

DECLINATION OF A POINT IN SPACE: The angular distance of a line from the center of the earth to that point, above or below the plane of the earth's equator. It is comparable to the latitude of a station on the earth.

FOCAL LENGTH, EQUIVALENT: The distance measured along the lens axis from the rear nodal point to the plane of the best average definition over the entire field used in the aerial camera.

FOCAL LENGTH, CALIBRATED: An adjusted value of the equivalent focal length so computed as to distribute the effect of lens distortion over the entire field used in the aerial camera. Also, the distance along the lens axis from the interior perspective center to the image plane, the interior center of perspective being selected so as to distribute the effect of lens distortion over the entire field.

NADIR POINT: The point at which a vertical line through the perspective center of the camera lens pierces the plane of the photograph.

GROUND NADIR: The point on the ground vertically beneath the prespective center of the camera lens. On a spherical earth the ground nadir of a photograph is equivalent to the sub-satellite point at the instant of exposure.

NODAL POINT: One of the two points on the optical axis of a lens (or a system of lenses) which has the property that when all object distances are measured from one point and all imagine distances from the other, they satisfy the simple lens relations (conjugate foci formula). Also, one of the two points on the optical axis of a lens which has the property that a ray emergent from the second point (of a perfect lens) is parallel to the rays incident at the first.

OPTICAL AXIS OF A LENS ELEMENT: A straight line which passes through the centers of curvature of the lens surfaces.

PERSPECTIVE CENTER: The point of origin or termination of bundles of perspective rays. The two such points usually associated with a survey photograph are the *interior perspective center* and the *exterior perspective center*. In a perfect lens-camera system, perspective rays from the interior perspective center to the photographic images enclose the same angles as do the corresponding rays from the exterior perspective center to the objects photographed.

PRINCIPAL DISTANCE: The perpendicular distance from the internal perspective center to the plane of a particular finished negative or print. This distance is equal to the calibrated focal length corrected for both the ratio of reduction and the shrinkage or expansion of film or paper. This maintains the same perspective angles at the internal perspective center to points on the finished negative or print as existed in the taking camera at the moment of exposure. This is a geometric property of each finished negative or print.

PRINCIPAL LINE: The trace of the principal plane upon the photograph, the line connecting the principal point and the nadir point.

PRINCIPAL PLANE: The vertical plane through the internal perspective center containing the photograph perpendicular of a tilted photograph.

PHOTOGRAPH PERPENDICULAR: The perpendicular from the interior perspective

center to the plane of the photograph. (See also Principal Distance.)

PRINCIPAL POINT: The foot of the perpendicular from the interior perspective center to the plane of the photograph, i.e., the foot of the photograph perpendicular.

RESECTION: The graphical or analytical determination of a position as the intersection of at least three lines of known direction to corresponding points of known position.

RIGHT ASCENSION OF A POINT IN SPACE: The angular distance in the plane of the earth's equator measured eastward from the vernal equinox to the hour circle through the point.

SPACE RESECTION: The analytical determination of the three rectangular coordinates of an exposure station with reference to the ground survey coordinate system.

REFERENCES

1. Bandeen, W. R., and Manger, W. P., "Angular Motion of the Spin Axis of the TIROS I Meteorological Satellite Due to Magnetic and Gravitational Torques," J. Geophys. Res. 65(9): 2992–2995, September 1960.
2. Church, E. F., "Revised Geometry of the Aerial Photograph," Syracuse University, New York, Aerial Photogrammetry Bulletin No. 15, June 1945.
3. Merritt, E. L., "Explicit Three-point Resection in Space," Photogrammetric Eng. 15(4): 649–665, December 1949.

U.S. GOVERNMENT PRINTING OFFICE: 1964 O—646-770